Transactions of the ASME®

Transactions of the ASME, Journal of Fluids Engineering (ISSN 0098-2202) is published quarterly (Mar., June, Sept., Dec.) for $150.00 per year by The American Society of Mechanical Engineers, 345 East 47th Street, New York, NY 10017. Second class postage paid at New York, NY and additional mailing offices. POSTMASTER: Send address changes to Transactions of the ASME, Journal of Fluids Engineering, c/o THE AMERICAN SOCIETY OF MECHANICAL ENGINEERS, 22 Law Drive, Box 2300, Fairfield, NJ 07007-2300.
CHANGES OF ADDRESS must be received at Society headquarters seven weeks before they are to be effective. Please send old label and new address.
PRICES: To members, $40.00, annually; to nonmembers, $150.00. Add $30.00 for postage to countries outside the United States and Canada.
STATEMENT from By-Laws. The Society shall not be responsible for statements or opinions advanced in papers or . . . printed in its publications (B7.1, Par. 3).

INDEXED by Applied Mechanics Reviews and Engineering Information, Inc.
Canadian Goods & Services Tax Registration #126148048

Journal of Fluids Engineering

Published Quarterly by The American Society of Mechanical Engineers

VOLUME 116 • NUMBER 4 • DECEMBER 1994

(Contents continued on p. 720)

Contents (continued)

Review: The Use of Kirchhoff's Method in Computational Aeroacoustics

A. S. Lyrintzis
Associate Professor,
School of Aeronautics and Astronautics,
Purdue University,
West Lafayette, IN 47907-1282;
Formerly, Aerospace
Engineering and Mechanics,
University of Minnesota,
Minneapolis, MN
Mem. ASME

A comprehensive review of the use of Kirchhoff's method in computational aeroacoustics is given. Kirchhoff's integral formulation allows radiating sound to be evaluated based on quantities on an arbitrary control surface S if the wave equation is assumed outside. The control surface S is assumed to include all the nonlinear flow effects and noise sources. Thus only surface integrals are needed for the calculation of the far-field sound. A numerical CFD method can be used for the evaluation of the flow-field solution in the near-field and thus on surface S. Kirchhoff's integral formulation has been extended to an arbitrary, moving, deformable piecewise-continuous surface. The available Kirchhoff formulations are reviewed and various aeroacoustic applications are given. The relative merits of Kirchhoff's method are also discussed.

Introduction

Flow-generated sound has been familiar to man for centuries. However, very little study of the mechanisms governing these sounds was done until after World War II. Since then the increased use of airplanes and helicopters has drawn attention to the noise they generate (e.g., Smith, 1989). The Federal Aviation Agency (FAA) has introduced several noise regulations for aircraft since 1971. (i.e., Federal Aviation Regulations (FAR) part 36). These regulations have been revised repeatedly and have led to a better understanding of the problem. Many airports impose extra noise-control restrictions that restrict entries of noise aircraft. Climb and descent noise-minimizing paths are used in most flights. Noise is now becoming a serious concern early in the design process rather than a problem to be corrected during the production stages, since in order to comply with the rules, aircraft manufacturers must have very good estimates of the detailed noise characteristics of the proposed aircraft. The High Speed Civil Transport (HSCT) and the civil tilt-rotor aircraft, two very advanced aircraft currently under development face major technical difficulties, in obtaining a the reduction of their noise emission. There is clearly a substantial need for intensive aircraft noise research.

For an airplane or a helicopter, aerodynamic noise generated from fluids is usually very important. There are many kinds of aerodynamic noise including turbine jet noise, impulsive noise due to unsteady flow around wings and rotors, broadband noise due to inflow turbulence and boundary layer separated flow, etc. (e.g., Lighthill, 1992). Accurate prediction of noise mechanisms is essential in order to be able to control or modify them to achieve required noise reductions. Both theoretical and experimental studies are being conducted to understand the basic noise mechanisms. Flight-test or wind-tunnel test programs can be used, but in either case difficulties are encountered such as high expense, safety risks, and atmospheric variability, as well as reflection problems for wind tunnel tests. As the available computational power increases numerical techniques are becoming more and more appealing. Although complete noise models have not yet been developed, numerical simulations with a proper model are increasingly being employed for the prediction of aerodynamic noise because they are low cost and efficient. This research has led to the emergence of a new field: Computational Aeroacoustics (CAA). A recent review of the status of CAA is given by Hardin and Hussaini, (1993). However, the use of Kirchhoff's method in CAA has not yet been adequately reviewed, and we felt that a review of the method is needed.

CAA is concerned with the prediction of the aerodynamic sound source and the transmission of the generated sound starting from the time-dependent governing equations. The full, time-dependent, compressible Navier-Stokes equations describe these phenomena. Although recent advances in Computational Fluid Dynamics (CFD) and in computer technology have made first-principles CAA plausible, direct extension of current CFD technology to CAA requires addressing several technical difficulties in the prediction of both the sound generation and its transmission.

Once the sound source is predicted, several approaches can be used to describe its propagation. The obvious strategy is to extend the computational domain for the full, nonlinear Navier-Stokes equations far enough to include the location where the sound is to be calculated. However, if the objective is to calculate the far-field sound, this direct approach requires prohibitive computer storage and leads to unrealistic CPU times. The best solution seems to be the separation of

Contributed by the Fluids Engineering Division for publication in the JOURNAL OF FLUIDS ENGINEERING. Manuscript received by the Fluids Engineering Division January 17, 1993; revised manuscript received September 6, 1994. Associate Technical Editor: D. P. Telionis.

the computation into two domains, one describing the nonlinear generation of sound, and other describing the linear propagation of sound.

There are several alternatives to describing the sound propagation once the source has been identified, the first of which is the acoustic analogy. In this method the governing Navier-Stokes equations (assumed to be valid in the source region) are rearranged to be in wave-type form. The far-field sound pressure is then given in terms of a volume integral over the domain containing the sound source. However, the volume integrals required lead to storage problems.

Another method is to use a CFD near-field solution plus a linearized Euler's equation. This method starts from the numerical calculation of the nonlinear near- and mid-field while the far-field is found from a linearized Euler solution. This method seems to have very good potential, however the solution still has to be found in the far-field numerically. Far-field mesh spacing, diffusion and dispersion errors have to be adequately resolved.

The final alternative is Kirchhoff's method, that is a nonlinear CFD solution plus Kirchhoff's integral for the far-field. A Kirchhoff's integral formulation allows the radiating sound to be evaluated based on quantities on an arbitrary control surface S, when the linear wave equation is assumed valid outside the control surface. Thus only surface integrals are needed and the dimension of the problem is reduced by one (compared to acoustic analogy). The control surface S is assumed to include all the nonlinear flow effects and noise sources. A numerical CFD method can be used for the evaluation of the flow-field solution in the near-field and on control surface S. The method has been extended for an arbitrary moving deformable surface (e.g., Farassat and Myers, 1988). Kirchhoff's method has been used in various acoustic problems, such as propeller noise, high-speed compressibility noise, blade-vortex interactions, etc.

In this paper we discuss briefly the various methods of computational aeroacoustic analysis, then review the evolution of the Kirchhoff formulations for various cases. Some typical Kirchhoff formulations are shown and their past and possible future aeroacoustic applications as well as a discussion of the relative merits of Kirchhoff's method over acoustic analogy are presented. Earlier, versions of this paper were presented by Lyrintzis (1993, 1994).

Methods of Computational Aeroacoustic Analysis

Sound can be considered as the propagating part of the entire flow-field. In a few cases the radiated sound can be found solving the entire flow field. In most cases of practical interest one cannot find a full numerical solution everywhere in the flow because of diffusion and dispersion errors caused by increasing mesh size in the far-field. In addition, the acoustic fluctuations are usually quite small (about three to five orders of magnitude less than the flow fluctuations). Thus, it is often advantageous, or even necessary, to develop ways of determining the far-field noise from near-field solutions. To do so the computation is separated into two domains, one describing the nonlinear generation of sound, the other describing the linear propagation of sound.

The main approaches used to find the far-field noise can be classified as follows:

1) *Full Flow-Field CFD*: This is a calculation of the full nonlinear flow field using CFD including far-field waves. However, since the dissipation and the dispersion properties of traditional CFD numerical schemes tend to damp the acoustic oscillations or sometimes generate artificial disturbances, high-order of accuracy schemes and grid refinement strategies are employed. Some outstanding recent examples of specialized CAA numerical operators are the Dispersion Relation Preserving (DRP) scheme (Tam and Webb, 1993), the compact finite difference schemes, (Lele, 1992), a third order upwind scheme (Sankar et al., 1993), an upwind version of the leapfrog scheme (Thomas and Roe, 1993) and various high order schemes (e.g., Lele, 1989; Goodrich, 1993; and Lockard et al., 1994). Lele's scheme was applied to compressible free-shear layer flows. However, the application of most of the above operators has been demonstrated only for relatively simple model problems. An example of an application of CFD techniques for the calculation of radiating waves from transonic blade-vortex interactions (BVI) is given by Baeder et al. (1986, 1987). The high-speed impulsive (HSI) noise was also investigated by Baeder et al. (1990, 1991, 1933) using the same technique. Various levels of approximation (i.e., small disturbance, Euler and Navier Stokes equations) were used. However, in order to numerically resolve the details of the acoustic three-dimensional far-field, a very fine mesh should be used, which makes these computations impractical, even with today's powerful supercomputers. The impracticality of straight CFD calculations for supersonic jet aeroacoustics was pointed out by Mankbadi et al. (1993). Furthermore, because the acoustic fluctuations are usually quite small, the use of a nonlinear equation (e.g., Euler, Navier Stokes) could result in errors (Stoker and Smith, 1993). Scott and Atassi (1990) and Fang and Atassi (1993) used the rapid distortion theory (Batchelor and Proudman, 1954) to simplify the CFD computations. The Euler equations were linearized about a nonlinear flow and acoustic radiation from airfoils in nonuniform flow was investigated. However, this method might not be very accurate for transonic flows, where nonlinear noise sources (i.e., shocks) are present.

2) *Acoustic Analogy*: This is a nonlinear near-field CFD calculation plus the application of an integral equation (e.g., Lighthill, 1952) for the far-field. In the acoustic analogy, the governing Navier-Stokes equations are rearranged to be in wave-type form. The far-field sound pressure is then given in terms of a volume integral using second derivatives over the domain containing the sound source. It should be noted that the sound sources (in the absence of solid bodies) are quadrupoles due to turbulence and/or shock waves including refraction and diffraction of the sound field. Several modifications to Lighthill's original theory have been proposed to account for the sound-flow interaction or other effects (e.g., Lilley, 1974; Phillips, 1960). In the presence of solid bodies more terms representing monopoles (e.g., expanding sphere) and dipoles (i.e., unsteady force) should be added to Lighthill's formula to construct the Ffowcs-Williams Hawkings equation (Ffowcs-Williams and Hawkings, 1969). All integrals are evaluated in the retarded (emission) time. The monopole and dipole terms are easy to evaluate, because they are surface integrals over the body surface. The nonlinear near- and mid-field can be evaluated using CFD techniques. Experimental data can also be used when available. The far-field is found from a linear Green's function formulation evaluated in terms of surface and volume integrals over the retarded time transformations of the near- and mid-field flow and body surfaces. The major difficulty with the acoustic analogy is the evaluation of the quadrupole term which requires a volume integral evaluation. In many aeroacoustics applications (e.g., jet noise, helicopter noise) the noise source is not compact (a source region of size 1 is compact when $\omega l/c$ is small, where ω is the frequency and c is the speed of sound; a compact source radiates like a concentrated source making calculations easier). Thus the volume integrals required when quadrupole sources are present (i.e., shock waves, turbulence) lead to storage problems. In transonic flow there are substantial difficulties in including the nonlinear quadrupole term (which requires second derivatives) in the volume integrals, especially around moving shock surfaces. Thus, many investigators of helicopter noise (e.g.,

Tadghighi et al., 1992) use near-field data only on the blade surface, a method that cannot be used in the transonic cases, since the effects of shocks are not accounted for. Near-field data can be evaluated either from experiments, or from CFD computations. Farassat and Tadghighi (1990) have tried to simplify the formulation of the shock related noise and apply it in some special cases (e.g., Tadghighi et al., 1991). However, we feel that there are still substantial difficulties preventing the wide use of their formulation. Some examples of the applications of acoustic analogy in helicopter aeroacoustics are given by Farassat and Brentner (1988), and Brentner and Farassat (1992).

3) *CFD plus Linearized Euler's*: This is a nonlinear CFD near-field solution plus linearized Euler's equation. This approach starts from the numerical CFD calculation of the nonlinear near- and mid-field and the far-field is found from a linearized Euler solution. Proper boundary conditions between the nonlinear near-field and the linearized far-field must be used. Although this method has not yet been extensively tested, it seems to have very good potential. However, since the solution still has to be found in the far-field numerically, far-field mesh spacing, diffusion and dispersion errors have to be adequately resolved. Applications of this technique for a model problem is given by Freund et al. (1993), for propeller noise is given by Lim et al. (1993) and for supersonic jet noise by Viswanathan et al. (1994). Hadin and Pope (1992) have proposed a two-part calculation where for the near-field CFD a time-dependent incompressible flow is used and for the acoustic radiation the inviscid perturbations about the incompressible flow are used, an approach that they later applied to evaluate the sound from a two-dimensional cavity (Hardin and Pope, 1993).

4) *Kirchhoff Method*: *CFD Near-Field Plus Kirchhoff Integral Formulation*: This is a calculation of the nonlinear near- and mid-field using CFD techniques with the far-field solutions found from a linear Kirchhoff formulation evaluated on a control surface S surrounding the nonlinear-field. The control surface S is assumed to include all the nonlinear flow effects and noise sources. The full nonlinear equations are solved in the first region (near-field), using CFD techniques, and a surface integral of the solution over the control surface gives enough information for the analytical calculation in the second region (far-field). This method provides an adequate matching between the aerodynamic nonlinear near-field and the acoustic linear far-field. The advantage of the method is that the surface integrals and the first derivatives needed can be easily evaluated from the near-field numerical data; full diffraction and focusing effects are included while eliminating the propagation of the reactive near-field. The method is simple and accurate as it accounts for the nonlinear shock-related noise in the far-field and is the method that we go on to investigate further in this paper.

Kirchhoff's Method

Introduction. Kirchhoff's method is an innovative approach to noise problems which takes advantage of the mathematical similarities between the aeroacoustic and electrodynamic equations. The considerable body of theoretical knowledge regarding electrodynamic field solutions can be utilized to arrive at the solution of difficult noise problems.

Kirchhoff's formula was first published in 1882 although primarily used in the theory of diffraction of light and in other electromagnetic problems, it has also many applications in studies of acoustic wave propagation (e.g., Pierce, 1981). The classical Kirchhoff formulation is limited to a stationary surface. Morgans (1930) derived a Kirchhoff formula for a moving surface (i.e. the interior region of an expanding sphere) using the Green's function approach. However, his analysis was lengthy and complicated. There has been some disagreement about the correctness of Morgans' final result. Ffowcs-Williams and Hawkings (1969) and Hawkings (1989) claim that there is an "error in the final formula, whereas Farassat and Myers (1988, 1989) claim that there is only an "ambiguity in the final result and it is clear from the derivation that Morgans was very much aware of the details that caused it. Munro (1981) also agrees that Morgans' formula is correct.

Khromov (1963) presented another extended Kirchhoff formulation. He converted the wave equation into a Laplace equation by introducing an imaginary part for the time variable. However, this novel approach is counter-intuitive and led to an error early in the derivation as pointed out by Ffowcs-Williams and Hawkings (1969) and shown by Farassat and Myers (1989).

Generalized functions can also be used for the derivation of an extended Kirchhoff formulation. A field function is defined to be identical to the real flow quantity outside a control surface S and zero inside. The discontinuities of the field function across the control surface S are taken as acoustic sources, represented by generalized functions. Ffowcs-Williams and Hawkings (1969) derived an extended Kirchhoff formulation for sound generation from a vibrating surface in arbitrary motion. However, in their formulation the partial derivatives were taken with respect to the observation coordinates and time and that is difficult to use in numerical computations. Farassat and Myers (1988) derived an extended Kirchhoff formulation for a moving, deformable, piecewise smooth surface. The same partial derivatives were taken with respect to the source coordinates and time. Thus their formulation is easier to use in numerical computations and their relatively simple derivation shows the power of generalized function analysis.

Morino and his co-workers have also developed various extended Kirchhoff formulations. Morino (1973, 1974, 1985) derived an extended Kirchhoff's formulation for the special case when control surface S moves in uniform translation with respect to the undisturbed air. He used the Green's function approach. The method is suitable for airplane aerodynamics and became the basis of direct panel methods which are widely used for the evaluation of aerodynamic loads in aircraft design. Subsequently, the more general term "boundary-element method was introduced a term that covers panel and lifting surface methods depending on the representation of the surface of the body. The method was extended to a rotating surface (e.g., helicopter rotor) by Morino et al. (1985) and finally to surface moving in an arbitrary motion Morino et al. (1987, 1988, 1990). Their formulation is based on the velocity potential Φ, but this is not a limitation, since pressure p can be found using Bernoulli's theorem. It should be noted that Morino's formulations were derived with aerodynamic applications in mind. However, they can be used in aeroacoustics, as well (e.g., Lyrintzis and George, 1988; Xue and Lyrintzis, 1993).

In the remaining parts of the paper, we are going to show some typical Kirchhoff formulations and discuss some aeroacoustic applications.

Theoretical Development of Typical Kirchhoff Formulation. In all subsequent formulations we will make the assumption of a rigid (i.e., not deformable) surface S, for simplicity. We will attempt to unify the nomenclature so the formulations will be easier to compare. It should be noted that there is a sign difference in the definition of distance r between Morino and Tseng (1990) and Farassat and Myers (1988) that causes a sign difference in their final formulas. The reader is referred to the original references for the exact formulations, detailed assumptions and derivations.

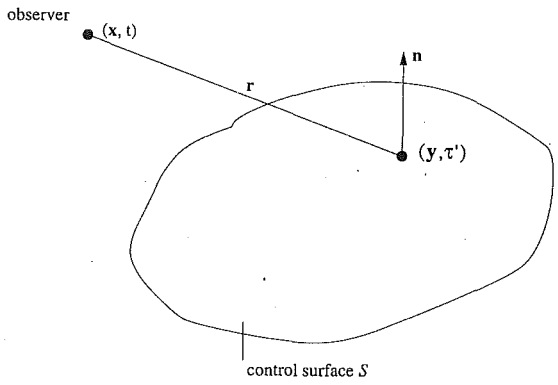

Fig. 1 Kirchhoff's surface S and notation

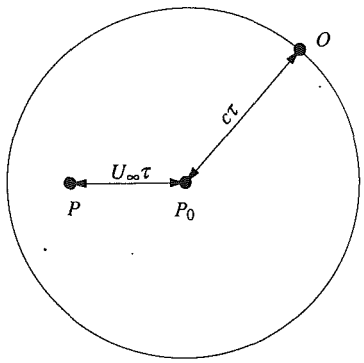

Fig. 2 Effect of retarded time τ for a source (point P) moving with a constant subsonic speed U_∞

1 Stationary Surface

A Kirchhoff's surface S (Fig. 1) is assumed to enclose all the nonlinear effects and sound sources. Outside this surface the acoustic flow field is linear and is governed by the wave equation. Let Φ be a quantity satisfying the wave equation (i.e., pressure, (disturbance) velocity potential) in the exterior of surface S:

$$\frac{1}{c^2}\frac{\partial^2\Phi}{\partial t^2} - \nabla^2\Phi = 0 \tag{1}$$

Φ and its first derivatives (i.e., $\partial\Phi/\partial t$, $\partial\Phi/\partial n$) should be continuous outside surface S. c is the speed of sound at ambient conditions.

In Morino's formulation, a Green's function approach is used to derive a representation for the solution of the convective wave equation in terms of the surface pressure and its derivatives. The Green function is a solution of the equation

$$\nabla^2 G - \frac{1}{c^2}\left(\frac{\partial}{\partial t}\right)^2 G = \delta(x-x', y-y', z-z', t-\tau') \tag{2}$$

where δ is the Dirac delta function. The observer location is $\mathbf{x} = (x, y, z, t)$ and $\mathbf{y} = (x', y', z', \tau')$ is the source. (Superscript $'$ is used to denote the source position.) G must satisfy the casuality condition for hyperbolic equations:

$$G = \frac{\partial G}{\partial t} = 0 \text{ for } t < \tau'. \tag{3}$$

The solution for the above equation for the subsonic case is given by

$$G = -\frac{\delta(\tau' - t + \tau)}{4\pi r}. \tag{4}$$

where τ' is the retarded (emission) time and τ is the time delay (r/c) between emission and detection

$$\tau' = t - \tau = t - \frac{r}{c} \tag{5}$$

The classical Kirchhoff formulation for a stationary control surface S (Fig. 1) can be written as (e.g., Pierce, 1981)

$$4\pi\Phi(\mathbf{x},t) = \int_S \left[\frac{\Phi}{r^2}\frac{\partial r}{\partial n} - \frac{1}{r}\frac{\partial\Phi}{\partial n} + \frac{1}{cr}\frac{\partial r}{\partial n}\frac{\partial\Phi}{\partial\tau}\right]_\tau dS \tag{6}$$

where:
$[\,]_\tau$ denotes evaluation in the retarded (emission) time, e.g., $[\Phi]_\tau = \Phi(\mathbf{y},\ t - r/c\ ]\ (\mathbf{x}, t)$ and $(\mathbf{y}, \tau')$ are the space-time variables of the observer and the source (surface, respectively, r is the distance between observer and source: $r = |\mathbf{x} - \mathbf{y}|$; it should be noted that $\cos\theta = \partial r/\partial n$ where θ is the angle between the normal vector on the surface $\mathbf{n}$ (pointing out) and the radiation direction $\mathbf{r} = \mathbf{x} - \mathbf{y}$.

Equation (6) is an integral representation of Φ at points exterior to S in terms of information prescribed on the control surface S. It can be used for the computation of noise at an arbitrary point, if the solution is known on surface S. The numerical simulations can provide Φ and its normal and time derivative. It should be noted that the first term has an $1/r^2$ dependence with distance r and it is not significant in the far-field. Furthermore, for the observer on or inside the surface, Φ equals zero. In fact, if the observer is on the surface, Eq. (1) is an integral equation for Φ on S. This is the basis of modern boundary-element methods (e.g., Morino, 1973, 1974). This also shows that Φ, $\partial\Phi/\partial\tau$, and $\partial\Phi/\partial n$ are not independent on the surface S.

2 Uniformly Moving Surface

2.1 Time-Domain Formulation

2.1.1 Subsonically Moving Surface. Now the outside flow is governed by the convective wave equation

$$\nabla^2\Phi - \frac{1}{c^2}\left(\frac{\partial}{\partial t} + U_\infty\frac{\partial}{\partial x}\right)^2\Phi = 0 \tag{7}$$

where U_∞ is the uniform velocity of the control surface S. If U_∞ is zero, the above equation reduces to the simple wave equation. If U_∞ is a subsonic speed, the solution for the Green's function becomes:

$$G = -\frac{\delta(\tau' - t + \tau)}{4\pi r_o} \tag{8}$$

where subscript o denotes evaluation at the Prandtl-Glauret transformation:

$$x_o = x, \quad y_o = \beta y, \quad z_o = \beta z. \tag{9}$$

Thus the distance between the observer and the surface point in Prandtl-Glauret coordinates is

$$r_o = \left[(x-x')^2 + \beta^2\left[(y-y')^2 + (z-z')^2\right]\right]^{1/2}, \tag{10}$$

The time delay τ is still uniquely defined for this case. The physical meaning of the time delay τ can be explained using Fig. 2. O is the observation point and P is the source point. P_O is the source point at the time of the emission. The time delay now becomes:

$$\tau = \frac{[r_o - \mathrm{M}_\infty(x - x')]}{c\beta^2} \tag{11}$$

where M_∞ is the free-stream Mach number and:

$$\beta = \left(1 - \mathrm{M}_\infty^2\right)^{1/2} \tag{12}$$

After some algebra, Φ can be expressed in terms of surface integrals (see Morino, 1985, equation 3.15):

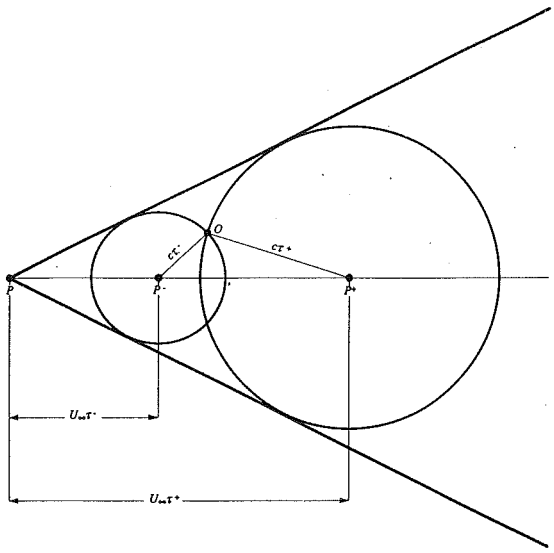

Fig. 3 Effect of retarded time τ for a source (point P) moving with a constant subsonic speed U_∞. Two emission positions P^+ and P^- with corresponding delay times τ^+ and τ^- exist in this case.

$$4\pi\Phi(\mathbf{x},t) = \int_{S_o}\left[\frac{\Phi}{r_o^2}\frac{\partial r_o}{\partial n_o} - \frac{1}{r_o}\frac{\partial \Phi}{\partial n_o} + \frac{1}{cr_o\beta^2}\frac{\partial \Phi}{\partial \tau}\left(\frac{\partial r_o}{\partial n_o} - \mathrm{M}_\infty\frac{\partial x_o}{\partial n_o}\right)\right]_\tau dS_o \quad (13)$$

where subscript o denotes the transformed variable, (e.g. $\mathbf{n}_o$ is the outward pointing vector normal to the surface S_o) and all the values are calculated at the retarded time. It can be easily checked that Eq. (13) reduces to Eq. (6) when U_∞ is zero.

2.1.2 Supersonically Moving Surface. The convecting wave Eq. (7) is still the governing equation and the solution for the Green's function is still given from Eq. (8). However, for a supersonically moving surface the time delay τ is not uniquely defined. As shown in Fig. 3 there are now two emission positions (P^+ and P^-) for source point P. Thus the signal for the observer O is the summation of two discrete cases. The time delay now becomes:

$$\tau^\pm = \frac{[\pm r_o - \mathrm{M}_\infty(x - x')]}{cB^2} \quad (14)$$

where:

$$B = \left(\mathrm{M}_\infty^2 - 1\right)^{1/2} \quad (15)$$

Subscript o denotes evaluation at the Prandtl-Glauret transformation:

$$x_o = x, \quad y_o = By, \quad z_o = Bz. \quad (16)$$

Thus the distance between the observer and the surface point in Prandtl-Glauret coordinates is

$$r_o = \left[(x - x')^2 + B^2\left[(y - y')^2 + (z - z')^2\right]\right]^{1/2}, \quad (17)$$

and Eq. (13) now becomes:

$$4\pi\Phi(\mathbf{x},t) = \int_{S_o}\left[\frac{\phi}{r_o^2}\frac{\partial r_o}{\partial n_o} - \frac{1}{r_o}\frac{\partial \Phi}{\partial n_o} + \frac{1}{cr_oB^2}\frac{\partial \Phi}{\partial \tau}\left(\pm\frac{\partial r_o}{\partial n_o} - \mathrm{M}_\infty\frac{\partial x_o}{\partial n_o}\right)\right]_{\tau^\pm} dS_o \quad (18)$$

where $[\,]_{\tau^\pm}$ implies evaluation at both retarded times τ^+ and τ^-. The $\pm$ signs in the third term are also used for the τ^+ and τ^- retarded times, respectively.

2.2 Frequency-Domain Formulation. An alternative approach to the above is to work in the frequency domain starting from the Helmholtz equation. In this approach, we write the function Φ as

$$\Phi(\mathbf{x},t) = \mathscr{R}\left\{\hat{\Phi}(\mathbf{x})e^{-i\omega t}\right\} \quad (19)$$

where $\mathscr{R}\{\}$ denotes the real part.

Substituting in Eq. (13) and accounting for the retarded time, we obtain

$$4\pi\Phi(\mathbf{x},t) = \mathscr{R}\left\{-e^{-i\omega t}\int_{S_o}\left[\frac{\hat{\Phi}}{r_o^2}\frac{\partial r_o}{\partial n_o} - \frac{1}{r_o}\frac{\partial \hat{\Phi}}{\partial n_o} + \frac{-i\omega}{c_\infty r_o\beta^2}\hat{\Phi}\left(\frac{\partial r_o}{\partial n_o} - \mathrm{M}_\infty\frac{\partial x'}{\partial n_o}\right)\right]\right\} \times\exp\left[i\frac{\omega}{c_\infty\beta^2}\left(r_o - \mathrm{M}_\infty(x - x')\right)\right]dS_o \quad (20)$$

This is the Kirchhoff's formulation in the frequency domain for a uniformly moving surface (the retarded time is the last term of the equation). Davis and Atassi (1991) have developed a two-dimensional Kirchhoff formulation in the frequency domain. Their formulation is interesting because it employs a modified Green's function that does not require the evaluation of the normal derivative (i.e. second term of the equation). The authors claim that the evaluation of the normal derivatives introduces numerical errors. However, the method has not yet been extended to three-dimensional problems. Furthermore, some testing with a point source and a cylindrical Kirchhoff surface for various approximations for the normal derivative showed that the grid resolution used in the CFD evaluation of jets is adequate for determining the normal derivative (Lyrintzis and Mankbadi, 1995). Equation (20) was used by Lyrintzis and Mankbadi (1995) in supersonic jet noise.

3 Arbitrarily Moving Kirchhoff Surface

The formulation for an arbitrary, subsonically-moving, rigid Kirchhoff's surface (e.g., Farassat and Myers, 1988) can be written as:

$$4\pi\Phi(\mathbf{x},t) = \int_S\left[\frac{\partial r/\partial n}{r^2(1 - \mathrm{M}_r)}\Phi - \frac{1}{r(1 - \mathrm{M}_r)}\times\left(\frac{\partial \Phi}{\partial n} + \frac{\mathrm{M}_n}{c}\frac{\partial \Phi}{\partial \tau}\right) + \frac{1}{c(1 - \mathrm{M}_r)}\frac{\partial}{\partial \tau}\times\left\{\frac{\partial r/\partial n - \mathrm{M}_n}{r(1 - \mathrm{M}_r)}\Phi\right\}\right]_\tau dS \quad (21)$$

where $\mathbf{y}$ and $\mathbf{r}$ are now a function of time: $\mathbf{y}(\tau')$, $\mathbf{r}(\tau')$, M_r is the Mach number in the direction of wave propagation from the source to the observer: $\mathrm{M}_r = \mathbf{v}\cdot\mathbf{r}/rc$ ($\mathbf{v}$ is the local source-surface velocity $\mathbf{v} = \partial\mathbf{y}/\partial\tau$), M_n is the local normal Mach number on S: v_n/c. (v_n is the local normal velocity of S with respect to the undisturbed medium). All the quantities are also evaluated for the retarded (emission) time which now is the root τ' of the equation

$$\tau - t + r(\tau)/c = 0 \quad (22)$$

This equation has a single root for the subsonic case. Note that for the steady surface: $\tau' = t - r/c$. For complicated motions, Eq. (22) has to be solved numerically (e.g., Newton-Raphson technique). The normal and the time derivatives of Φ, i.e., $\partial\Phi/\partial\tau$, and $\partial\Phi/\partial n$, are taken with respect to source coordinates and time which makes the formula easy to apply in computations.

It should be noted that the time derivative in the last term

of Eq. (21) can be evaluated analytically, so Eq. (21) can be written as:

$$4\pi\Phi(\mathbf{x},t) = \int_S \left[\frac{E_1}{r(1-\mathrm{M}_r)} + \frac{\Phi E_2}{r^2(1-\mathrm{M}_r)}\right]_\tau dS \quad (23)$$

where

$$E_1 = \left(\mathrm{M}_n^2 - 1\right)\frac{\partial\Phi}{\partial n} + \mathrm{M}_n\mathbf{M}_t\cdot\nabla'\Phi - \frac{\mathrm{M}_n}{c}\dot{\Phi} + \frac{1}{c(1-\mathrm{M}_r)}\left[\left(\dot{n}_r - \dot{\mathrm{M}}_n - \dot{n}_M\right)\Phi + \left(\frac{\partial r}{\partial n} - \mathrm{M}_n\right)\dot{\Phi}\right] + \frac{1}{c(1-\mathrm{M}_r)^2}\times\left[\dot{\mathrm{M}}_r\left(\frac{\partial r}{\partial n} - \mathrm{M}_n\right)\Phi\right] \quad (24)$$

$$E_2 = \frac{1-\mathrm{M}^2}{(1-\mathrm{M}_r)^2}\left(\frac{\partial r}{\partial n} - \mathrm{M}_n\right) \quad (25)$$

Here the dot over $\mathbf{M}$ and $\mathbf{n}$ denotes derivative with respect to source time. In addition:

$$\dot{\mathrm{M}}_r = \dot{\mathbf{M}}\cdot\hat{r}, \quad \dot{n}_r = \dot{\mathbf{n}}\cdot\hat{\mathbf{r}}, \quad \dot{\mathrm{M}}_n = \dot{\mathbf{M}}\cdot\mathbf{n}, \quad \dot{n}_\mathrm{M} = \dot{\mathbf{n}}\cdot\mathbf{M}, \quad \dot{\mathbf{n}} = \omega\times\mathbf{n}$$

where: $\hat{\mathbf{r}} = \mathbf{r}/r$, ∇' is the surface gradient operator, and ω is the angular velocity of surface S (S is assumed rigid).

The simplified expression for E_2 was given by Myers and Hausmann (1990). In the original paper of Farassat and Myers (1988) a more complicated formula for E_2 is given. Simplified expressions for E_1 and E_2 for a rigid surface in uniform rectilinear motion were given by Myers and Hausmann (1992).

The above formulation is valid when the observer is stationary and the surface is moving at an arbitrary subsonic speed. However, for the case of an advancing rotating blade the observer is usually moving with the free flow speed (e.g., helicopter rotor in a wind tunnel with a free stream not equal to zero). The formulation can be adjusted for this case by allowing the observer to move with the free stream instead of being stationary in Eq. (22) of the retarded time. In fact for the case of a uniformly moving surface, we started from Eq. (23) and derived Morino's formula (Eq. 13) for a uniformly moving surface and moving observer at the same speed.

In Farassat's formulation the Kirchhoff surface is assumed to be moving subsonically. Extension to supersonically-moving surfaces can be made, but the analysis becomes lengthy and complicated (Farassat and Myers, 1986) and the complete form of the formulation has not yet been published, but it is now developed (Farassat, 1994).

Morino's formulation for an arbitrary subsonically-moving surface (e.g., Morino and Tseng, 1990) can be written as

$$4\pi\Phi(\mathbf{y}_*,\tau_*) = \int_S \left[-\frac{\partial}{\partial\hat{n}}\left(\frac{1}{r(1-\mathrm{M}_r)}\right)\Phi - \frac{1}{r(1-\mathrm{M}_r)}\frac{\partial\Phi}{\partial\tilde{n}} + \frac{1}{(1-\mathrm{M}_r)}\frac{\partial\Phi}{\partial\tau}\left(\frac{\partial\tau'}{\partial\tilde{\mathbf{n}}} - \frac{v_n}{c^2}\right)\right]_\tau dS \quad (26)$$

where:

$$\frac{\partial}{\partial\tilde{n}} = \frac{\partial}{\partial n} - \frac{v_n}{c^2}\mathbf{v}\cdot\nabla' \quad (27)$$

$$\frac{\partial}{\partial\tilde{n}} = -\mathbf{n}\cdot\nabla - \frac{v_n}{c^2}\frac{d}{d\tau} \quad (28)$$

Superscript $'$ is used to denote the source point and τ' is still the solution of the retarded time Eq. (22)

Note that in Eq. (26) the solution is evaluated for the source (surface) coordinates, that means that the observer is moving with the same velocity as the surface, whereas in Eq. (23) the observer is stationary. The formulation of Eq. (23) could be more useful for the noise in cases of a fixed observer and a moving source. However, the formulation of Eq. (26) could be used for a comparison check of Kirchhoff's formulation with a CFD solution, since in both techniques rotating coordinates are usually used. Equation (26) will also reduce to Eq. (13) for a uniformly moving surface and to Eq. (6) for a stationary surface. It should be noted that Morino's formulation (Eq. 26) can be easily extended to supersonically moving surfaces (Morino and Tseng, 1990) by just summing the values at all the retarded times τ', whereas Farassat's formulation (Eq. (23)) cannot be easily extended. The two formulations are mathematically equivalent (Farassat, 1994). This is easy to see for the case of a uniformly moving surface.

Isom et al. (1987) developed a nonlinear Kirchhoff formulation (Isom's formulation) for some special cases (i.e., stationary surface at the sonic cylinder, high frequency approximation and observer on the rotation plane). They have included in their formulation some nonlinear effects using the transonic small disturbance equation. The nonlinear effects are generally accounted for with a volume integral (e.g., Morino and Tseng, 1990). However, they showed that for the above special cases the nonlinear effects can be reduced to a surface integral.

For the case where the Kirchhoff control surface S coincides with the body surface the effects of interaction between turbulence and solid surface S should be considered. In both the derivations of Ffowcs-Williams and Hawkings (1969) and Farassat and Myers (1988) the turbulence effects were assumed small and neglected at the onset of the derivations. Wu and Akay (1992) included turbulence effects. They showed that source cancellations take place within the surface integral when turbulence effects are present. Using dimensional analysis, the volume integral was shown to be negligible when the source is in rectilinear motion at low Mach numbers. The effects of the turbulent stress field are included and the extended Kirchhoff formulation is modified due to the cancellations mentioned above.

Finally, for the case where the Kirchhoff control surface S coincides with the body surface, there are some nonuniqueness difficulties in the prediction of the radiated acoustic sound in the exterior region whenever the frequency coincides with one of the Dirichlet eigenfrequencies. These problems were analyzed for the stationary Kirchhoff surface by Wu and Pierce (1990) and for moving Kirchhoff surfaces by Wu (1993b).

Applications. Kirchhoff's formula has been extensively used in light diffraction and other electromagnetic problems, aerodynamic problems, i.e., boundary-elements (e.g., Morino and Tseng, 1990), as well as in problems of wave propagation in acoustics (e.g., Pierce, 1981). Here, we will review the aeroacoustic applications of Kirchhoff's formula.

Kirchhoff's integral formulation has been used extensively for the prediction of acoustic radiation in terms of quantities on boundary surfaces (the Kirchhoff control surface coincides with the body). Some examples are the method of weighted residuals (Fenlon, 1969), the simplified Helmholtz integral program (Rogers, 1973), the boundary-integral/boundary-element method, (Seybert et al., 1984, 1985) the method of variational principles, (Wu et al., 1987; Wu, 1989; and Ginsberg et al., 1990) as well as CHIEF (Schenck, 1968 and Seybert and Rengarajan, 1987) and CONDOR (Burton and Miller, 1971, and Meyer et al., 1978) codes.

Kirchhoff's method has also been used for the computation of acoustic scattering from rigid bodies (e.g., Gallman et al., 1991 and Myers and Hausmann, 1992) using a boundary element technique with the Galerkin method. Finally, Wu and Wang (1993) and Wu (1993b) have also used the extended Kirchhoff formulation of Wu and Akay (1992) to

evaluate the sound radiation from vibrating cylinders in motion and transient sound vibration from impulsively accelerated bodies, respectively.

However, we feel the main power of Kirchhoff's formulation is to extend near-field aeroacoustic calculations to the far-field for nonlinear problems (e.g., transonic flow, jets). The nonlinear aerodynamic near-field can be evaluated using CFD techniques. This idea of matching between a nonlinear aerodynamic near-field and a linear acoustic far-field was first proposed by Hawkings (1977), and has been used by some investigators in various problems. The separation of the problem into linear and nonlinear regions allows the use of the most appropriate numerical methodology for each. We have been referring to this technique as the "Kirchhoff method."

The use of Kirchhoff's method is based on Kirchhoff formulations (e.g., Eqs. (6), (13), (23), (26)). The values of the pressure (or velocity potential) and its normal and time derivatives on an arbitrary surface S are enough to give the far-field radiation at any external point. The surface S is assumed to enclose all the nonlinear flow effects and noise sources. Pressure (or velocity potential) and its derivatives are numerically calculated from an aerodynamic near-field code. Since it is assumed that the linear wave equation is valid outside this control surface, S, this surface must be chosen large enough to include the region of nonlinear behavior. However, the accuracy of the numerical solution is limited to the region immediately surrounding the near-field, because of the usual increase of mesh spacing with distance. Thus, since the size of S is limited by the accuracy in the numerical solution for the mid-field, a judicious choice of S is required for the effectiveness of the Kirchhoff method. For example, Patrick et al. (1993) recommended that the deviation of the velocity at S from its average value should not be allowed to be more than five percent. Xue and Lyrintzis (1991) relate the size of the Kirchhoff surface for transonic blade-vortex interactions to the transonic similarity parameter for a given vortex strength. However, the more accurate procedure seems to be testing the wave propagation of the CFD solution for a ray of points in order to find the appropriate linear region and place the Kirchhoff surface there (e.g., George and Lyrintzis, 1988, Lyrintzis and George, 1989). The results should be independent of the placement of the Kirchhoff surface, as long as the surface stays in the linear region. Another idea, not tested yet, is to substitute directly into the right-hand side of the integral Kirchhoff equation and measure the difference between the predicted (i.e., the left-hand side of the equation) and the actual value. If the difference is low we are in the linear region.

By making calculations with different surfaces, it was found by Lyrintzis and George (1989b) that the tip surface or cylinder base contributions of the Kirchhoff surface have only a small effect in most cases. The effect of mesh size, wave thickness, numerical or analytical (when available) derivatives was also studied by Lyrintzis (1988) and Lyrintzis and George (1989b). They used some simple analytical cases to evaluate the effects of the above factors. It should be noted that sometimes a finer CFD mesh is needed to resolve details such as the high frequency content of the solution on the Kirchhoff surface S before the numerical evaluation of the surface integral. Some simple analytical cases to demonstrate the effectiveness of Kirchhoff's formulation were also performed by Myers and Hausmann (1990) and Jaeger and Korkan (1990). Finally, Meadows and Atkins (1994) tested the use of Kirchhoff's method in the evaluation of the noise due to an oscillating sphere. They examined the effect of the order of integration for the surface integrals and the number of points per period and per wavelength in the retarded time.

Now let use review some "real-life aeroacoustic applications of Kirchhoff's method. Hawkings (1977) used a stationary-surface Kirchhoff's formula to predict the noise from high-speed propellers and helicopter rotors. Forsyth and Korkan (1987) calculated high-speed propeller noise using the Kirchhoff formulation of Hawkings (1977). Jaeger and Korkan (1990) used a special case of the Farassat and Myers (1988) formulation for a uniformly moving surface to extend the calculation to advancing propellers. In the above applications, the Kirchhoff surface S was chosen to be a cylinder enclosing the rotor.

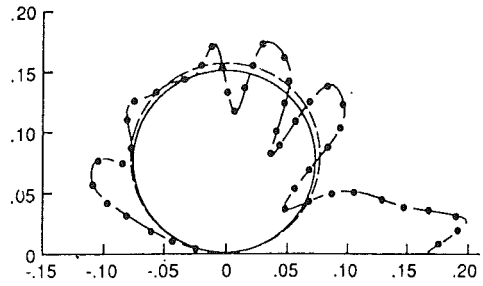

Fig. 4 Comparison between far-field directivity of acoustic pressure values using the Kirchhoff method (– – –) and the direct calculation method (– · –) for a three percent thick Joukowski airfoil in a transverse gust at $k_1 = 1.0$; M = 0.1. The semi analytical results (—) for a flat plate encountering the same gust are also shown (from Davis and Atassi, 1991).

Davis and Atassi (1991), Atassi et al. (1993), and Patrick et al. (1993) have used Kirchhoff's method for the evaluation of acoustic radiation from airfoils in nonuniform subsonic flows. They employed rapid distortion theory to calculate the near-field CFD. A sample comparison for the far-field directivity of the acoustic pressure using the Kirchhoff method and the direct calculation method (i.e., rapid distortion theory, Scott and Atassi, 1990) is given in Fig. 4 (from Davis and Atassi, 1991) for a three percent thick Joukowski airfoil in a transverse gust at $k_1 (= \omega c/2V_\infty) = 1$ and M = 0.1. The semi-analytical results for a flat plate encountering the same gust are also shown in Fig. 4 and are very close to the results from Kirchhoff's method. The figure indicates that the direct calculation method is not accurate in the far-field, as the direct simulation results are very different from the semi-analytical and the Kirchhoff results. This is due to discretization errors. However, this CFD code is accurate in the near-field and the Kirchhoff method should be used instead in the far-field, as indicated in Fig. 4.

The Kirchhoff method for a uniformly moving surface was also used in two-dimensional transonic blade-vortex interactions (BVI) to extend the numerically calculated nonlinear aerodynamic BVI results to the linear acoustic far-field (George and Lyrintzis, 1988; Lyrintzis and George, 1989a; Lyrintzis and Xue, 1991). Typical results from this application are shown in Fig. 5; in this figure the CFD solution for a two dimensional transonic BVI case is compared to the Kirchhoff solution while the unsteady transonic small disturbance code VTRAN2 is used for the CFD calculations for a point P $(-0.35, -0.186, 0)$ just outside the Kirchhoff surface, upstream and beneath the blade, for a NACA 64A006 airfoil, Mach number M = 0.822, vortex strength $C_{lv} = 0.4$, ($C_{lv} = 2\Gamma/U_\infty c$, where Γ is the vortex strength, U_∞ is the free-stream velocity and c is the vortex strength) y_0 (vortex miss distance) $= -0.5$, $x_s = 0.25, 125$, $y_s = \pm 1.8$, $z_s = 8$ (all distances are in chords). The vortex moves at constant speed U_∞ (fixed vortex path). The initial vortex position is $x_0 = -9.51$ chords and the free-stream velocity is one (arbitrary units) so the vortex passes below the airfoil leading edge at time $T = 9.51$. The agreement between the CFD and the Kirchhoff method results is excellent. The Kirchhoff method was used to test ideas for BVI noise reduction (Xue and Lyrintzis, 1993b). The method was also extended to study

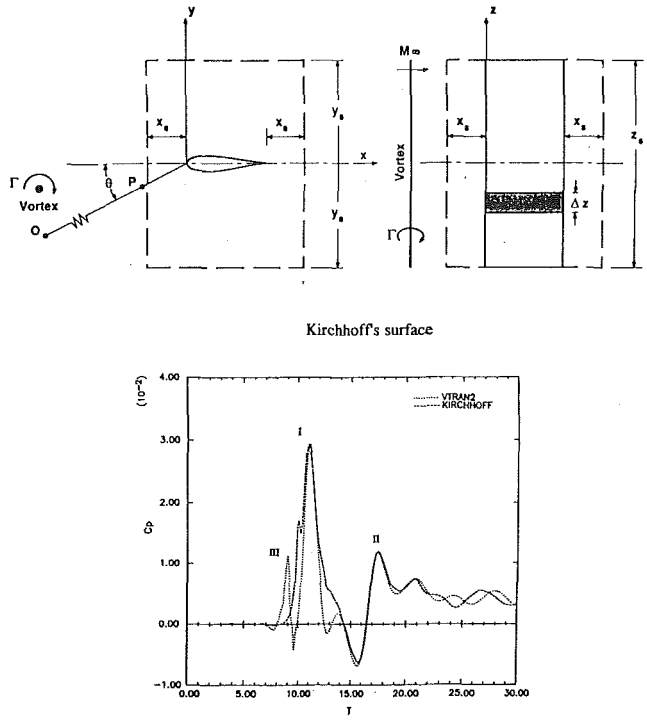

Fig. 5 CFD and Kirchhoff's method results for 2-D BVI at point P (-0.35, -0.186, 0); NACA 64A006, Mach number M = 0.822, vortex strength $C_{lv} = 0.4$, ($C_{lv} = 2\Gamma/U_\infty c$, where Γ is the vortex strength, U_∞ is the free stream velocity and c is the vortex strength), y_0 (vortex miss distance) =-0.5, $x_s = 0.25, 1.25$, $y_s = \pm 1.8$, $z_s = 8$ (all distances are in chords), fixed vortex path (from George and Lyrintzis, 1988).

noise due to other unsteady transonic flow phenomena (i.e., oscillating flaps, thickening-thinning airfoil) by Lyrintzis et al. (1992, 1994c).

Kirchhoff's method has been applied to hover High-Speed Impulsive (HSI) noise. Baeder et al. (1993) and Strawn et al. (1993) used a stationary Kirchhoff surface that encloses the entire rotor. The state-of-the-art Transonic Unsteady Rotor Navier Stokes (TURNS) code was used for the near-field CFD calculations. An unstructured grid was used by Strawn et al. (1993). Kirchhoff's method predicted the HSI hover noise very well using about half the CPU of the straight CFD calculation. The results are also compared with a linear (i.e., monopole plus dipole sources) acoustic analogy method (RAPP code). The acoustic analogy results were inaccurate for tip Mach numbers higher than 0.7, because of the omission of quadrupole sources. Figure 6 shows some typical acoustic HSI signals from Baeder et al. (1993) at a distance of 3.09 rotor radii and compares with experiments by Purcell (1988). Results from Strawn et al. (1993) are similar. The method was recently extended to an advancing rotor HSI noise by Strawn and Biswas (1994). It should be noted that, detailed CFD information out to the stationary Kirchhoff cylinder is necessary as an input. In addition, the aerodynamic input, which is usually in rotating blade coordinates, has to be transformed to stationary coordinates, a process that introduces some errors. Since the cylinder surface is not included, the method seems to be well suited for HSI noise calculations where the main signal is on the rotor plane. However, the application of this method for BVI noise, where noise radiation occurs also in downward directions and detailed CFD information is needed near the blade, is doubtful.

Isom et al. (1987), and Purcell (1988, 1989) used a modified Kirchhoff method which also included some nonlinear effects for a stationary surface, to calculate high-speed compressibility noise for the hover case. Results (not shown here) show good agreement with experimental data.

Another Kirchhoff method used in helicopter noise is the rotating Kirchhoff method (i.e., the surface rotates with the blade). The method was used for three-dimensional transonic BVI's for a hovering rotor by Xue and Lyrintzis (1993, 1994). The near-field was calculated using the Full Potential Rotor (FPR) code. The rotating Kirchhoff formulation allows the Kirchhoff surface to rotate with the blade; thus a smaller cylinder surface around the blade can be used. No transformation of data is needed because the CFD input is also rotating. Since more detailed information is utilized for the accurate prediction of the far-field noise this method is more efficient. We feel that the rotating Kirchhoff formulation is needed for the BVI problem, since the details of the flow around the airfoil caused by the vortex are important in determining the far-field noise. Typical results (pressure versus rotor azimuthal angle Ψ) are shown in Fig. 7, where the CFD solution is compared to the Kirchhoff solution at point P $(x, y, z) = (0.56, 9.89, 0.705$ chords) just outside the Kirchhoff surface. A rotating formulation is used for the Kirchhoff method and the FPR is used for the CFD calculations. It should be noted that both solutions are in the rotating (i.e., blade fixed) coordinate system (i.e., Morino's formulation, Eq. (26)). The Kirchhoff control surface coincides with the grid lines, $L = 11$ is used in this case. The results are almost the same. The small errors are probably due to the relatively coarse mesh used in the FPR calculations. The rotating Kirchhoff method (Farassat's formulation) compares very well with experimental results (Purcell, 1988), as shown in Fig. 8, where results from Purcell (1988) (Isom's formulation) are also included. FPR is used in both cases. It should be noted that a more detailed grid resolution near the rotor tip was used in reference by Purcell (1988). Finally, the method was extended for an advancing rotor (Lyrintzis et al. 1994b) and was applied to HSI noise (Lyrintzis et al., 1994a). However, a slight drawback of the method is that the rotating speed of the tip of the rotating surface needs to remain subsonic, because Farassat's formulation is currently limited to subsonically moving surfaces. An extension to supersonically moving surfaces is needed. This imposes limits to the position of the tip of the rotating Kirchhoff surface in very high Mach number cases (e.g., M = 0.92–0.95 for hover). However, Farassat and Myers (1994) are currently extending the formulation to supersonically moving surfaces. We expect that this extension will be employed in the rotating Kirchhoff formulation in the near future.

Kirchhoff's method has also been applied in the estimation of supersonic jet noise. Soh (1994) used the stationary Kirchhoff method (Eq. (6)) and Lyrintzis and Mankbadi (1995) used the uniformly moving formula (Eqs. (13) and (20)) and compared time and frequency domain formulations. It should be noted that for some complicated noise problems (e.g., supersonic jet noise) three computational domains might be needed: a complicated near-field (e.g., using Large Eddy Simulations-LES), a simplified mid-field with some nonlinear effects, and a linear Kirchhoff's method for the far-field. Kirchhoff's method can also be applied to ducted fan noise. Exploratory results were shown by Ozyoruk and Long (1994). Finally, a nonlinear extension of Kirchhoff's method could possibly be used in the evaluation of sonic boom to extend near-field CFD solutions to a distance where the acoustic field is axisymmetric; then, the ray tracing can begin from this point.

Concluding Remarks

Kirchhoff's method consists of the calculation of the nonlinear near-and mid-field usually numerically with the far-field solutions found from a linear (or nonlinear) Kirchhoff formulation evaluated on a surface S surrounding the nonlin-

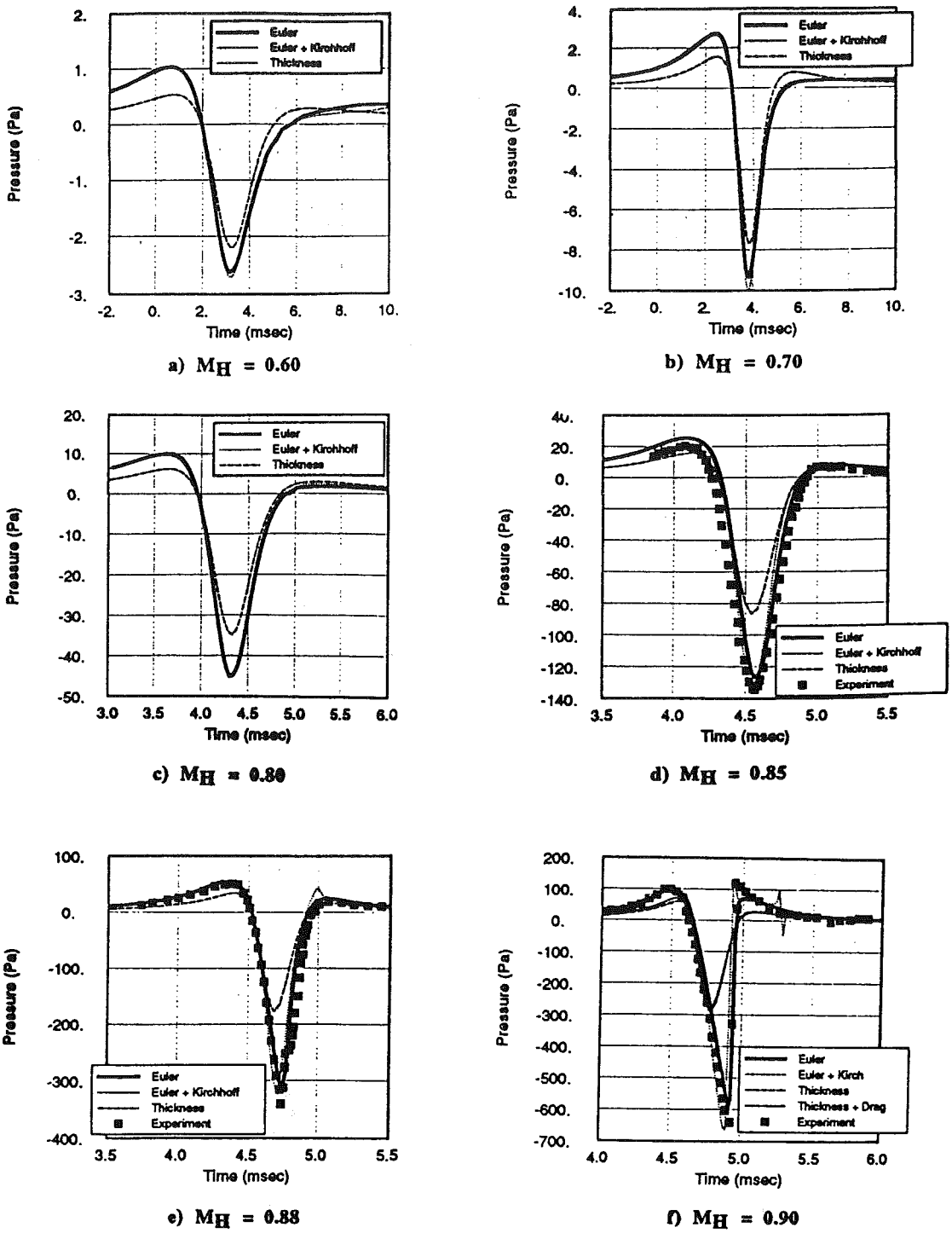

Fig. 6 Comparison of the predicted pressure time histories in the plane of the rotor at 3.09 rotor radii for untwisted UH-1H for three methods at various tip Mach numbers (from Baeder et al., 1993)

ear-field. The surface S is assumed to include all the nonlinear flow effects and noise sources. The separation of the problem into linear and nonlinear regions allows the use of the most appropriate numerical methodology for each. The advantage of this method is that the surface integrals and the first derivatives needed can be evaluated more easily than the volume integrals and the second derivatives needed for the evaluation of the quadrupole terms when acoustic analogy is used. The method is simple and accurate and accounts for the nonlinear quadrupole noise in the far-field. Full diffraction and focusing effects are included while eliminating the propagation of the reactive near-field. Some results indicative of the uses of Kirchhoff's method were shown here, but the reader is referred to the original references for further details.

Kirchhoff's method is a powerful technique for calculating the far-field noise utilizing numerical aerodynamic results that simulate complex phenomena, because it gathers all near-field complicated nonlinear effects that are necessary for far-field accurate acoustic prediction. The use of Kirch-

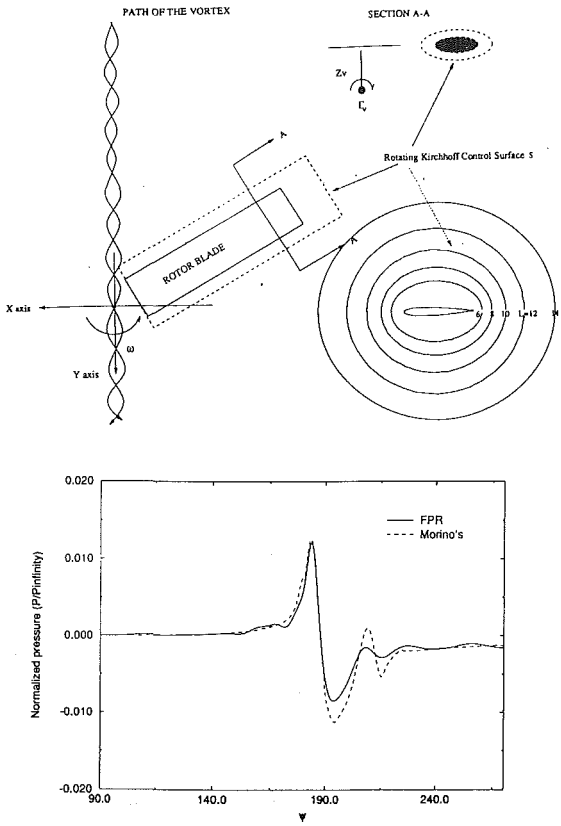

Fig. 7 CFD and Kirchhoff's method results (pressure versus rotor azimuthal angle) for 3-D BVI at point P (0.56, 9.89, 0.705 chords) on L = 11; NACA 0012, tip Mach number $M_{tip} = 0.75$, vortex strength $\Gamma_v = \Gamma/Mc = 0.2$, vortex miss distance $Z_v = 0.26$, (from Xue and Lyrintzis, 1993a).

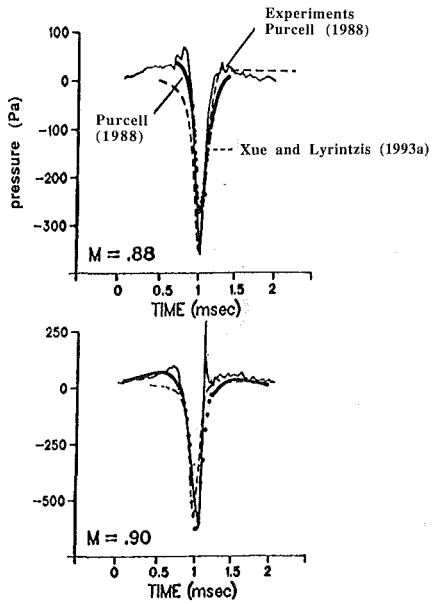

Fig. 8 HSI acoustic pressure predictions for two hover tip Mach numbers, M = 0.88, 0.90 at distance R = 3 radii. Experiments and computations from reference Purcell (1988) are also shown, (from Xue and Lyrintzis, 1993a).

hoff's method has increased substantially the last 5–10 years, because of the development of reliable CFD methods that can be used for the evaluation of the near-field. It can be used to study various acoustic problems, such as propeller noise, high-speed compressibility noise, blade-vortex interactions, jet noise, ducted fan noise, etc.

A simple set of portable Kirchhoff subroutines can be developed to calculate the far-field noise from inputs supplied by any aerodynamic near/mid-field code. Some issues that need to be addressed before the wide-spread application of Kirchhoff subroutines are the determination of proper Kirchhoff surface placement, the choice of an adequate grid, and the choice between time and frequency domain. Finally, the subroutines should be extended to handle supersonically moving surfaces. However, as these subroutines develop and become mature, Kirchhoff's method may very well replace the Acoustic Analogy method used today for acoustic problems when nonlinear quadrupole terms are present.

Acknowledgments

The author wishes to acknowledge the support of the University of Minnesota Supercomputer Institute (MSI) and Cray Research Inc.

References

Atassi, H. M., Dusey, M., and Davis, C. M., 1993, "Acoustic Radiation from a Thin Airfoil in Nonuniform Subsonic Flows," *AIAA Journal*, Vol. 31, No. 1, Jan. pp. 12–19.

Baeder, J. D., McCroskey, W. J., and Srinivasan, G. R., 1986, "Acoustic Propagation Using Computational Fluid Dynamics," *Proceedings of the 42nd Annual Forum of the American Helicopter Society*, Washington, DC, Vol. 1, pp. 551–562.

Baeder, J. D., 1987, "Computation of Non-Linear Acoustics in Two-Dimensional Blade-Vortex Interactions," Paper No. 1-1, 13th European Rotorcraft Forum, Arles, France.

Baeder, J. D., 1990, "Euler Solutions to Nonlinear Acoustics of Non-Lifting Hovering Rotor Blades," 16th European Rotorcraft Forum, Glasgow, Scotland.

Baeder, J. D., 1991, "Euler Solutions to Nonlinear Acoustics of Non-Lifting Rotor Blades," *Proceedings of AHS/RAeS International Technical Specialists meeting on Rotorcraft Acoustics and Rotor Fluid Dynamics*, Philadelphia, PA, Oct.

Baeder, J. D., Gallman, J. M., and Yu, Y. H., 1993, "A Computational Study of the Aeroacoustics of Rotors in Hover," *Proceedings of the 49th Annual Forum of the American Helicopter Society*, St. Louis, MO, May, Vol. I, pp. 55–71.

Batchelor, G. K., and Proudman, I., 1954, "The Effect of Rapid Distortion of a Fluid in Turbulent Motion," *Quart. J. Mech. Appl. Math.*, Vol. 1, pp. 83–103.

Brentner, K. S., and Farassat, F., 1992, "Helicopter Noise Prediction: The Current Status and Future Direction," *Journal of Sound and Vibration*, Vol. 170(1), pp. 79–96.

Burton, A. J., and Miller, G. F., 1971, "The Application of the Integral Equation Method to the Numerical Solution of Some Exterior Boundary Value Problems," *Proceedings of Royal Society*, Vol. 323A, pp. 202–210.

Davis, C. M., and Atassi, H. M., 1991, "The Far-Field Acoustic Pressure of an Airfoil in Nonuniform Subsonic Flows," presented at the *Symposium of Flow Noise Modeling, Measurement and Control*, NCA-Vol. 11/FED-Vol. 130, pp. 107–117, ASME Winter Annual Meeting, Atlanta, GA, Dec.

Fang, J., and Atassi, H. M., 1993, "Direct Calculation of Sound Radiated from a Loaded Cascade in a Gust," *Computational Aero- and Hydro-Acoustics*, FED Vol. 147, Mankbadi, R. R., Lyrintzis, A. S., Baysal, O., Povinelli, L. A., and Hussaini, M. Y., eds., pp. 111–116, ASME Fluids Engineering Conference, Washington, DC, June.

Farassat, F. and Myers, M. K., 1986, "The Moving Boundary Problem for the Wave Equation: Theory and Application," *First IMACS International Symposium on Computational Acoustics*, Yale University, 6–8 August.

Farassat, F., and Brentner, K. S., 1988, "The Uses and Abuses of the Acoustic Analogy in Helicopter Rotor Prediction," *Journal of the American Helicopter Society*, Vol. 33(1), pp. 29–36.

Farassat, F., and Myers, M. K., 1988, "Extension of Kirchhoff's Formula to Radiation from Moving Surfaces," *Journal of Sound and Vibration*, Vol. 123, No. 3, pp. 451–460.

Farassat, F., and Myers, M. K., 1989, Author's Reply to "Comments on the Extension of Kirchhoff's Formula to Radiation from Moving Surfaces," *Journal of Sound and Vibration*, Vol. 132, No. 3, p. 511.

Farassat, F., and Tadghighi, H., 1990, "Can Shock Waves on Helicopter Rotors Generate Noise? A Study of the Quadrupole Source," *Proceedings of the 46th Annual Forum of the American Helicopter Society*, Washington, DC, May, Vol. I, pp. 323–346.

Farassat, F., and Myers M. K., 1994, "Kirchoff Formula for Super-

sonic Surfaces," presented at the *Symposium on Acoustic Radiation and Wave Propagation*, ASME 115th Congress, Chicago, IL, Nov.

Felton, F. H., 1969, "Calculation of the Acoustic Radiation Field at the Surface of a Finite Cylinder by the Method of Weighted Residuals," *Proceedings of IEEE*, Vol. 57, No. 3, pp. 291–306.

Ffowcs-Williams, and Hawkings, D. L., 1969, "Sound Generation by Turbulence and Surfaces in Arbitrary Motion," *Philosophical Transactions of The Royal Society*, London, Vol. 264A, pp. 321–342.

Forsyth, D. W., and Korkan, K. D., 1987, "Computational Aeroacoustics of Propeller Noise in the Near- and the Far-Field," AIAA paper 87-0254, AIAA 25th Aerospace Science Meeting, Reno, NV.

Freund, J. B., Lele, S. K., and Moin, P., 1993, "Matching of Near/Far-Field Equation Sets for Direct Computations of Aerodynamic Sound," AIAA paper 93-4326, AIAA 15th Aeroacoustics Conference, Long Beach, CA.

Gallman, J. M., Myers, M. K., and Farassat, F., 1991, "Boundary Integral Approach to the Scattering of Nonplanar Acoustic Waves by Rigid Bodies," *AIAA Journal*, Vol. 29, No. 12, pp. 2038–2046.

Goodrich, J. W., 1993, "Application of a New High-Order Difference Scheme to Acoustic Propagation With the Linearized Euler Equation," *Computational Aero- and Hydro-Acoustics*, FED Vol. 147, Mankbadi, R. R., Lyrintzis, A. S., Baysal, O., Povinelli, L. A., and Hussaini, M. Y., eds., pp. 53–61, ASME Fluids Engineering Conference, Washington, DC, June.

George, A. R., and Lyrintzis, A. S., 1988, "Acoustics of Transonic Blade-Vortex Interactions," *AIAA Journal*, Vol. 26, No. 7, July 1988, pp. 769–776.

Ginsberg, J. H., Chen, P. T., and Pierce, A. D., 1990, "Analysis Using Variational Principles of the Surface Pressure and Displacement Along an Axisymmetrically Excited Elastic Disk in a Baffle," *Journal of Acoustical Society of America*, Vol. 88, pp. 548–559.

Hardin, J. C., Hussaini, M. Y., 1993, *Computational Aeroacoustics*, Springer-Verlag, New York.

Hardin, J. C., and Pope, D. S., 1992, "A New Technique for Aerodynamic Noise Calculation," *Proceedings of the DGLR/AIAA 14th Aeroacoustics Conference*, Aachen, Germany, pp. 448–456.

Hardin, J. C., and Pope, D. S., 1993, "Sound Generation By Flow Over a Two-Dimensional Cavity," AIAA paper 93-4327, AIAA 15th Aeroacoustics Conference, Long Beach, CA.

Hawkings, D. L., "Noise Generation by Transonic Open Rotors," Westland Research Paper 599, 1979.

Hawkings, D. L., 1989, "Comments on the Extension of Kirchhoff's Formula to Radiation from Moving Surfaces," *Journal of Sound and Vibration*, Vol. 132, No. 1, p. 160.

Isom, M. P., Purcell, T. W., and Strawn, R. C., 1987, "Geometrical Acoustics and Transonic Sound," AIAA paper 87-2748, AIAA 11th Aeroacoustics Conference, Sunnyvale, CA.

Jaeger, S., and Korkan, K. D., 1990, "On the Prediction of Far-Field Computational Aeroacoustics of Advanced Propellers," AIAA paper 90-3996, AIAA 13th Aeroacoustics Conference, Oct.

Khromov, V. A., 1963, "Generalization of Kirchhoff's Theorem for the Case of a Surface Moving in an Arbitrary Way," *Soviet Physics-Acoustics*, Vol. 9, 68–71.

Lele, S., 1989, "Direct Numerical Simulation of Compressible Free Shear Flows," AIAA paper 89-0374, AIAA 27th Aerospace Science Meeting, Reno, NV.

Lele, S., 1992, "Compact Finite Difference Schemes with Spectral-like Resolution," *Journal of Computational Physics*, Vol. 103, pp. 16–42.

Lighthill, M. J., 1952, "On Sound Generated Aerodynamically, I. General Theory," *Proceedings of The Royal Society*, London, Vol. 221A, pp. 564–587.

Lighthill, M. J., 1992, "A General Introduction to Aeroacoustics and Atmospheric Sound," ICASE Report 92-52, NASA Langley Research Center, Hampton, VA.

Lilley, G. M., 1974, "On the Noise from Jets: Noise Mechanisms," AGARD-CP-131, Mar. 1974, 13.1–13.12.

Lim, T. B., Sankar, L. N., Hariharan, N., and Reddy, N. N., 1993, "A Technique for the Prediction of Propeller Induced Acoustic Loads on Aircraft Structures," AIAA-93-4340, 15th AIAA Aeroacoustics Conference, Long Beach, CA.

Lockard, D. P., Brentner, K. S., and Atkins, H. L., 1994, "High Accuracy Algorithms for Computational Aeroacoustics," AIAA paper 94-0460, AIAA 32nd Aerospace Science Meeting, Reno, NV.

Lyrintzis, A. S., 1988, "Transonic Blade-Vortex Interactions," Ph.D. dissertation, Sibley School of Mechanical and Aerospace Engineering, Cornell University, Ithaca, NY.

Lyrintzis, A. S., 1993, "The Use of Kirchhoff Method in Aeroacoustics," *Computational Aero- and Hydro-Acoustics*, FED Vol. 147, Mankbadi, R. R. Lyrintzis, A. S., Baysal, O., Povinelli, L. A., and Hussaini, M. Y., eds., pp. 53–61, ASME Fluids Engineering Conference, Washington, DC, June.

Lyrintzis, A. S., 1994, "A Review of the Uses of Kirchoff's Method on Computational Aeronautics," presented at the *Symposium on Acoustic Radiation and Wave Propagation*, ASME 115th Congress, Chicago, IL, Nov.

Lyrintzis, A. S., and George, A. R., 1989a, "Far-Field Noise of Transonic Blade-Vortex Interactions," *American Helicopter Society Journal*, Vol. 34, No. 3, pp. 30–39.

Lyrintzis, A. S., and George, A. R., 1989b, "The Use of Kirchhoff Method in Acoustics," *AIAA Journal*, Vol. 27, No. 10, Oct., pp. 1451–1453.

Lyrintzis, A. S., and Xue, Y., 1991, "A Study of the Noise Mechanisms of Transonic Blade-Vortex Interactions," *AIAA Journal*, Vol. 29, No. 10, pp. 1562–1572.

Lyrintzis, A. S., Lee, J., and Xue, Y., 1992, "Mechanisms and Directivity of Unsteady Transonic Flow Noise," presented at the *International Symposium on Flow Induced Vibration and Noise III, Vol. 3: Flow-Structure and Flow-Sound Interactions*, Farabee, T. M., Paidoussis, M. P., eds., pp. 85–113, ASME Winter Annual Meeting, Anaheim, CA, Nov.

Lyrintzis, A. S., Xue, Y., and Kilaras, M. S., 1994a, "A Prediction of High-Speed Rotor Noise Using a Rotating Kirchhoff Formulation," AIAA paper 94-0463, AIAA 32nd Aerospace Science Meeting, Reno, NV.

Lyrintzis, A. S., Kilaras, M. S., and Xue, Y., 1994b, "Transonic 3-D BVI Noise Using a Rotating Kirchhoff Formulation for Advancing Rotors," *Proceedings of the AHS 50th Annual Forum of the American Helicopter Society*, Vol. I, Washington, DC, May, pp. 115–127.

Lyrintzis, A. S., Lee, J., and Xue, Y., 1994c, "Mechanisms and Directivity of Unsteady Transonic Flow Noise," ASME JOURNAL OF FLUIDS ENGINEERING, Vol. 6, pp. 649–652.

Lyrintzis, A. S., and Mankbadi, R. R., 1995, "On the Prediction of the Far-Field Jet Noise Using Kirchhoff's Method," AIAA Paper No. 95-0508 to be presented at the 33rd Aerospace Science Meeting, Reno, NV.

Mankbadi, R. R., Hayder, M. E., and Povinelli, L. A., 1994, "The Structure of Supersonic Jet Flow and Its Radiated Sound," *AIAA Journal*, Vol. 32, No. 5, May, pp. 897–906.

Meadows, K., and Atkins, H. L., 1994, "Evaluation of a Hybrid Kirchhoff-CFD Approach for Computational Aeroacoustics," presented at the 14th IMACS World Congress, July, Atlanta, GA.

Meyer, W. L., Bell, W. A., Zinn, B. T., and Stallybrass, M. P., 1978, "Boundary Integral Solutions of Three-Dimensional Acoustic Radiation Problems," *Journal of Sound and Vibration*, Vol. 59, pp. 245–262.

Morgans, R. P., 1930, "The Kirchhoff Formula Extended to a Moving Surface," *Philosophical Magazine*, 9, s.7, No. 55, pp. 141–161.

Morino, L., 1973, "Unsteady Compressible Potential Flow Around Lifting Bodies: General Theory," AIAA paper No. 73-196.

Morino, L., 1974, "A General Theory of Unsteady Compressible Potential Aerodynamics," NASA Contractor Report CR-2464, December 1974.

Morino, L., 1980, "Steady, Oscillatory, and Unsteady Subsonic and Supersonic Aerodynamics—Production Version 1.1 (SOUSSA-P, 1.1), Vol. 1, Theoretical Manual," NASA Contractor Report CR-159130.

Morino, L., 1985, "Mathematical Foundations of Integral Methods," *Computational Methods in Potential Aerodynamics*, Morino, L., ed., Springer-Verlag, New York, pp. 271–291.

Morino, L., Freedman, M. I., Deutsch, D. J., and Sipcic, S. R., 1985, "An Integral Equation Method for Compressible Potential Flows in an Arbitrary Frame of Reference," *Computational Methods in Potential Aerodynamics*, L. Morino, ed., Computational Mechanics Publications, Southampton, UK.

Morino, L., Bharadvaj, B. K., Freedman, M. I., and Tseng, K., 1988, "BEM for Wave Equation With Boundary in Arbitrary Motion and Applications to Compressible Potential Aerodynamics of Aeroplanes and Helicopters," *Advanced Boundary Element Methods*, T. A. Cruse, ed., Springer-Verlag, New York.

Morino, L., and Tseng, K., 1990, "A General Theory of Unsteady Compressible Potential Flows With Applications to Airplanes and Rotors," *Developments in Boundary Element Methods*, Vol. 6, Banerjee, P. K., and Morino, L., eds., Elsevier Applied Science Publisher, Barking, UK, pp. 183–245.

Munro, D. H., 1980, "The Production of Sound by Moving Objects," Ph.D. dissertation, Massachusetts Institute of Technology.

Myers, M. K., and Hausmann, J. S., 1990, "On the Application of the Kirchhoff Formula for Moving Surfaces," *Journal of Sound and Vibration*, Vol. 139, pp. 174–178.

Myers, M. K., and Hausmann, J. S., 1992, "Computation of Acoustic Scattering from a Moving Rigid Surface," *Journal of the Acoustical Society of America*, Vol. 91(5), pp. 2594–2605.

Ozyoruk, Y., and Long, L. N., 1993, "A Navier-Stokes/Kirchhoff Method for Noise Radiation from Ducted Fans," AIAA paper 94-0462, AIAA 32nd Aerospace Science Meeting, Reno, NV.

Patrick, S. M., Davis, C. M., and Atassi, H., 1993, "Acoustic Radiation from a Lifting Airfoil in Nonuniform Subsonic Flows," *Computational Aero- and Hydro-Acoustics*, FED Vol. 147, Mankbadi, R. R., Lyrintzis, A. S., Baysal, O., Povinelli, L. A., and Hussaini, M. Y., eds., pp. 41–46, ASME Fluids Engineering Conference, Washington, DC, June.

Phillips, O. M., 1960, "On the Generation of Sound by Supersonic Turbulent Shear Layers," *Journal of Fluid Mechanics*, Vol. 9, pp. 1–28.

Pierce, A. D., 1981, *Acoustics: An Introduction to Its Physical Principles and Applications*, McGraw-Hill, New York.

Purcell, T. W., Strawn, R. C., and Yu, Y. H., 1987, "Prediction of High-Speed Rotor Noise With a Kirchhoff Formula," *Proceedings of the American Helicopter Society National Specialists' Meeting on Aerodynamics and Aeroacoustics*, Arlington, TX.

Purcell, T. W., 1988, "CFD and Transonic Helicopter Sound," Paper No. 2, 14th European Rotorcraft Forum.

Purcell, T. W., 1989, "A Prediction of High-Speed Rotor Noise," AIAA 89-1130, AIAA 12th Aeroacoustics Conference, San Antonio, TX.

Rogers, P. H., 1973, "Formal Solution of the Surface Helmholtz Integral Equation at a Nondegenerate Characteristic Frequency," *Journal of Acoustical Society of America*, Vol. 54, pp. 1662–1666.

Sankar, L. N., Reddy, N. N., and Hariharan, N., 1993, "A Third-order Accurate Upwind Scheme for Aeroacoustic Applications," AIAA paper 93-0149, AIAA 31st Aerospace Science Meeting, Reno, NV.

Schenck, H. A., 1968, "An Improved Integral Formulation for Acoustic Radiation Problems," *Journal of Acoustical Society of America*, Vol. 44, pp. 41–58.

Scott, J. R., and Atassi, H. M., 1990, "Numerical Solution of the Linearized Euler Equations for Unsteady Vortical Flows Around Lifting Airfoils," AIAA paper No 90-0064, AIAA 28th Aerospace Science Meeting, Reno, NV.

Seybert, A. F., Soenarko, F. J., Rizzo, F. J., and Shippy, D. J., 1984, "Application of BIE Method to Sound Radiation Problems Using an Isoparametric Element," ASME *Journal of Vibration, Acoustics, Stress and Reliability and Design*, Vol. 106, pp. 414–420.

Seybert, A. F., Soenarko, F. J., Rizzo, F. J., and Shippy, D. J., 1985, "An Advanced Computational Method for Radiation and Scattering of Acoustic Waves in Three-Dimensions," *Journal of Acoustical Society of America*, Vol. 77, pp. 362–368.

Seybert, A. F., and Rengarajan, T. K., 1987, "The Use of CHIEF to Obtain Unique Solutions for Acoustic Radiation Using Boundary Integral Equations," *Journal of Acoustical Society of America*, Vol. 81, pp. 1299–1306.

Smith, M. J. T., 1989, *Aircraft Noise*, Cambridge University Press, New York.

Soh, W. Y., 1994, "Unsteady Jet Flow Computation-Towards Noise Prediction," AIAA paper 94-0138, AIAA 32nd Aerospace Science Meeting, Reno, NV.

Stoker, R. W., and Smith, M. J., 1993, " An Evaluation of Finite Volume Direct Simulation and Perturbation Methods in CAA Applications," AIAA 93-0152, AIAA 31st Aerospace Science Meeting, Reno, NV.

Strawn, R. C., Garceau, M., and Biswas, R., 1993, "Unstructured Adaptive Mesh Computations of Rotorcraft High-Speed Impulsive Noise," AIAA paper 93-4359, presented at the 15th AIAA Aeroacoustics Conference, Long Beach, CA.

Strawn, R. C., Biswas, R., 1994, "Computation of Helicopter Rotor Acoustics in Forward Flight," presented at the 19th Army Science Conference, June, Orlando, FL.

Tadghighi, H., Holtz, R., Farassat, F., and Lee, Y-J, 1991, "Development of Shock Noise Prediction Code for High-Speed Helicopters—The Subsonically Moving Shock," *Proceedings of the 47th Annual Forum of The American Helicopter Society*, Phoenix, AZ, May, pp. 773–789.

Tadghighi, H., Hassan, A. A., and Charles, B., 1992, "Prediction of Blade-Vortex Interaction Noise Using Airloads Generated by a Finite-Difference Technique," *Journal of the American Helicopter Society*, Vol. 37(4), pp. 38–47.

Tam, K. W., and Webb, J. C., 1993, "Dispersion-Relation-Preserving Finite Difference Schemes for Computational Acoustics," *Journal of Computational Physics*, Vol. 107, pp. 262–283.

Thomas, J. P., and Roe, P. L., 1993, "Development of Non-Dissipative Numerical Schemes for Computational Aeroacoustics," AIAA paper 93-3382, AIAA 24th Fluid Dynamics Conference, Orlando, FL.

Viswanathan, K., Sankar, L. K., Reddy, N. N., 1994, "A Fluid/Acoustic Coupled Simulation of Supersonic Jet Noise," AIAA paper 94-0137, AIAA 32nd Aerospace Science Meeting, Reno, NV.

Wu, S. F., 1987, "Faster Calculations of Sound Radiation from Vibrating Cylinders Using Variational Formulations," ASME *Journal of Vibration, Acoustics, Stress, and Reliability in Design*, Vol. 111, pp. 101–107.

Wu, S. F., 1993a, "Nonuniqueness of Solutions to Extended Kirchhoff Integral Formulations," *Journal of the Acoustical Society of America*, Vol. 93, No. 2, Feb., pp. 683–695.

Wu, S. F., 1993b, "Transient Sound Radiation from Impulsively Accelerated Bodies," *Journal of the Acoustical Society of America*, Vol. 94, No. 1, July, pp. 542–553.

Wu, S. F., and Pierce, A. D., 1990, "Nonuniqueness of Solutions to Variationally Formulated Acoustic Radiation Problems," ASME *Journal of Vibration and Acoustics*, Vol. 112, pp. 263–267.

Wu, S. F., and Akay, A., 1992, "Sound Radiation from Vibrating Bodies in Motion," *Journal of the Acoustical Society of America*, Vol. 91, No. 5, pp. 2544–2555.

Wu, S. F., and Wang, Z., 1993, "Extended Kirchhoff Integral Formulations for Sound Radiation from Vibrating Cylinders in Motion," ASME *Journal of Vibration and Acoustics*, Vol. 115, No. 3, July, pp. 324–331.

Xue, Y., and Lyrintzis, A. S., 1991, "Noise Reduction for Transonic Blade-Vortex Interactions," *Proceedings of AHS/RAeS International Technical Specialists meeting on Rotorcraft Acoustics and Rotor Fluid Dynamics*, Philadelphia, PA, Oct.

Xue, Y., and Lyrintzis, A. S., 1993a, "The Use of a Rotating Kirchhoff Formulation for 3-D Transonic BVI Noise," *Proceedings of the 49th Annual Forum of the American Helicopter Society*, St. Louis, MO, May.

Xue, Y., and Lyrintzis, A. S., 1993b, "Transonic Blade-Vortex Interactions: Noise Reduction Techniques," *AIAA Journal of Aircraft*, Vol. 30, No. 3, May–June, pp. 408–411.

Xue, Y., and Lyrintzis, A. S., 1994, "Rotating Kirchhoff Formulation for 3-D Transonic BVI Noise for a Hovering Rotor," *AIAA Journal* , Vol. 32, No. 2, July, pp. 1350–1359.

Investigation of Fully Developed Turbulent Flow in a Straight Duct With Large Eddy Simulation

M. D. Su
Tsinghua University,
Beijing, 100084
PR China

R. Friedrich
Lehrstuhl für
Fluidmechanik,
TU München
80333 München, Germany

Large eddy simulations have been performed in straight ducts with square cross section at a global Reynolds number of 49,000 in order to predict the complicated mean and instantaneous flow involving turbulence-driven secondary motion. Isotropic grid systems were used with spatial resolutions of $256*64^2$. The secondary flow not only turned out to develop extremely slowly from its initial conditions but also to require fairly high resolution. The obtained statistical results are compared with measurements. These results show that the large eddy simulation (LES) is a powerful approach to simulate the complex turbulence flow with high Reynolds number. Streaklines of fluid particles in the duct show the secondary flow clearly. The database obtained with LES is used to examine a statistical turbulence model and describe the turbulent vortex structure in the fully developed turbulent flow in a straight duct.

1 Introduction

The study of viscous flows in straight ducts has been of fundamental interest to fluid dynamicists. Most such flows encountered in engineering equipments are turbulent. Many investigations show that the flow in noncircular straight ducts is accompanied by secondary motions in the plane perpendicular to the streamwise flow direction. This secondary motion can be caused by different mechanisms and seriously depends on the Reynolds number, geometry of cross-section (for example, aspect ratio of the section) etc. Secondary flow not only induces a reduction in the volumetric flow rate, but it also causes the axial velocity field to be distorted with an outward shift of the contours of constant velocity. Furthermore, the secondary motion produces an increase in the wall shear stress towards the corners, and a significant influence on the heat transfer at the walls. The secondary flow can also increase the lateral spreading of any tracer discharged into the channel. A clear understanding of the evolution and consequences of the secondary flow in ducts in its fully developed state is quite important. Besides, little is known about the structure of internal turbulent flows, even in straight ducts.

A considerable number of experimental investigations and numerical predictions has been carried out on turbulent flow in straight square ducts. Most of the experimental investigations of duct flows aimed at measuring the statistical time-averaged velocities and Reynolds stresses. Almost all numerical predictions have been carried out with turbulence models. In the paper of Demuren and Rodi (1984) experimental investigations and statistical models were presented, described and compared in detail. As we know, the secondary flow in a straight square duct is very weak and the velocity components are of the order of 2~3 percent of the main flow velocity. The measurement of this secondary motion becomes prohibitively difficult. In the past decades, several researchers measured the secondary flow and got some useful results (for example, Brundett and Baines, 1964; Gessner, 1964; Gessner and Emery, 1981). Kline (1981) found that the length required for full flow development in a pipe may exceed 140 diameters. According to this viewpoint, only in a few experiments fully developed flow has been achieved (for example, Brundett and Baines (1964), Gessner (1964)). The present results will be compared with Gessner (1964 and 1981) data.

As a result of the rapid development of supercomputer, the large eddy simulation (LES) method is successfully used to simulate complex turbulence. Because an accurate prediction of the secondary flow needs models of high order accuracy, this flow can be considered to be a good candidate to examine the quality of LES methods. Using LES, Miyake and Kajishima (1991) investigated the origin of secondary flows that are observed in straight ducts of square cross section. This work, however, does not contain a complete investigation of this flow, since it lacks spatial resolution. Recently, Madabhushi and Vanka (1991) used the same technique and compared their results with experimental data of higher Reynolds numbers. The agreement is obviously not satisfying. The authors declare the comparisons between the experimental data and their numerical results are only qualitative and not quantitative, because there is a large difference in Reynolds numbers. The analysis of the turbulence structure in a straight duct has not been confirmed till now.

An important role of numerical simulation (DNS or LES) is that the database generated with numerical simulation can

Contributed by the Fluids Engineering Division for publication in the JOURNAL OF FLUIDS ENGINEERING. Manuscript received by the Fluids Engineering Division July 1, 1993; revised manuscript received May 2, 1994. Associate Technical Editor: J. A. C. Humphrey.

be used to test the correctness of the statistical turbulent model and put forward suggestion to improve modelling. Demuren and Rodi's algebraic modelling was tested in the present paper.

It is the object of the present work to use the LES method in the simulation of fully-developed turbulent flows in straight ducts. The object can be divided into the following parts:

- To show the reliability of the LES method in numerical simulation of complex turbulent flows in straight ducts by comparison with experimental data.
- To analyze the mechanism of the secondary flow in a square duct.
- To establish a database of turbulent flows in a square duct for examination of statistical turbulence modellings, to analyze various statistical values and correlations, and to display visually the turbulent motion and different structures in the turbulent flow.

2 Description of Basic Theory and Numerical Method

The following basic assumptions are made: the fluid is incompressible and Newtonian; fluid properties like the kinematic and dynamic viscosity are constant; the gravitational and other external forces are ignored; in the fluid flow, the influence of heat exchange is ignored.

The governing equations of LES are obtained through filtering Navier-Stokes (NS) equations over space.

In the present paper, the box filter is used, because it has a simple and clear physical meaning:

$$G(\mathbf{r}|\mathbf{r}')=\begin{cases}\dfrac{1}{\Delta_1\Delta_2\Delta_3} & -\dfrac{\Delta i}{2}\le x_i\le\dfrac{\Delta_i}{2}\\ 0 & |x_i|>\dfrac{\Delta_i}{2}\end{cases} \tag{1}$$

where $x_i=(\mathbf{r}-\mathbf{r}')_i \quad i=1, 2, 3$

The scale of the grid is chosen as a filter scale:

$$\Delta=\sqrt[3]{\Delta V}=\sqrt[3]{\Delta x_1\Delta x_2\Delta x_3} \tag{2}$$

The physical quantities are averaged over the grid volume or over its side surfaces in the process of box filtering equations. The physical quantities (f) are divided into two parts: large-scale and small-scale parts ($\bar{f}$ and f').

The filtered NS equations, in a cartesian coordinate system are as follows:

Continuity equation

$$\begin{aligned}&(\Delta A_1^{+\Delta A_1^+}\,\overline{v_1}-\Delta A_1^{-\Delta A_1^-}\,\overline{v_1})\\&+(\Delta A_2^{+\Delta A_2^+}\,\overline{v_2}-\Delta A_2^{-\Delta A_2^-}\,\overline{v_2})\\&+(\Delta A_3^{+\Delta A_3^+}\,\overline{v_3}-\Delta A_3^{-\Delta A_3^-}\,\overline{v_3})=0\end{aligned} \tag{3}$$

Momentum equation

$$\begin{aligned}\Delta V\frac{\partial}{\partial t}{}^{\Delta V}\overline{v_i}+\sum_{l=1}^{3}&(\Delta A_l^{+\Delta A_l^+}\overline{v_l}^{\Delta A_l^+}\overline{v_i}-\Delta A_l^{-\Delta A_l^-}\overline{v_l}^{\Delta A_l^-}\overline{v_i})\\&+(\Delta A_l^{0\Delta A_l^+}\overline{p}-\Delta A_l^{0\Delta A_l^-}\overline{p})\\&-\sum_{l=1}^{3}(\Delta A_l^{+\Delta A_l^+}\overline{\tau_{il}^*}-\Delta A_l^{-\Delta A_l^-}\overline{\tau_{il}^*})=0\end{aligned}$$

$$\overline{\tau_{il}^*}=-\overline{v_i'v_l'}+\frac{1}{\mathrm{Re}}\bar{S}_{il} \tag{4}$$

where ΔA_i^+ is side surface of volume ΔV with normal direction $\mathbf{e}_i$, and ΔA_i^- with $-\mathbf{e}_i$. Moreover $v_i'v_l'$ is a second-order correlation of small-scale values. It is called the subgrid-scale (SGS) stress. These are not the second order small values in turbulence and should be calculated from large scale values by means of SGS-modeling. Here the modified Schumann's SGS-model is used, which is described in detail in Su (1993).

In the present paper the fully developed turbulent flow in a straight square duct is simulated numerically, using the coordinate system shown in Fig. 1. The cross section of the duct is a square with side H, the length of the duct is $L=4H$. In the main direction of flow, i.e., x_1-direction, the periodic condition for velocities and pressure p' ($=p-x(dp/dx)_0$) are used. The time-mean pressure gradient $(dp/dx)_0$ is given. At the walls, the velocities are zero. The initial velocity field satisfies the equation of continuity.

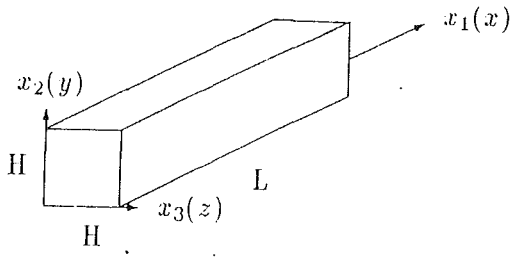

Fig. 1 Coordinate system

In the present paper the staggered grid is used. The equations of momentum are solved with an explicit "leap-frog," finite-difference scheme. The Poisson equation for the pressure is solved with a fast spectral method.

3. Numerical Results and Discussions

Outline of Computational Examples. The numerical results show that the second order correlations of fluctuating velocities at two points in main direction are nearly zero, if the distance between the two points is more than 2H. That means the chosen length of the duct is large enough to get correct results in the numerical simulation of fully developed turbulent flow in a straight duct. According to Arnal and Friedrich (1991), there is some influence of the shape of the grid cell on the computational results. Anisotropic grids produce a spurious exchange of fluctuating energy among the three velocity components. The best computational results were obtained with 'isotropic' grids for which $\Delta x_1=\Delta x_2=\Delta x_3$. The reason is that different filter widths do different filtering in the three directions. In isotropic turbulence this would obviously have an unwanted effect.

Three large-eddy simulations of the turbulent flow in a straight duct have been performed. The Reynolds number of the flow was 49000. Their parameters are as follows:

Table of parameters of LES of turbulent flow in straight duct

Case	L/H	Δx	Δy	Δz
I	4.0	0.0625	0.03125	0.03125
II	4.0	0.03125	0.03125	0.03125
III	4.0	0.015625	0.015625	0.015625

Case	number of grids	number of time steps	CPU of Cray-YMP
I	$64\times32\times32$	45500	10.8 h
II	$128\times32\times32$	52000	24 h
III	$256\times64\times64$	36000	137 h

To reduce the number of time-steps, in cases II and III, the initial fields were obtained by interpolation of the computational results of cases I and II, respectively. In the following discussion the results of case III are presented and compared with experiment.

Distribution of Mean Axial Velocity. Contours of the mean axial velocity in a cross section of the duct are compared with Gessner's (1964) experimental data (dots) in Fig. 2. Here the averaged velocity is normalized with the maximum velocity. The agreement is acceptable.

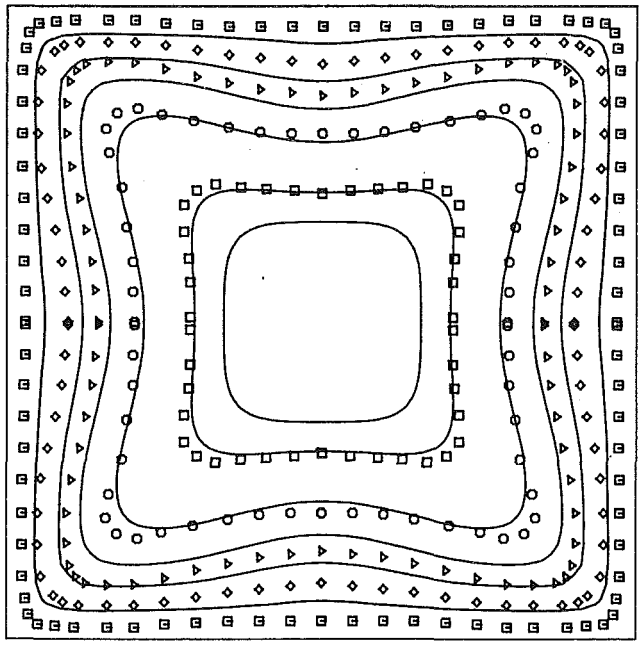

Fig. 2 Contours of averaged velocity and their comparison with Gessner's data indicated by symbols

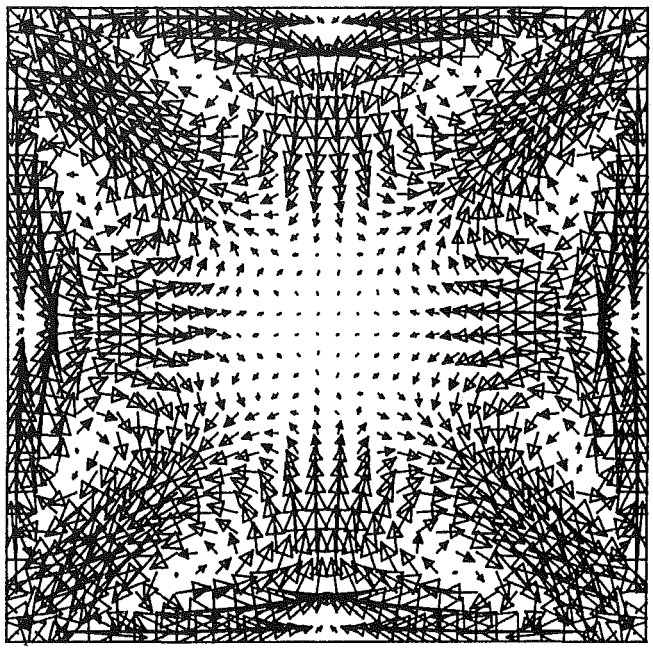

Fig. 4 Velocity vectors of the secondary flow

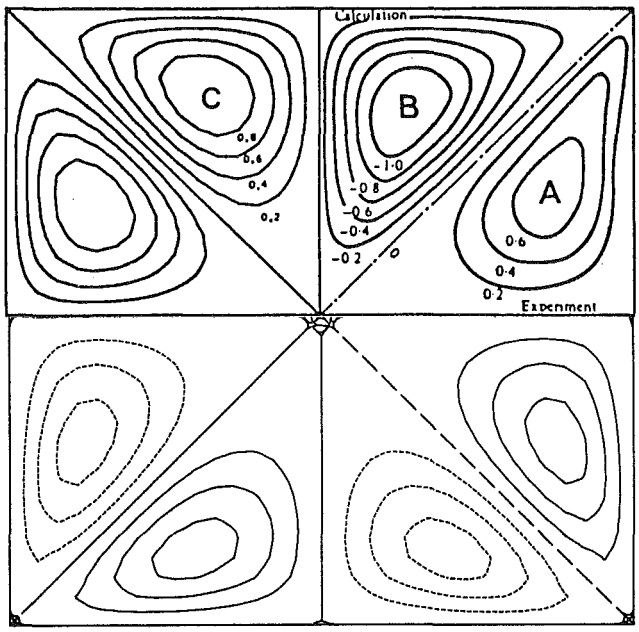

Fig. 3 Streamlines of the secondary flow (A) Gessner; (B) Nakayama; (C) Hur; other—present result

One finds that the contours of the mean axial velocity are not convex everywhere. They are deformed towards the corners of the duct. This is produced by the secondary flow in the duct. In this flow, the fluid moves from the center of the duct towards its corners. Close to the corners it turns rapidly with small radius of curvature and flows along the walls. In the center of the side wall two secondary streams meet and take a 90 deg turn towards the duct center. Thus, the eight recirculation zones of the secondary flow are formed (see Fig. 3). The momentum of the fluid is convected from the central part of the duct towards the corners. However, the fluid near the centers of the side walls is decelerated close to the stagnation line of the secondary flow. The difference between the present and Gessner's contours of the axial velocity is produced from the different Reynolds number (the present number is 49,000, Gessner's is 250,000.) Larger Reynolds numbers lead to stronger secondary flow.

Pattern of Secondary Flow and Mechanism of Its Production. The instability of an unidirectional mean axial turbulent flow and the appearance of secondary flow in the transverse plane of a pipe with noncircular cross section was first recognized by Nikuradse (1926). Many experiments have shown that the secondary flow velocities of fully developed turbulent flow in a straight square duct are small and equal to ~2–3 percent of the magnitude of the axial velocity.

In the present simulation, the secondary flow appears very clearly in the shape of eight recirculation zones (Fig. 3), it is symmetrical with four symmetry axes. In Fig. 3 a comparison between the streamlines of the secondary flow in the present simulation and those in experimental measurement and numerical predictions (A) Gessner (1964), (B) Nakayama (1988), and (C) Hur (1988)) is shown. There is good agreement among all the data. A vector plot is presented in Fig. 4.

In the following, the mechanism for the development of the secondary flow is discussed using the results obtained in the present large eddy simulation. The time averaged velocity field of the fully developed turbulent flow in a straight duct is quasi-steady and two dimensional.

The mean longitudinal vorticity satisfies the following differential equation:

$$\langle v\rangle \frac{\partial\langle\omega_x\rangle}{\partial y}+\langle w\rangle \frac{\partial\langle\omega_x\rangle}{\partial z}=\nu\left(\frac{\partial^2\langle\omega_x\rangle}{\partial y^2}+\frac{\partial^2\langle\omega_x\rangle}{\partial z^2}\right) -\frac{\partial^2(\langle\tilde{w}\tilde{w}\rangle-\langle\tilde{v}\tilde{v}\rangle)}{\partial y\partial z}-\frac{\partial^2\langle\tilde{v}\tilde{w}\rangle}{\partial y^2}+\frac{\partial^2\langle\tilde{v}\tilde{w}\rangle}{\partial z^2} \quad (5)$$

where $(\tilde{\cdot})=(\cdot)-\langle(\cdot)\rangle$, $\langle\cdot\rangle$ is the time averaged value. In fully developed laminar flow, $\langle\tilde{v}\tilde{v}\rangle=0$, $\langle\tilde{w}\tilde{w}\rangle=0$ and $\langle\tilde{v}\tilde{w}\rangle=0$, so that $\langle\omega_x\rangle=0$, that means there is no secondary flow in the laminar case. In fully developed turbulent flow, the existence of a secondary flow is directly tied to the presence of a nonzero axial mean vorticity $\langle\omega_x\rangle$. The axial vorticity source term in (5) given by

$$\frac{\partial^2(\langle\tilde{w}\tilde{w}\rangle-\langle\tilde{v}\tilde{v}\rangle)}{\partial y\partial z}+\frac{\partial^2\langle\tilde{v}\tilde{w}\rangle}{\partial y^2}-\frac{\partial^2\langle\tilde{v}\tilde{w}\rangle}{\partial z^2}$$

is the cause of the secondary flow. The pressure $\langle p\rangle$ is divided

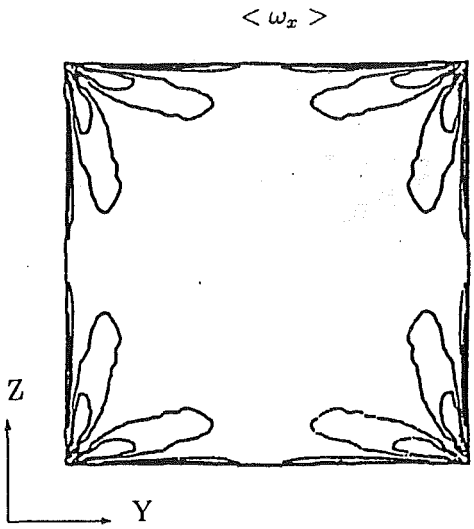

Fig. 5 Contours of $\langle\omega\rangle_x$

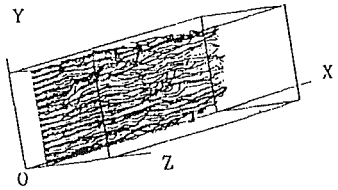

Fig. 6 Streaklines of fluid particles

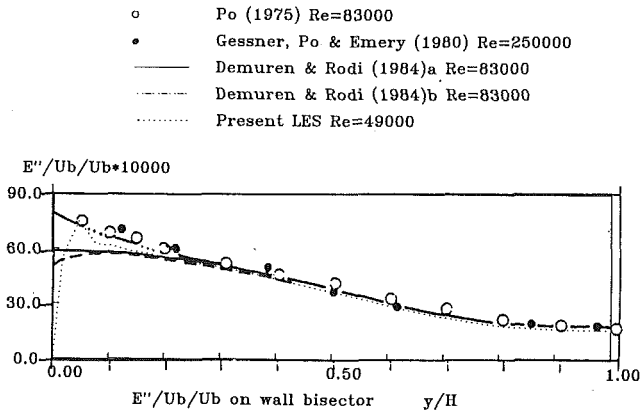

Fig. 7(a)

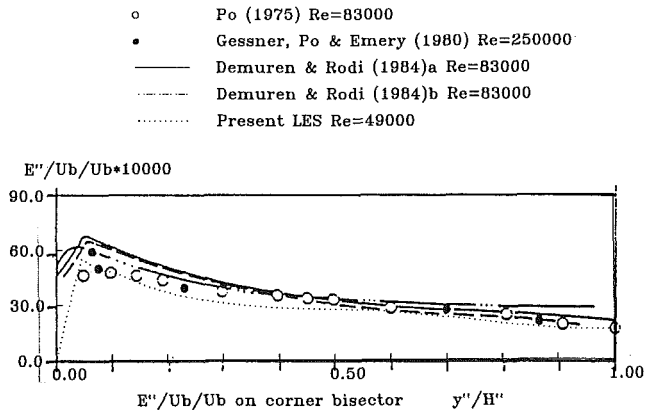

Fig. 7(b)

Fig. 7 Profile of turbulence kinetic energy along (*a*) wall bisector and (*b*) corner bisector

into $\langle p\rangle_N$ attributed to the normal stress $(-\partial\langle\tilde{v}\tilde{v}\rangle / \partial y, -\partial\langle\tilde{w}\tilde{w}\rangle / \partial z)$ and $\langle p\rangle_S$ attributed to the shear stress $(-\partial\langle\tilde{v}\tilde{w}\rangle/\partial z, -\partial\langle\tilde{v}\tilde{w}\rangle/\partial y)$. They can be determined by solving the following Poisson equation:

$$\frac{\partial^2\langle p\rangle_N}{\partial y^2}+\frac{\partial\langle p\rangle_N}{\partial z^2}=-\frac{\partial^2\langle\tilde{v}\tilde{v}\rangle}{\partial y^2}-\frac{\partial^2\langle\tilde{w}\tilde{w}\rangle}{\partial z^2} \tag{6}$$

$$\frac{\partial^2\langle p\rangle_S}{\partial y^2}+\frac{\partial^2\langle p\rangle_S}{\partial z^2}=-2\frac{\partial^2\langle\tilde{v}\tilde{w}\rangle}{\partial y\partial z} \tag{7}$$

The calculated results of these two pressure fields show that the pressure $\langle p\rangle_S$ is very small, so that one can conclude that the secondary flow is generated essentially by the gradient of the normal turbulent stresses.

Contours of ω_x are displayed in Fig. 5. They show that the driving forces for the secondary motion are concentrated in regions close to the four corners. These conclusions agree with the Speziale (1982) analysis and Miyake and Kajishima's (1991) discussion.

Motion of Particles in Duct. To visualize the turbulent flow, streaklines are computed. They can be compared with photos, obtained from visualization experiments. Streaklines are shown in Fig. 6.

Distributions of Turbulence Kinetic Energy and Reynolds Stresses. In Figs. 7 and 8, the numerical and measured profiles of the turbulent kinetic energy $\langle\tilde{E}\rangle$ and the Reynolds stress $\langle\tilde{u}\tilde{v}\rangle$ along the wall- and corner-bisectors are compared. They show that the agreement is fairly good, but there are certain discrepancies near the wall and the corner. The present LES results are closer to the experiment than the results obtained with turbulence models, especially in the vicinity of the side walls. As we know, most of the turbulent kinetic energy is produced in the buffer layer close to the wall. In this region the turbulent kinetic energy $\langle\tilde{E}\rangle$ and the Reynolds stress $\langle\tilde{u}\tilde{w}\rangle$ have their maximum values. Therefore it is necessary to choose an appropriate turbulence model and a numerical approach to correctly simulate this region.

The contours of the Reynolds stress $\langle\tilde{u}\tilde{w}\rangle$, which are obtained by the present simulation are compared in Fig. 9 with those of Hur (1988) and Myong (1988). The agreement among these results is quite good.

4 Examination of Phenomenological Turbulence Models With LES-Database

The fully developed turbulent flow in a straight duct was predicted by numerous authors through different statistical turbulence models. These turbulence models were developed by means of phenomenology and experimental data. Many unmeasurable values, for example, correlations between fluctuating pressure and velocity, are calculated with empirical formulae in turbulence models.

There are also numerous empirical constants in these models, which are determined from experimental data or numerical experience. The correctness of the turbulence models can be examined with the help of experiments or high-level numerical simulations: Large Eddy Simulation (LES) and Direct Numerical Simulation (DNS).

In this paper the database obtained from LES is used to examine Launder, Reece and Rodi's turbulence model (LRR-model), (Demuren and Rodi's work 1984). Consistent with the local equilibrium assumption, they assume equality between production P and dissipation ϵ of turbulent kinetic energy. According to this assumption, the following simplified formula is obtained:

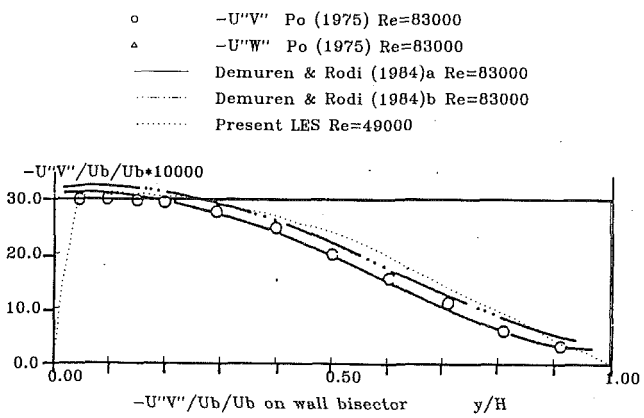

Fig. 8(*a*)

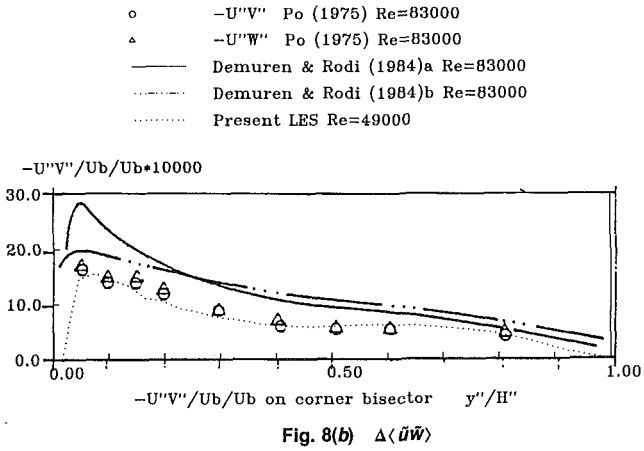

Fig. 8(*b*) $\Delta\langle\tilde{u}\tilde{w}\rangle$

Fig. 8 Profile of turbulence Reynolds stress $\langle\tilde{u}\tilde{v}\rangle$ along (*a*) wall bisector and (*b*) corner bisector

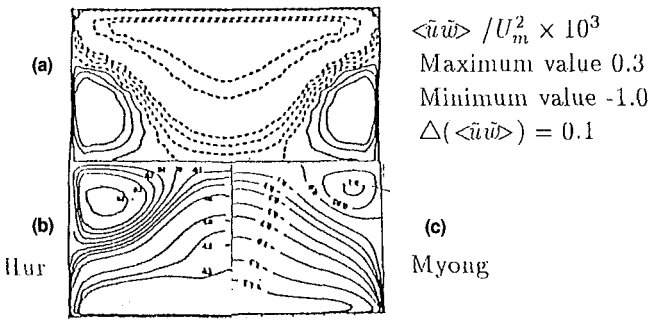

Fig. 9 Contours of $\langle\tilde{u}\tilde{w}\rangle$. $\langle\tilde{u}\tilde{w}\rangle/U_m^2 \times 10^3$. Maximum value 0.3, minimum value −1.0, $\Delta(\langle\tilde{u}\tilde{w}\rangle) = 0.1$. (*a*) present, (*b*) Hur (1988), and (*c*) Myong (1988)

$$(1-\alpha)\left(-\overline{\tilde{u}_i\tilde{u}_l}\frac{\partial V_j}{\partial x_l}-\overline{\tilde{u}_j\tilde{u}_l}\frac{\partial V_i}{\partial x_l}\right)$$
$$-\beta\left(-\overline{\tilde{u}_i\tilde{u}_l}\frac{\partial V_l}{\partial x_j}-\overline{\tilde{u}_j\tilde{u}_l}\frac{\partial V_l}{\partial x_i}\right)-\gamma k\left(\frac{\partial V_j}{\partial x_i}+\frac{\partial V_i}{\partial x_j}\right)$$
$$-\frac{\epsilon}{k}\left[c_1\,\overline{\tilde{u}_i\tilde{u}_j}+\frac{2}{3}(1-\alpha-\beta-c_1)\delta_{ij}k\right]=0 \quad (8)$$

where k is the turbulent kinetic energy, ϵ the dissipation of turbulent kinetic energy. The overbar denotes statistical averages. V_i is the mean velocity. Constants are defined as follows:

$$\alpha=0.7636-0.06f,\ \gamma=0.182,\ \beta=0.1091+0.06f,$$
$$c_1=1.5-0.50f$$

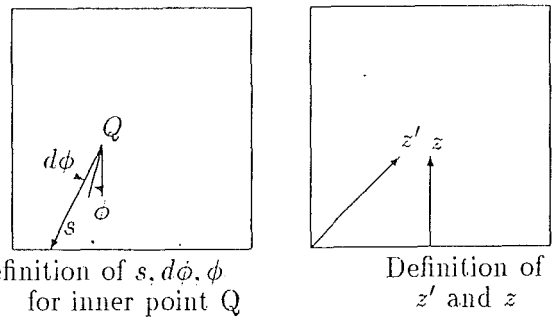

Fig. 10 Definition of s, $d\phi$, ϕ for inner point Q; definition of z' and z

where f is a function of the dimensionless wall distance. Demuren and Rodi use two different wall-damping functions: namely, a linear and a quadratic one

$$f=\frac{L}{\langle y^n\rangle},\ \text{with}\ \frac{1}{\langle y^n\rangle}=a\int_0^{2\pi}\frac{d\phi}{s^n}. \quad (9)$$

with $n=1$, $a=1/2$ and $n=2$, $a=2/\pi$. The lengthscale L is determined from $L = (c_\mu^{3/4}/\kappa) \cdot (K^{3/2}/\epsilon)$. The coefficient $c_\mu^{3/4}/\kappa$ in this definition of L has been chosen so that f takes the value of unity in regions near plane walls. s is the distance from the considered point to the surrounding surfaces, see Fig. 10.

From the velocity correlation appearing in the last bracketed term in Eq. (8), the individual stress components can be obtained, and are given in Demuren and Rodi (1984).

$$\underbrace{\frac{Dk}{Dt}\equiv V_2\frac{\partial k}{\partial x_2}}_{\text{Convection of } k}$$

$$\underbrace{-\frac{\partial}{\partial x_l}\overline{\tilde{u}_l\left(\frac{\tilde{p}}{\rho}+\frac{1}{2}\overline{\tilde{u}_i\tilde{u}_i}\right)}}_{\text{Pressure and convective diffusion of } k}\ \underbrace{-\ \overline{\tilde{u}_i\tilde{u}_k}\frac{\partial U_k}{\partial x_l}}_{\text{Production of } k}$$

$$\underbrace{+\nu\frac{\partial}{\partial x_l}\overline{u_k\left(\frac{\partial\tilde{u}_k}{\partial x_l}\right)}}_{\text{Viscous diffusion}}\ \underbrace{-\nu\overline{\frac{\partial\tilde{u}_k}{\partial x_l}\left(\frac{\partial\tilde{u}_l}{\partial x_k}+\frac{\partial\tilde{u}_k}{\partial x_l}\right)}}_{\text{Dissipation of } k} \quad (10)$$

In this equation the left-hand term and the first three right-hand terms can be calculated in the large eddy simulation. For high Reynolds number flows the viscous diffusion term in the region far from wall is negligible and thus the dissipation of k can be computed.

The result of calculation shows that the production of k is roughly equal to the dissipation of k in the greatest part of the flow field. Therefore this result is in agreement with Demuren and Rodi's assumption. So that in the calculation, the dissipation of k can be replaced by the production of k.

In the calculation of the function f, it is found that the decline of the dissipation of k from the near wall region to the central region of the duct is faster than the decline of k. Thus, it is impossible that the function f has a value of unity in the near-wall region and a value of zero as the point remotes from the walls, because the value of $k^{3/2}/\epsilon$ does not tend to zero, but it is large in the central region of the duct. Here the value

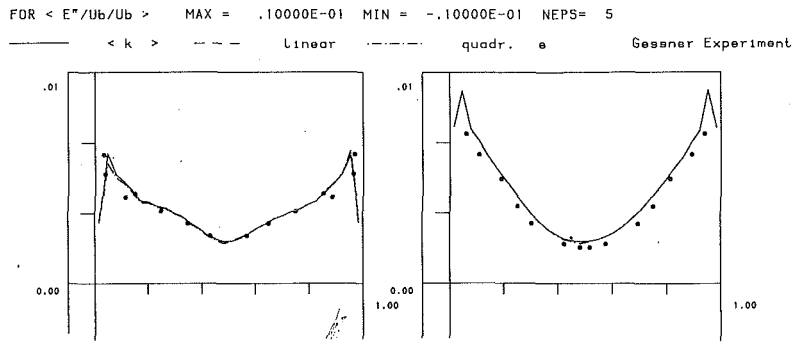

Fig. 11(*a*) *k* versus z'/H'; *z/H* (right)

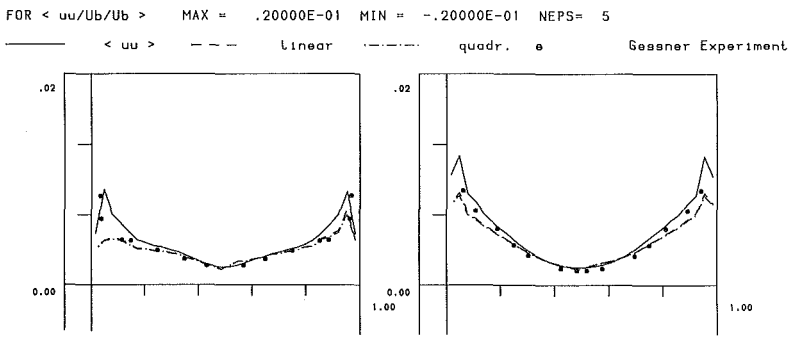

Fig. 11(*b*) $\langle \overline{uu} \rangle$ versus z'/H'; *z/H* (right)

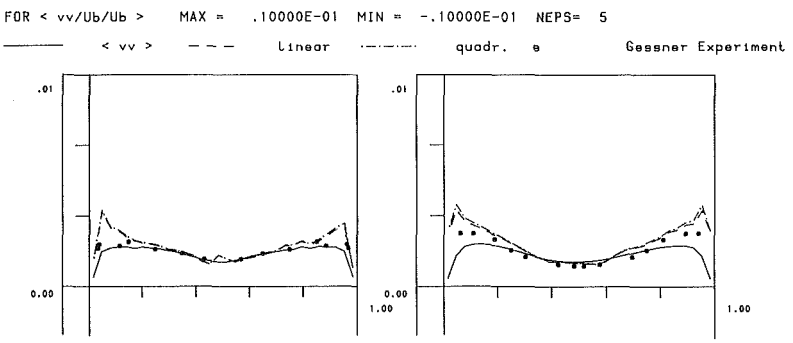

Fig. 11(*c*) $\langle \overline{vv} \rangle$ versus z'/H'; *z/H* (right)

of $\langle y \rangle$ at the nearest-corner point is chosen as L for linear relationship, and the value of $\langle y^2 \rangle$ as L^2 for quadratic relationship.

Using the above-mentioned function f and the time-averaged values of the LES-database, the predicted Reynolds stresses can be evaluated using the individual stress component equation of Demuren and Rodi (1984). These results are compared with the LES and the experimental data in Figs. 11(*a*)–(*e*).

Figure 11(*a*) shows that the distributions of k from LES and predicted results are almost identical. Figures 11(*b*) and (*c*) show that in the distributions of the turbulent kinetic energy in two different directions there are differences among predicted, LES results and experimental data.

Figures 11(*d*) and (*e*) show the distributions of $\langle \tilde{u}\tilde{v} \rangle$, $\langle \tilde{u}\tilde{w} \rangle$. The agreement between the LES result and the experimental data is better than that between the predicted result and the experimental data. The difference between the predicted result and the experimental data becomes more distinct near the wall and corner.

5 Distribution of the Inclination Angle of the Vorticity Vector

As Moin and Kim (1985) pointed out, the distribution of the inclination angle of the vorticity vector is one of the relevant quantities for the determination of the vorticity structure in a turbulent flow. The present method to obtain this distribution is different from Moin and Kim's method. The duct is divided into four parts (four triangular prisms) by two diagonal planes. Every part contains a side wall of the duct. The inclination angle θ is defined as an angle between the neighboring wall of the considered point and the projection of the vorticity vector into the plane normal to this wall and parallel to the duct's axis. The inclination angle ψ is defined as an angle between the projection of the vorticity vector onto the duct's cross section (y, z)-plane and the neighboring wall of the considered point. The statistics are carried out along 8 lines parallel to the axial direction. Every eight lines constitute a group. They have four symmetry planes: horizontal and vertical planes through the axis of duct as well as two diagonal planes of the duct.

The results of the statistics are shown in Figs. 12 and 13. The histogram at each line group (with eight lines) is generated by calculating the angle θ at all the grid points. The contribution of each grid point is weighted with the magnitude of the vorticity vector. y and z in Figs. 12 and 13 are coordinates of one line in a group.

From the distribution of θ, one can find that there are two

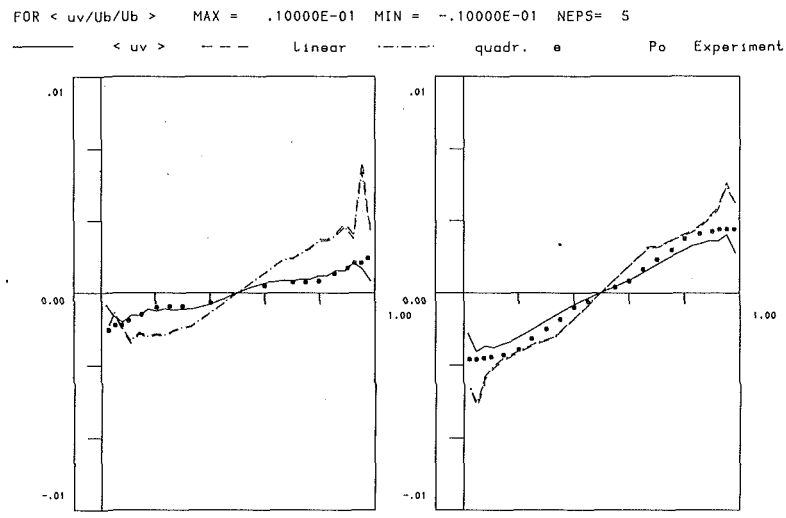

Fig. 11(*d*) $\langle \overline{uv} \rangle$ versus z'/H'; z/H (right)

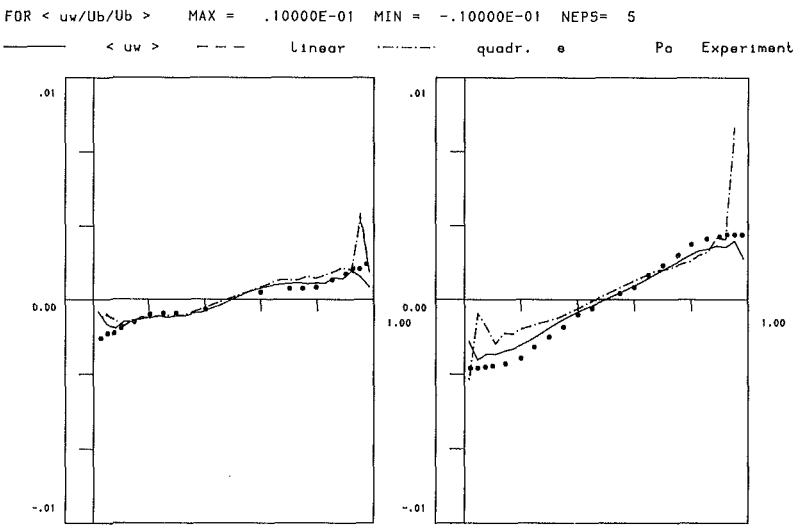

Fig. 11(*e*) $\langle \overline{uw} \rangle$ versus z'/H'; z/H (right)

Fig. 11 Comparison between prediction/LES/experiment (solid line: LES)

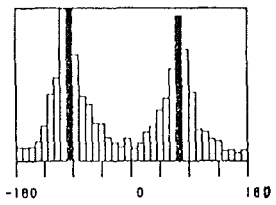

a) $z = \frac{1}{32}H, y = \frac{1}{2}H;$

Fig. 12(*a*) $z = 1/32$ *H*, $y = 1/2$ *H*;

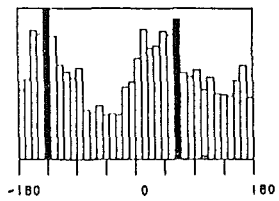

b) $z = \frac{1}{2}H, y = \frac{1}{2}H;$

Fig. 12(*b*) $z = 1/2$ *H*; $y = 1/2$ *H*;

Fig. 12 Distribution of θ along different line-groups

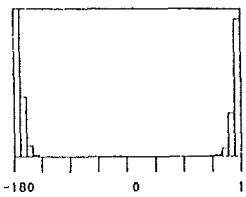

a) $z = \frac{1}{32}H, y = \frac{1}{2}H;$

Fig. 13(*a*) $z = 1/32$ *H*, $y = 1/2$ *H*;

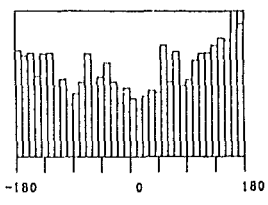

b) $z = \frac{1}{2}H, y = \frac{1}{2}H;$

Fig. 13(*b*) $z = 1/2$ *H*, $y = 1/2$ *H*.

Fig. 13 Distribution of ψ along different line-groups

peaks for every group. The positions of the two peaks for all groups are almost in regions from 45 to 90 deg and from -90 to 135 deg, and the distance between the positions of the two peaks is nearly 180 deg. That means the vorticity vectors of higher strength can be found between planes inclined from 45 to 90 deg. At distances $z = 1/32$ H from their neighboring walls, the vorticity vectors of higher strength have a greater tendency to occur in planes inclined at 80 or -100 deg to the neighboring walls. With the increase of the distance between the lines and their neighboring walls, this angle varies in the region from 45 to 90 deg or from -90 to -135 deg. For the fully developed turbulent flow in a straight channel, the principal axes of the mean-strain-rate tensor, S_{ij}, are inclined at 45 deg to the neighboring walls. For the fully developed turbulent flow in a straight duct, the principal axes of the mean-strain-rate tensor, S_{ij}, are not inclined at 45 deg but at a variable angle to the neighboring wall due to the existence of the side walls.

The inclination angles between the projections of vorticity vectors into (y, z)- planes and the neighboring walls, i.e., ψ were also calculated. In the vicinity of the wall, the distribution

of ψ has a peak, which is close to 180 deg (or -180 deg). Away from the wall, the distributions become broader. However, the concentration of vorticity vectors pointing in the spanwise direction (the direction of the mean-vortex lines) remains appreciable until the normal distance $n \sim 0.35\,H$. The distribution shows symmetry about $\psi = 0$ approximately. In the center of the duct, the peak is smeared.

The above study shows that the information about the structure of the flow that can be extracted is useful, but limited. Nevertheless, horseshoe-vortices were found as well as other kinds of vorticity lines. A detailed discussion can be found in Su (1993).

5 Conclusions

From the investigations the following conclusions can be obtained:

- The agreement between experimental data and LES results shows that the method of LES with a modified Schumann SGS model can be used to predict the various features of the turbulent flow with fair accuracy.
- Although the secondary motion is very weak and varies sensitively with the geometry of ducts and Reynolds number, the numerical simulation can describe it clearly. In addition, the cause of the production of the secondary flow can be explained through the analysis of the database produced with the numerical simulation.
- The comparison between LES and Demuren-Rodi's result shows that the LES method is a more promising approach.
- In the regions, which are near side-walls but far away from corners, the turbulent structure is similar to that of turbulent flow in a straight channel.

The work reported here was sponsored by the Deutsche Forschungsgemeinshaft (DFG). The first author would like to thank the referees for their comments, which has led to substantial improvement of the manuscript.

References

Arnal, M., and Friedrich, R., "Large-Eddy Simulation of a Turbulent Flow with Separation," Notes on Numerical Fluid Mechanics, (1991), Vieweg Verlag.

Brundett, E., and Baines, W. D., "The Production and Diffusion of Vorticity in the Duct Flow," *J. Fluid Mech.*, (1964), Vol. 19, pp. 375–394.

Demuren, A. O., and Rodi, W., "Calculation of Turbulence-Driven Secondary Motion in Non-Circular Ducts," *Journal of Fluid Mechanics*, (1984), Vol. 140, pp. 189–222.

Gessner, F. B., "Turbulence and Mean-Flow Characteristics of Fully Developed Flow in Rectangular Channels," Ph.D. Thesis, Dept. Mech. Engng. Purdue University (1964).

Gessner, F. B., and Emery, A. F., "A Length-Scale Model for Developing Turbulent Flow in a Rectangular Duct," ASME JOURNAL OF FLUIDS ENGINEERING, (1981), Vol. 103, pp. 445–455.

Hur, N., "Numerical Study of Secondary Flows in Curved Ducts," Ph.D. thesis, Stevens Institute of Technology, April (1988).

Kline, A., "Review: Turbulent Developing Pipe Flow," ASME JOURNAL OF FLUIDS ENGINEERING (1981), Vol. 103, pp. 243–249.

Madabhushi, R. K., and Vanka, S. P., "Large-Eddy Simulation on Turbulence-Driven Secondary Flow in a Square Duct," *Physics & Fluids* (1991), A., Vol. 3 (11), pp. 2734–2745.

Miyake, Y., and Kajishima, T., "Explanation of the Origin of the Secondary Flow in a Straight Square Duct on the Basis of LES," *Separated Flows and Jets*, V. V. Kozlov, A. V. Dovgal, eds., Springer-Verlag, Heidelberg, 1991, pp. 149–152.

Moin, P., and Kim, J., "Numerical Investigation of Turbulent Channel Flow," *Journal of Fluid Mechanics*, (1985), Vol. 155, pp. 441–464.

Myong, H. K., "Fundamental Studies on Two-Equation Turbulence Model for Numerical Predictions of Wall-Bounded Shear Flow and Heat Transfer," Dr. Eng. thesis, the University of Tokyo, Tokyo, (1988).

Nakayama, A., "Three-Dimensional Flow Within Conducts of Arbitrary Geometrical Configurations," Ph.D. thesis, University of Illinois at U-C (1988).

Naot, D., and Rodi, W., "Numerical Simulations of Secondary Currents in Channel Flow," *Journal of Hydraulics Division*, ASCE (1982), Vol. 7, p. 151.

Nikuradse, J. V. D. I., Forschungsheft, (1926), Heft 70, p. 1229.

Po, J. K., "Developing Turbulent Flow in the Entrance Region of a Square Duct," MS thesis, University of Washington (1975).

Speziale, C. G., "On Turbulent Secondary Flows in Pipes of Noncircular Cross-Section," *International Journal of Engineering Science*, Vol. 20, No. 7, (1982), pp. 863–872.

Su, M. D., "Large-Eddy-Simulation Vollentwickelter Turbulenter Strömungen in Kanälen ohne und mit Längskrümmung," Dissertation in der TUM, Maschinenwesen (1993).

Velocity Characteristics of a Confined Highly-Turbulent Swirling Flow Near a Swirl Plate

(Data Bank Contribution*)

R. X. Shi
Graduate Student. Currently, Engineer, Navistar International Corp., Melrose Park, IL

B. Chehroudi
Assistant Professor.

UIC Engine Laboratory, Department of Mechanical Engineering, University of Illinois at Chicago, P. O. Box 4348, M/C 251, Chicago, IL 60680

Axial and tangential components of the velocity vector are measured using a Laser Doppler Velocimeter (LDV) system in a confined highly turbulent isothermal swirling flow near a swirl plate. The flow has essential features of swirl-stabilized flame combustors. Throughout this study, a constant "nominal" swirl number of 0.36 is generated by air jets from a set of slots in a swirl plate. A low-speed coflowing air, referred to as dilution air, is uniformly distributed around the swirling flow by use of an annular-shaped honeycomb. Three different swirling air flow rates with a fixed dilution flow rate are studied and results are discussed. Detailed mean axial and tangential velocity profiles at several axial locations show that the size and the strength of the central recirculation zone are strongly dependent on the swirling air flow rate. Increasing the swirl air flow rate increases both the radial extent and the axial length of the central recirculation zone. Mean total and reversed air flow rates are calculated by integrating the mean axial velocity profiles. In the setup used in this study and up to the axial positions investigated, the reversed flow rate as a percent of the total flow rate seems to be linearly proportional to the reversed-flow zone area, being independent of the swirl air flow rate at a fixed nominal swirl number value. As swirl air flow rate is increased, the root mean square (rms) of the axial and tangential velocity fluctuations increase monotonically at almost all radial positions except sufficiently away from the swirl plate and near the chamber axis. Several velocity biasing correction methods are reviewed. A simple velocity biasing correction scheme is applied in this study to investigate its effect on the conclusions reached in the study.

1 Introduction

Swirling flows have many practical engineering applications such as in gas turbine engines, industrial furnaces, diesel engines, boilers, etc. In these combustion systems, swirl is a major contributor to improved combustion efficiency, enhanced flame stabilization, better fuel-air mixing, improved blow-off limits, and lower pollutant formation. Due to its importance, there have been experimental and theoretical investigations on swirling flows in a variety of applications and geometries. Our emphasis in this paper is the swirling flows of relevance to furnaces, oil burners, and gas turbine combustors. Many of these works are summarized by Gupta et al. (1984). In these studies different chamber geometries and swirl generation designs were considered by researchers. For example see, Khalil et al. (1977), Habib and Whitelaw (1979), Fujii et al. (1981), Vu and Gouldin (1982), Gouldin et al. (1985), Altgeld et al. (1983), Ramos and Somer (1985), Heitor and Whitelaw (1986), Brum and Samuelsen (1987), Samimy and Langenfeld (1988), and Nejad et al. (1989). In these works, although many conclusions were apparatus-specific, several general observations were also made. In particular, swirling flow was found to generate flow reversal or tendency for flow reversal at some distance from the swirling jet exit plane. The strength and size of the recirculation zone were greatly dependent on the "swirl number." Swirl number is a nondimensionalized parameter equal to the axial flux of the swirl momentum divided by the axial flux of axial momentum, times the equivalent swirler (or nozzle) radius, see Gupta et al. (1984). The higher the swirl number, the stronger and larger the recirculation zones become. The character and the size of the recirculation zone have important effects on flame stabilization in these combustors. The recirculated mass flow rate was shown to be proportional to the swirl number. Tangential (or swirl) velocity profiles showed forced vortex behavior inside the "central" recirculation zone and nearly free vortex outside of it. Combustion was also found to greatly affect the formation of the recirculation zone and to increase the turbulence intensity. In most

*Data have been deposited to the JFE Data Bank. To access the file for this paper, see instructions on p. 892 of this issue.

Contributed by the Fluids Engineering Division for publication in the JOURNAL OF FLUIDS ENGINEERING. Manuscript received by the Fluids Engineering Division May 24, 1993; revised manuscript received March 21, 1994. Associate Technical Editor: M. Gharib.

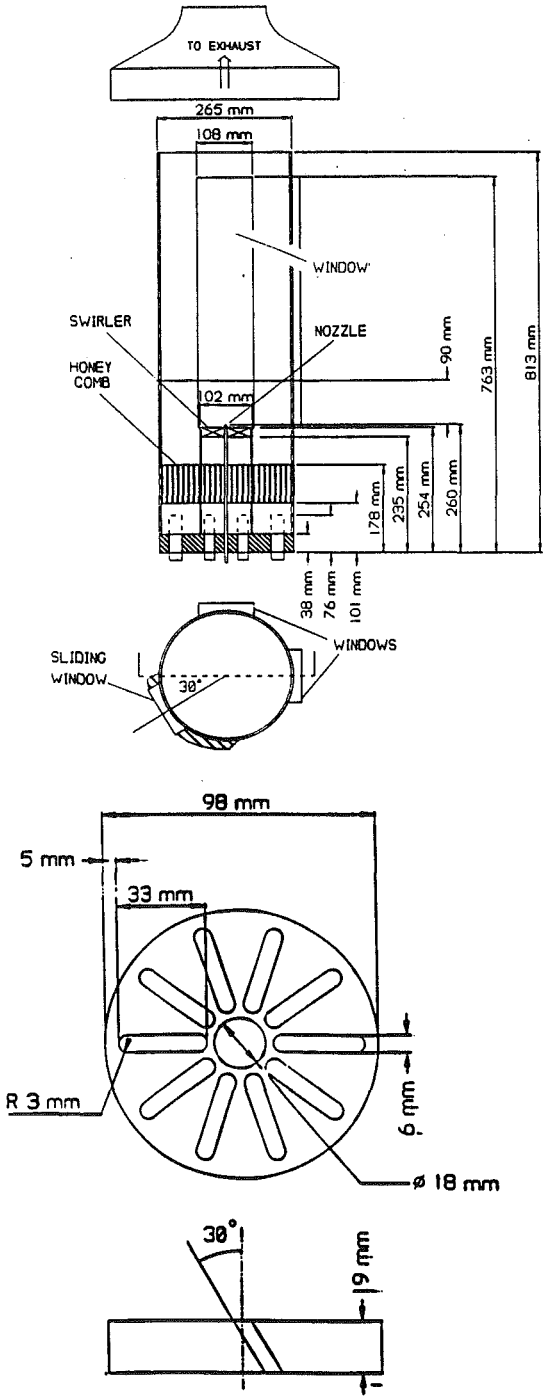

Fig. 1 Schematic of the test rig and the swirl pate

cases, combustion made the recirculation zone stronger and wider in radial direction as compared to the isothermal cases. LDV was generally used because of the nonintrusive nature of the measurement and the existence of flow reversal.

Swirlers are generally designed considering manufacturing, economical, and application factors. In this paper, we would like to report experimental results and observations near a particular design of a swirl "plate." The employed design simulates a class of simple swirlers used in swirl-stabilized combustors such as oil burners and furnaces. Here, the main objective is to understand the effects of "swirl flow rate" at a constant nominal swirl number on the flow field near the swirl plate in a model swirl-stabilized combustor configuration possessing important features of practical combustors which have swirl, high turbulence intensity, and flow recirculation. Test conditions and, in particular, measurement positions were chosen such that these results provide assistance in understanding the effects of swirl flow rate, combustion, and droplet/air interaction in our current and future efforts on liquid fuel spray combustion using the same chamber, see Chehroudi and Ghaffarpour (1991), (1992), and (1993)(*a*),(*b*).

2 Experiment

2.1 Experimental Setup. The combustor used in this study is identical to the one used by Chehroudi and Ghaffarpour (1991), (1992), and (1993)(*a*),(*b*). A somewhat self-explanatory schematic drawing of the combustor is shown in Fig. 1. Compressed air is ducted through regulators and filters and divides into two passages, one for swirl air (the inner 216 mm long by 102 mm diameter pipe) and the other for low-speed co-flowing air referred to as dilution air (annular region within the outer and inner pipes). For more details on the rig refer to the aforementioned references where it was used.

For the swirling air, a swirl plate is located just inside the upper edge of the inner cylinder. There are ten radial slots of 33 mm in length and 6 mm in width equally spaced tangentially, see Fig. 1. Each slot produces 30 degree exit velocity jet with respect to the chamber axis. The central hole in this plate is where the fuel nozzle is positioned. This swirl plate design is similar to and simulates what is employed in some industrial furnaces and oil burners. Looking from the top, the swirl plate slots generate a clockwise swirling flow with a calculated nominal swirl number of about 0.36. The slot width/length ratio is about 0.27, ensuring that the air jet angle from each slot is the same as the one for the slot itself (i.e., 30 deg to the vertical axial in Fig. 1), see Gupta et al. (1984). Note that for a given swirl plate design, assuming a uniform velocity profile (plug flow) for the slot jets, the swirl number is only dependent on the swirl plate geometry and not the "swirl flow rate." In fact, the herein reported swirl number referred to as nominal is based on these assumptions, see Beer and Chigier (1972). The actual swirl number does change with the swirl flow rate to some degree. However, various type of swirl numbers calculated on a different basis using different measurements and different assumptions provided a reasonably fair agreement, see Kihm et al. (1990). In this work the above-mentioned swirl plate design was selected since it produced the widest stable flame region in our chamber. The effects of "swirl flow rate" were then investigated near the plate (with a fuel nozzle in place but no fuel spray injection) at a constant nominal swirl number value of 0.36.

2.2 Measurement System. The measurement system in this study includes: A TSI LDV system model 9100-7, a TSI optical table model 9127 with a motorized control system, a a LEXEL Ion Laser model 95, a TSI counter-type signal processor model 1990B (+/−1 nanosecond resolution), a lab interface box and a 386 IBM compatible PC for data acquisition and analysis. A 3.75X beam expander was employed to obtain a smaller measurement volume providing a higher signal-to-noise ratio. Fringe spacing of 1.90 μm with +/− 0.1 % accuracy was produced in the measurement volume with 70 μm in diameter and 508 μm in length. Back scattering system was used throughout the measurements with a collecting lens of 152 mm O.D. and 480 mm focal length. This arrangement was used because of geometrical constraints imposed by other optical setups, see Chehroudi and Ghaffarpour (1991), (1992), (1993)(*a*). A Bragg cell provided frequency shift of 40 Mhz on one beam to cause directional sensitivity and minimize LDV fringe bias. Frequency mixer was bypassed upon parametric study (to obtain optimum counter and photomultiplier tube settings) since it was found to introduce noise into the system. The high low pass filters are set at 20 and 50 Mhz respectively. Sixty-four number of cycles were used for counting process with percent comparison of 7 percent. Cumulative uncertainty

(due to counter processor resolution, fringe spacing calculation, digital data acquisition, and Bragg cell frequency) of an individual measurement was estimated to be less than about 1 percent. Total sample data changed between minimum of 1000 to maximum of 3000 depending on the measurement position. Total acquisition time per position was limited to maximum of five minutes. Velocity Probability Distribution Function (PDF) was constructed and data points beyond 3.5 standard diviations was rejected. The statistical uncertainties were estimated to about $+/-3$ percent and $+/-$ 7 percent for the mean and rms of velocity fluctutations, respectively. Use of 40 Mhz frequency shifting with 0.01 percent accuracy decreases the accuracy for small velocities. The resolution of small velocity measurement was estimated to be approximately 0.06 m/s. For example, a 1 m/s velocity can be measured with about 6 percent accuracy. Digital output of the TSI counter processor was interfaced to an IBM-compatible PC for fast data acquisition and analysis. Data acquisition and processing programs were from Yas Diagnostics Inc. using Fortran and Assembly languages. A seeder similar to the one used by Chehroudi (1983) was constructed to provide stable and uniform seeds in the flow field. A seed rate of about 100 seeds per second in the measurement volume is estimated from the geometry and speed of the eletrical motor. Seed was titanium dioxide powder with average size of less than 1 μm.

3 Results and Discussions

Both axial and tangential velocity profiles were measured at six different axial locations (z = 15, 25, 40, 55, 70, 90 mm from the tip of the fuel nozzle). These axial positions were chosen to coincide with measurements of Chehroudi and Ghaffarpour (1991), (1992), (1993) when liquid fuel spray injection and combustion were considered. In addition, they found no liquid fuel droplets at distances higher than the 90 mm with combustion, hence no droplet/air interaction exists above this position. At each axial position, the horizontal traverse line of the measurement volume was located in a vertical plane that includes the chamber axis and passes through the middle of two slots on the swirl plate. Three-different swirl air flow rates, referred to as "high," "medium,"and "low," were used to investigate effects of the swirling air flow rate on the flow field inside the combustor. Dilution volumetric air flow rate (at atmospheric condition) was fixed at 1.55 m^3/min. Swirl air flow rates of 3.7, 2.9, and 1.41 m^3/min were used for this study. The accuracy of these values are to within $+/-$ 2.5 percent of the readings. These flow rates were chosen since high (3.7 m^3/min) and "low" (1.41 m^3/min) swirl flow rates corresponded to the boundary beyond which flame could not exist in this combustor as reported by Chehroudi and Ghaffarpour (1993). The character of the flame and the nature of its instability near the high and low swirl flow rates were found to be different. The medium swirl (2.9 m^3/min) case was for the most stable flame condition observed by them at the dilution flow rate mentioned above.

3.1 Velocity Profiles. Figure 2 shows radial profiles of the mean and rms of axial velocity fluctuations at six axial locations and with three different swirl air flow rates. In the initial measurements, results were collected on both sides of the geometrical axis at each axial position to investigate flow symmetry in the "measurement plane." However, this practice was not continued due to time constraint, difficulty in reaching far radial distances, and the finding that profiles looked fairly symmetric particularly for positions beyond 15 mm. Laser sheet visualization passing through the geometrical axis at several different orientations also showed good flow symmetry in the plane of the laser sheet. Flow reversal (negative mean axial velocity) is seen around the centerline at all conditions except at z = 15 mm for the low swirl air flow rate case. The right margin in these plots is the position of the combustor inner side walls. Extrapolating the results, it seems that, in some cases, a small negative velocity appears to exist near the chamber inner side walls. This is because dilution-flow mean axial momentum is not large enough to overcome or influence the pressure gradient pattern created by the strong swirling flow. Based on the uniform inlet velocity profile assumption, a 1.55 m^3/min dilution air flow rate can only produce 0.62 m/s air velocity, while the "medium" swirl air flow rate of 2.9 m^3/min has an slot exit axial air velocity of 29.4 m/s, which is much higher than the 0.62 m/s.

The two peaks in the mean axial velocity profiles at z = 15 mm and also the tendency of a twin-peak in that of z = 25 mm are due to the non-uniform initial flow distribution of the jets exiting from the slots (with 30 degree angle) in the swirl plate. Because individual jets exiting different slots of the swirl plate do not have sufficient time to be fully mixed at lower axial locations (that is before z = 15 mm or z = 25 mm) one would observe two peaks corresponding to the jets from the two adjacent slots (i.e., flow is three-dimensional). Similar twin-peak profile can also be seen in tangential velocity plots in Fig. 3. However, for the axial velocity the second peaks are shifted closer to the centerline compared to the peak locations of the tangential velocity profiles. This double-peak structure disappears further downstream from the swirl plate as the swirling jets from the slots are fully and uniformly mixed (i.e., flow is two-dimensional).

Profiles of the rms of the axial velocity fluctuations in Fig. 2 reveal that the higher swirl air flow rate has higher peak rms value resulting from higher shear stresses. Around (but not at) the centerline of the combustion chamber, rms of the axial velocity fluctuations has less radial gradient (slope) for the low swirl flow rate at axial locations below 90 mm. The rms axial velocity profiles also show that the three swirl levels have the same fluctuation level at locations close to the chamber side walls. They are also equal in magnitude near the centerline for axial positions larger than 40 mm and for all the measured swirl flow rates. In addition all rms profiles show a local minimum at the centerline position. The rms profiles seem to peak at about the inflection point of the mean axial velocity profiles. This can be clearly seen for medium and high swirl flow rates. With low swirl air flow rate, turbulence is almost flat in shape for all axial locations. The turbulence level (i.e., rms value) in this study is quite large. At higher locations, turbulence intensities (i.e., rms/mean ratio) are over 50 percent in some cases.

Tangential mean velocity profiles are shown in Fig. 3. At z = 15 mm, all three different swirl flow rates have similar profiles with higher swirl flow rate having higher magnitude for the tangential velocity. However, starting from z = 25 mm, mean tangential velocities for the medium and high swirl flow cases are different from those of low swirl values. Tangential mean velocity profile for the lowest swirl case exhibits solid body rotation with zero mean velocity being on the geometrical axis of symmetry of the combustor, while medium and high swirl flow rate cases have their mean zero velocity away from this axis. For the latter two cases, there is a noticeable region around the axis in which the mean tangential velocity is zero and hence flow goes downward toward the nozzle. This phenomenon was also noticed by Vu and Gouldin (1982) and Gouldin et al. (1985). Their explanation was that since fluid entered the recirculation bubble by turbulent diffusion across the bounding streamline and recirculation zone was confined to the center of the vortex core, the tangential velocity would be very small. However, in the present study there is another possibility. It is possible that the swirling air velocity in the center of the recirculation zone diminishes because the recirculation zone has an open-upper-end and thus air can enter the recirculation zone with no or very little swirl velocity. For both closed-upper-end and open-upper-end bubbles, the swirl velocity within the recirculation zone is expected

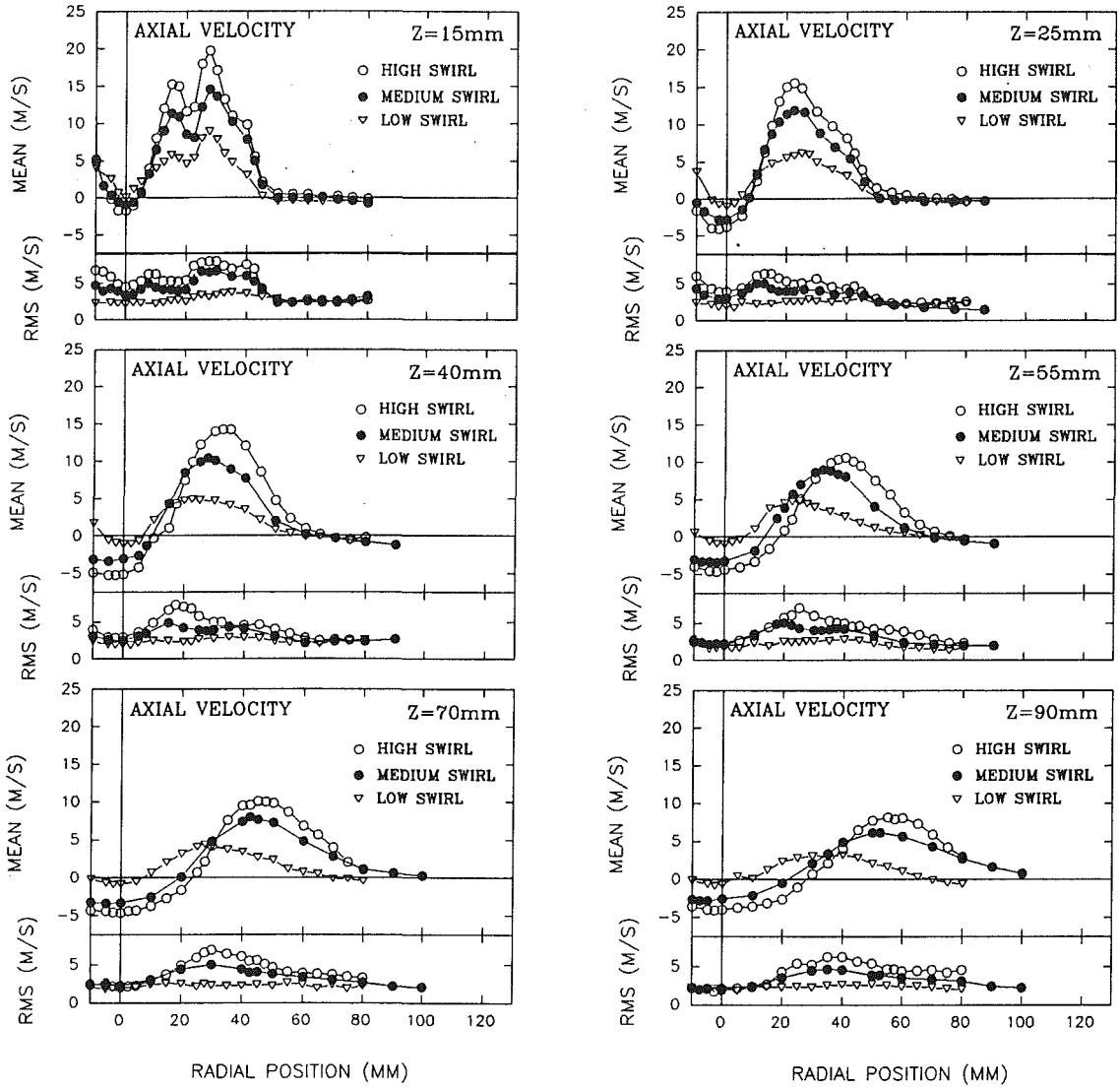

Fig. 2 Axial velocity profiles at various axial locations. The "high," "medium," and "low" swirl refer to swirl flow rates of 3.7, 2.9, and 1.41 m^3/min, respectively. Statistical uncertainties: +/− 3 percent and +/− 7 percent for the mean and rms of velocity fluctuations (before LDV velocity biasing correction).

to be close to zero. since the recirculation zone for the lowest swirl is most likely to be a closed-upper-end bubble in shape and has a smaller radius, solid body rotation remains valid in this case.

The rms of tangential velocity profiles from Fig. 3 show a double-peak character for medium and high swirl flow except at z = 90 mm. One peak occurs almost at the chamber centerline and can clearly be seen for z = 15 and z = 25 mm cases. This peak seems to occur at about the point where the mean tangential velocity just reaches a zero value. But since recirculation zone is wider at higher locations, this peak moves away from the centerline axis as this zero-mean-tangential-velocity point moves. There is another peak shown in the rms profiles in Fig. 3 easily observed for locations less than 70 mm and for medium and high swirl flow rates. This peak seems to correlated with the peak tangential velocity, shown in velocity profiles at axial locations lower than 70 mm.

Centerline mean axial and tangential velocity values are plotted versus axial positions in Fig. 4(*a*) and Fig. 4(*b*). The greater initial rate of change in centerline mean axial velocity reveals a higher pressure gradient which produces a stronger recirculation bubble. Extrapolation of these curves to zero mean axial velocity indicates that for the medium and high swirl flow rates the mean stagnation points are at the same axial position, being different than that for the low swirl case. The rms of the centerline tangential and axial velocity fluctuations also show a steep change for the high swirl flow rate case at lower axial locations. The interesting point is that the high gradient for the tangential centerline rms velocity as compared with the axial one is due to the existence of a near-axis peak with a relatively high rms of the tangential velocity fluctuations as shown in Fig. 3 and Fig. 4(*b*). This is believed to be due to the precession of the recirculation zone which has also been observed by Heitor and Whitelaw (1986). Also in Fig. 4(*b*), the centerline mean tangential velocity shows a weakly oscillating character around the zero value which is similar to the helix vortex line suggested by Farokhi et al. (1989). By since the values are small, it is not conclusive to determine whether a helix vortex line exists or not in this study.

Figure 5 shows contours for the radial positions of the peak and the zero of the mean velocity profiles for both axial and tangential components of the velocity vector. Note that at some

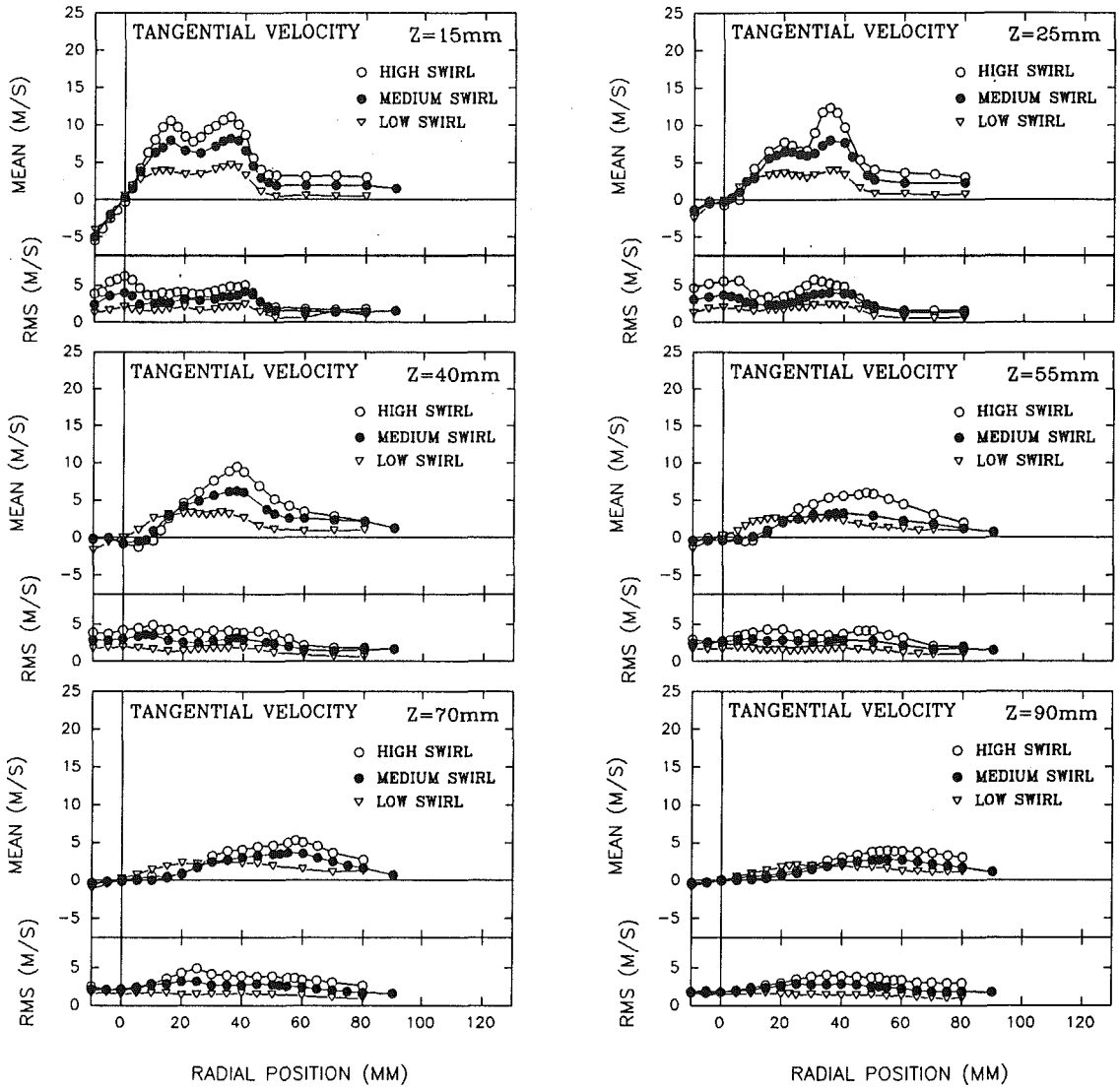

Fig. 3 Tangential velocity profiles at various axial locations. The "high," "medium," and "low" swirl refer to swirl flow rates of 3.7, 2.9, and 1.41 m^3/min, respectively. Statistical uncertainties: +/− 3 percent and +/− 7 percent for the mean and rms of velocity fluctuations (before LDV velocity biasing correction).

axial locations (mainly closer to the swirl plate) two velocity peaks are indicated in this figure. They are indicative of the two adjacent slot jets from the swirl plate as mentioned before. At low axial locations, z = 15 and 25 mm, mean profiles for all three swirl values seem to have the same peak mean velocity radial locations in Fig. 5(*a*). This suggests that the slot jet directions are unaffected by the flow rate and, consequently, the swirl plate is properly designed. At higher axial positions, the location of the peak mean axial velocity profile for different swirl air flow levels starts to diverge. This indicates different slot jet expansion behavior at different swirl flow rate. Note that the initial jet momentum increased swirl flow rate. Lowest swirl flow rate has the smallest radial position at which the peak mean axial velocity occurs, indicating that the swirling flow is weakly expanding. This is because of the low angular momentum at the swirling flow due to low swirl-to-dilution mass flow rates ratio. At medium and high swirl flow rates, the peaks of the axial velocity profile continue to expand rapidly at nearly constant rates (constant slopes of the curves.) Looking at the zero mean axial velocity radial positions in Fig. 5(*a*), since stronger swirl flow rate causes a greater radial pressure gradients, it creates a larger recirculation bubble even possible to create an open upper-ended reversed-flow zone. With medium and high swirls, diameter of the "reversed-flow zone" (at each axial position it is defined as diameter of a circular area in which negative mean axial velocity exists) increases from z = 15 to z = 90 mm, although the rate of increase from z = 70 to z = 90 mm is lower than that from z = 40 to z = 70 mm. In the case of low swirl flow rate, there is no (mean) recirculation (no negative mean axial velocity) at z = 15 mm and the diameter of the "reversed-flow zone" is roughly unchanged from z = 40 to z = 70 mm. It indicates that higher than this swirl air flow rate results in a wider recirculation zone. The top of this zone is at about z = 90 mm for this condition. At medium swirl case, the radial size of the reversed-flow zone ceases to increase at the last two axial positions indicating weakening of the recirculation. At the "high" swirl case, the size of this zone increases monotonically even up to z = 90 mm.

Figures 5(*b*) shows a possible minimal-change situation for the peak velocity locations of the tangential velocity at the low swirl air flow rate. Apparently flow does not have sufficient

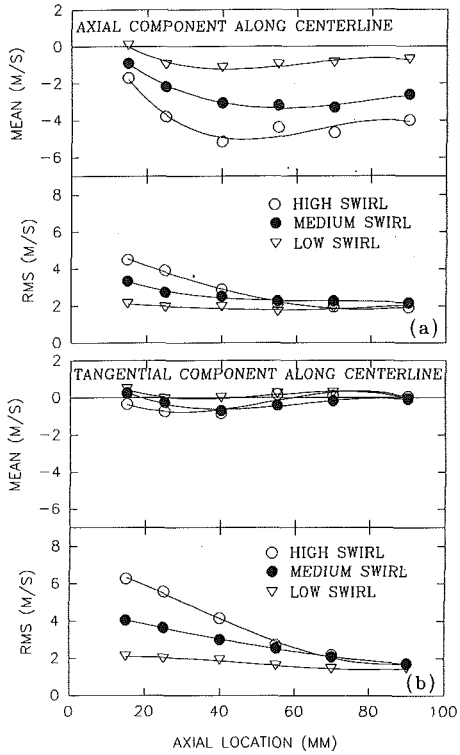

Fig. 4(*a*) and (*b*) Centerline velocity profiles. Statistical uncertainties: +/− 3 percent and +/− 7 percent for the mean and rms of velocity fluctuations. (*a*) For axial component; (*b*) for tangential component.

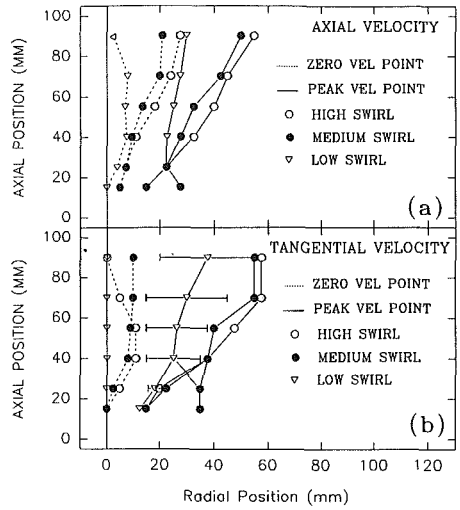

Fig. 5(*a*) and (*b*) Contours of the maximum and zero mean velocity locations. Accuracy: +/− 1 mm. (*a*) For axial component; (*b*) for tangential component.

momentum to rapidly spread the swirling jet under this condition. Note that profiles for the mean tangential velocity in Fig. 3 are much flatter than the axial ones, particularly for the low swirl flow rate. The horizontal band around the down-triangle symbol in Fig. 5(*b*) is a reflection of this fact. For this reason (definitive) descriptive behavior of the peak position for this condition is not clear. At the two higher swirl flow rates, the swirling flow expands rapidly at lower axial locations from $z = 25$ to $z = 70$ mm. But at higher locations, $z = 70$ to $z = 90$ mm, the peak locations remain unchanged. The zero-velocity-location contour of the tangential velocity shows the size of the region within the recirculation zone where the tangential velocity is small or close to zero.

3.2 LDV Bias. The question here is that to what extent, if any, results presented and conclusions reached so far are changed by LDV biasing. After a short review of the biasing, an approach is selected to direct the answer. The subject of LDV velocity biasing has been an important issue since McLaughlin and Tiederman (1973) predicted that the time-average of velocities measured by LDV systems was biased towards higher velocities in turbulent flows. This is because seed particles with higher velocities had higher chance to sweep through the LDV measurement volume. This effect has been observed experimentally by Quigley and Tiederman (1977), Stevenson et al. (1982), Johnson et al. (1983), and Craig and Nejad (1985). However, proper weighting factor can be used to correct mean and rms of velocity fluctuations. Since the average number of realizations per unit time is proportional to the magnitude of the mean velocity vector, if one assumes uniform seed density and spherical measurement volume, McLaughlin and Tiederman (1973) proposed an inverse-velocity-vector weighting scheme for velocity biasing correction. Due to the difficulties in practical measurements, they simplified this correction method to a one-dimensional scheme using inverse of the measured velocity component as a weighting factor. Although simple, it is only adequate to correct the time-average mean and rms of velocities when the other unmeasured two components are small compare to the measured component or when all velocity components were closely correlated. However, since there are regions of close-to-zero velocity, the inverse weighting of the one velocity component is likely to over-correct this velocity component. Other weighting methods, such as particle transit-time and particle interarrival time weightings were also proposed and used, see Hoesel and Rodi (1977), Adams and Eaton (1988) and Petrie et al. (1988), Johnson et al. (1983), Edwards and Jensen (1983), and Edwards (1987).

On an extension of the one-dimensional correction method, either two-dimensional velocity-inverse weighting function, see McLaughlin and Tiederman (1973) and Johnson et al. (1983), or inverse velocity vector with an estimated third-component, see Nakayama (1985), could be used as good correction methods for low turbulence intensity cases. Where two velocity components measured simultaneously, two-dimensional correction is expected to correct biased data up to turbulence intensity of 35 percent, see Gould et al. (1989). Although an estimated third component could be significant when both of the two measured velocity components approach zero, Johnson et al. (1983), Petrie et al. (1988) reasoned that the two-dimensional scheme was accurate enough since the z-component was small in most cases.

Constant time sampling technique was used by many researchers, for example Edwards et al. (1990) and Samimy and Langenfeld (1988). This approach is believed to be one of the most effective methods even for high turbulence intensity as long as the sampling data rate is an order of magnitude less than the valid data rate, Gould et al. (1989) and Stevenson et al. (1984). However, it requires a large seeding rate and a long sampling time which is not always available, and it might still be biased when two consecutively sampled bursts are strongly correlated, see Adams et al. (1984).

In this work, we chose to use a simpler method suggested by Nakao et al. (1987). In this approach, the acquired data is post-processed for biasing correction. They proposed a new weighting function based on the shape of the Probability Distribution Function (PDF) of the velocity data. This study showed good agreement between theirs and the two-dimensional method up to a "corrected" turbulence intensity of about 0.6. Their approach assumes a weighting function of

$$W_i = [1 + (\overline{U}_{en} - U_i)/\overline{U}_{en}]^{1.5}$$

in which $\overline{U}_{en}$ = the mean velocity calculated by the standard (unweighted) ensemble average, and U_i = the ith velocity realization. Extensive comparison was made between corrected and uncorrected velocities. Correction was applied only at locations where the corrected turbulence intensity was lower than 56 percent. In our study, the turbulence intensities are so high that only the velocities around the peak are validated for this correction procedure. However, since velocity biasing affects larger velocities more than the lower ones, this correction scheme should provide some improvement in the flow rate correlations described in the next section. As an example, after correction, the peak mean axial velocity drops by about 16 percent with little change in the rms velocity values at $Z = 40$ mm and for the high-swirl-flow-rate case. *The important observation was that the locations of the peak velocity in the profiles have remained unchanged.* This means that the conclusions drawn from the trends of the uncorrected data in the previous section are still valid.

An effort was made to use interarrival time correction during the process. The correction did not have any effect on the mean velocity profiles. Apparently, the data rate was too low (approximately 30 to 200 data per second) to validate particle interarrival-time weighting scheme, see Edwards and Jensen (1983) and Petrie et al. (1988). The particle interarrival-time correction is not valid when the mean measurement interarrival time per turbulence coherent time (or the velocity persistence time, which is defined as time interval in which the velocity essentially stays unchanged) scale is less than 0.1.

3.3 Volume Flow Rate Correlation. Volumetric flow rates were calculated from the mean axial velocity profiles by

$$\dot{V} = \int_0^{r_c} U(r) \cdot 2\pi r \cdot dr$$

in which $U(r)$ is the mean axial velocity, and r_c is the radius of the circular area of interest (i.e., radius of the inner combustor walls for the total volumetric flow rate, and radius of the reversed-flow zone for the recirculation flow rate. Since no measurements were made for the radial positions larger than the 80 mm (for most conditions) due to the difficulties in reaching these points, all velocities in these regions were assumed to be zero. This will cause underestimating the total volumetric flow rate at higher axial positions as shown later.

Comparison between the "calculated" (using LDV results) and "directly-measured" (using inlet rotameters and pressure gauges) volumetric flow rates are shown in Fig. 6. Best agreement seems to occur around 40 to 60 mm (axial) range and for medium to high flow rates. The solid symbols in this figure show results after velocity biasing correction. It should be clear, that this correction brings down the results in Fig. 6. Note that turbulence intensities are higher than 60 percent at almost all locations and the velocity biasing correction scheme of Nakao et al. (1987) becomes invalid. Interpretation of this figure is made difficult due to several factors; among them are: (*a*) interacting individual slot jets at lower axial position. (*b*) Assumption of angular symmetry for the LDV-calculated flow rates. (*c*) Unmeasured data point beyond radial position of 80 mm. (*d*) Possible existence of a secondary reversed-flow region beyond 80 mm radial position for medium and high swirl flow rates, see Fig. 2. (*e*) LDV-velocity biasing.

The LDV-calculated results are lower than the measured values at all axial locations when lowest flow rate is used. It is possible that the unmeasured small velocity values at the radial positions larger than the 80 mm produce such a behavior. A simple calculation assuming outside velocity of 0.4 m/s (average exit velocity for dilution flow) can change flow rate by about 14×10^{-3} m^3/s. The trends for the two higher flow rates are very similar. At lowest axial positions the imperfect flow-field angular symmetry is an important reason for poor agreement, see also Farokhi et al. (1989). As individual slot

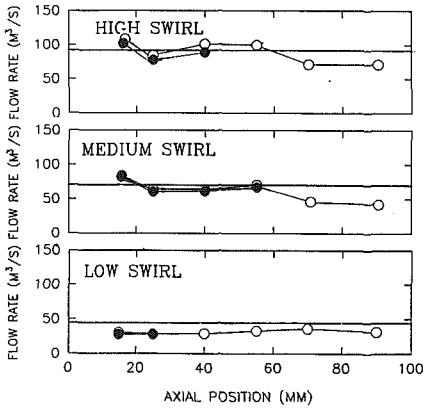

Fig. 6 Total directly measured and LDV-calculated volumetric flow rate at different axial positions. Hollow symbol, before velocity biasing correction; solid symbol, after biasing correction; solid horizontal line, directly measured total inlet flow rate. Estimated accuracy: +/− 5 percent. Scale for the vertical axis is magnified by a factor of 1000.

jets mix and produce a more uniform flow field better agreements are reached from 40 to 60 mm axial range. This important observation indicates that good angular flow-field symmetry and near-complete slot-jet mixing are achieved by about 40 mm from the swirl plate used in this study. This was also confirmed by laser sheet illumination and results in Fig. 2. This seems to be a conservative estimate. Hence, if the results at this position (i.e., 40 mm) are selected to judge the "improvement" brought about by biasing correction approach used here, it is seen that results are improved only at the highest swirl flow rate while no or small change occurs for the medium flow rate condition. Lower LDV-calculated values at the highest axial positions are believed to be due to unmeasured axial velocity beyond the radial position of about 80 mm. Finally, oscillatory flow pattern behavior can contribute to the disagreement. This was indicated by Samimy et al. (1988) who found strong flow oscillations in their dump combustor with swirling air. Flow visualization with laser sheet showed very weak flow oscillations in our chamber. The size and shape of the recirculation zone with its high turbulence is crucial to flame stability and performance of the swirl-stabilized combustors. In previous works of swirling flows, both free and confined, it was demonstrated that the fraction of the mass recirculated correlates with swirl number, see Gupta et al. (1984). This correlation was also demonstrated with combustion for the average and maximum value of recirculated flow by Khalil et al. (1977). In our study, effects of swirl flow rate instead of swirl number was investigated. This was mainly to understand the effects of flow rate on spray flame stability for the most stable swirl plate design in Fig. 1, see Chehroudi and Ghaffarpour (1991), (1992), (1993). The swirl number for the swirl plate design used here can be shown to be proportional to the tangent of the slot angles with respect to the vertical axis, see Gupta et al. (1984), and hence is reasonably justified to be "nominally" constant although some degree of variation is expected. The percentages of the total flow that is recirculated (or reversed) are shown at different axial locations in Fig. 7(*a*). The general behavior for this type of plot is a rise to an axial position with maximum recirculated flow and a decline to a location where mean reversed flow ceases to exist. Figure 7(*a*) indicates that as swirl flow rate increases the length of the recirculated region increases while its onset position remains roughly constant (on the average). Figure 7(*b*) shows plots of the percent of the total flow that is reversed at any axial position as a function of the local reversed-flow zone area. The local reversed-flow zone area is the area of the circle within which negative mean axial velocity exists. In Fig. 7(*b*), except the last point for the "medium" flow rate case, the

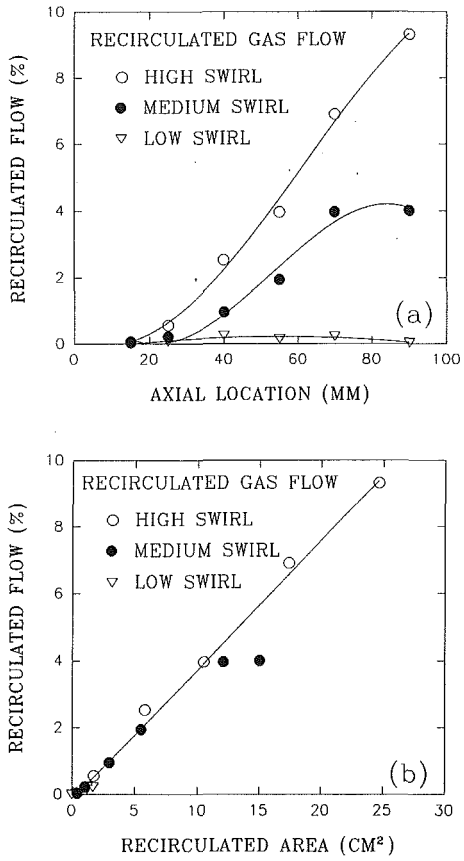

Fig. 7(*a*) and (*b*) Recirculated volumetric flow rate correlation: (*a*) Reversed (or recirculated) flow (as a percent of total flow) versus axial position; (*b*) reversed (or recirculated) flow (as a percent of total flow) versus the local reversed-flow zone area.

percent recirculated flow seems to correlate (linearly) and scale with the recirculated area. This in turn indicates that the cross-sectional averaged reversed-flow axial velocity is a linear function of the total flow rate. In other words, for a given total input flow rate, this cross-sectional averaged recirculated velocity is the same at all the measured axial positions. This result cannot be generalized as sufficient data is not available for the entire recirculated flow zone and/or for other geometrical variables.

4 Conclusions

Present work investigated a highly turbulent confined swirling flow near a swirl plate (similar to a type used in some applications) in a cylindrical swirl-stabilized combustor under isothermal condition. Central recirculation zone is observed in all cases that have been studied. Results for three different "swirl flow rates" at a constant nominal swirl number show that the size of the recirculation zone strongly depends on the swirl strength (swirl air flow rate). Stronger swirl air flow rate increases both the radial extent and the axial length of the recirculation zone. Also, high swirl flow rate generates high maximum negative axial velocity and high maximum positive axial and tangential velocity components. In our setup and up to the axial positions measured, the recirculated flow rate as a percent of the total flow rate (calculated based on the LDV-measured axial velocity) seems to be linearly proportional to the reversed-flow zone area, independent of the swirl air flow rate at the fixed nominal swirl number value used in this study.

Very close to the swirl plate (about less than 25 mm), the swirling flow generated by the plate is highly nonuniform with neighboring slot jets exhibiting their individual structures. At about 40 mm the slot jets from the swirl plate are fully mixed.

As swirl air flow rate is increased, the rms of axial and tangential velocity fluctuations increase monotonically at almost all radial positions except sufficiently away from the fuel nozzle and near the chamber axis, and for positions approaching the chamber inner walls.

Solid body rotation near the chamber axis is only valid for the lowest swirl air flow rate. As swirl becomes stronger, air within the recirculation zone assumes a near-zero tangential velocity possibly because the recirculation bubble becomes open-ended and air enters the bubble from far downstream in the combustion chamber and/or because swirl velocity can only be transferred into the recirculation zone by turbulent diffusion.

Velocity biasing effect is found to be important at the highest flow rate for this high-turbulence-intensity flow. A simple velocity biasing correction scheme developed by Nakao et al. (1987) is shown to be marginally useful for the flow reported in this paper.

Data Bank Contribution

The data files provided on a disk contain information on radial profiles of the Mean and RMS of the axial and tangential components of the velocity vector measured at six axial positions from the nozzle (Z = 15, 25, 40, 55, 70, and 90 mm) and for three different swirl flow rates.

References

Adams, E. W., and Eaton, J. K., 1988, "An LDA Study of the Backward-facing Step Flow, Including the Effects of Velocity Bias," ASME JOURNAL OF FLUIDS ENGINEERING, Vol. 110, pp. 275–282.

Altgeld, H., Jones, W. P., and Whilhelmi, J., 1983, "Velocity Measurements in a Confined Swirl Driven Recirculating Flow," *Experiments in Fluids*, Vol. 1, pp. 73–78.

Beer, J. M., and Chigier, N. A., 1972, Combustion Aerodynamics, *Applied Science*, pp. 100–146.

Brum, R. D., and Samuelsen, G. S., 1987, "Two-Component Laser Anemometer Measurements of Non-reacting and Reacting Complex Flows in a Swirl-stabilized Model Combustor," *Experiments in Fluids*, Vol. 5, pp. 95–102.

Chehroudi, B., 1983, "Scanning Laser Doppler Anemometer and Its Applications in Turbulent Separated Flows," Ph.D. dissertation. Department of Mechanical Engineering, Southern Methodist University.

Chehroudi, B., and Ghaffarpour, M., 1991, "Spray Drop Size and Velocity Measurements in a Swirl-Stabilized Combustor," ASME paper 91-GT-43, 36th ASME Int. Gas Turbine and Aeroengine Congress and Exposition, Orlando, FL.

Chehroudi, B., and Ghaffarpour, M., 1992, "Structure of a Hollow-Cone Spray With and Without Combustion," ASME paper 92-GT-124, 37th ASME Int. Gas Turbine and Aeroengine Congress and Exposition, Cologne, Germany.

Chehroudi, B., and Ghaffarpour, M. 1993, "Experiments on Spray Combustion in a Gas Turbine Model Combustor," *Combustion Science and Technology*, Vol. 92, pp. 173–200.

Chehroudi, B., and Ghaffarour, M., 1994, "Experiments on a Swirl-Stabilized Spray Flame," *Combustion Science and Technology*, (submitted).

Craig, R. R., and Nejad, A. S., 1985, "Velocity Biasing of Two-Component LDV Data in Low-Turbulent Flows," *AIAA Journal*, Vol. 23, pp. 973–974.

Edwards, R. V., 1987, "Report of the Special Panel on Statistical Particle Bias Problems in Laser Anemometer," ASME JOURNAL OF FLUIDS ENGINEERING, Vol. 109, pp. 89–93.

Edwards, R. V., and Jensen, A. S., 1983, "Particle Sampling Statistics Laser Anemometers: Sample-and-Hold Systems and Saturable Systems," *Journal of Fluid Mechanics*, Vol. 133, pp. 397–411.

Edwards, C. F., Rudoff, R. C., and Bachalo, W. D., 1990, "Measurement of Correlated Droplet Size and Velocity Statistics, Size Distribution, and Volume Flux in a Steady Spray Flame," *5th Symp. on Appl. of Laser Tech. to Fluid Mech.*, Lisbon Portugal, July.

Farokhi, S., Taghavi, R., and Rice, E. J., 1989, "Effect of Initial Swirl Distribution on the Evolution of a Turbulent Jet," *AIAA Journal*, Vol. 27, pp. 700–706.

Fujii, S., Eguchi, K., and Gomi, M., 1981, "Swirling Jets With and Without Combustion," *AIAA Journal*, Vol. 19, pp. 1438–1442.

Gould, R. D., Stevenson, W. H., and Thompson H. D., 1989, "Parametric Study of Statistical Bias in Laser Doppler Velocimetry," *AIAA Journal*, Vol. 27, pp. 1140–1142.

Gouldin, F. C., Depsky, J. S., and Lee, S.-L., 1985, *Velocity Field Characteristics of a Swirling Flow Combustor," AIAA Journal*, Vol. 23, pp. 95–102.

Gupta, A. K., Lilley, D. G., and Syred, N., 1984, *Swirl Flows*, Abacus.

Habib, M. A., and Whitelaw, J. H., 1979, "Velocity Characteristics of a Confined Coaxial Jets," ASME JOURNAL OF FLUIDS ENGINEERING, Vol. 101, pp. 521–529.

Habib, M. A., and Whitelaw, J. H., 1980, "Velocity Characteristics of Confined Coaxial Jets With and Without Swirl," ASME JOURNAL OF FLUIDS ENGINEERING, Vol. 102, pp. 47–53.

Heitor, M. V., and Whitelaw, J. H., 1986, "Velocity Temperature, and Species Characteristics of the Flow in a Gas-Turbine Combustor," *Combustion and Flames*, Vol. 64, pp. 1–32.

Hoesel, W., and Rodi, W., 1977, "New Biasing Elimination Method for Laser-Doppler Velocimeter Counter Processing," *Review of Scientific Instruments*, Vol. 48, pp. 910–919.

Johnson, D. A., Modaress, D., and Owen, F. K., 1983, "An Experimental Verification of Laser-Velocimeter Sampling Bias and Its Correction," ASME JOURNAL OF FLUIDS ENGINEERING, Vol. 106, pp. 5–12.

Khalil, K. H., El-mahallawy, F. M., and Moneib, H. A., 1977, "Effect of Combustion Air Swirl on the Flow Pattern in a Cylindrical Oil Fired Furnace," *16th Symposium on Combustion*, pp. 135–143.

Kihm, K. D., Chigier, N., and Sun, F., 1990, "Laser Doppler Velocimetry Investigation of Swirler Flow Fields," *AIAA Journal of Propulsion and Power*, Vol. 6, No. 4, pp. 364–374.

McLaughlin, D. K., and Tiederman, W. G., 1973, "Biasing Correction for Individual Realization of Laser Anemometer Measurements in Turbulent Flows," *Physics of Fluids*, Vol. 16, pp. 2082–2088.

Nakao, S., Terao, Y., and Hirata, K., 1987, "New Method for Eliminating the Statistical Bias in Highly Turbulent Flow Measurements," *AIAA Journal*, Vol. 25, pp. 443–447.

Nakayama, A., 1985, "Measurements of Separating Boundary Layer and Wake of an Airfoil Using Laser Doppler Velocimetry," AIAA paper 85-0181.

Nejad, A. S., Vanka, S. P., Favaloro, S. C., Samimy, M., and Langenfeld, C., 1989, "Application of Laser Velocimetry for Characterization of Confined Swirling Flow," *Journal of Energy*, Gas Turbine and Power, Vol. 111, pp. 36–44.

Petrie, H. L., Samimy, M., and Addy, A. L., 1988, "Laser Doppler Velocity Bias in Separated Turbulent Flows," *Experiments in Fluids*, Vol. 6, pp. 80–88.

Quigley, M. S., and Tiederman, W. G. Jr., 1977, "Experimental Evaluation of Sampling Bias in Individual Realization Laser Anemometer," *AIAA Journal*, Vol. 15, pp. 266–268.

Ramos, J. J., and Somer, H. T., 1985, "Swirling Flow in a Research Combustor," *AIAA Journal*, Vol. 23, pp. 241–248.

Samimy, M., Nejad, A. S., Langenfeld, C. A., and Favaloro, S. C., 1988, "Oscillatory Behavior of Swirling Flows in a Dump Combustor," AIAA paper 88-0189.

Samimy, M., and Langenfeld, C. A., 1988, "Experimental Study of Isothermal Swirling Flows in a Dump Combustor," *AIAA Journal*, Vol. 26, pp. 1442–1449.

Stevenson, W. H., Thompson, H. D., and Craig, R. R., 1984, "Laser Velocimeter Measurements in Highly Turbulent Recirculating Flows," ASME JOURNAL OF FLUIDS ENGINEERING, Vol. 106, pp. 173–180.

Stevenson, W. H., Thompson, H. D., and Roesler, T. C., 1982, "Direct Measurement of Laser Velocimeter Bias Errors in a Turbulent Flow," *AIAA Journal*, Vol. 20, pp. 1720–1723.

Vu, B. T., and Gouldin, F. C., 1982, "Flow Measurements in a Model Swirl Combustor," *AIAA Journal*, Vol. 20, pp. 642–651.

A Simple Method for Estimating Velocity Distributions in Swirling Flows

D. Kinnear

P. A. Davidson

Department of Mechanical Engineering, Imperial College, London, SW7 2BX, England

We describe the important structural features of swirling recirculating flows induced by a rotating boundary. A knowledge of this structure has allowed us to match the core flow to the boundary layer using a momentum-integral technique. In particular, we derive a single integro-differential equation, valid for any shape of container, which predicts the distribution of swirl, secondary recirculation, and wall shear stress. This momentum-integral approach has been applied to three cases: flow between parallel disks; flow in a cone; and flow in a hemisphere. The results compare favorably with published experimental data, and with computed numerical results. Our momentum-integral approach complements numerical solution methods. For simple geometries all the important information can, in principle, be derived using the momentum-integral approach, and this is particularly useful for establishing the scaling laws. In more complex geometries a numerical approach may be more appropriate. However, even in such cases, the scaling laws derived using the momentum-integral analysis are still useful as they allow extrapolation of a single computation to a wide range of high Reynolds number flows.

1 Introduction

In this paper we consider swirling, recirculating flow induced in an axisymmetric container by rotation of one of the walls. The container may be of any shape, (e.g., cylindrical, conical, spherical) and the flow is considered to be turbulent. Such flows are important in a number of engineering devices where rotating surfaces are used to create recirculation. One example of this is the rotating-disk-contactor (RDC) shown in Fig. 1. In this device Ekman layers form on rapidly rotating disks, where the fluid gains energy, and on the stator disks where energy is dissipated. The intense shearing action in the Ekman layers provides thorough mixing of the two phases and therefore an efficient extraction process.

In recent years, momentum-integral methods have been some what displaced by more general computational techniques. The ubiquitous k-ϵ turbulence model, in conjunction with wall functions and finite difference algorithms, offers the possibility of simulating turbulent flows in relatively complex geometries. However, for simple geometries, momentum-integral methods can often provide a useful insight into the flow. In this paper, we discuss the structure of swirling recirculating flow, and use the momentum-integral technique to establish the scaling laws for the flow and to provide engineering estimates of the velocity field.

The essential nature of an enclosed, swirling flow is perhaps best illustrated by reference to the textbook problem of "spin-down" of a stirred cup of tea. The main body of fluid is essentially in a state of inviscid rotation. The centrifugal force is balanced by a radial pressure gradient. This pressure gradient is imposed throughout the boundary layer on the bottom of the cup. In the boundary layer, however, the fluid rotates less rapidly than in the core and so there is a local imbalance

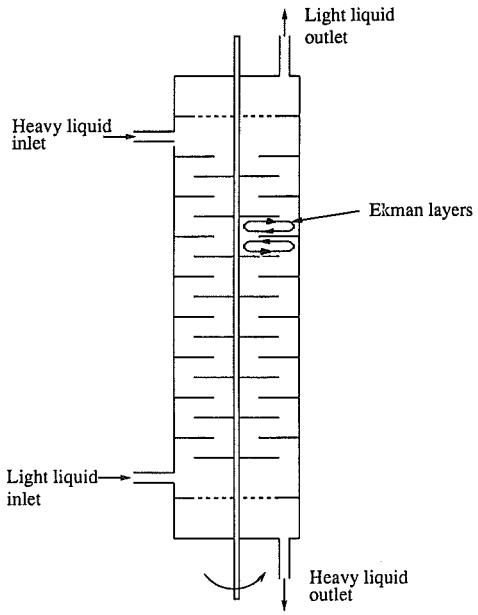

Fig. 1 Formation of Ekman layers in a rotating disk contactor

Contributed by the Fluids Engineering Division for publication in the JOURNAL OF FLUIDS ENGINEERING. Manuscript received by the Fluids Engineering Division July 2, 1993; revised manuscript received August 10, 1994. Associate Technical Editor: R. Metcalfe.

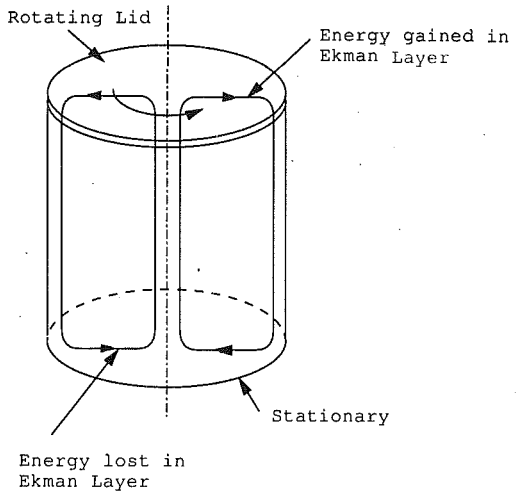

Fig. 2 Energy transfer to and from the fluid due to Ekman-layers

between the imposed pressure gradient and the centripetal acceleration. The result is a radial inflow with the fluid drifting up and out of the (Ekman) boundary layer. As each element of fluid passes through the Ekman layer, it loses a significant fraction of its kinetic energy. The tea finally comes to rest when all the contents of the cup have been flushed through the boundary layer at the base of the cup.

Spin-down is, of course, an unsteady flow. However, many of these features also manifest themselves in forced steady flows with swirl. Here Ekman layers act as a source of dissipation, destroying the kinetic energy imparted to the fluid by the external forcing (see Davidson, 1992). In cases where the flow is driven by rotation of one or more boundary, Ekman layers can both generate and dissipate kinetic energy. If the wall rotates faster than the fluid, then the fluid is centrifuged radially outward, picking up energy in the process. Conversely if the wall is stationary and the fluid rotates, a radial inflow is created with the fluid losing energy as it passes through the boundary layer (see Fig. 2).

The flows above are characterized by the presence of high speed wall-jets within the Ekman layers. Typically, these jets entrain and detrain fluid at such a rate that the entire body of fluid is flushed through the narrow boundary layers (Davidson, 1992 and Davidson, 1993). The continual recycling of fluid through all the wall jet ensures that the structure of the entire flow field is controlled by the dynamics of these narrow sub domains. If one wishes to compute such a flow, then it is essential that these wall jets are well resolved. This can make the numerical simulation of such flows somewhat troublesome. (Wall functions, which are generally used to resolve turbulent boundary layers, cannot be produced to describe wall jets.) On the other hand, such flows are particularly well suited to momentum-integral techniques, where the wall jets and core flow are modeled separately and the solutions matched. Indeed, Kármán first developed the momentum-integral method to analyze flow over a rotating disk.

Momentum-integral techniques have already been applied to swirling flows in a number of specific configurations. Flow over a single disk, or between two disks rotating at different speeds are examples (Greenspan, 1968; Kármán, 1921, Schlichting, 1979, and Daily and Nece, 1960). Here we build on the earlier work and produce a particularly simple formulation suitable for axisymmetric containers of arbitrary shape. We start in Section 2 by describing the overall structure of these flows, establishing the relationship between the inviscid core flow and the Ekman layers which bound it. In Section 3, we develop a particularly simple form of the momentum-integral method suitable for swirling turbulent flows. This furnishes a single integro-differential equation, valid for any shape of container from which the distribution of swirl, recirculation and wall stress can be calculated. In Section 4 this equation is solved for flow between parallel disks. The predictions are compared with numerical simulations using a k-ϵ turbulence model and published experimental data. In Section 5, we look at the case of flow in a cone, again comparing theoretical results with the results of numerical simulations. Finally, in Section 6, we apply the analysis to flow in a hemisphere.

2 General Structure of the Core Flow

Consider the flow shown in Fig. 3. Fluid is held in a closed container and swirl is induced by rotation of the top surface. The Reynolds number is assumed to be high and the flow may be either laminar or turbulent. Consider first a laminar flow. Using cylindrical polar coordinate (r, θ, z), the equations of motion for the recirculation is,

$$\frac{D\mathbf{u}_p}{Dt} = -\nabla\left(\frac{p}{\rho}\right) + \frac{\Gamma^2}{r^3}\hat{\mathbf{e}}_r + \nu\nabla^2\mathbf{u}_p \tag{1}$$

where $\mathbf{u}_p$ is the poloidal velocity (u_r, 0, u_z) and Γ is the angular momentum, $u_\theta r$. The corresponding transport equations for angular momentum and azimuthal vorticity are,

$$\frac{D\Gamma}{Dt} = \nu\nabla_1^2\Gamma \tag{2}$$

$$\frac{D}{Dt}\left(\frac{\omega_\theta}{r}\right) = \nu\nabla_2^2\left(\frac{\omega_\theta}{r}\right) + \frac{\partial}{\partial z}\left(\frac{\Gamma^2}{r^4}\right) \tag{3}$$

Nomenclature

ρ = density
ν = kinematic viscosity
p = pressure
$\mathbf{u}_p$ = poloidal velocity vector
u_r = radial velocity
u_θ = swirl velocity
u_z = axial velocity
$\hat{u}_s$ = characteristic curvilinear velocity
$\hat{u}_r$ = characteristic radial velocity
Γ = angular momentum $u_\theta r$
Γ_c = core angular momentum
Γ_w = angular momentum of fluid in contact with lid
ψ = streamfunction
ϕ = cone angle
τ_θ = azimuthal shear stress on stationary walls
τ'_θ = azimuthal shear stress on the rotating surface
τ_r = radial shear stress
Δ = core angular velocity $\Gamma_c/\Omega r^2$
δ = boundary layer thickness
$\dot{q}$ = volume flow rate
χ_1, χ_2 = shape functions
κ_1, κ_2 = friction coefficients
ω_θ = vorticity
T = driving torque on the rotating surface
Ω = angular velocity of the rotating surface
Re = Reynolds number $\Omega R^2/\nu$
$\mathbf{x}$ = vector tangential to a streamline
R = outer radius
z = axial coordinate
r = radial coordinate
θ = azimuthal coordinate
s = curvilinear coordinate
n = normal curvilinear coordinate
t = tangential curvilinear coordinate
z_s = axial coordinate
r_s = radial coordinate
$\hat{\mathbf{e}}_r$ = radial unit vector
$\hat{\mathbf{e}}_\theta$ = azimuthal unit vector

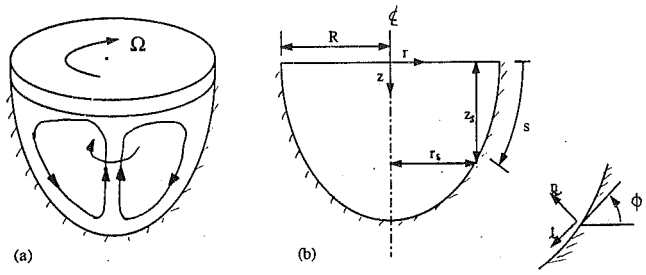

Fig. 3 Flow Geometry: (*a*) general flow pattern; (*b*) coordinate system

where, the Laplace-like operators ∇_1^2 and ∇_2^2 are defined as,

$$\nabla_1^2 \equiv \frac{\partial^2}{\partial z^2} + r\frac{\partial}{\partial r}\left[\frac{1}{r}\frac{\partial}{\partial r}\right], \quad \nabla_2^2 \equiv \frac{\partial^2}{\partial z^2} + \frac{1}{r^3}\frac{\partial}{\partial r}\left[r^3\frac{\partial}{\partial r}\right]$$

The recirculation, $\mathbf{u}_p$ can be written in terms of the Stoke's streamfunction ψ,

$$\mathbf{u}_p = \nabla \times [(\psi/r)\hat{\mathbf{e}}_\theta], \quad \nabla_1^2\psi = -r\omega_\theta$$

so that the instantaneous velocity field is uniquely determined by the two scalars Γ and ψ, or equivalently Γ and ω_θ.

Now intuitively, we expect the flow-field to be as shown in Fig. 3(*a*). Fluid is sucked up into the top Ekman layer, where it is centrifuged radially outward, picking up energy in the process. This energy is then lost in the side-wall boundary layer. We may therefore expect the magnitude of the recirculation to be controlled by Ekman pumping. If this is so, then continuity requires that in the core $|\mathbf{u}_p| \ll u_\theta$, and consequently Eq. (3) demands that Γ is independent of z (to the appropriate order). This is reminiscent of the Taylor-Proudman theorem. Although substantially correct, this argument requires some formal justification. We shall follow the arguments given by Davidson (1993).

If we integrate (1) along a closed streamline, s, then we obtain,

$$\oint_s \frac{\Gamma^2}{r^3}\,dr + \nu\oint_s \nabla^2\mathbf{u}_p.d\mathbf{x} = 0 \tag{4}$$

The two terms in this equation represent the rate of generation and dissipation of the energy associated with the recirculation. There are only three ways of satisfying (4) in the high Reynolds number limit. First, Γ could be constant along a streamline, to order ν. In this case slow (Batchelor) diffusion between streamlines will eventually reduce such subdomains to regions where Γ and ω_θ/r are uniform (see Batchelor, 1956; Davidson and Hunt, 1987; and Davidson, 1993). However, such a structure cannot exist when the axis of symmetry is included in the flow field. The other two options are:

(*a*) Γ is independent of z throughout the core, to order ν;

(*b*) every streamline passes through a boundary layer, δ, where gradients in $\mathbf{u}_p$ scale as $\nu^{1/2}$.

In fact, it is readily shown that both (*a*) and (*b*) must hold true. For example, suppose the flow satisfies (*a*). Then Eq. (2) applied to the core gives us $\mathbf{u}_p = u_z(r)\hat{\mathbf{e}}_z$, so that every streamline passes out of the core and into the Ekman layers. This then ensures that (*b*) also holds true. Conversely, suppose that the flow satisfies (*b*). Then continuity requires that $\mathbf{u}_p$ in the core is of order $\delta\Omega$. The left-hand side of Eq. (3) is then of order $\delta^2\Omega^2/R^3$, requiring that axial gradients in Γ throughout the core are of order $\Gamma\delta^2/R^3$. We therefore conclude that the core flow satisfies,

$$\Gamma_c = \Gamma_c(r) + O[(\delta/R)^2] \tag{5}$$

$$\mathbf{u}_p = u_z(r)\hat{\mathbf{e}}_z \tag{6}$$

These two equations define the state of the core flow. The same arguments may also be applied to a turbulent flow, where ν is replaced by an eddy viscosity.

3 Momentum-Integral Analysis

In the rest of this paper we shall restrict ourselves to turbulent boundary layers, largely because most flows encountered in engineering are turbulent. The analysis could be readily adapted to laminar flows. In addition to the cylindrical coordinates r, z, it is convenient to introduce curvilinear coordinates s and n to define a point relative to the wall (see Fig. 3). The normal and tangential vectors are $\mathbf{n}$ and $\mathbf{t}$, and ϕ defines the local angle of inclination of the surface. We shall let $\Gamma_c(r)$ represent the core angular momentum, and $\Gamma_w = \Omega r^2$ be the angular momentum of the fluid in contract with the lid.

If we integrate (2) across the Ekman layer on the side wall we obtain the momentum-integral equations,

$$\frac{d}{ds}\left[r_s\int_0^\delta [\Gamma_c - \Gamma]u_s dn\right] - \frac{\dot{q}}{2\pi}\frac{d\Gamma_c}{ds} = \frac{r_s^2}{\rho}\tau_\theta \tag{7}$$

Here u_s is the tangential velocity in the boundary layer, τ_θ is the wall shear stress and $\dot{q}$ is the volumetric mass flux in the boundary layer,

$$\frac{\dot{q}}{2\pi r_s} = \int_0^\delta u_s dn \tag{8}$$

The equivalent equation for the boundary layer on the lid is,

$$\frac{d}{dr}\left[r\int_0^\delta [\Gamma - \Gamma_c]u_r dz\right] + r\int_0^\delta u_r dz\frac{d\Gamma_c}{dr} = \frac{r^2\tau'_\theta}{\rho}$$

where τ'_θ is the surface shear stress on the lid. Now Eq. (6) implies that at a given radius, the mass flux through the top and side boundary layers must be the same. It follows that we may rewrite the equation above as,

$$\frac{d}{dr}\left[r\int_0^\delta [\Gamma - \Gamma_c]u_r dz\right] + \frac{\dot{q}}{2\pi}\frac{d\Gamma_c}{dr} = \frac{r^2\tau'_\theta}{\rho} \tag{9}$$

Next we substitute for τ_θ and τ'_θ using the well-known seventh power law fit to the law of the wall (see Schlichting, 1979). This relates the wall shear stress, τ, to the local slip velocity, u, by the relationship, $\tau = 0.0225\,\rho u^2(\nu/u\delta)^{1/4}$. This gives,

$$r^2\tau_\theta/\rho = \kappa_1\Gamma_c^2;\ r^2\tau'_\theta/\rho = \kappa_2(\Gamma_w - \Gamma_c)^2$$

where κ_1 and κ_2 are friction coefficients given by,

$$\kappa_1 = 0.0225[\Gamma_c\delta/\nu r_s]^{-1/4} \tag{10}$$

$$\kappa_2 = 0.0255[(\Gamma_w - \Gamma_c)\delta/\nu r]^{-1/4} \tag{11}$$

In addition, it is convenient to introduce the shape functions for the side and top Ekman layers, χ_1 and χ_2 defined by,

$$\int_0^\delta (\Gamma_c - \Gamma)u_s dn = \chi_1\Gamma_c\frac{\dot{q}}{2\pi r_s}$$

$$\int_0^\delta (\Gamma - \Gamma_c)u_r dz = \chi_2(\Gamma_w - \Gamma_c)\frac{\dot{q}}{2\pi r}$$

We shall treat χ_1 and χ_2 as independent of s. We may estimate their magnitudes by assuming the velocity profiles in the Ekman layers follow the seventh power law.

Following Kármán (1921), we assume,

$$\Gamma/\Gamma_c = (n/\delta)^{1/7};\ u_s = \hat{u}_s(n/\delta)^{1/7}[1 - (n/\delta)]$$

at the side wall, and

$$(\Gamma_w - \Gamma)/(\Gamma_w - \Gamma_c) = (n/\delta)^{1/7},\ u_r = \hat{u}_r(n/\delta)^{1/7}[1 - (n/\delta)]$$

for the top boundary layer. (Here $\hat{u}$ is a characteristic velocity.) It follows that $\chi_1 = \chi_2 = 1/6$ and so the two momentum-integral equations reduce to,

$$\frac{1}{6}\frac{d}{dr}\left[\Gamma_c\frac{\dot{q}}{2\pi}\right] - \frac{\dot{q}}{2\pi}\frac{d\Gamma_c}{dr} = \kappa_1\Gamma_c^2\frac{ds}{dr_s} \tag{12}$$

$$\frac{1}{6}\frac{d}{dr}\left[(\Gamma_w-\Gamma_c)\frac{\dot{q}}{2\pi}\right]-\frac{\dot{q}}{2\pi}\frac{d\Gamma_c}{dr}=\kappa_2(\Gamma_w-\Gamma_c)^2 \tag{13}$$

Provided we can evaluate δ, and hence find the coefficients κ_1 and κ_2, we have two equations in two unknowns, $\Gamma_c(r)$ and $\dot{q}(r)$. Now the coefficients, κ_1 and κ_2, will typically vary as $r^{-1/4}$. However this variation is much less marked than the dependence of Γ^2 on $r(\Gamma^2 \sim r^4)$, which is the parameter they multiply. Consequently we shall evaluate κ_1 and κ_2 at the outer radius ($r = R$) and treat the friction coefficients as constant. This is a relatively crude approximately, but is not inconsistent with the errors associated with treating χ_1 and χ_2 as constant. The next step is to integrate (12), giving an explicit expression for $\dot{q}$. We can thus eliminate the mass flux from (13) to give an integro-differential equation for $\Gamma_c(r)$. The result is,

$$\frac{\dot{q}}{2\pi}=6\kappa_1\Gamma_c^5\int_0^r\Gamma_c^{-4}\frac{ds}{dr_s}\,dr \tag{14}$$

$$\frac{d}{dr}[\Gamma_c^5\Gamma_w]\int_0^r\Gamma_c^{-4}\frac{ds}{dr_s}\,dr=-\Gamma_c(\Gamma_w-\Gamma_c)\frac{ds}{dr_s}+\left(\frac{\kappa_2}{\kappa_1}\right)[\Gamma_w-\Gamma_c]^2 \tag{15}$$

where,

$$\frac{\kappa_2}{\kappa_1}=\left[\frac{\Gamma_c}{\Gamma_w-\Gamma_c}\right]_{r=R}^{1/4} \tag{16}$$

For a given shape of container $s(r_s)$ we can integrate (15) to give the core angular momentum distribution $\Gamma_c(r)$. Equation (14) then gives the boundary layer mass flux while the driving torque applied to the top surface is,

$$T=2\pi\rho\kappa_2\int_0^R[\Gamma_w-\Gamma_c]^2dr \tag{17}$$

Consequently, we have a simple system of equations which completely describe the flow in an arbitrary geometry.

It only remains to evaluate δ and hence the friction coefficient κ_2. This is furnished by the radial momentum-integral equation for the top surface.

$$\frac{d}{dr}\left[r\int_0^\delta u_r^2dz\right]=\frac{1}{r^2}\int_0^\delta[\Gamma^2-\Gamma_c^2]dz-\frac{r\tau_r}{\rho}$$

Following Kármán (1921), we take

$$\tau_r=\frac{\hat{u}_r}{(\Gamma_w-\Gamma_c)/r}\tau_\theta'$$

In addition, we can evaluate the integrals in the momentum equation using the shape functions for Γ and u_r invoked earlier. The result is the differential equation,

$$\frac{d}{dr}\left[\left(\frac{\dot{q}}{2\pi}\right)^2\frac{1}{r\delta}\right]=\frac{\delta(\Gamma_w-\Gamma_c)(8\Gamma_c+\Gamma_w)}{44.7r^2}-1.73\kappa_2\frac{\dot{q}}{2\pi r}\frac{(\Gamma_w-\Gamma_c)}{\delta} \tag{18}$$

Given the radial variations of $\dot{q}$ and Γ_c, this equation allows δ and hence κ_2 to be evaluated. Equations (14) to (18) give a complete description of the problem. We now look at three different cases of increasing complexity: flow between parallel disks; flow in a cone; and flow in a hemisphere.

4 Flow Between Parallel Disks

If we take $ds/dr_s = -1$, then our system of equations describe flow between two parallel, enclosed disks where the gap between the disks is much less than the disk radius. This simple geometry has been extensively studied in the past (see, Greenspan, 1968, Schlichting, 1979; and Daily and Nece, 1960). Previous momentum-integral analyses have either assumed a value for Γ_c, or else deduced it using a scheme specific to the geometry. (For example, Schlichting, 1979 and Daily and Nece, 1960.) Here our analysis is quite general. Equation (15) is satisfied by the rigid-body rotation expression.

$$\frac{\Gamma_c}{\Omega r^2}=0.345 \tag{19}$$

It follows from (14) and (17) that the boundary layer mass flux and drive torque are given by,

$$\frac{\dot{q}}{2\pi r}=0.347\kappa_2\Omega r^2$$

$$\frac{T}{\rho\Omega^2R^5}=0.539\kappa_2$$

It only remains to evaluate the friction coefficient κ_2. This is furnished by substituting for $\dot{q}$ and Γ_c in Eq. (18). The result is,

$$\kappa_2=0.0396\left[\frac{\Omega R^2}{\nu}\right]^{-1/5}=0.0396\ \mathrm{Re}^{-1/5}$$

where Re is the Reynolds number based on the maximum fluid velocity. Eliminating κ_2 from the expressions above gives,

$$\frac{\dot{q}}{2\pi r}=0.0137\Omega r^2\mathrm{Re}^{-1/5} \tag{20}$$

$$\frac{T}{\rho\Omega^2R^5}=0.0214\ \mathrm{Re}^{-1/5} \tag{21}$$

We might compare our predictions with the experimental data of Daily and Nece (1960). They found some variation with gap size, but typically,

$$\frac{\Gamma_c}{\Omega r^2}=0.41\rightarrow0.46$$

$$\frac{T}{\rho\Omega^2R^5}=(0.020\rightarrow0.022).\mathrm{Re}^{-1/5}$$

Our theory appears to underestimate the core rotation rate by 15–25 percent, although the prediction of the drive torque corresponds closely to the measurements. Schlichting (1979) also reports measurements of the torque, and these are best approximated by the expression,

$$\frac{T}{\rho\Omega^2R^5}=0.020\ \mathrm{Re}^{-1/5}$$

Again there is a reasonable correspondence with predictions.

For this and other geometries we have performed numerical simulations of the flow. We have used a standard version of the fluid flow modeling code FLUENT. This code divides the flow domain into cells, integrates the Navier-Stokes equations over each cell and represents the resulting equations using finite differences. The discretization uses a second order accurate quadratic upwind scheme for convection terms and the usual second order finite difference approximation for the diffusion term. The SIMPLE algorithm is used to find a steady flow solution in terms of the primitive variables. The discretization and solution algorithm are well documented and can be found in, for example, Pantanker (1980). The turbulence is modeled using the standard k-ϵ method where transport equations for the turbulent kinetic energy k and dissipation ϵ are solved in addition to the momentum equations. An "effective viscosity" can then be found from k and ϵ. Details of the particular implementation of the k-ϵ model used in the code are given by Rodi (1984). At the solid boundaries the shear stress is modeled using wall functions. In essence, this relates the slip

velocity near the wall to the wall shear using the universal log-law of the wall. This is also discussed in detail by Rodi (1984).

To demonstrate the accuracy of the computational models we have used two grids, 40 × 56 and 79 × 111, to compute the flow. An aspect ratio of 0.1 (gap to radius) was used and the other parameters were $\Omega = 10$ rad/s, $R = 0.364$ m, $\nu = 0.9 \times 10^{-6}$ m^2/s, and $\rho = 10^3$ kg/m^3. The shape of the recirculation is shown in Fig. 4, where the role of Ekman pumping is evident. The computed values of u_θ midway between the disks are also shown in Fig. 4, where they are compared with the theoretical prediction (19). The computational results show a small radial variation in the angular velocity in the core. To compare the results of the momentum-integral analysis with the computations, we took the value of the angular velocity midway between the disks and at a radial location $r = 0.8 \times R$. The computed values of $\Gamma/\Omega r^2$, $T/\rho\Omega^2 R^5$ and maximum boundary layer mass flux $\dot{q}/2\pi R$ are shown in Table 1 along side our theoretical predictions. There is a good correspondence between the two. Note that, doubling the grid size in both directions effected the computed core rotation by 2.2 percent, the torque by 2.8 percent, and the boundary layer mass flux by 5.9 percent. The momentum-integral analysis appears to underestimate the computed core rotation rate by 21 percent but predicts the torque and boundary layer mass flux well. The computed core rotation and torque are in good agreement with the experimental results.

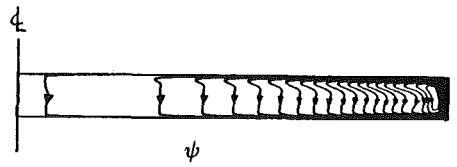

Fig. 4(a)

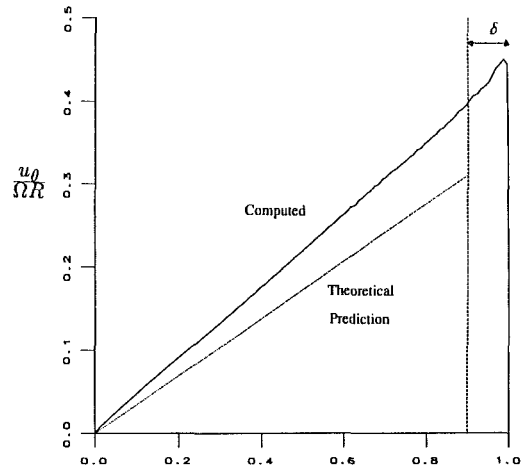

Fig. 4(b)

Fig. 4 Finite difference solutions for the flow between parallel disks (a) streamfunction; (b) computed and theoretical core rotation u_θ

5 Flow in a Cone

We now consider flow in a cone, with a half angle of $\pi/2 - \phi$. Equation (15) is again satisfied by the rigid-body rotation expression,

$$\frac{\Gamma_c}{\Omega r^2} = \Delta \tag{22}$$

Here Δ is a constant which is determined by the algebraic equation,

$$7\cos\phi\left[\frac{1-\Delta}{\Delta}\right]^{7/4} - 5\left[\frac{1-\Delta}{\Delta}\right] - 12 = 0 \tag{23}$$

Values of Δ range from 0.345, for $\phi = 0$ deg, to 0, for $\phi = 90$ deg. Expressions (14) and (17) then give the boundary layer mass flux and drive torque as,

$$\frac{\dot{q}}{2\pi r} = \frac{6\kappa_1 \Delta \Omega r^2}{7\cos\phi}$$

$$\frac{T}{\rho\Omega^2 R^5} = \frac{2\pi\kappa_2}{5}(1-\Delta)^2$$

As before, we can evaluate the friction coefficients by substituting for $\dot{q}$ and Γ_c into Eq. (18). This gives,

$$\kappa_2 = 0.0267[1 + 1.4\Delta] f(\Delta) \mathrm{Re}^{-1/5}$$

where,

$$f(\Delta) = \frac{(1+8\Delta)^{1/10}}{(1-0.365\Delta)^{1/10}(1-\Delta)^{2/5}(1+1.4\Delta)^{4/5}}$$

The function $f(\Delta)$ differs from unity by at most, 0.5 percent. In view of the other approximations it is reasonable to take $f(\Delta) = 1$. In this case the boundary layer mass flux and drive torque are given by,

$$\frac{\dot{q}}{2\pi r} = 0.0320(1-\Delta)^2 \Omega r^2 \,\mathrm{Re}^{-1/5} \tag{24}$$

$$\frac{T}{\rho\Omega^2 R^5} = 0.0336(1-\Delta)^2(1+1.4\Delta)\mathrm{Re}^{-1/5} \tag{25}$$

Expressions (22) to (25) give a complete description of the flow. Consider by way of illustration the two cases of $\phi = 30$ deg and $\phi = 70$ deg. These correspond to cone half-angles of 60 and 20 deg, respectively. Our theory predicts:

$$\frac{\Gamma_c}{\Omega r^2} = 0.320$$

$$\frac{\dot{q}}{2\pi r} = 0.0148 \Omega r^2 \,\mathrm{Re}^{-1/5}$$

$$\frac{T}{\rho\Omega^2 R^5} = 0.0225 \,\mathrm{Re}^{-1/5}$$

for the 60 deg cone, and for the 20 deg cone,

$$\frac{\Gamma_c}{\Omega r^2} = 0.177$$

$$\frac{\dot{q}}{2\pi r} = 0.0217 \Omega r^2 \,\mathrm{Re}^{-1/5}$$

Table 1 Comparison between the analysis, computations, and experimental results for the rotating disk problem (Re = 1.47 × 10^6)

Rotating disks	Momentum-Integral analysis	Numerical computations 40×56	79×111	Experimental results
$\Gamma_c/\Omega r^2$	0.345	0.429	0.438	0.41–0.46
$T/\rho\Omega^2 R^5$	1.25×10^{-3}	1.20×10^{-3}	1.16×10^{-3}	1.17–1.29×10^{-3}
$\dot{q}/2\pi R$	1.06×10^{-3}	1.09×10^{-4}	1.03×10^{-3}	—

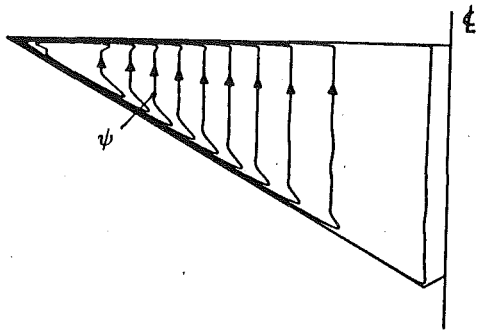

Fig. 5(a)

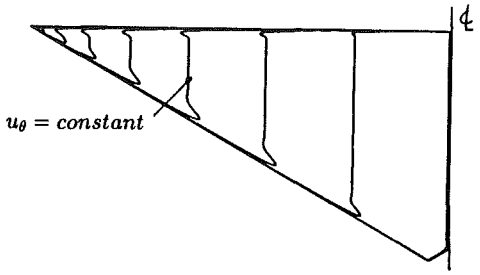

Fig. 5(b)

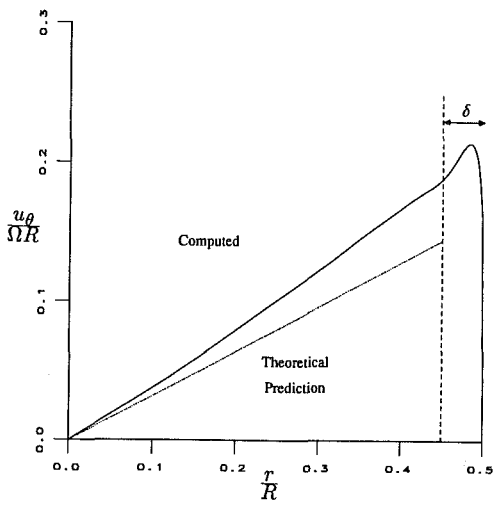

Fig. 5(c)

Fig. 5 Finite difference solutions for the flow in a 60 deg cone: (a) streamfunction; (b) contours of constant u_θ; (c) computed and theoretical core rotation u_θ at the mid-height

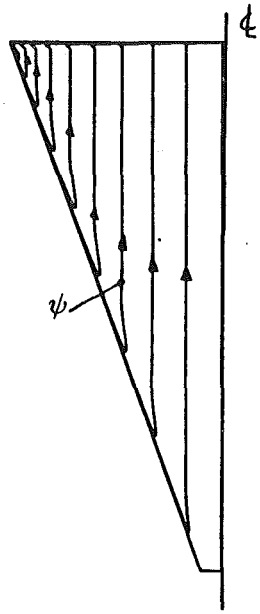

Fig. 6(a)

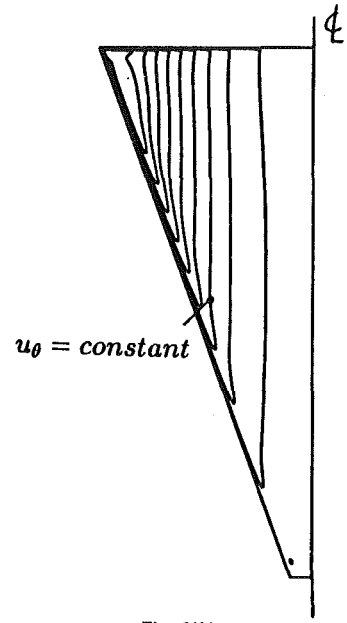

Fig. 6(b)

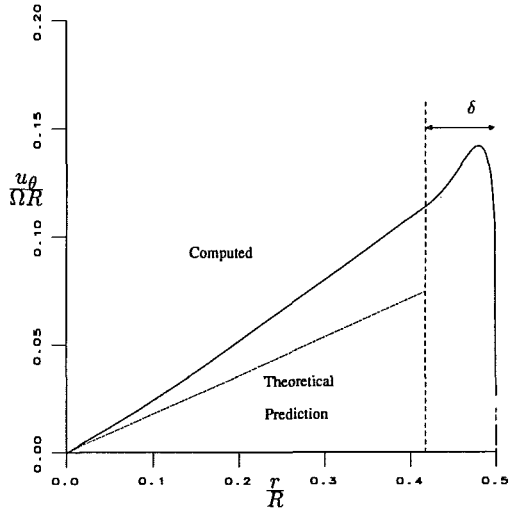

Fig. 6(c)

Fig. 6 Finite difference solutions for the flow in a 20 deg cone: (a) streamfunction; (b) contours of constant u_θ; (c) computed and theoretical core rotation u_θ at the mid-height

$$\frac{T}{\rho\Omega^2 R^5} = 0.0284\ \mathrm{Re}^{-1/5}$$

We have computed these flows using the finite difference code described in the previous section. Grids of 119 × 58 and 77 × 107 were used for the 20 and 60 deg cones, respectively. The values of Ω, R, ν, and ρ are the same as those specified in Section 4. The results are shown in Figs. 5 and 6. Each figure shows the streamfunction for the recirculation, the contours of constant u_θ, and a comparison of the computed and predicted core velocity at the mid-height of the cone.

It is clear from the streamfunction contours that all of the streamlines do pass through the boundary layers. Moreover, the contours of u_θ show that Γ_c is virtually independent of z, as predicted. As before core rotation rate does vary slightly with radius so comparisons between theory and computations are made at $r = 0.8 \times R$ and at the mid-height of the cone.

The computed values of $\Gamma_c/\Omega r^2$ and $T/\rho\Omega^2 R^5$ are compared with those calculated using the momentum-integral analysis in Table 2. As before, the momentum-integral analysis tends to underpredict the core rotation rate, this time by 23 percent for the 60 deg cone and 34 percent for the 20 deg cone. The dimensionless torque, $T/\rho\Omega^2 R^5$, is again predicted reasonably well.

In order to examine the scaling of $T/\rho\Omega^2 R^5$ with Reynolds number, we have repeated the computations for the 60 deg cone at $\Omega = 50$ rad/s. The computed values are given in Table 2. We find that $T/\rho\Omega^2 R^5 \propto \mathrm{Re}^{-0.207}$, which is in good agreement with the predicted scaling.

6 Flow Induced in a Hemisphere

As our third illustration of the analysis, we consider flow induced in a hemispherical container with a rotating lid. Here we make an additional simplification in the theory. Equation (16) gives κ_2/κ_1 in terms of $\Gamma_c/\Omega r^2$ evaluated at $r = R$. However, in our numerical computations we have found that the angular velocity is relatively uniform so we can take,

$$\frac{\kappa_2}{\kappa_1} = \left[\frac{\Gamma_c}{\Gamma_w - \Gamma_c}\right]_{r=0}^{1/4}$$

Table 2 Comparison between the analysis and computations for the cone problems (Re = 1.47×10^6 and Re = 7.35×10^6 for lid rotation of 10 rad/s and 50 rad/s, respectively)

Cone	Dimensionless parameter	Momentum-integral analysis	Numerical computations
60 deg 10 rad/s	$\Gamma_c/\Omega r^2$	0.320	0.418
	$T/\rho\Omega^2 R^5$	1.31×10^{-3}	1.13×10^{-3}
60 deg 50 rad/s	$\Gamma_c/\Omega r^2$	0.320	0.358
	$T/\rho\Omega^2 R^5$	0.950×10^{-3}	0.810×10^{-3}
20 deg 10 rad/s	$\Gamma_c/\Omega r^2$	0.177	0.270
	$T/\rho\Omega^2 R^5$	1.66×10^{-3}	1.48×10^{-3}

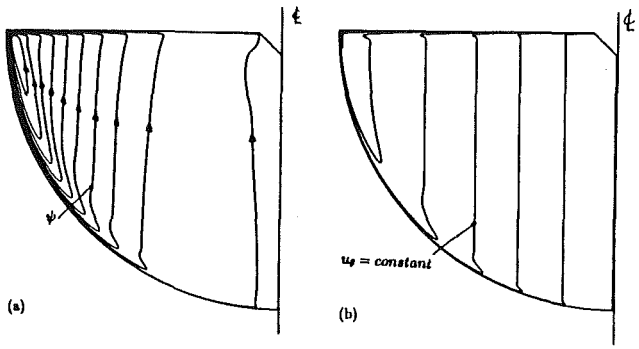

Fig. 7(a,b)

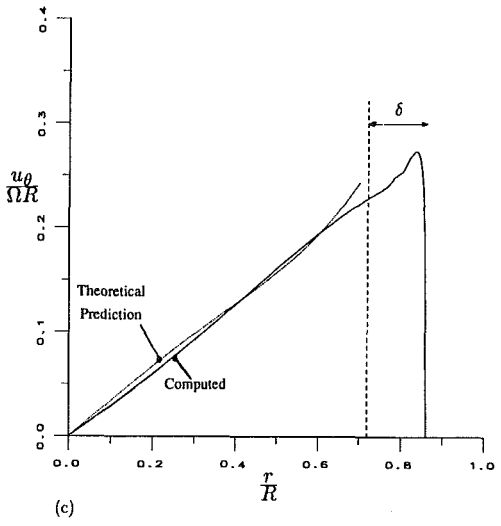

Fig. 7(c)

Fig. 7 Finite difference solutions for the flow in a hemisphere (a) streamfunction; (b) contours of constant u_θ; (c) computed and theoretical core rotatoin u_θ at $z = R/2$

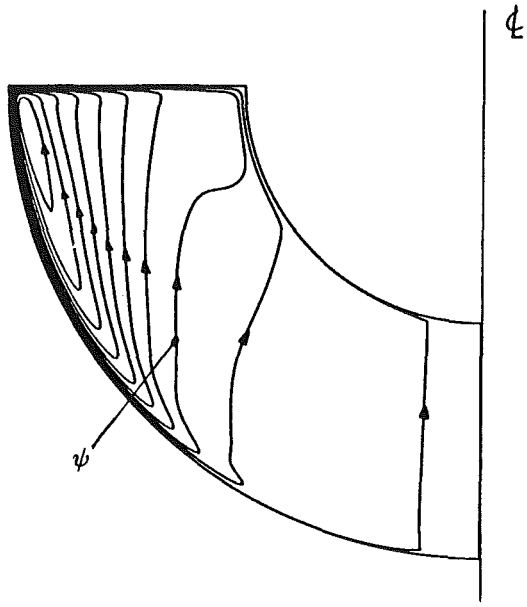

Fig. 8(a)

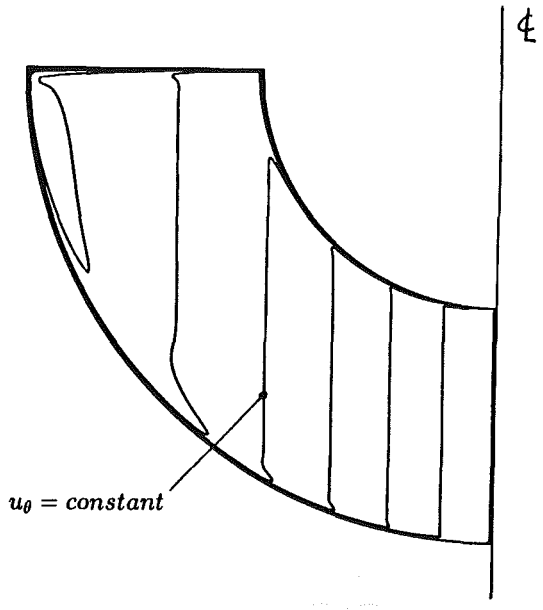

Fig. 8(b)

Fig. 8 Finite difference solutions for the flow between concentric hemispheres: (a) streamfunction; (b) contours of constant u_θ

with little loss of accuracy. Introducing the dimensionless core angular velocity, $\Delta(r)$, defined by,

$$\Delta(r) = \Gamma_c(r)/\Omega r^2$$

Equation (15) becomes,

$$\frac{1}{r^4}\frac{d}{dr}[\Delta^5 r^{12}]\int_0^r \Delta^{-4} r^{-8}\frac{ds}{dr_s}\,dr = -\Delta(1 - \Delta)\frac{ds}{dr_s} + (1-\Delta)^2\left[\frac{\Delta_0}{1-\Delta_0}\right]^{1/4} \quad (26)$$

where Δ_0 is $\Delta(0)$. Noting that

$$\frac{ds}{dr_s} = \frac{-1}{\sqrt{1-(r/R)^2}}$$

it is readily confirmed that the power series solution of (26) is

$$\Delta = 0.345[1 - 0.723(r/R)^2 + 1.515(r/R)^4) + \ldots] \quad (27)$$

Figure 7 shows the finite difference calculation of this flow using a 119 × 58 grid. Again the same values have been taken for Ω, R, and ν. As for the conical geometry, all of the streamlines pass through the boundary layers, and Γ_c is virtually independent of z. Figure 7 shows a comparison of the computed

theoretical values of u_θ at $z = R/2$. We see that there is very good agreement in the range where the expansion is valid.

Finally, we note that the arguments of Section 2 were entirely general, so that we would expect the core of any contained swirling flow to satisfy (5) and (6). This certainly seems to be the case for the three geometries considered so far. To further test this hypothesis we have computed the flow between concentric hemispheres where a radial lid is attached to the rotating inner hemisphere. Here the inner hemisphere rotates at 10 rad/s. The physical properties of the fluid and outer radius are as for the previous problems. The streamfunction and contours of constant u_θ are shown in Fig. 8. Again we see the same flow structure. In the core the streamlines and contours of constant u_θ are parallel to the axis. In addition, wall jets form on both the rotating and stationary surfaces. However the stream function contours show some variation with axial location, perhaps due to shear stress away from the boundaries near the region where the rotating surface is axial.

7 Discussion

For certain geometries and Reynolds numbers, multiple eddy structures could appear in the core. Our technique is not valid in such cases. However, when only one eddy forms, we have developed a comprehensive picture of the flow. Away from the boundaries, the flow exhibits no axial variation in angular momentum. This results in streamlines that are parallel to the axis. Near the boundaries, wall jets form which entrain or detrain fluid from the core. The result is that all the fluid is flushed through these narrow wall regions. This is evident in the numerical solutions which show all streamlines passing through the boundary layers.

These rather general features of the flow allows us to apply a momentum-integral technique. We have derived a single integro-differential equation, valid for any shape of container, and used this to predict the flow in several geometries. Unlike previous applications of the momentum-integral approach, our method determines the core flow through the explicit matching with the boundary layer. This momentum-integral analysis is seen to provide a reasonable prediction the core rotation rate and torque on the rotating boundaries.

A knowledge of this flow structure is useful even when the flow is to be computed numerically. In particular, it highlights the need for a refined mesh in regions where a wall jet forms. As the Reynolds number increases these wall jets become more intense and narrow, and so require a corresponding increase in grid resolution.

These two methods of solution therefore complement each other. For simple geometries all the important formation can (in principle) be derived using the momentum-integral approach. For more complicated geometries, which are best analyzed numerically, a prior understanding of the flow structure provides guidance for constructing a first mesh. Moreover, the scaling derived using the momentum-integral analysis is general, and thus allows the results of a single computation to be applied at different values of the Reynolds number. In particular, it offers the possibility of extrapolating the results to very high Reynolds number problems which are more difficult to compute numerically.

Acknowledgments

The finite difference code used was FLUENT, made available by Dr. F. Boysan of FLUENT Europe.

References

Batchelor, G. K., 1956, "On Steady Laminar Flows with Closed Streamlines at Large Reynolds Number," *Journal of Fluid Mechanics*, Vol. 1, pp. 177–398.

Daily, J. W., and Nece, N. E., 1960, "Chamber Dimension Effects on Induced Flow and Frictional Resistance of Enclosed Rotating Disks," ASME *Journal of Basic Engineering*, Vol. 82, pp. 217–232.

Davidson, P. A., Flood, S. C., and Kinnear, D., 1993, "Recirculating Flow due to a Rotational Body Force," *7th Beer-Sheva Conference on MHD Flows and Turbulence*, Feb., Proceedings in press.

Davidson, P. A., 1992, "Swirling Flow in an Axisymmetric Cavity of Arbitrary Profile, Driven by a Rotating Magnetic Field," *Journal of Fluid Mechanics*, Vol. 245, pp. 669–699.

Davidson, P. A., 1993, "Similarities in the Structure of Swirling and Buoyancy-Driven Flows," *Journal of Fluid Mechanics*, Vol. 252, pp. 357–382.

Davidson, P. A., and Hunt, J. C. R., 1987, "Swirling Recirculating Flow in a Liquid-Metal Column Generated by Rotating Magnetic Field," *Journal of Fluid Mechanics*, Vol. 185, pp. 67–106.

Greenspan, H. P., 1968, *The Theory of Rotating Fluids*, Cambridge University Press.

Kármán, Th. Von., 1921, "Uber Laminare and Turbulente Reibung," *Zeitschrift fur angewandte Mathematik und Mechanik*, Vol. 1, pp. 233–252.

Patankar, S. V., *Numerical Heat Transfer and Fluid Flow*, Hemisphere, 1980.

Rodi, W., 1984, "Turbulence Models and Their Application in Hydraulics—A State of the Art Review.

Schlichting, H., 1979, *Boundary Layer Theory*, McGraw-Hill.

A Numerical Study of Confined Turbulent Jets

J. Zhu

T.-H. Shih

Center for Modeling
of Turbulence and Transition,
ICOMP,
NASA Lewis Research Center,
Cleveland, OH 44135

A numerical investigation is reported of turbulent incompressible jets confined in two ducts, one cylindrical and the other conical with a 5 deg divergence. In each case, three Craya-Curtet numbers are considered which correspond, respectively, to flow situations with no, moderate, and strong recirculation. Turbulence closure is achieved by using the K-ϵ *model and a recently proposed realizable Reynolds stress algebraic equation model. Calculations are carried out with a finite-volume procedure. Second-order accurate differencing schemes and sufficiently fine grids are used to ensure numerical accuracy. The calculated results are compared with experimental data. It is shown that the numerical methods presented are capable of capturing the essential flow features observed in the experiments and that the realizable Reynolds stress algebraic equation model performs better than the* K-ϵ *model for this class of flows.*

1 Introduction

This paper is concerned with numerical computations of confined turbulent jets. The general features of the flow considered are sketched in Fig. 1. At the entrance, two uniform flows, a jet of high velocity and an ambient stream of low velocity, are discharged into the duct. Due to turbulent entrainment, the jet increases its mass flux while spreading and this causes an equal decrease in the mass flux of the ambient stream. An adverse pressure gradient is thus set up by the decrease in the velocity of the ambient stream which can be considered as an inviscid flow. When the ratio of jet to ambient velocities at the entrance is above a critical value and the jet to duct diameter ratio is small, a recirculation zone occurs at the duct wall downstream of the inlet plane. These features are common to many flows involving two streams of different velocities in industrial apparatus, in particular, in combustion chambers. Therefore, the understanding of confined jet flows is of great practical importance to the design of such devices.

Numerical calculations of confined jets have been reported by Gosman et al. (1979), Jones and Marquis (1985) and Zhu (1986). In these calculations, turbulence effects were represented either by the K-ϵ model or by second-moment closures. The success of numerical methods depends, to a large extent, on the performance of the turbulence model used. These numerical studies showed that the calculations with the K-ϵ model could reproduce some basic flow characteristics observed in the experiments in general, but large discrepancies were present in detail. The discrepancies were mostly attributed to inherent imperfections of the model such as the isotropic eddy-viscosity representation and the insensitivity to streamline curvature effects. Second-moment closures have no such drawbacks and represent a higher level of turbulence modeling beyond the eddy-viscosity level. However, it was found in a systematical numerical study (Zhu, 1986) that second-moment closures, whether of the algebraic or of the transport form, did not manifest themselves to be significantly superior to the K-ϵ model in the computation of confined jets.

Recently, Shih and Lumley (1993) have shown that the Reynolds stress, being a second rank tensor, can be expressed as a sixth-order polynomial of the mean velocity gradients. This is the most general stress-strain relationship within the framework of algebraic turbulence modeling, with the linear stress-strain relation in the Boussinesq's eddy-viscosity concept being its first-order approximation. Based on this, Shih et al. (1993) have recently proposed a quadratic stress-strain relation in conjunction with the two modeled equations of K and ϵ for practical calculations. Realizability constraints have been used to derive appropriate expressions for the model coefficients, in particular, the coefficient C_μ has been naturally related to the time scale ratio of the turbulence to the mean strain rate. As a result, the model ensures the positivity of individual turbulent normal stresses, an important feature that is not present in most existing turbulence models. As the model appears promising as a competitive alternative in the turbulence modeling arsenal, it is of interest to test its performance for confined jets which, due to their complicated flow structures

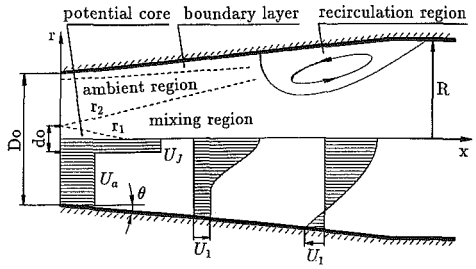

Fig. 1 Flow configuration and notations

Contributed by the Fluids Engineering Division for publication in the JOURNAL OF FLUIDS ENGINEERING. Manuscript received by the Fluids Engineering Division May 14, 1993; revised manuscript received April 15, 1994. Associate Technical Editor: O. Baysal.

such as strong recirculation coupled with severe adverse pressure gradients, constitute a challenge to the turbulence modeling.

To this end, calculations are performed for the flows studied experimentally by Barchilon and Curtet (1964) in a cylindrical duct and by Binder and Kian (1983) in a conical duct with 5 deg divergence. These two experiments have been chosen in this study because of their diverse flow conditions which vary gradually from no to strong recirculation. The standard K-ϵ model is also used, since it is the most popular turbulence model used today in calculations of complicated flows and can also be used to highlight the performance of the new model. The numerical accuracy of solutions is ensured by using second-order accurate differencing schemes and sufficiently fine grids. The performances of the models are examined through comparisons with experimental data.

2 Calculation Approach

Incompressible turbulent flows are governed by the following statistically averaged continuity and Navier-Stokes equations:

$$U_{i,i}=0 \tag{1}$$

$$(\rho U_j U_i-\mu U_{i,j}-\tau_{ij})_{,j}=-p_{,i} \tag{2}$$

The Reynolds or turbulent stresses $\tau_{ij}(=-\rho\overline{u_i u_j})$ appearing in these equations are calculated by using the following two models:

1) K-ϵ model (Launder and Spalding, 1974)

$$\tau_{ij}=\mu_t(U_{i,j}+U_{j,i})-\frac{2}{3}\rho K\delta_{ij} \tag{3}$$

$$\mu_t=C_\mu\rho K^2/\epsilon, \quad C_\mu=0.09 \tag{4}$$

where the turbulent kinetic energy K and its dissipation rate ϵ are calculated, respectively, by the following transport equations:

$$\left[\rho U_j K-\left(\mu+\frac{\mu_t}{\sigma_K}\right)K_{,j}\right]_{,j}=G-\rho\epsilon \tag{5}$$

$$\left[\rho U_j \epsilon-\left(\mu+\frac{\mu_t}{\sigma_\epsilon}\right)\epsilon_{,j}\right]_{,j}=(C_1 G-C_2\rho\epsilon)\frac{\epsilon}{K} \tag{6}$$

where

$$G=\tau_{ij}U_{i,j} \tag{7}$$

$$C_1=1.44, \quad C_2=1.92, \quad \sigma_K=1, \quad \sigma_\epsilon=1.3 \tag{8}$$

2) Realizable Reynolds stress algebraic equation (RRSAE) model (Shih et al., 1993)

$$\tau_{ij}=\mu_t(U_{i,j}+U_{j,i})+T_{ij}-\frac{2}{3}\rho K\delta_{ij} \tag{9}$$

$$\mu_t=C_\mu\rho K^2/\epsilon, \quad C_\mu=\frac{2/3}{A_1+\eta} \tag{10}$$

where

$$T_{ij}=-\frac{\rho K^3}{(A_2+\eta^3)\epsilon^2}\left[C_{\tau 1}\left(U_{i,k}U_{k,j}+U_{j,k}U_{k,i}-\frac{2}{3}\Pi\delta_{ij}\right)\right.$$
$$\left.+C_{\tau 2}\left(U_{i,k}U_{j,k}-\frac{1}{3}\tilde{\Pi}\delta_{ij}\right)+C_{\tau 3}\left(U_{k,i}U_{k,j}-\frac{1}{3}\tilde{\Pi}\delta_{ij}\right)\right] \tag{11}$$

$$\Pi=U_{k,l}U_{l,k}, \quad \tilde{\Pi}=U_{k,l}U_{k,l} \tag{12}$$

$$\eta=K(2S_{ij}S_{ij})^{1/2}/\epsilon, \quad S_{ij}=(U_{i,j}+U_{j,i})/2 \tag{13}$$

and the model constants are

$$C_{\tau 1}=-4, \quad C_{\tau 2}=13, \quad C_{\tau 3}=-2, \quad A_1=5.5, \quad A_2=1000. \tag{14}$$

The K and ϵ in the RRSAE model are calculated with the same equations as in the K-ϵ model. It can be seen that the RRSAE model reduces to the K-ϵ model if the quadratic terms T_{ij} are set to zero.

Computational boundaries involved are inlet, outlet, axis of symmetry and solid wall. Among them, the inlet conditions require special attention because they have a considerable influence on the calculations (Zhu et al., 1987). At the inlet, the jet and the ambient flow have uniform velocities U_J and U_a (Fig. 1), but the flow conditions in the initial shear layer between the jet and the ambient flow are unknown and determination of these conditions is not a trivial matter. In the present work, the parabolic entrance region scheme of Zhu et al. (1987) is used to specify the initial shear layer conditions. The outlet boundary is placed at $x=10D_o$ which is sufficiently far away from the main region of interest. At this boundary streamwise gradients of all variables are set to zero. Along the axis of symmetry the normal velocity component and the normal gradients of the other variables are set to zero. The standard wall-function approach (Launder and Spalding, 1974) is used to bridge the viscous sublayer at the duct wall, which is based on two considerations: 1. the RRSAE model in its present form is only valid for high Reynolds number turbulent flows; 2. since the maximum turbulent stresses occur in a region far away from the wall, the present computations are not sensitive to the near-wall turbulence modeling, except for the wall shear stress.

The computations are carried out using a conservative finite-volume method designed for calculating incompressible elliptic flows with complex boundaries. The method uses a non-staggered variable arrangement. The momentum interpolation procedure of Rhie and Chow (1983) is used to avoid checkerboard oscillations usually associated with non-staggered grids. The velocity-pressure coupling is achieved via the SIMPLEC algorithm (Van Doormal and Raithby, 1984). To ensure numerical accuracy and stability, the convection terms of all the transport equations are differenced by the hybrid linear/parabolic approximation (HLPA) of second-order accuracy (Zhu, 1991a), and all the other terms by the conventional central differencing scheme. The governing equations are solved in a sequential manner. The resulting set of algebraic difference equations is solved with the strongly implicit procedure of Stone (1968). The calculation is started from an assumed fully-developed turbulent field and the iterative solution process is regarded as converged when the maximum normalized residue of all the dependent variables is below 0.5 percent. The details of the present numerical procedure are given in Zhu (1991b).

3 Results

The experiments of Barchilon and Curtet (1964) and Binder and Kian (1983) were taken as the test cases, hereinafter terms BC- and BK-case, respectively. The geometrical dimensions and the inlet flow conditions of both cases are given in Tables 1 and 2. In the BK-case, the velocity field and the pressure field were measured separately using the different inlet velocities as shown in Table 2. The Craya-Curtet number C_t is defined by

$$C_t=\frac{1}{\sqrt{m}}, \quad m=\frac{S}{Q^2}\int_S\left(U^2+\frac{p}{\rho}\right)dS-\frac{1}{2} \tag{15}$$

where Q and S are the total flow rate and the duct area, respectively.

Calculations were made on the Cray YMP computer. The grid-dependency of solutions was examined using two convection schemes, HLPA and HYBRID (central/upwind differencing), and three grid consisting of 50×40 (grid 1), 86×50 (grid 2), and 120×80 (grid 3) points, respectively. The HYBRID scheme that is highly diffusive in the presence of both convective dominance and flow-to-grid skewness was used here

Table 1 Geometrical dimensions of the ducts

case	D_o (cm)	d_o (cm)	θ (degree)	L (cm)
BC	16	1.2	0	
BK	16	1.6	2.5	64

Table 2 Inlet flow conditions

case	C_t	U_J (cm/s)	U_a (cm/s)
BC	0.976	1293.6	84.48
	0.506	1253.8	39.81
	0.152	1296.2	7.42
BK (velocity field)	1.230	40	4.885
	0.775	40	2.662
	0.590	40	2.330
BK (pressure field)	1.090	650	61.38
	0.842	650	46.58
	0.570	650	29.90

Table 3 Separation and reattachment points (x_s/D_o, x_r/D_o)

case	C_t	experiment	K-ϵ	RRSAE
BC	0.506	1.70, 3.07	1.37, 2.7	1.6, 3.03
	0.152	0.45, 3.07	0.40, 2.95	0.5, 3.15
BK	0.775	2.50, 3.4~3.8	1.82, 3.17	2.15, 3.79
	0.590	1.50, 3.4~3.8	1.43, 3.22	1.45, 3.81

only to highlight the importance of using higher-order accurate schemes. Test results obtained with the RRSAE model at $C_t = 0.506$ are shown in Fig. 2(a) for the axial velocity U-profiles, normalized by the sectional mean velocity U_m, and Fig. 2(b) for the turbulent shear stress $\overline{uv}$-profiles, both at the same downstream location $x/D_o = 1.875$. It can be seen that the results of HLPA on the coarse grid 1 are already very close to those on the fine grid 3 for both the U- and the $\overline{uv}$-profiles, while significant differences exist between the corresponding results of HYBRID. The HLPA results on the intermediate grid 2 can be considered as grid-independent because the refinement from the grid 2 to the grid 3 produced differences too small to be seen on the graph. The HYBRID solutions, however, responded to the grid refinement in such a slow manner that they still had not reached the grid-independent stage on the finest grid. The numbers of iterations and CPU-time in minutes required for the calculations with HLPA were 196 and 0.2 on grid 1, 640 and 1.4 on grid 2 and 1874 and 9.3 on grid 3. The calculations with HYBRID took about 0.6~0.8 of these numbers. The grid 2 and HLPA were used for all subsequent calculations.

Figure 3 shows the axial mean velocity profiles at four downstream locations, at the smallest value of C_t in each case. In the BC-case, the RRSAE model results are in excellent agreement with the experimental data whereas noticeable discrepancies exist in the K-ϵ model results at the last three downstream locations. In the BK-case, the results of RRSAE model are also better than those of the K-ϵ model, but the agreement is less satisfactory than in the BC-case. At the location $x/D_o = 1.25$, the experimental profile shows no constant ambient velocity portion while the calculated profiles by both models still have a vertical plateau around $r/R = 0.6$. The comparison at the location $x/D_o = 2.5$ indicates that the width of the predicted reverse-flow region is somewhat too thin. Comparing the corresponding profiles in the BC-case which has a much stronger recirculation, the experimental velocity minimum at the last location seems to be too far away from the duct wall. It is to be noted that the flow is highly perturbed in the recirculation region in which the measurement uncertainty is likely to be greatest.

The separation and reattachment points are given in Table 3. In the BK-case, only a range of $3.4 \sim 3.8 D_o$ was given experimentally for the reattachment point due to the high unsteadiness of the recirculation bubbles. The experiments in both

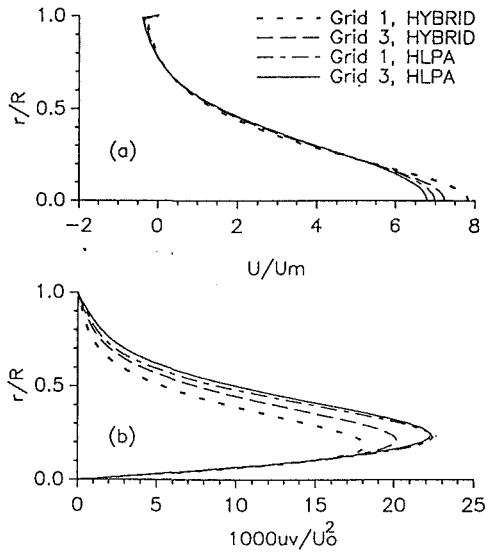

Fig. 2 Numerical accuracy test at $C_t = 0.506$

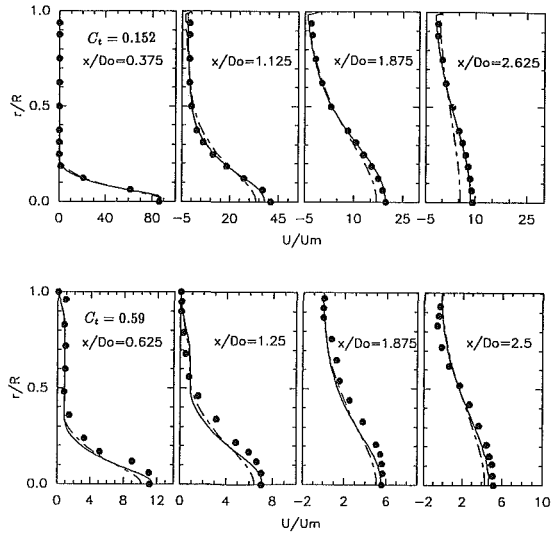

Fig. 3 Axial mean velocity profiles: —·— K-ϵ model; — RRSAE model; • experiment

the BC- and BK-cases revealed that as C_t decreased, the separation points moved upstream while the reattachment points remained basically unchanged. The RRSAE model captured this feature well and predicted the locations of the recirculation bubbles better than did the K-ϵ model.

In order to study the jet spreading, the excess flow rate Q_j has been introduced which is defined as $Q_j = 2\pi \int_0^{r_2} (U - U_1) r dr$, where U_1 is the ambient velocity (Fig. 1). In the recirculation region, the ambient velocity has no physical meaning and is defined as the minimum velocity (having negative value) for analytical convenience. Fig. 4 shows the variation of Q_j with x and C_t. As a consequence of the turbulent entrainment, the excess flow rate increases first, passes through a maximum and then decreases in case of recirculation which corresponds to $Q_j/Q \geq 1$. This variation becomes more pronounced as C_t decreases. The calculations agreed well with the experiments at large C_t, but the agreement deteriorated as recirculation intensified. At small C_t (< 0.6), the calculation underpredicted the maximum excess flow rate. It should be pointed out that the excess flow rate, due to its definition, is a quantity that is highly sensitive to errors in the velocity profiles so that a small change in U_1, especially in the recirculation zone, will result

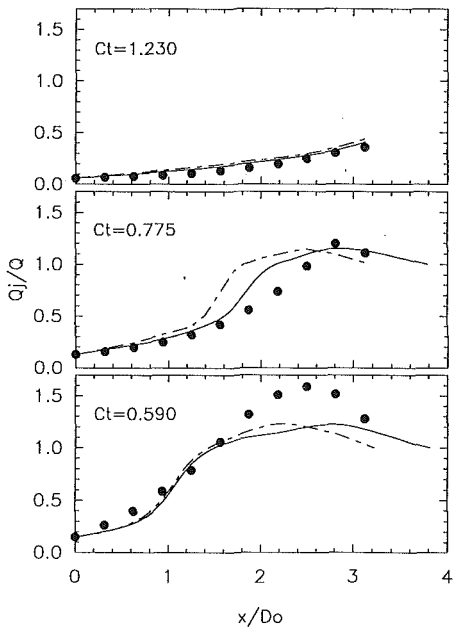

Fig. 4 Excess flow rate (legend as in Fig. 3)

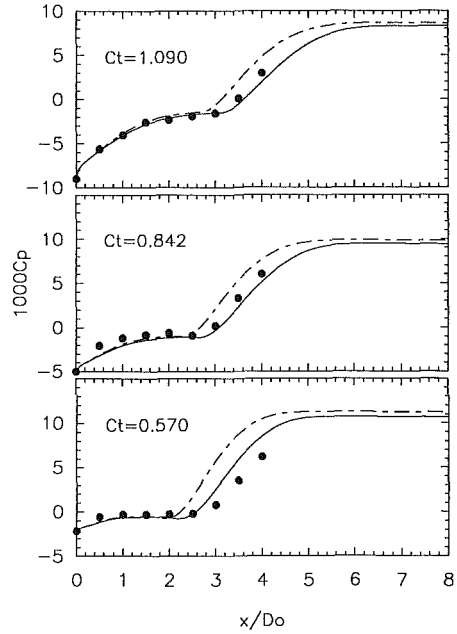

Fig. 5 Pressure coefficient along the duct wall (legend as in Fig. 3)

in a large difference in Q_j. Regarding the comparison between the two models, the RRSAE model clearly performed better than did the K-ϵ model.

Figure 5 shows the variation of pressure coefficients along the duct walls. Here, $C_p = (\Delta p - 0.5\rho U_a^2)/(0.5\rho U_j^2)$ and Δp is the pressure difference between the location x and the entrance. The pressure gradient is governed by the jet entrainment, the contraction and expansion of the flow caused by recirculating eddies as well as the geometry of the duct. The entrainment and the divergence of the duct can only produce a maximum pressure difference equal to $\rho U_a^2/2$, while the pressure difference created by the divergence of streamlines in the downstream part of the recirculating bubble can be much larger than $\rho U_a^2/2$. This explains the variation of C_p with C_t seen in Fig. 5. Regarding the comparison between predictions and experiments, it can be seen that although both models predict prac-

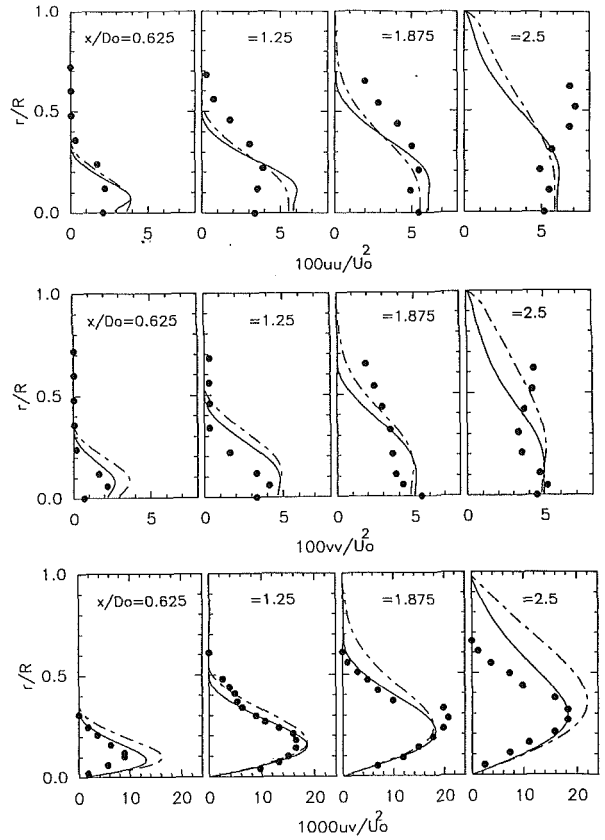

Fig. 6 Turbulent stress profiles at $C_t = 0.59$ (legend as in Fig. 3)

tically the same total pressure rises, the RRSAE model captures the location where the pressure starts to shoot up much better than the K-ϵ model at all the C_t numbers.

Detailed experimental data for the turbulent stresses $\overline{uu}$, $\overline{vv}$ and $\overline{uv}$ are available only in the BK-case at $C_t = 0.59$. The computed and measured radial profiles of these quantities at four downstream locations are compared in Fig. 5. With regard to the turbulent normal stresses $\overline{uu}$ and $\overline{vv}$, the experimental data are basically followed by the results of both the RRSAE model and the K-ϵ model, with the former predicting more anisotropy than the latter. The experimental data at $x/D_o = 2.5$ are seen to exhibit a different trend for both $\overline{uu}$ and $\overline{vv}$, which may possibly be due to measurement errors. The flow visualization in the experiment indicated that the global flow pattern was highly unsteady in the presence of recirculation. With due regard to flow complexities and measurement difficulties, the agreement between the predictions and measurements seen in Fig. 6 should be considered as reasonably good, but it is difficult to judge which model performs better for the turbulent normal stresses, overall. For the turbulent shear stress $\overline{uv}$, the results obtained with the RRSAE model are clearly better than those with the K-ϵ model for all the locations considered. The large discrepancy seen at $x/D_o = 2.5$ is partially due to the underprediction of the width of the backflow region and partially due to the experimental uncertainty, as evidenced by the fact that in the experimental data, the change in sign of the shear stress profile occurs much further away from the duct wall than the velocity minimum.

4 Concluding Remarks

A numerical study has been conducted on axisymmetric confined jets in two ducts with and without divergence. The focus of the study was on the performance of the two turbulence

models under various flow conditions ranging from no to strong recirculation. The RRSAE model is new, and its capability to predict this type of flows needs to be tested. The K-ϵ model was applied to the same problem before, but we believe that a re-assessment is necessary because the previous studies were made on an inaccurate numerical basis (first-order differencing together with very coarse grids). This study has shown that the confined jet calculations are very sensitive to the convective approximation of the transport equations. In order to achieve a numerically credible solution without involving excessive grid points, higher-order differencing schemes have to be adopted. In this regard, the second-order accurate HLPA scheme behaves quite well. Therefore, it can be concluded with a sufficient degree of confidence that the present calculations reflect the real predictive capability of the models for the confined jets.

The calculations have been compared with the experiments. The comparison clearly shows that superiority of the RRSAE model over the K-ϵ model under all the circumstances considered, which is mainly due to the two important properties of the RRSAE model for separated flows: 1. the anisotropic representation of the Reynolds stresses; 2. the new formulation of C_μ which leads to a reduction in μ_t in regions of high η value. Only for the maximum reverse flow rate, an important parameter to characterize the performance of combustion chambers, does the RRSAE model result in little improvement. Since this quantity is directly related to the flow near the wall in the recirculation region, the use of the wall function may constitute a source of error and also measurement errors should not be excluded in this highly perturbed region. Overall, the RRSAE model is shown to be able to predict confined jets with an accuracy sufficient for engineering applications.

References

Barchilon, M., and Curtet, R., 1964, "Some Details of the Structure of an Axisymmetric Confined Jet with Backflow," ASME *Journal of Basic Engineering*, Vol. 86, pp. 777–787.

Binder, G., and Kian, K., 1983, "Confined Jets in a Diverging Duct," *Proceedings, Turbulent Shear Flows 4*, Karlsruhe, pp. 7.18–7.23.

Gosman, A. D., Khalil, E. E., and Whitelaw, J. H., 1979, "The Calculation of Two-Dimensional Turbulent Recirculating Flows," *Turbulent Shear Flows 1*, F. Durst, B. E. Launder, F. W. Schmidt, and J. H. Whitelaw, eds., Springer-Verlag, pp. 237–255.

Jones, W. P., and Marquis, A. J., 1985, "Calculation of Axisymmetric Recirculating Flows with a Second Order Turbulent Model," *Proceedings, Turbulent Shear Flows 5*, Cornell University, Ithaca, pp. 20.1–20.6.

Launder, B. E., and Spalding, D. B., 1974, "The Numerical Computation of Turbulent Flows," *Computer Methods in Applied Mechanics and Engineering*, Vol. 3, pp. 269–289.

Rhie, C. M., and Chow, W. L., 1983, "A Numerical Study of the Turbulent Flow Past an Isolated Airfoil with Trailing Edge Separation," *AIAA Journal*, Vol. 21, pp. 1525–1532.

Shih, T.-H., and Lumley, J. L., 1993, "Remarks on Turbulent Constitutive Relations," *Math. Comput. Modelling*, Vol. 18, pp. 9–16.

Shih, T.-H., Zhu, J., and Lumley, J. L., 1993, "A Realizable Reynolds Stress Algebraic Equation Model," NASA TM 105993.

Stone, H. L., 1968, "Iterative Solution of Implicit Approximations of Multidimensional Partial Differential Equations," *SIAM J. Num. Anal*, Vol. 5, pp. 530–558.

Van Doormal, J. P., and Raithby, G. D., 1984, "Enhancements of the SIMPLE Method for Predicting Incompressible Fluid Flows," *Numerical Heat Transfer*, Vol. 7, pp. 147–163.

Zhu, J., 1986, "Calcul des jets turbulents confinés avec recirculation," Doctoral dissertation, l'Institut National Polytechnique de Grenoble, France.

Zhu, J., Binder, G., and Kueny, J. L., 1987, "Improved Predictions of Confined Jets with a Parabolic Computation of the Entrance Region," *AIAA Journal*, Vol. 25, pp. 1141–1142.

Zhu, J., 1991a, "A Low Diffusive and Oscillation-Free Convection Scheme," *Communications in Applied Numerical Methods*, Vol. 7, pp. 225–232.

Zhu, J., 1991b, "FAST-2D: A Computer Program for Numerical Simulation of Two-Dimensional Incompressible Flows with Complex Boundaries," Rept. No. 690, Institute for Hydromechanics, University of Karlsruhe.

P. S. Cumber

M. Fairweather

British Gas plc,
Research and Technology,
Gas Research Centre,
Loughborough LE11 3QU, England

S. A. E. G. Falle
Department of Applied Mathematics,
The University of Leeds,
Leeds LS2 9JT, England

J. R. Giddings
Mantis Numerics Ltd.,
46 The Calls,
Leeds LS2 7EY, England

Predictions of the Structure of Turbulent, Moderately Underexpanded Jets

A mathematical model capable of predicting the structure of turbulent, underexpanded jets is described. The model is based on solutions of the fluid flow equations obtained using a second-order accurate, finite-volume integration scheme coupled to an adaptive grid algorithm. Turbulence within these jets is modelled using a k-ϵ approach coupled to the compressible dissipation rate model of Sarkar et al. (1991a). Comparison of model predictions and experimental data, reported in the literature, on a number of moderately underexpanded jets demonstrate significant improvements over results derived using the standard k-ϵ approach, and the adequacy of the compressibility corrected turbulence model for predicting such jets.

Introduction

Underexpanded, axisymmetric free jets are one of the simplest flows involving both turbulent mixing and compressibility effects. As well as being of interest to fundamental studies of the interaction of turbulence and compressibility, the ability to predict the detailed structure of such flows has numerous practical applications ranging from the design of rocket propulsion systems to consequence and risk assessments of leaks of high pressure gas. A final motivation for studying the simple axisymmetric case is that detailed measurements of a number of such jets exist in the literature. In the absence of detailed measurements on more complex flows, these data provide the opportunity to validate rigorously mathematical models of turbulent, underexpanded jets such that their predictions can be applied with confidence to other, more complex, compressible flow situations.

The flow pattern of a jet issuing from a straight or convergent nozzle depends primarily on the ratio of the pressure at the nozzle exit to the ambient pressure. Three types of flow are possible depending on this pressure ratio, these being subsonic, moderately underexpanded and highly underexpanded jets. The values of pressure ratio separating these three generic flow regimes are dependent on the physical properties of the gas issuing from the nozzle, although the variation from one gas to another is small. For the case of air, moderately underexpanded jets, the subject of the present paper, exist in the range P_0/P_a from $\simeq 1.1$ to 2.1 and are characterized by a system of oblique shocks downstream of the nozzle exit which is embedded in the potential core of the jet. The potential core itself is surrounded by a mixing region that diffuses inward, ultimately dissipating the core. Downstream of the core, once the jet is subsonic, the spread and decay of the jet are similar to the totally subsonic case.

A number of research groups have derived mathematical models of such jets. Dash and Wolf (1983) and Chuech et al. (1989) based predictions on simplified forms of the fluid dynamic equations derived by neglecting streamwise diffusion. This approach simplifies the computational algorithm required for solution of the system of differential equations, allowing results to be derived using efficient marching procedures. However, although this approach has been used to model the three-dimensional case of a supersonic jet issuing from a rectangular nozzle (Dash et al., 1986), the complexities associated with its extension to more complex three-dimensional flows makes its general application difficult.

The present study describes a mathematical model capable of predicting the structure of turbulent, underexpanded jets, and validates predictions of the model against available experimental data on moderately underexpanded releases. The model described differs from the theoretical approaches referred to above in deriving solutions from the elliptic versions of the fluid flow equations using a second-order accurate, finite-volume integration scheme coupled to an adaptive grid algorithm. These techniques allow sonic releases to be modeled economically, and offer the potential for ultimate application to predicting such flows not only in axisymmetry but also in more complex three-dimensional geometries.

Mathematical Model

Governing Equations. The flow from a circular nozzle is governed by the steady-state, axisymmetric form of the fluid

Contributed by the Fluids Engineering Division for publication in the JOURNAL OF FLUIDS ENGINEERING. Manuscript received by the Fluids Engineering Division May 12, 1993; revised manuscript received February 23, 1994. Associate Technical Editor: R. W. Metcalfe.

flow equations. Solutions of the density-weighted (Favre) averaged, high Reynolds number form of these equations (Jones and Whitelaw, 1982), expressing conservation of mass, momentum, and scalar transport (mixture fraction), were used as the basis of the predictions reported later, with density-weighted averaging being used as most appropriate for the variable density flows of interest. Closure of this set of equations was achieved through the use of a standard two-equation, k-ϵ turbulence model (Jones and Launder, 1972). Modelling constants employed were standard values found to give acceptable agreement between theoretical predictions and experimental data in a wide range of flows (Jones and Whitelaw, 1982).

In addition to the equations outlined above, a conservation equation for the total energy of the fluid, E, was also solved. For solution, the equation was written in a form appropriate to axisymmetric flows but, for reasons of brevity, is given below in Cartesian tensor form:

$$\frac{\partial}{\partial x_j}[\tilde{U}_j(\bar{\rho}\tilde{E}+\bar{P})]=\frac{\partial}{\partial x_j}(\tilde{U}_i\bar{\tau}_{ij})+\frac{\partial}{\partial x_j}\left(\frac{\mu_t}{\sigma_E}C_p\frac{\partial\tilde{T}}{\partial x_j}\right). \quad (1)$$

In the above, turbulent transport has again been represented using a gradient diffusion model, and the stress tensor was specified in line with the k-ϵ turbulence model assumptions. The total energy is defined as

$$\tilde{E}=\tilde{e}+1/2\,\tilde{U}_i^2+k, \quad (2)$$

where e is the internal energy of the gas. The constant σ_E was assigned the standard value of 0.9. For the air jet simulations considered later a constant value of C_p was employed, whereas C_p was taken as a function of chemical composition for the natural gas jet studied. The temperature dependence of C_p was neglected because of the absence of strong shocks in the experiments considered (Pai, 1959). Finally, the system of equations was augmented by the ideal gas law for solution.

Turbulence Models. The k-ϵ turbulence model used in the present work may be expressed in its conventional form (Jones and Whitelaw, 1982) as

$$\frac{\partial}{\partial x_j}(\bar{\rho}\tilde{U}_j k)=\frac{\partial}{\partial x_j}\left(\frac{\mu_t}{\sigma_k}\frac{\partial k}{\partial x_j}\right)-\bar{\rho}\,\widetilde{u_i''u_j''}\frac{\partial\tilde{U}_i}{\partial x_j}-\bar{\rho}\epsilon \quad (3)$$

$$\frac{\partial}{\partial x_j}(\bar{\rho}\tilde{U}_j\epsilon)=\frac{\partial}{\partial x_j}\left(\frac{\mu_t}{\sigma_\epsilon}\frac{\partial\epsilon}{\partial x_j}\right)-C_1\frac{\epsilon}{k}\bar{\rho}\,\widetilde{u_i''u_j''}\frac{\partial\tilde{U}_i}{\partial x_j}-C_2\bar{\rho}\frac{\epsilon^2}{k}, \quad (4)$$

with

$$\mu_t=C_\mu\bar{\rho}\frac{k^2}{\epsilon}. \quad (5)$$

This model has been used extensively for predicting incompressible flows, although for compressible flows the standard model stated is known to overpredict turbulence levels, and hence mixing rates, because it does not account for the effect of compressibility on turbulence dissipation. This has been observed in many experimental studies, for example, as reported by Papamoschou and Roshko (1986). It is therefore important to accurately model such effects if reliable predictions of jet velocity and concentration are required.

A number of authors have suggested modifications, or alternatives, to Eqs. (3) to (5) in order to incorporate compressibility effects into turbulent flow calculations. Dash and Wolf (1983) evaluated a number of different turbulence models for such flows; namely, the standard k-ϵ turbulence model (Jones and Launder, 1972), a compressibility corrected k-ϵ model, and the k-W model of Spalding (1971) with the turbulence model constants calibrated using compressible free jet data. These authors considered the latter model as the most capable of predicting the free jet data considered. However, the k-W model requires special treatment near walls to correctly model the damping of turbulence by solid boundaries, and as a consequence is not easily applied to wall-bounded shear flows. The compressibility corrected k-ϵ model used differed from the standard version in that the turbulent viscosity was considered to be a function of the turbulent Mach number, a dimensionless velocity scale based on the local maximum value of k, with the latter equation being multiplied by $f(M_\tau)$. The functional dependence of the turbulent viscosity on M_τ was then derived by calibrating the model with measured spreading rate data obtained from supersonic shear layers (Birch and Eggers, 1973), with μ_τ, and hence turbulence levels, decreasing with increasing M_τ.

Chuech et al. (1989) used a similar approach, and derived a compressible turbulent viscosity model based on a convective Mach number, M_c; a dimensionless velocity scale associated with large scale structures in a shear layer. The functional dependence of the turbulent viscosity on M_c was then derived using the measured spreading rate data obtained by Papamoschou and Roshko (1986) and other researchers. However, although the modified turbulent viscosity models proposed by both Dash and Wolf (1983) and Chuech et al. (1989) resulted in good agreement between model predictions and experimental data on sonic jets, adjusting the turbulent viscosity to account for reduced mixing does not model the underlying physical mechanism responsible for reduced turbulence generation, only the net effect, and so the approach cannot be expected to be general.

Nomenclature

a = local speed of sound
C_p = specific heat at constant pressure
C_1, C_2, C_μ = turbulence model constants
d = nozzle diameter
e = internal energy
E = total energy
f = mixture fraction
k = turbulence kinetic energy
M = Mach number [$= U/a$]
M_c = convective Mach number
M_τ = turbulent Mach number [$=(2k)^{0.5}/a$]
P = pressure
r = radial coordinate
S_k = additional source term in transport equation for k
T = temperature
u'' = fluctuating velocity
U = mean velocity
U_a = reference velocity [$=(P_a/\rho_a)^{0.5}$]
W = fluctuating vorticity parameter
x = general coordinate
z = axial coordinate
α_1 = constant in compressible dissipation rate model
Δr = grid spacing in r direction
Δz = grid spacing in z direction
ϵ = dissipation rate of k
μ_t = turbulent viscosity
ρ = density
σ_E, σ_k, σ_ϵ = Prandtl/Schmidt numbers
τ = stress tensor

Subscripts

a = ambient value
c = compressible
j = in jth direction
o = nozzle exit condition

Superscripts

$^-$ = conventional time average
$\sim$ = density-weighted average

Other authors have proposed multi-turbulence length scale modifications to the standard k-ϵ model in order to incorporate compressibility effects, for example Abdol-Hamid and Wilmoth (1989) and Brescianini (1992). However, although such approaches show improvements over the predictions of the single scale model, further understanding of the details and importance of multi-scale effects in such flows is required.

Recently, direct numerical simulation of simple compressible turbulent flows has provided sufficient insight to allow the underlying physical mechanism responsible for reduced mixing to be identified. Lee et al. (1991) simulated decaying compressible turbulence using this method and observed the formation of shocks, or eddy shocklets, in the instantaneous flow field. These eddy shocklets are formed by compression waves generated by the mixing of high speed and low speed fluid in the instantaneous field. Sarkar et al. (1991a) analyzed the exact equations for the transport of Reynolds stress in compressible flows, finding the important sink terms in the turbulent kinetic energy budget generated by the eddy shocklets; namely a compressible turbulence dissipation rate and to a lesser extent the pressure-dilatation term. For the case of low Mach number, isotropic turbulence, as studied by the latter authors, the pressure-dilatation term was found to be negligibly small. For the compressible dissipation rate, Sarkar et al. (1991a) proposed the model

$$\epsilon_c = \alpha_1 M_\tau^2 \epsilon, \tag{6}$$

derived from an asymptotic analysis of the compressible Navier-Stokes equations over an acoustic time scale, and calibrated using direct numerical simulations. This model was subsequently incorporated into a second-order turbulence closure model by Speziale and Sarkar (1991) and the composite model, with the constant α_1 set to one to allow for the neglected pressure-dilatation term, applied to predicting a simple supersonic mixing layer. The model was found to faithfully reproduce the functional dependence of the shear layer growth rate on convective Mach number, although its ability to predict the detailed features of compressible flows was not assessed.

A number of alternative models for both the compressible dissipation rate and the pressure-dilatation term have been derived using direct numerical simulations of compressible turbulent homogeneous shear flows (Sarkar et al., 1991b) and compressible turbulence subjected to shear and a rapid compression (Zeman, 1991). Sarkar et al.'s (1991a) model is, however, the simplest of the alternative models, and its use in the validation studies discussed later suggests that it is adequate for modelling compressible free jets. The implication of using the latter model in the present work is that an additional sink term is introduced into the transport equation for turbulence kinetic energy, Eq. (3):

$$S_k = -\bar{\rho} M_\tau^2 \epsilon, \tag{7}$$

with the turbulent viscosity for compressible flows, Eq. (5), now being replaced by

$$\mu_t = C_\mu \bar{\rho} \frac{k^2}{(1+M_\tau^2)\epsilon}. \tag{8}$$

Computational Procedure and Boundary Conditions. To compare predictions of the model with the experimental data considered later, solution of the axisymmetric form of six (for air jets) or seven (for natural gas jets) coupled partial differential equations is required. Solutions were obtained by expressing the equation set in cylindrical co-ordinates, and integrating the time-dependent form of these equations numerically by time-marching to a steady state.

Integration of the equations was performed using a second-order accurate finite-volume scheme. Discretization of the descriptive equations therefore followed a conservative, control volume approach, with values of the dependent variables stored at the centers of the computational cells over which the differential equations were integrated. Diffusion and source terms in the modeled equations were approximated using central differencing, whilst approximations to the inviscid (advective and pressure) fluxes were derived using a second-order accurate (in space) variant of Godunov's method. The latter method was derived from a conventional first-order Godunov scheme by introducing gradients within computational cells using a nonlinear, slope-limiting function which ensures monotinicity. In its fully explicit, time-accurate form the method uses a predictor-corrector procedure, where the predictor stage is spatially first-order and is used to provide an intermediate solution at the half-time between time-steps. This in turn is used at the corrector stage for the calculation of second-order fluxes.

To increase the rate of convergence a diagonalized implicit scheme was used. This scheme first calculates the explicit rate of change to second-order space accuracy, as described above, and then applies diagonalized implicit operators in each of the space directions to make the scheme implicit for sound waves and diffusion. This allows the calculation to proceed using much larger time-steps, based on advection velocities rather than sound waves, than would be required using the explicit scheme alone. Further details of the numerical algorithm may be found elsewhere (Falle, 1991).

Using a second-order accurate scheme makes it feasible to capture the shock structure in compressible free jets, but only with fine computational grids in the vicinity of shocks. The computational cost of capturing shock structures was reduced in the present work by using an adaptive finite-volume grid algorithm which employed a two-dimensional, rectangular mesh, with adaption being achieved by overlaying successively refined layers of computational grids. Each layer was generated from its predecessor by doubling the number of computational cells in each space direction. In the results given later, up to five levels of grid were used. Further details of the adaptive algorithm may be found in Falle and Giddings (1992).

In all the simulations a symmetry boundary was imposed along the center-line of a jet represented by the z axis at $r=0$, with a fixed pressure boundary condition being used in the z direction at $+r$ and the downstream boundary of the computational domain, at $+z$, being taken as an outflow surface. The location of the latter boundaries was varied in order to ensure that solutions were insensitive to the boundary conditions imposed on these surfaces. The release itself was represented as a hole in a flat plate. Flat profiles of all dependent variables were prescribed at the nozzle exit for the experiments of Seiner and Norum (1979 and 1980), and of Birch et al. (1984 and 1987), which used plug flows, whilst the fully developed pipe flow used by Chuech et al. (1989) was represented using profiles obtained from Hinze (1977). In the absence of experimental data, the plug flow simulations used initial turbulence kinetic energy levels corresponding to 5 percent of the mean velocity, with ϵ specified by assuming a turbulence length scale of $0.05d$.

The fineness of computational grid required to obtain grid independent solutions was examined for each of the jets studied. As an example, simulations of Seiner and Norum's (1979 and 1980) jet, which contains particularly strong shocks, required a grid spacing of $\Delta r = \Delta z = d/64$ for essentially grid independent resolution of the shock structure. For a uniform non-adaptive grid, this corresponds to approximately 123 k nodes required to cover the computational domain of interest, whereas the adaptive simulation required only 52 k nodes. Figure 1 shows the sensitivity of mean and fluctuating streamwise velocity predictions at one downstream station of Chuech et al.'s (1989) jet to the grid resolution used in the computations.

Results and Discussion

The performance of the numerical model was evaluated by

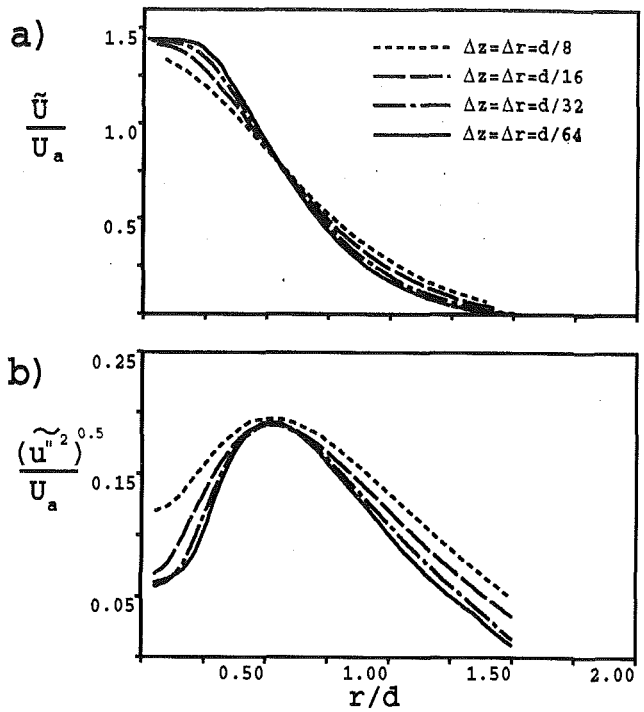

Fig. 1 Effect of grid resolution on radial predictions of (*a*) mean streamwise velocity and (*b*) fluctuating streamwise velocity at $z/d = 5$ for Chuech et al.'s (1989) air jet ($d = 9.5$ mm, $P_o/P_a = 1.2$, M = 1)

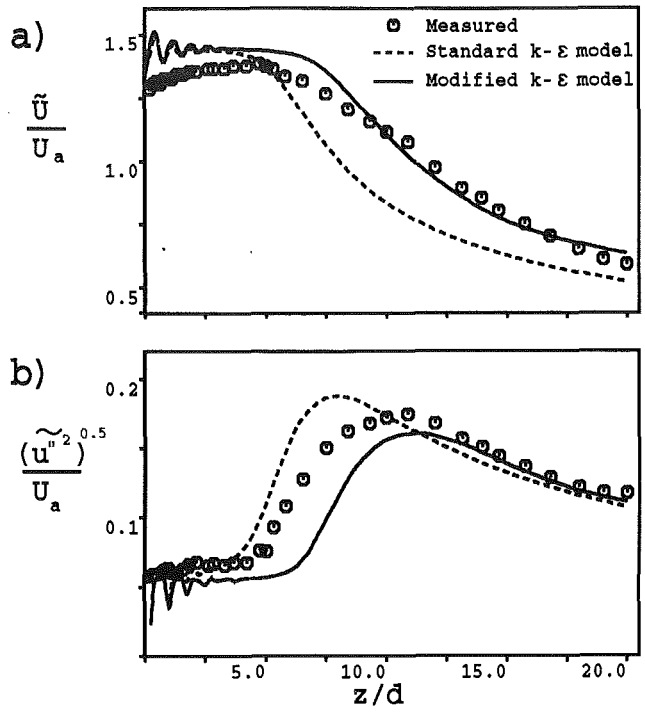

Fig. 2 Center-line values of (*a*) mean streamwise velocity and (*b*) fluctuating streamwise velocity for Chuech et al.'s (1989) air jet ($d = 9.5$ mm, $P_o/P_a = 1.2$, M = 1)

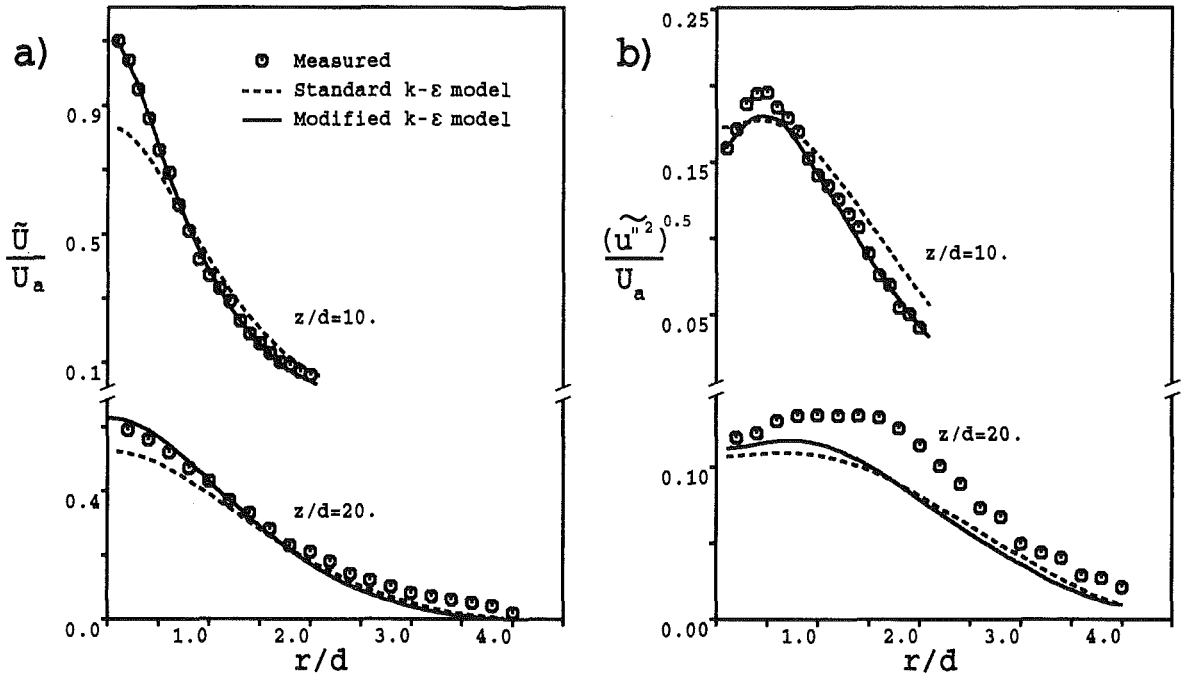

Fig. 3 Radial values of (*a*) mean streamwise velocity and (*b*) fluctuating streamwise velocity at two downstream stations for Chuech et al.'s (1989) air jet ($d = 9.5$ mm, $P_o/P_a = 1.2$, M = 1)

comparing predicted fluid flow properties with measured data for four jets studied by Chuech et al. (1989), Seiner and Norum (1979 and 1980), and Birch et al. (1984 and 1987). The jets are considered in ascending order of pressure ratio.

The air jet studied by Chuech et al. (1989) has a pressure ratio of 1.2 and an exit Mach number of one. Figure 2 compares predicted streamwise velocities along the center-line of this jet with experimental data. In the near field of the jet, predictions obtained using both the standard and compressibility corrected k-ϵ models overpredict, and differ qualitatively, from measured mean velocities (Fig. 2(*a*)). The predicted velocities oscillate due to the presence of oblique shocks in the potential core of the jet, as observed by Chuech (1987), whereas measured values are relatively smooth. However, the latter measurements were obtained using laser Doppler anemometry techniques, and a deficiency of this technique when applied to shock containing regions, noted by Chuech (1987), is the poor response of seeding particles to the rapidly changing velocity

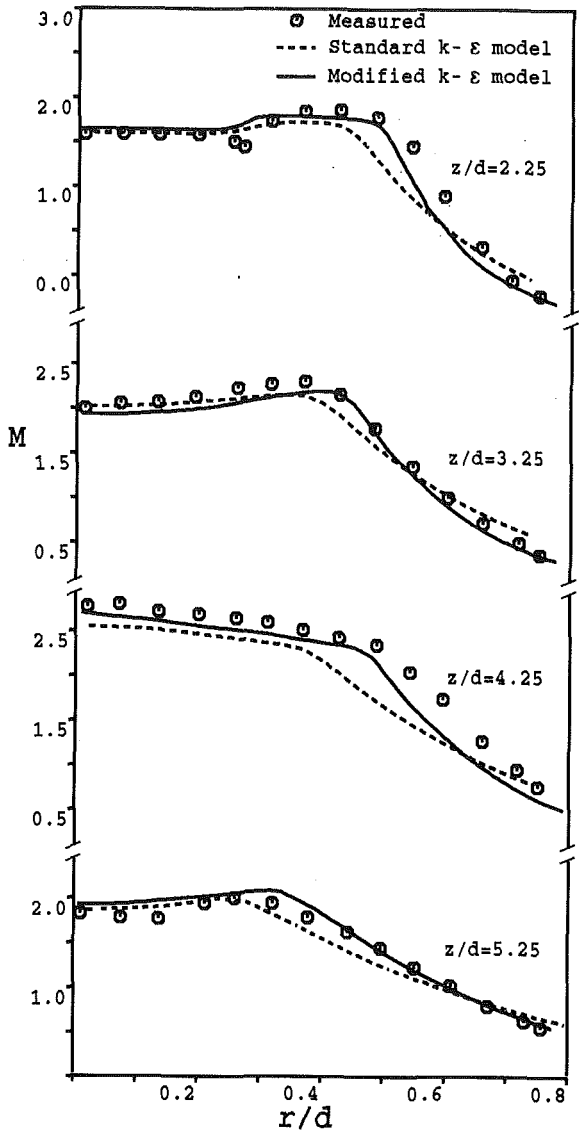

Fig. 4 Radial values of Mach number at four downstream stations for Seiner and Norum's (1979 and 1980) air jet ($d = 50$ mm, $P_o/P_a = 1.45$, M = 2)

field. The accuracy of the results can be expected to be high from approximately 7 diameters downstream of the nozzle where variations in pressure become small (Chuech, 1987). From this point, predictions obtained using the compressibility corrected turbulence model are in good agreement with measurements, with the rate of decay of velocity being adequately reproduced. In contrast, results obtained using the standard k-ϵ turbulence model underpredict measured mean velocities from approximately 5 diameters downstream due to the overprediction of turbulence production dissipating the velocity on the axis. This is confirmed by the results shown in Fig. 2(b) which again demonstrate good agreement between the compressibility corrected turbulence model and experimental data, particularly in terms of the location of the peak fluctuating velocity. Some underprediction of data is, however, evident between $z = 7d$ and $10d$.

Figure 3 compares equivalent results for radial profiles within the jet at two downstream locations. Mean velocities (Fig. 3(a)) predicted by the compressibility corrected k-ϵ model are again in closer accord with experimental data than those of the standard model at both locations, although the former model does tend to slightly underpredict the width of the jet at $z/d = 20$. Predictions of streamwise fluctuating velocities (Fig. 3(b)) are less satisfactory, although both sets of results agree qualitatively with the measured data, with the peak fluctuating velocity off-axis in the near field tending towards the center-line with increasing downstream distance. Quantitatively, results obtained using compressibility corrections are again superior.

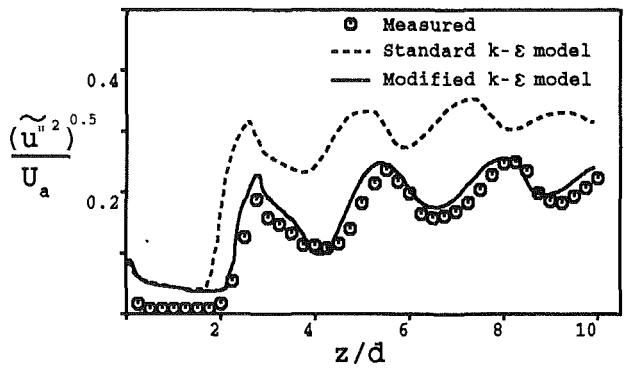

Fig. 5 Axial values of fluctuating streamwise velocity at $r/d = 0.5$ for Seiner and Norum's (1979 and 1980) air jet ($d = 50$ mm, $P_o/P_a = 1.45$, M = 2)

The second underexpanded jet used to evaluate the model was studied by Seiner and Norum (1979 and 1980). This jet differs from the others examined in this section in that the nozzle used had a convergent-divergent shape which gave flat exit profiles and a Mach number of 2 at a pressure ratio of 1.45. The latter pressure ratio is only 20 percent more than for Chuech et al.'s (1989) jet, but the supersonic flow significantly increases the effect of compressibility on turbulence dissipation.

Figure 4 compares radial values of Mach number at four downstream locations within the jet. Predictions obtained using Sarkar et al.'s (1991a) modifications are in close agreement with the measured data. Mach numbers derived from the standard k-ϵ turbulence model suffer from the same deficiency observed for the mean velocity field in Chuech et al.'s (1989) jet because of an underprediction of the turbulence energy dissipation rate in the shear layer. Unfortunately, the measurement stations are too closely spaced to permit a more thorough evaluation of the models' ability to predict the Mach number field of this jet, but the level of agreement obtained when compressibility effects are modelled is encouraging.

Streamwise fluctuating velocities along a line parallel to the center-line of the jet, and extending from the nozzle lip, are compared in Fig. 5. The assumed initial turbulence kinetic energy profiles and levels, noted earlier, are seen to result in an overestimate of the actual turbulence level close to the nozzle, although the turbulent kinetic energy field was found to be insensitive to the prescribed nozzle exit values apart from in the vicinity of the nozzle itself. Qualitatively, both predictions of fluctuating velocity are in agreement with the measured data, correctly predicting the increase in fluctuating velocity in regions of compression and the decrease in regions of rarefaction. Quantitatively, the predictions obtained using the standard k-ϵ turbulence model overpredict the measured data by approximately 40 percent, whereas results based on Sarkar et al.'s (1991a) modifications are in good agreement with observations.

The final comparison for this jet is given in Fig. 6 which shows pressures along the jet center-line. Predicted pressures obtained using the standard k-ϵ turbulence model are seen to be in agreement with experimental data in the near field of the jet, up to 2 diameters downstream, although a slight phase error is present in the shock structure due to the predicted rarefaction wave emanating from the nozzle lip intersecting the jet axis downstream of the measured location. This finding is consistent with there being a boundary layer attached to the nozzle wall. Thus, although the nozzle employed in the ex-

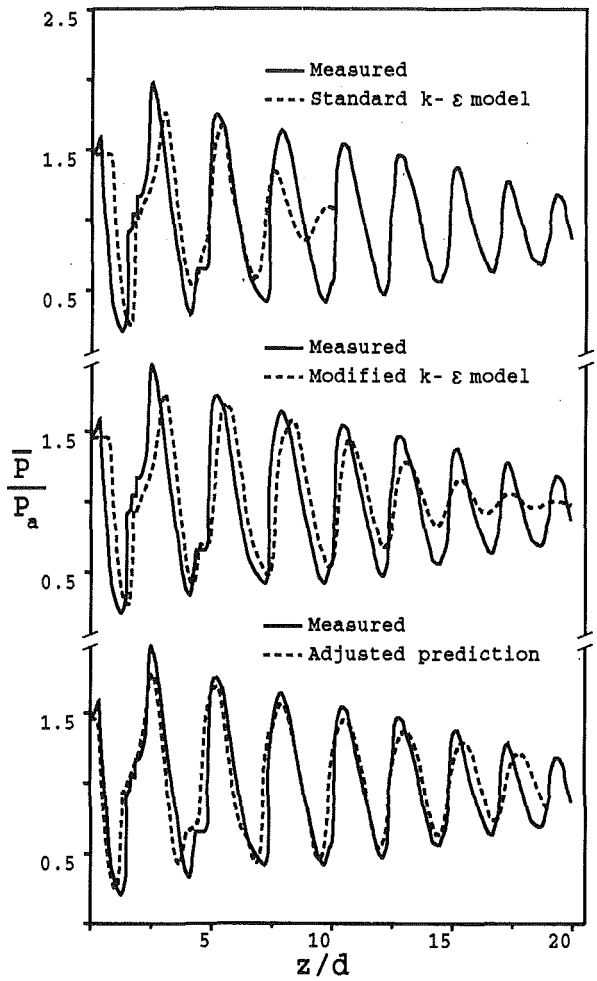

Fig. 6 Center-line values of pressure for Seiner and Norum's (1979 and 1980) air jet ($d = 50$ mm, $P_o/P_a = 1.45$, M = 2)

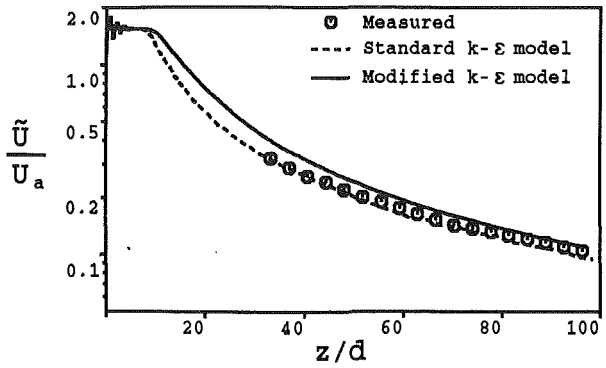

Fig. 7 Center-line values of mean streamwise velocity for Birch et al.'s (1987) air jet ($d = 2.7$ mm, $P_o/P_a = 2.05$, M = 1)

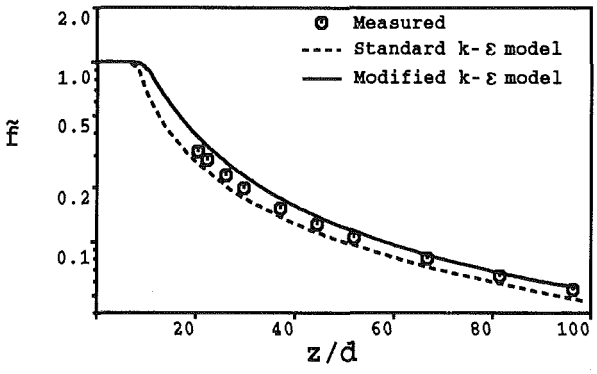

Fig. 8 Center-line values of mean mixture fraction for Birch et al.'s (1984) natural gas jet ($d = 2.7$ mm, $P_o/P_a = 1.88$, M = 1)

periments was designed to give flat profiles at the nozzle exit, as used in the simulations, in reality a turbulent boundary layer would have developed adjacent to the nozzle wall. The presence of the remnants of this boundary layer downstream of the nozzle exit in the experiments, not accounted for in the simulations, would cause the rarefaction wave emanating from the nozzle to be reflected back into the inviscid potential core of the jet at a point closer to the nozzle than predicted, since in the simulations this wave would be reflected further downstream by the free jet boundary. Later on in the jet, the predicted shock strength is dissipated prematurely because of an overprediction of the spreading rate of the shear layer.

Incorporation of the compressible dissipation rate into the turbulence model is seen to significantly improve agreement with experimental data, with the shock strength and location now being well predicted for the first 12 diameters downstream. As for predictions of the standard k-ϵ approach, an initial phase error still persists for the reasons stated above, but in this case the phase error is propagated downstream to approximately 15 diameters suggesting the shock frequency is correctly predicted in this region. Further downstream, the shock strength underpredicts the measured data, again due to an overprediction of the spreading rate of the shear layer.

The final set of predictions given in Fig. 6 was derived by adjusting the constant C_2, used in Eq. (4), from 1.92 to 1.8; a change within the limits of uncertainty on this modelling constant (Rodi, 1980). This has the effect of reducing the spreading rate of the shear layer. In addition, the affine transformation (Walker, 1988)

$$\frac{z}{d} \leftarrow 0.98\left(\frac{z}{d} - 0.5\right) \tag{9}$$

was also applied to the downstream coordinate of the predicted pressure. The $d/2$ shift in this transformation removes the phase error due to the presence of the nozzle boundary layer noted above, and rescaling the downstream coordinate by the factor 0.98 is equivalent to assuming the boundary layer attached to the nozzle wall had a width corresponding to 2 percent of the nozzle diameter, making the appropriate length scale in the experiment $0.98d$. In total, the adjustments noted above significantly improve agreement between observations and predictions of the compressibility corrected turbulence model, although in the absence of more detailed experimental data on the nozzle exit conditions and far field turbulence levels it is impossible to quantitatively evaluate the improvements gained, nor to recommend adjustments to the value of C_2 for predicting sonic jets. These results do, however, demonstrate the sensitivity of model predictions to initial conditions, and the requirement for further experimental data.

Finally, Figs. 7 and 8 compare model predictions with experimental data obtained by Birch et al. (1984 and 1987) for, respectively, the center-line variation of mean streamwise velocity in an air jet, and of mixture fraction (fuel mass fraction) in a jet of natural gas. Although the experimental techniques used by the latter authors were not capable of yielding reliable results in compressible regions of the flow, the agreement between predictions of the compressibility corrected turbulence model and experimental data in the far field of the jets is good. In addition, although results derived from the standard k-ϵ model are in better agreement with mean velocity data over significant portions of the air jet, they do tend to slightly underpredict observations in the far field of both jets. This underprediction of experimental data in the subsonic regions of these jets may, to some extent, be attributable to the fact

that the standard k-ϵ approach is known to overpredict the spreading rate of incompressible round jets.

Conclusions

A mathematical model capable of predicting the structure of turbulent underexpanded jets has been described, and the model has been used to simulate a number of underexpanded jets that span the range of pressure ratio which gives rise to moderately underexpanded jets. The model's ability to predict the detailed flow structure of these jets has been assessed by comparing predictions with measured fluid flow properties, and in the majority of cases use of a compressibility corrected (Sarkar et al., 1991a) turbulence model was found to lead to significant improvements over results derived using a standard k-ϵ approach. In addition, the comparisons with experimental data suggest that predictions derived using a k-ϵ turbulence model coupled to the compressible dissipation rate model are adequate for predicting the flow field of moderately underexpanded jets. Application of the model to highly underexpanded releases will be considered in a separate publication.

Acknowledgments

The calculations reported in this paper were made using a modified version of the Mantis Numerics Ltd. code, COBRA. This paper is published by permission of British Gas plc.

References

Abdol-Hamid, K. S., and Wilmoth, R. G., 1989, "Multiscale Turbulence Effects in Underexpanded Supersonic Jets," *American Institute of Aeronautics and Astronautics Journal*, Vol. 27, pp. 315–322.

Birch, A. D., Brown, D. R., Dodson, M. G., and Swaffield, F., 1984, "The Structure and Concentration Decay of High Pressure Jets of Natural Gas," *Combustion Science and Technology*, Vol. 36, pp. 249–261.

Birch, A. D., Hughes, D. J., and Swaffield, F., 1987, "Velocity Decay of High Pressure Jets," *Combustion Science and Technology*, Vol. 52, pp. 161–171.

Birch, S. F., and Eggers, J. M., 1973, "A Critical Review of the Experimental Data for Developed Free Turbulent Shear Layers," *Free Turbulent Shear Flows Conference Proceedings*, NASA SP-321, pp. 11–40.

Brescianini, C. P., 1992, "Modified k-ϵ Model for Compressible Free Shear Flows," *American Institute of Aeronautics and Astronautics Journal*, Vol. 30, pp. 2161–2163.

Chuech, S. G., 1987, "Kinematic and Scalar Structure of Turbulent Underexpanded Sonic Jets," Ph.D. thesis, Pennsylvania State University.

Chuech, S. G., Lai, M.-C., and Faeth, G. M., 1989, "Structure of Turbulent Sonic Underexpanded Free Jets," *American Institute of Aeronautics and Astronautics Journal*, Vol. 27, pp. 549–559.

Dash, S. M., and Wolf, D. E., 1983, "Shock-Capturing Parabolized Navier Stokes Model (SCIPVIS) for the Analysis of Turbulent Underexpanded Jets," American Institute of Aeronautics and Astronautics Paper 83-0704.

Dash, S. M., Wolf, D. E., Sinha, N., and Lee, S. H., 1986, "Progress in the Development of Parabolized Navier Stokes (PNS) Methodology for Analyzing Propulsive Jet Mixing Problems," American Institute of Aeronautics and Astronautics Paper 86-1115.

Falle, S. A. E. G., 1991, "Self-Similar Jets," *Monthly Notices of the Royal Astronomical Society*, Vol. 250, pp. 581–596.

Falle, S. A. E. G., and Giddings, J. R., 1992, "Body Capturing Using Adaptive Cartesian Grids," *Proc. ICFD Conf. on Numerical Methods for Fluids*, 7th–10th April.

Hinze, J. O., 1977, *Turbulence*, McGraw-Hill, New York.

Jones, W. P., and Launder, B. E., 1972, "The Prediction of Laminarization with a Two-Equation Model of Turbulence," *International Journal of Heat and Mass Transfer*, Vol. 15, pp. 301–314.

Jones, W. P., and Whitelaw, J. H., 1982, "Calculation Methods for Reacting Turbulent Flows: A Review," *Combustion and Flame*, Vol. 48, pp. 1–26.

Lee, S., Lele, S. K., and Moin, P., 1991, "Eddy Shocklets in Decaying Compressible Turbulence," *Physics of Fluids A*, Vol. 3, pp. 657–664.

Pai, S. I., 1959, *Introduction to the Theory of Compressible Flow*, McGraw-Hill, New York.

Papamoschou, D., and Roshko, A., 1986, "Observations of Supersonic Free Shear Layers," American Institute of Aeronautics and Astronautics Paper No. 86-0162.

Rodi, W., 1980, "Turbulence Models and their Application in Hydraulics—A State of the Art Review," Int. Association for Hydraulic Research, Delft, The Netherlands.

Sarkar, S., Erlebacher, G., Hussaini, M. Y., and Kreiss, H. O., 1991a, "The Analysis and Modelling of Dilatational Terms in Compressible Turbulence," *Journal of Fluid Mechanics*, Vol. 227, pp. 473–493.

Sarkar, S., Erlebacher, G., and Hussaini, M. Y., 1991b, "Compressible Homogeneous Shear: Simulation and Modelling," Eighth Symposium on Turbulent Shear Flows, 9th–11th September.

Seiner, J. M., and Norum, T. D., 1979, "Experiments on Shock Associated Noise of Supersonic Jets," American Institute of Aeronautics and Astronautics Paper No. 79-1526.

Seiner, J. M., and Norum, T. D., 1980, "Aerodynamic Aspects of Shock Containing Jet Plumes," American Institute of Aeronautics and Astronautics Paper No. 80-0965.

Spalding, D. B., 1971, "Concentration Fluctuations in a Round Turbulent Free Jet," *Chemical Engineering Science*, Vol. 26, pp. 95–107.

Speziale, C. G., and Sarkar, S., 1991, "Second-Order Closure Models for Supersonic Turbulent Flows," American Institute of Aeronautics and Astronautics Paper No. 91-0217.

Walker, P. M. B., ed., 1988, *Chambers Science and Technology Dictionary*, W. & R. Chambers Ltd. and Cambridge University Press, Cambridge.

Zeman, O., 1991, "Compressible Turbulence Subjected to Shear and Rapid Compression," Eighth Symposium on Turbulent Shear Flows, 9th–11th September.

Fei-Bin Hsiao
Professor,
Institute of Aeronautics and Astronautics,
National Cheng Kung University,
Tainan, Taiwan

Jiann-Min Huang
Associate Research Scientist,
Aeronautical Research Laboratory,
CSIST,
Taichung, Taiwan

On the Dynamics of Flow Structure Development in an Excited Plane Jet

Coherent structure dynamics in the developing region of a plane jet under acoustic excitation is studied experimentally by means of hot-wire measurements and smoke-wire flow visualization. The mean and fluctuation velocity properties, such as mean and fluctuation intensities in both streamwise and transverse directions, turbulent shear stress variations, and the turbulent energy production and energy convection phenomena, are carefully investigated. The results indicate that flow property behavior is closely related to vortex formation and the merging processes, which are the dominant mechanisms governing flow behavior in the developing region of a plane jet.

1 Introduction

The study of coherent structure induction in turbulent shear flow dates from the early 1970's by Crow and Champagne (1971) and Brown and Roshko (1971). It has since been found that the evolution and interaction of these large-scaled organized structures are the major mechanism for turbulent shear flow spreading and momentum transfer by Winant and Browand (1971) and Ho and Huang (1982). Ho (1981) proposed a subharmonic evolution model which interpreted the relationship between subharmonic instability evolution and the mechanism of vortex merging from a hydrodynamic instability point of view. Amplified subharmonic instability is considered to be the primary catalyst for the occurrence of the vortex merging.

For jets, initial shear layers are originated from the development of Kelvin-Helmholtz instability. Through linear and nonlinear interactions, vortex formation and subsequent merging processes occur, dominating the flow dynamics downstream of the shear layers. One of the objectives of this paper is the investigation of variations in mean and fluctuating flow properties under such a vortex interaction mechanism. Although fluctuation energy budget characteristics in jets have been extensively studied by Sami (1967), Gutmark and Wygnanski (1976), Everitt and Robins (1978), and Miau and Karlsson (1986), most of these researches concentrated on the self-preserving region at the further downstream of the end of the potential core. Our previous papers (Hsiao and Huang, 1988, 1990a, 1990b) focused on instability mode dynamics as well as their sideband instabilities in the developing region of a plane jet. The present work continues our works on the plane jet developing region and emphasize flow structure dynamics and interaction processes. Relevant flow properties, as well as mean and fluctuating velocity properties together with other major terms of the fluctuation energy budget, are also examined and related to jet vortex behavioral dynamics.

2 Experimental Apparatus and Procedure

The experimental layout of the plane jet is shown in Fig. 1. The air source was supplied by a 3 HP centrifugal blower which was followed in line by a 180 × 180 × 170 cm noise reduction chamber. The honeycomb and screens managed flow quality. The jet nozzle was a fifth-order polynomial profile with a height (H) of 15 mm at the nozzle exit, giving an aspect ratio of 20 at this point. The operating velocity throughout the experiment was fixed at 10 m/s, with the turbulence intensity at the nozzle exit center being 0.2 percent. Twenty earphones were used as loudspeakers in locally exciting the jet flow. These earphones were equi-distantly spaced along both sides of the nozzle exit. DISA 55M10 constant-temperature anemometers with a 5 μm Pt single-wire and X-wire probes were utilized for the velocity measurements. Digitized data at a sampling rate of 50 μs was obtained by a MDAS 7000 data acquisition system equipped with a 12-Bit A/D converter. The smoke-wire technique was employed in visualizing jet flow development. Flow pictures were taken by a 35 mm camera equipped with a timing controlled flash. A more detailed description of the experimental conditions can be found in our previous paper (Hsiao and Huang, 1990a).

3 Results and Discussion

3.1 The Basic Flow Conditions of the Plane Jet. Initial boundary layers at the natural jet nozzle exit are first examined in order to ensure that they are laminar over various jet exit velocities. The initial fundamental instability frequency, f_0, measured from frequency spectra of streamwise velocity fluctuations, is related to the jet exit velocity by:

$$f_0 \propto U^{3/2}.$$

Contributed by the Fluids Engineering Division for publication in the JOURNAL OF FLUIDS ENGINEERING. Manuscript received by the Fluids Engineering Division October 29, 1991; revised manuscript received May 17, 1993. Associate Technical Editor: Ho, Chih-Ming.

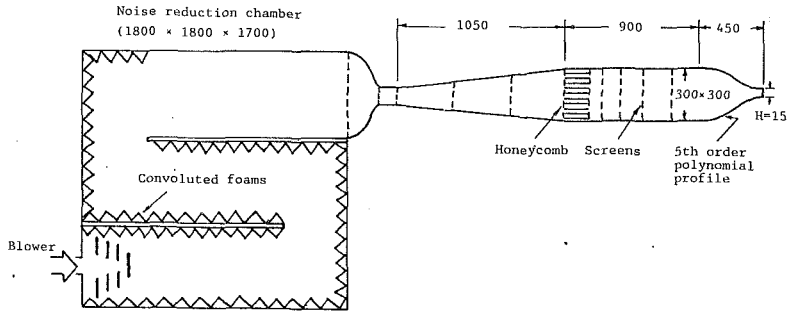

Fig. 1 The experimental layout of the plane jet (all units are in mm)

For the jet exit velocities between 5–30 m/s, the initial Strouhal number, given by the following equation:

$$\mathrm{St}_0 = f_0\theta_0/U_0,$$

falls within the 0.0092–0.0117 range. Gutmark and Ho (1983) pointed out that since the initial Strouhal number is not constant but varies from 0.01 to 0.018 over a number of identical experiments, this suggests that a low level, spatially coherent disturbance frequency existing in the individual facilities determines the initially predominant frequency, and is responsible for spreading the initial Strouhal number over a wide range. Zaman and Hussain (1980) found the natural roll-up frequency of the exit shear layer to occur near an St_0 of 0.012. This exit shear layer natural roll-up frequency is lower than the most amplified, acoustically excited frequency determined with a St_0 of 0.017. In the present experiment, the measured fundamental frequency (f_0) corresponds to the natural vortex roll-up frequency of the shear layer and is used as a reference parameter for acoustic excitation frequency selection in shear flow control analysis. The experiments in this paper maintain a 10 m/s jet exit velocity with the jet flow being acoustically excited at its fundamental frequency (f_0). After excitation, the initial boundary layer at the nozzle exit is monitored to ensure that it remains laminar. The initial Strouhal number based on initial momentum thickness corresponds to $\mathrm{St}_0 = f_0\theta_0/U_0 = 0.0092$, while that based on the nozzle exit width of the plane jet corresponds to $\mathrm{St}_H = f_0H/U_0 = 0.726$.

3.2 The Determination of the Vortex Merging Locations. According to Ho's subharmonic evolution model (1981), vortex formation and merging processes are mainly due to evolution of related instability waves. He defined the merging location as the position where the neighboring two vortices are vertically aligned due to amplifying subharmonics. Their

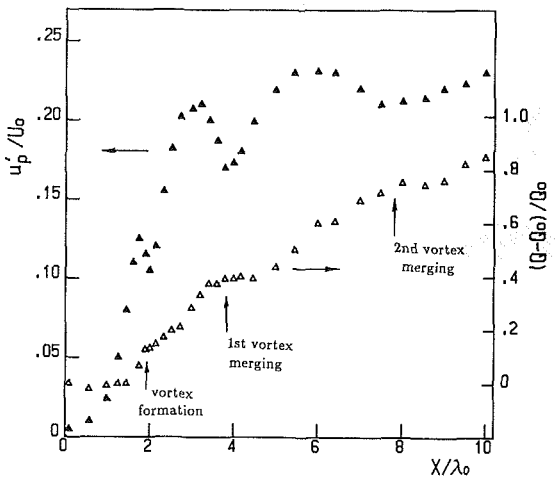

Fig. 2 The downstream development of peak streamwise velocity fluctuations and flow entrainment in an excited plane jet (from Hsiao and Huang, 1990b). (Uncertainty in u_p'/U_0 = 2.5 percent and in X/λ_0 = 0.01 percent)

energy contents are found to reach saturation here. He also pointed out that in a shear flow, vortex induced perturbations are able to propagate upstream where they excite the flow field near the nozzle exit. As a result, a feedback loop is established from the incipience of initial instability at the nozzle exit down to the vortex merging location.

The ith vortex merging location in a low subsonic jet can be determined from the following relationship:

$$X_i = 2^{i+1}\lambda_0.$$

Nomenclature

A_1 = fluctuation energy convection by streamwise mean motion
A_2 = fluctuation energy convection by transverse mean motion
A_{12} = fluctuation energy convection term ($= A_1 + A_2$)
f_0 = the fundamental frequency
H = height of the plane jet exit
Q = the entrainment rate of fluid volume ($= \int_0^{Y_{0.1}} U dY$)
Q_0 = the entrainment rate of fluid volume at the plane jet nozzle exit
P_1 = fluctuation energy production due to turbulent shear stress
P_2 = fluctuation energy production due to normal stresses
P_{12} = the fluctuation energy production term ($= P_1 + P_2$)
Re = Reynolds number ($= U_0H/\nu$)
St_0 = the initial Strouhal number ($= f_0\theta_0/U_0$)
U = the streamwise mean velocity
U_0 = the mean velocity at the plane jet nozzle exit
u' = the streamwise rms velocity fluctuation
u_p' = the peak streamwise velocity fluctuation along the Y axis
$\overline{u'v'}$ = turbulent shear stress
V = the transverse mean velocity
v' = the transverse rms velocity fluctuation
v_p' = the peak transverse velocity fluctuation along the Y axis
$W|_\theta$ = the integrated value of W ($= \frac{1}{\theta}\int_0^{Y_{0.1}} W dY$)
X, Y = the streamwise and transverse coordinates
Y_a = transverse position where $U = aU_c$, a = 0.99, 0.9, ..., etc.
θ = momentum thickness
θ_0 = initial boundary layer momentum thickness
δ_0 = initial boundary layer displacement thickness
ν = kinetic viscosity
λ_0 = initial instability wavelength ($= U_0/2f_0$)

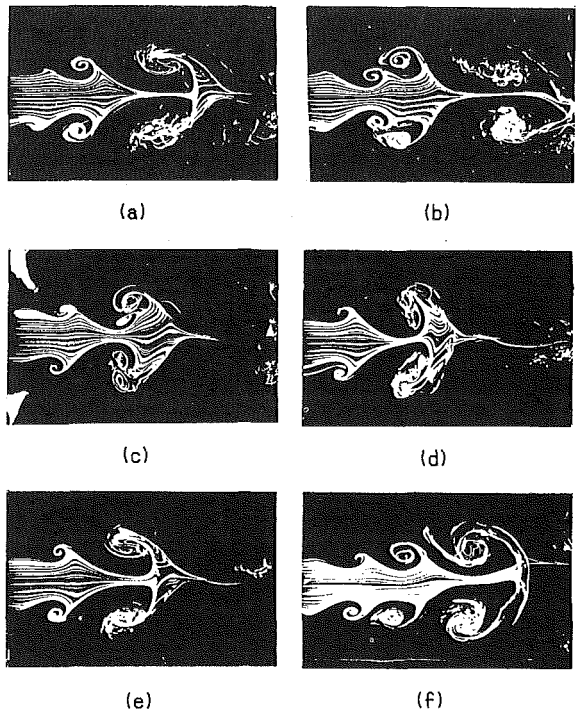

Fig. 3(*a*)–(*f*) Flow patterns during the vortex merging process

This relationship indicates that a vortex formation forms at $X = 2\lambda_0$, with the first and second vortex merging location being at $\mathbf{X} = 4$ and $8\lambda_0$, respectively. These positions were also identified in our earlier research on instability mode analysis (Hsiao and Huang, 1990a and 1990b).

The downstream development of peak streamwise velocity fluctuations and flow entrainment in an excited jet is shown in Fig. 2 (see also Hsiao and Huang, 1990b). Since the two interacting vortices vertically align at the merging location, the jet ceases to spread near the $\mathbf{X} = 2$, 4 and $8\lambda_0$ downstream positions. The shear layer induces large flow mixing in the former position of the merging process. This region encompasses the point where merging starts, and extends through the major merging locations (e.g., $2\lambda_0 < X < 4\lambda_0$). Further downstream, however, the merging process is unable to induce prominent flow entrainment in the shear layer. This region is knwn as the latter portion of the merging process.

The results of the vortex merging process obtained by the smoke-wire technique are clearly illustrated in Figs. 3(*a*)–(*f*). Due to the fact that turbulent diffusion at high velocities degrades visual quality, jet flow was operated to an U_0 value of 3.15 m/s and excited at its fundamental frequency ($f_0 = 70$ Hz). The former portion of the vortex merging process is illustrated in Figs. 3(*a*)–(*c*), while that of the latter portion is shown in Figs. 3(*d*)–(*f*). The merging location, the point where two interacting vortices vertically align, is depicted in stage III (Fig. 3(*c*)) and is related to the $X = 4\lambda_0$ event shown in Fig. 2. Likewise, the flow structure at stage II (Fig. 3(*b*)) is analogous to the situation at $X = 3\lambda_0$.

3.3 Mean and Fluctuating Flow Field. Streamwise and transverse mean velocity contours are shown in Figs. 4(*a*) and (*b*). Note that the spread of the transverse velocity V/U_0 distribution is similar to that of U/U_0, except at high transverse mean velocities where it is concentrated within the shear layer region. Also note that at the outer edge of the shear layer, the transverse velocity demonstrates negative motion, indicating that outer fluid is entrained inward through the shear layer. Moreover note that in the stream near the

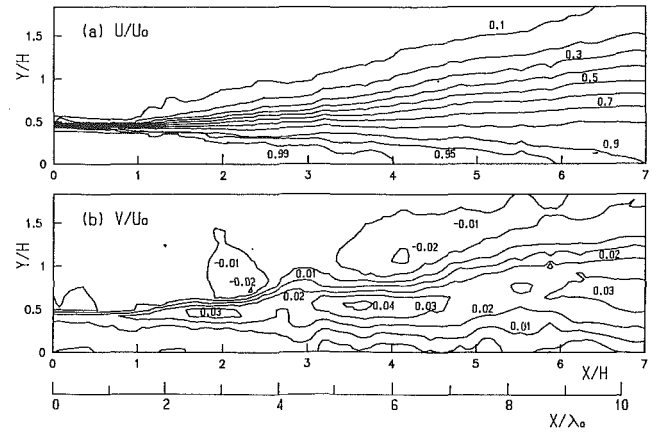

Fig. 4 Streamwise (*a*) and transverse (*b*) mean velocity contours in the jet flow field. (Uncertainty in $U/U_0 = 1.5$ percent, $V/U_0 = 1.5$ percent)

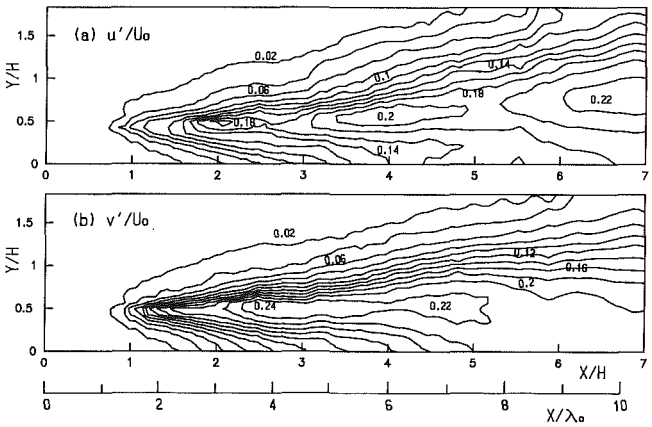

Fig. 5 Jet flow field intensity plots for streamwise (*a*) and transverse (*b*) velocity fluctuations. (Uncertainty in $u'/U_0 = 2.5$ percent and in $v'/U_0 = 2.5$ percent)

outer edge of the shear layer, especially around $\mathbf{X} = 3$, 6 and $10\lambda_0$ (see Fig. 4(*b*)), the local maximum and the absolute value of the negative transverse mean velocity occur a little further downstream than those of the local maximum and the positive transverse mean velocity within the shear layer. These flow characteristics correspond to the former portion of the merging process. Transverse mean velocity induction is mainly due to transverse displacement of interacting vortices by their amplified subharmonics formed during the merging process. The vortex merging process entrains a significant amount of fluid into the jet column, resulting in a shear flow which spreads rapidly around the above mentioned λ_0 locations, but decreases in intensity near the vortex mergings regions ($\mathbf{X} = 4$ and $8\lambda_0$). In these regions, two interacting vortices become vertically aligned and no longer expand transversely.

Jet flow field intensity contour plots for streamwise and transverse velocity fluctuations are depicted in Figs. 5(*a*) and (*b*). Note that the fluctuation intensities are much more intense within the shear layer than those in the potential core region; a direct result of their quick growth. In the former portion of the vortex merging process, local v'/U_0 maximum values at $\mathbf{X} = 3$, 6 and $10\lambda_0$, occur further downstream than those of u'/U_0.

The downstream variation in u'_p/U_0 and v'_p/U_0 peak fluctuation intensities are shown in Fig. 6. Note that the local minimum for one component corresponds to the local maximum of the other. This interchange of energy between u' and v' is associated with the vortex interaction mechanism namely,

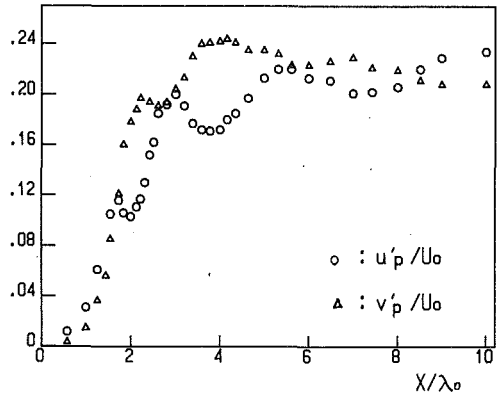

Fig. 6 The downstream variation in streamwise and transverse peak velocity fluctuation intensities. (Uncertainty in $u'_p/U_0 = 2.5$ percent and in $v'_p/U_0 = 2.5$ percent)

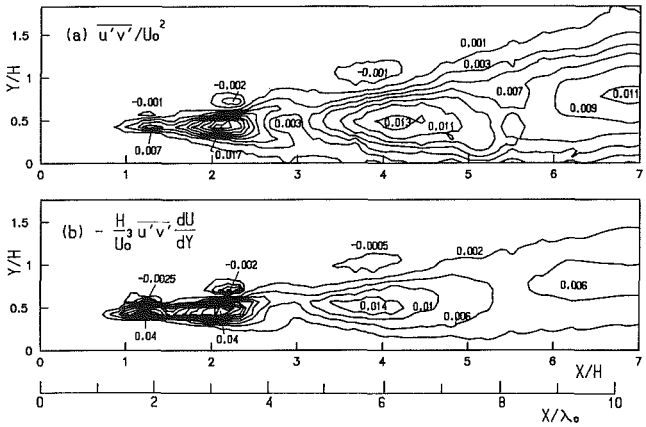

Fig. 7 Jet flow field contour plots of turbulent shear stress (*a*) and fluctuation energy production (*b*). (Uncertainty in $\overline{u'v'}/U_0^2 = 5.0$ percent)

vortex formation and the merging process. These results are in agreement with those defined in our previous research on vortex simulation. In earlier research, we found that while u'/U_0 local maxima and v'/U_0 local maxima correspond to the point at which two interacting vortices are approxmately inclined 30 deg with respect to the streamwise direction in the former portion of the merging process (i.e., stage II in Fig. 3(*b*)), u'/U_0 local maxima and v'/U_0 local maxima correspond, respectively, to points where the vortex forms and merges. At the latter location in the induced streamwise velocity, vertically aligned vortices experience their largest cancellation, but produce their largest transverse velocity (i.e., stage III in Fig. 3(*c*)). Although u' and v' have the same growth rate when $\mathbf{X} < 1.8\lambda_0$, the value of v' becomes larger in the developing region dominated by the vortex interaction mechanism ($1.8\lambda_0 < X < 8\lambda_0$). With such a large transverse fluctuation motion, rapid fluid entrainment occurs. An examination of Figs. 6 and 2 reveals, that even though the u'_p values in the former measured by an **X**-wire probe appear to be slightly lower than those in the latter which were measured by a single-wire probe, u'_p evolves in a consistent manner.

Due to the existence of the negative mean velocity gradient in the shear layer region, positive turbulent shear stress, $\overline{u'v'}$, in this area induces positive fluctuation energy production, while negative turbulent shear stress exhibits negative production. Flow field turbulent shear stress distribution and the corresponding fluctuation energy production are shown in Figs. 7(*a*) and (*b*), respectively. Note the presence of local maxima in the shear layer center near the downstream $\mathbf{X} =$

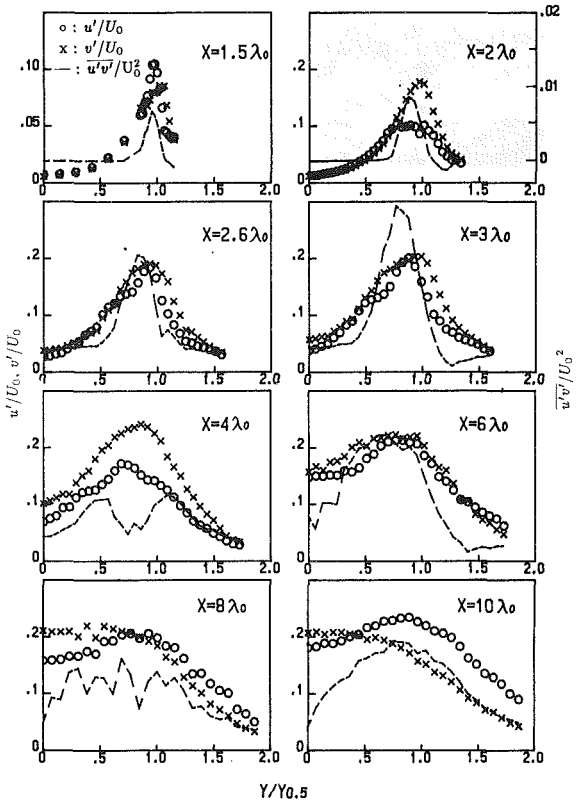

Fig. 8 Streamwise and transverse velocity fluctuation intensity and turbulent shear stress distribution along the transverse direction. (Uncertainty in $u'/U_0 = 2.5$ percent, in $v'/U_0 = 2.5$ percent and in $\overline{u'v'}/U_0^2 = 5.0$ percent)

1.8, 3 and $6\lambda_0$ positions, and in the former portion of the vortex formation and merging process region. The vortex formation and merging locations near $\mathbf{X} = 2$, 4 and $8\lambda_0$ retain local minimum shear stresses (or the production), resulting in a decrease of turbulent energy.

Note that the shear flow structures exhibit negative production behavior in the latter portion of the merging process, where the vorticity distribution tilts upstream on the low speed side of the shear layer (i.e., stage IV to VI in Figs. 3(*d*)–(*f*)). Browand and Ho (1983) pointed out that negative production of turbulence in free shear layers was associated with the turning of elliptical vortex structures forming in the flow (i.e., the vortex nutation effect). In this situation, the momentum flux opposes shear layer flow, resulting in a decrease of flow field turbulent energy. In the present experiment, due to randomly induced fluctuations and jittering in the merging process, no apparent negative production was observed in the long-time-averaged flow. In actuality, this phenomenon of negative production has only been detected in shear flow under higher amplitude excitation by Zaman and Hussain (1980) and Oster and Wygnanski (1982).

In contrast, negative turbulent shear stresses were observed near the outer edge of the shear layer in the former portion of the vortex formation and merging process region (see Fig. 7(*a*)), indicating that fluctuation energy is reversed back into the mean flow in this area. Based on their mixing layer investigations, Miau and Hsu (1987) suggested that reverse turbulent energy production occurs when the local velocity fluctuation intensity exceeds the level provided by the mean flow; a supposition that reasonably explains our negative production results. In the former portion of the vortex interaction process, fluctuation energy increases abruptly due to a rapid amplification of the instability waves. Near the outer edge of the shear layer, however, the local

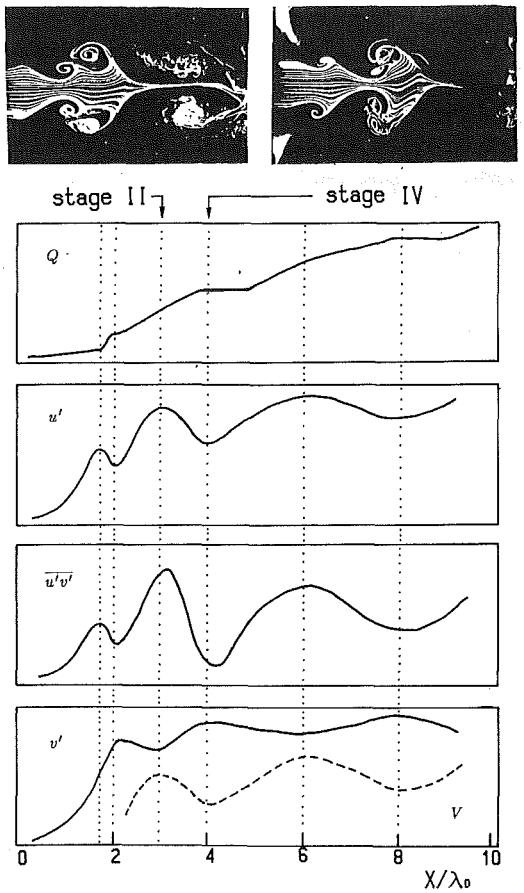

Fig. 9 Flow property variation during the vortex merging process

mean velocity is so low that it no longer sustains a high fluctuating motion, which leads to the occurrence of negative production.

The variation in u'/U_0, v'/U_0 and $\overline{u'v'}/U_0^2$ streamwise and transverse velocity fluctuating velocity and turbulent shear stress along the transverse direction are shown in Fig. 8. Note that their velocity fluctuation peaks occur near the velocity center of the shear layer, and that while u' and v' values are similar around the former portion of the merging process ($\mathbf{X} = 3, 6\lambda_0$), v' becomes larger at the vortex formation and merging locations ($\mathbf{X} = 2, 4\lambda_0$) due to transverse expansion of the interacting vortices. Also note that while at the first merging location ($\mathbf{X} = 4\lambda_0$), turbulent shear stress exhibits double peaks owing to the vertical alignment of two vortices. This phenomenon is less prominent at the second merging location ($\mathbf{X} = 8\lambda_0$) due to the increased effect of diffusion on the vortex structures.

Induced flow properties resulting from vortex interaction processes in the developing region of a jet are summarized in Fig. 9. In the shear layer region of the former portion of vortex formation and the merging processes ($\mathbf{X} = 1.8, 3, 6\lambda_0$), V, u' and $\overline{u'v'}$ exhibit local maxima, whereas v' contains local minima. Conversely, at the vortex formation and merging locations ($\mathbf{X} = 2, 4, 8\lambda_0$), V, u' and $\overline{u'v'}$ exhibit local maxima, whereas v' contains local maxima. Moreover at these positions, jet spreading ceases to increase until the next merging process starts and local V and $\overline{u'v'}$ negative zones are observed near the outer edge of the shear layer. The u' and v' energy exchange behavior results from variations in vortex orientation as well as vortex deformation during vortex formation and the merging process. For a related discussion, the reader is referred to our previous paper (Hsiao and Huang, 1990b).

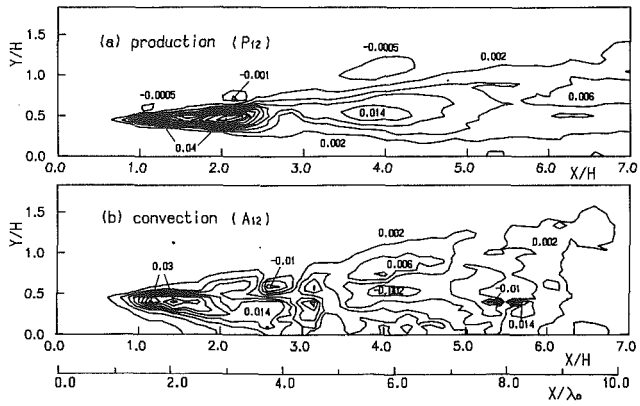

Fig. 10 Jet flow field contour plots of the total fluctuation energy production term (*a*) and the total fluctuation energy convection term (*b*). (Uncertainty in P_{12} = 5.0 percent and in A_{12} = 5.0 percent)

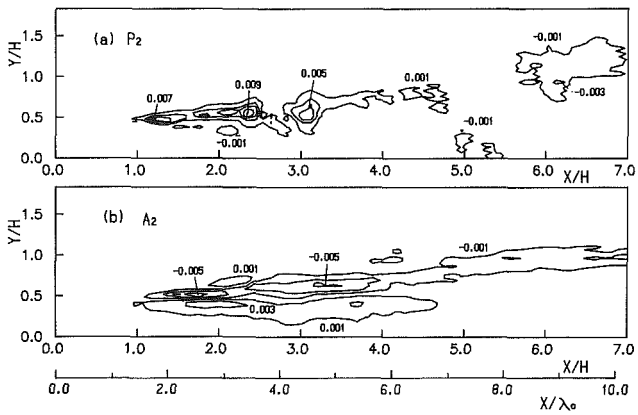

Fig. 11 Jet flow field contour plots of fluctuation energy production by normal stresses difference (*a*) and fluctuation energy convection by transverse motion (*b*). (Uncertainty in P_2 = 5.0 percent and in A_2 = 5.0 percent)

3.4 Fluctuation Energy Transport Behavior. The investigation of fluctuation energy transport behavior was based on our velocity results and takes into account two-dimensional flow structure characteristics. According to the turbulent kinetic energy equation, the total fluctuation energy production term, P_{12}, is generated from both the turbulent shear stress and normal stresses and can be written in the form:

$$P_{12} = P_1 + P_2 = -\frac{H}{U_0^3}\left[\overline{u'v'}\frac{\partial U}{\partial Y} + \left(\overline{u'^2} - \overline{v'^2}\right)\frac{\partial U}{\partial X}\right] \quad \text{(A)}$$

The total fluctuation energy convection term, A_{12}, contributes to fluctuation kinetic energy convection by mean flow motion in both streamwise and transverse directions, and can be obtained from:

$$A_{12} = A_1 + A_2 = \frac{H}{U_0^3}\left[\frac{U}{2}\frac{\partial}{\partial X}\left(\overline{u'^2} + \overline{v'^2}\right) + \frac{V}{2}\frac{\partial}{\partial Y}\left(\overline{u'^2} + \overline{v'^2}\right)\right] \quad \text{(B)}$$

The P_{12} and A_{12} spatial distributions in the near field of the jet are shown in Figs. 10(*a*) and (*b*), respectively. Note that Fig. 10(*a*) is almost identical to Fig. 7 in which turbulent shear stress is depicted, indicating that the shear layer motion does indeed govern the flow field within the developing region of the jet. Although the fluctuation energy production due to normal stress difference, P_2, is also concentrated

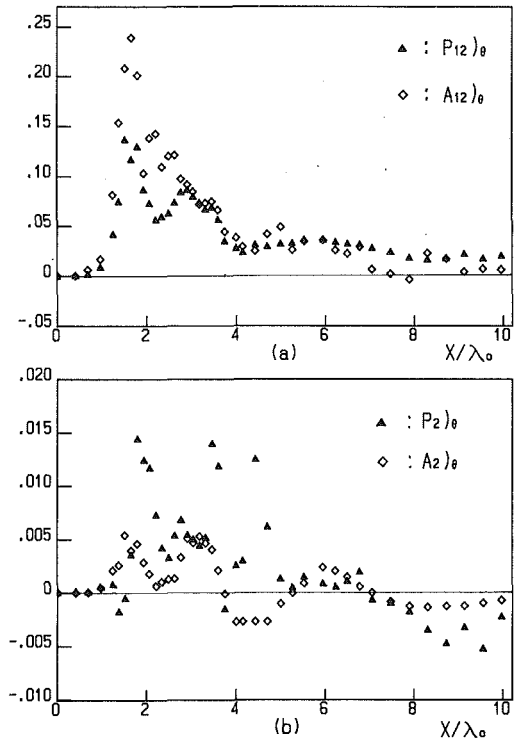

Fig. 12(*a*)(*b*) The downstream variation in the integrated values for fluctuation energy production and fluctuation energy convection. (Uncertainty is the same as in Figs. 10 and 11.)

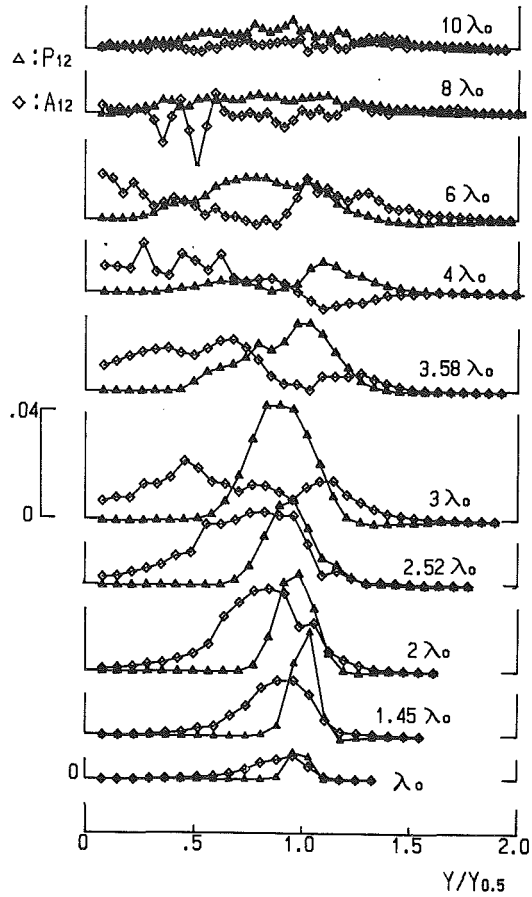

Fig. 13 Total fluctuation energy production and total fluctuation energy convection distribution along the transverse direction. (Uncertainty is the same as in Fig. 10.)

within the shear layer center as shown in Fig. 11(*a*), it exhibits little influence on the total fluctuation energy production. The growth and decay of the total fluctuation energy production were found to behave in a manner that correlates to the coherent structure interaction discussed in the previous section. As for the convective behaviors, the fluctuation energy is largely convected along in the streamwise direction by the streamwise mean motion (refer to Figs. 10(*b*) and 11(*b*)). Due to the low value of the V component, the transverse convective development (A_2) tends to be very limited.

The downstream variation in integrated total fluctuation energy production, $P_{12}|_\theta$, and convection, $A_{12}|_\theta$, are shown in Fig. 12(*a*). Note that local $P_{12}|_\theta$ minima near $\mathbf{X} = 2$, 4, and $8\lambda_0$ are consistent with the vortex formation and merging locations predicted previously. Local $P_{12}|_\theta$ maxima near $\mathbf{X} = 1.8$, 3, and $8\lambda_0$ correspond to the former portion of these vortex interaction processes. Conversely for energy convection, the maximum $A_{12}|_\theta$ value occurs near to where the initially, most amplified fundamental instability wave reaches saturation; in other words, where the vortex forms. Note that the energy convection values are higher than those of energy production in the $X < 3\lambda_0$ region, indicating that the large amount of the fluctuation energy gained there is due to the upstream to downstream convection mechanism. The downstream variations in the integrated values for $P_2|_\theta$ and $A_2|_\theta$ are depicted in Fig. 12(*b*). Note that the transverse convection motion, $A_2|_\theta$, varies in accordance with the vortex interaction processes, signifying that local $A_2|_\theta$ maxima occur in the former portion of the vortex interaction process ($\mathbf{X} = 1.8$, 3 and $8\lambda_0$). These results further confirm that $A_2|_\theta$ possesses a high capacity for transverse momentum transport in this region. The fact that local $A_2|_\theta$ minima near $\mathbf{X} = 2$, 4 and $8\lambda_0$ are positioned at the vortex formation and merging locations also lends support to the above statement. The P_{12} and A_{12} transverse variation at a number of streamwise locations is shown in Fig. 13. Note that the P_{12} values are consistently higher near the velocity center of the shear layer ($Y_{0.5}$) where turbulent shear stress is highest. Also note that a large energy convection occurs close to the inner edge of the shear layer.

4 Concluding Remarks

In the developing region of a plane jet, jet spreading is essentially dominated by coherent structure dynamics. The jet spreads in a stepwise manner as a result of vortex interaction processes, which include the mechanism of vortex formation and vortex merging. The vortex formation and merging locations are determined from the point at which the transverse velocity fluctuations for the corresponding primary instabilities, namely the fundamental and its subharmonics, reach saturation. Within the shear layer, the local transverse mean velocity (V), streamwise velocity fluctuation (u'), and turbulent shear stress ($\overline{u'v'}$) (representing fluctuation energy production) minima, are sustained, while the transverse velocity fluctuation (v') experiences a local maximum. Furthermore, in this region, jet spreading ceases to increase until the next merging process starts and local V and $\overline{u'v'}$ negative zones are observed near the outer edge of the shear layer. Maximum V, u', and $\overline{u'v'}$ values are obtained in the former portion of the vortex merging processes, whereas v' contains local minima. Variations in these turbulent flow dynamics are mainly due to variations in vortex orientation as well as vortex deformation during the merging process.

References

Browand, F. K., and Ho, C. M., 1983, "The Mixing Layer: An Example

of Quasi Two-Dimensional Turbulence," *Journal of Mechanics and Theoretical Applications*, pp. 665–672.

Brown, F. K., and Roshko, A., 1974, "On Density Effects and Large Structure in Turbulent Mixing Layers," *Journal of Fluid Mechanics*, Vol. 64, pp. 775–816.

Crow, S. C., and Champagne, F. H., 1971, "Orderly Structure in Jet Turbulence," *Journal of Fluid Mechanics*, Vol. 48, pp. 547–591.

Everitt, K. W., and Robins, A. G., 1978, "The Development and Structure of Turbulent Plane Jets," *Journal of Fluid Mechanics*, Vol. 88, pp. 563–583.

Gutmark, E., and Ho, C. M., 1983, "Preferred Modes and Spreading Rates of Jets," *Physics of Fluids*, Vol. 26, pp. 2932–2938.

Gutmark, E., and Wygnanski, I., 1976, "The Planar Turbulent Jet," *Journal of Fluid Mechanics*, Vol. 73, pp. 465–495.

Ho, C. M., 1981, "Local and Global Dynamics of Free Shear Layers," *Proceedings of the Symposium on Numerical and Physical Aspects of Aerodynamic Flow* (Long Beach), pp. 521–533.

Ho, C. M., and Huang, L. S., 1982, "Subharmonics and Vortex Merging in Mixing Layers," *Journal of Fluid Mechanics*, Vol. 119, pp. 443–473.

Hsiao, F. B., and Huang, J. M., 1988, "Subharmonic Evolution of Coherent Structures in an Excited Plane Jet," *First National Fluid Dynamics Congress* (Cincinnati), AIAA paper 88-3609.

Hsiao, F. B., and Huang, J. M., 1990a, "Near-Field Flow Structures and Sideband Instabilities in an Initially Laminar Plane Jet," *Experiments in Fluids*, Vol. 9, pp. 2–12.

Hsiao, F. B., and Huang, J. M., 1990b, "On the Evolution of Instabilities in the Near Field of a Plane Jet," *Physics of Fluids A*, Vol. 2, pp. 400–412.

Miau, J. J., and Hsu, C. T., 1987, "Concerning the Wake Effect on the Initial Instability Development of a Mixing Layer," *2nd International Symposium on Transport Phenomena in Turbulent Flows* (Tokyo).

Miau, J. J., and Karlsson, S. K. F. K., 1986, "Evolution of Flow in the Developing Region of the Mixing Layer with a Skew Laminar Wake as an Initial Condition," *Physics of Fluids*, Vol. 29, pp. 3598–3607.

Oster, D., and Wygnanski, I., 1982, "The Forced Mixing Layer Between Parallel Streams," *Journal of Fluid Mechanics*, Vol. 123, pp. 91–130.

Sami, S., 1967, "Balance of Turbulence Energy in the Region of Jet-Flow Establishment," *Journal of Fluid Mechanics*, Vol. 29, pp. 81–92.

Winant, C. D., and Browand, F. K., 1974, "Vortex Pairing—The Mechanism of Turbulent Mixing-Layer Growth at Moderate Reynolds Number," *Journal of Fluid Mechanics*, Vol. 63, pp. 237–255.

Zaman, K. B. M. Q., and Hussain, A. K. M. F., 1980, "Vortex Pairing in a Circular Jet Under Controlled Excitation. Part 1: General Jet Response," *Journal of Fluid Mechanics*, Vol. 101, pp. 449–491.

Surface Disturbance Evolution and the Splattering of Turbulent Liquid Jets

Sourav K. Bhunia

John H. Lienhard V

W. M. Rohsenow Heat and Mass Transfer Laboratory, Department of Mechanical Engineering, Massachusetts Institute of Technology, Cambridge, MA 02139

In this study, we investigate the growth of surface disturbances on turbulent liquid jets in air and its relation to the amount of splattering when the jet strikes a target. A laser-based optical technique is used to measure the instantaneous local amplitude of fluctuations on jets produced by fully-turbulent tube nozzles. Measurements were made over the portion of the jet between 0.2 and 45 nozzle diameters downstream of the nozzle. Jets of water, an isopropanol-water mixture, and water with a surfactant were studied. The local rms amplitude of surface disturbances scales with the jet Weber number and the dimensionless distance from the target. The measurements show a nonexponential growth of the rms amplitude as the liquid moves downstream. Power spectra of the disturbance amplitudes show broadband turbulent disturbances to be dominant over any single wavenumber Rayleigh-type instability. The measured rms amplitude of roughness on the jet surface correlates well with the fraction of impinging liquid splattered, as hypothesized in previous models of splattering. A mathematical model of the free-surface/turbulence interaction is also given. The spectrum of surface disturbances is calculated based on the pressure spectrum of isotropic, homogeneous turbulence. Both the theoretical model and the experiments show that the high-wavenumber portion of the spectrum decays as $k^{-19/3}$ owing to the damping effect of capillary forces on the turbulent pressure spectrum that drives surface roughening.

1 Introduction

The disturbances on the free surface of a turbulent liquid jet cause splattering of liquid when the jet strikes a surface and are thus critical to the control of jet impingement cooling and cleaning processes. The rate of surface roughening is also important to absorption in jet systems (Kim and Mills, 1989) and to jet atomization processes. No detailed measurements of the instantaneous amplitudes of these disturbances are available in the literature. Many photographic studies of turbulent jets have been reported (e.g., Hoyt et al., 1974), but photography does not generally provide sufficient temporal resolution for high-frequency time-series analysis or spectral determination. The only time-resolved measurements of the turbulent-disturbance amplitude that the authors have found were by Chen and Davis (1964), who presented a few rms amplitude measurements obtained with an electrical conductivity probe. The accuracy of those data was severely limited by the interference of the instrument with the flow.

In the present work, we use a laser-based optical technique to measure the amplitudes of fluctuations on the free surface of a turbulent jet in air (following Tadrist et al., 1991). This instrument, consisting of a laser light sheet, a photosensor, and lenses, is capable of measuring fluctuations in jet diameter at frequencies up to about 1 MHz. The jets were produced by fully developed turbulent pipe flow issuing from straight tube nozzles.

A key objective of this study is to assess the relationship between jet surface roughness and splattering during jet impingement. In a previous study, we examined the process by which liquid droplets are splattered when a turbulent jet impacts a solid surface normal to its axis (Bhunia and Lienhard, 1994). Splattering was found to occur when disturbances on the jet are carried into the liquid moving along the target, where they are amplified and cause droplets to be ejected. The results of that study showed that spattering increases as the dimensionless jet length increases and as the jet Weber number increases (i.e., as surface tension decreases). Since turbulent roughening of the jet surface is greater for longer jets and for jets of lower surface tension, these trends were credited to an increasingly rough jet surface when the jet reached the target. The present measurements allow a direct test of the correlation between jet surface-roughness and the fraction of incoming liquid that is splattered.

A mathematical model of free-surface response to turbulence is also developed. At modest values of air-side Reynolds number, the free surface deforms in response to turbulent pressure fluctuations in the liquid. Capillary pressure provides the restoring force that balances the turbulent pressure, and this

Contributed by the Fluids Engineering Division for publication in the JOURNAL OF FLUIDS ENGINEERING. Manuscript received by the Fluids Engineering Division September 15, 1993; revised manuscript received May 10, 1994. Associate Technical Editor: M. W. Reeks.

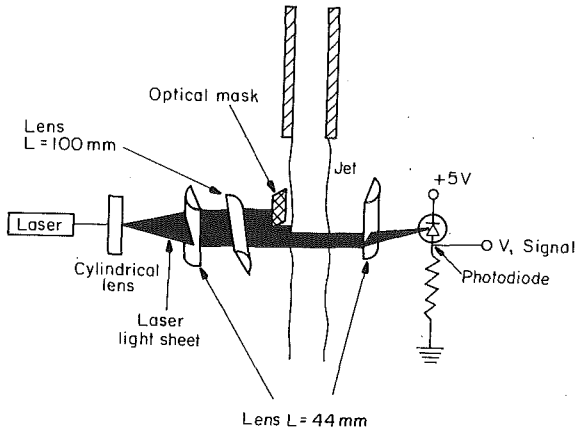

Fig. 1 Optical probe for measuring the instantaneous amplitude of surface disturbances

balance determines the amplitude and evolution of the free-surface disturbances. Here, the high wavenumber (small scale) range of the turbulent pressure spectrum is modeled using results for homogeneous, isotropic turbulence. A force balance between turbulent and capillary pressure is used to calculate the high wavenumber spectrum of the surface disturbances. The theory shows the spectrum to decay as the $-19/3$ power of wavenumber, owing to the capillary damping of the turbulent pressure spectrum. This result is in good agreement with the measured spectra.

2 Experiments

A laser-based optical instrument (Fig. 1) was used to measure the fluctuation amplitudes on the free surface of a turbulent jet in air. A similar instrument was used earlier by Tadrist et al. (1991) to measure the surface disturbances on laminar liquid jets. A 2.4 mW He-Ne laser beam was transformed into a collimated sheet of light by sending it successively through a glass rod and a cylindrical lens (focal length, $L = 44$ mm). This light sheet was further thinned and focused onto the liquid jet by passing it through the axis of a cylindrical lens ($L = 100$ mm) so that an approximately 0.1 mm thick light sheet intersected the jet perpendicular to its axis. A collecting lens ($L = 44$ mm) focused the portion of the light sheet unintercepted by the jet onto a photosensor.

The photosensor was based on an EG&G Vactec photodiode (VTP 8552) and had a dynamic range of about 1 MHz. A 5 Vdc reverse bias was applied to the photodiode, reducing the junction capacitance to 44 pF. The voltage drop across a resistor placed in series with the photodiode provided a signal corresponding to the amount of laser light power incident on the diode. Static calibration showed perfectly linear voltage variation of the measuring system with the width of the intercepted portion of the collimated laser sheet. The rms deviation from linearity was 1 percent of the full scale, i.e., of the voltage reading corresponding to the entire laser sheet. Precise measurements of the diameters of transparent glass rods with this instrument indicated that refraction of light by the object measured has negligible influence on the data. The glass rod (or liquid jet) acts as a diverging lens, and only a negligible portion of the laser sheet is refracted into the direction of the collecting lens. In other words, the jet is effectively an opaque obstruction to the laser sheet.

The output of the photosensor was analyzed by a digital oscilloscope (Hewlett Packard 54200 A/D) and a spectrum analyzer (GenRad 2512A). The oscilloscope provided the true rms voltages over time intervals of the signal. Several such rms voltage outputs were recorded to obtain the rms of the total voltage signal (AC + DC), called V_{tot}, at a given jet axial location. The rms AC component of the signal, V_{ac}, was also recorded at each location. Then, to measure the amplitude of fluctuations at one point on the jet surfce, half of the width of the light sheet incident on the jet was obstructed by an optical mask, so that only the fluctuations from one side of the jet contributed to the fluctuating light power received by the photosensor. The corresponding AC rms signal is denoted by $V_{1/2}$. In addition, the steady voltage signal corresponding to the entire light sheet, *without* any interception by the jet, was obtained as V_0. Owing to the linearity of photodetector response, the ratio of rms amplitude of surface fluctuations to the mean jet diameter[1] can be obtained from these measurements as

$$\frac{\delta_{rms}}{d} = \frac{V_{1/2}}{V_0 - \sqrt{V_{tot}^2 - V_{ac}^2}} \tag{1}$$

The GenRad 2512A spectrum analyzer had a frequency band-

[1]The contraction coefficient for turbulent jets leaving pipe nozzles is essentially unity. Throughout this study, we treat nozzle diameter and initial mean jet diameter interchangeably.

Nomenclature

d = nozzle diameter, m
$F(k)$ = three-dimensional isotropic turbulent pressure spectrum, N^2/m
$G(\eta)$ = power spectrum of the amplitude of free surface disturbances, Eq. 8
k = wavenumber, 1/m
k_1, k_2, k_3 = $j(x, y, z)$ Cartesian components of the wavenumber vector, $k^2 = k_1^2 + k_2^2 + k_3^2$, 1/m
k_p = resultant wavenumber in the (x, y) plane, $\sqrt{k_1^2 + k_2^2}$, 1/m
l = integral scale of turbulence or distance of target from nozzle, m
p = fluctuating component of pressure, N/m^2
t = time, s
u = jet free surface speed, m/s
u_f = jet bulk velocity at the nozzle exit, m/s
u' = rms turbulent speed in liquid, m/s
We_d = jet Weber number, $\rho u_f^2 d/\sigma$
x = distance from the nozzle exit along the jet axis, m
(x, y) = Cartesian coordinates in the plane of the mean liquid surface, m
δ = instantaneous height of the jet surface disturbances, i.e., instantaneous radius minus local mean radius, m
$\overline{\delta^2}$ = ensemble average of δ^2, m^2
δ_{rms} = rms height of surface disturbances, $\sqrt{(\overline{\delta^2})}$, m
η = dimensionless wavenumber of the free surface disturbances, $l\sqrt{k_1^2 + k_2^2}$
ξ = splattered fraction of incoming jet's liquid
ρ = liquid density, kg/m^3
σ = surface tension between jet liquid and surrounding gas, N/m

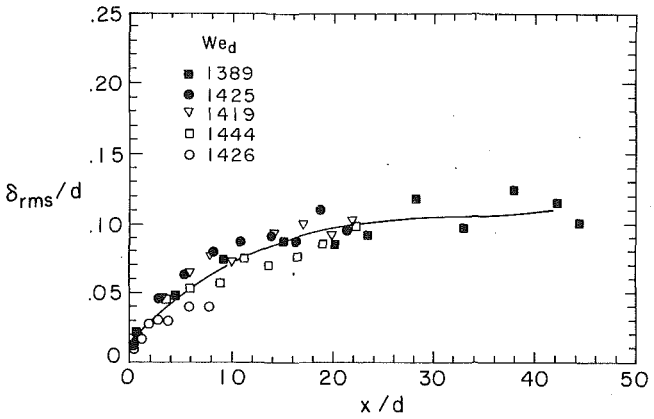

Fig. 2 Variability in repeated measurements of the rms disturbance amplitude: water, $d = 5.8$ mm

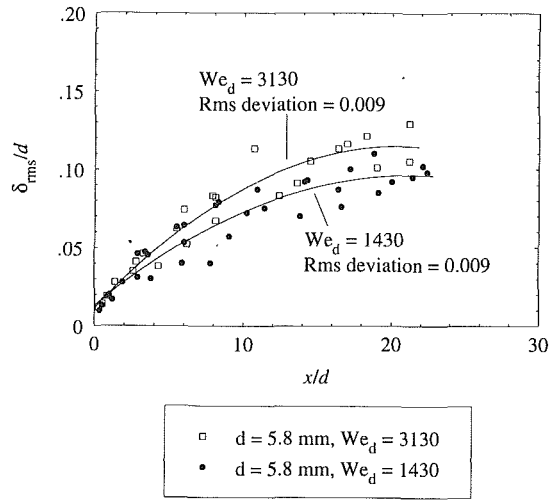

Fig. 3 Measurements of δ_{rms} at two different Weber numbers. For each We_d, a second-order least-squares curve is shown, together with the rms deviation from it

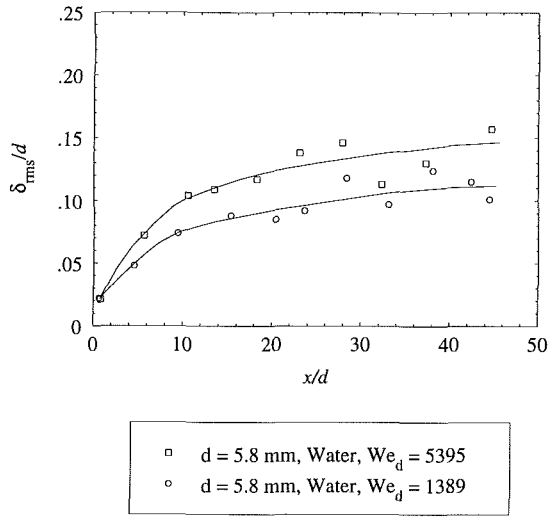

Fig. 4 Measurements of δ_{rms} at two different Weber numbers, with faired curves for each

width of dc to 100 kHz and an amplitude range of 6 decades for the power spectra.

Jets were produced by fully developed turbulent pipe flow from tube nozzles of diameter $d = 2.7 - 5.8$ mm. Measurements were made over the portion of the jet between 0.2 and 45 nozzle diameters downstream of the nozzle. Most experiments were conducted with water; however, for some runs the surface tension was varied by using isopropanol-water mixtures or by using a surfactant detergent. In each case, the surface tension was measured with a ring gauge. Direct measurement of the flow rates (by volume collection) provided the jet Weber numbers with ± 3 percent uncertainty (at 20:1 odds).

Full details of the jet apparatus are given by Bhunia and Lienhard (1994). That study also reports measurements of the fraction of the jet liquid splattered, ξ, during jet impingement on smooth, solid targets under isothermal conditions. As described in that report, the jet Reynolds number has only a very weak influence on the turbulence intensity of jets produced by fully developed pipe flows. Therefore, in the present report, the jet Reynolds numbers are not mentioned, although they can be calculated easily from the nozzle diameters and Weber numbers provided with each data set. The Reynolds number here ranges from 20,000 to 49,000.

Each measurement of δ_{rms} is based on an estimated number of 1000 samples. The actual number of samples varied because of the sampling technique used by the oscilloscope, which reported an rms voltage based on samples that typically had about 100 points. Ten to twelve of the resulting values of δ^2 were averaged to obtain the reported results. Some additional uncertainty can enter into the measurements when the jet Weber number and the length of the jet, x/d, become large enough that droplets are stripped off the jet surface and enter the air flow around the jet. For the measurements reported here, however, this droplet stripping was either absent or of a negligibly low amount.

3 Results of Experiments

Figures 2, 3, and 4 show the rms amplitude of disturbances on turbulent water jets in air. To determine the run-to-run variability of the measurements, several tests were repeated at nearly identical conditions (Fig. 2). The Weber numbers for each test were equal to within the uncertainty limits of ± 3 percent. The rms deviation of the measurements from a second or third order least-squares fit was 0.009, which is about 9 percent of the maximum rms disturbance for this case. The 90 percent confidence intervals of the measurements (according to a chi-squared test of 1000 sample points) are so small that they have essentially the same size as the symbols plotted.

Figure 3 shows the fitted curves for repeated measurements of δ_{rms}/d at two different jet Weber numbers. Although the ranges of variability for the two data sets overlap, the averaged curves show a dependence of the surface disturbance amplitude on the Weber number. This dependence is more pronounced in Fig. 4, which compares jets having a larger difference in Weber numbers.

The amplitudes of disturbances are very small near the nozzle. As the liquid moves downstream, the disturbances grow, but they do not exhibit the exponential increase with x/d that would be expected from Rayleigh's capillary instability theory (Drazin and Reid, 1981; Lienhard et al., 1992). Some consideration of the graphs also shows that the disturbance growth rate parameter predicted by Rayleigh's theory, $(x/d)/\sqrt{We_d}$, cannot correlate the disturbance amplitude data for jets of different diameters and Weber numbers.

Figure 5 compares the surface roughness evolution for liquids of different surface tension. One case represents a mixture of 10 percent by volume isopropanol in water, which has a static surface tension 58 percent lower than pure water (0.042 N/m versus 0.072 N/m). The evolution of δ_{rms} compares favorably with the data for a water jet at the same Weber number and x/d.

Figure 5 also show data for a surfactant-water jet. At rest, the surfactant solution has a surface tension of only 0.027 N/m. Our previous study of splattering (Bhunia and Lienhard,

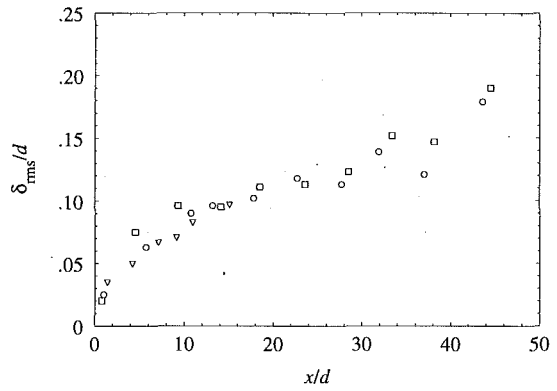

▽ d = 5.8 mm, Soap-water, We_d = 8509(3191)
□ d = 5.8 mm, Isopropanol/Water, We_d = 3042
○ d = 5.8 mm, Water, We_d = 3123

Fig. 5 Comparison of δ_{rms} evolution among liquids with different surface tensions. The Weber number in parentheses is based on pure-water surface tension

1994) showed that surfactants have no effect on splattering behavior: the splattering scaled with a Weber number based on the surface tension of pure water, rather than the surface tension of the static surfactant mixture. From this, it appeared that the turbulent jet surface never achieves a sufficient concentration of surfactant to exhibit a lowered surface tension, either because the diffusion timescales are too long relative to x/u_f or because turbulent free-surface renewal limits the surfactant's surface concentration. Figure 5 supports that conclusion, since the roughness evolution of the surfactant jet is identical to that of a pure water jet having the same size and speed. For those data, the higher Weber number shown is based on the static surface tension, while the lower is based on the surface tension of pure water. The lower value equals that of the pure water jet.

When a turbulent liquid jet impinges onto a solid target, droplets are splattered off the liquid sheet that moves across the target. Figure 6 reproduces measurements of the fraction of incoming jet liquid splattered, ξ, reported earlier (Bhunia and Lienhard, 1994). Near the nozzle ($x/d < 10$, say), ξ changes very little as the jet Weber number varies from 1400 to 7300. Similarly, the variation in δ_{rms}/d with the jet Weber number in Figs. 3 and 4 is also relatively weak near the nozzle. Farther downstream, the dependence on jet Weber number is stronger both for δ_{rms}/d and ξ. These observations suggest a correlation between the two variables, and such a correlation was the basic hypothesis of previous models of splattering (Lienhard et al., 1992). We may now examine this correlation quantitatively.

Figure 7 shows the splatter fraction, ξ, as a function of the rms amplitude of jet surface disturbances. Each point on this graph is obtained by plotting a previously measured splatter fraction ξ (Bhunia and Lienhard, 1994) against δ_{rms}/d from present experiments for jets of same Weber number and $x/d = l/d$. Each set of data for a given nozzle diameter and Weber number consists of measurements at several different axial locations, x/d. The correlation is reasonably clear, given that both δ_{rms} and ξ have significant variability, and this provides further evidence that the jet impingement splattering results from the presence of surface disturbances on turbulent jets and is governed by the amplitude of those disturbances.

For more unusual liquids, various surface-tension phenomena can be expected to alter the surface-roughness evolution and its relation to splattering. For example, surface polymerizing agents (such as are often used to suppress to jet breakup)

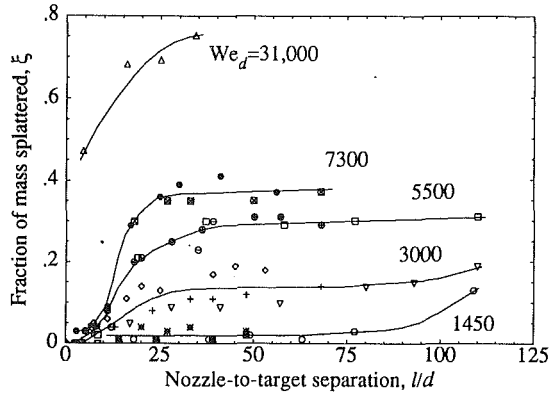

△ d=4.4 mm, Re_d=98097, We_d=31243
⊠ d=4.4 mm, Re_d=48284, We_d=7564
● d=2.7 mm, Re_d=37141, We_d=7096
⊖ d=5.8 mm, Re_d=47800, We_d=5628
⊕ d=4.4 mm, Re_d=41437, We_d=5420
□ d=2.7 mm, Re_d=31868, We_d=5373
◇ d=5.8 mm, Re_d=35986, We_d=3101
+ d=4.4 mm, Re_d=30090, We_d=2858
▽ d=2.7 mm, Re_d=24580, We_d=3108
✱ d=5.8 mm, Re_d=24507, We_d=1479
■ d=4.4 mm, Re_d=20988, We_d=1430
○ d=2.7 mm, Re_d=16320, We_d=1409

Fig. 6 Splattering as a function of nozzle-to-target separation and jet Weber number. The solid lines are fitted curves through groups of data having We_d constant to within its uncertainty (±3 percent)

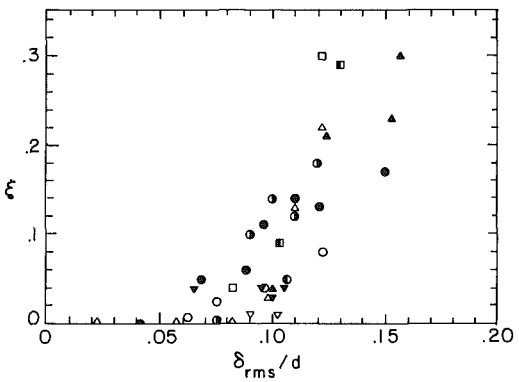

Fluid	d (mm)	We_d
● Isopropanol / Water	5.8	3200
▲ Water	5.8	5500
●		3120
▼		1450
□ Water	4.4	7535
△		5290
○		2850
▽		1400
◙ Water	2.7	7000
◐		3175

Fig. 7 Dependence of the splattering fraction on the rms amplitude of surface disturbances

may be expected to suppress splattering significantly. As another example, long chain alcohols in aqueous solution require a finite time to establish the static surface tension at a freshly formed liquid surface (Addison, 1945), owing to their tendency

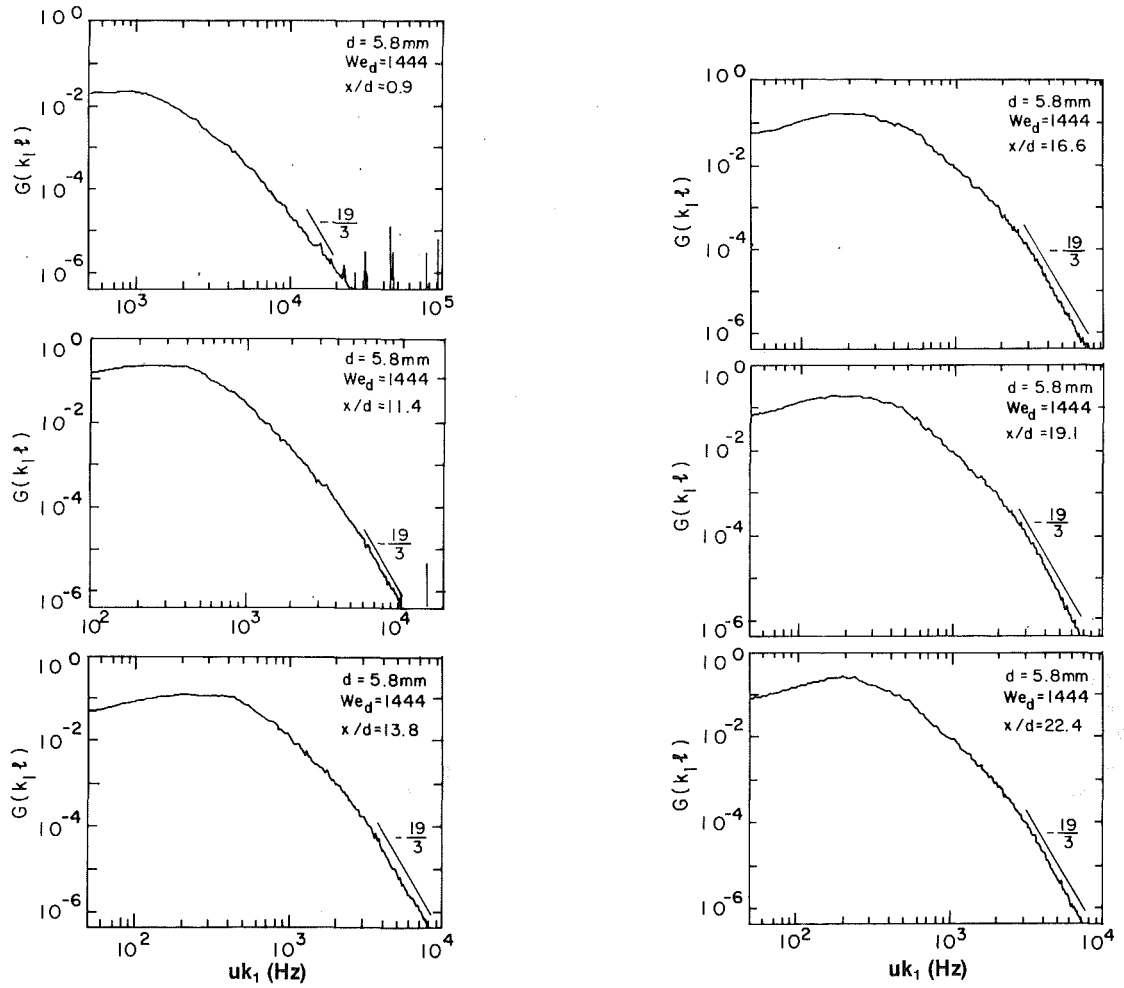

Fig. 8 Measured spectra of free-surface disturbances on a turbulent liquid jet at different axial locations. The ordinate is *proportional* to $G(k_1 l)$

to form a surface monolayer. Thus, for long chain alcohol solutions, a simple Weber number may not effectively scale roughness evolution and splattering, in contradiction to our observations for isopropanol.

3.1 Roughness Spectra. The local distribution of disturbance wavelengths on the jet surface can elucidate the mechanism of surface roughening. Figure 8 shows the spectra of surface-disturbance amplitudes at several different axial locations. The ordinate is proportional to the power spectrum of the free surface disturbance amplitude, $G(k_1 l)$ (see Eq. (8)) and the abscissa is uk_1, where k_1 is the wavenumber in the direction of the jet axis, u is the free surface velocity, and l is the integral scale of turbulence. The spikes at very high frequencies are a reproducible noise signature of the electronics.

These graphs of power spectrum versus disturbance wavenumber show that broad-band turbulent disturbances are more prevalent than any single-wavenumber disturbance related to a Rayleigh-type instability. In the sense of Rayleigh's capillary instability, the low wavenumbers are unstable and the high wavenumbers are stable; the most unstable wavenumber corresponds to $uk_1 = 1017$ Hz. Although this frequency is within the portion of the spectrum that contributes most strongly to the variance of surface roughness (the "knee"), the spectra retain the general appearance of a turbulent cascade from low to high wavenumber. The coupling of the turbulent pressure to the capillary pressure drives the spectral distribution.

These log-log spectral plots show a portion of very nearly linear decrease in the spectral amplitude, characteristic of high wavenumber turbulence. Except for measurement locations very close to the nozzle, the slope of this linear portion is $-19/3$. This novel result is explained in detail in the following section. Similar spectra were obtained for jets of other sizes and the other We_d.

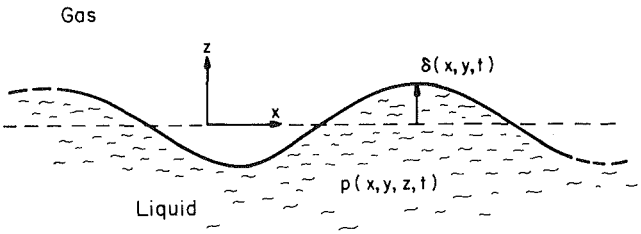

Fig. 9 Geometry of the free surface over a turbulent liquid

4 A Model for Turbulence-Induced Free Surface Disturbances

To examine the relationship between the disturbance spectrum and the pressure spectrum, let us consider a planar free surface of infinite dimensions with a turbulent liquid of infinite depth on one side of it (Fig. 9). A rectangular Cartesian coordinate system is positioned so that the (x, y) plane coincides with the mean location of the free surface and negative values of z lie within the liquid below the surface. Let $\delta(x, y, t)$ be the instantaneous amplitude of small surface disturbances relative to the mean free surface position, and let $p(x, y, z, t)$ be

the fluctuating component of liquid pressure at any location (x, y, z). Since the pressure fluctuations on the free surface are balanced by the surface tension, we have at $z \cong 0$

$$p = -\sigma\left(\frac{\partial^2\delta}{\partial x^2}+\frac{\partial^2\delta}{\partial y^2}\right) \tag{2}$$

Let us define Fourier transforms of δ and p as follow:

$$\delta = \int_{-\infty}^{\infty}\int_{-\infty}^{\infty} \Delta(k_1, k_2, t)e^{-i(k_1x+k_2y)}dk_1dk_2 \tag{3}$$

and

$$p = \int_{-\infty}^{\infty}\int_{-\infty}^{\infty}\int_{-\infty}^{\infty} P(k_1, k_2, k_3\ t)e^{-i(k_1x+k_2y+k_3z)}dk_1dk_2dk_3 \tag{4}$$

Substituting into Eq. (2), we get

$$\int_{-\infty}^{\infty} P(k_1, k_2, k_3, t)dk_3 = \sigma(k_1^2+k_2^2)\Delta(k_1, k_2, t) \tag{5}$$

To describe any time-evolution of the statistical moments of δ and p, the Navier-Stokes equation with proper boundary and initial conditions must be used. In this model, we restrict our attention to the instantaneous statistical relation between p and δ. We suppose the statistics to be taken over spatial intervals large compared to the turbulent integral scales but small compared to the axial distance over which the surface disturbances evolve significantly. In practice, this means wavelengths of a few jet diameters or less. Since the actual measurements are time averages taken at a single spatial location, we are in effect applying the usual Taylor hypothesis (Monin and Yaglom, 1975) to obtain the wavenumber spectrum from the frequency spectrum, with frequency $= uk_1$. Thus, while the statistics of p and δ in the subsequent analysis are instantaneous spatial averages, the measured parameters correspond to time-averages at any spatial location.

Assuming the turbulent pressure fluctuations to be a spatially homogeneous stationary random process, the three-dimensional turbulent pressure spectrum, $F(k)$, can be defined in the usual way by taking a one-point ensemble-average moment of Eq. (4):

$$\overline{p^*p} = \ldots = \int_{-\infty}^{\infty}\int_{-\infty}^{\infty}\int_{-\infty}^{\infty} F(k)dk_1dk_2dk_3 \tag{6}$$

where the * indicates a complex conjugate.[2] Multiplying Eq. (3) by its complex conjugate and ensemble averaging, we obtain with Eqs. (5) and (6)

$$\overline{\delta^2} = \overline{\delta^*\delta} = \int_{-\infty}^{\infty}\int_{-\infty}^{\infty} \frac{1}{\sigma^2(k_1^2+k_2^2)^2}\int_{-\infty}^{\infty} F(k)dk_3dk_2dk_1 \tag{7}$$

For isotropic, homogeneous turbulence (George et al., 1984),

$$F(k) \sim 0.26\rho^2u'^4l^3(kl)^{-13/3},\ kl \gg 1$$

where u' is the rms fluctuating component of turbulent velocity and l is the integral scale of turbulence. Let us define the one-dimensional spectrum of disturbances, $G(\eta)$, by the following equation:

$$\frac{\overline{\delta^2}}{l^2} = \int_0^{\infty} G(\eta)d\eta \tag{8}$$

Here, η is the wavenumber of the free surface disturbances nondimensionalized with the integral scale of turbulence, l. From Eqs. (7) and (8), it follows that at high wavenumbers $(\eta \gg 1)$ the disturbance spectrum is

$$G(\eta) \sim 0.26 \times 2\pi \frac{\rho^2u'^4}{\sigma^2}\frac{l^{-13/3}}{k_p^3}\int_{-\infty}^{\infty}\frac{dk_3}{(k_p^2+k_3^2)^{13/6}} \tag{9}$$

where we have transformed from Cartesian to polar coordinates in the wave number plane $[(k_1, k_2) \rightarrow (k_p, \theta)]$, with $\eta = k_pl$. Upon evaluating the integral, the spectrum of free-surface turbulent disturbances is found to be

$$G(\eta) \sim 2.41\left(\frac{\rho^2u'^4l^2}{\sigma^2}\right)\eta^{-19/3},\ \eta \gg 1 \tag{10}$$

This result explains the observed $-19/3$ slope in the log-log plots of the disturbance spectra as being a consequence of the $k_1^{-7/3}$ variation of the one-dimensional spectrum of the pressure fluctuations (George et al., 1984) and a factor of k_1^{-4} introduced by the derivatives of δ in the capillary force balance equation. It should be noted that this is the *steepest possible slope* for wave numbers less than the Kolmogorov scale. For free surfaces over liquid having a significant mean shear stress, we expect different slopes at high wavenumber, since the corresponding pressure spectra have different slopes (George et al., 1984). For example, in the case of jets, near the nozzle we should see slopes different from $-19/3$ at high wave numbers. These conclusions are each confirmed by the measured spectra (Fig. 8).

The success of this model is due in part to its focus on the high wavenumbers: theoretical and experimental studies of otherwise-homogeneous turbulence near a plane interface show that the higher wavenumbers retain a homogeneous character near the free surface (Hunt and Graham, 1978; Brumley, 1984).

Finally, it is interesting to note that for small amplitudes, the mean increase in jet surface area is proportional to $\int_0^{\infty}\eta^2G(\eta)d\eta$, as can be shown by manipulation of the integral for surface area in terms of $\delta(x, y)$. This implies that the high wavenumber spectrum of the surface-energy increase of the jet is proportional to $\eta^2G(\eta) \sim \eta^{-13/3}$.

5 Conclusions

A nonintrusive optical technique has been used to measure the instantaneous amplitude of surface disturbances on turbulent liquid jets and to study the evolution of rms surface roughness. The spectrum of disturbance amplitudes has also been measured, and a simple theory for its high wavenumber behavior has been developed.

- Measurements show a nonexponential growth of the rms amplitude of jet surface disturbances as the jet travels downstream. The disturbance evolution depends on Weber number and x/d.
- Surface-tension effects on jet roughness scale with the jet Weber number, as demonstrated by comparing results for water jets and isopropanol-water jets. Surfactants have no effect on the roughness, presumably because the surfactant is unable to reach the surface concentration necessary to alter surface tension.
- The amplitude of turbulent jet surface disturbance is correlated with the fraction of liquid splattered during jet impingement.
- The spectra of surface disturbances show that turbulent disturbances dominate over any single-wavelength Rayleigh-type unstable disturbance. The log-log slope of the disturbance spectrum at high wavenumber is $-19/3$. Near the nozzle, the high wavenumber slopes are different owing to alteration of the pressure spectrum by the residual mean shear force in the bulk liquid.
- A mathematical model of free-surface/turbulence interaction is developed. The model predicts the observed $k^{-19/3}$ high wavenumber decay of the disturbance spectrum.

Acknowledgment

This work was supported by the National Science Foundation under grant number CBTE-8858288.

[2]For wavevectors $\vec{k}'$ and $\vec{k}$, $\overline{P^*(\vec{k}')P(\vec{k})} = F(k)\,\delta_{\text{Dirac}}(\vec{k}' - \vec{k})$ if p is a stationary random function.

References

Addison, C. C., 1945, "The Properties of Freshly Formed Surfaces. Part IV. The Influence of Chain Length and Structure on the Static and Dynamic Surface Tensions of Aqueous Alcoholic Solutions," *Journal of Chemical Society*, pp. 98–106.

Bhunia, S. K., and Lienhard V, J. H., 1994, "Splattering During Turbulent Liquid Jet Impingement on Solid Targets," ASME JOURNAL OF FLUIDS ENGINEERING, Vol. 116, No. 2, pp 338–344.

Brumley, B., 1984, "Turbulence Measurements Near the Free Surface in Stirred Grid Experiments," *Gas Transfer at Water Surfaces*, W. Brutsaert and G. H. Jirka, eds., Reidel Publishing Co., pp. 83–92.

Chen, T.-F., and Davis, J. R., 1964, "Disintegration of a Turbulent Water Jet," *J. Hydraulics Division*, Proc. ASCE, HY 1, Jan., pp. 175–206.

Drazin, P. G., and Reid, W. H., 1981, *Hydrodynamic Stability*, Cambridge University Press, Cambridge, UK.

George, W. K., Beuther, P. D., and Arndt, R. E. A., 1984, "Pressure Spectra in Turbulent Free Shear Flows," *Journal of Fluid Mechanics*, Vol. 148, pp. 155–191.

Hoyt, J. W., Taylor, J. J., and Runge, C. D., 1974, "The Structure of Jets of Water and Polymer Solution in Air," *Journal of Fluid Mechanics*, Vol. 63, pp. 635–640.

Hunt, J. C. R., and Graham, J. M. R., 1978, "Free-Stream Turbulence Near Plane Boundaries," *Journal of Fluid Mechanics*, Vol. 84, pp. 209–235.

Kim, S., and Mills, A. F., 1989, "Condensation on Coherent Turbulent Liquid Jets: Part I—Experimental Study," ASME *Journal of Heat Transfer*, Vol. 111, Nov., pp. 1068–1074.

Lienhard V, J. H., Liu, X., and Gabour, L. A., 1992, "Splattering and Heat Transfer During Impingement of a Turbulent Liquid Jet," ASME *Journal of Heat Transfer*, Vol. 114, May, pp. 362–372.

Monin, A. S., and Yaglom, A. M., 1975, *Statistical Fluid Mechanics: Mechanics of Turbulence*, Vol. 2, MIT Press, Cambridge, MA, p. 449.

Tadrist, L., Alaoui, E. K. O., Occelli, R., and Pantaloni, J., 1991, "Experimental Study of a Liquid Jet Flowing Into Another Immiscible Liquid, 'A Local Analysis of the Interface'," *Experiments in Fluids*, Vol. 12, pp. 67–75.

T. M. Spielbauer
Senior Materials Development Engineer,
3M,
3M Center Bldg.,
St. Paul, MN 55144-1000

C. K. Aidun
Associate Professor,
Institute of Paper Science and Technology
and School of Mechanical Engineering
Georgia Institute of Technology,
500 10th St., N.W.,
Atlanta, GA 30318-5403

The Wave-Thinning and Breakup of Liquid Sheets

In this study, the radially thinning liquid sheets formed by a simple splash plate nozzle were investigated. These sheets, observed using high-speed video and 16 mm photography, were found to breakup by way of a localized rupture mechanism. The sheet is thinned by geometric distortion due to the radial expansion of the sheet, and by stretching caused by the presence of large amplitude sinuous waves. The downstream sheet thickness in the wave-thinned region was calculated from experimentally measured perforation growth rates. These thicknesses were found to be about 12 percent of the predicted value for an undisturbed sheet. Trends in the downstream position at which significant thinning due to sinuous waves is predicted to occur agree with trends in experimentally measured rates of hole formation.

Introduction

The breakup of liquid sheets has been the subject of extensive investigation, and a number of disintegration mechanisms have been proposed. Dombrowski and Fraser (1954) described two mechanisms of bulk sheet breakup, one involves waves and subsequently ligament formation, and the second mechanism is based on sheet perforations.

A simplified description of the wave mechanism of breakup presented by Fraser et al. (1962), is as follows. Wave-like disturbances present in the sheet grow as the liquid expands downstream. When the wave reaches some critical amplitude, the sheet breaks at uniform, half-wave length intervals forming bands of fluid. These bands contract into cylinders, and in a mechanism similar to that for jets, these cylinders break up into drops.

Hagerty and Shea (1955) performed an analytical investigation of the growth of waves in a planar inviscid sheet. They showed that only two wave forms could exist: sinuous waves, for which the upper and lower sheet surfaces move in phase, and dilational waves, for which the motion of the surfaces is out of phase. It has been demonstrated (Hagerty and Shea, 1955; Crapper et al., 1975a,b) that the sinuous disturbances always grow faster than the dilational disturbances, and that there is a single sine wave of optimum growth.

Dombrowski and Johns (1963) included the effects of the liquid phase viscosity, and found that the growth rate of all disturbances was reduced; however, a single wave of optimum growth was still predicted to exist. Weihs (1978) included the effects of the radially thinning geometry in his analysis of viscous liquid sheet stability. Again, a single wave of optimum growth was predicted. The wavelength of the optimum disturbance was predicted to be a function of the sheet thickness and the liquid viscosity.

In the second mechanism of breakup, perforations, are formed in the sheet. As these holes expand under the action of surface tension forces, thick rims are formed. These rims interact to form a web of strands which breaks up into drops.

The source of the perforations described by Dombrowski and Fraser (1954) has been investigated. Possible causes of sheet rupture include the presence of suspended solid particles (Dombrowski and Fraser, 1954), and particle impingement (Fraser et al., 1962).

A broad distribution of drop sizes is a common feature of the sprays formed by sheet producing nozzles. This distribution is believed to be a consequence of random variations in the physical steps involved in the formation, destabilization, and disintegration of the liquid sheet. In this study, experimental and analytical investigation of the liquid sheets formed by a simple splash plate nozzle has been performed in order to identify the key steps in the breakup process. Emphasis has been placed on determining the processes causing the formation of a distribution of drop sizes.

Experimental Approach

A sketch of the flow loop used in this study is shown in Fig. 1. A 1.2 m × 1.2 m (4 ft. × 4 ft.) galvanized steel tank acts as a reservoir for the test fluid. The bottom of the tank slopes toward a drain located in the center of the base, providing 380 liters (100 gallons) of storage capacity. Plexiglass walls extend upward on all four sides to constrain the spray. These transparent walls provide flexibility in locating the lighting sources needed to image the sprays. In addition, a 0.5 m × 0.5 m (20 in. × 20 in.) Plexiglass window installed in the bottom of the tank allows the spray to be illuminated.

Six nozzles were used to produce straight jets. The orifice diameter of each nozzle was measured using a telescope gage. The reported diameter is the average of four measurements made at equally spaced locations around the orifice. All of the nozzles were selected to mate with a 1/2 in. nominal female pipe connection. The entrance region, where the flow area decreased from the 1/2 in. pipe to the final orifice dimension, varied with nozzle design. The exit of five of the nozzles was

Contributed by the Fluids Engineering Division for publication in the JOURNAL OF FLUIDS ENGINEERING. Manuscript received by the Fluids Engineering Division September 25, 1992; revised manuscript received March 21, 1994. Associate Technical Editor: M. W. Reeks.

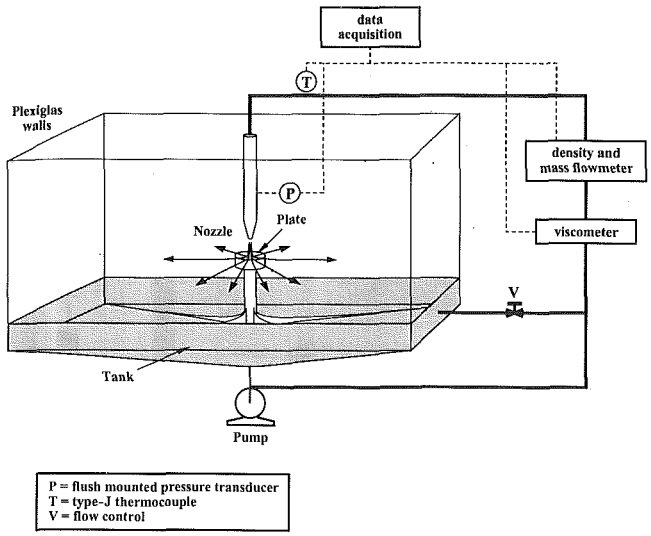

Fig. 1 Sketch of the spray apparatus

a straight length at the final orifice diameter. The sixth nozzle was a sharp edged orifice.

A threaded support rod, welded to the base of the tank directly below the discharge orifice of the nozzle, provides support for a polished, silicone coated, stainless steel plate. The plate is 5.08 cm (2 in.) in diameter. Threaded positioning bars connect the support rod to four equally spaced locations on the base of the reservoir. Using these positioning bars, the support rod can be adjusted to ensure that the plate surface is horizontal. Because the plate was mounted in the center of the reservoir, the liquid sheet, formed from the impact of the jet on the plate, travels a minimum distance of 0.6 m (2 ft) before striking the Plexiglass walls encompassing the spray chamber.

A Xybion high-speed video camera recorded images of the spray during breakup. The Xybion obtains images at a constant rate of 30 frames per second; however, the exposure time can be varied continuously from 25 nanoseconds to 10 milliseconds. The short exposure times were necessary to effectively freeze the motion of the sheet so that details of the breakup process could be observed. A Hycam high-speed 16 mm camera was also used to collect images of the spray on Kodak Tri-X and 4-X film. Rates of 4000–7000 frames per second were used. The exposure time for the Hycam is equal to 1/2.5 times the reciprocal of the framing rate.

Results

Radial Distribution of Perforations. Liquid sheets were formed by the perpendicular impingement of a circular jet on a polished disc. The jet diameter was varied by using three nozzles with different orifice sizes (#1–3). Each nozzle was operated over its practical range of jet velocities using a glycerol/water solution as the test liquid (viscosity = 62 ± 3 cp; density = 1215 ± 1 kg/m^3). For each nozzle there was a minimum critical jet velocity, below which radially thinning sheets could not be formed. Rather, the fluid spreading out from the plate surface collapsed in on itself forming bells as described by Taylor (1959). The maximum jet velocity that could be investigated was fixed by the mechanical limitations of the pump. The range of jet velocities are provided in Table 2.

The high-speed video camera was focused on a small area of the sheet, downstream from the plate edge. Images were collected for approximately one minute; thus, about 2000 images were obtained during each trial. This process was repeated at a series of downstream positions. One thousand images were viewed for each combination of nozzle diameter, jet velocity,

Table 1 Orifice diameters of the straight jet nozzles used to produce splash plate sheets

I.D.	Nozzle	Measured diameter
#1	Bete Fog NF-6000	4.83 mm
#2	Bete Fog NF-8000	5.56 mm
#3	Bete Fog NF-10000	6.07 mm
#4	S.S. Co. QU-00120	6.56 mm
#5	S.S. Co. QU-00200	8.45 mm
#6	Sharp Edge	6.36 mm

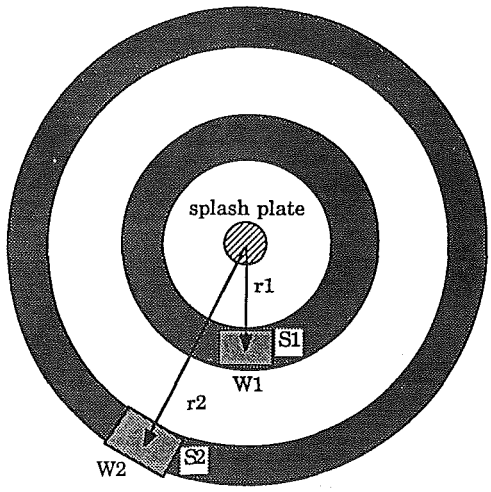

Fig. 2 Representative imaging areas for the perforation count experiments

and downstream location. The perforations observed in these images were counted, and the size and scale of the images were recorded.

The imaging area was independent of the downstream location; thus, the fraction of the total circumferential area of the spray observed varied with the radial position. Therefore, to provide a uniform basis for comparison, the observed perforation counts were normalized. The area corrected perforation count, $(Np)_{area}$, was obtained by first multiplying the number of perforations observed, $(Np)_{obs}$, by the ratio of the circumference of the spray sheet at the imaging position, r, to the width of the imaging area, W. This value was then divided by the radial span of the imaging area, S, to obtain

$$(Np)_{area} = (Np)_{obs} \times \left(\frac{2\pi r}{WS}\right), \quad (1)$$

where:

r = radial position of the center of the imaging area [m];
$(Np)_{obs}$ = number of perforations observed at downstream position, x;
$(Np)_{area}$ = area corrected number of perforations per centimeter of radial span;
W = lateral width of the imaging area [m]; and
S = radial span of the imaging area [cm].

The width and span are defined in Fig. 2 for two representative locations.

In order to estimate the number of new perforations formed in a given range of downstream positions, the area corrected perforation count at each location was modified to exclude the perforations accounted for at positions upstream of that location. Thus, if the sheet is imaged at some number of radial positions, M, then the number of perforations reported for the mth position (where $2 \le m \le M$) is given by

Table 2 Operating conditions for the perforation number density experiments

Nozzle	Number of trials	Number of locations	Range of locations (cm)	Range of jet velocities (m/s)
#1	22	5	13–21	15–20
#2	38	7	8–21	12.5–22.5
#3	16	3	10–20	12.5–22.5

$$(Np)_{\text{rep},m} = (Np)_{\text{area},m} - \sum_{j-1}^{m-1} (Np)_{\text{rep},m} \quad (m \geq 2). \tag{2}$$

The reported number of perforations is equal to the area corrected number of perforations for the first radial location; therefore, for $m = 1$,

$$(Np)_{\text{rep},1} = (Np)_{\text{area},1}. \tag{3}$$

In the discussion that follows, the term "perforation count" refers to $(Np)_{\text{rep},m}$.

For each perforation count experiment, the number of holes observed was counted for ten sets of 100 images. An estimate for the error in the reported number of perforations per 1000 images can be obtained from the standard deviation in the number of perforations observed in these sets of 100 images. Based on these data, the uncertainty at the 95 percent confidence level was calculated.

When the number of observed perforations was small (less than 10 holes/1000 images) the uncertainty limits were large and include zero perforations in their range. Excluding these trials, the average uncertainty in the observed perforations per 1000 images is $+/-25$ percent.

The range of operating conditions investigated is given in Table 2. The radial perforation distribution as a function of the jet velocity is shown for two nozzle orifice diameters in Figs. 3 and 4. As can be seen in these plots, only a small percentage of the total number of perforations observed occurred in the region near the splash plate ($r < 16$ cm). This relatively undisturbed portion of the spray was followed by a narrow band of downstream positions in which a rapid increase in the number of observed perforations was recorded. The downstream location at which this transition occurred varied with the orifice diameter and the jet velocity. In general, for a fixed orifice diameter, the downstream position at which a large increase in the number of perforation occurred decreased with increasing jet velocity.

The relation for the sheet thickness is given by (for derivation, see Watson, 1964)

$$H(r) = \left(\frac{2\pi^2}{3\sqrt{3}}\right)\left(\frac{\nu(r^3+\Gamma^3)}{Qr}\right), \tag{4}$$

where Q is the volumetric flow rate ($Q = \pi d_2^0 U_0/4$; ν is the kinematic viscosity; and Γ is a characteristic length scale which can be obtained from

$$\Gamma = 0.330 d_0 \text{Re}_{\text{jet}}^{1/3}, \tag{5}$$

as derived by Watson (1964). The numerical constant in this expression has been corrected for differences in the definitions for the length scale and the Reynolds number between this work and the original work by Watson. Here, the Reynolds number is defined as

$$\text{Re}_{\text{jet}} = \frac{\rho_{\text{liq}} d_0 U_0}{\mu_{\text{liq}}}, \tag{6}$$

where U_0 is the average jet velocity. After substituting the definitions for the Reynolds number, the volumetric flow rate, and the characteristic length scale, Eq. (4) can be made dimensionless by dividing through by the theoretical inviscid sheet thickness $H_{\text{inv}}(r) = d_0^2/8r$, thus obtaining

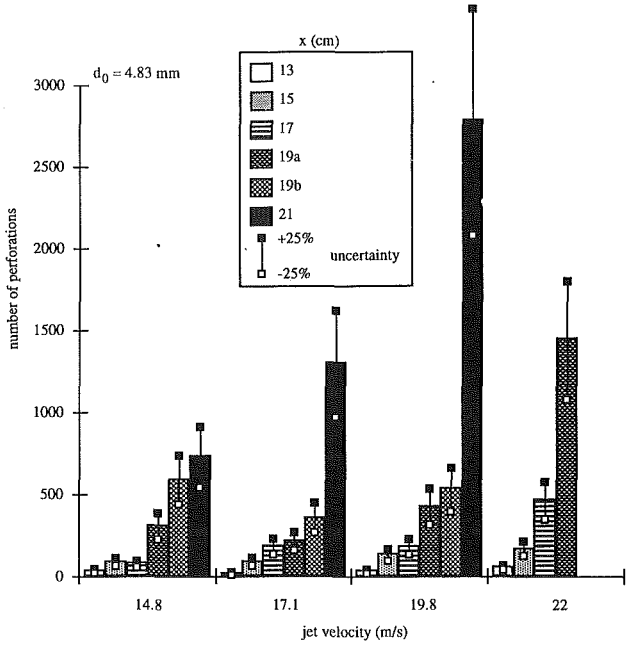

Fig. 3 Number of perforations reported for $d_0 = 4.83$ mm

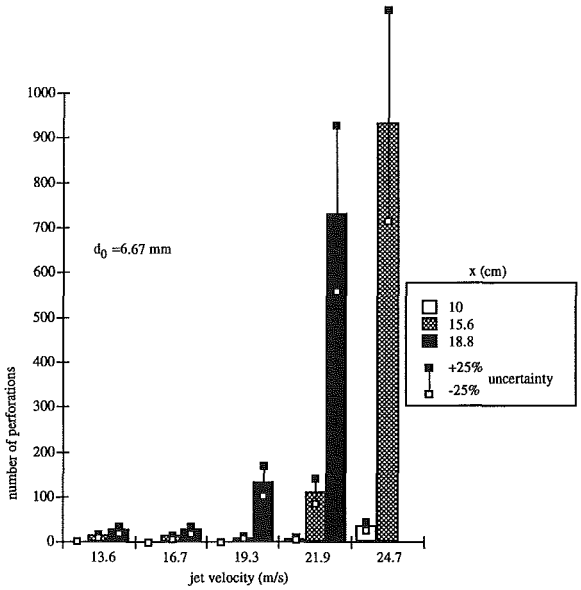

Fig. 4 Number of perforations reported for $d_0 = 6.67$ mm

$$\frac{H(r)}{H_{\text{inv}}(r)} = 1.39 + \frac{38.7}{\text{Re}_{\text{jet}}}\left(\frac{r}{d_0}\right)^3. \tag{7}$$

The sheet thickness ratios predicted with this equation were compared to experimental values obtained for the splash plate nozzle used in this study. The sheet thickness was measured using three mechanical probes spaced 120 deg apart, all located 2.14 ± 0.04 cm downstream from the center of jet impact on the plate. The vertical position of each probe was adjusted with a micrometer until the tip just contacted the top surface of the spreading liquid. The thickness of the sheet was taken as the difference between this position and the reference location of the top surface of the plate. A summary of the range of operating conditions investigated is given in Table 3.

The sheet thicknesses measured by each of the three probes were used to calculate an average sheet thickness and the standard deviation of the probe measurements. The normalized

Table 3 Range of operating conditions investigated in the sheet thickness studies

Nozzle style	d_0 (mm)	Number of trials	Velocity (m/s)	Viscosity (cp)	Density (kg/m^3)	Reynolds number
#1	4.66	18	8.6–24.9	69–85	1220	900–3200
#6	6.36	21	5.9–17.2	51–67	1210	1300–4400
#4	6.56	14	5.6–18.3	79–102	1220	700–2500
#5	8.45	17	3.0–12.6	85–96	1220	500–2400

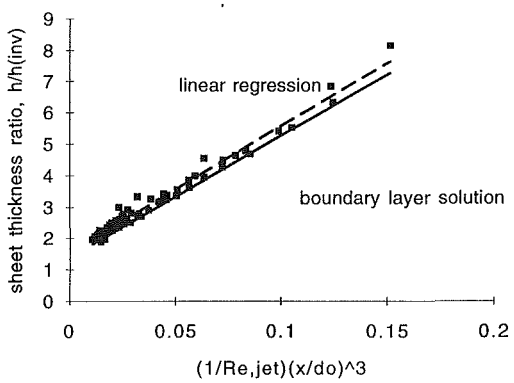

Fig. 5 Dimensionless sheet thickness correlation

standard deviation (the standard deviation divided by the average sheet thickness) varied from one to 20 percent, with an average value of six percent.

The average thicknesses were made dimensionless with respect to the inviscid sheet thickness and plotted versus $(1/\mathrm{Re}_{\mathrm{jet}})\,(r/d_0)^3$, as shown in Fig. 5. Equation (7) is shown as a solid line, while the best fit linear regression is shown as a dashed line. The slope of the regression line (40 ± 1) agrees with the predicted value within the 95 percent confidence intervals. The experimental intercept (1.55 ± 0.08) is greater than predicted; thus, the thickness of the sheet is underpredicted by an average of 7 percent in all cases. This may be a result of neglecting momentum losses which occur in the region of jet impact.

Downstream Sheet Thickness. Once the liquid leaves the plate to form a free, radially thinning sheet, viscous forces will no longer decrease its velocity, and the sheet velocity is assumed to be equal to the average sheet velocity at the plate edge. Thus, if the thickness of the sheet at the plate edge is known, and if the sheet is assumed to be axisymmetric, then the downstream thickness of the sheet can be calculated from a simple mass balance given by

$$2\pi r_p H(r_p)\, U_{\mathrm{avg}}(r_p)\rho_{\mathrm{liq}} = 2\pi r H(r)\, U_{\mathrm{avg}}(r_p)\rho_{\mathrm{liq}}, \qquad (8)$$

where the subscript p denotes the value of a parameter at the edge of the plate. Upon arrangement the downstream sheet thickness can be written as

$$H(r) = \frac{r_p H(r_p)}{r}, \quad \text{for} \quad r > r_p. \qquad (9)$$

The operating conditions for each perforation count experiment were used in conjunction with Eq. (7) to calculate the sheet thickness at the edge of the splash plate (r_p = 2.50 cm). Equation 9 was then used to calculate the thickness of the sheet at the center of each imaging area.

The perforations counts, previously plotted versus the distance downstream and jet velocity, are now replotted versus the calculated downstream sheet thickness, as shown in Fig. 6. Six additional experiments were performed in which the perforations were too numerous to count. Many of the images collected during these trials showed clumps, strands, and drops

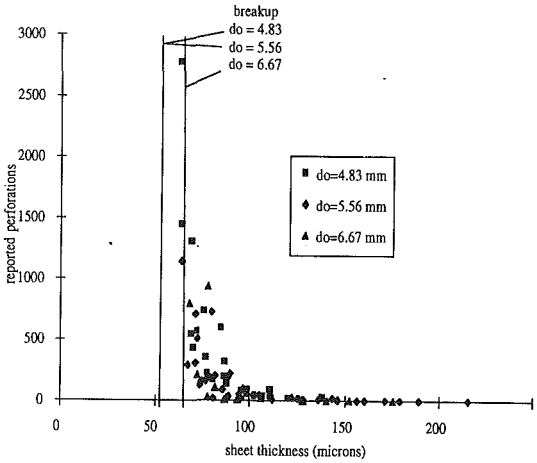

Fig. 6 Number of perforations versus the predicted downstream thickness

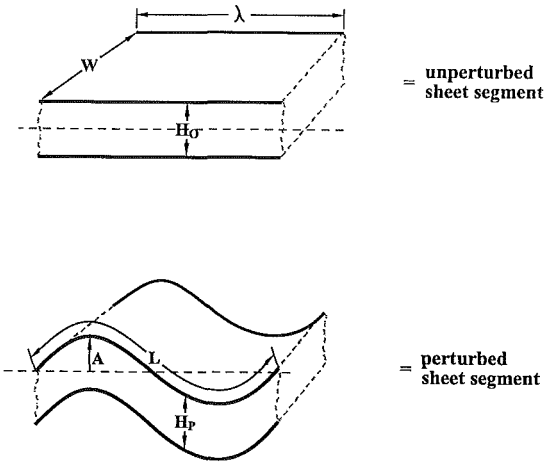

Fig. 7 A planar and a perturbed liquid sheet

of liquid. The range of sheet thicknesses calculated for these six trials is labeled the breakup region in Fig. 6.

The number of perforations formed per centimeter of radial span appears to increase rapidly when the sheet thickness is reduced to about 70 microns. The breakup of the sheet into the clumps and strands which precede drop formation is completed before the calculated sheet thickness is reduced below 50–60 microns.

Wave-Thinning. The downstream sheet thickness values estimated in the preceding section were based on an undisturbed, radially thinning sheet; however, previous investigators (Dombrowski and Fraser, 1954; Fraser et al., 1962) have shown that sinuous waves will be present. Such waves were observed in this study as well. A sinuous wave will stretch the sheet and decrease its thickness relative to an undisturbed sheet. In the following section, we will estimate the magnitude of this wave-thinning as a function of the amplitude and wavelength.

A planar and sinuously perturbed sheet segment is sketched in Fig. 7. This section of the sheet is one wavelength, long, has a uniform thickness, H_0, and an arbitrary span, W. The mass contained in this unperturbed segment, m_u, is then

$$m_u = H_0 W \lambda \rho_{\mathrm{liq}}. \qquad (10)$$

If the axially symmetric sheet is assumed to thin uniformly over one wavelength, the mass contained in the perturbed segment, m_p, will be

$$m_p = H_p W L \rho_{\mathrm{liq}}. \qquad (11)$$

In Eq. (11) L is the length of sinuously perturbed sheet segment as measured along the surface of the sheet (see Fig. 7). These expressions can be set equal to each other and rearranged to obtain an expression for the thickness of a sheet perturbed by a sinuous wave, that is

$$H_p = H_0(\lambda/L). \tag{12}$$

If the sheet segment is assumed to be perturbed by a single sinuous wave of amplitude A and wavelength λ, then the length of the perturbed section will be given by

$$L = \frac{2\lambda(1+p^2)^{1/2}}{\pi} E(\pi/2, q), \tag{13}$$

where $p = 2\pi A/\lambda$, $q = (1+p^2/p)^{1/2}$, and $E(\pi/2, q)$ is the complete elliptic integral of the second kind.

Details for the derivation of Eq. (13) are given in Spielbauer (1992). Hagerty and Shea (1955) used linear stability analysis to develop an expression for the growth rate of sinuous waves in planar inviscid sheets. The general disturbance is decomposed into normal modes described by

$$A = A_0 e^{(st+ikz)}, \tag{14}$$

where s is the temporal growth rate, and k is the wavenumber. The growth rate of a disturbance with wavenumber k was reported to be

$$s_{\text{inv}} = \left(\frac{k^2 U_s^2 \gamma - k^2 \sigma/\rho_{\text{liq}}}{kH/2}\right)^{1/2}, \tag{15}$$

where γ is the density ratio ($\rho_{\text{gas}}/\rho_{\text{liq}}$), and σ is the surface tension. The assumption that $kH/2$ is small, such that $\tanh(kH/2) = kH/2$, was used in deriving this expression and applies to all the sheets formed in this study.

Weihs (1978) developed a similar expression for the growth rate of sinuous waves in a planar viscous sheet. His result is presented here as

$$s_{\text{vis}} = \frac{\nu}{2}\left(-k^2 + \left(\frac{8(\rho_{\text{gas}} U_s k - k^2\sigma)}{\rho_{\text{liq}}\nu^2 H/2}\right)\right)^{1/2}. \tag{16}$$

In this study, the viscous effects cannot be neglected (Spielbauer and Aidun, 1994) and therefore, the equations derived by Weihs (1978) are used to determine the growth rate and a wavelength of the optimum mode.

If the values of s and k are assumed to be real only, then the amplitude of the optimum wave (k_{opt}) at any position x can be determined from Eq. (14) by substituting $t = x/U_s$. Using results presented by Gaster (1962), Asare et al. (1981) showed that this transformation between a temporal growth rate and a spatial growth rate was valid, provided the wave speed was equal to the sheet velocity. Morris (1981) showed that these velocities were approximately equal, provided the density ratio ($\rho_{\text{gas}}/\rho_{\text{liq}}$) was much less than $\tanh(kH/2)$ and if $(kH/2)/\tanh(kH/2)$ is of order unity. Both these conditions were met for all experiments performed in this study; thus, the transformation to a spatial growth rate was used.

Using the wavelength and growth rate for the optimum disturbance in a viscous sheet, and an assumed initial disturbance amplitude of 1 micron, the downstream thickness could be calculated for each of the perforation count experiments. These sheet thicknesses are plotted in Figs. 8 and 9. As can be seen, there is a gradual decrease in the sheet thickness as it spreads out from the plate. This is due to the radial thinning of the sheet, as the wave amplitudes are so small they do not significantly affect the sheet thickness. At some critical distance downstream, a rapid decrease in the sheet thickness is predicted. In this region, the sinuous wave amplitude is large enough such that the sheet thickness is significantly reduced relative to a planar sheet. The downstream location of rapid thinning decreases with increasing jet velocity and jet diameter.

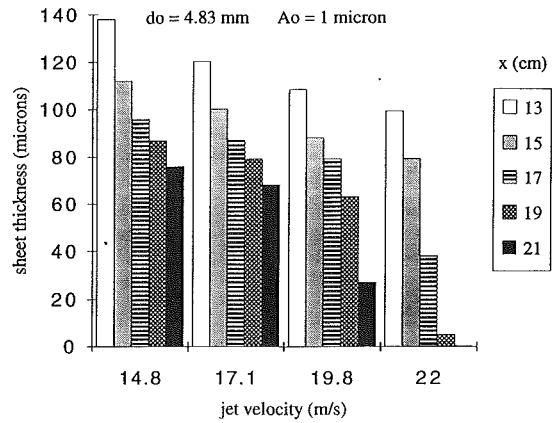

Fig. 8 Calculated wave-thinned sheet thickness for $d_0 = 4.83$ mm

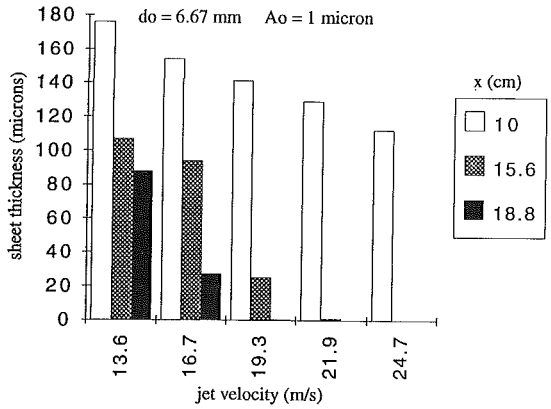

Fig. 9 Calculated wave-thinned sheet thickness for $d_0 = 6.67$ mm

Comparing the behavior seen in the perforation count experiments and the sheet thickness predictions, there appears to be good qualitative agreement. However, quantitative comparisons can not be made as the initial disturbance is unknown, and thus, the location downstream at which the rapid wave-thinning occurs cannot be predicted. Clark and Dombrowski (1972) point out the effect of the flow characteristics in the nozzle on sheet breakup. Specifically, they show that when the nozzle Reynolds number is above 9000, ripples form and propagate resulting in a more rapid sheet breakup. This is consistent with the wave thinning effect that we discuss here. Our experiments show that the distance from rapid thinning and breakup region to the nozzle decreases as the nozzle Reynolds number increases.

An indirect method was used to measure the downstream thickness of a sheet thinned by sinuous waves. Fraser et al. (1962) showed that the growth rate of a hole in a liquid sheet is inversely proportional to the square root of the sheet thickness. High-speed 16 mm films of expanding perforations were used to measure these growth rates. The perforation diameter was measured both radially (in the direction of flow) and laterally (perpendicular to the direction of flow). The lateral growth rates were corrected to account for the stretching of a perforation which occurs due to the radial expansion of the sheet. This correction was less than 5 percent in all cases.

The lateral diameter was found to increase linearly with time, as predicted by Fraser et al. (1962). The radial diameter increased linearly in the early stages of growth, but the growth rate then appeared to decrease. The behavior is related to the optical distortion of the perforations which results from obtaining a two-dimensional image of a three-dimensional structure. That is, as the perforation grows in the downstream direction, it will follow the sinuous shape of the sheet. Any

Table 4 A summary of the sheet thicknesses calculated from perforation growth rate data

Trial	U_0 (m/s)	μ_{liq} (kg/ms)	Position (cm)	$2h^{(a)}$ (μm)	Perforations measured	Range of $2h^{(b)}$(μm)	Average $2h^{(b)}$(μm)
1	15.3±0.5	0.060±0.002	16	45	4	4–20	8
2	15.5±0.5	0.056±0.002	20	35	4	2–6	3
3	16.1±0.5	0.128±0.002	39	50	6	9–40	20
4	17.7±0.6	0.126±0.002	39	50	17	8–30	14
5	19.1±0.6	0.123±0.002	39	48	8	6–23	13

(*a*) predicted sheet thickness based on radial expansion alone
(*b*) sheet thickness calculated from perforation growth rate data

motion perpendicular to the imaging plane (parallel to the centerline of the sheet) will not be visible in the images. Due to this image distortion, the lateral perforation growth rates were used to calculate the downstream wave-thinned sheet thickness.

In all cases, there is a significant reduction in the thickness caused by the sinuous distortion of the sheet, as shown in Table 4.

The uncertainty in the sheet thicknesses calculated from the perforation growth rate data was approximately 18 percent.

Discussion

The formation and disintegration of a radially thinning liquid sheet formed by a splash plate nozzle was investigated. Based upon the high-speed video and 16 mm images obtained, the experimental sheet thickness and perforation count data collected, and the results of the additional analytical investigations, the following description of the breakup process was developed.

The sheet is formed by the perpendicular impingement of a circular jet on a flat plate. This sheet thins due to both the radial expansion of the sheet and the growth of sinuous waves resulting from the hydrodynamic instability of disturbances. As the fluid spreads out radially, viscous shear at the plate surface slows the sheet and increases its thickness relative to an inviscid sheet. This increase in the relative sheet thickness is proportional to $1/\mathrm{Re}_{jet}\ (x/d_0)^3$; thus, for fixed fluid properties, the relative sheet thickness at the plate edge will increase with a decrease in the jet velocity or nozzle diameter. Because the inviscid sheet thickness is proportional to d_0^2, the sheet thickness may decrease with a decrease in the orifice diameter, even though the ratio of the viscous to inviscid sheet thickness increases.

As the liquid releases from the edge of the plate, a radially thinning free sheet is formed. In this free sheet, shear forces will no longer be significant, and the velocity of the sheet is related to an average velocity of the sheet at the edge of the plate. As the sheet travels downstream, it continues to thin due to the geometric expansion of the liquid. This thinning is enhanced by instability and growth of waves.

In this study, sinuous waves were predicted to result in breakup before dilational waves. Based on linear theory, the optimally growing sine wave in an inviscid sheet is independent of the sheet thickness; however, in a viscous sheet, the wavelength increases with an increase in either the sheet thickness or the liquid viscosity. Using a growth rate expression available in the literature, a cubic equation was derived (Spielbauer, 1992 and Spielbauer and Aidun, 1994) which relates the wave number of optimum growth in a viscous sheet to the wave number of optimum growth in an inviscid sheet. This ratio was found to be a function of a single dimensionless parameter, Ω. Examination of this equation showed that the rate of increase in the wavelength of the optimum sinuous wave with the liquid viscosity is a function of the gas and liquid phase densities, the surface tension, the sheet thickness, and the sheet velocity.

The viscous dispersion equations were used to predict the wave-thinned downstream thickness of the sheet. When the amplitude of the wave was small, the presence of the disturbance did not enhance the radial thinning of the sheet appreciably; however, as the wave grew, the sheet thickness decreased significantly over a narrow range of downstream position. The downstream position of this rapid decrease in sheet thickness is predicted to decrease with increasing jet velocity and nozzle orifice diameter. As the waves grow downstream, aerodynamic interaction with vortices generated in the surrounding air, as shown by Crapper et al. (1975a,b), results in nonlinear effects. The linear analysis will no longer be valid.

The radially thinning free sheet was imaged using a high shutter speed video camera. These images were used to count the number of perforations formed in the sheet as a function of the nozzle orifice diameter, the jet velocity, and the radial position downstream. The number of perforations formed was found to increase rapidly at a critical position downstream which varied with the orifice diameter and jet velocity.

The predicted effects of the jet velocity and orifice diameter on the sheet thickness correspond qualitatively to their observed effects on the number of perforations formed. It was concluded that the combination of the radial and wave thinning reduces the sheet thickness to a critical value, at which point rupture occurs.

The fluid contained in a thin liquid film possessed different thermodynamic properties that does the same fluid in a bulk phase (Sheludko, 1967). Short range forces such as electric double layer interaction and London dispersion forces affect the stability of such films.

Patzer and Homsey (1975), performed a theoretical analysis on the stability of spherically concentric, draining, fluid sheets. They predicted a critical film thickness for rupture on the order of one micron. This value is expected to be an upper bound, as the stabilizing effects of electric double layer repulsion were neglected.

Pandit and Davidson (1990), studied the rupture of thin, draining spherical films experimentally. They found a critical rupture thickness of 0.05–0.09 microns. High ionic strength salts were added to the liquids in sufficient concentration to suppress the effects of the electric double layer; thus, these values may be considered an upper bound for the spontaneous rupture thickness, as well.

Images obtained with a high-speed 16 mm camera were used to measure the growth rates of perforations in the sheet. These growth rates were used to calculate the thickness of the sheet. The calculated thicknesses are normally above 50 microns and, therefore, significantly less than the thickness predicted in the absence of waves. This provides support for a wave-thinning induced sheet rupture mechanism; however, the measured thickness was still one to two orders of magnitude larger than the maximum sheet thickness predicted for spontaneous rupture; thus, other mechanisms of rupture may be important.

The formation of perforations has been attributed to a number of causes. Point disturbances were observed by Dom-

browski and Fraser[1] (1954). These disturbances were shown to have originated at the nozzle orifice and were believed to be the result of turbulence. However, spontaneous rupture was ruled out as the source of perforations.

A perfectly axisymmetric radially expanding sheet with no external disturbances would eventually break into circular axisymmetric ligaments. However, as first discussed by Clark and Dombrowski (1972), flow characteristics in the nozzle upstream of the sheet and other disturbances generate locally thin regions which may rupture spontaneously if the thickness is reduced below a critical value. This diminishes the breakup length of the sheet. They show that at Reynolds number (based upon the hydraulic mean diameter of the orifice) above 9000, ripples form and propagate, markedly reducing the length of the sheet.

Other mechanisms include particle impingement (Fraser et al., 1962), wave interaction (Clark and Dombrowski, 1971), dissolved air, suspended particles (Dombrowski and Fraser, 1954), and small air bubbles. These mechanisms and their relative importance are described elsewhere (Spielbauer and Aidun, 1994) and will not be repeated here.

References

Asare, H. R., Takahashi, R., and Hoffman, M. A., 1981, "Liquid Sheet Jet Experiments: Comparison with Linear Theory," ASME JOURNAL OF FLUIDS ENGINEERING, Vol. 103, Dec., pp. 595–604.

Clark, C. J., and Dombrowski, N., 1971, "The Dynamics of the Rim of a Fan Spray Sheet," *Chemical Engineering Science*, Vol. 26, pp. 1949–1952.

Clark, C. J., and Dombrowski, N., 1972, "Aerodynamic Instability and Disintegration of Inviscid Liquid Sheets," *Proceedings of the Royal Society of London*, Series A, Vol. 329, pp. 467–478.

Crapper, G. D., Dombrowski, N., and Jepson, W. P., 1975a, "Large Amplitude Kelvin-Helmholtg Waves on Thin Liquid Sheets," *Proceedings of the Royal Society of London*, Series A, Vol. 342, pp. 209–224.

Crapper, G. D., Dombrowski, N., and Jepson, W. P., 1975b, "Wave Growth on Thin Sheets of non-Newtonian Liquids," *Proceedings of the Royal Society of London*, Series A, Vol. 342, pp. 225–236.

Dombrowski, N. and Fraser, R. P., 1954, "A Photographic Investigation into the Disintegration of Liquid Sheets," *Philosophical Transactions of the Royal Society of London*, Vol. 247A, Sept., pp. 101–130.

Dombrowski, N., and Johns, W. R., 1963, "The Aerodynamic Instability and Disintegration of Viscous Liquid Sheets," *Chemical Engineering Science*, Vol. 18, pp. 203–213.

Fraser, R. P., Eisenklam, P., Dombrowski, N., and Hasson, D., 1962, "Drop Formation from Rapidly Moving Liquid Sheets," *American Institute of Chemical Engineers Journal*, Vol. 8(5), Nov., pp. 672–680.

Gaster, M., 1962, "A Note on the Relation between Temporally-Increasing and Spatially-Increasing Disturbances in Hydrodynamic Instability," *Journal of Fluid Mechanics*, Vol. 14, pp. 222–224.

Hagerty, W. W., and Shea, J. F., 1955, "A Study of the Stability of Plane Fluid Sheets," ASME *Journal of Applied Mechanics*, Vol. 22, Dec., pp. 509–514.

Morris, P. J., A note appended to Asare et al. (1981).

Pandit, A. B., and Davidson, J. F., 1990, "Hydrodynamics of the Rupture of Thin Liquid Films," *Journal of Fluid Mechanics*, Vol. 212 pp. 11–24.

Patzer, J. F., and Homsey, G. M., 1975, "Hydrodynamic Stability of Thin Spherically Concentric Fluid Shells," *Journal of Colloid and Interface Science*, Vol. 51(3), June, pp. 499–508.

Sheludko, A., 1967, "Thin Liquid Films," *Advances in Colloid and Interface Science*, Elsevier Publishing Company, Amsterdam, Vol. 1, pp. 391–464.

Spielbauer, T., 1992, "The Stability and Disintegration of Radially Thinning Liquid Sheets," Ph.D. thesis, Institute of Paper Science and Technology, Atlanta, GA., June.

Spielbauer, T., and Aidun, C. K., 1994, "The Cause and Origin of Perforations in a Radially Thinning Liquid Sheet," *Journal of Liquid Atomization and Spray*, Vol. 4, pp. 405–436.

Taylor, G. I., 1959, "The Dynamics of Thin Sheets of Fluid: Part I. Water Bells," *Proceedings of the Royal Society of London*, Series A, Vol. 253, pp. 289–295.

Watson, E. J., 1964, "The Radial Spread of a Liquid Jet over a Horizontal Plane," *Journal of Fluid Mechanics*, Vol. 20 (Part 3), pp. 481–499.

Weihs, D., "Stability of Thin, Radially Moving Liquid Sheets," *Journal of Fluids Mechanics*, Vol. 7, Part 2, pp. 289–298.

[1]They reported an assumed critical sheet thickness of 10^{-7} m based on work by Fisher (1948), while the minimum sheet thickness they obtained was reported to be 10^{-4} m. These values for sheet thickness appear to be excessively small. It seems likely that a typographical error occurred as values of 10^{-7} cm (10^{-3} m) and 10^{-4} cm (1 m) are consistent with other data presented in the article. For instance, Dombrowski and Fraser report that sheet thickness in microns is approximately equal to 14 divided by the distance downstream in centimeters. If the reported minimum observed sheet thickness value of 10^{-4} m is correct, the corresponding downstream distance would be 1.4×10^5 cm. If, however, the value 10^{-4} cm is used, the corresponding downstream distance would be 14 cm.

Donald F. Elger
Associate Professor,
Mechanical Engineering.

Sam. J. Taylor
Graduate Student,
Mechanical Engineering.

Chyr P. Liou
Associate Professor,
Civil Engineering.

University of Idaho,
Moscow, ID, 83844

Recirculation in an Annular-Type Jet Pump

For some annular-type jet pump applications, it is important to avoid formation of a recirculation zone in the mixing region. The goals of this research were to find (i) when recirculation occurs and (ii) the size and location of the resulting recirculation zone. Experiments were performed using air in a straight-walled, annular-type, ducted jet. Area ratio A_j/A_s varied from 0.39 to 0.89; here, A is flow area, and j and s identify the jet and secondary flows, respectively. Data showed that recirculation correlates with J, where $J \approx P_j/(P_j + P_s)$, and P is rate of momentum. For the area ratios studied, recirculation begins when J exceeds a value ranging from 0.89 to 0.94. This paper also presents data showing the recirculation zone boundaries and presents a discussion of jet pump design.

Introduction

Jet pumps have been used for many different applications, and the technical literature on jet pumps, which exceeds 400 articles, is reviewed by Blevins (1984) and by Bonnington et al. (1976). The most common jet pump, the center-type, uses a center jet to entrain an annular secondary flow. This research focuses on a less commonly used jet pump, the annular-type, which uses an annular jet to entrain a central secondary flow. Recent works on the annular-type jet pump include the study by Shimuzu et al. (1987) and the study by Enderlin et al. (1988).

An annular-type jet pump, because of its geometry (Fig. 1), is well suited for applications involving hydraulic transport of large solids. Examples of solids pumped include live fish, large cylindrical capsules used in pipelines to transport bulk materials, and food products such as whole potatoes and onions. When pumping delicate materials, such as potatoes or fish, minimizing the pumping damage to the solids is often the main design goal. While it might be expected that an annular-type pump would pump solids with little damage, observations from the authors' laboratory showed that this was not the case. As a large solid object passed through the mixing region, its motion was very chaotic—sometimes the object was vigorously rotated and flung about, sometimes the object actually paused for an instant, and at other times the object would strike the mixing region wall rather violently.

The erratic motion of objects is caused by the flow pattern in the mixing region. In particular, for certain operating conditions, a recirculation zone forms in the center of the mixing region, Fig. 2(*a*), and a solid must find a path around this zone. Hence, a study of recirculation was motivated.

Figures 2(*a*) illustrates the geometry of the study. This geometry can be labeled as an annular-type, confined, ducted jet; or as a straight, Annular-type Jet Pump (AJP). The aims

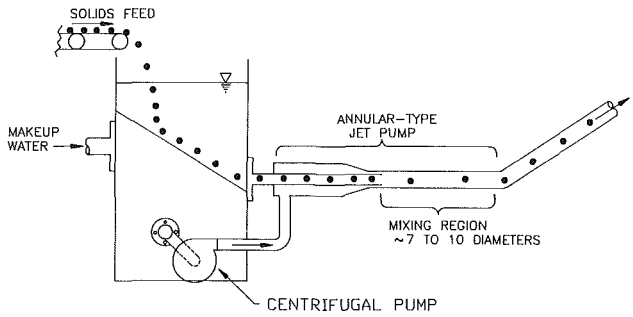

Fig. 1 An annular-type jet pump being used to pump large solids

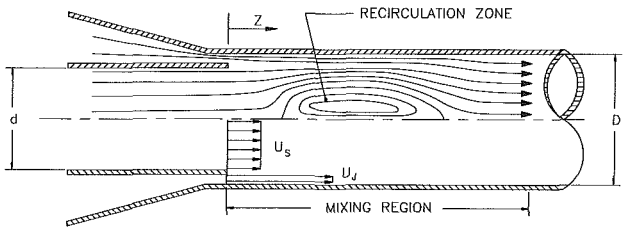

Fig. 2(*a*)

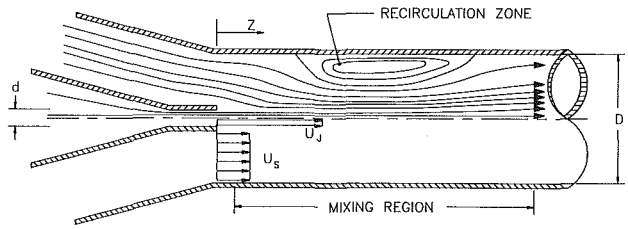

Fig. 2(*b*)

Fig. 2 The flow field in ducted jets: (*a*) annular-type, and (*b*) center-type. Each sketch shows streamlines in the top half and velocity profiles in the bottom half.

Contributed by the Fluids Engineering Division for publication in the JOURNAL OF FLUIDS ENGINEERING. Manuscript received by the Fluids Engineering Division March 16, 1992; revised manuscript received April 25, 1994. Associate Technical Editor: Wing-Fai Ng.

of this work are to quantify for an AJP (i) the onset of recirculation, and (ii) the size and location of the resulting recirculation region. Both the jet and secondary flows are assumed to be single phase, incompressible and to have the same density. Dimensions and operating conditions were selected, based on the authors' experience, to be typical of those used in application.

To the best of the authors' knowledge, this work is the first reporting of recirculation in an AJP. However, there have been several studies of recirculation in center-type, confined ducted jets (Hill, 1965; Curtet and Ricou, 1964; Barchilon and Curtet, 1964; and Exley and Brighton, 1971). Rajaratnam (1976) reviews these studies, and only the main results are described here.

Figures 2(*b*) shows a typical recirculation region in a center-type confined jet. The occurrence of recirculation can be explained using the concept of entrainment. As the jet flows through the mixing region, it expands in diameter due to entrainment of the secondary flow. Recirculation occurs when all of the secondary flow is entrained before the jet has expanded to reach the walls of the mixing region. Hence, the recirculation bubble can be visualized as a mechanism to provide the additional fluid needed for the jet to fully expand.

Hill (1965) showed that the presence of a recirculation region in a centertype confined jet correlates with d/D, and with a second group H which is given as

$$H=\frac{Q_m/D}{\sqrt{\pi W/(2\rho)}}, \tag{1}$$

where Q_m is the volume flow rate in the mixing region pipe,

$$W=\int_0^{D/2}[P_m'(r,z)+\rho u_m^2(r,z)]rdr, \tag{2}$$

and P_m' is the static pressure in the mixing region.

Before Hill's work, Craya and Ricou (1964) suggested that recirculation correlates with d/D and with C_t, a group which is now called the Craya-Curtet number. Similarly, Becker et al. (1962) suggested using d/D and a group m. However, Rajaratnam (1976) showed that approaches are equivalent because H, C_t, and m are related by

$$H=\frac{1}{\sqrt{1+2m}}=\frac{1}{\sqrt{1+2/C_t^2}}. \tag{3}$$

Rajaratnam (1976) summarizes the available data on the onset of recirculation. While there is moderate data scatter, it appears that when D/d is low, recirculation occurs when $H \leq \approx 0.6$, and when D/d is large, recirculation occurs when $H \leq \approx 0.46$.

Methods

Dimensional analysis was used to identify the parameters which quanify recirculation. The onset and nature of recirculation were studied experimentally.

Dimensional Analysis. Because the flow pattern in an AJP depends on six dimensional variables (u_j, u_s, d, D, μ, and ρ), data can be correlated with three dimensionless groups. One possible choice of these groups is the area ratio A_j/A_s, the Reynolds number ($\mathrm{Re} = u_m D\rho/\mu$), and a momentum ratio J which is conceptually given by

$$J\approx\frac{P_j}{P_j+P_s}, \tag{4}$$

where P_j, the rate at which momentum is carried into the mixing region by the jet, is given as

$$P_j=\int_{d/2}^{D/2}\rho u_j^2(r)\,2\pi r dr. \tag{5}$$

The term P_s is similarly defined as the rate of momentum carried by the secondary flow. For this project, all flows were assumed to be single-phase, and P_j and P_s were approximated using average velocities: $P_j \equiv \rho_j u_j^2 A_j$ and $P_s \equiv \rho_s u_s^2 A_s$. Because the jet and secondary flows were assumed to have the same density, J can be defined as

$$J\equiv\frac{u_j^2 A_j}{u_j^2 A_j+u_s^2 A_s}. \tag{6}$$

There are several reasons for defining J using average velocities. First, in an industrial environment, the pointwise data needed to evaluate a term like Eq. (5) is not likely to be available. Even in a research laboratory, making an accurate measurement is difficult because of the small dimensions of the jet, and because of large velocity gradients near walls. Second, plug-like velocity profiles likely occur in both the jet and the secondary flows. This is because the jet flow is usually near the end of a contraction and the secondary flow is typically turbulent and fully developed or nearly so. Hence, the average velocity approximation will likely give a good estimate of the integral term. Third, it is very unusual to use an integral term to define a dimensionless group.

The dimensional analysis presented here differs somewhat from that used by researchers studying center-type jets. They used two groups (H and D/d), while three groups were used here because of the inclusion of viscosity. For several reasons, J was selected rather that H. As previously discussed, an integral term is difficult to measure accurately. In addition, note that Eq. (2) requires measurement of pointwise pressure because the radial pressure distribution in an AJP is nonuniform (Elger, et al., 1991). Another reason for not using H is that this group is based on a concept that doesn't apply very well to an AJP. This concept is that a submerged jet (i.e., a jet discharging into a quiescent reservoir of the same fluid) and

Nomenclature

A_j = jet flow area = $(\pi/4)(D^2-(d+2t)^2)$ (m^2)
A_s = secondary flow area = $(\pi/4)d^2$ (m^2)
B = bias limit
d = inside diameter of the secondary pipe (m)
D = inside diameter of the mixing region pipe (m)
H = Hill number; defined by Eq. (3) (dimensionless)
J = momentum ratio; defined by Eq. (6) (dimensionless)
J_c = the momentum ratio at which recirculation begins (dimensionless)
P = precision limit
P' = static pressure (Pa)
Re = Reynolds number as defined by $\mathrm{Re} = u_m D\rho/\mu$ (dimensionless)
Q = volume flow rate (m^3/s)
r = radial position (m)
t = wall thickness of the secondary flow pipe
u = average axial velocity = Q/A (m/s)
U = total uncertainty
z = axial position measured from the mixing region inlet (m)
z_0 = axial location at which recirculation begins (m)
μ = viscosity (kg/m-s)
ρ = density (kg/m^3)

Subscripts

j = jet pipe
m = mixing region pipe
s = secondary pipe

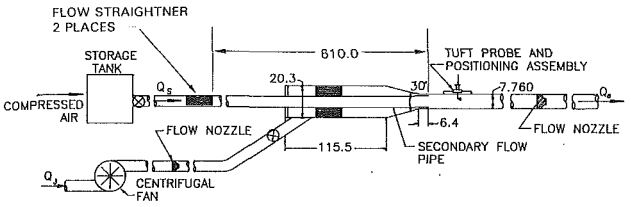

Fig. 3 The experimental apparatus

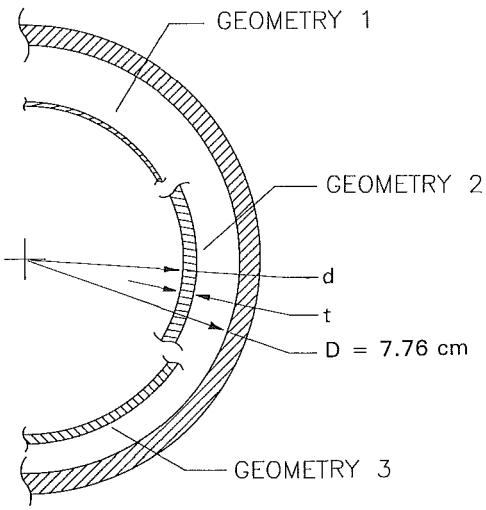

Fig. 4(*a*)

Geometry	Secondary pipe* inside diameter d (cm)	Secondary pipe* outside diameter d + 2t (cm)	A_j/A_s**
1	5.563	5.715	0.890
2	5.715	6.198	0.668
3	6.350	6.680	0.387

*Uncertainties in dimensions: P = ± 0.014 cm, B = ± 0.003 cm, U = ± 0.015 cm
**Uncertainties in A_j/A_s: P = ± 0.010, B = ± 0.002, U = ± 0.010

Fig. 4(*b*)

Fig. 4 The three geometries which were tested: (*a*) section view at the mixing region inlet, and (*b*) dimensions

a ducted center-type jet are similar with respect to axial momentum transport: A submerged jet has constant axial momentum with axial location, and a ducted center-type jet, if wall shear stress is ignored, has a constant pressure plus axial momentum integral with axial location (i.e., W given by Eq. (2) is constant with axial location). However, this similarity is much weaker for an AJP because wall friction cannot be neglected. In summary, it did not seem wise to use H for correlating data for an AJP, and no attempts were made to either use H or to compare J and H.

Experimental Methods. Figure 3 illustrates the experimental apparatus. Air was used, and flow rates were controlled using valves in the secondary and jet pipes. Conditioning of the jet and secondary flows was provided by flow straighteners and by straight runs of pipe. The secondary flow pipe length varied from 96 to 110 diameters. The relevant jet pipe length (6.4 cm in Fig. 3) varied from 3.1 to 5.9 hydraulic diameters (the relevant hydraulic diameter is twice the dimension of the gap between the secondary and jet flow pipes).

To study the effects of geometry, three secondary flow pipes were used, Fig. 4. These geometries were selected based on the following considerations. An AJP with an area ratio much larger than geometry 1 will tend to use an excessive amount of fluid in the jet. Also, when such a geometry is used to pump a liquid, it will be the most prone to limiting cavitation. Geometries 2 and 3 are typical of jet pumps used in application. Note that a jet pump with a smaller area ratio is sometimes used; for example, Shimuzu et al. (1987) report data for an AJP with $A_j/A_s = 0.19$. As shown in Fig. 4, the wall thickness is not constant. While constant wall thickness is desirable, hardware availability and design considerations precluded this.

To detect the onset of recirculation, a small tufted probe was used. It was comprised of a 0.32-cm-diameter rod with five 1.91-cm-long nylon threads attached. The probe was inserted into the mixing region through a long rectangular access slot machined in the mixing region wall. To facilitate positioning of the probe, while providing a leak free seal, the access slot was covered with a seal made of foam, rubber and PVC.

To record data giving the onset of recirculation, the experimental apparatus was operated at a fixed jet velocity, and the secondary velocity was adjusted so that no recirculation was occurring. Next, the secondary velocity was reduced by a small amount, and after approximately 75 s, the small probe was moved throughout the mixing region in order to check recirculation, with recirculation indicated if the threads on the probe were all pointing upstream. If recirculation was not indicated, then the secondary velocity was again reduced and the process was repeated.

After a recirculation zone formed, the boundaries were mapped using a large tufted probe. The large probe was comprised of 10 nylon threads, each 1.9-cm-long, attached to the eye of a needle. The needle was held parallel to the flow using a 0.56-cm-diameter rod. The boundary of the recirculation region was identified as the location where some of the probe threads were pointing upstream and some were pointing downstream, a situation which is pictured in photographs presented in Taylor (1990). The first step in mapping the recirculation region was to locate the upstream and downstream ends. Next, the probe was moved inside the recirculation zone to an axial location on the center axis, just behind the upstream end of the recirculation region. To map the radial boundary at this point, the probe was moved radially outward until it was out of the recirculation region, and then slowly moved inward until a few of the threads pointed upstream. This process was then repeated for different axial locations.

During the boundary mapping process, the probe was positioned using a Velmex 3-axis positioning system, and location measurements were made using integrated vernier scales accurate to 0.05 mm.

Air volume flow rates were measured using short-radius flow nozzles at the positions shown in Fig. 3. Flow rate calculation and nozzle installation detail followed ASME standards (Bean, 1971). The differential pressure across each flow nozzle was measured with a temperature-compensated piezoresistive pressure transducer.

All pressure transducer outputs were collected and processed with a computerized data acquisition system comprised of a PC and a MetraByte DAS 16/16F data acqusition board. All analog voltages were digitized and then averaged to remove electronic and flow noise.

Uncertainty Analysis. For each data point reported, a precision limit P and a bias limit B were estimated. These limits were then combined to give an uncertainty U: $U \equiv (P^2 + B^2)^{1/2}$. The precision limit was found by using replicated measurements to estimate variance and then using Student's t distribution to find a 95 percent confidence interval. The bias limit was found by using the standard root-mean-squared formula to track error propagation through each appropriate equation.

Table 1 Raw data: oxial location and momentum ratio at the onset of recirculation; uncertainties for these data are presented in Table 2.

Geometry 1		
Re	z_o/D	J_c
45400	2.0	0.94
53300	1.9	0.94
54500	1.6-1.9	0.94
62900	1.9	0.94
67300	1.6-1.9	0.95
68800	1.9	0.94

Geometry 2		
Re	z_o/D	J_c
39400	1.9	0.93
49400	2.0	0.93
58600	2.0	0.92
64000	1.9	0.92
64200	1.9	0.92
69700	2.0	0.91
70100	2.0	0.91

Geometry 3		
Re	z_o/D	J_c
38300	2.0	0.89
48000	1.9-2.1	0.90
48900	2.2	0.89
49000	1.8-2.3	0.89
55700	2.1	0.89
63100	2.0	0.89
67300	1.8-2.0	0.89

Table 2 Averaged results: momentum ratio and oxial location at the onset of recirculation

	J_c				z_o/D			
	avg.	uncertainty			avg.	uncertainty		
		P	B	U		P	B	U
Geom. 1	0.94	± 0.0048	± 0.010	± 0.011	1.9	± 0.11	± 0.052	± 0.12
Geom. 2	0.92	± 0.0057	± 0.013	± 0.014	1.9	± 0.026	± 0.052	± 0.06
Geom. 3	0.89	± 0.0033	± 0.017	± 0.017	2.0	± 0.12	± 0.052	± 0.13

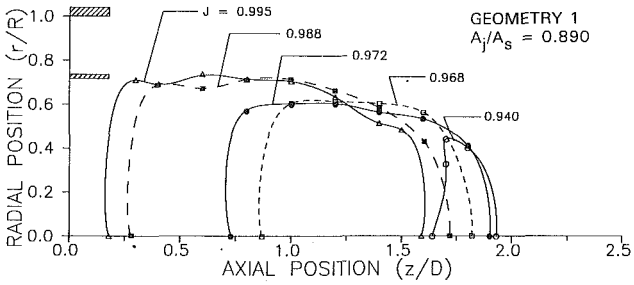

Fig. 5(*a*)

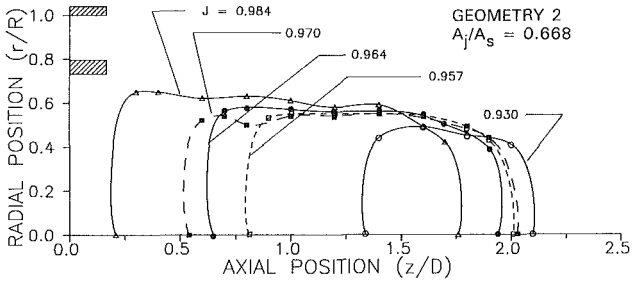

Fig. 5(*b*)

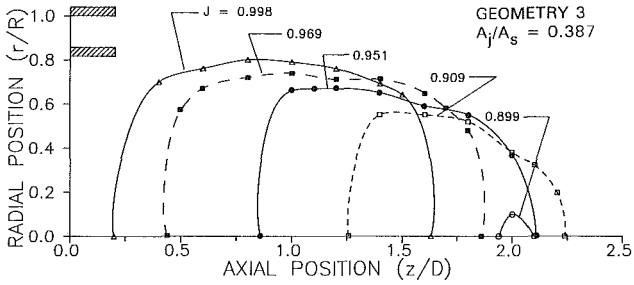

Fig. 5(*c*)

UNCERTAINTIES FOR THE FIGURES

VARIABLE	P	B	U
z/D	± 0.069	± 0.052	± 0.086
r/D	± 0.14	± 0.10	± 0.17
J	± 0.010	± 0.017	± 0.020

Fig. 5(*d*)

Fig. 5 Boundaries of the recirculation zone; data are shown with symbols and are connected by lines for clarity; the insets on the vertical axis show the pipe walls at the mixing region inlet

Results

This section gives (i) data describing the onset of recirculation, (ii) data giving the size and location of the recirculation zone, and (iii) a discussion of how the results might be applied to designing an annular-type jet pump.

The Onset of Recirculation. Table 1 lists the raw data describing the onset of recirculation. The critical momentum ratio J_c identifies the onset of recirculation: when $J \geq J_c$, a recirculation zone forms in the mixing region. The data show that, over the range of data taken, J_c is independent of Reynolds number. Hence, the Table 1 data were averaged and used to estimate the precision limit; Table 2 gives these results.

Tables 1 and 2 show that J_c varies with area ratio, and that the variation, while small, is significant compared to the precision error. When J_c is plotted as a function of area ratio, the result is a straight line which can be written as

$$J_c = (0.0974)A_j/A_s + (0.854) \tag{7}$$

Of course, Eq. (7) is based on only three data points, and more data would provide better proof that the relationship is linear. Recall that Eq. (7) is based on data for $0.39 \leq A_j/A_s \leq 0.89$.

Notice that for a given area ratio, the onset of recirculation occurs at a constant value of flow ratio (Q_s/Q_j). This is easily shown because the definition of J, Eq. (6), can be rewritten as

$$J = \frac{1}{1 + (Q_s/Q_j)^2(A_j/A_s)}. \tag{8}$$

Hence for geometry 1, values of $J_c = 0.94$ and $A_j/A_s = 0.89$ can be substituted into Eq. (8) to show that recirculation occurs when $Q_s/Q_j \leq 0.27$. Similarly for geometries 2 and 3, recirculation develops when $Q_s/Q_j \leq 0.36$ and $Q_s/Q_j \leq 0.56$, respectively.

Table 1 also shows the axial location z_o/D at which recirculation begins. When a single value of z_o/D is listed, the recirculation zone was very small, and the tufted probe indicated recirculation at a single point. When two values of z_o/D are listed, the recirculation zone appeared to form over a larger region. Since the z_o/D results also appear to be Reynolds number independent, they have been statistically processed, Table 2. In these calculations, when two values of z_o/D were listed in Table 1, both values were used. For the geometries studied, Table 2 shows that recirculation tends to begin about two diameters (D) downstream of the mixing region inlet.

The Size and Location of the Recirculation Zone. When an AJP is operated so that J exceeds J_c, a recirculation region will occur, with the region's size and location dependent on

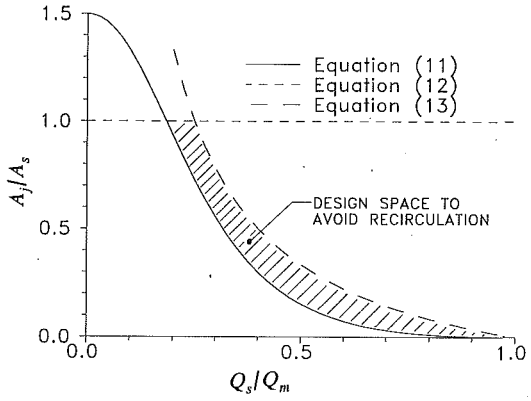

Fig. 6 The design space to avoid recirculation

J. Figure 5(*a*) shows the data from geometry 1. As *J* increases, the recirculation region becomes both longer and wider. Also, both the upstream and downstream endpoints of the recirculation region move upstream.

The recirculation region shape, for most values of *J*, is approximately that of a cylinder. However, note the appearance of the radial boundary (eg. see the boundary for $J = 0.988$ in Fig. 5(*a*)). This boundary, which slopes towards the centerline, provides an excellent visualization of how the jet expanded to fill the mixing region pipe. A similar trend is apparent for most of the shapes shown in Fig. 5.

Figures 5(*b*) and 5(*c*) show the recirculation region boundaries for geometries 2 and 3, respectively. Similar to geometry 1, these results show that the recirculation region is cylindrical in shape, and as *J* is increased, the region becomes longer and wider and tends to move upstream. Notice that the recirculation zone size is very sensitive to the value of *J*. Also, as *J* approaches its maximum value of $J = 1$, the recirculation zone expands to a diameter which approximately matches the inside diameter of the secondary flow pipe. Aside from this effect, the shape of the recirculation region is not strongly influenced by the value of the area ratio.

Applications to Design. This section presents a discussion of the design of an AJP which operates without forming a recirculation zone. The experimental data show that recirculation will not occur when

$$J < J_c. \tag{9}$$

Rewriting this equation by using *J* from Eq. (8) gives

$$\frac{1}{1+(Q_s/Q_j)^2(A_j/A_s)} < J_c. \tag{10}$$

Next, continuity (i.e., $Q_m = Q_j + Q_s$) was used to rewrite the left side of Eq. (10), and then the J_c correlation from this study (Eq. 7) was used to rewrite the right side, giving

$$\frac{1}{1+\left(\frac{Q_s/Q_m}{1-Q_s/Q_m}\right)^2\left(\frac{A_j}{A_s}\right)} < (0.0974)(A_j/A_s)+(0.854). \tag{11}$$

Equation (11) provides a design guideline, the results of which are shown graphically in Fig. 6. A recirculation zone will not form so long as a jet pump operates in the region to the right of the Eq. (11) line.

Several practical limitations prevent a jet pump from operating so Eq. (11) is satisfied. First, an AJP is usually not practical unless.

$$A_j/A_s < 1. \tag{12}$$

Second, the jet velocity u_j must exceed the secondary stream velocity u_s. Typically, u_j is 5 to 6 times larger than u_s. At a minimum

$$u_j \geq 3u_s. \tag{13}$$

The design space to avoid recirculation is shown on Fig. 6 by plotting Eqs. (11) through (13).

Figure 6 has several qualifications. First, Fig. 6 uses the curve fit for J_c (i.e, Eq. 7) for the range $0 \leq A_j/A_s \leq 1.5$, when it is based on data for $0.39 \leq A_j/A_s \leq 0.89$. Second, Eq. (13) is only an estimate. If one replaces Eq. (13) with, say $u_j/u_s \geq 5$, then the possible design space shrinks to almost nothing.

Despite the qualifications, Fig. 6 strongly suggests that an engineer will have difficulty designing a practical AJP to operate without recirculation. This idea is proposed because Fig. 6 shows that the possible design space, at best, is quite limited. Moreover, other design criteria, not shown on Fig. 6, will further shrink the design space. These criteria include matching the jet pump to other components in the system and designing to avoid limiting cavitation.

Probably the best way to avoid recirculation is to use a variable-area jet pump. One such concept is to design so the jet flow, as it enters the mixing region, is converging. Another concept is to use a converging/diverging mixing region pipe. Additional study is need on these concepts and on other possible concepts.

Conclusions

For suitable combinations of parameters, a recirculation zone will form in the mixing region of an annular-type jet pump. The onset and resulting size of the recirculation zone correlates with three parameters: jet pump geometry, Reynolds number and momentum ratio (*J*). To identify the influence of these parameters, experiments were performed in straight-geometry, annular-type jet pumps with flow areas spanning the range $0.39 \leq A_j/A_s \leq 0.89$.

For the range of parameters studied, the onset of recirculation depends primarily on momentum ratio, with a small dependence on A_j/A_s and no dependence on Reynolds number. Recirculation begins about two diameters (*D*) downstream of the mixing region inlet. Once formed, the recirculation zone usually has a cylindrical plug shape, whose size correlates strongly with momentum ratio (Fig. 5). As momentum ratio is increased, the recirculation zone moves upstream and becomes longer and wider.

The data on the onset of recirculation were used to study the design of an annular-type jet pump which is intended to operate without recirculation. This analysis showed that the possible design space is very limited. Hence, the straight-geometry, annular-type jet pump does not appear suitable for a design which will operate without recirculation.

Acknowledgments

This financial support of the J. R. Simplot Company, Food Division, is gratefully acknowledged. Thanks to Ed McLam, Don Mecham, and Rich Dinius for help with the experimental apparatus.

References

Barchilon, M., and Curtet, R., 1964, "Some Details of the Structure of an Axisymmetric Confined Jet With Backflow," ASME *Journal of Basic Engineering*, Vol. 86, pp. 777-787.

Bean, H. S., ed., 1971, *Fluid Meters, Their Theory and Application*, 6th Edition, ASME, New York, pp. 47-49.

Becker, H. A., Hottel, H. C., and Williams, G. C., 1962, "Mixing and Flow in Ducted Turbulent Jets," *Proc. 9th Int. Symp. Combustion*, pp. 7-20.

Blevins, Robert D., 1984, *Applied Fluid Dynamics Handbook*, Van Nostrand, New York, pp. 257-262.

Bonnington, S. T., and King, A. L., Hemmings, J. A. G., 1976, *Jet Pumps and Ejectors, A State of the Art Review and Bibliography*, 2nd Ed., Cranfield, Bedford, England, BHRA Fluid Engineering.

Curtet, R., and Ricou, F. P., 1964, "On the Tendency to Self-Preservation

in Axisymmetric Ducted Jets," ASME *Journal of Basic Engineering*, Vol. 86, pp. 765–776.

Elger, D. F., McLam, E. T., and Taylor, S. J., 1991, "A New Way to Represent Jet Pump Performance," ASME JOURNAL OF FLUIDS ENGINEERING, Vol. 113, pp. 439–444.

Enderlin, C., Gore, R., Lagrande, R., Steinbach, D., Crowe, C. T., Lee, J., Ushimara, K., Bernstein, S., 1988, "An Experimental Study of Performance and Erosion of an Annular Slurry Jet Pump," *Third International Symposium on Liquid Solid Flow*, ASME FED, Vol. 75, pp. 195–202.

Exley, J. T., and Brighton, J. A., 1971, "Flow Separation and Reattachment in Confined Jet Mixing," ASME *Journal of Basic Engineering*, Vol. 93, pp. 192–198.

Hill, P. G., 1965, "Turbulent Jets in Ducted Streams," *Journal of Fluid Mechanics*, Vol. 21, No. 1, pp. 161–186.

Rajaratnam, N., 1976, *Turbulent Jets*, Elsevier, New York, pp. 148–183.

Shimizu, Y., Nakamura, S., Kazuhara, S., and Kurata, S., 1987, "Studies of the Configuration and Performance of Annular Type Jet Pumps," ASME JOURNAL OF FLUIDS ENGINEERING, Vol. 109, pp. 205–212.

Taylor, S. J., 1990, "Flow Patterns in the Mixing Region of Straight Annular-Drive Jet Pumps," M.S. thesis, University of Idaho.

Development of Prototype Pump Using a Vibrating Pipe With a Valve

Hiroyuki Hashimoto
Tohoku University,
2-1-1 Katahira, Aobaku,
Sendai-shi, 980 Japan

Hirokuni Hiyama
Ebara Research Co., Ltd.,
4-2-1 Honfujisawa,
Fujisawa-shi, 251 Japan

Rokuro Sato
Tohoku University,
2-1-1 Katahira, Aobaku,
Sendai-shi, 980 Japan

Tests were conducted on a prototype pump which has an extremely simple structure and excellent controllability. Its structural and hydrodynamic features are different from those of previous conventional reciprocating pumps. The pump structure constitutes a leak-proof short vibrating pipe equipped with a nonreturn valve on the edge of its outlet. The authors developed a prototype pump which uses a 25 mm diameter vibration pipe and an electromagnetic excitation device. The pump performance, intentionally changed by adjusting the coil voltage or the coil current frequency, featured a maximum pressure of approximately 1.0 bars, a maximum flow rate of approximately 40 liters per minute, and a maximum efficiency of approximately 30 percent. Results of both a one-year test run, using water as the working medium, and a three-month durability test, using concentrated nitric acid as the working fluid, assuming application as a chemical pump, indicated favorable results.

Introduction

It is possible to raise liquid up a vertical pipe, i.e., a pipe whose lower end is submerged in a liquid and whose upper end is equipped with a spring-controlled non-return valve, by vibrating the pipe in the direction of its axis. After the rising liquid reaches the upper end of the pipe, it is discharged through the valve, thus constituting a pumping action. The discharge pressure and flow rate of the liquid could be controlled by regulating the excitation (vibratory) conditions. A pump featuring this pumping effect has many advantages, such as: simple design, easy maintenance, a good leak-proof feature, etc.

Although there has been much research done on vibratory flows in a pipe, no report features the pumping effects of a vibrating pipe such as mentioned above. The closest, would be a report on the pumping effect of a vibration nozzle equipped on the lower end of a pipe submerged in a liquid (Ганиев et al., 1987). Another would be a report on the pumping effect of a capillary tube using ultra high frequency vibration (Дежкунов et al., 1980). However, both of these cases are dissimilar to the present research on a new prototype pump, which is discussed in the following, in terms of configuration and flow mechanism. The prototype pump discussed in the following is different from conventional reciprocating pumps, in that there are no pistons or diaphragms used.

The authors have succeeded in clarifying the principles of the self-priming effect (Hiyama et al., 1987) and the circulating pump effect (Hiyama et al., 1984), both theoretically and experimentally, of this innovative pumping method. The prototype pump (electromagnetically driven chemical pump) features this new pumping method. The pumping characteristics and design factors of this prototype pump are discussed in the following report. Also discussed are its safe and simple use, and its excellent controllability over a wide field of application.

Pumping Principle and Pump Features

Figure 1 shows the basic configuration of the present prototype pump. Its basic components are the vibrating pipe and the valve equipped on its upper end. The lower end of the vibrating pipe is connected to the stationary pipe with bellows.

The section from the lower end of the stationary pipe to

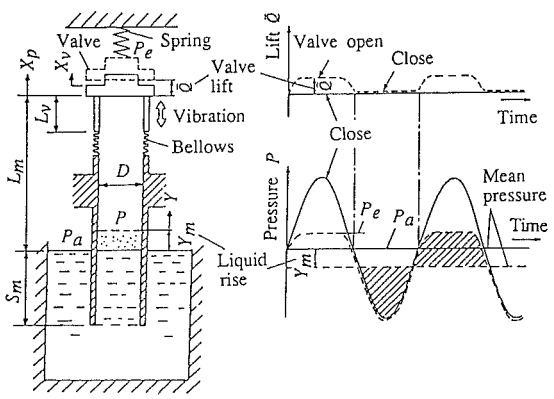

Fig. 1 Working principle

Contributed by the Fluids Engineering Division and presented at the Fluids Engineering Conference, Washington, D.C., June 20–24, 1993, of The American Society of Mechanical Engineers. Manuscript received by the Fluids Engineering Conference, August 11, 1993; revised manuscript received October 6, 1993. Associate Technical Editor: L. Nelik.

the upper end of the vibrating pipe of the present prototype pump is referred in this paper as the suction pipe. The process in which a liquid rises to the upper end of the vibrating pipe is referred to as the self-priming operation, while a pumping operation when the interior of the pump is filled with liquid is referred to as the circulating pump operation.

Self-Priming Operation. During a self-priming operation, a liquid free surface exists inside the suction pipe. When the vibrating pipe is vibrated along its axis, the liquid column inside the pipe starts vibrating in proportion to the periodical pressure fluctuation of gases inside the pipe. The valve at the upper end of the pipe opens when the gas pressure builds up inside the pipe, and the gas is then discharged from the valve. Such discharge of gas occurs once every vibratory cycle. Figure 1 shows the rough curves of the pressure fluctuation of a gas column in such a situation. The mean pressure inside the pipe, per one vibratory cycle, becomes lower than the atmospheric pressure and the liquid inside the pipe rises approximately in proportion to the difference in pressure. Accordingly, it becomes possible to increase the rising speed of the liquid surface by controlling the pressure fluctuation amplitude to a greater value, as doing so will cause the liquid surface to rise per each vibratory cycle. The optimum excitation frequency condition matches with the resonance point of the vibratory system (gas column, liquid column and valve) in the pipe. The method, which will be explained later on, features small amplitude excitation, which is practical. Generally speaking, the self-priming operation, provided the total suction pipe is 1 m in length (the vibrating pipe length is about 0.05 m) and with an internal diameter of 0.025 m, can be carried out favorably at low vibratory frequencies of below 10 Hz.

Circulation Pump Operation. In a circulation pump operation, the suction pipe is filled with water. The opening of the valve and the discharge of the liquid follows roughly the same process as that of the self-priming operation, i.e., by the pressure fluctuation of the liquid column inside the suction pipe proportional to the motion of the vibrating pipe. However, the compression of the liquid inside the pipe is different from that of the self-priming operation, meaning that resonance point of the liquid inside the pipe does not necessarily constitute the optimum pumping condition.

Figure 2 shows some actual measured data on the valve and vibrating pipe, liquid column pressure P in the suction pipe, and flow rate Q per one vibratory cycle during a circulation pump operation. It is acknowledged that the pressure inside the suction pipe rises roughly during the upward motion of the vibrating pipe. This causes the valve to open and the liquid to flow into the chamber outside the valve disk. In contrast, the pressure inside the pipe decreases roughly during the downward motion of the vibrating pipe, causing the valve to become shut. The piston effect during the next upward motion of the vibrating pipe causes the liquid to discharge downstream of the valve through the discharge pipe. This means that the present prototype pump achieves both the suction and discharge process by one valve and one short vibrating pipe. Generally, a well-known process in a conventional piston pump necessitates two valves (suction and discharge). As the present prototype pump has only one valve, the liquid which is provided a significant amount of kinetic energy from the pressure fluctuation caused by vibration of the vibrating pipe, is made to flow directly from the suction side to the discharge side while the valve is open.

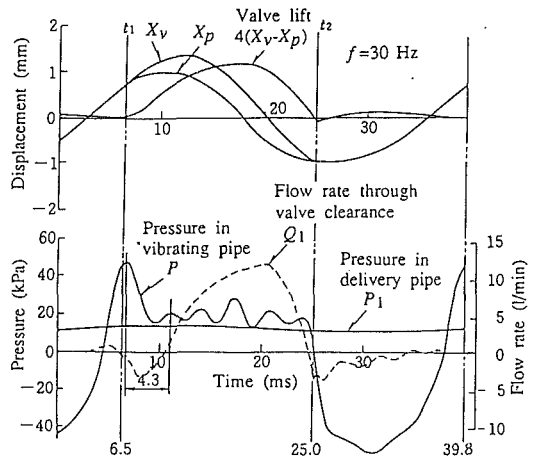

Fig. 2 Displacement, pressure and flow rate in pumping system

Pump Features and Application. As can be gathered from the above, the present prototype pump works on a unique pumping principle based on the vibration phenomena of fluids. The following are some features and points of interest.

(*a*) It is compact, lightweight, with minimal parts, its maintenance is easy, and it can be manufactured at relatively low cost.

(*b*) It can be made leak-proof and measures against corrosiveness can be set easily (the flow path is not complicated and materials can be selected easily).

(*c*) It carries a self-priming performance and its operation can be controlled easily.

(*d*) Its use as a high lift pump (e.g., discharge pressure exceeding 2 bars) or a large-scale pump (e.g., diameter exceeding 0.1 m) is not favorable.

(*e*) The discharged liquid will feature a pulsating flow (no constant flow rate at pump discharge outlet).

Considering the above points, it is assumed that the present prototype pump is most applicable as a small-scale pump for pumping special fluids that need to be handled with caution. It can be used for pumping chemical fluids such as acids and alkalis, corrosion-resistant-high temperature fluids such as molten salt and liquid metals, or bio-related fluids such as cell culture fluids and blood. There is a case, where a high temperature pump driven by the air actuator was operated experimentally for pumping Heat Transfer Salt mixture with

Nomenclature

D = internal diameter of pipe
f = frequency
f_a = optimum frequency
g = acceleration of gravity
H = pump head
I = electric current
k = spring constant of valve spring
L_m = suction pipe length above water
L_v = vibrating pipe length
m = mass of valve
P = gas column pressure
P_l = liquid column pressure
P_a = atmospheric pressure
P_e = valve set pressure
Q = flow rate
Q_1 = flow rate through valve clearance
Q = valve lift
S_m = submerged length of suction pipe
t = time
t_m = given time
V = voltage
X_p = displacement of vibrating pipe
X_v = displacement of valve
X_{vi} = initial spring contraction
X_0 = peak to center displacement of vibration
Y = liquid displacement
Y_m = liquid rise height
η = pump efficiency
θ_c = temperature rise of coil
γ = polytropic index

Table 1 Nondimensional parameters

$\omega = 2\pi f$, $T = \omega t$, $T_m = \omega t_m$, $Y' = Y/L_m$, $Y'_m = Y_m/L_m$, $K = kX_0)/(\text{mg})$, $P'_a = P_a/(\rho g L_m)$, $V_0 = (dY/dt)_0/(\omega X_0)$, $M' = \pi D^2 \rho L_m/(4m)$, $Q_i = X_{vi}/X_0$, $Q' = (X_v/X_0) - \sin T$, $B_1 = K/G$, $B_2 = -1/G - KQ_i/G - M' Y'_m/G$, $B_3 = 1 - K/G - M' a(Y'_m + S'_m)/(1 - a)$, $B_4 = M'(Y'_m + S'_m)\sqrt{a}\{V_0 - a/(a-1)\}$

$NaNO_3$ heated to 410°C (770°F). The pump performance indicated a maximum flow rate of 15 liters/min at low pressure. In the biomedical field, there are cases of an out-of-body auxiliary blood circulation pump used for artificial hearts. A prototype blood circulation pump (Nitta et al., 1991) was tried, it was driven by an electromagnetic-permanent magnet system which uses a soft elastic membrane for reducing any damage to blood cells. Its practicality has been confirmed through in vivo and in vitro hemolysis tests were carried out on a goat. An electomagnetic pump was also developed for moving culture fluids into bio-reactors. Full consideration is given to sanitation therefore the sections of the pump which come in contact with the fluids are made of AISI316L and Teflon®. The interior of the entire pump system can be disinfected using steam, without having to disconnect any piping, since the pump valve can be opened by applying a pressure of approximately 0.1 bar to its suction side.

As indicated above, the present prototype pump can be used for handling special fluids. Further research and development are expected to broaden its application into new fields.

Self-Priming Performance

Let us here attempt a theoretical estimation of the liquid rise characteristic of the present prototype pump, i.e., applying a pumping fluid theory considering the areas of vibration in the suction flow passage along the axial symmetry shown in Fig. 1.

When calculating pressure P of the gas column inside the pipe at a given time t_m, the excitation vibration displacement X_p of the vibration pipe is sinusoidal $X_p = X_0 \sin(2\pi f t)$, where t is time, f is exciting frequency, X_0 is the amplitude of the vibration (Hiyama et al., 1987). The displacement of the liquid surface due to vibration is sufficiently small compared to the total height of the liquid column from the liquid surface in the pipe to the bottom end of the suction pipe, so the extremely small secondary term is able to be omitted. Finally, the gas pressure P is:

$$\frac{P - P_a}{\rho g L_m} = -Y'_m - \frac{\gamma(P'_a - Y'_m)}{1 - Y'_m}\frac{X_0}{L_m}\left(\sin T - \sin T_m - \frac{Y}{X_0}\right) \quad (1)$$

where nondimensional parameters are shown in Table 1.

When calculating the valve movement X_v and the dimensionless excitation acceleration $G = (2\pi f)^2 X_0/g$, necessary for opening the valve, the relation of the excitation acceleration to the relative displacement of the valve versus the pipe is obtained by solving simultaneously three equations; the gas pressure (Eq. (1)), the liquid column motion and the valve motion. The liquid column motion equation and the valve motion equation are indicated as follows:

$$\frac{d^2Y'}{dT^2} + aY' = a(\sin T - \sin T_m) \quad (2)$$

$$\frac{d^2Q'}{dT^2} + B_1 Q' = B_2 + B_3 \sin T + B_4 \sin(\sqrt{a}T) \quad (3)$$

When examining the optimum excitation vibration frequency, i.e., regarding the optimum pumping condition as the minimal dynamic force for opening the valve (Hiyama et al., 1987), the optimum conditions match with the resonance point (the natural frequency) of the gas/liquid system inside the pipe.

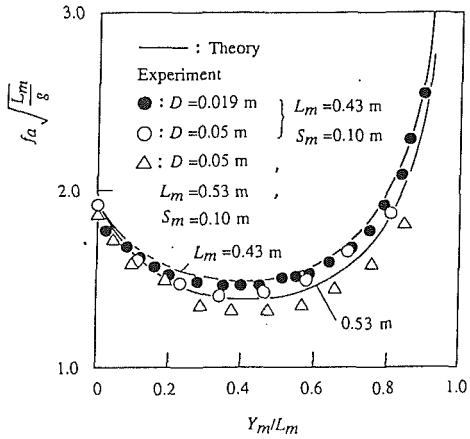

Fig. 3 Optimal liquid-lifting conditions. (Experimental uncertainty in $f_a/L_m/g$ = ± 5 percent and in Y_m/L_m = ±1 percent at 20:1 odds)

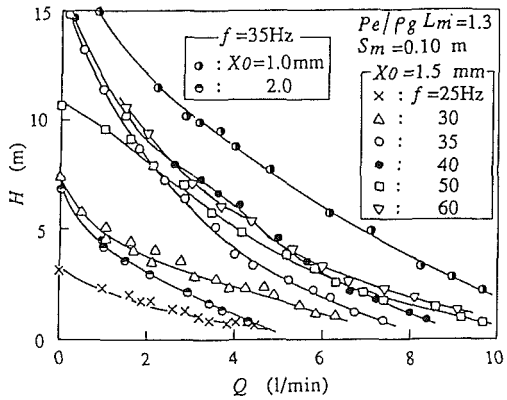

Fig. 4 Relationship between head H and flow rate Q. (Experimental uncertainty in H = ±7 percent and in Q = ±13.3 percent at 20:1 odds)

The optimum conditions are given as follows:

$$a = 1,\ a = \frac{\gamma g(P'_a - Y'_m)}{\omega^2 L_m(1 - Y'_m)(Y'_m + S'_m)} \quad (4)$$

Figure 3 shows an example of an optimum vibration frequency, indicating the most favorable self-priming effect and the comparison between the theoretical result and the experiment, i.e., the change in the resonance vibration frequency of the flow system inside the suction pipe due to the liquid surface height. The theoretical curve is obtained from equation. It was confirmed theoretically and experimentally, that there was almost no effect on the nondimensional optimum vibration frequency $f_a\sqrt{L_m/g}$ by changes in the suction pipe length and pipe diameter; where f_a is a natural frequency, g is acceleration of gravity, L_m is indicated in Fig. 1. As acknowledged in the optimum Eq. (4), the value of the optimum vibration frequency also became relatively smaller as the submerged depth of the pipe became greater.

Pump Output

Figure 4 shows an example of pump performance in a 19 mm diameter suction pipe. The performance of the present prototype pump was roughly similar to that of a conventional turbo pump, wherein the pressure decreases as the flow rate increases, the only difference being that changes in performance were almost linear. It is acknowledged that the pump head increases along with the vibration frequency when the amplitude is at a constant, and also with the amplitude when the frequency is at a constant in the range of the present

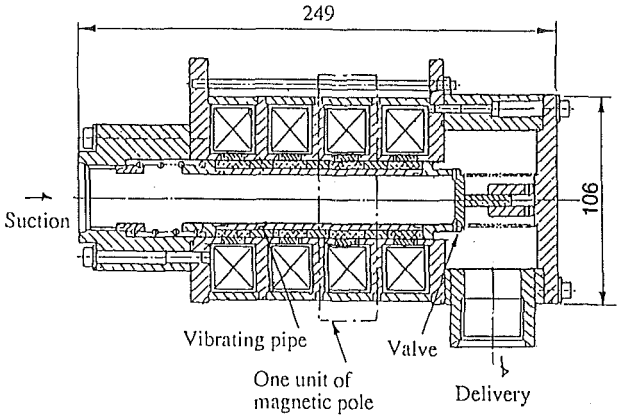

Fig. 5 Sectional view of chemical pump

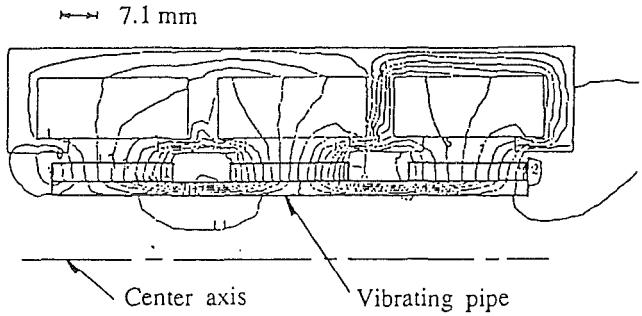

Fig. 6 Magnetic flux lines (3-units)

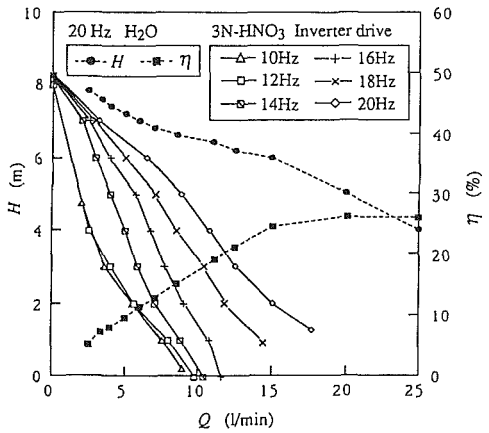

Fig. 7 Pump performance of chemical pump. (Experimental uncertainty in $H = \pm 12.5$ percent and in $Q = \pm 13.3$ percent at 20:1 odds)

experiment. As acknowledged from the example of pump performance, it is possible to control the flow rate of the present prototype pump over a wide region by changing the excitation conditions such as the vibration frequency and the amplitude (Hiyama et al., 1984).

The following discusses the flow states bringing on the pumping effect, i.e., in terms of work by the vibrating pipe per one cycle of excitation.

While the valve is closed, the vibrating pipe undergoes both a reciprocating (piston) movement which affects the liquid in the chamber outside the valve disk and an accumulation of kinetic energy which affects the liquid in the vibrating pipe, the latter of which is provides the rise of the liquid in the suction pipe. In this situation, the internal pressure of the vibrating pipe builds up due to the kinetic energy of the inflow liquid inside the suction pipe. This causes the valve to open and the liquid is discharged. One pumping cycle of the present prototype pump includes the discharge of liquid while the valve is open and the reciprocating effect (the back side of valve works as a piston disk) of the vibrating pipe while the valve is closed. Generally, a favorable pumping performance can be obtained by setting a higher excitation frequency than the optimum frequency of the self-priming operation. The kinetic energy building up in the liquid column in the suction pipe, while the valve of the present prototype pump is closed, is greater than the work rate by the reciprocating (piston) effect of the vibrating pipe. The fluid efficiency η_h (ratio between the work rate effective for pumping versus the overall energy of the liquid provided by the vibration of the pipe) depends on the kinetic energy accumulated in the liquid column and the energy caused by the piston effect (Hiyama et al., 1991).

Prototype of Electromagnetic Chemical Pump

Figure 5 shows a sectional view of an electromagnetic prototype chemical pump. The basic configurational element of this pump is just the vibrating pipe with its upper end sealed off by a valve excluding the excitation device. Magnetized permanent magnets are attached in the radial direction on the external surface of the vibrating pipe. An electromagnetic coil is equipped inside the casing. When an electric current passes through the coil, the intensity of the bias magnetic field generated by the permanent magnets becomes changed by the magnetic field of the coil, resulting in an axial direction force applying on the vibrating pipe. This means that the vibrating pipe vibrates along its axial direction when an electric current passes through the coil. The prototype pump features an electromagnetic excitation method, especially developed for this pump, and a non-seal structure as it was built for use as a chemical pump.

The electromagnetic excitation device is compact and the excitation it generates is large. As for the design of this device, an attempt was made to optimize its magnetic pole configuration by analyzing its magnetic field. The magnetic pole configuration of the coil was simplified and made into a unit. This made it possible to simply assemble magnetic pole units to match the number of magnetic stages. As the driving force increases in proportion to the number of magnet stages, it became possible to increase the pump head by adding more units. Figure 6 shows an example of magnetic field analysis results, for a case where three stages of magnetic pole units were used. The displacement and driving force characteristics of this electromagnetic excitation device were estimated theoretically. This theoretical estimation revealed that the pump performance (the displacement amplitude) suddenly increases when the electric current passing through the coil is increased within a certain range of the vibrating pipe position.

Another important feature of the pump is that the pump can be installed at any angle, except in the case where it is used for a self-priming operation.

Figure 7 shows the pump performance for water, and for nitric acid solvents as a chemical pump. Changes in the performance for nitric acid solvents versus vibration frequencies are shown. An invertor was used for providing the driving force here. A long, continuous pumping operation was carried out under $Q = 5$ liters/min and $H = 6$ m (Aq) and confirmation was made that there were no irregularities in the pump performance and pump parts.

The performance for water was also obtained using a different electric power source from that for the nitric acid solvents case. The maximum efficiency for water, including that of the excitation device, was approximately 28 percent under a vibration frequency of 20 Hz and an electric voltage of 60 W.

Design Procedures

The pumping effect of the present prototype pump, as was

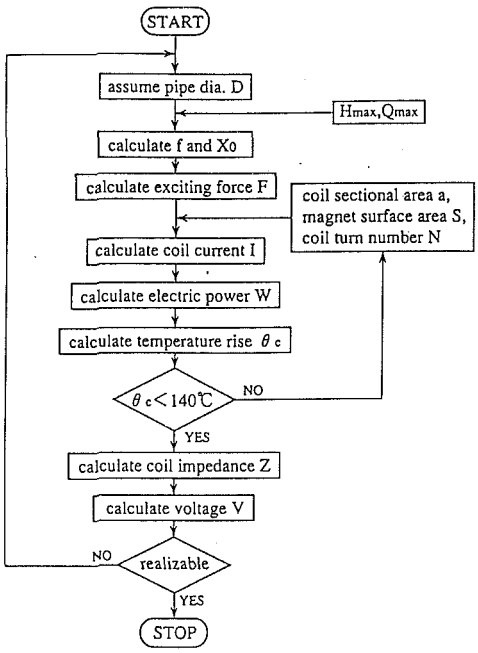

Fig. 8 Block diagram of determining design parameters

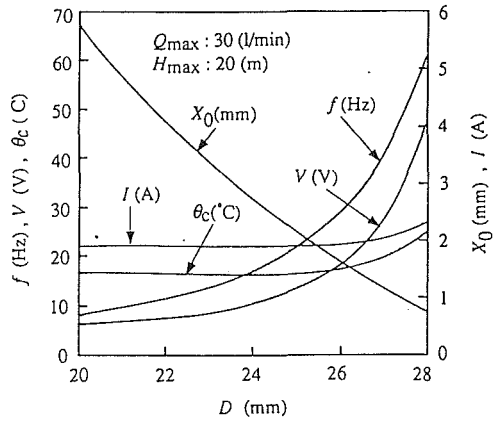

Fig. 9 Calculation results of design parameters

Table 2 Parameter values

Design parameter	H_{max} (m)	Q_{max} (l/min)	D (mm)	I (A)	f (Hz)	X_0 (mm)
Range of value	$H_{max} \leqq 15$	$Q_{max} \leqq 50$	$D \leqq 50$	$I \leqq 7$	$10 \leqq f \leqq 50$	$X_0 \leqq 10$

mentioned earlier, is generated by the pressure fluctuation, induced by the vibrating pipe, in the liquid inside the pipe. As this pumping effect is an unsteady phenomenon, it is relatively difficult to make a precise estimation on pump performance by theoretical calculations. Pump performance also depends on the characteristics of the valve used and the configuration of the pump itself. However, the performance of the present prototype pump can be estimated approximately, provided its shutoff pressure and maximum flow rate values can be known. This is because the pressure in this pump is linearly in reverse proportion to the flow rate. A simplified design procedure which uses experimental equations has been set up for the electromagnetic prototype pump shown in Fig. 5.

Figure 8 shows the design procedures. Empirical equations for calculating the excitation force F, excitation amplitude X_0, maximum flow rate Q_{max}, and maximum pressure H_{max} must be decided beforehand. Figure 9 shows an example of the calculated results for the amplitude X_0, frequency f, temperature rise of coil θ_c, coil current I and coil voltage V. The recommended values of critical design parameters for the high performance-prototype pump are shown in Table 2.

Summary

The pumping principle and characteristics of a new type pump were clarified. This pump features effective use of a pumping method based on vibrating a pipe, whose one end is sealed with a valve, along its axial direction, thus causing liquid to rise inside the pipe and to become discharged through the valve. A prototype chemical pump was developed using this pumping method and tested. Test results indicated that this pump capabilities were sufficient for it to become practical.

References

Дежкунов, Н. В. and Прохоренко, П, П., 1980, "Зависимость Воздействия Ультраэвука на Подбем Жидкости в Капилляре от ее Свойств," *Inzhenerno Fizicheskii Zhurnal*, Vol. 39, No. 3, pp. 513–519.

Ганиев, Р. Ф., Малышев, П. А., Чистяков, Ю, Г, 1978, "Вибрачионное Перемешение Жидкости в Сосудах," *Prikladnaia Mekhanika*, Vol. 14, No. 11, pp. 126–129.

Hiyama, H., Hashimoto, H., and Sato, R., 1984, "Pumping Characteristics of Liquid in a Vibrating Pipe (Liquid-Lifting Effect by a Vibrating Pipe)," *Proceedings of China-Japan-Vibration-Joint Conference 84*, Shanghai, pp. 351–358.

Hiyama, H., Hashimoto, H., and Sato, R., 1987, "The Effect of Pumping in a Vertically Vibrating Pipe (3rd Report, Theoretical Analysis of Liquid Rising Characteristics in a Suction Pipe with Abrupt Sectional Change)," *Trans. Jpn. Soc. Mech.*, Vol. 53, No. 490, B, pp. 1716–1722 (in Japanese).

Hiyama, H., Hashimoto, H., Sato, R., and Yamamoto, K., 1991, "The Effect of Pumping in a Vertically Vibrating Pipe (Experimental Study on Flow Mechanism in a Pump)," *JSME International Journal*, Vol. 34, pp. 333–339.

Nitta, S., Katahira, Y., Yanbe, T., Sonobe, T., Tanaka, M., Miura, M., Sato, N., Mohri, H., Hiyama, H., Aoki, M., and Hashimoto, H., 1991, "An Electromagnetically Driven Univalved Artificial Heart," *Artificial Heart*, Vol. 3, pp. 87–91.

Hydrodynamics and Erosion Modeling of Fluidized Bed Combustors

Chunyuan Li

Victor Zakkay

Department of Applied Science,
New York University,
26-36 Stuyvesant Street,
New York, NY 10003

Hydrodynamics and erosion of Fluidized Bed Combustors (FBCs) containing tubes have been analyzed through the use of the hydrodynamic model, which has been developed at New York University, utilizing a CRAY Y-MP/832 supercomputer and a CONVEX C210 minisupercomputer. Particle velocity fields and bed dynamics including bubble formation and motion and bed expansion and collapse were analyzed for high pressure cold and hot beds. The cold beds were studied by (a) optimizing tube models for simulating a circular tube, (b) varying the distance from distributor plate to the tubes, (c) changing tube size, and (d) using vertical tubes. Atmospheric and pressurized fluidized bed combustors were also simulated and compared to each other for bubble size, bubble frequencies, particle jets, and tube erosion. In particular, the computation revealed bubble coalescence which causes high particle jets. Threshold velocity has been analyzed utilizing Hertz contact theory and the maximum shear theory (Tresca). Tube erosion was predicted utilizing the Finnie erosion model and the modified Finnie model, which considers the threshold velocity and compared to each other. Computed results show that the distance from distributor to the tubes, tube size, tube orientation and operating pressure have significant effect on bed dynamics and tube erosion. The threshold velocity is found to significantly influence the prediction of erosion.

1 Introduction

Fluidized bed combustion has become a highly competitive technology for the clean combustion of coal; however erosion of in-bed heat exchangers is limiting this technology. In order to analyze the erosion of the in-bed tubes, some experimental work has been performed (Vicent et al., 1987; Witherell et al., 1988; Levy et al., 1989; Podolski et al., 1987, 1991; Levy et al., 1991; Sethi et al., 1991). Since erosion is a local behavior which concerns particle impact velocity and impingement frequency, it is extremely difficult, time consuming and expensive to obtain those local erosion data through experiment. High speed computers make it possible to analyze the bed dynamics and to predict tube erosion. Hydrodynamics and erosion of FBCs have been analyzed through the use of the computers for some bed configurations and operating conditions (Bouillard et al., 1991; Lyczkowski et al., 1987, 1991; Chang et al., 1991); however, research is confined to the simulation of cold beds containing horizontal square tubes (Lyczkowski et al., 1991; and Chang et al., 1991). Due to the complexity of the hydrodynamics variation of bed configuration and operating condition may also influence flow fields and therefore tube erosion.

In bubbling beds, as the bubbles pass the tubes they carry the particles in their wakes with various velocities. The larger the bubbles within the tube bank, the higher is the variation in the local velocity in the neighborhood of the tube (Zakkay and Krishna, 1987). The bubble size depends not only on the fluidizing velocity, but also on the space between distributor and tubes. When this space becomes larger, the bubbles may have enough space to coalesce and become larger. Larger bubbles cause higher particle jets and thus result in serious damages of the tubes. Erosion is severe for a horizontal tube arrangement due to the direct impact of the particles. Different tube arrangement and size may change bubble size so that smaller tubes could result in smaller bubbles. This may reduce tube erosion and in addition heat transfer rates may be improved since surface is increased.

The horizontal heat exchanger tube design is preferred by the boiler industries because of the substantial experience gained in this configuration. However, vertical heat exchangers appear to provide clear advantages over horizontal types such as enhanced particle mobility, resistance to erosion, scope for increasing the volumetric solidity of in-bed tubes and thus higher heat loadings (Zakkay et al., 1986). For horizontal tube banks, particle jets impact on the tubes directly and they are the main contributors to the erosion; however in vertical tube banks, the tube configuration makes the bubbles pass the tubes smoothly and the particle jets move tangentially to the tubes, thereby reducing tube erosion. Thus far, only limited research has been conducted on vertical heat exchangers since its original suggestion by Zakkay in 1978.

Contributed by the Fluids Engineering Division for publication in the JOURNAL OF FLUIDS ENGINEERING. Manuscript received by the Fluids Engineering Division April 17, 1993; revised manuscript received June 3, 1994. Associate Technical Editor: A. F. Ghoniem.

Atmospheric fluidized bed combustors (AFBCs) are already enjoying some success in the industrial marketplace as a highly competitive technology for producing heat and process steam. AFBCs provide fuel flexibility, meet emission standards for SO_2, reduce NO_x, and increase thermal efficiency. Pressurized fluidized bed combustors (PFBCs) offer the promise of further enhancement of some of AFBCs design advantages and may reduce bubble size due to higher pressure, and therefore lower erosion.

The particles circulate in fluidized bed combustors and each particle possesses different velocities depending on its size and orientation. When the moving particles impact on the tubes, erosion may be produced; however when the velocity of the particles is lower than a certain level (threshold), only elastic deformation takes place. The inclusion of the threshold velocity in the model could have significant effect on the computation of the erosion. The threshold phenomenon has been reported by Stringer (1987) and Podolski et al. (1991). In FBCs, some particles have lower velocity than the threshold velocity so that the elastic deformation energy in the model, which does not contribute to the erosion, should be excluded in the erosion calculation.

This paper presents (i) the analyses of threshold velocity and the modification of the Finnie erosion model, (ii) the development of hydrodynamic model utilizing computers, and (iii) the analyses of the hydrodynamics and erosion in fluidized bed combustors containing tubes for the variation of the distance from the distributor to the tubes; the tube arrangement; the tube orientation; and the operating pressure.

2 Threshold Velocity

In fluidized bed combustors, the particles in the wakes of rising bubbles have a higher velocity than the adjacent particles. When the particle velocity impacting on the tube is lower than the threshold velocity, only elastic deformation takes place and no erosion is produced. Therefore, erosion should take into account only those particle velocities which are higher than the threshold velocity.

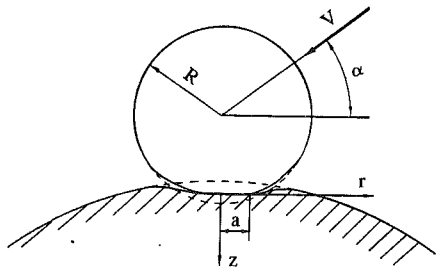

Fig. 1 A particle impacting on a tube

The threshold velocity can be obtained by the theory of elasticity. Assuming that the particle which is hitting the tubes is spherical and the ratio of the particle diameter to the tube diameter approaches zero, Hertz contact theory (Laudau and Lifshitz, 1986) shows that the contact area is a circle and maximum pressure P_o takes place at the center of contact surface, which is

$$P_o = \frac{3}{2\pi D}\sqrt{\frac{h_o}{R}} \tag{1}$$

where h_o is the distance of the deepest penetration of the particle into the tube, R the radius of the particle and

$$D = \frac{3}{4}\left(\frac{1-\nu^2}{\mathrm{E}} + \frac{1-\nu'^2}{\mathrm{E}'}\right) \tag{2}$$

where ν and ν' are Poisson's ratios of the target (the tube) and the spherical particle, and E and E′ are Young's moduli of the two bodies.

As a spherical particle with velocity V impacts on a target with angle α as shown in Fig. 1, both the normal stresses and

Nomenclature

a = contact radius
b = length of the tetrahedral edge, m
c = compaction modulus
C = threshold velocity constant
C_m = maximum of threshold velocity constant
C_{dy} = drag coefficient in y-direction
d_p = particle diameter, m
D_e = function for threshold velocity, Pa^{-1}
E, E' = Young's modulus, Pa
F = erosion rate of the Finnie model, m/s
g = acceleration due to gravity, m/s^2
G = solid elastic modulus, Pa
h_o = maximum contact approach, m
m = particle mass, kg
$\dot{m}$ = mass flux of solids, $kg/(m^2 \cdot s)$
P = pressure in fluidized bed combustors, Pa
P_s = hardness of eroded body, Pa
P_o = maximum pressure of two contact bodies, Pa
F' = erosion rate considering V_t, m/s
Q = local time-averaged erosion rate, m/s
R, R' = curvature radii of two contact bodies, m
R_{ey} = Reynolds number in y-direction
S = surface area of spherical particle, m^2
t = time, s
U_g, U_s = gas and solids phase velocities in the x-direction, respectively, m/s
V = particle impact velocity, m/s
V_g, V_s = gas and solids phase velocities in the y-direction, respectively, m/s
V_z = normal velocity of the particle, m/s
V_t = threshold velocity for spherical particle, m/s
$V_{t,tip}$ = threshold velocity for particle with tip, m/s
W = material weight removed by particle, kg
x, y = lateral and axial coordinates in fluidized bed, respectively, m
z = normal coordinates for elastic deformation of two contact bodies, m
α = impingement angle
β_x, β_y = fluid-particle friction coefficient in the x- and y-directions, respectively, $kg/(m^3 \cdot s)$
ϵ = porosity
ϵ^* = compaction gas volume fraction
τ_{max} = maximum shear stress, Pa
τ_{zr} = shear stress in target, Pa
ν, ν' = Poisson's ratio
σ_r, σ_z = compressive stresses in r- and z-directions, respectively, Pa
σ_y = yield stress of materials, Pa
ρ = density of the eroded material, kg/m^3
ρ_g, ρ_s = gas and particle densities, respectively, kg/m^3
μ = friction coefficients for contact bodies
μ_g = gas dynamic viscosity, $kg/(m \cdot s)$
Φ_s = particle shape factor

Superscripts

$= d/dt$

shear stress appear inside the target. The normal stresses in the target are σ_z in the z-direction and σ_r in the r-direction, and the shear stress is τ_{zr} due to friction. The distributions of σ_z and σ_r along the z-axis are given by Engel (1978). If compressive stresses are taken as positive,

$$\sigma_z = \frac{a^2}{a^2+z^2} P_o \tag{3}$$

$$\sigma_r = -P_o \left\{ (1+\nu) \left[\frac{z}{a} \arctan\left(\frac{a}{z}\right) - 1 \right] + \frac{a^2}{2(a^2+z^2)} \right\} \tag{4}$$

where a is the contact radius.

If the impingement angle α is less than a certain value, the sphere will slip on the target. Most of the particles in fluidized beds hit the tubes almost tangentially (Podolski et al., 1991). The tangential force of friction between the moving sphere and the target is porportional to the normal force by Coulomb's law and the friction traction has the same distribution as the normal pressure. According to Johnson (1985), the shear stress inside the target along the z-direction has the same distribution as σ_z and it is written:

$$\tau_{zr} = \mu P_o \frac{a^2}{a^2+z^2} \tag{5}$$

The relationship between the maximum pressure, P_o, and the impact velocity of the sphere, V, can be obtained by the principle of energy conservation (Laudau and Lifshitz, 1986). In collision, the maximum contact approach h_o is

$$h_o = \left(\frac{5mD}{4\sqrt{R}} \right)^{2/5} V_z^{4/5} \tag{6}$$

where m is mass of the spherical particle. The maximum pressure becomes

$$P_o = \frac{1}{2} \left(\frac{405}{\pi^4} \right)^{1/5} \frac{\rho_s^{1/5} V_z^{2/5}}{D^{4/5}} \tag{7}$$

where ρ_s is the density of the particle and $V_z = V \sin \alpha$. A similar expression of Eq. (7) has been given by Davies (1949); however, his model only includes one of the elastic moduli of two contact bodies and thus it may only be used for the case where the sphere has much higher hardness than the target. According to the theory of maximum shear stress (Tresca), the criterion of limiting elastic stress state (Jaeger, 1956 and Popov, 1976), in which no permanent deformation takes place, is

$$\tau_{\max} = \sqrt{\left(\frac{\sigma_z - \sigma_r}{2} \right)^2 + \tau_{zr}^2} < \frac{\sigma_y}{2} \tag{8}$$

where σ_y is the yield stress of the target material without considering the effect of hardening due to multiple impacts.

With the help of Eqs. (3), (4), and (5), Eq. (8) becomes

$$CP_o = \frac{1}{2} \left(\frac{405}{\pi^4} \right)^{1/5} \frac{C \rho_s^{1/5} V_z^{2/5}}{D^{4/5}} < \frac{\sigma_y}{2} \tag{9}$$

where

$$C = \left\{ \left[\frac{\frac{3a^2}{2(a^2+z^2)} + (1+\nu) \left[\frac{z}{a} \arctan\left(\frac{a}{z}\right) - 1 \right]}{2} \right]^2 + \left(\frac{\mu a^2}{a^2+z^2} \right)^2 \right\}^{1/2} \tag{10}$$

The maximum normal velocity, V_z, to satisfy Eq. (9) is called the threshold velocity, V_t, as the constant C reaches the maximum, C_m. Consequently, the threshold velocity becomes

$$V_t = 0.49 C_m^{-5/2} \rho_s^{-1/2} \sigma_y^{5/2} D^2 \tag{11}$$

where the constant, 0.49, results from $\pi^2/\sqrt{405}$.

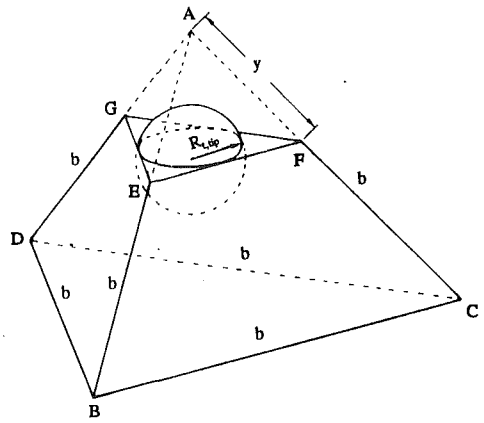

Fig. 2 Idealized tetrahedral particle

The particles in fluidized bed combustors are not perfect spheres. Some particles may have sharp tips so that they erode the tube more seriously than the spherical particles. The threshold velocity for a particle with the sharp tip of R_{tip} is

$$\frac{V_{t,\text{tip}}}{V_t} = \left(\frac{R_{\text{tip}}}{R} \right)^{3/2} \tag{12}$$

Equation (12) indicates that the threshold velocity of the particles with sharp tip is $(R_{\text{tip}}/R)^{3/2}$ times as small as the spherical ones.

The particles in fluidized beds have different shapes and the character of the shape is represented by an average sphericity which is defined as the ratio of the surface of a spherical particle to the surface of actual particle on the basis of same volume (Kunii and Levenspiel, 1969). The rougher the particles, the lower the sphericity. For example, a tetrahedron has a sphericity of 0.671 and a perfect sphere has a sphericity of 1.0. In spite of the variety of the particles, some typical particles, such as tetrahedral particles, could be used to obtain the relation between threshold velocity and sphericity. To facilitate the analysis, each broken tip of the tetrahedron is simplified as a part of an inscribed sphere whose radius is the curvature radius of the tip, as shown in Fig. 2; the broken edges are not taken into account. Referring to Fig. 2, the curvature radius of the broken tip is

$$R_{\text{tip}} = \frac{\sqrt{6}}{8} y \quad 0 \le y \le \frac{b}{2} \tag{13}$$

where y is the distance from the tip. The particle is considered to be a sphere and its radius is

$$R = b \left\{ \frac{\sqrt{2}}{16\pi} \left[1 - 4\left(\frac{y}{b}\right)^3 + \frac{7\sqrt{3}\pi}{36} \left(\frac{y}{b}\right)^3 \right] \right\}^{1/3} \tag{14}$$

The surface of the spherical particle is $S = 4\pi R^2$ and the actual surface of the particle is

$$A = b^2 \left[\sqrt{3} - 2\sqrt{3} \left(\frac{y}{b}\right)^2 + \frac{\pi}{6} \left(\frac{y}{b}\right)^2 \right] \tag{15}$$

Therefore, the sphericity $\phi = S/A$ and R_{tip}/R can be obtained by utilizing the above relations. $V_{t,\text{tip}}/V_t$ approximately linearly decreases with ϕ, as shown in Fig. 3.

The quantity $V_{t,\text{tip}}$ may be used in the erosion models (Bitter, 1963a,b; Neilson and Gilchrist, 1968; Hashish, 1987) which include threshold velocity and V_t might be involved in the models (Hutchings et al., 1976; Rickerby and Macmillan, 1980; and Sriram and Kosel, 1987) which apply for high impact velocity. Since Finnie's model (Finnie, 1958, 1963) has a simple form and easily obtainable parameters, it is used here to predict erosion. In erosion processes, no erosion is produced when the normal velocity ($V \sin \alpha$) of the particle is lower than $V_{t,\text{tip}}$. When $V \sin \alpha$ is higher than $V_{t,\text{tip}}$, erosion takes place; however

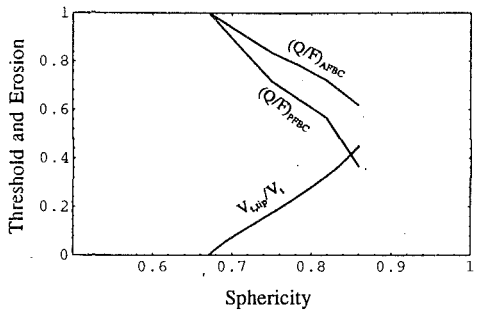

Fig. 3 Computed normalized erosion and threshold versus sphericity. $(Q/F)_{AFBC}$ is the ratio of the modified model to the Finnie model in a AFBC.

elastic deformation energy does not contribute to the erosion (Bitter, 1963a,b). Therefore, the Finnie model

$$F=\frac{\dot{m}V^2}{8P_s}f(\alpha) \tag{16}$$

might be modified as

$$Q=\frac{\dot{m}[(V\cos\alpha)^2+(V\sin\alpha-V_{t,tip})^2]}{8P_s}f(\alpha) \tag{17}$$

where F and Q are erosion rate, $\dot{m}$ the particle mass flux, P_s the hardness of eroded body and

$$f(\alpha)=\begin{cases}\sin 2\alpha-3\sin^2\alpha & \alpha\le 18.43^\circ\\ \dfrac{\cos^2\alpha}{3} & \alpha\ge 18.43^\circ\end{cases} \tag{18}$$

Utilizing Eq. (17), computed erosion rates for AFBC and PFBC at the underside of the central tube are shown in Fig. 3. Erosion almost linearly decreases with increasing sphericity and erosion in PFBC decreases more rapidly than in AFBC.

The threshold velocity varies with the particle shape; for fairly rough particles, $V_{t,tip}$ vanishes; however for particles close to perfect spheres, $V_{t,tip}$ approaches V_t. Unfortunately, the expression of $V_{t,tip}$ for each individual particle in fluidized beds can not be developed thus far. The actual particles are neither idealized angular ($V_{t,tip}$ = 0) nor perfect sphere ($V_{t,tip}$ = V_t). Erosion might be predicted by an appropriate average of the two extreme cases; idealized angular particles and perfect spheres. This may be performed because erosion has approximately linear relation versus sphericity as shown in Fig. 3. For the idealized angular particles, erosion is calculated by the Finnie model (Eq. (16)) and for the perfect spheres, it may be predicted by the following model.

$$F'=\frac{\dot{m}[(V\cos\alpha)^2+(V\sin\alpha-V_t)^2]}{8P_s}f(\alpha) \tag{19}$$

Therefore, the average erosion which considers threshold might be approximated by

$$Q=F-\frac{\phi-\phi_o}{-\phi_o}(F-F') \tag{20}$$

where ϕ_o is the minimum sphericity. The average sphericity of the particles in fluidized beds is around 0.75 (Kunii and Levenspiel, 1969; Almstedt and Zakkay, 1990) and the minimum sphericity is about 0.5 (Kunii and Levenspiel, 1969). In this study, ϕ_o = 0.5 and ϕ = 0.75 are taken.

3 Hydrodynamic Model of Fluidization

Hydrodynamic model of fluidization uses the principles of conservation of mass, momentum, and energy. The separate phase continuity equations and the momentum equations for two-dimensional, transient, isothermal two-phase flow (in Cartesian coordinates) are given as follow (Lyczkowski et al., 1987). See nomenclature for the definition of the symbols.

Gas Phase Continuity

$$\frac{\partial}{\partial t}(\rho_g\epsilon)+\frac{\partial}{\partial x}(\rho_g\epsilon U_g)+\frac{\partial}{\partial y}(\rho_g\epsilon V_g)=0 \tag{21}$$

Solid Phase Continuity

$$\frac{\partial}{\partial t}[\rho_s(1-\epsilon)]+\frac{\partial}{\partial x}[\rho_s(1-\epsilon)U_s]+\frac{\partial}{\partial y}[\rho_s(1-\epsilon)V_s]=0 \tag{22}$$

Gas Phase Momentum in x-Direction

$$\frac{\partial}{\partial t}(\rho_g\epsilon U_g)+\frac{\partial}{\partial x}(\rho_g\epsilon U_gU_g)+\frac{\partial}{\partial y}(\rho_g\epsilon V_gU_g)=-\epsilon\frac{\partial P}{\partial x}+\beta_x(U_s-U_g) \tag{23}$$

Solid Phase Momentum in x-Direction

$$\frac{\partial}{\partial t}[\rho_s(1-\epsilon)U_s]+\frac{\partial}{\partial x}[\rho_s(1-\epsilon)U_sU_s]+\frac{\partial}{\partial y}[\rho_s(1-\epsilon)V_sU_s]=-(1-\epsilon)\frac{\partial P}{\partial x}+\beta_x(U_g-U_s)+G(\epsilon)\frac{\partial\epsilon}{\partial x} \tag{24}$$

Gas Phase Momentum in y-Direction

$$\frac{\partial}{\partial t}(\rho_g\epsilon V_g)+\frac{\partial}{\partial x}(\rho_g\epsilon U_gV_g)+\frac{\partial}{\partial y}(\rho_g\epsilon V_gV_g)=-\epsilon\frac{\partial P}{\partial y}+\beta_y(V_s-V_g)-\epsilon\rho_g g \tag{25}$$

Solid Phase Momentum in y-Direction

$$\frac{\partial}{\partial t}[\rho_s(1-\epsilon)V_s]+\frac{\partial}{\partial x}[\rho_s(1-\epsilon)U_sV_s]+\frac{\partial}{\partial y}[\rho_s(1-\epsilon)V_sV_s]=-(1-\epsilon)\frac{\partial P}{\partial y}+\beta_y(V_g-V_s)-\rho_s(1-\epsilon)g+G(\epsilon)\frac{\partial\epsilon}{\partial y} \tag{26}$$

In the equations, gas and solid viscous stresses have been deleted because for this application they are unimportant and result in longer computing time (Rivard and Torrey, 1979). The solid phase stresses in the equations are used to prevent the particles from compacting to unreasonably high density and the solid elastic modulus, $G(\epsilon)$, is

$$G(\epsilon)/G_o=\exp[-c(\epsilon-\epsilon^*)] \tag{27}$$

where c = 500 and ϵ^* = 0.422 and G_o = 1.0 Pa (Gidaspow and Syamlal, 1985).

In the equations β_x and β_y are friction coefficients between the gas and the particles and a set of those parameters are given by Ettehadieh et al. (1984) as follows.

$$\beta_y=150\frac{(1-\epsilon)^2\mu_g}{\epsilon(d_p\Phi_s)^2}+1.75\frac{\rho_g|V_g-V_s|(1-\epsilon)}{d_p\Phi_s} \quad \epsilon\le 0.8 \tag{28}$$

$$\beta_y=\frac{3}{4}C_{dy}\frac{\epsilon(1-\epsilon)|V_g-V_s|\rho_g}{d_p\Phi_s}\epsilon^{-2.65} \quad \epsilon>0.8 \tag{29}$$

$$C_{dy}=\frac{24}{R_{ey}}(1+0.15R_{ey}^{0.687}) \quad R_{ey}<1{,}000 \tag{30}$$

$$C_{dy}=0.44 \quad R_{ey}\ge 1{,}000 \tag{31}$$

$$R_{ey}=\frac{\epsilon\rho_g|V_g-V_s|d_p}{\mu_g} \tag{32}$$

The expression for the friction coefficient in the x-direction is the same as that in the y direction.

The seven unknown quantities are the gas density, ρ_g; the void fraction, ϵ; the pressure, P; the gas velocity components U_g and V_g and the solids velocity components U_s and V_g in the x- and y-directions, respectively. The six equations above

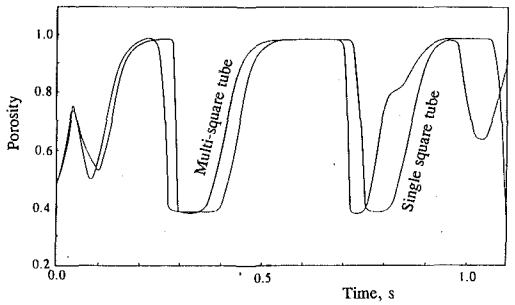

Fig. 4 Computed bubble frequencies at bottom sides of tube 3 for multi-square and single square tubes

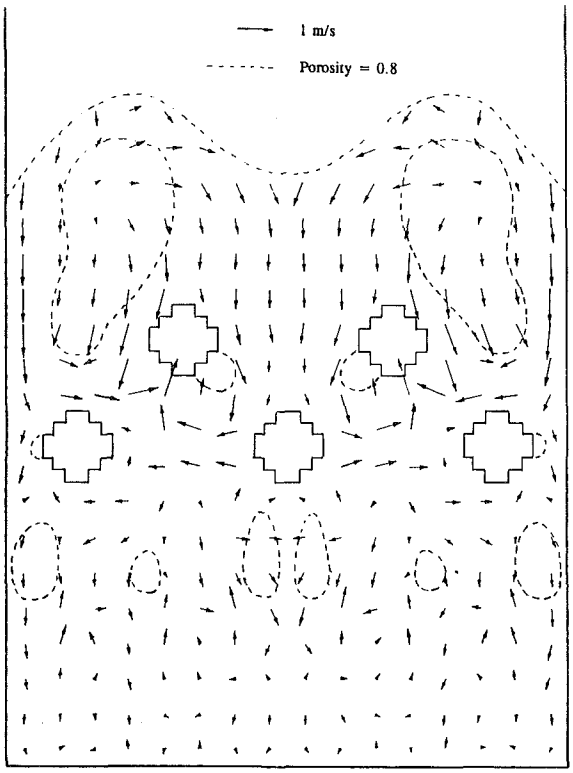

Fig. 5 Computed porosity and particle velocity vector plots of multi-square tube bed at 0.75 s

(Eqs. (21)–(26)), plus the equation of state for the gas, $P = P(\rho_g)$, are sufficient to determine all the unknowns for given boundary and initial conditions.

Numerical solutions of Eqs. (21)–(26) can be obtained through the use of high speed computers; however solving the partial differential equations requires means for representing the fields, and a way to calculate changes in the fields through time from a prescribed set of initial conditions, subject to given boundary conditions. In this study, a finite difference method (Harlow and Amsden, 1975) is used to solve the equations. The equations are solved in two parts. The first part of a calculation cycle performs the explicit time advancement (t_{n+1}) of those quantities that do not need to be determined in the implicit iteration loop. From Eq. (22), the density of solids-phase can be obtained explicitly for time t_{n+1} and therefore the porosity. The second part to be solved are those of the simultaneous implicit transport of gas density and the momentum of both fields, which involves an iteration procedure. The first step is to obtain a pressure increment ΔP for every computational cell. With ΔP the gas density and the velocities for new sweep can be obtained through iteration. Iterative

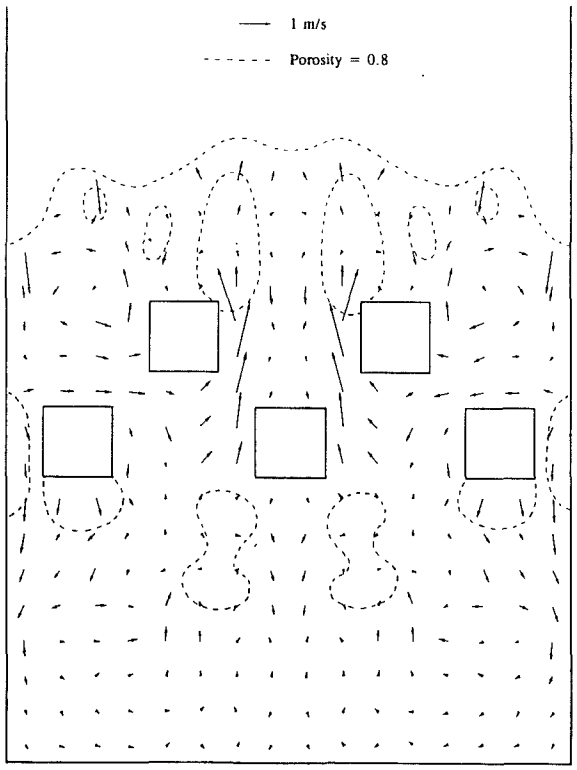

Fig. 6 Computed porosity and particle velocity vector plots of single square tube bed at 0.75 s

accumulation of changes in the pressure and the other field variables continues until the error of gas phase mass conservation is sufficiently small, at which time the changes in pressure is small enough and the iterative quantities have converged to their final values for the cycle. The program has been developed utilizing New York University CONVEX C210 mini-supercomputer. This computer model can perform hydrodynamic computations for cold, hot or high pressure isothermal fluidized bed.

In the simulation process, a proper tube model is needed to represent a circular tube for a better hydrodynamics prediction. In order to optimize the tube models, two types of the tube models, multi-square (24 cells) as shown in Fig. 5 and single square (6 × 6 cells) as shown in Fig. 6, are chosen to represent the circular tube. The multi-square tube model has the volumetric solidity of 14.8 percent, the single square has 22.2 percent, and the circular tube with the same tube spacing has 17.5 percent. If the tube model is represented by a multi-square of 76 smaller cells having 16 corners, the solidity is 16.9 percent; however, computing time will increase about 10 times because both the cell dimension and the timestep decrease.

A bed model, 40.8 cm wide by 88.4 cm high as shown in Figs. 5 and 6, is simulated. During the simulation, glass beads, diameter of 1500 μm; sphericity of 1.0; and a density of 2490 kg/m^3, were used for the solid phase. Air was used as fluid carrier at a temperature of 65.5 °C (see Table 1). The no-slip boundary conditions are used, i.e., all velocities on solid surfaces are set to be zero. This is always true except for the tangential particles under elastic deformation condition; however there is difficulty in addressing with this problem. At the inlet, uniform fluidizing velocity of 1.22 m/s is used and there are no particles entering. Initially, the axial (vertical) gas velocity is equal to the gas phase velocity and all the other velocities are zero. The initial bed porosity is uniform at 0.494 as computed from the Ergun equation (Ergun, 1952) and initial bed height is 38.35 cm. The initial pressure distribution corresponds to the hydrostatic bed height.

Table 1 Operating conditions

Parameter	Value
Particle diameter (μm)	1500
Particle density (kg/m^3)	2490
Particle sphericity	1.0
Minimum-fluidized porosity	0.42
Fluidizing velocity (m/s)	1.22
Temperature (°C)	65.5
Pressure at top of bed (kPa)	101.3
Fluid carrier	Air

Table 2 Computed average erosion rates Unit: μm/1000 hr

	Tube 1		Tube 2		Tube 3		Tube 4		Tube 5	
	F	Q	F	Q	F	Q	F	Q	F	Q
Single square tube	706	353	459	232	1245	856				
Multi-square tube	185	93	114	57	336	220				
Higher bed	384	221	519	319	253	133	411	260	518	310
Lower bed	314	164	307	181	211	116	208	110	429	274
Larger size tube	1440	748	342	173	743	454				
Smaller size tube	418	243	279	141	336	168	458	245	566	315
Vertical tube	111	56	331	166	95	49				
AFBC	574	367	568	337	641	444				
PFBC	395	200	171	86	301	162				

Note: 1) For the distribution of the erosion rates around the tubes, see reference Li (1993).
2) F is the erosion rate of the Finnie model and Q is the one of the modified model.

The symmetric condition may result in reduced computing time. The bed geometry and the boundary conditions are symmetrical about the center line. During the computation, x and y coordinates were set on the distributor and the left wall of the bed, respectively, and no symmetry was assumed in advance. The entire bed containing 5 tubes was computed utilizing 4992 cells. The computed results show that all the variables are symmetrical about the center line. This implies that only half the bed needs to be computed and therefore the computational time could be cut in half. In the computations, a fixed timestep of 10 μs was used for this bed model. On a CONVEX C210 mini-supercomputer, running time for 2496 cells is about 10 hours for each second of transient time.

Figure 4 shows the bubble frequencies (the number of bubbles/sec passing a given point) for those two types of the tube models at the underside (near 6 o'clock) of the upper level tubes up to 1.1 s of transient time. The bubble frequencies are approximately 3 Hz, which is in excellent agreement with the experimental results, 2–4 Hz (Podolski et al., 1991). The bubbles which last for longer times as shown in Fig. 4 indicate the larger bubbles. In the bed, bubbles grow and break; some bubbles coalesce and form larger ones. Figure 5 shows the coalesced bubbles due to combination of the bubbles in the tube bank. The coalescing bubbles become larger than the single one and cause higher particle jets in their wakes. The phenomenon of bubble coalescence has been reported by Levy et al. (1991), where the effect of bubble coalescence on the tubes in an experimental bed containing one row of tubes was studied; however, no result has been reported on bubble coalescence within tube banks. Figure 6 presents the particle velocity distribution and porosity contours for the single square tube model with the maximum particle jets of 1.6 m/s, about 1.5 times as large as that of multi-square one (1.1 m/s) and therefore higher erosion. This difference could be attributed to the tube corners.

The hydrodynamic model developed here is capable of computing gas and solid velocities, bubble frequencies, and porosity in the vicinity of the tubes in fluidized bed combustors, which may be used to predict erosion. Utilizing the Finnie erosion model and the modified model, the average erosion rates of the tubes were computed and are presented in Table 2 for one second transient time (0.1 – 1.1 s) assuming that the tube material is steel SAE 1045 (the yield stress of 631 MPa) and the threshold velocity for spherical particles is 0.336 m/s according to Equation 11 for $\mu = 0.2$. Computed results show that the threshold velocity has a significant effect on the erosion calculation. The average erosion rates predicted by the Finnie model (no threshold) are about double of those predicted by the modified model. For the multi-square tube, the maximum average erosion rate predicted by the Finnie model is 366 μm/1000 hr; however that by the modified Finnie model is 220 μm/1000 hr which is in good agreement with the experimental average result; 127 μm/1000 hr (Podolski et al., 1991). As shown in Table 2, the average erosion of the single square tube has four times higher erosion than the multi-square tube. This implies that the modified Finnie model may be utilized to predict erosion and the multi-square tube model consisting of 16 cells could be a good representation of the circular tube.

4 Analyses of Hydrodynamics and Erosion

(i) Influence of Distributor-Tube Space. Influence of distributor-tube space to bed dynamics and erosion is analyzed here through the simulation of two beds. The only difference between these two beds is the distance from distributor to the tubes. The higher bed has the double height (distributor-tube space) of the lower one as shown in Figs. 7 and 8 and each bed contains 9 horizontal tubes. During the computation, both beds have the same operating conditions as presented in Table 1 and a fixed timestep of 5 μs was used. Computations of these two beds were performed on a CRAY Y-MP/832 supercomputer. Running time is 18.5 hours for the higher bed and 15 hours for the lower bed for 2 seconds of transient time.

Computed bubble frequencies are about 3 Hz for the lower bed. The bubble frequencies for the higher bed are slightly lower, however the bubble size is larger. This may result from bubble coalescence due to the larger distance between the distributor plate and the tubes. Figures 7 and 8 present porosity contours and particle velocity vector plots which show typical particle jets in the wakes of the bubbles. The jets around the upper level tubes in the lower bed are about 1.1 m/s; however, the jets in the higher bed is 2.7 m/s. These higher jets result in serious damage to the tubes. The computed average erosion rates of the two beds are presented in Table 2 and show that the distance from the distributor plate to the tubes affects erosion with the larger distance resulting in higher erosion. In particular, the local erosion rate of the higher bed is about 50 percent higher than that of the lower bed, see Li (1993) for the distribution of erosion around the tubes. This may suggest that the tube should be brought as close as possible to the distributor plate to avoid establishing a higher bubble size and to reduce erosion in a freely bubbling bed. This criterion is limited to the minimum space that should be provided for the combustion to take place between the distributor plate and the bottom of the tubes.

(ii) Influence of Tube Arrangement and Size. Bubble size in a tube bank may be influenced by tube arrangement since the bubble diameter is proportional to the tube spacing (Zakkay and Krishna, 1987). The tube banks consisting of smaller tubes may resist the formation of larger bubbles due to smaller tube spacing and smaller changes of the cross-sectional area of the tubes, and therefore could result in more uniform flow fields and lower erosion. Influence of tube arrangement and tube size on the hydrodynamics was studied by simulating the beds which contain different sizes of tubes. The bed containing 5 larger tubes 5.1 cm in diameter has a tube volumetric solidity of 16.7 percent, as shown in Fig. 9. The other bed containing 9 smaller tubes 2.55 cm diameter as shown in Fig. 10 has the same solidity as the larger tube bed, 16.7 percent. For sim-

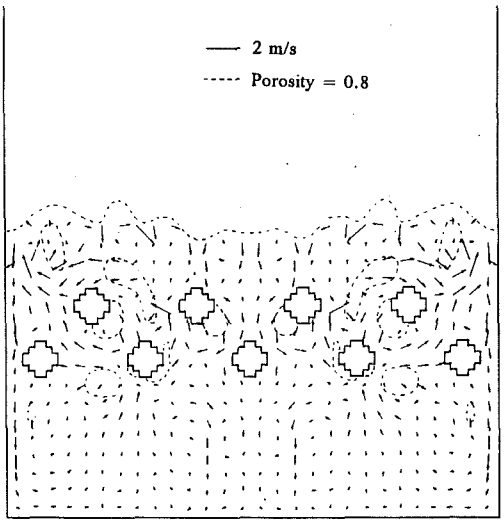

Fig. 7 Computed porosity and particle velocity vector plots of lower bed at 0.8 s

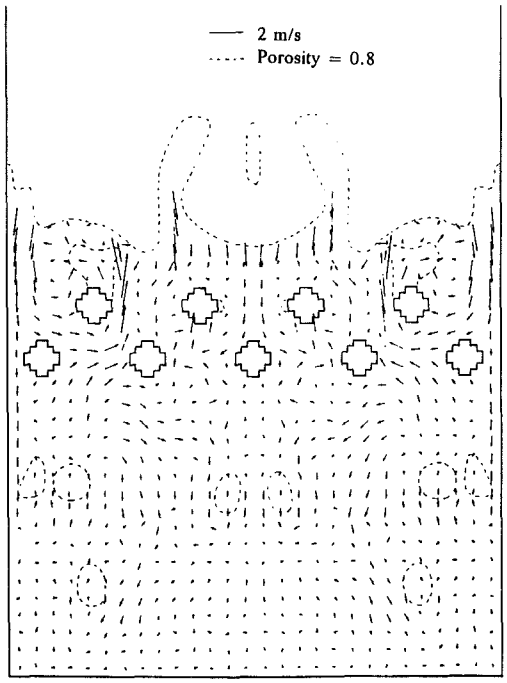

Fig. 8 Computed porosity and particle velocity vector plots of higher bed at 1.1 s

plicity, the tube model for both beds is represented by a single square. The larger tube model has 4 × 4 cells and the smaller one has 2 × 2. The opening conditions of the two beds are the same as presented in Table 1.

Computed bubble frequencies around the tubes are about 3 Hz for both beds. This indicates that tube arrangement does not significantly influence bubble frequency; however, it influences bubble size. The larger tubes cause larger bubbles since they have larger tube spacing. Figure 9 presents the porosity and particle velocity vector plots for the larger tube bed at 0.7 s with a jet velocity of about 1.3 m/s. For the bed containing smaller tubes, the bubbles within the tube banks are smaller and therefore result in lower jets (about 0.7 m/s) as shown in Fig. 10, thus effectively reducing tube erosion. The average erosion rate of the larger tube of the upper level is 454 μm/1000 hr as shown in Table 2; however the erosion

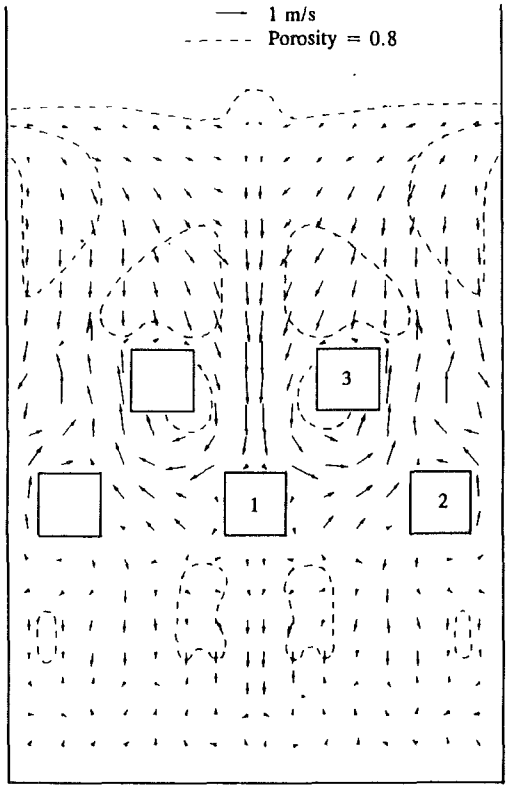

Fig. 9 Computed porosity and particle velocity vector plots of larger tube bed at 0.7 s

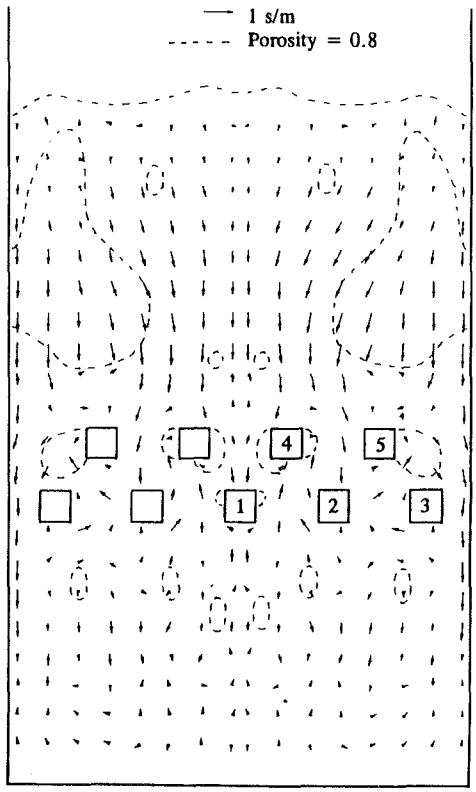

Fig. 10 Computed porosity and particle velocity vector plots of smaller tube bed at 0.7 s

rate of the smaller tube is only 315 μm/1000 hr, about 50 percent lower. This may lead to the conclusion that smaller tubes should be used to reduce erosion.

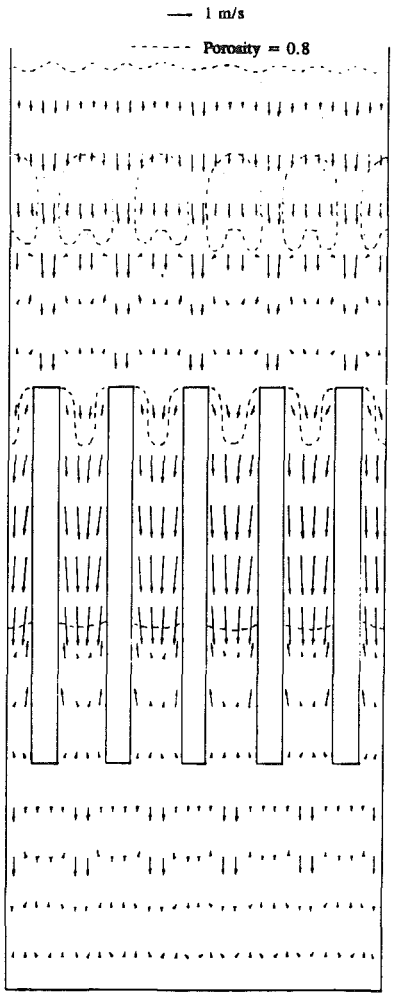

Fig. 11 Computed porosity and particle velocity vector plots of vertical tube bed at 1.0 s

(iii) Vertical Tube Bed. Motion of bubbles causes particle jets in their wakes. In a horizontal tube arrangement, the jets impact on the tubes directly and result in erosion. However in vertical tube arrangement, motion of particles is tangential to the tube orientation and erosion could be reduced since it avoids the direct impact of the particle and large variation in velocity. Figure 11 is a two-dimensional bed model which contains 5 vertical tubes. Tube solidity is 16.7 percent which is the same as the bed containing the smaller horizontal tubes in Fig. 10. The tube model simulates a tube of diameter 2.55 cm and a length of 38.25 cm. Operating conditions are the same as presented in Table 1.

Computed frequencies at the lower end of the tubes are very close to those of horizontal tubes, about 3 Hz and the frequencies of the upper end are slightly lower than those of the lower end due to coalescence of the bubbles. Particles move tangentially to the tubes and have lower normal impact velocity as shown in Fig. 11 due to the influence of the tube orientation; therefore lower tube erosion is produced as shown in Table 2. The highest average erosion rate of vertical tubes is 166 μm/1000 hr; compared to the horizontal tube of 315 μm/1000 hr, and therefore a vertical tube has approximately one half the erosion of the horizontal tube. This would suggest that vertical tubes could be used to avoid the direct impact of the particles on the tubes and to reduce tube erosion.

(iv) AFBC and PFBC. Variation of pressure in fluidized bed combustors may result in different size bubbles and flow fields and therefore produce different tube erosion. AFBC has

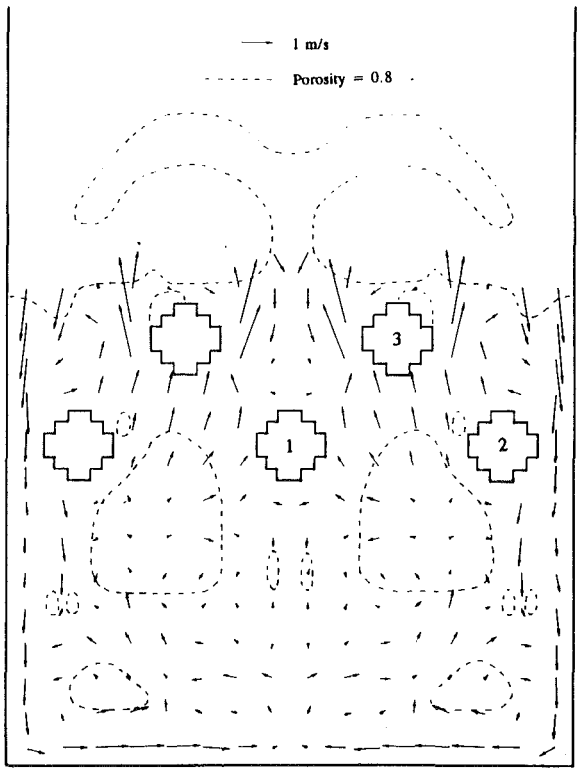

Fig. 12 Computed porosity and particle velocity vector plots of AFBC at 1.3 s

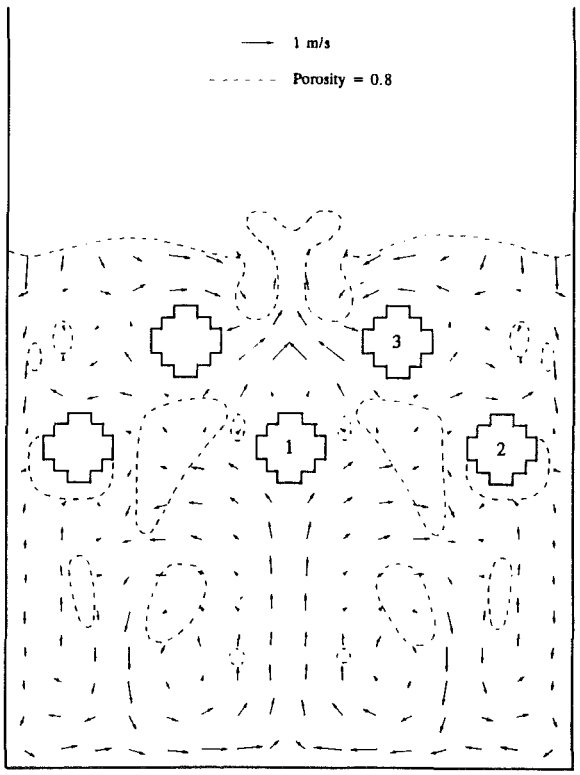

Fig. 13 Computed porosity and particle velocity vector plots of PFBC at 1.3 s

lower pressure which results in lower drag force so that fluidizing velocity has to be increased; this may result in larger bubbles which cause higher particle jets in their wakes and thus give rise to higher tube erosion. However, an increase of

the operating pressure (PFBC) results in an increase of the drag force, and therefore lower fluidizing velocity with the same drag force. This could result in smaller bubbles and reduced erosion. Hydrodynamics and erosion of AFBC and PFBC were analyzed by the simulation of a bed, 40.8 cm wide containing 5 multi-square tubes. In the computation, particle diameter was 800 μm and the air temperature was 871 °C. Exit pressure is 1 atm for AFBC and 10 atm for PFBC. Superficial fluidizing velocity is uniform at 1 m/s for AFBC and 0.599 m/s for PFBC in order to maintain the same drag force as AFBC.

Computed bubble frequencies around the tubes for both AFBC and PFBC are 4–5 Hz. It indicates that increase of pressure does not significantly influence the circulation rate of particles. However, the bubble sizes are quite different as shown in Figs. 12 and 13. The bubbles are much smaller in PFBC than in AFBC so that the particle jets in PFBC are much lower. The jet velocity is about 1 m/s in PFBC and 2 m/s in AFBC. The smaller bubbles may improve the heat transfer and make particles interact well so that SO_2 may be removed more efficiently. In addition, PFBC can either be designed to be smaller or convert more energy since the gas mass flux in this case is higher.

The tube erosion rates for both AFBC and PFBC were averaged from 1.0 to 2.0 s in order to eliminate the influence of slugging flow of AFBC since it occurs before 0.7 s. This behavior may result from uniform porosity at the initial and higher fluidizing velocities, but it disappears after 0.7 s. Slugging was minimum for PFBC. Computed erosion rate of the upper level tubes in the AFBC is 436 μm/1000 hr as shown in Table 2; however that of the PFBC is 162 μm/1000 hr, more than two times lower. The threshold velocity has a significant effect in PFBC because of the lower particle velocity, as shown in Table 2. The higher erosion of AFBC results from the higher particle jets caused by the larger bubbles. This result concludes that increasing the pressure decreases the erosion rates and improves bed dynamics, a result which has already been observed by several researchers.

8 Conclusions

Hydrodynamics and erosion of fluidized bed combustors containing tubes have been analyzed and compared to one another for a given fluidized bed configuration and operating conditions through the use of the computer model which has been developed here. Computed results show that the bed configuration and the operating pressure have significant effects on the bed dynamics and tube erosion and also show the flexibility and reliability of the computerized hydrodynamic model.

Threshold velocity has been used to modify the Finnie model. Computed results show that the threshold velocity has a significant effect on erosion prediction, particularly at lower impact velocity. The modified model predicts erosion closer to the experimental values (Podolski et al., 1991) than the Finnie model. The comparison of two types of tube models indicates that the multi-square tube model results in better hydrodynamic results which are closer to the experimental data. Moreover the predicted erosion is in good agreement with experiments (Podolski et al., 1991). This leads to the conclusion that the computation should be performed (if possible) for circular tubes; however prohibitive computational time is necessary.

The computed results of horizontal tubes for different distributor-tube space indicate that the larger distance from distributor to the tubes may result in larger bubbles which cause higher jets and higher tube erosion. Therefore, the tubes should be brought as close as possible to the distributor plate to avoid establishing a larger bubble size. The hydrodynamics simulation for the beds containing different tube arrangements indicates that the smaller tubes could reduce bubble size due to the smaller tube spacing and the smaller change of the cross-sectional area of the tubes and thus could produce lower erosion. This may imply that smaller size tubes should be used to reduce bubble size within the tube banks and to reduce erosion. Hydrodynamics and erosion computations for vertical tubes indicate that the orientation of the tubes has significant effect on the erosion process to the tubes. Vertical tubes could produce lower erosion since particles travel tangentially to the tubes.

The simulation of Atmospheric Fluidized Bed Combustor (AFBC) and Pressurized Fluidized Bed Combustor (PFBC) shows some advantages of PFBC over AFBC. PFBC produces smaller bubbles, lower particle jets and lower tube erosion. In addition, the smaller PFBC can be designed because of higher gas mass flux. In another words, PFBC has larger energy conversion capacity.

Most of the conclusions reached here have already been discovered experimentally. The purpose of this paper is to demonstrate the flexibility of utilizing this model for future research and design.

Acknowledgment

The computation has been supported by Pittsburgh Supercomputing Center. The authors acknowledge the help of Dr. Frances Bauer and Edward Friedman at Academic Computing Facility of New York University.

References

Almstedt, A. E., and Zakkay, V., 1990, "An Investigation of Fluidized-Bed Scaling Capacitance Prob Measurements in a Pressurized Fluidized-Bed Combustor and a Cold Model Bed," *Chemical Engineering Science*, Vol. 45, No. 4, pp. 1071–1078.

Bitter, J. G. A., 1963, "A Study of Erosion Phenomena, Part 1," *Wear*, Vol. 6, pp. 5–21.

Bitter, J. G. A., 1963, "A Study of Erosion Phenomena, Part 2," *Wear*, Vol. 6, pp. 169–191.

Bouillard, J. X., Lyczkowski, R. W., Floga, S., Gidaspow, D., and Berry, G. F., 1989, "Hydrodynamics of Erosion of Heat Exchanger Tubes in Fluidized Bed Combustors," *The Canadian Journal of Chemical Engineering*, Vol. 67, Apr.

Chang, S. L., Lyczkowski, R. W., and Berry, G. F., 1991, "Spectral Dynamics of Computer-Simulated Two-Dimensional Few-Tube Fluidized Bed Combustors," *International Journal of Heat Mass Transfer*, Vol. 34, No. 7, pp. 1773–1781.

Davies, R. M., 1949, "The Determination of Static and Dynamic Yield Stress Using a Steel Ball," *Proc. Royal Society of London*, series A, Vol. 197, London, pp. 416–432.

Engel, P., 1978, *Impact Wear of Materials*, Elsevier Scientific Publishing Company, Amsterdam.

Ergun, S., 1952, "Fluid Flow Through Packed Columns," *Chemical Engineering Progress*, Vol. 48, No. 2, pp. 89–94.

Ettehadieh, B., Gidaspow, D., and Lyczkowski, R. W., 1984, "Hydrodynamics of Fluidization in a Semicircular Bed with a Jet," *AIChE Journal*, Vol. 30, No. 4, pp. 529–536.

Finnie, I., 1958, "The Mechanism of Erosion of Ductile Metals," *Proc. 3rd U.S. National Congress of Applied Mechanics, Wear*, pp. 527–532.

Finnie, I., 1960, "Erosion of Surfaces by Solid Particles," *Wear*, Vol. 3, pp. 87–103.

Gidaspow, D., and Syamlal, M., 1985, "Solid-Gas Critical Flow," 74e, AIChE Annual Meeting, Vol. 9, Chicago.

Harlow, F. H., and Amsden, A. A., 1975, "Numerical Calculation of Multiphase Fluid Flow," *Journal of Computational Physics*, Vol. 17, pp. 19–52.

Hashish, M., 1987, "An Improved Model of Erosion by Solid Particle Impact," *Proc. 7th Int. Conf. on Erosion by Liquid and Solid Impact*, J. E. Field and J. P. Dear, eds., Cambridge, England, pp. 66-1–66-9.

Hutchings, I. M., Winter, R. E., and Field, J. E., 1976, "Solid Particle of Metals: The Removal of Surface Material by Spherical Projectiles," *Proc. Roy. Soc., London Series A*, Vol. 348, pp. 379–392.

Jaeger, J. C., 1956, *Elasticity, Fracture and Flow*, Wiley, pp. 89–95.

Johnson, K. L., 1985, *Contact Mechanics*, Chambridge University Press, pp. 18–28.

Kunii, D., and Levenspiel, O., 1969, *Fluidization Engineering*, Wiley, New York, p. 65.

Laudau, L. D., and Lifshitz, E. M., 1986, *Theory of Elasticity*, 3rd Edition, Vol. 7, Oxford, pp. 26–31.

Levy, A. V., Wang, B. Q., and Geng, G. Q., 1989, "Characteristics of Erodent Particles in Fluidized Bed Combustors," *Proc. 1989 Int. Conf. on Fluidized*

Bed Combustion, A. M. Manaker, ed., Vol. 2, ASME, New York, pp. 945–951.

Levy, E. K., and Stallings, J. W., 1991, "Tube Erosion in Bubbling Fluidized Beds," *Proc. 1991 Int. Conf. on Fluidized Bed Combustion*, J. E. Anthony, ed., Vol. 3, ASME, pp. 1139–1144.

Li, C., 1993, "Hydrodynamics and Erosion Modeling of Fluidized Bed Combustors Containing Tubes," Ph.D. thesis, Department of Applied Science, New York University.

Lyczkowski, R. W., Bouillard, J. X., Berry, G. F., and Gidaspow, D., 1987, "Erosion Calculations in a Two-Dimensional Fluidized Bed," *Proc. 1987 Int. Conf. on Fluidized Bed Combustion*, J. P. Mustonen, ed., Vol. 2, American Society of Engineers, New York, pp. 697–706.

Lyczkowski, R. W., Gamwo, I. K., and Dobran, F., 1991, "Comparison of Experimental and Computed Solids Motion and Bed Dynamics for Fluidized Bed Containing Obstacles," *Proc. 1991 Int. Conf. on Fluidized Bed Combustion*, E. J. Anthony, ed., Vol. 1, ASME, pp. 325–333.

Neilson, J. H., and Gilchrist, A., 1968, "Erosion by a Stream of Solid Particles," *Wear*, Vol. 11, pp. 112–122.

Popov, E. P., 1976, *Mechanics of Materials*, 2nd Ed., Prentice-Hall, pp. 235–248.

Podolski, W. F., Reimann, K. J., Swift, W. M., and Carls, E. L., 1987, "Metal Wastage in Fluidized-Bed Combustors," *Proc. 1989 Int. Conf. on Fluidized Bed Combustion*, A. M. Manaker, ed., Vol. 2, ASME, New York, pp. 837–846.

Podolski, W. F., Lyczkowski, R. W., and Montrone, E., 1991, "A Study of Parameters Influencing Metal Wastage in Fluidized Bed Combustion," E. J. Anthony, ed., Vol. 2, ASME, pp. 609–617.

Rickerby, D. G., and Macmillan, N. H., 1980, "On the Oblique Impact of a Rigid Sphere Against a Rigid-Plastic Solid," *Int. J. Mech. Sci.*, Vol. 22, pp. 491–494.

Rivard, W. R., and Torrey, M. D., 1979, "K-FIX: A Computer Program for Transient Two Fluid Flow—THREED: An Extension of the K-FIX Code for Three-Dimensional Calculations, Los Alamos Scientific Laboratory Report LA-NUREG-6623, Supplement 2, (Jan.).

Sethi, V. K., Wright, I. G., Dooley, R. B., Stallings, J. W., Stringer, J., and Wheeldon, J. M., 1991, "Relative Performance of Wear Control Strategies for Evaporator Tube Wastage in FBCs," *Proc. 1991 Int. Conf. on Fluidized Bed Combustion*, E. J. Anthony, ed., Vol. 2, ASME, pp. 737–742.

Sriram, T. S., and Kosel, T. H., 1987, "Computer Modeling of the Rebound Characteristics of Spherical Erodent Particles," *Proc. 7th Int. Conf. on Erosion by Liquid and Solid Impact*, Cambridge, England, pp. 67-1 to 67-8.

Stringer, J., 1987, "Current Information on Metal Wastage in Fluidized Bed Combustiors," *Proc. 1987 Int. Conf. on Fluidized Bed Combustion*, J. P. Mustonen, ed., Vol. 2, American Society of Engineers, New York, pp. 685–696.

Vincent, R. Q., Poston, J. M., and Smith, B. F., 1987, "Erosion Experience of the TVA 20-MW AFBC Boiler," *Proc. 1987 Int. Conf. on Fluidized Bed Combustion*, J. P. Mustonen, ed., Vol. 2, American Society of Engineers, New York, pp. 672–684.

Zakkay, V., Sellakumar, K. M., Radhakrishnan, R., and McClung, J. D., 1986, "Vertical Heat Exchanger for High Pressure Fluidized Bed Coal Combustors," *Energy Progress*, Vol. 6, No. 4, Dec., pp. 248–253.

Zakkay, V., and Krishna Sastri, V. M., 1987, "Modeling of Boiler Tube Erosion in Fluidized Bed Combustor," Department of Applied Science, New York University.

Predrag Marjanović
Senior Research Fellow,
Centre for Industrial Bulk Solids Handling,
Department of Physical Sciences,
Glasgow Caledonian University,
Cowcaddens Road,
Glasgow G4 0BA, United Kingdom

Vladan Djordjević
Head of Fluid Mechanics Department,
Faculty of Mechanical Engineering,
University of Belgrade,
27.marta 80, 11000 Belgrade, Yugoslavia

On the Compressible Flow Losses Through Abrupt Enlargements and Contractions

The well-known structure of incompressible flow through abrupt enlargements and contractions is applied to the subsonic compressible flow through the same area change. Using the basic system of equations for 1-D model of flow, both cases are solved for adiabatic and isothermal conditions. The changes for all flow parameters (M, v, p, p_0, T, T_0, s) are obtained analytically and shown graphically. The results are compared with the available experimental data.

1 Introduction

Exact, or at least accurate prediction of separation losses that occur in a pipe, whenever its area or its direction is changed, is of invaluable importance for any engineer who is involved in calculation of fluid flow in pipes. Head loss due to separation of fluid flow from the walls of a pipe makes a constitutive part of the generalized Bernoulli's equation, without which even a very simple problem of fluid flow through pipes can hardly be solved. As is well known from a basic fluid mechanics course, the generalized Bernoulli's equation is derived from the momentum equation, or, more precisely, from its differential form when it is integrated between two characteristics cross-sections of the pipe. Consequently, head loss due to separation can only be accurately deduced if all the terms in the momentum equation are known, and, in particular, if the reaction force, i.e., the force which the fluid exerts on the pipe walls, is known. Thus, the accurate value of the reaction force represents the key parameter for an analytic evaluation of the separation loss. In general, due to the complicated, usually 3-D structure of the flow in separation losses, it is not possible to predict its value. Hence, the corresponding head loss in Bernoulli's equation cannot be predicted either, and can be determined only by experiments.

However, there are two exceptions: the flow in an abrupt enlargement (Fig. 1) and the flow in an abrupt contraction with a Borda mouthpiece (Fig. 2(*a*)). In both of these the reaction force consists mainly of the pressure force exerted on the annular area. In the first case, the pressure over the annular area is approximately uniform and equal to the pressure in upstream station 1, while in the second case, it is approximately equal to the total pressure in station 1. For an incompressible flow the corresponding reaction forces straightforwardly lead to the following expressions for the head loss:

$$Y_l=\frac{1}{2}(v_1-v_2)^2 \quad \text{— for abrupt enlargement (Borda-Carnot formula)}$$

$$Y_l=\frac{1}{2}v_2(v_2-v_1) \quad \text{— for the abrupt contraction with a Borda mouthpiece } (l>D_2/2)$$

where v_1 and v_2 are mean velocities in stations 1 and 2, respectively.

As far as we know, the problem of a subsonic compressible flow through sudden area changes, whose structure can be

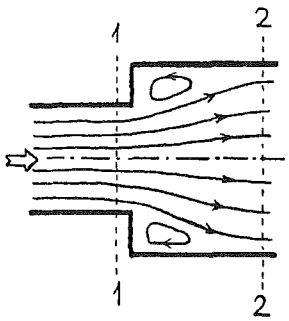

Fig. 1 Flow through an abrupt enlargement

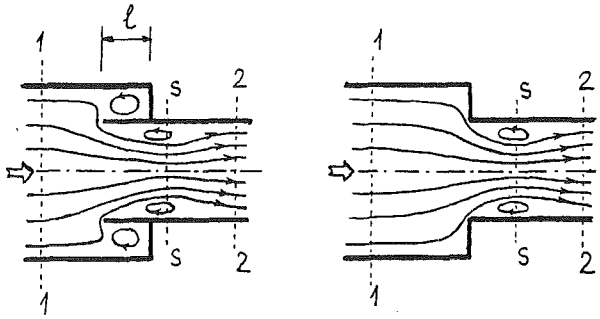

Fig. 2 Flow through an abrupt contraction

Contributed by the Fluids Engineering Division for publication in the JOURNAL OF FLUIDS ENGINEERING. Manuscript received by the Fluids Engineering Division January 17, 1993; revised manuscript received February 23, 1994. Associate Technical Editor: R. W. Metcalfe.

supposed to be very similar to the incompressible flow and for which the corresponding reaction force attains approximately the same values, has been only partially and incompletely treated in the existing literature, for example, Hall and Orme (1952) or numerous papers by Benedict et al. (1966–1980). In this paper, the complete theory of that problem for both adiabatic and isothermal flow conditions is presented. For the flow through a sudden contraction, the problem of choking is also discussed, and the upstream critical Mach number is evaluated.

2 Flow Model

A one-dimensional model of flow has been adopted here for studying the problem, with two characteristic stations: 1 (before the area change) and 2 (after the area change, when fluid flow is reattached to the pipe wall). At the same time, the subsonic case is considered and hence the static pressure at the face of the step is equal either to p_1 (for abrupt enlargement) or to p_{01} (for abrupt contraction with Borda mouthpiece). Both values were confirmed experimentally, for instance by Benedict (1966b).

For each of the two cases of area change, both adiabatic and isothermal flow are considered in conjunction with the ideal gas law:

$$\frac{p_1}{\rho_1 T_1}=\frac{p_2}{\rho_2 T_2}=R \tag{1}$$

and conservation of mass:

$$\dot{m}=\rho_1 v_1 A_1=\rho_2 v_2 A_2 \tag{2}$$

There are various ways to present the obtained analytical solutions, some of which have been used in already published papers and textbooks. However, the most suitable way to present, analyze and use the results in practice is to express the simple ratio of the values of a variable after and before the area change as a function of the gas property (γ), area ratio (A), and upstream Mach numbe (M_1):

$$\frac{x_2}{x_1}=f(\gamma, A, M_1)$$

This form is used for all four cases that are considered in this paper, which enables the simple comparison of the results.

3 Abrupt Enlargement

For this type of area change (Fig. 1) the conservation of momentum is

$$-p_1(A_2-A_1)=p_1A_1-p_2A_2+\dot{m}(v_1-v_2) \tag{3}$$

The fourth equation is dependent upon the thermodynamic conditions of the flow. For the sake of simpler presentation, the area ratio $A=(A_2/A_1)>1$ is used.

3.1 Adiabatic Flow. When the gas flows through a thermally insulated pipe, the flow can be considered as adiabatic ($T_0=$ const) and therefore the conservation of energy stays as

$$\frac{\gamma}{\gamma-1}\frac{p_1}{\rho_1}+\frac{v_1^2}{2}=\frac{\gamma}{\gamma-1}\frac{p_2}{\rho_2}+\frac{v_2^2}{2} \tag{4}$$

A quadratic equation appears when solving the presented set of equations. It is interesting to note that one of the possible solutions actually corresponds to the shock wave case in a pipe, as then $A_1=A_2$ and all governing equations have an identical form as in the flow through a shock. Of course, this solution has been rejected in this context.

The obtained results are presented in the following way:

$$\frac{v_2}{v_1}=F_1 \tag{5}$$

$$\frac{\rho_2}{\rho_1}=\frac{1}{F_1 A} \tag{6}$$

$$\frac{p_2}{p_1}=\frac{F_2}{F_1 A} \tag{7}$$

$$M_2=M_1\frac{F_1}{\sqrt{F_2}} \tag{8}$$

$$\frac{p_{02}}{p_{01}}=\frac{F_2}{F_1 A}\left(\frac{1+\frac{\gamma-1}{2}\frac{F_1^2}{F_2}M_1^2}{1+\frac{\gamma-1}{2}M_1^2}\right)^{\gamma/\gamma-1} \tag{9}$$

$$\frac{T_2}{T_1}=F_2 \tag{10}$$

$$\frac{s_2-s_1}{R}=\frac{1}{\gamma-1}\ln\left(\frac{T_2}{T_1}\right)^{\gamma}\left(\frac{p_1}{p_2}\right)^{\gamma-1}=\ln\frac{p_{01}}{p_{02}} \tag{11}$$

Both F_1 and F_2 depend upon γ, A, and M_1 and are given in the Appendix. All ratios in Eqs. (5) to (11) can now be easily tabulated or presented graphically.

The majority of the results for this case have been already known theoretically and confirmed experimentally by Hall and Orme (1952) and by Benedict et al. in a number of papers and books (1966–1980). Here attention will be paid to an interesting result concerning the density changes. It can be seen from Eqs. (3) and (4) that the velocity decrease causes both pressure and temperature increases. The change of density, however, depends on the rate of change of both pressure and temperature. It can be shown that there is a characteristic area ratio

$$A_c=\frac{\gamma+1}{\gamma-1}\quad(=6 \text{ for air}) \tag{12}$$

at which, regardless of M_1, fluid does not change its density and hence its velocity changes in an "incompressible manner" ($v_1/v_2=A_c$). The change of density (Eq. (6)) is presented in Fig. 3 (full lines) for three different inlet Mach numbers and this characteristic value can be seen quite clearly. Therefore, when gas flows through a sudden enlargement under adiabatic conditions, it either compresses (for $A<A_c$), when pressure increase prevails upon temperature increase, or expands (for $A>A_c$), when the temperature increase is the dominant factor.

Nomenclature

A = area, m^2
c = specific heat capacity, J/kgK
k = coefficient
M = Mach number
$\dot{m}$ = mass flow rate, kg/s
p = static pressure, N/m^2
p_0 = total pressure, N/m^2
q = heat exchange rate, J/kg
R = gas constant, J/kgK
s = entropy, J/kgK
T = static temperature, K
T_0 = total temperature, K
v = gas velocity, m/s
Y_l = head loss, J/kg
γ = c_p/c_v
ρ = gas density, kg/m^3
ψ = coefficient of contraction

Subscripts

1 = inlet conditions
2 = outlet conditions
c = critical conditions
s = vena contracta

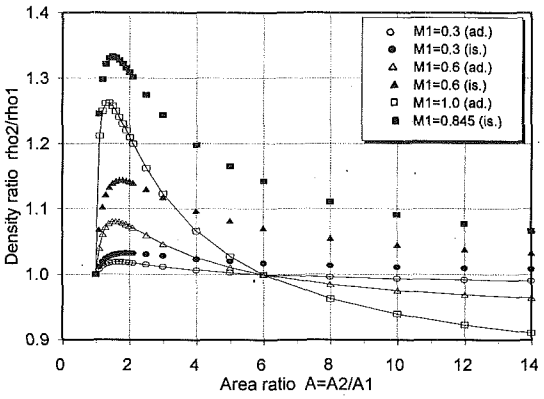

Fig. 3 The influence of area ratio A and inlet Mach number M_1 on the gas density change for adiabatic and isothermal flow through abrupt enlargement

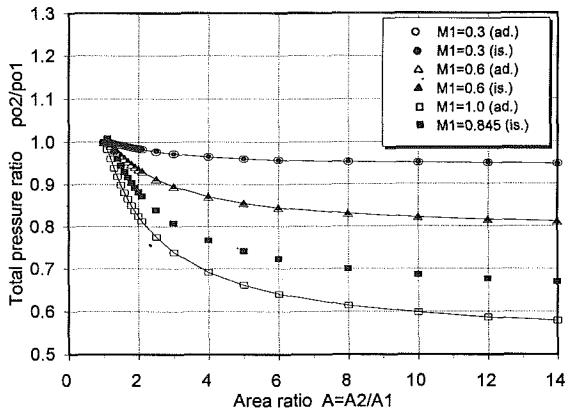

Fig. 5 The influence of area ratio A and inlet Mach number M_1 on the total pressure change for adiabatic and isothermal flow through abrupt enlargement

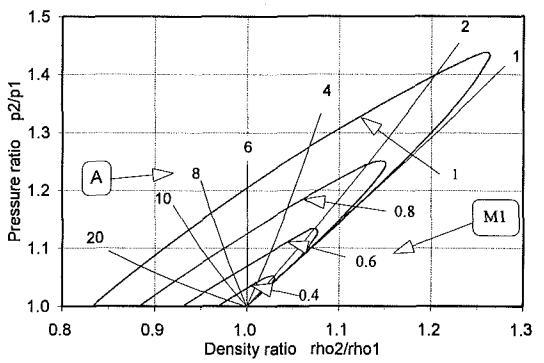

Fig. 4 The influence of area ratio A and inlet Mach number M_1 on the gas density and pressure change for adiabatic flow through abrupt enlargement

As far as the equation of continuity is concerned, it means that for a large ratio A, an obvious velocity drop is not sufficient to keep that gas flow rate constant, and a density decrease is required. However in any case, the gas density does not change dramatically and, for most values of A and M_1 it varies within ± 10 percent. The only exception is the combination of a very high inlet Mach number M_1 and a very low area ratio A where that change just exceeds 20 percent (the absolute maximum is $(\rho_2/\rho_1)_{max} = 1.2632$ for $A = 1.357$ and $M_1 = 1$).

The absolute maximum of the static pressure ratio $(p_2/p_1)_{max} = 1.4387$ occurs at $M_1 = 1$ and the slightly higher area ratio $A = 1.523$. All local maximum values of density and static pressure (for $M_1 = \text{const.}$) occur at different values of area ratio A. This can also be elucidated in another type of diagram (Fig. 4), which usefully and instantaneously gives values for change of pressure and density for the given enlargement (A) and inlet conditions (M_1).

Finally, a diagram representing the influence of M_1 and A onto the total pressure is given in Fig. 5. This is presented in order to predict the energy loss in this case, as well as for the comparison with the isothermal flow through the same configuration.

3.2 Isothermal Flow. When the pipe is not insulated, intensive heat transfer with surroundings occurs and hence, $T = \text{const.}$ In order to solve this problem, a set of three equations (1)–(3) is used, which, as for the adiabatic conditions, will give one solution in the supersonic region that cannot be used as the assumption for the reaction force is not valid. The other solution, for subsonic flow, can be presented as follows:

$$\frac{v_2}{v_1} = F_3 \tag{13}$$

$$\frac{\rho_2}{\rho_1} = \frac{p_2}{p_1} = \frac{1}{F_3 A} \tag{14}$$

$$M_2 = F_3 M_1 \tag{15}$$

$$\frac{T_{02}}{T_{01}} = \frac{1 + \frac{\gamma - 1}{2} F_3^2 M_1^2}{1 + \frac{\gamma - 1}{2} M_1^2} \tag{16}$$

$$\frac{p_{02}}{p_{01}} = \frac{1}{F_3 A} \left(\frac{1 + \frac{\gamma - 1}{2} F_3^2 M_1^2}{1 + \frac{\gamma - 1}{2} M_1^2} \right)^{\gamma/\gamma - 1} \tag{17}$$

$$\frac{s_2 - s_1}{R} = \ln \frac{p_1}{p_2} = \ln (F_3 A) \tag{18}$$

The parameter $F_3 = f(\gamma, A, M_1)$ is given in the Appendix. As with isothermal flow in a constant area pipe (Rayleigh flow), when friction losses are encountered only, the characteristic Mach number $M = 1/\sqrt{\gamma}$ ($= 0.8452$ for air) occurs too.

The analysis of all ratios obtained can be carried out in the same way as for the adiabatic flow. In this paper, only the change of density (here identical to the change of static pressure) in Fig. 3 and the change of total pressure in Fig. 5 are shown (in both cases only with symbols). For the majority of values of M_1 and A, the behavior of the change of the flow parameters for adiabatic and isothermal flow is very similar and the difference in actual values of the ratios is in the order of a few percent.

However, apart from the already mentioned characteristic Mach number, which in isothermal flow takes the place that critical Mach number has in adiabatic flow, there are two other qualitative differences. The first one can easily be seen from Fig. 3; for the isothermal flow through the abrupt enlargement the gas density will always increase as the pressure increases and temperature remains constant. For the same values of M_1 and A, that increase of density is higher for isothermal flow. The local maximum values appear at different values for area ratio A and inlet Mach number M_1; the absolute maximum here is $(\rho_2/\rho_1)_{max} = (p_2/p_1)_{max} = 1.3333$ for $M_1 = 0.8452$ and $A = 1.5$.

The other difference appears for the change of total pressure at the area ratio close to unity (see Fig. 6). For those ratios a very small increase in total pressure is obtained by this one dimensional approach. It results as the consequence of the

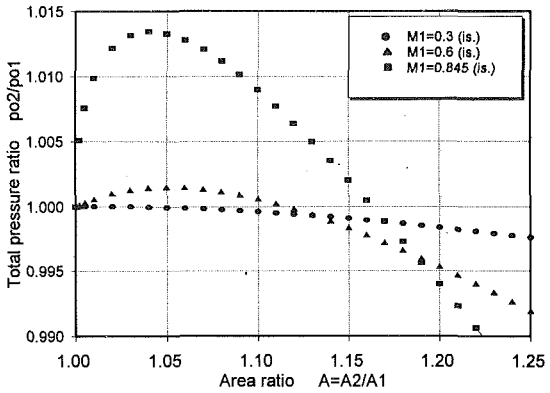

Fig. 6 The total pressure change for isothermal flow through abrupt enlargement with the small area ratio

overwhelming influence of pressure increase, compared with the decrease of Mach number.

As the total temperature decreases here, it is obvious that in this case gas emits heat to the surroundings. The heat exchange rate can be calculated from the conservation of energy:

$$q=\frac{1}{2}(v_2^2-v_1^2) \tag{19}$$

4 Abrupt Contraction

There are two basic designs for an abrupt contraction: with or without a Borda mouthpiece (see Fig. 2). The difference between those two designs, from the point of view of the flow model which has been adopted here, is in the reaction force on the face plane. This force depends upon the pressure at that surface which is equal to total pressure p_{01} if the Borda mouthpiece is incorporated (with $l>D_2/2$) and is less than p_{01} for the other design. However, it is not possible to determine the exact value of this latter pressure and hence to predict the exact value of the reaction force in the momentum equation. Therefore, the analytical procedure will be carried out only for the first design (Fig. 2(a)). Unfortunately, there are no experimental data for this design which could be used for the verification of the obtained results. For the second design (Fig. 2(b)), there are some published expressions, based predominately on the empirical data. The experimental data obtained by Benedict et al. (1966b) and Benedict (1980) will be used in this paper in the first instance for the qualitative verification of the results obtained for the flow through an abrupt contraction with the Borda mouthpiece, and then, to a certain extent, for the quantitative analysis of the same results.

Unlike the enlargements, the flow in the contractions may be choked and therefore one of the targets in this paper is to determine either maximum inlet Mach number M_1 for a given area ratio $A=(A_1/A_2)>1$ or a maximum area ratio for a given inlet Mach number. However, due to the flow pattern in the contraction, the sonic flow will appear at the station s (vena contracta) first, and the coefficient of contraction should be taken into account. Its theoretical value, for inviscid flow and very high area ratio, is given by Kirchof, published by Milne-Thomson (1955):

$$\psi=\frac{A_s}{A_2}=\frac{\pi}{\pi+2}=0.611 \tag{20}$$

However, it does depend strongly upon the area ratio A, specially when A is closer to unity, as then only a partial contraction occurs. That dependence can be obtained only by experiments, and only two examples are given here:

— by Weissbach, published by Benedict (1980):

$$\psi=0.61375+\frac{0.13318}{A^2}-\frac{0.26095}{A^4}+\frac{0.51146}{A^6} \tag{21}$$

— by Altshul (1982):

$$\psi=0.57+\frac{0.043A}{1.1A-1} \tag{22}$$

Apart from the difficulty which arises when this or similar relations are used in the basic system of equations, applied for stations 1 and s, there is another, more severe problem. Namely, it is impossible to define the reaction force on the control volume chosen between those two stations. Therefore, the basic system of equations will be applied here on the flow between stations 1 and 2, but the choked flow conditions (i.e., when the downstream Mach number M_2 is close to unity) will be excluded from the domain of application. These choked flow conditions will be approximately determined using one of the empirical expressions for the coefficient of contraction ψ.

Regarding the used notation, all basic equations for stations 1 and 2 will remain identical as for abrupt enlargement, apart from the conservation of momentum, which is here:

$$kp_{01}(A_1-A_2)=p_1A_1-p_2A_2+\dot{m}(v_1-v_2) \tag{23}$$

where coefficient $k=1$ (for Borda mouthpiece, Fig. 2(a)) or else $k<1$, as discussed earlier.

4.1 Adiabatic Flow. This flow model is defined by four basic equations: ideal gas law (Eq. (1)), conservation of mass (Eq. (2)), energy (Eq. (4)) and momentum (Eq. (23)). The results are as follows:

$$\frac{v_2}{v_1}=\frac{F_4(1-F_5)}{M_1^2A} \tag{24}$$

$$\frac{\rho_2}{\rho_1}=\frac{M_1^2A^2}{F_4(1-F_5)} \tag{25}$$

$$\frac{p_2}{p_1}=F_4(1+\gamma F_5) \tag{26}$$

$$M_2=\sqrt{\frac{1-F_5}{1+\gamma F_5}} \tag{27}$$

$$\frac{T_2}{T_1}=\frac{F_4^2}{M_1^2A^2}(1+\gamma F_5)(1-F_5) \tag{28}$$

$$\frac{p_{02}}{p_{01}}=F_4(1+\gamma F_5)\left(\frac{1+\frac{\gamma-1}{2}\frac{1-F_5}{1+\gamma F_5}}{1+\frac{\gamma-1}{2}M_1^2}\right)^{\gamma/\gamma-1} \tag{29}$$

$$\frac{s_2-s_1}{R}=\ln\frac{p_{01}}{p_{02}} \tag{30}$$

As in the previous cases, both F_4 and F_5 depend on γ, A and M_1 and are included in the Appendix. The diagrams which represent the change of Mach number, density and total pressure are given in Figs. 7, 8, and 9. The theoretical boundary ($M_2=1$) has been drawn with dashed lines; the real limit ($M_s=1$) will be discussed later. The theoretical maximum value of the area ratio, at which is $M_2=1$, can be obtained by solving Eq. (27):

$$A_{th}=\left(\frac{A_1}{A_2}\right)_{th}=$$

$$=\frac{(1+\gamma M_1^2-F_A)\{F_A+M_1\sqrt{(\gamma+1)[2+(\gamma-1)M_1^2]}\}}{(\gamma+1)[2+(\gamma-1)M_1^2]M_1^2-F_A^2} \tag{31}$$

where the parameter $F_A=f(\gamma, A, M_1)$ is given in the Appendix. Equation (31) is presented in Fig. 10 with a dashed line.

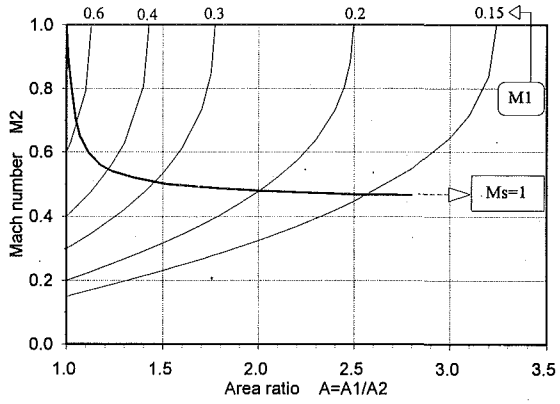

Fig. 7 The influence of area ratio A and inlet Mach number M_1 on the outlet Mach number M_2 for adiabatic flow through abrupt contraction

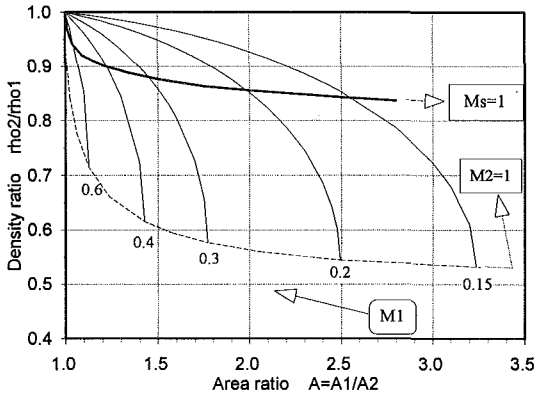

Fig. 8 The influence of area ratio A and inlet Mach number M_1 on the gas density change for adiabatic flow through abrupt contraction

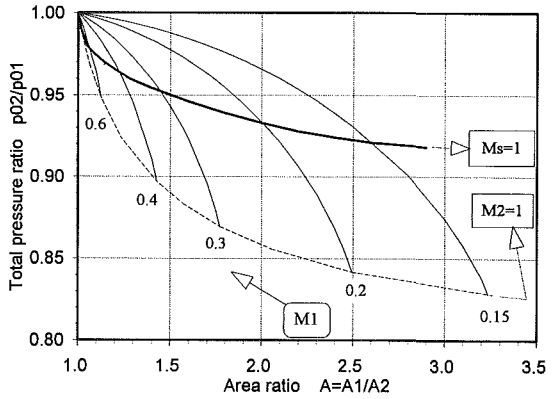

Fig. 9 The influence of area ratio A and inlet Mach number M_1 on the total pressure change for adiabatic flow through abrupt contraction

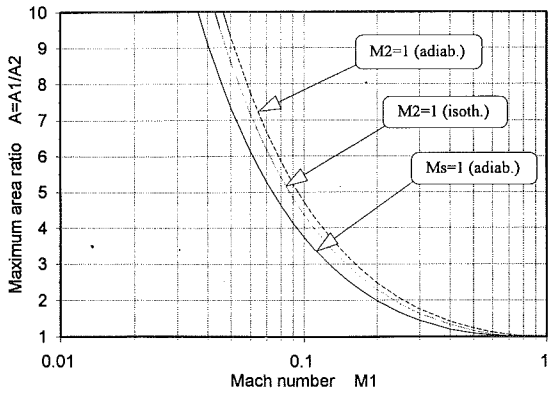

Fig. 10 The maximum area ratio $A = A_1/A_2$ for abrupt contraction and different flow conditions

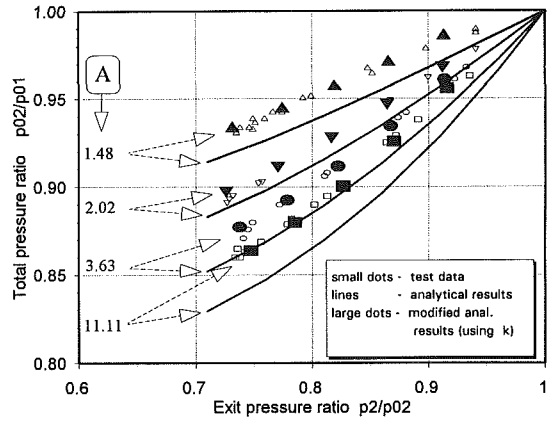

Fig. 11 The comparison of the analytical solutions with the experimental data (Benedict et al., 1966b) for adiabatic flow through abrupt contraction

In order to find the effect of the flow contraction, three basic equations should be applied to the stations 1 and s. There are two possible ways of defining station s: by area A_s or by area A_2. The problem with the first one lies in the application of the conservation of momentum, as neither the area of the jet between the inlet of the smaller bore pipe and station s, nor the pressure at that surface can be determined (the pressure changes along the surface, too). Therefore, it is not possible in this case to predict the reaction force within a 1-D flow model.

The only assumption which has to be made in the second case is that the pressure at station s, which incorporates the whole area of the smaller bore pipe, is constant and equal to the static pressure p_s of the core flow. Then, the set of the basic equations will be:

$$kp_{01}\left(A_1-\frac{A_s}{\psi}\right)=p_1A_1-p_s\frac{A_s}{\psi}+\dot{m}(v_1-v_s) \tag{32}$$

$$\dot{m}=\rho_1v_1A_1=\rho_sv_sA_s \tag{33}$$

$$\frac{\gamma}{\gamma-1}\frac{p_1}{\rho_1}+\frac{v_1^2}{2}=\frac{\gamma}{\gamma-1}\frac{p_s}{\rho_s}+\frac{v_s^2}{2} \tag{34}$$

As this set of equations is used only to determine the choked flow conditions ($M_s=1$), the solution for Mach number M_s is the only one which is interesting:

$$M_s=\sqrt{\frac{1}{\psi}\frac{1-F_{5s}}{1+\gamma F_{5s}}} \tag{35}$$

where $F_{5s}=f(\gamma, A, M_1)$ is included in the Appendix. In order to determine the real maximum area ratio ($A_{\text{real}}<A_{th}$), an additional equation for coefficient of contraction has to be used (Eq. (22) is used here). Due to the empirical type of this equation, only the iterative procedure can be used. The boundary which represents choked flow conditions is superimposed with full lines onto the diagrams in Figs. 7 to 10.

In order to compare these analytical results with some test data, the results of Benedict (1966b) have been used, as they were carried out under the conditions which are the nearest to the assumptions used in this analysis. However, due to the different design (Benedict used contraction without a Borda mouthpiece) and hence the flow pattern, it was expected that the total pressure ratio p_{02}/p_{01} (Eq. (29)) is less than the measured one. This expectation has been confirmed in Fig. 11, where

the difference between test results (open symbols) and analytical results (lines) is in the order of 1.5 percent (for lower area ratios) to 3 percent (for higher area ratios).

As mentioned earlier, the problem with the simple abrupt contraction is the unknown pressure at the face plane ($p = kp_{01}$, see Eq. (23)). Therefore, two sets of results from Fig. 11 (experimental and analytical) were used to determine the approximate value of k, which should depend on the area ratio A and the flow conditions at station 1. As the latter one is probably of the lesser influence, only the former one was taken into account and a single value for k was determined for each of four area ratios (the iterative procedure was inevitable here, too). The obtained values are: $k = 0.970$ (for $A = 1.48$), $k = 0.990$ (for $A = 2.02$), $k = 0.993$ (for $A = 3.63$) and $k = 0.9975$ (for $A = 11.11$) and some analytical results, modified by using k, are presented in Fig. 11 with filled symbols. Qualitatively, those results are realistic, as k is very close to unity for high area ratio and it decreases as area ratio decreases.

4.2 Isothermal Flow. Using the analogous analytical procedure as in the previous case, the following results are obtained for this flow model:

$$\frac{v_2}{v_1} = \frac{A}{F_6} \tag{36}$$

$$\frac{\rho_2}{\rho_1} = \frac{p_2}{p_1} = F_6 \tag{37}$$

$$\mathrm{M}_2 = \frac{\mathrm{M}_1 A}{F_6} \tag{38}$$

$$\frac{T_{02}}{T_{01}} = \frac{1 + \dfrac{\gamma - 1}{2} \dfrac{A^2 \mathrm{M}_1^2}{F_6^2}}{1 + \dfrac{\gamma - 1}{2} \mathrm{M}_1^2} \tag{39}$$

$$\frac{p_{02}}{p_{01}} = F_6 \left(\frac{1 + \dfrac{\gamma - 1}{2} \dfrac{A^2 \mathrm{M}_1^2}{F_6^2}}{1 + \dfrac{\gamma - 1}{2} \mathrm{M}_1^2} \right)^{\gamma/\gamma - 1} \tag{40}$$

$$\frac{s_2 - s_1}{R} = \ln \frac{p_1}{p_2} = \ln \frac{1}{F_6} \tag{41}$$

where $F_6 = f(\gamma, A, \mathrm{M}_1)$ is given in the Appendix.

If one compares the absolute values of the ratios of different flow parameters for isothermal and adiabatic model of flow, one finds that the difference is in the order of a few percent. For the same area ratio A and inlet Mach number M_1, only velocity v_2 is higher for isothermal flow than the corresponding one for the adiabatic flow; all other outlet flow parameters (M_2, p_2, ρ_2, and p_{02}) are lower. The theoretical maximum value of the area ratio, at which choked flow conditions will occur (when $\mathrm{M}_2 = 1/\sqrt{\gamma}$), is also lower for the isothermal flow; the relationship is obtained in the same way as for the adiabatic flow:

$$A_{th} = \left(\frac{A_1}{A_2} \right)_{th} = \frac{\left(1 + \dfrac{\gamma - 1}{2} \mathrm{M}_1^2 \right)^{\gamma/\gamma - 1} (F_A + 2\mathrm{M}_1 \sqrt{\gamma})}{4\gamma \mathrm{M}_1^2 - F_A^2} \tag{42}$$

This relationship is presented with a dotted line in the Fig. 10. Finally, in this case gas absorbs heat from the surroundings (see Eq. (19)).

5 Application Limits

The basic idea explored in this paper is to apply known flow patterns for 1-D incompressible flow onto 1-D compressible flow. Therefore, the first obvious application limit is on the subsonic flow throughout the whole enlargement or contraction piece. In the case of an enlargement, it means that the inlet Mach number could be $\mathrm{M}_1 \leq 1$. It is very likely that the area ratio does not represent any limit, as the Borda-Carno formula for incompressible flow gives good results even for $A \to \infty$ (outlet of a pipe into a large reservoir).

For the contraction however, due to possible choked flow conditions at the vena contracta, the limit of the inlet Mach number is lower and depends upon the area ratio A (see Fig. 10). The area ratio probably influences the accuracy of the assumption of the value of the reaction force (see Eq. (23) and Fig. 11), depending also on the actual design of the contraction piece.

Generally, the accuracy of the results obtained from the presented 1-D theory for subsonic compressible flow depend upon the correctness of the assumption concerning the reaction force, which is the key to solving the 1-D flow model. The best way to prove the accuracy of this assumption is to compare with the experimental data. This comparison with available experiments has been very encouraging, although more test data are needed over as wide a range of flow and geometric conditions as possible for reliable conclusions. Another possible approach would be to carry out numerical integration of Euler's equations, but it is beyond the scope of this paper, as the main aim here is the application of 1-D model. However, comparison with test data is essential.

6 Conclusions

A complete theory for 1-D subsonic flow model for the flow through the pipes with the abrupt area change is given in this paper and several interesting and useful results have been obtained. For example, it has been shown that gas flows as an incompressible fluid through the abrupt enlargement of the characteristic area ratio A_c, if adiabatic conditions are imposed; the obtained results enable the design of the abrupt enlargement which will provide the maximum static pressure, or alternatively maximum density; the choked flow conditions in the abrupt contraction are analyzed in more detail, etc. As the agreement with the published experimental data is very good, it is proved that the 1-D flow model can be accurate and efficient, if the reaction force can be predicted beforehand. All presented results and conclusions encourage and lead toward the possible application of the 1-D model for other, even more complex flow patterns.

References

Altshul, A. D., 1982, *Hydraulic Resistances*, 2nd edition, Nedra, Moscow (in Russian).

Benedict, R. P., 1966a, "On the Determination and Combination of Loss Coefficients for Compressible Fluid Flows," ASME *Journal of Engineering for Power*, Vol. 88, pp. 67–72.

Benedict, R. P., Carlucci, N. A., and Swetz, S. D., 1966b, "Flow Losses in Abrupt Enlargements and Contractions," ASME *Journal of Engineering for Power*, Vol. 88, pp. 73–81.

Benedict, R. P., 1973, "Some Generalizations in Compressible Flow Characteristics," ASME *Journal of Engineering for Power*, Vol. 95, pp. 65–74.

Benedict, R. P., 1976, "Generalized Flow Across an Abrupt Enlargement," ASME *Journal of Engineering for Power*, Vol. 98, pp. 327–334.

Benedict, R. P., 1980, *Fundamentals of Pipe Flow*, Wiley, New York.

Hall, W. B., and Orme, E. B., 1952, "Flow of a Compressible Fluid Through Sudden Enlargement in a Pipe," *Proceedings of the Institution of Mechanical Engineers*, 1B, pp. 1007–1020.

Milne-Thompson, L. M., 1955, *Theoretical Hydrodynamics*, MacMillan & Co., London, p. 296.

APPENDIX

The following parameters has been used throughout the paper:

$$F_1 = \frac{1}{(\gamma+1)M_1^2}\left[(\gamma M_1^2 + A) - \sqrt{M_1^4 + 2(\gamma A - \gamma - 1)M_1^2 + A^2}\right]$$

$$F_2 = 1 + \frac{\gamma-1}{2} M_1^2 (1 - F_1^2)$$

$$F_3 = \frac{1}{2\gamma M_1^2}\left[(A + \gamma M_1^2) - \sqrt{(A+\gamma M_1^2)^2 - 4\gamma M_1^2}\right]$$

$$F_4 = \frac{1}{\gamma+1}\left[A(1+\gamma M_1^2) - (A-1)\left(1 + \frac{\gamma-1}{2} M_1^2\right)^{\gamma/\gamma-1}\right]$$

$$F_{4s} = \frac{1}{\gamma+1}\left[A(1+\gamma M_1^2)\psi - (A\psi - 1)\left(1 + \frac{\gamma-1}{2} M_1^2\right)^{\gamma/\gamma-1}\right]$$

$$F_5 = \sqrt{1 - \frac{M_1^2 A^2 [2 + (\gamma-1)M_1^2]}{(\gamma+1)F_4^2}}$$

$$F_{5s} = \sqrt{\frac{1}{\gamma}\left[1 + \frac{(\gamma^2-1)(\gamma+1)}{1+\gamma(2\psi-1)}\right] - \frac{M_1^2 A^2 [2 + (\gamma-1)M_1^2]\psi^2}{1+\gamma(2\psi-1)F_{4s}^2}}$$

$$F_A = 1 + \gamma M_1^2 - \left(1 + \frac{\gamma-1}{2} M_1^2\right)^{\gamma/\gamma-1}$$

$$F_6 = \frac{\gamma+1}{2} F_4 + \sqrt{\frac{(\gamma+1)^2}{4} F_4^2 - \gamma M_1^2 A^2}$$

Experimental Study of Interactions of Shock Wave With Free-Stream Turbulence

A. Honkan

C. B. Watkins

J. Andreopoulos

Department of Mechanical Engineering,
City College of The City
University of New York,
New York, NY 10031

Phenomena related to turbulence interactions with shock waves have been studied in detail. The present investigation is focused on interactions of a normal shock wave with homogeneous/grid-generated turbulence. When a shock wave formed in a shock-tube is passed through a grid, the induced flow behind the shock has the features of a compressible flow with free-stream turbulence. The decaying turbulence is subjected to an interaction with the reflected shock traveling in the opposite direction. Data were sampled simultaneously from four channels of high frequency response pressure transducers and dual hot-wires probes. A cold-wire was used to provide instantaneous total temperature measurements while a single hot-wire provided instantaneous mass flux measurements. Amplification of velocity and temperature fluctuations and dissipative length scales has been found in all experiments. Velocity fluctuations of large eddies are amplified more than the fluctuations of small eddies. The dissipative length scale, however, of the large eddies is amplified less than the length scale of the small eddies.

1 Introduction

The interactions of shock waves with turbulent flows are of great practical importance in engineering applications since they considerably modify the fluid field by vorticity and entropy production and transport. Most of the previous work on shock wave/viscous flow interactions is confined to three cases only, namely: shock wave/boundary layer interaction, shock wave/free shear layer interaction and traveling normal shock/compressible pipe flow interaction, in a shock tube.

In the first two cases the shear flow, bounded or free, interacts with an oblique shock wave generated by a compression corner. In the first category, large gradients in static pressure, skin-friction, and mass-flow rate occur and if the turning angle of the compression corner is large enough the flow separates and becomes unsteady due to shock oscillation (Settles, et al., 1979; Adamson and Messiter, 1980; Dolling and Murphy, 1982; Agrawal and Messiter, 1984; Andreopoulos and Muck, 1987; Smits and Muck, 1987; Ardonceau, 1984). Previous work by Settles et al. (1982), Hayakawa et al. (1984), and Samimy and Addy (1985) in shock wave/free shear layer interactions indicate similar results as far as the turbulence behavior is concerned: considerable amplification of all turbulence intensities across the shock that depends on the shock strength. However, in all previous work on oblique shock wave/shear layer interactions some additional phenomena were involved which made the emerging flow picture and, therefore, the flow behavior, rather complicated. These phenomena were: (*a*) oscillation of the shock wave in the longitudinal direction and wrinkles in the spanwise direction; (*b*) separation, occurring downstream of the shock, in cases of high turning angles which causes even more unsteadiness; (*c*) compression continuing after the shock; (*d*) streamline curvature; and (*e*) wall proximity which results in high turbulence intensity and, therefore, high flow anisotropy. As a consequence of all these influences, the phenomenon of turbulence amplification as a direct result of the Rankine-Hugoniot jump conditions is considerably distorted and all previous results are masked by these additional effects.

The third category includes flows where turbulence intensities have been considerably amplified after the passage of a shock. This category includes flows inside a shock tube where a traveling normal shock is reflected on the end wall and then interacts with the flow induced by the incident shock, (Trolier and Duffy, 1985; Hartung and Duffy, 1986). In these cases turbulence is mainly produced in regions of high velocity gradients close to the wall and then transported toward the centerline of the tube. Despite the large scatter of the measured data and the fact that the r.m.s. level of the incident flow was rather low, turbulence amplification was strongly evident. Keller and Merzkirch (1990) measured the density fluctuations in a similar interaction between a traveling wave and the wake of a perforated plate by using speckle photography. They also demonstrated that density fluctuations are considerably amplified. Haas and Sturtevant (1987) and Hesselink and Sturtevant (1988), investigated the interaction of a weak shock wave with a single discrete gaseous inhomogeneity and statistical uniform medium, respectively. It was found that the shock induced Rayleigh-Taylor instability enhances mixing considerably, in that turbulent scales seem to decrease after passage of the shock. The latter is in contrast to all previous work mentioned earlier (see for example Smits and Muck, 1987) and most probably is due to the Rayleigh-Taylor instability which is as a result of a nonlinear interaction of two pre-existing

Contributed by the Fluids Engineering Division for publication in the JOURNAL OF FLUIDS ENGINEERING. Manuscript received by the Fluids Engineering Division July 27, 1993; revised manuscript received May 1, 1994. Associate Technical Editor: Wing-Fai Ng.

modes in the flow namely, that of the vorticity mode and that of entropy.

From a simplistic point of view the shock wave can be considered as a very steep pressure gradient. Information from experiments and computations of low speed flows with such pressure gradients indicates that "rapid distortion" concepts hold and, in the limit of extremely sharp gradients the Reynolds stresses and turbulent intensities are "frozen," since there is insufficient residence time in the gradient for the turbulence to alter at all (Hunt, 1973). The physics, associated with the compressibility phenomena that are responsible for this amplification, are not well understood.

The first attempt to predict such turbulence amplification is attributed to Ribner (1955). His predictions were verified by experiments conducted by Sekundov (1974) and Dosanjh and Weeks (1964). Several analytical and numerical studies of this phenomenon by Chang (1955), Morkovin (1960), McKenzie and Westphal (1968), Zang et al. (1982), Anyiwo and Bushnell (1982), Viecelli (1989), Rotman (1989), and Lee et al. (1991) show very similar turbulence enhancement. Chu and Kovasznay (1950) indicated that there are three fluctuating modes that are coupled and are responsible for the turbulence amplification: 1) acoustic (fluctuating pressure and irrotational velocity model); 2) turbulence (fluctuating vorticity mode); and 3) entropy (fluctuating temperature mode). These modes are, in general, nonlinearly coupled and the Rankine-Hugoniot jump conditions across the shock indicate that when any of one of the three fluctuation modes is transferred across a shock wave, it not only generates the other two fluctuation modes, but it may itself also be considerably amplified. The present work focuses on the turbulence fluctuation mode. Specifically, we have investigated the transfer of homogeneous and isotropic turbulence across an unsteady normal shock propagating inside the flow. Previous work on this subject is rather limited if nonexisting. The reason is that it is rather difficult to experimentally set up a configuration where a decaying, grid-generated turbulence will interact with a plane shock in a wind tunnel. Debieve et al. (1985), for instance, attempted to generate homogeneous and isotropic turbulence by installing a grid inside the settling chamber of a supersonic wind tunnel. The flow, however, became anisotropic after it passed through the contraction of the wind tunnel.

One way to simulate experimentally the aforementioned interaction is by taking advantage of the induced flow behind a moving shock in a shock tube. This flow is passed through a turbulence generating grid and the decaying turbulence behind the incident shock interacts with the shock wave after it has been reflected from the end wall (see Fig. 1). The present work is aimed at a better understanding of the interaction of a moving shock wave with the decaying turbulence. This paper describes the experimental techniques used and reports on new results of an on going investigation which complement previous work (Honkan and Andreopoulos, 1990, 1992).

2 Experimental Setup and Techniques

The work was carried out in the 44.5 mm diameter shock tube of the Department of Mechanical Engineering. The stainless steel tube had a length of approximately 3.05 m and a wall thickness of 6.35 mm and consisted of three different sections bolted together with stainless steel flanges. Thin aluminum plates were used as diaphragms installed in the driver section. All the results were obtained with the same geometrical and opening/rupture characteristics of the aluminum diaphragms. The end wall was removed and a 305 mm extension of the tube was constructed and used as the working section. This additional piece was tightly bolted to the tube through flanges. The turbulence generating grid was installed between the two flanges and with the help of four rubber gaskets a leak-free operation was achieved. Several ports were drilled in this extension at

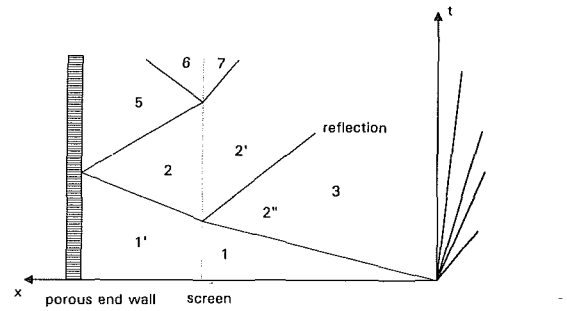

Fig. 1 Schematic of the shock wave turbulence interaction

Table 1 Flow parameters. (Data in [ ] are from one-dimensional inviscid theory with mean pressures as input.)

		Upstream	Downstream
p	Pa	199,955	347,508
ρU	kg/m^{2}s	318 [330]	86 [64]
U	m/s	150 [180]	29 [22]
T_o	K	391 [399]	433 [416]
T	K	379 [378]	433 [416]
ρ	kg/m^3	2.10 [1.97]	2.80 [2.91]
Mach no. (flow)		0.385 [0.48]	0.069 [0.053]
M_s (incident shock)		[1.354]	
M_R (reflected shock)		[1.240]	
Re $= UM/\nu$		30,480	9,090

different locations from the grid. These ports were used to plug in two pressure transducers and a dual hot-wire probe. A stainless-steel screen with a mesh size 10×10 was used as a grid. In order to avoid choking of the flow through the grid the open area of the grid should be higher than the corresponding sonic throat area for a given pressure ratio/Mach number. To elaborate more on this issue, continuity, momentum and energy equations have been evaluated for a stationary observer and for a control volume including the screen:

$$\rho_2 U_2 = \rho_{2'} U_{2'} \tag{1}$$

$$\Delta p + p_2 + \rho_2 U_2^2 = p_{2'} + \rho_{2'} U_{2'}^2 \tag{2}$$

$$C_p T_2 + \frac{U_2^2}{2} = C_p T_{2'} + \frac{U_{2'}^2}{2} \tag{3}$$

where Δp is the pressure loss through the screen. From continuity and equations of state for (2) and (2′) we can obtain

$$\frac{p_2}{p_{2'}} = \frac{M_{2'}}{M_2}\left[\frac{T_2}{T_{2'}}\right]^{1/2}$$

Since total temperature is constant

$$\frac{T_2}{T_0} = \frac{1}{[2+(\gamma-1)M_2^2]} \quad \text{and} \quad \frac{T_{2'}}{T_0} = \frac{1}{[2+(\gamma-1)M_{2'}^2]}$$

Therefore

$$\frac{p_2}{p_{2'}} = \frac{M_{2'}}{M_2}\left[\frac{2+(\gamma-1)M_{2'}^2}{2+(\gamma-1)M_2^2}\right]^{1/2}$$

This relation can be rearranged to provide $M_{2'}$ when M_2 and the pressure ratio $p_2/p_{2'}$ are known:

$$(\gamma-1)M_{2'}^4 + 2M_{2'}^2 - \left(\frac{p_2}{p_{2'}}\right)^2 M_2^2[2+(\gamma-1)M_2^2] = 0 \tag{4}$$

For a given pressure ratio $p_2/p_{2'}$, Eq. (4) has two real roots for $M_{2'}$ one negative and one positive. Since the first is not physical only the second root is acceptable. Table 1 where the bulk data of the present experiment are summarized, shows that $M_2 = 0.385$ and therefore Eq. (4) gives $M_{2'} = 0.33$ if $p_2/p_{2'} = 0.9$ is assumed. This value for $M_{2'}$ indicates that the

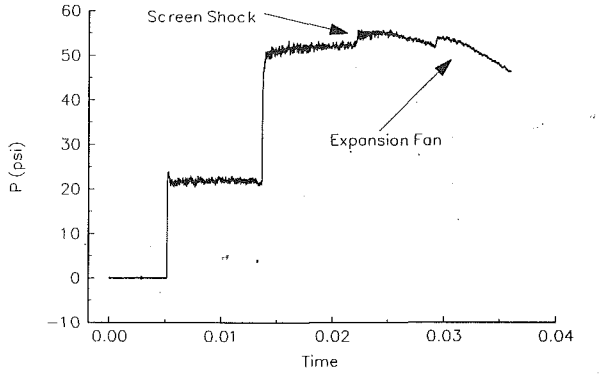

Fig. 2 Wall pressure signal. Arrows indicates the arrival of the shock reflected on the screen or the arrival of the reflected expansion wave.

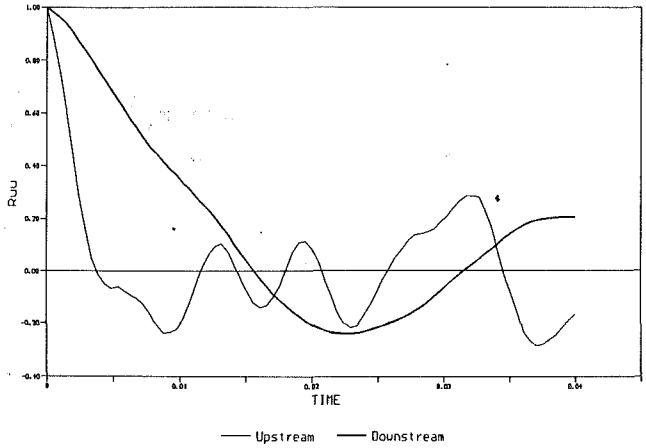

Fig. 3 Plot of autocorrelation function $R_{uu}(\tau)$

sonic area ratio A^*/A is 0.526. Consequently any screen with open area larger than this value will result in nonchoked flow. In the present experiment a screen with 0.65 open area ratio was used.

To obtain a nonzero velocity flow field behind the reflected shock the end wall was replaced by a Rigimesh disk. Rigimesh is a rigid multi-screen arrangement which resulted in a plane reflection of the shock while, at the same time allowed for some of the shock tube flow to be discharged in the environment. Nitrogen was used as driver and air as the driven gas.

Two high-frequency response subminiature Kulite pressure transducers type XCQ-062-500 were used to measure instantaneous pressures. Shock speeds were calculated first by measuring the traveling time of the shock between two locations and second by measuring the pressure rise and using one-dimensional inviscid flow theory. Most of the measurements were carried out with 2 MHz sampling frequency per channel with 16k samples per channel. The present data indicated that the frequency content of the viscous scales of the flow did not extend beyond, approximately, 65 kHz while the viscous length scale was of the order of 0.018 mm. The latter determines the spatial resolution of the hot-wire probe, which was approximately 44 viscous lengths. The frequency response of the hot wire as it was measured during the passage of the shock, was found to be of the order of 100 kHz. Similar value was found for the frequency response of the pressure transducers. The cold wire had a frequency response up to 40 kHz after compensation. The hot-wire and data processing techniques developed and used for this particular investigation are not straightforward. These are described in considerable detail by Honkan et al. (1993).

The duration of useful data downstream of the reflected shock was limited because of the arrival at the measuring location of either the reflected expansion wave coming from the end wall of the driver section or the reflected shock on the screen/grid (second reflection). The reflected shock impinges on the screen for a second time as it travels upstream in the opposite direction. This creates a weak reflected shock traveling downstream and therefore terminating our "integration" or "observation" time. This is shown in Fig. 2 where the reflected on-the-screen shock arrives after the passage of the reflected shock followed by the arrival of expansion waves.

Although all signals were visually inspected for such events, a more objective criterion was used to determine whether the data were seriously biased or contaminated by these reflections: The mean time derivative, $\overline{\partial Q}/\partial t$ was computed for the quantity Q where Q can be any one of U, ρU, T_0, or p. This derivative was computed by summing up the difference ΔQ between two successive points:

$$\frac{\overline{\partial Q}}{\partial t} = \frac{1}{N}\sum_{i=1}^{N}\frac{\Delta Q_i}{\Delta t}$$

where Δt is the sampling interval and N is the number of samples under consideration. If this mean slope was not close to zero within a small quantity e, the number of samples N was reduced and the computation of statistical averages was repeated until the criterion of $\overline{\partial Q}/\partial t < e$ was satisfied.

The results include statistical averages which were computed over several ensembles, i.e., tube firings. Each ensemble contained several statistically independent realizations, i.e., large eddies and therefore statistical convergence was achieved within a few events. The integral time scale, $\mathcal{L}_t$ was used to determine the number of samples for each ensemble. It is defined as

$$\mathcal{L}_t = \int_0^\infty R_{uu}(\tau)\,d\tau$$

where τ is the time delay. $R_{uu}(\tau)$ is the autocorrelation function defined as

$$R_{uu}(\tau) = \frac{\overline{u(t)\cdot u(t-\tau)}}{\overline{u^2}}$$

Figure 3 indicates a typical autocorrelation function obtained at $x/M = 15$. To calculate the time scale, numerical integration of $R_{uu}(\tau)$ was carried out up to the first zero crossing point for the preshock and postshock flow regions. This particular figure shows that the time scale is about 0.025 ms and 0.0075 ms for the upstream and the downstream of the shock eddies, respectively. For a total sampling time roughly between 0.6 and 1 or more ms about 100–300 eddies per ensemble were considered in the statistical analysis. The results have been obtained by taking the mean value over the calculated ensemble averages. By invoking Taylor's hypothesis the integral length scales $\mathcal{L}_x$ can be estimated from the relation $\mathcal{L}_x = \mathcal{L}_t U$. In this particular case this length scale is reduced through the interaction to 3/5 of its initial value upstream value.

3 Results

Several diagnostic tests were carried out in order to evaluate the quality of the shock wave and the homogeneity and isotropy of the flow. These tests indicated that the incident and reflected shocks were plane and normal to the tube axis. Monitoring of the arrival time of the shock wave by the two transducers and hot-wire probes, placed at the same distance from the grid, indicated that the shock front contained no measurable ripples of any kind in the region between $x/M = 10$ and 60 where measurements were carried out.

In flows where turbulence is distorted by a rapidly applied mean strain across $s = (\partial U/\partial x)_{\text{s.w.}}$ the shock wave controlling parameter of the interaction is the ratio of the time scale of turbulence $L/(Q,q)$ to the time scale of the applied strain $1/s$:

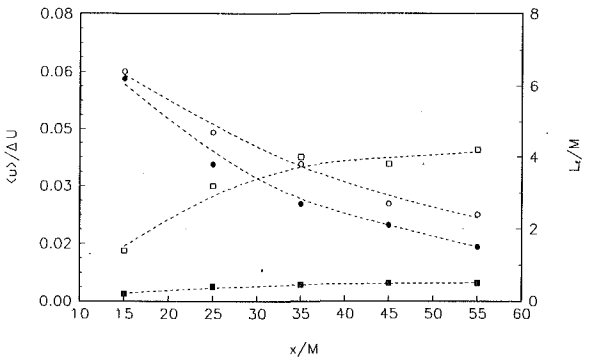

Fig. 4 Graph of $\langle u\rangle/\Delta U$ (●, ○) and L_ϵ/M (■, □) versus x/M. Filled symbols represent values before the interaction and open symbols after the interaction. Uncertainty in mean velocity and turbulence intensity ≈ 16 percent

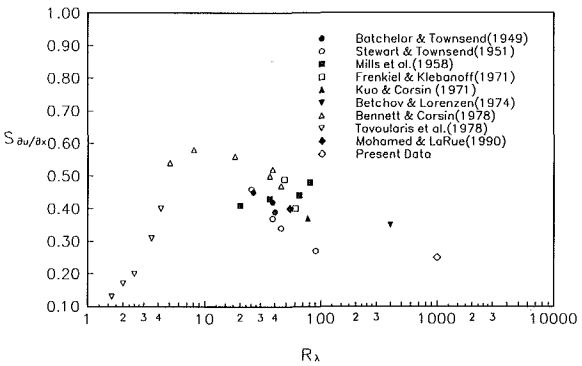

Fig. 5 Graph of skewness of the velocity derivative $S_{\partial u/\partial x}$

$$r=\frac{Ls}{q}$$

with

$$\overline{q^2}=1/2(\overline{u^2}+\overline{v^2}+\overline{w^2})=3/2(\overline{u^2})$$

and

$$q=(\overline{q^2})^{1/2}$$

Since

$$L=(\overline{q^2})^{3/2}/\epsilon$$

where ϵ is the dissipation rate then

$$r=\frac{s\overline{q^2}}{\epsilon}.$$

The strain rate s can be approximated by

$$s=\frac{\partial\overline{U}}{\partial x}=\frac{U_5-U_2}{\Delta x_s}$$

where Δx_s is the shock wave thickness which according to Thompson (1972) can be estimated by

$$\Delta x_s=\frac{12\gamma p_2}{(\gamma+1)(p_5-p_2)}\Lambda$$

where Λ is molecular mean free path.

In flows where the parameter r reaches small values, inviscid rapid distortion theory (Hunt, 1973) and its extension to compressible flows (Debieve et al., 1985) may be invoked to describe several bulk characteristics of the interaction.

Since the extra strain rate s is what is causing the interaction, the velocity difference $\Delta\overline{U}=\overline{U}_2-\overline{U}_5$ may be an appropriate velocity scale to nondimensionalize the turbulence intensity data as it has been suggested by Debieve and Larcharme (1985).

Measurements of turbulence intensities before and after the passage of the shock are shown in Fig. 4. Distances from the turbulence generating grid are nondimensionalized by the grid size M. As it can be seen from the present data, values of $\langle u\rangle/\Delta\overline{U}$ after the interaction are higher than those upstream of the shock by an amount which varies from 10 percent at $x/M=15$ to 48 percent at the farthest station downstream $x/M=55$.

The distribution of the dissipative length scale L_ϵ defined as

$$-\overline{U}\frac{\partial\overline{u^2}}{\partial x}=\frac{(\overline{u^2})^{3/2}}{L_\epsilon}$$

is also shown in Fgi. 4. L_ϵ was determined from the above equation and a power-law fit of $\overline{u^2}$ in the form of $(x/M-x_0/M)^{-n}$ as it has been described by Hancock and Bradshaw (1989). It can be seen from this figure that the present flow provides a variety of length scales and turbulence intensities as different inputs to the interaction with a shock of the same strength. It is also obvious that the flow response characteristics are not the same for all x/M positions. The power-law of the $\overline{u^2}$ decay is a characteristic behavior of a homogeneous and isotropic flow. The fact that the present data exhibit a decay of $\overline{u^2}$ obeying this power-law with coefficients within the well-established ranges (see Mohamed and LaRue, 1990) indicates indirectly that the flow is indeed isotropic. However, direct evidence of the isotropy of the present flow was obtained from the skewness of velocity fluctuations as well as the skewness of the derivative $\partial u/\partial x$. The skewness of the velocity fluctuations S_u was found to be close to zero. According to the analysis of Taylor (1983), skewness of the velocity derivative $S_{\partial u/\partial x}$ represents the average rate of production of mean-square vorticity by vortex stretching. Batchelor (1953) indicated that $S_{\partial u/\partial x}$, at sufficiently large Reynolds numbers should be constant. This constant, however, has been found to be a function of turbulent Reynolds number

$$\mathrm{R}_\lambda=\frac{(\overline{u^2})^{1/2}\lambda}{\nu},$$

where λ is the "Taylor microscale." Figure 5 shows the variation of $S_{\partial u/\partial x}$ with R_λ. The results of Batchelor and Townsend (1949), Stewart and Townsend (1951), Miles et al. (1958), Frenkiel and Klebanoff (1971), Kuo and Corrsin (1978), Mohamed and LaRue (1990), and Tavoularis et al. (1978) are also plotted for comparison. The data, despite the considerable scatter, indicate a decrease of $S_{\partial u/\partial x}$ with increasing R_λ. The present value of this skewness is well within this trend.

The gains or amplification ratios of turbulence quantities are among the characteristics of the interaction. They are defined as

$$G_u=\frac{[\langle u\rangle/\Delta\overline{U}]_o}{[\langle u\rangle/\Delta\overline{U}]_i}\quad\text{for the turbulence intensities and}$$

$$G_L=\frac{[L_e/M]_o}{[L_e/M]_i}\quad\text{for the dissipative length scales.}$$

Subscript i refers to the flow upstream of the reflected shock i.e., input to the interaction and subscript o refers to the flow immediate downstream of the shock i.e., output of the interaction. These amplification ratios are plotted in Fig. 6. The present data clearly show that G_u and G_L are not the same for all downstream distances. G_u, for instance, varies from 1.1 close to the grid to 1.48 at $x/M=55$. Since, both $\langle u\rangle$ and L_e vary considerably with x/M, it appears plausible to conclude that G_u as well as G_L depend also on the local velocity and turbulence length scale, in addition to the shock i.e., Mach number of the interaction. Lee et al. (1991) calculated the amplification ratio G_u as function of Mach number by extending the rapid distortion theory and Ribner's (1953, 1987) linear analysis to three dimensions. For the present Mach number in the shock fixed coordinates their predictions indicate that the gain of turbulence intensity $\langle u\rangle$ 1.24 by using the

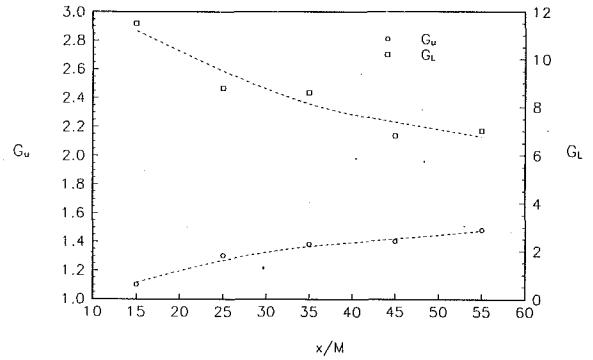

Fig. 6 Graph of amplification ratios G_u and G_L

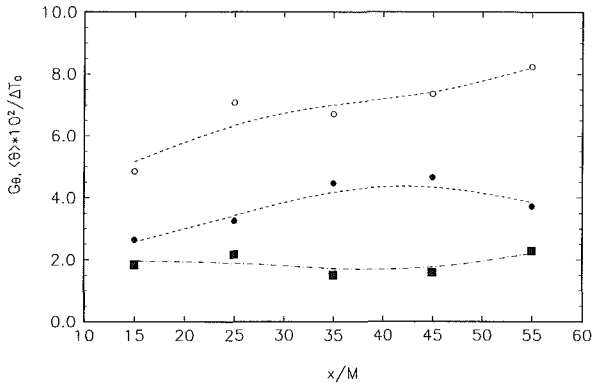

Fig. 7 Graph of the distribution of total temperature fluctuations before and after the interaction (●, ○) and of amplification ratio G_θ (■). Uncertainty in temperature measurements ≈ 12 percent

rapid distortion theory and 1.47 by using Ribner's analysis, respectively. Although these predictions are significantly different from each other, they fall within the range of the present measured values. None of the theories, however, predicts the length scale and turbulence intensity dependence of both amplification ratios G_u and G_L. Also none of them predicts the length scale dependence of G_u as it has been found in the present experiments, which indicates that the velocity fluctuations of large scales are amplified more than those of small scales.

Total Temperature Fluctuations. The distribution of the r.m.s. of total temperature fluctuations behind the grid, as it has been directly measured with the cold-wire, is shown in Fig. 7. The r.m.s. values have been normalized by the total temperature gradient $\Delta\overline{T}_o = (\overline{T}_o)_o - (\overline{T}_o)_i$ across the shock according to Debiéve et al. (1985). The level of $\langle\theta\rangle/\Delta\overline{T}_o$ is rather small, with values in the range of 2.5 to 4.6 percent in the incident flow region, upstream of the shock and 4.85 to 8.25 percent in the downstream region.

Amplification of total temperature fluctuations is expected since $\Delta\overline{T}_o \neq 0$. The amplification ratio, defined as

$$G_\theta = \frac{[\langle\theta\rangle/\Delta\overline{T}_o]_o}{[\langle\theta\rangle/\Delta\overline{T}_o]_i}$$

is also shown in Fig. 7. The results indicate that total temperature fluctuations are amplified across the shock by a factor of 1.875 on average and that no preferential amplification is apparent at any x/M position in the flow.

Wall Pressure Fluctuations. Figure 8 shows the distribution of the r.m.s. of wall pressure fluctuations downstream of the grid for both flow regions, upstream and downstream of the shock. The results are nondimensionalized by the pressure

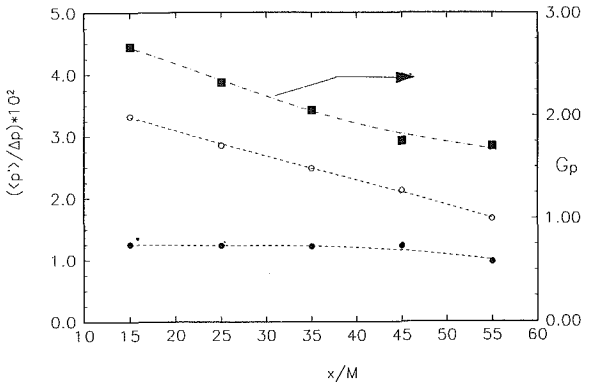

Fig. 8 Graph of the distribution of wall pressure fluctuations (●, ○) and of amplification ratio G_p (■). Uncertainty in pressure measurements ≈ 3 percent

rise across the shock $\Delta\overline{p} = (\overline{p})_o - (\overline{p})_i$, which is causing the interaction. The level of the r.m.s. is between 0.96 to 1.25 percent for the incident flow and 1.66 to 3.32 percent for the downstream flow. Both distributions decay with downstream distance as is expected. The amplification ratio

$$G_p = \frac{[\langle p\rangle/\Delta\overline{p}]_o}{[\langle p\rangle/\Delta\overline{p}]_i}$$

also shown in Fig. 8, indicates considerable difference in the level of amplification with downstream position. G_p is higher close to the grid than at the farthest position $x/M = 55$.

In trying to interpret the behavior of wall pressure fluctuations several other considerations should be taken into account. First, wall pressure fluctuations are closely related to the local wall shear stress. In fact, Willmarth and Wooldridge (1962) found that the r.m.s. of pressure fluctuations is 2.19 times the local wall stress. The presence of free-stream turbulence increases the local skin friction and therefore the wall pressure fluctuations, roughly by 3 percent for each 1 percent r.m.s. increase of the longitudinal intensity (see Hancock and Bradshaw, 1989). The turbulence intensity of the free stream of the incident flow is about 5 percent at $x/M = 15$ and decays down to 1.5 percent at $x/M = 55$. These values indicate a 15 percent increase of pressure fluctuations at $x/M = 15$ and about 4.5 percent at $x/M = 55$. This may explain the slow decay of pressure fluctuations r.m.s. with downstream distance. However, the above picture is further complicated by the fact that the boundary layer flow went through the turbulence generating grid. Since the grid mesh size M is smaller than the boundary layer thickness it is expected that the large eddies are reduced in size after the screen. In addition, the flow is further complicated by the passage of the reflected shock. It appears that the boundary layer region responds differently from the free stream region to the new boundary conditions imposed by the end wall. Because the velocity inside the boundary layer is lower than the external velocity U_2, the propagation speed of the reflected shock W_R is higher inside the boundary layer than the propagation speed in the free stream. The implication is that the reflected shock propagates faster and is inclined forward inside the boundary layer. Had the end wall been nonporous, the velocity U_5 would be zero and massive separation of the boundary layer would have occurred. The porosity of the end wall imposes a nonzero velocity behind the reflected shock which improves significantly the overall flow quality in the free stream region. Because the velocity behind the oblique part of the shock and that behind the normal shock do not match in the area around the bending position, a slip line or better, a shear layer should develop. Some flow visualization pictures, found in the text book by Thompson (1972) and due to R. North of N.P.L. indeed indicate the forward inclination of the shock inside the boundary layer and the existence of

the shear layer/slip line in a flow with non-porous end wall. The latter clearly complicates further the flow in this region since it considerably disturbs the flow. This flow disturbance will reach the centerline region after some time. In addition, if the boundary layer is thick, the free-stream region where the flow is homogeneous and isotropic may be very small and, therefore, the reflected shock may be planar over only a limited area around the axis of symmetry. In order to minimize this effect, the measuring positions were very close to the reflecting end wall. In addition, the observation time has been terminated shortly after the passage of the shock due to reasons explained earlier. For these two reasons, the boundary layer was thin during the observation time and consequently the flow was relatively uniform in the free-stream region.

4 Further Discussion and Concluding Remarks

The present results indicate that turbulence intensities of velocity, pressure and temperature, dissipative length scales, and time scales are considerably amplified through a moving shock. In this investigation the effects of shock waves on turbulence do not contain any additional effects caused by shock wave oscillation and unsteadiness due to downstream flow separation or streamline curvature and downstream compression. The fact, however, is that similar conclusions were reached by Smits and Muck (1987) in compression corner flows where all the above mentioned additional effects were present, indicating that turbulence amplification is a rather general characteristic of shock wave/turbulent flow interactions. The second major conclusion of the present investigation is that turbulence amplification depends on the input r.m.s. level of velocity fluctuations and length scales. Less energetic eddies away from the screen have their intensity amplified three times more than those eddies closer to the screen. The measurements show that the dissipative length scale amplification is higher closer to the screen where eddies are smaller and more energetic than further downstream where eddies are larger with smaller fluctuations. However, integral length scales in the longitudinal direction may be reduced through the interaction. The present limited analysis indicated a 40 percent reduction in $\mathcal{L}_x$ after the passage of the shock wave.

Although the incident flow upstream of the shock is isotropic the downstream flow may have strong anisotropies developed due to different amplifications of the velocity fluctuations of the other two components since the vorticity components are amplified by different amounts. Previous experiments in compression corners conducted by Ardonceau (1984) and Smits and Muck (1987) indicated that the anisotropy ratio $\langle u \rangle / \langle v \rangle$ which in the present flow is close to 1 for the incident flow, is reduced considerably through the shock due to larger amplification of the v-fluctuations. Return to isotropy, however, may be achieved at some further distance downstream.

The present investigation was aimed at better understanding of the fundamentals of the shock wave/turbulence interactions and at the same time providing data that may be used in testing calculation methods. Calculations of flows involving shock wave interaction with a turbulent boundary layer or free shear layer perform rather poorly because of inadequate modeling of the turbulence behavior. Testing of calculation methods requires much simpler flows without streamline curvature and mean shear or other additional parameters so that the effects of various closures and assumptions become very clear. Compression of a decaying homogeneous turbulence by a moving shock wave may exhibit a test case for a better understanding of turbulence which may lead to a better modeling of compressible turbulence.

One major problem in the calculations for the present flow is the description of the initial turbulent field since calculating the flow through the turbulence generating grid is not feasible. Traditional modeling of the flow by extrapolating subsonic flow concepts may be inadequate mainly because time-averaged equations are used. Several new ideas in defining the initial turbulence have been attempted by Rotman (1989) and Lee et al. (1993). Initial time-dependent "turbulent" flow conditions have been prescribed in a box through which a plane shock wave is passing. Rotman and Lee et al. have successfully shown qualitatively the increase in turbulent kinetic energy caused by the shock. The present data are aiming at providing guidance in modeling and testing calculation methods such as those mentioned above. However, further experiments are needed to establish turbulence behavior for a wider range of initial intensities and length scales.

Acknowledgment

The financial support provided by the National Science Foundation grant #91-04767 is gratefully acknowledged.

References

Adamson, T. C., and Messiter, A. F., 1980, "Analysis of Two Dimensional Interactions Between Shock Waves and Boundary Layers," *Annual Review of Fluid Mechanics*, Vol. 12, p. 103.

Agrawal, S., and Messiter, A. F., 1984, "Turbulent Boundary Layer Interaction with a Shock-Wave at a Compression Ramp Corner," *Journal of Fluid Mechanics*, Vol. 143, p. 23.

Anderson, J. D., 1982, *Modern Compressible Flow*, McGraw-Hill, New York.

Andreopoulos, J., and Muck, K. C., 1987, "Some New Aspects of the Shock-Wave Boundary Layer Interaction in Compression Ramp Corner," *Journal of Fluid Mechanics*, Vol. 180, p. 405.

Ardonceau, P. L., 1984, "The Structure of Turbulence in a Supersonic Shock-wave/Boundary-Layer Interaction," *AIAA Journal*, Vol. 22, No. 9, p. 1254.

Anyiwo, J. C., and Bushnell, D. M., 1982, "Turbulence Amplification in Shock-Wave Boundary Layer Interaction," *AIAA Journal*, Vol. 20, No. 7, p. 893.

Batchelor, G. K., and Townsend, A. A., 1949, "The Nature of Turbulent Motion at High Wave Numbers," *Proceedings of Royal Society*, Series A 199, p. 238.

Bushnell, D. M., Carry, A. M., and Harris, J. E., 1976, "Calculation Methods for Compressible Boundary Layers," NASA report SP-422.

Chang, C. T., 1955, "On the Interaction of Weak Disturbances and a Plane Shock of Arbitrary Strength in a Perfect Gas," Ph.D. thesis, The Johns Hopkins University, Baltimore, MD.

Chu, B. T., and Kovasznay, L. S. G., 1957, "Non-linear Interactions in a Viscous Heat-Conducting Compressible Flow," *Journal of Fluid Mechanics*, Vol. 3, p. 494.

Coakley, T. J., Viegas, J. R., and Horstman, C. C., 1977, "Evaluation of Turbulence Models for Three Primary Types of Shock-Wave Turbulence Boundary Layer Interaction," AIAA Paper 77-692.

Debieve, J. F., and Lacharme, J. P., 1985, "A Shock Wave Free Turbulence Interaction," *IUTAM Symposium on Turbulent Shear Layer/Shock Wave Interactions*, J. Delery, ed., Springer-Verlag, Paris.

Dolling, D. S., and Murphy, M., 1982, "Wall Pressure in Supersonic Separated Compression Ramp Flow Field," AIAA Paper 82-0986.

Dosanjh, D. S., and Weeks, T. M., 1964, "Interaction of a Starting Vortex as Well as Karman Vortex Streets with Traveling Shock Wave," AIAA Paper 64-425.

Frenkiel, F. N., and Klebanoff, P. S., 1971, "Statistical Properties of Velocity Derivatives in Turbulent Field," *Journal of Fluid Mechanics*, Vol. 48, p. 183.

Grande, E., and Oates, G. C., 1973, "Unsteady Flow Generated by Shock-Turbulent Boundary Layer Interactions," AIAA Paper 73-168.

Green, J. E., 1970, "Interactions Between Shock Waves and Turbulent Boundary Layers," *Progress in Aeronautical Science*, Vol. 11, pp. 235-340.

Haas, J. F., and Sturtevant, B., 1987, "Interaction of Weak Shocks Waves with Cylindrical and Spherical Gas Inhomogeneities," *Journal of Fluid Mechanics*, Vol. 181, p. 41.

Hancock, P. E., and Bradshaw, P., 1989, "Turbulence Structure of a Boundary Layer Beneath a Turbulent Free Stream," *Journal of Fluid Mechanics*, Vol. 205, p. 45.

Hartung, L. C., and Duffy, R. E., 1986, "Effects of Pressure on Turbulence in Shock-Induced Flows," AIAA Paper 86-0127.

Hayakawa, K., Smits, A. J., and Bogdonoff, S. M., 1984, "Turbulence Measurements in a Compressible Re-attaching Shear Layer," *AIAA Journal*, Vol. 22, No. 7, p. 889.

Hesselink, L., and Sturtevant, B., 1988, "Propagation of Weak Shocks Through Random Medium," *Journal of Fluid Mechanics*, Vol. 196, p. 513.

Honkan, A., and Andreopoulos, J., 1990, "Experiments in a Shock Wave/Homogeneous Turbulence Interaction," AIAA Paper 90-1647.

Honkan, A., and Andreopoulos, J., 1992, "Rapid Compression of Grid-generated Turbulence by a Moving Shock Wave," *Physics of Fluids A.*, Vol. 4, No. 11, pp. 2562-2572.

Honkan, A., Andreopoulos, J., and Watkins, C. B., 1993, "Application of Hot-Wire Anemometry in Shocktube Flows," *Third International Symposium on Thermal Anemometry*, ASME Fluids Engineering Conference, Washington, DC.

Horstman, C. C., Settles, G. S., Williams, D. R., and Bogdonoff, S. M., 1981, "A Reattaching Free Shear Layer in Compressible Turbulent Flow," AIAA Paper 81-0333R.

Horstman, C. C., Settles, G. S., Vas, I. E., Bogdonoff, S. M., and Hung, C. M., 1977, "Reynolds Number Effects on Shock-Wave Turbulent Boundary Layer Interactions," *AIAA Journal*, Vol. 15, No. 9, p. 1152.

Hunt, J. R. C., 1973, "A Theory of Turbulent Flow Round Two-Dimensional Bluff Bodies," *Journal of Fluid Mechanics*, Vol. 61, p. 625.

Jacquin, L., Blin, E., and Geffroy, P., 1991, "Experiments on Free Turbulence/Shock Wave Interaction," *8th Symposium on Turbulent Shear Flows*, Munich.

Keller, J., and Merzkirch, W., 1990, "Interaction of a Normal Shock Wave with a Compressible Turbulent Flow," *Experiments in Fluids*, Vol. 8, p. 241.

Kovasznay, L. S. G., 1950, "The Hot-Wire Anemometer in Supersonic Flow," *Journal of the Aeronautical Sciences*, Vol. 17, pp. 565–573.

Kuo, A. Y., and Corrsin, S., 1971, "Experiments on Internal Intermittency and Fine Structure Distribution Functions in Fully Turbulent Flows," *Journal of Fluid Mechanics*, Vol. 50, p. 285.

Kussoy, M. I., and Horstman, C. C., 1975, "An Experimental Documentation of a Hypersonic Shock-wave Turbulent Boundary Layer Interaction Flow with and Without Separation," NASA TMX-62412.

Lee, S., Lele, S. K., and Moin, P., 1993, "Direct Numerical Simulation of Isotropic Turbulence Interacting with a Weak Shock Wave," *Journal of Fluid Mechanics*, Vol. 251, pp. 533–562.

Lee, S., Lele, S. K., and Moin, P., 1991, "Direct Numerical Simulation and Analysis of Shock Turbulence Interaction," AIAA Paper 91-0523. 29th Aerospace Science Meeting, Reno, NV.

Mateer, G. G., Brosh, A., and Viegas, J. R., 1976, "A Normal Shock-Wave Turbulent Boundary Layer Interaction at Transonic Speeds," AIAA Paper 76-161.

McKenzie, J. F., and Westphal, K. O., 1968, "Interaction of Linear Waves with Oblique Shock Waves," *Physics of Fluids*, Vol. 11, No. 11, pp. 2350-2362.

Mills, R. R., Kistler, A. L., O'Brien, V., and Corrsin, S., 1958, "Turbulence and Temperature Fluctuations Behind a Heated Grid," N.A.C.A. Tech. Note No. 4288.

Morkovin, M. V., 1962, "Effects of Compressibility on Turbulent Flows," *Mechanique de la Turbulence*, A. Farre, ed., Paris: CNRS, pp. 367–380.

Morkovin, M. V., 1960, "Note on Assessment of Flow Disturbances at a Blunt Body Traveling at Supersonic Speeds Owing to Flow Disturbances in Free Stream," ASME *Journal of Applied Mechanics*, Vol. 27, pp. 223–229.

Mohamed, M. S., and LaRue, J. C., 1990, "The Decay of Power Law in Grid Generated Turbulence," *Journal of Fluid Mechanics*, Vol. 219, p. 195.

Ribner, H. S., 1955, "Convection of a Pattern of Vorticity Through a Shock Wave," NACA Report 1233.

Rose, W. C., 1973, "The Behavior of a Compressible Turbulent Boundary-Layer in a Shock-Wave Induced Adverse Pressure Gradient," NASA TN-D-7092.

Rotman, D., 1989, "Shock Wave Effects on a Turbulent Flow," UC Lawrence Livermore Report 101798.

Samimy, M., and Addy, A. L., 1985, "A Study of Compressible Turbulent Reattaching Free Shear Layers," AIAA Paper 85-1646.

Sekundov, A. N., 1974, *Supersonic Flow Turbulence and Interaction with a Shock Wave*, Akademia Nauk SSSR, Izvestia Mekhanika Zhidkosti i Gaza, Mar.-Apr.

Settles, G. S., Baca, B. K., Williams, D. R., and Bogdonoff, S. M., 1982, "A Study of Reattachment of a Free Shear Layer in Compressible Turbulent Flow," *AIAA Journal*, Vol. 20, No. 1, p. 60.

Settles, G. S., Fitzpatrick, T. J., and Bogdonoff, S. M., 1979, "Detailed Study of Attached and Separated Compression Corner Flow Fields in High Reynolds Numbers Supersonic Flow," *AIAA Journal*, Vol. 17, p. 579.

Smits, A. J., and Muck, K. C., 1987, "Experimental Study of Three Shock Wave/Boundary Layer Interactions," *Journal of Fluid Mechanics*, Vol. 182, pp. 291–314.

Smits, A. J., Muck, K. C., and Hayakawa, K., 1983, "Constant Temperature Anemometer Practice in Supersonic Flows. Part 1. The Normal Wire," *Experiments in Fluids*, Vol. 2, p. 23.

Stewart, R. W., and Townsend, A. A., 1951, "Similarity and Self Preservation in Isotropic Turbulence," *Philosophical Transactions of The Royal Society*, Series A 243, p. 359.

Tavoularis, S., Bennett, J. C., and Corrsin, S., 1978, "Velocity-Derivative Skewness in Small Reynolds Number, Nearly Isotropic Turbulence," *Journal of Fluid Mechanics*, Vol. 88, p. 63.

Taylor, G. I., 1938, "Production and Dissipation of Vorticity in a Turbulent Fluid," *Proceedings of the Royal Society*, Series A 164, p. 15.

Thompson, P. A., 1972, *Compressible Fluid Mechanics*, McGraw-Hill, New York, 1972.

Troiler, J. W., and Duffy, R. E., 1985, "Turbulent Measurements in Shock-Induced Flows," *AIAA Journal*, Vol. 23, No. 8, p. 1172.

Viecelli, J. A., 1989, "Implosion and Shock Compression of Two Dimensional Eddy Structures," *Physics of Fluids A*, Vol. 1, No. 4, p. 753.

Visbal, M., and Knight, D. D., 1983, "Evaluation of the Baldwin-Lomax Turbulent Model for Two-Dimensional Shock-Wave Boundary Layer Interactions," AIAA Paper 83-1697.

Walker, D. A., Ng, W. F., and Waker, M. D., 1989, "Experimental Comparison of Two Hot-Wire Techniques in Supersonic Flow," *AIAA Journal*, Vol. 27, No. 8, p. 1074.

Willmarth, W. W., and Wooldridge, C. E., 1962, "Measurements of the Fluctuating Pressure at the Wall Beneath a Thick Boundary Layer," *Journal of Fluid Mechanics*, Vol. 14, p. 187.

Zang, T. A., Hussaini, N. Y., and Bushnell, D. M., 1982, "Numerical Computations of Turbulence Amplification in Shock Wave Interactions," AIAA Paper 82-0293 and *AIAA Journal*, Vol. 23, No. 1, p. 1984.

Numerical Simulation of a Dilute Particulate Flow (Laminar) Over Tube Banks

Yong-Du Jun

Widen Tabakoff

Department of Aerospace Engineering and Engineering Mechanics, University of Cincinnati, Cincinnati, OH 45221

This paper presents an investigation of numerical simulation for a dilute particle laden flow (laminar) over in-line tube banks. Particles behavior of two different sizes and density (100 μm sand and 40 μm fly ash) is demonstrated through the present study for a fixed geometry and flow condition, that is, a square in-line tube bank of two rows deep with pitch-to-diameter ratio of two at Reynolds number 400. Dilute particulate flow assumption is used and the drag force is considered as the only external force term that affects the particles behavior in the flow. Experimental rebounding data and semiempirical equation for the erosion estimation are used. It was found through the present simulation that the particles behavior of the different sizes and density in tube bank system is quite different in their trajectories, impact and the erosion pattern. The protective role of the first row of cylinders could be supported with respect to the particles collision on the cylinder but not necessarily to the erosion point of view. Also the information at impact such as the impact velocity and the impact angle which affect the erosion (Tabakoff et al., 1988) can be estimated by using the numerical simulation shown in the present study.

1 Introduction

Particles behavior in a gas-particle mixture is important in many industrial fields such as: fluidized bed, pulverized coal burning, powder transportation, erosion in turbomachinery and heat exchangers, and design of inertia and impingement filters. Erosion with particulate flows is a major problem in the power industry, especially in the reheaters and economizers of coal fired boilers utilizing fluidized bed combustors.

The problems of erosion due to particle-laden flows in heat exchangers started with the basic flow patterns such as the flow over a cylinder. Early works in this concern includes Michael and Norey (1969) who introduced the concept of collision efficiency of particle to the collector (sphere). Morsi and Alexander (1972) theoretically studied the particle trajectories in the two-phase flow system introducing the expression for the drag coefficient which approximates to the standard experimental drag-Reynolds number relationship. However, in these two cases the flows were assumed inviscid and studies were limited to the particle collision in which case information about the particles behavior after the impact was not available. The experimental measurement of particle restitution coefficients by Tabakoff and his colleagues (Grant and Tabakoff, 1975; Tabakoff et al., 1988) enabled the trajectory simulation after the particle impact to the solid surface. For the tube bank system, a study by Schuh et al. (1989) showed some numerical results for particle-laden gas flows past in-line tubes. In this study, they computed the flow over in-line tube banks to simulate particle trajectories and erosion distribution. However, the turbulent flow field obtained from the numerical simulation especially for the in-line tube bank case showed discrepancy compared with the experimental observation reported by Zukauskas (1972).

Although turbulent flows are of practical importance in many engineering problems, the authors think that the study of laminar gas-particle suspension flows can describe some important characteristics of the flows with complex geometry.

The present work shows some of the results obtained from the numerical simulation of the flow and the particles behavior in dilute particulate flows using the experimental data for particle restitution coefficients (Grant and Tabakoff, 1975) and the erosion correlation (Hamed, 1992). Flow field is calculated separately from the particle trajectory calculation based on the further assumption that particle-particle interactions and the viscous loss of the fluid flow due to the particles are negligible. The analysis was done for the flow over square in-line tube banks up to two rows deep, with pitch-to-diameter ratios 2.0×2.0, at Reynolds numbers 400 based on the tube diameter and maximum flow velocity through the channel. Particles behavior including the particle trajectories, impact and the erosion distribution is studied for 100 μm sand particles and 40 μm fly ash particles, respectively.

2 Governing Equations

2.1 Flow Field. The vorticity-stream function approach

Contributed by the Fluids Engineering Division for publication in the JOURNAL OF FLUIDS ENGINEERING. Manuscript received by the Fluids Engineering Division March 18, 1993; revised manuscript received June 10, 1994. Associate Technical Editor: M. W. Reeks.

is used for solving the two-dimensional incompressible Navier-Stokes equations because of its simplicity over the primitive variable approach. The governing nondimensionalized vorticity transport equation and stream function equation in general two-dimensional curvilinear coordinates (ξ, η) are:

$$J\frac{\partial\omega}{\partial t}+\frac{\partial}{\partial\xi}(\Psi_\eta\psi)-\frac{\partial}{\partial\eta}(\Psi_\xi\omega)$$
$$=\frac{1}{\mathrm{Re}_r}\left[\frac{\partial}{\partial\xi}\left(\frac{\alpha}{J}\frac{\partial\omega}{\partial\xi}-\frac{\beta}{J}\frac{\partial\omega}{\partial\eta}\right)+\frac{\partial}{\partial\eta}\left(\frac{\gamma}{J}\frac{\partial\omega}{\partial\eta}-\frac{\beta}{J}\frac{\partial\omega}{\partial\xi}\right)\right] \quad (1)$$

and

$$-J\omega=\frac{\partial}{\partial\xi}\left(\frac{\alpha}{J}\frac{\partial\Psi}{\partial\xi}-\frac{\beta}{J}\frac{\partial\Psi}{\partial\eta}\right)+\frac{\partial}{\partial\eta}\left(\frac{\alpha}{J}\frac{\partial\Psi}{\partial\eta}-\frac{\beta}{J}\frac{\partial\Psi}{\partial\xi}\right) \quad (2)$$

where the metric coefficients, α, β, and γ, and the Jacobian, J, are defined as

$$\alpha=x_\eta^2+y_\eta^2$$
$$\beta=x_\xi x_\eta+y_\xi y_\eta$$
$$\gamma=x_\xi^2+y_\xi^2$$
$$J=\frac{\partial(x,y)}{\partial(\xi,\eta)}=x_\xi y_\eta-x_\eta y_\xi \quad (3)$$

Here Ψ and ω are the nondimensionalized stream function and vorticity with respect to free stream velocity, U_∞, and cylinder radius, r.

2.2 Numerical Grid Generation. The numerical, body-fitted, two-dimensional grids are generated by solving the transformed Poisson equations.

$$\alpha x_{\xi\xi}-2\beta x_{\xi\eta}+\gamma x_{\eta\eta}=-J^2(Px_\xi+Qx_\eta)$$
$$\alpha y_{\xi\xi}-2\beta y_{\xi\eta}+\gamma y_{\eta\eta}=-J^2(Py_\xi+Qy_\eta) \quad (4)$$

where (ξ, η) represent the coordinates in the computational domain and P and Q are terms which control the point spacing in the interior of the domain.

2.3 Particle Trajectory and Rebounding. The trajectory of a particle in a moving fluid is governed by the rate of change of momentum and the external forces acting upon it. The equations of motion of a particle of mass m in Cartesian coordinates are as follows:

$$m\frac{d^2x}{dt^2}=f_x$$
$$m\frac{d^2y}{dt^2}=f_y \quad (5)$$

where x, y are the coordinates of the particle.

Among the forces acting on the nonrotating spherical particles in the flow field, only the drag and body forces are considered significant for typical low speed dilute gas-particle flows where the density ratio of fluid and the particle is of the order of 10^{-3} (Rudinger, 1980). Side forces such as Magnus force (Rubinow and Keller, 1961) and Saffman's force (Saffman, 1965) are not considered in the present study. Also the gravitational body force, even though not negligible in magnitude, is not included in the present simulation to avoid the complexity in the discussion depending on the direction of the gravity relative to the flow direction and tube arrangement.

Based on the assumption that the drag is the only dominant external force acting on the spherical particle, then the components of the drag, f_x and f_y, in the direction of the relative velocity, w_r, are defined by:

$$f_x=\frac{1}{8}\pi\rho_f d^2C_d(u_f-u)w_r$$
$$f_y=\frac{1}{8}\pi\rho_f d^2C_d(v_f-v)w_r \quad (6)$$

where the drag coefficient, C_d, for a spherical particle from Hussein and Tabakoff (1973) is used which approximates to the standard experimental drag-Reynolds number relationship.

2.4 Impact and Rebound Phenomena of Particles. The velocity of a rebounding particle is calculated using the restitution coefficients, e_t ($\equiv V_{2t}/V_{1t}$) and e_n ($\equiv V_{2n}/V_{1n}$), that is measured by experiments. The rebound particle velocity components, V_{2t} and V_{2n}, are then calculated by the following manner,

$$V_{2t}=e_tV_{1t}$$
$$V_{2n}=e_nV_{1n} \quad (7)$$

It should be noted here that the restitution ratios, which are determined experimentally, vary according to the flow velocity, and the combination of particles and target materials. For the present simulation, existing experimental data from Grant and Tabakoff (1975) for sand particles impacting on the 410 stainless steel was used for demonstration, which has the following expressions for the restitution ratios:

$$e_t\equiv\frac{V_{2t}}{V_{1t}}=1.0-2.12\beta_1+3.0775\beta_1^2-1.1\beta_1^3$$
$$e_n\equiv\frac{V_{2n}}{V_{1n}}=1.0-0.4159\beta_1+0.4994\beta_1^2-0.292\beta_1^3 \quad (8)$$

Nomenclature

c_p = pressure coefficient, Fig. 4
d = particle diameter, Eq. (6)
E_n = collision efficiency for nth row of cylinders
f_x, f_y = external forces, Eq. (5), (6)
J = Jacobian, Eq. (3)
m = particle mass, Eq. (5)
P, Q = forcing function or control function, Eq. (4)
Re = Reynolds number based on cylinder diameter and the free stream velocity for flow over a cylinder; Reynolds number based on cylinder diameter and maximum velocity through the channel for tube bank flows
Re_p = Reynolds number based on particle diameter and relative velocity, w_r
Re_r = Reynolds number based on cylinder radius, Eq. (1)
r = cylinder radius
t = time
V = velocity
w_r = relative velocity of the particle to the flow
x = Cartesian coordinate (nondimensionalized)
y = Cartesian coordinate (nondimensionalized)
α, β, γ = metric coefficient, Eq. (3)
θ = angle from the leading edge of the cylinder, Figs. 10 and 11
ρ = density
τ = particle relaxation time, = $(1/18)(d^2\rho_p/\nu\rho_f)$
Ψ = streamfunction, nondimensionalized
ω = vorticity, nondimensionalized
ξ, η = coordinates in the computational domain

Subscripts

p = refers to particle
1 = refers the condition before impact
2 = refers the condition after impact
t = particle velocity component tangential to the surface
n = particle velocity component normal to the surface

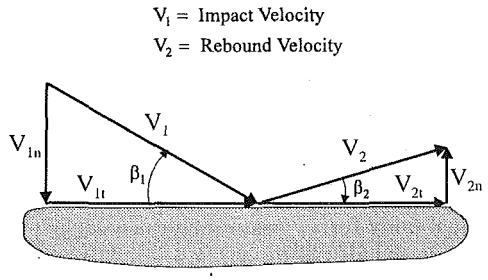

Fig. 1 Velocity and angle notations

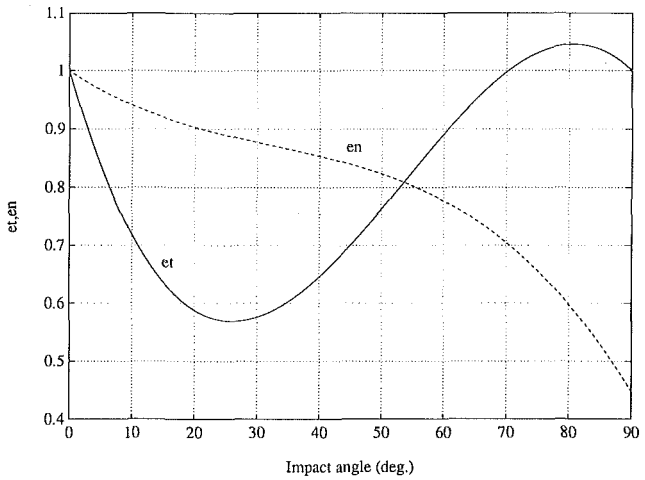

Fig. 2 Typical restitution ratios (e_t, e_n) from experiments (Grant and Tabakoff, 1975)

where β_1 is an impact angle in radian as defined in Fig. 1. The rebounding coefficients of Eq. (8) are shown in Fig. 2.

2.5 Erosion Due to the Particle Impact. The experimental data from the erosion tests were used to obtain the following semiempirical equation (Hamed, 1992) for the erosion mass parameter, ϵ_r, which is defined as the ratio of the eroded mass of the target material to the mass of the impinging particles and has the unit of mg/gm.

$$e_r = 278.90\left[\left(\frac{V_1}{100}\right)^{2.47}\cos^2\beta_1(1-e_t^2) + 0.0832\left(\frac{V_1}{100}\right)^{2.344}\sin^2\beta_1(1-e_n^2)\right] \quad (9)$$

where V_1 is in meter/s. Figure 3 shows the correlation represented by Eq. (9).

3 Numerical Procedure

3.1 Flow Field. The stream function and vorticity transport form of the equations of motion are solved using a factored ADI scheme developed by Davis et al. (Davis, 1972; Hill, 1979). Calculations were conducted for the flow over a cylinder and two rows of square in-line tube banks, respectively. A tube bank flow with pitch-to-diameter ratios of 1.5×1.5 was selected to compare the present result with Fujii et al. (1984). For the simulation of particles behavior, a square in-line tube bank with pitch-to-diameter ratios of 2.0×2.0 at $\mathrm{Re} = 400$ was selected. For this case, symmetry boundary condition is applied along the upper and lower boundaries of the channel and free stream boundary condition is used for far upstream and far downstream. The upstream boundary is located at four cylinder diameter upstream from the center of the first cylinder and the downstream boundary is specified at 18 cylinder diameter downstream from the center of the first cylinder. On the cylinder surface, no-slip condition is applied.

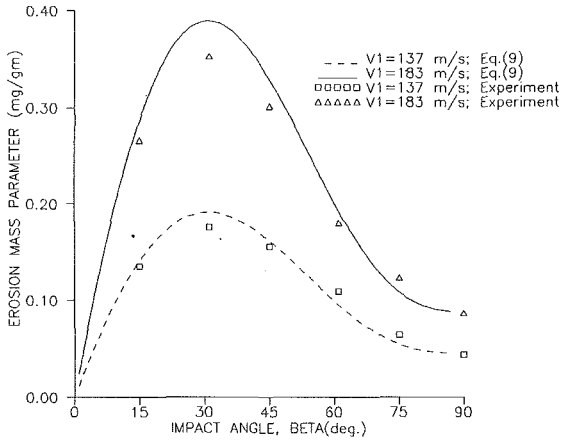

Fig. 3 Typical erosion mass parameter curves (Hamed, 1992)

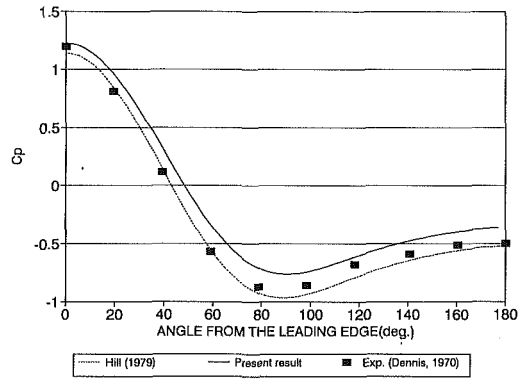

Fig. 4 Pressure coefficient over a cylinder (Re = 40)

3.2 Particles Behavior. Once the steady-state solution of the flow field is obtained, the equations for the particle trajectory, Eq. (5), are integrated with the given initial conditions (location and velocity components) to get the particle location and velocity components at any time. This initial value problem is solved numerically by using fourth order Runge-Kutta method. When the particle approaches any solid surface, the time step size is adjusted to locate the closest point of impact by trial and error method until the distance between the particle and the surface becomes less than the prescribed limit. If the particle impacts solid surface, the particle rebounding coefficients in Eq. (8) are used to continue the particle trajectory simulation after the impact and the amount of erosion due to the particle impact is estimated by using Eq. (9).

4 Results and Discussion

Flows over the following configurations were studied: (*a*) one cylinder and (*b*) square in-line tube banks.

4.1 Flow Field. Our calculated results for the flow over a cylinder were checked with the results of Hill (1979) and Dennis and Chang (1970) for flow at $\mathrm{Re} = 40$ based on the free stream velocity and the cylinder diameter. For this purpose, a concentric grid with 129×129 points, was used to get the steady solution of the flow field. Calculated streamlines agreed well with the results by Hill (1979) and by Dennis and Chang (1970) in terms of the recirculating wake length while the nondimensionalized pressure showed slight deviation as shown in the Fig. 4, which seems to be the effect of the accumulated truncation error with the first-order accurate boundary condition.

A square in-line tube bank with a pitch-to-diameter ratios of 1.5×1.5 was selected as a test case to compare the calculated

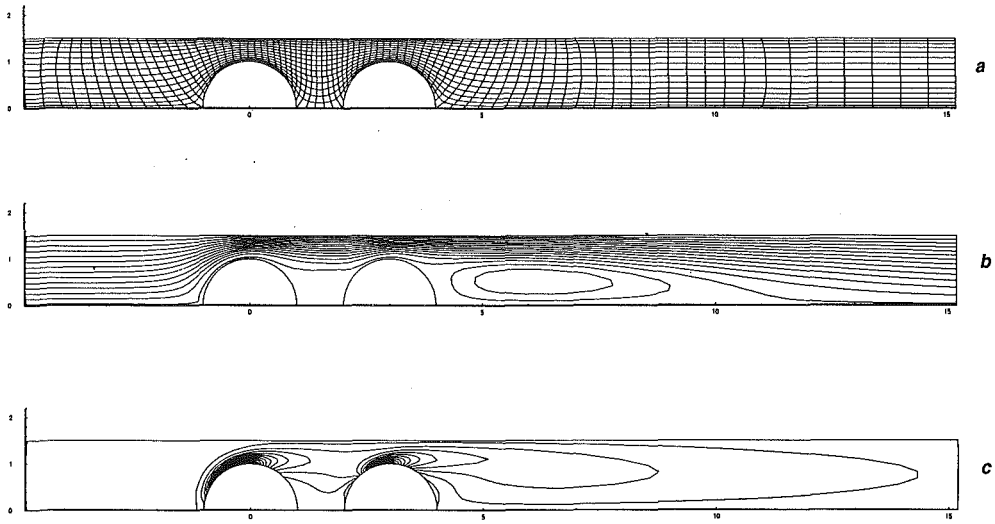

Fig. 5 Flow over two rows of in-line tube banks (1.5 x 1.5) at Re = 120; (*a*) Part of 201 x 16 grid, (*b*) streamlines, and (*c*) iso-vorticity lines

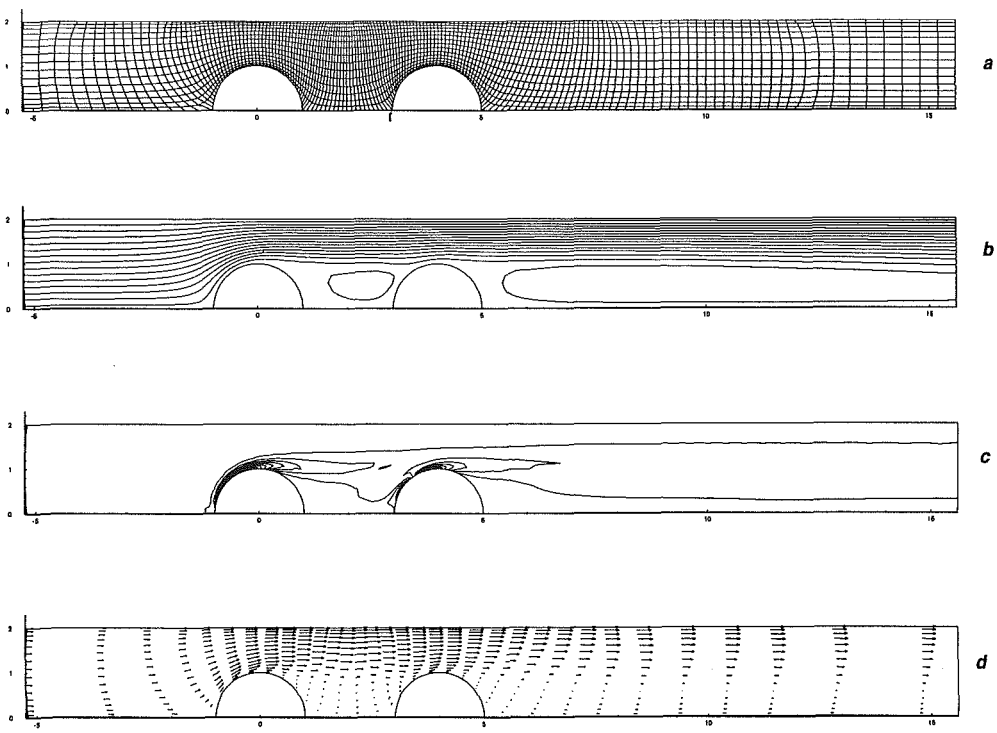

Fig. 6 Flow over two rows of in-line tube banks (2.0 x 2.0) at Re = 400; (*a*) Part of 201 x 16 grid, (*b*) streamlines, (*c*) iso-vorticity lines, and (*d*) velocity profile

results with those of Fujii et al. (1984) who calculated the flow (laminar) for an in-line square tube bank up to five rows deep, with the same pitch-to-diameter ratios. The flow fields were calculated at three different Reynolds numbers (Re = 60, 120, 300) based on the maximum velocity through the channel and the cylinder diameter. Figures 5(*a*) to 5(*c*) show the grid (201×16), the streamlines and the iso-vorticity lines of the flow at Re = 120. Compared with the results of Fujii et al. (1984), the streamlines and iso-vorticity lines showed similar contour and in both simulations the stagnation point (or the position of the impact point) on the inner cylinder surface was found to be about 45 deg from the center line according to the iso-vorticity lines in Fig. 5(*c*). Finally a square in-line tube bank of two rows with pitch-to-diameter ratios 2.0×2.0, Fig. 6, was selected for the particles trajectory simulation. Using a 401×31 numerically generated grid, flow fields were obtained for 201×16 points at Re = 80, 200, and 400. Fully converged flow solutions were obtained for flows at Re = 80 and 200, however at Re = 400 the vorticity field was not stable enough to meet the prescribed convergence criteria on the local maximum error, $|(f_{i,j}^{N+1} - f_{i,j}^{N})/\Delta t|_{\max} < 10^{-4}$, while the stream function converged relatively fast. It is reported that the vorticity field is slower in convergence than the streamfunction (Ghia et al., 1989) but the coarse grid seems to be the limiting condition for the high Reynolds number flow simulation.

The calculated flow at Re = 400 for two rows of in-line tube bank is shown in Fig. 6: (*a*) part of the 201×16 grid, (*b*) the streamlines, (*c*) the iso-vorticity, and (*d*) the velocity profile.

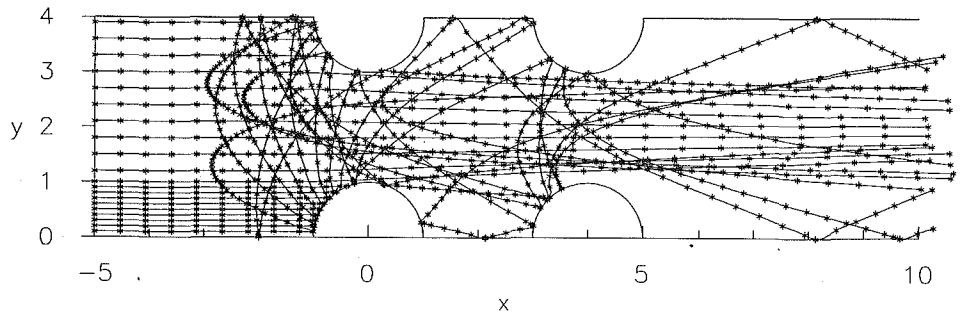

Fig. 7 Particle trajectories over in-line tube banks (Re = 400); sand, $D_p = 100\ \mu m$, $(V_p/V_f)_i = 0.8$

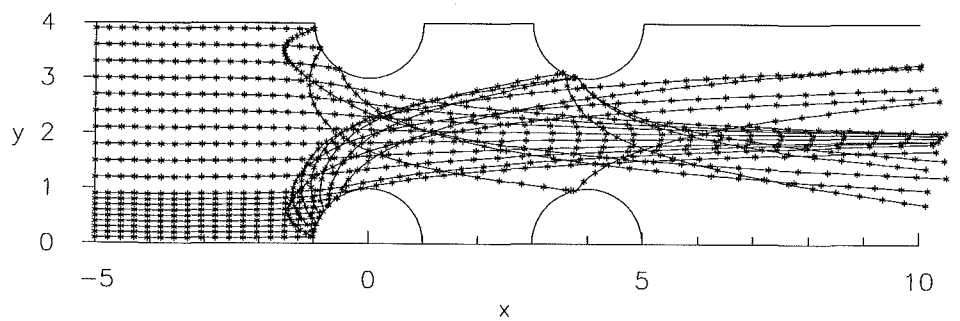

Fig. 8 Particle trajectories over in-line tube banks (Re = 400); fly ash, $D_p = 40\ \mu m$ $(V_p/V_f)_i = 0.8$

A wake has formed between the two cylinders and is followed by a major recirculation zone after the second row of cylinders. Uniform flow from upstream accelerates approaching the first cylinder and attains its maximum velocity near the top of the first cylinder. The flow then separates from the cylinder surface because of the adverse pressure gradients along the cylinder surface and is divided into two parts, the main stream and the recirculation zone. The main stream continues with higher velocity than the uniform stream (approximately two times the uniform velocity for the present case) while the velocity in the recirculation zones are very slow as can be seen in Fig. 6(*d*).

It is important to notice that the flow pattern which directly affects the particle behavior in the flow is basically determined by the geometric configuration (tube diameter, transverse and longitudinal spacing) and the incoming flow velocity.

4.2 Particle Trajectory, Impact, and Erosion in Tube Banks. The solid particles of assumed spherical shape are introduced into the calculated flow field, Fig. 6, to simulate their trajectories, impact and finally to estimate the erosion of the tube material. The dimensions used for this simulation are as follows:

Type of arrangement	: square in-line tube bank.
Number of rows	= 2
Pitch (S_l, S_t)	= two times the cylinder diameter.
Flow Re	= 400
Cylinder diameter	= 3.175 mm
Flow (air) density	= 1.2042 Kg/m^3
Particle density	= 2444.0 Kg/m^3 (Sand)
	1665.9 Kg/m^3 (Fly Ash)
Partile diameter	= 40 μm and 100 μm
Kinematic viscosity	= 1.46E-5 m^2/s
Tube material	: Rene 41
Density of Rene 41	= 8190 Kg/m^3
Free stream velocity	= 0.9197 m/s

Here the relaxation time for 100 μm sand particles is 77.1 ms and that for 40 μm fly ash particles is 8.4 ms, respectively. Particles are introduced with an assumed initial particle-to-flow velocity ratio of 0.8.

For larger sand particles (100 μm) as shown in Fig. 7, most of the rebounded particles from the first cylinder cross the mainstream and impact on the neighboring cylinder surface either on the first or on the second row. Therefore considerable amount of secondary impact occur on the first cylinder surface either on the front side or on the back side to the main stream. Part of the impact on the back side of the first cylinders comes after the impact on the second cylinders while others come from the neighboring first cylinders. It is interesting to note that the particle introduced in the wake do not change the direction much because the particle inertia is dominant compared with the aerodynamic forces acting on it. From this, one can see that there is more chance of impact on the first row of cylinders in this tube bank than the case of one cylinder because of the secondary impact from the neighboring cylinders.

For smaller fly ash particles (40 μm) as shown in Fig. 8, most of the impact on the first cylinders are the primary impact while most of the impact on the second cylinders are the secondary impact from the first row of cylinders. An interesting feature of the impact on the second cylinders is that they are concentrated in a limited area on the tube surface in this particular case.

To estimate the relative impact frequency on the cylinders the collision efficiency, E_n, is defined to be the ratio of the total number of impact on the nth row cylinder to the number of particles uniformly introduced over a transverse pitch (two times the cylinder diameter for the present geometry). For this one hundred uniformly distributed particles over a transverse pitch were introduced for the simulation.

Figure 9 shows the collision efficiency of the two particle group for the first and the second row, respectively. According to the figure, the larger particles (100 μm sand) showed higher collision efficiency than the smaller ones (40 μm fly ash) for the first row, which reflects the contribution from the neighboring cylinders with the secondary impact. Lower collision efficiencies on the second row cylinders seems to partially support the protective role of the first row cylinders in regard to the particles collision. Also higher E_2 with larger particles

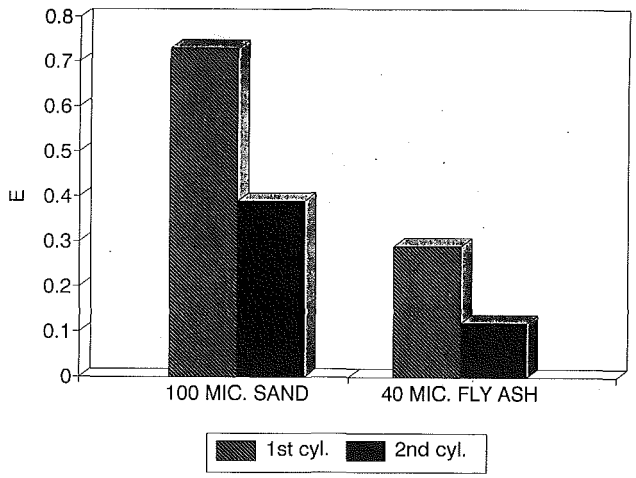

Fig. 9 Collision efficiency of in-line tube banks (2.0 × 2.0) at Re = 400

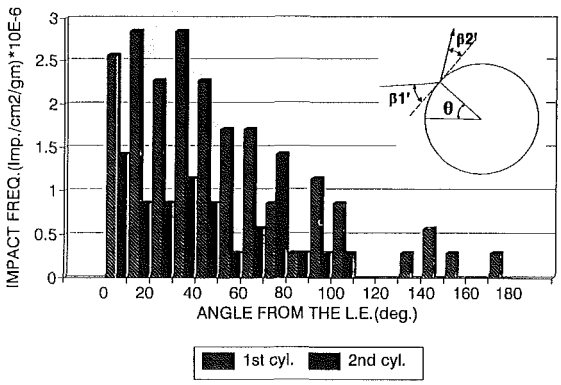

Fig. 10(*a*) Impact frequency

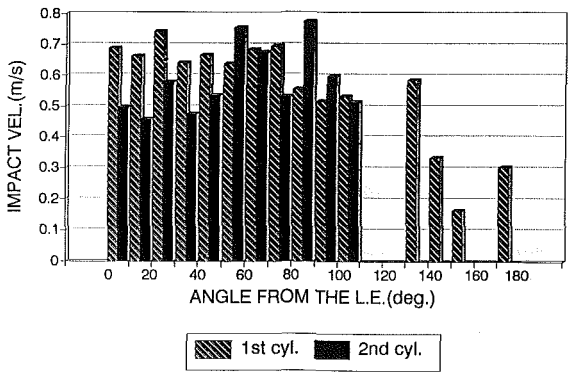

Fig. 10(*b*) Impact velocities

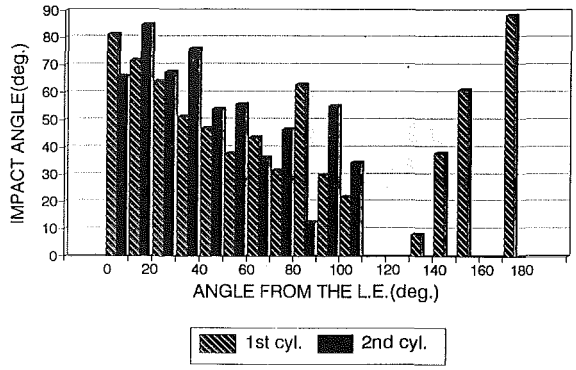

Fig. 10(*c*) Impact angles

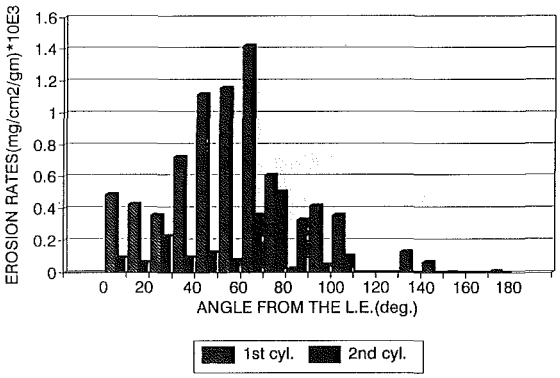

Fig. 10(*d*) Erosion rates

Fig. 10 Impact characteristics for 100 μm sand

than that with smaller ones suggests the more inertia dominated nature of the larger particles in the particles behavior.

Figures 10 and 11 represent the impact and erosion characteristics of the tube bank in the particulate environment.

For larger particles, Figs. 10(*a*) through 10(*d*), impact occurs mostly on the front side of the first cylinders and it occurs less frequently on the front side of the second cylinder and on the back side of the first cylinder, as presented in Fig. 10(*a*). Figure 10(*b*) shows the averaged impact velocities on both the first and the second cylinders. The small velocity difference with regard to the initial velocity (0.736 m/s) reflects the fact that there was not enough time for these particles to adjust themselves to the changes in the flow field. According to the results from the simulation the maximum erosion occurred at 40 to 70 deg from the leading edge, Fig. 10(*d*), even though the maximum impact frequency occurred at 0 to 50 deg from the leading edge, Fig. 10(*a*). This is mostly because of the smaller impact angle (about 30 to 45 deg) at that location (40 to 70 deg from the leading edge) with which the target surface is vulnerable to severe erosion as demonstrated by Fig. 3. The second cylinders also have impact along the front side and part of the back side near the top. However the impact frequency and erosion on the second cylinders are much less than those on the first cylinders.

The impact characteristics for 40 μm fly ash particles are shown in Figs. 11(*a*) through 11(*d*). The impact frequency and impact angles are high near the leading edge and decreases as the wetted area decreases while the impact velocity increases slightly as the angle from the leading edge approaches 90 deg. This effect is due to the accelerated flow field. It is interesting to note from Fig. 3 that the combination of high impact velocity and low impact angle maximizes the erosion. This situation occurs near the top of the second cylinder (60 to 90 deg from the leading edge), Figs. 11(*b*) through 11(*d*). As a result of these conditions, the erosion of the second cylinder surface is no longer smaller than the erosion of the first cylinder surface. As can be sen in Fig. 11(*d*), the local maximum erosion now occurs on the second cylinders around 60 to 70 deg from the leading edge. This phenomenon is the outcome of the secondary impact from the neighboring cylinders combined with high main stream velocity defined by the tube arrangement. It should be noted that the erosion does not necessarily follow the trend of the impact frequency as could be seen in Figs. 10 and 11.

Figures 12 and 13 are representing the impact frequency and the erosion over the half cylinders for the two cases. It can be seen that the impact occur more frequently on the first cylinders than on the second cylinders in both cases. However, more serious erosion may happen on the second cylinders and it is depending on the particle sizes.

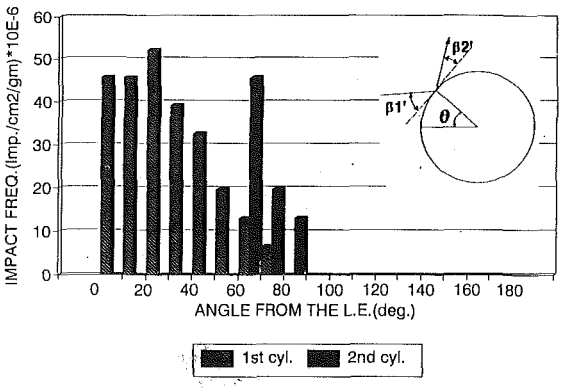

Fig. 11(*a*) Impact frequency

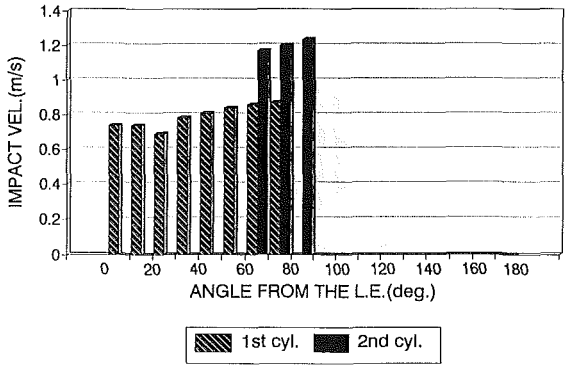

Fig. 11(b) Impact velocities

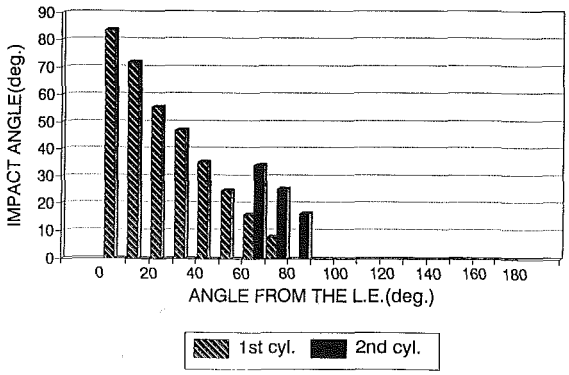

Fig. 11(*c*) Impact angles

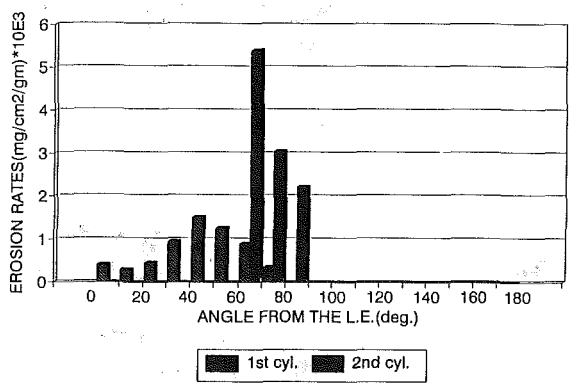

Fig. 11(*d*) Erosion rates

Fig. 11 Impact characteristics for 40 μm fly ash

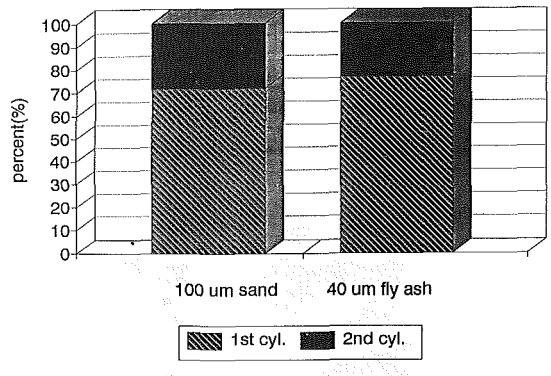

Fig. 12 Overall impact distribution on the first and the second cylinder surface

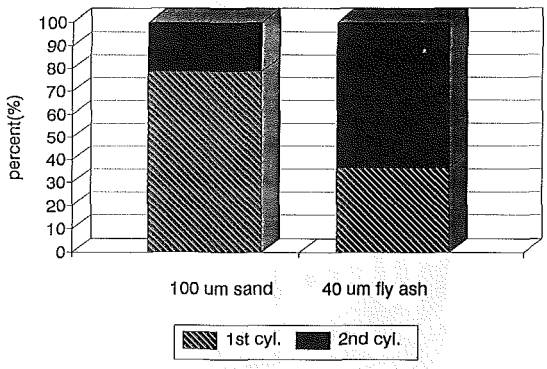

Fig. 13 Overall erosion rate distribution on the first and the second cylinder surface

5 Conclusions

The particles behavior in tube banks are basically different from that over a cylinder due to the different aerodynamic condition made by the neighboring cylinders. The tube spacing (transverse, longitudinal) and arrangement, cylinder diameter and the flow velocity of the gas seem to be the important factors affecting the particles trajectory, the impact, and the erosion when the particle properties are fixed. Different particles behavior of two different sizes and density are demonstrated through the present study for the fixed geometry and the flow condition as an in-line tube bank system.

Based on the simulation results, the followings could be concluded:

1. Depending on the mass and size of the particles, the particles behavior in tube bank system showed significant difference in their trajectories, impact and the erosion pattern.
2. The protective role of the first row of cylinders could be supported by the present simulation with respect to the particles impact only but not necessarily to the erosion.
3. The information that affects the erosion estimation at impact such as the impact velocity and the impact angle can be estimated by using the numerical simulation shown as in the present study.

Uncertainties. The restitution coefficients such as used for the present simulation are determined from empirical correlations of the restitution parameters based on the experimental data obtained by using Laser Doppler Velocimetry. They represents the most probable direction and magnitude of each rebounding particle velocity.

Acknowledgment

This research work was partially supported by NSF grant CTS-90123209.

References

Beam, R. M., and Warming, R. F., 1978, "An Implicit Factored Scheme for the Compressible Navier-Stokes Equations," *AIAA Journal*, Vol. 16, No. 4, Apr.

Chow, C. Y., 1979, *An Introduction to Computational Fluid Mechanics*, Wiley, New York, NY.

Dennis, S. C. R., and Chang, G. Z., 1970, "Numerical Solutions for Steady Flow Past a Circular Cylinder at Reynolds Numbers up to 100," *Journal of Fluid Mechanics*, Vol. 42, Part 3, pp. 471–489.

Davis, R. T., 1972, "Numerical Solution of the Navier-Stokes Equations for Symmetric Laminar Incompressible Flow Past a Parabola," *Journal of Fluid Mechanics*, Vol. 51, p. 417.

Fujii, M., Fujii, T., and Nagata, T., 1984, "A Numerical Analysis of Laminar Flow and Heat Transfer of Air in an In-Line Tube Banks," *Numerical Heat Transfer*, Vol. 7, pp. 89–102.

Ghia, K. N., Osswald, G. A., and Ghia, U., 1989, "Analysis of Incompressible Massively Separated Viscous Flows Using Unsteady Navier-Stokes Equations," *International Journal for Numerical Methods in Fluids*, Vol. 9, pp. 1025–1050.

Grant, G., and Tabakoff, W., 1975, "Erosion Prediction in Turbomachinery Resulting from Environmental Solid Particles," *Journal of Aircraft*, Vol. 12, No. 5, AIAA Paper 74-16.

Hamed, A., 1992, "An Investigation in the Variance in Particle Surface Interactions and Their Effects in Gas Turbines," *Journal of Aircraft for Gas Turbines and Power*, Vol. 114, pp. 235–241.

Hill, J. A., 1979, "Development of a Factored ADI Scheme for Solving the Navier-Stokes Equations in Streamfunction Vorticity Variables," M.S. thesis, University of Cincinnati, Cincinnati.

Hussein, M. F., and Tabakoff, W., 1973, "Three Dimensional Dynamic Characteristics of Solid Particles Suspended by Polluted Air Flow in a Turbine Stage," AIAA Paper No. 73-140.

Laitone, J. A., 1983, "Characterization of Particle Rebound Phenomena in the Erosion of Turbomachinery," *Journal of Aircraft*, Vol. 20, No. 3.

Michael, D. H., and Norey, P. W., 1969, "Particle Collision Efficiencies for a Sphere," *Journal of Fluid Mechanics*, Vol. 37, Part 3, pp. 565–575.

Morsi, S. A., and Alexander, A. J., 1972, "An Investigation of Particle Trajectories in Two Phase Flow System," *Journal of Fluid Mechanics*, Vol. 55, p. 193.

Rubinow, S. I., and Keller, J. B., 1961, "The Transverse Force on a Spinning Sphere Moving in a Viscous Fluid," *Journal of Fluid Mechanics*, Vol. 11, pp. 447–459.

Rudinger, G., 1980, *Fundamentals of Gas-Particle Flow*, Elsevier Scientific Publishing, pp. 7–11.

Saffman, P. G., 1965, "The Lift of a Small Sphere in a Slow Shear Flow," *Journal of Fluid Mechanics*, Vol. 22, Part 2, pp. 385–400.

Schuh, M. J., Schuler, C. A., and Humphrey, J. A. C., 1989, "Numerical Calculation of Particle-Laden Gas Flows Past Tubes," *AIChE Journal*, Vol. 35, No. 3.

Tabakoff, W., Hamed, A., and Wenglarz, R., 1988, "Particulate Flow and Blade Erosion," von Karman Institute for Fluid Dynamics Lecture Series 1988–89.

Zukauskas, A., 1972, "Heat Transfer from Tubes in Cross-Flow," *Advances in Heat Transfer*, Vol. 8, p. 93.

Effect of Selective Modification of Turbulence on Two-Equation Models for Particle-Laden Turbulent Flows

K. D. Squires
Department of Mechanical Engineering,
The University of Vermont,
Burlington, VT 05405

J. K. Eaton
Department of Mechanical Engineering,
Stanford University,
Stanford, CA 94305

The effect of selective modification of turbulence by particles on $K-\epsilon$ models for dilute two-phase flows has been evaluated using data from direct numerical simulation of particle-laden isotropic turbulence. Simulation results were obtained using as many as 64^3 grid points and up to 10^6 particles. The ratio of the particle time constant to large-eddy turbulence time scale varied from 0.14 to 1.50 and particle mass loadings of 0.0, 0.1, 0.5, and 1.0 were used in the simulations. Simulation results demonstrate that the balance between enstrophy production by turbulent vortex stretching and viscous destruction is disrupted by momentum exchange with the particle cloud. Selective modification of the turbulence by lighter particles results in a significant attenuation of enstrophy production by turbulent vortex stretching. The decrease in enstrophy production causes the model constant $C_{\epsilon 2}$ to increase for large mass loading. Heavy particles are found to act as a sink of enstrophy for all mass loadings used in the simulations. Preferential concentration of lighter particles by turbulence, however, can generate vorticity fluctuations, especially at higher mass loadings. For these cases conventional modeling of the destruction of dissipation by particles term in the ϵ equation requires that $C_{\epsilon 3}$ be negative.

1 Introduction

Numerical predictions of particle-laden turbulent flows are complicated by the fact that, in addition to the considerations which arise in the prediction of single-phase turbulence, one must account for particle interactions with the underlying turbulent flow field. For dilute flows in which there is no phase change the principle interactions which must be modeled are turbulent dispersion of particles and modification of turbulence due to momentum exchange with the particle cloud. Accurately incorporating these effects into the Eulerian transport equations used to predict turbulence properties is difficult since these interactions are inherently Lagrangian, i.e., they occur along the trajectories of individual particles. The increase in the relevant parameter space for particle-laden flows over single-phase turbulence further complicates the modeling of particle interactions with turbulence. Factors such as particle size, particle inertia, mass loading, and particle concentration distribution all influence particle interactions with turbulence and should necessarily be reflected by numerical predictive techniques.

There are a large number of techniques which may be used to predict particle-laden turbulence. The majority of the techniques used for engineering analysis involve solution of the Reynolds-averaged Navier–Stokes equations. In this approach the Navier–Stokes equations are averaged over time (or ensembles) to yield transport equations for the mean flow variables. As is well known, this averaging procedure gives rise to turbulent stresses which must be modeled using some level of approximation. Typically, the turbulent stresses are modeled using a gradient transport hypothesis in which closure of the mean equations is obtained through specification of the turbulent eddy viscosity. There are a large number of methods for determining the turbulent eddy viscosity. In one of the most widely used methods the eddy viscosity is specified in terms of the turbulence kinetic energy and dissipation rate, i.e., the $K-\epsilon$ model. In the $K-\epsilon$ model, two additional transport equations are solved for K and ϵ (e.g, see Launder et al., 1975, Rodi, 1980). For particle-laden turbulence in which the coupling between phases is from fluid to particles only (i.e., "one-way" coupling, Crowe, 1982) there is, in principal, no difficulty in predicting the properties of the turbulence since the fluid is assumed to be unaffected by the presence of the dispersed phase. Thus, for this class of flows, the $K-\epsilon$ model is unchanged. However, for the class of flows in which the properties of the turbulence may be modified by momentum exchange with the particle cloud it is necessary to explicitly model the effect of particles on the turbulence in the K and ϵ equations.

There have been a number of modifications proposed to the

Contributed by the Fluids Engineering Division for publication in the JOURNAL OF FLUIDS ENGINEERING. Manuscript received by the Fluids Engineering Division July 20, 1993; revised manuscript received May 3, 1994. Associate Technical Editor: M. W. Reeks.

$K-\epsilon$ model to account for the effect of particles on the turbulence kinetic energy and dissipation rate. Elghobashi & Abou-Arab (1983) derived the exact transport equations for K and ϵ for flows in which the particle cloud volume fraction is not negligible. These investigators used gradient-transport type closures for the correlations in the K and ϵ equations and introduced three new constants into the model to represent the effect of particle interaction with turbulence. Using this model, Elghobashi and Abou-Arab and Elghobashi et al. (1984) obtained reasonable agreement between computations of particle-laden jets and the experimental measurements of Modarress et al. (1982, 1984), though adjustment of one of the three new model constants was required to account for different particle sizes. Shuen et al. (1985) formulated a $K-\epsilon$ model for dilute particle-laden turbulence and compared model predictions to experimental measurements of particle-laden round jets. Reasonable agreement between computation and experiment was obtained but the model constant of the term in the dissipation equation representing the effect of particles on ϵ varied from 0.1 to 5.0. Mostafa et al. (1989) used a $K-\epsilon$ model derived by Mostafa and Mongia (1987) to compute particle-laden jets. They had to adjust the values of some of the model constants recommended by Mostafa and Mongia in order to obtain reasonable agreement between computations and experimental measurements. Chen (1986) used a multiple-scale $K-\epsilon$ model for dilute flows, derived by Chen and Wood (1985), to compute particle-laden pipe flow and a confined particle-laden jet. In Chen and Wood's model particles are assumed to act strictly as dissipation of both turbulence kinetic energy and the dissipation rate. Rizk and Elghobashi (1989) formulated a $K-\epsilon$ model for low-Reynolds number turbulence which also accounted for the presence of a wall on the interactions between particles and turbulence. The constants in the model representing the effect of particles on K and ϵ were different than those recommended by Elghobasi and Abou-Arab (1983). Berlemont et al. (1990) used a $K-\epsilon$ model identical to that developed by Shuen et al. (1985) to compute particle-laden turbulent jets. The model constants employed in these computations, however, were different than those used by Shuen et al. (1985). Azevedo and Pereira (1991) have used both a standard $K-\epsilon$ model as well as a multiple-scale model to compute swirling jets. As is also the case in the model of Chen and Wood (1985), these investigators assumed the effect of the particles to be strictly a dissipation of both K and ϵ.

Though the work cited above is not exhaustive, it does provide a representative overview of $K-\epsilon$ modeling of particle-laden turbulent flows. Implicit in all of these previous efforts are assumptions regarding the basic mechanisms by which a cloud of dispersed particles interact with turbulence. For example, the "single-phase" terms in the $K-\epsilon$ model, i.e., those terms which would arise for flows in which there is no dispersed phase, are assumed to be unchanged by momentum exchange with the particle cloud. The model constants multiplying these terms also have the same value as for single-phase turbulence. Thus, no accounting is given of the possibility that particle interactions with turbulence may interfere with certain dynamical processes of the turbulence itself. Futhermore, the presence of the dispersed phase is also represented in these models as "extra dissipation" of both K and ϵ. Gore and Crowe (1989) have compiled experimental measurements obtained from particle-laden turbulent jets and have demonstrated that turbulence kinetic energy can be enhanced if the particles are large relative to turbulence length scales. Aside from the fact that the particles are considered as extra dissipation, parameterizations of the effect of particles on K and ϵ are nearly identical to those used for the corresponding single-phase terms. Since the single-phase model expressions are often obtained through some approximate analysis, e.g., by considering a model form of the turbulence energy spectrum, simply assuming the analogous terms representing the effect of particles on K and ϵ to behave in a similar manner may be grossly in error. Similar model expressions for the particles and fluid will only be valid if the mechanisms by which particles and turbulence influence K and ϵ are the same.

Perhaps the principal reason for deficiencies in $K-\epsilon$ modeling of particle-laden turbulence has been the inability to directly evaluate the various assumptions and expressions associated with these models. It is simply not possible to measure in laboratory experiments most of the statistical correlations in the K and ϵ equations. An alternative to using data from laboratory experiments in model evaluation is utilization of the database generated from direct numerical simulation (DNS). In DNS the Navier-Stokes equations are solved without approximation (other than those associated with the numerical method) and the simulation provides a detailed, three-dimensional, time-dependent description of the flow. Since DNS resolves all scales of motion it is necessarily restricted to low Reynolds numbers. Recently, DNS has been utilized to study the fundamental physics of particle interactions with homogeneous turbulence. Squires and Eaton (1990) have examined turbulence modification by particles in simulations of forced, isotropic turbulence and have found that turbulence kinetic energy can be decreased by as much as 50 percent due to momentum exchange with the dispersed phase. Elghobashi and Truesdell (1993) have used DNS of decaying isotropic turbulence to study turbulence modification and find that particles interfere with energy transfer from large to small scales. Aside from increasing the basic understanding of particle interactions with turbulence in these flows, the simulations also provide a detailed database for evaluation of turbulence models for particle-laden flows. The objective of the present study, therefore, is to use the database from DNS to evaluate $K-\epsilon$ models for particle-laden turbulence. Use of DNS data permits, for the first time, examination of the assumptions inherent to existing $K-\epsilon$ models for particle-laden flows. The simulation database used in this study is that compiled by Squires and Eaton (1990), who examined particle interactions with turbulence in the simplest type of flow: homogeneous, isotropic turbulence. In isotropic turbulence there are no mean-flow gradients and consequently no production of turbulence energy. Therefore, it is the dissipation terms in the K and ϵ equations which are examined in this study.

2 Background

2.1 $K-\epsilon$ Equations for Dilute Particle-Laden Turbulence. The $K-\epsilon$ equations for dilute particle-laden turbulent flows can be expressed symbolically as

$$\frac{DK}{Dt}, \frac{D\epsilon}{Dt} = \text{Production} - \text{Dissipation} + \text{Transport} \qquad (1)$$

where $D(\cdot)/Dt$ denotes the substantial derivative and K and ϵ are the turbulence kinetic energy and dissipation rate, respectively. For homogeneous turbulence the transport terms in (1) are zero and the $K-\epsilon$ equations for this case may be expressed as

$$\frac{dK}{dt} = \mathcal{P}_K - \epsilon - \epsilon_p \qquad (2)$$

where $\mathcal{P}_K$ is the turbulence production and ϵ_p represents the source or sink of K due to momentum exchange with the particle cloud. The ϵ equation is

$$\frac{d\epsilon}{dt} = \mathcal{P}_\epsilon - \mathcal{D} - \mathcal{D}_p. \qquad (3)$$

In (3), $\mathcal{P}_\epsilon$ represents production of dissipation by turbulence interaction with mean gradients, $\mathcal{D}$ is the combination of the turbulent production and viscous destruction terms, and $\mathcal{D}_p$ is the source or sink of ϵ due to interaction with the particle

cloud. The terms $\mathcal{P}_K$, $\mathcal{P}_\epsilon$, and $\mathcal{D}$ are the same as for single-phase turbulence, i.e.,

$$\mathcal{P}_K = -\overline{u_i u_j}\,\overline{S}_{ij}, \tag{4}$$

$$\mathcal{P}\epsilon = -2\nu\,(\overline{u_{i,k}u_{j,k}} + \overline{u_{k,i}u_{k,j}})\,\overline{S}_{ij} \tag{5}$$

and

$$\mathcal{D} = 2\nu\,\overline{u_{i,j}u_{i,k}u_{j,k}} + 2\nu^2\,\overline{u_{i,jk}u_{i,jk}} \tag{6}$$

where $\overline{S}_{ij}$ is the strain-rate tensor of the mean velocity field, $\overline{S}_{ij} = (\overline{U}_{i,j} + \overline{U}_{j,i})/2$, u_i is the velocity fluctuation in the ith direction, and ν the kinematic viscosity of the fluid. The additional terms in the $K<\epsilon$ equations due to the presence of the dispersed phase are given by

$$\epsilon_p = \overline{u_i f_i} \tag{7}$$

and

$$\mathcal{D}_p = 2\nu\,\overline{u_{i,j}f_{i,j}} \tag{8}$$

where f_i is the fluctuating component of the force on the particles.

2.2 Closure of the $K-\epsilon$ Equations. Closure of the K equation requires specification of ϵ_p in (2). The term ϵ_p is a correlation between the fluctuating fluid velocity and force of the fluid on the particles. It is natural, therefore, to model ϵ_p using the particle equation of motion. In fact, it can be shown that construction of the turbulent velocity fluctuations along the particle path enables closure of ϵ_p without introduction of additional model constants (e.g., see Berlemont et al., 1990). Lagrangian models for particle dispersion require that the turbulent velocity fluctuations along the particle path be calculated. Thus, ϵ_p can be calculated directly given an accurate dispersion model. It may be remarked that construction of the turbulent velocity fluctuations along the particle path requires prescription, either directly or indirectly, of the correlation of fluid velocities along the particle path as well as the integral time scale of those fluctuations. It is important to emphasize that this correlation is a "particle-Lagrangian" function, i.e., it is dependent upon the motion of a particle which does not follow the turbulent fluctuations exactly. Recent findings, both from computations (Squires and Eaton, 1991a) and laboratory experiments (e.g., Longmire and Eaton, 1992, Lazaro and Lasheras, 1992; Fessler et al., 1993), have demonstrated that the fluid neighborhood encountered by a particle which is very responsive to the turbulent fluctuations can be different from the fluid velocities encountered by a heavier particle which does not respond as well to the spectrum of turbulent velocities. Since modeling particle dispersion by turbulence is beyond the scope of the present work specific closure models for ϵ_p are not examined in this study. The reader is referred to Squires and Eaton (1991b) for a discussion of closure assumptions employed in particle dispersion models.

Closure of the ϵ equation requires models for each of the terms on the right-hand side of (3). The production term is typically modeled as

$$\mathcal{P}_\epsilon = -2\nu\,(\overline{u_{i,k}u_{j,k}} + \overline{u_{k,i}u_{k,j}})\,\overline{S}_{ij} \approx C_{\epsilon 1}\,\frac{\epsilon}{k}\,\mathcal{P}_K \tag{9}$$

where $C_{\epsilon 1}$ is around 1.4 (e.g., see Launder et al., 1975). Since $K-\epsilon$ models were evaluated using simulations of isotropic turbulence the mean strain rate, $\overline{S}_{ij}$, is zero and there is no production of either K or ϵ by turbulence interaction with mean-field gradients. Therefore, closure models for the production terms are not addressed in this study.

The destruction of dissipation term, $\mathcal{D}$, is composed of two parts. The physical interpretation of these terms can be more easily seen by expressing $\mathcal{D}$ in terms of the vorticity fluctuations:

$$+2\nu^3\,\overline{\omega_{i,j}\omega_{i,j}}. \tag{10}$$

In (10) the fluctuating vorticity is ω_i and the strain-rate tensor of the fluctuating field is denoted as s_{ij}. The first term on the right-hand side of (10) corresponds to production of ϵ by turbulent vortex stretching while the second term is viscous destruction of ϵ. For single-phase turbulent flows these two terms are very nearly in balance and are therefore modeled together (e.g., see Smith and Reynolds, 1991). An expression for $\mathcal{D}$ can be obtained using a model form of the turbulence energy spectrum. Assuming high-Reynolds number turbulence and a $-5/3$ slope for the inertial subrange the following expression may be obtained for $\mathcal{D}$ (Reynolds, 1976)

$$\mathcal{D} \approx C_{\epsilon 2}\,\frac{\epsilon}{K}\,\epsilon. \tag{11}$$

The constant $C_{\epsilon 2}$ is calibrated from measurements of the decay of grid turbulence and is typically about 1.9.

In the majority of $K-\epsilon$ models the effect of particles on ϵ, $\mathcal{D}_p$, is parameterized analogously to that of $\mathcal{D}$, i.e.,

$$\mathcal{D}_p \approx C_{\epsilon 3}\,\frac{\epsilon}{K}\,\epsilon_p. \tag{12}$$

It is important to note that while (11) can be deduced based upon a model form of the energy spectrum, (12) is an *ad hoc* parameterization of the effect of particles on ϵ. The value of $C_{\epsilon 3}$ is usually calibrated to yield good agreement with a particular laboratory experiment. The fact that there is a wide range of values for $C_{\epsilon 3}$ currently used in K-ϵ models would indicate that (12) may be an inappropriate model for $\mathcal{D}_p$.

2.3 Overview of the DNS Database. In the earlier work by Squires and Eaton (1990) simulations of isotropic turbulence were performed to investigate particle response and turbulence modification by particles. Only the relevant properties of the turbulence and particles are summarized here. The reader is referred to Squires and Eaton (1991a, 1991b) for other details of the numerical method and computations.

In the simulations performed by Squires and Eaton (1990) the incompressible Navier–Stokes equations were solved using a Fourier-series, pseudo-spectral method. A steady, spatially non-uniform body force was added to the low wavenumber components of the velocity field in order to obtain a statistically stationary flow. Simulations using both 32^3 and 64^3 grid points were performed and the Taylor-microscale Reynolds numbers were nearly identical for each grid size (39.3 for the 32^3 grid, 38.7 for the 64^3 grid). Particle motion in the simulations was assumed to be governed by

$$\frac{dv_i}{dt} = \frac{u_i[X_j(t),t] - v_i(t)}{\tau_p} \tag{13}$$

where v_i is the ith component of the particle velocity and u_i is the fluid velocity at the instantaneous particle position. The particle time constant in (13) is denoted τ_p and the drag around the particle is assumed to be governed by Stokes law of resistance.

For each simulation the two phases were uncoupled and time advanced to reach a statistically stationary state. The momentum equation of the fluid was then coupled to the particle momentum equation with a specified mass loading. The mass loading is defined as the ratio of the total mass of particles to the total mass of fluid, i.e., $\phi = M_p/M_f$. Once the phases were coupled the 32^3 simulations were time advanced slightly over 12 eddy turnover times while the 64^3 simulations were advanced approximately six eddy turnover times. This provided a long enough time sample for adequate convergence of all statistical measures of interest. For each particle time constant simulations using mass loadings of 0.0, 0.1, 0.5, and 1.0 were performed. Ratios of the time constant τ_p to the large-eddy time scale T_f (defined using the longitudinal integral length scale and turbulence kinetic energy) ranged from 0.14 to 1.50.

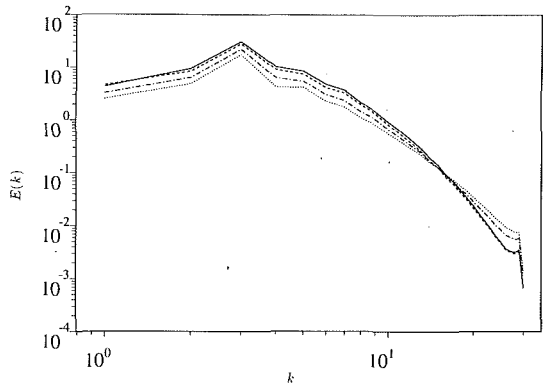

Fig. 1(*a*)

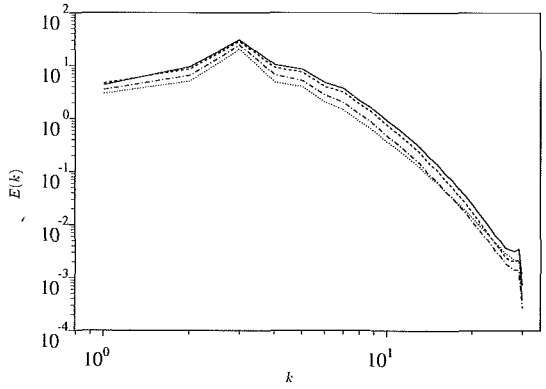

Fig. 1(*b*)

Fig. 1 Effect of mass loading on turbulence energy spectra. Note that the axes of both figures have been made dimensionless in terms of computationally convenient reference scales. (*a*) $\tau_p/T_f = 0.15$. (*b*) $\tau_p/T_f = 0.52$. — $\phi = 0$; — — — — $\phi = 0.1$; —·— $\phi = 0.5$; ····· $\phi = 1.0$.

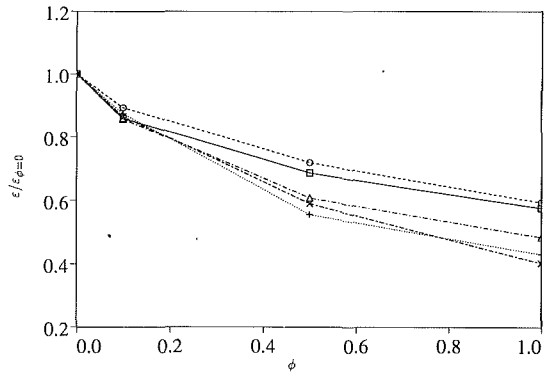

Fig. 2 Effect of mass loading on turbulence dissipation rate. ⊟—⊟ $\tau_p/T_f = 0.14$; ⊙--⊙ $\tau_p/T_f = 0.15$; ☆·☆ $\tau_p/T_f = 0.75$; ✳--✳ $\tau_p/T_f = 1.50$.

As mentioned previously, simulations of forced isotropic turbulence were employed in this study. True isotropic turbulence is statistically non stationary since the turbulence decays in the absence of any production mechanism. Most analytical approaches to isotropic turbulence assume the flow is statistically stationary and in practical applications there is usually a source of turbulence energy to maintain a stationary condition. Both experiments and analyses of decaying turbulence are complicated because the length, velocity, and time scales are continually changing, and because the initial conditions have a persistent effect on the evolution of the flow that is not easily quantified. This is an even more significant problem in particle-laden flows where the ratio of the particle time constant to the fluid time scale changes as the flow evolves. Particles may provide either a sink or source of energy to the turbulence which is dependent on seemingly irrelevant quantities such as the evolution time of the flow, the initial spectrum of the turbulence, and the initial conditions of the particle velocity field. To alleviate complications from these factors, the present simulations were made statistically stationary through application of a body force applied at the largest scales of motion.

3 Results

3.1 Effect of Particles on Turbulence Energy and Dissipation Rate. The effect of particles on the turbulence energy spectrum for $\tau_p/T_f = 0.15$ and $\tau_p/T_f = 0.52$ is shown in Figs. 1(*a*) and 1(*b*). Comparison of these figures shows that attenuation of turbulence energy by particles with $\tau_p/T_f = 0.52$ is more uniform than for particles with $\tau_p/T_f = 0.15$. It can be observed from Figure 1a that for simulations in which $\tau_p/T_f = 0.15$ the small-scale energy of the fluid increases for larger mass loadings. Squires and Eaton (1991a) have previously shown that particles with $\tau_p/T_f = 0.15$ exhibit significant effects of preferential concentration in regions of low vorticity and high strain rate. The effect of high concentrations of particles in these regions evidently leads to an increase in small-scale turbulent velocity fluctuations. This production of small-scale fluctuations subsequently causes the viscous dissipation rate *in the fluid* to be increased for simulations in which lighter particles interact with the flow. This effect is illustrated in Fig. 2 which shows the equilibrium value of the dissipation rate as a function of the mass loading for each of the particle time constants used in the simulations. As can be observed from the figure, the reduction in the dissipation rate with increasing mass loading is less for those simulations in which the turbulence is attenuated by lighter particles. Thus, the dissipation rate, which is weighted more toward the small-scale motions, is selectively modified by preferential concentration of particles.

Figures 1–2 provide further insight into the relative changes in turbulence quantities for increasing mass loadings. At zero mass loading the production of turbulence kinetic energy by forcing is balanced entirely by viscous dissipation. For non-zero particle mass loading drag about a particle provides an additional means for dissipating turbulence energy. Since the total dissipation of turbulence energy must match the production from the force field, viscous dissipation in the fluid is reduced (see Fig. 2) with increases in mass loading since an increasing fraction of the total dissipation is accounted for by particles. At the largest mass loadings dissipation of turbulence energy by the particle load accounts for as much as 50 percent of the total.

3.2 Effect of Particles on Turbulence Dissipation. As shown in Section 2.2 the destruction of dissipation term is composed of two parts:

$$\mathfrak{D} = -2\nu\overline{\omega_i\omega_j s_{ij}} + 2\nu^2\overline{\omega_{i,j}\omega_{i,j}} \qquad (14)$$

where the first term represents production of ϵ by vortex stretching and the second term is the viscous destruction of ϵ. The effect of mass loading on these terms for the particle time constants used in the 64^3 simulations is shown in Fig. 3. In this figure the production and destruction terms have been made dimensionless by their corresponding value at zero mass loading. It may be observed from the figure that both production and destruction of ϵ are attenuated by increased mass loadings for either particle time constant with reductions as large as 65 percent at the largest mass loading. For both particle time constants the production of ϵ term is reduced more than

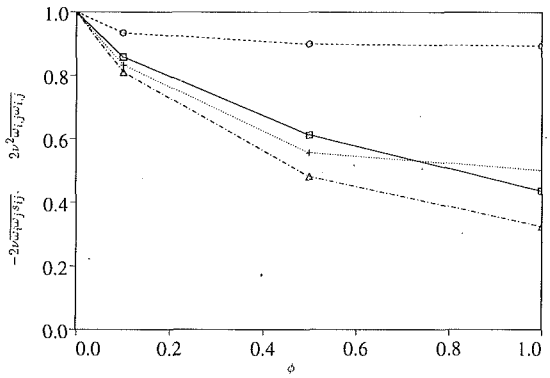

Fig. 3 Effect of mass loading on production and destruction of ϵ. ⊟——⊟ production of ϵ for $\tau_p/T_f = 0.15$; ⊖--⊖ destruction of ϵ for $\tau_p/T_f = 0.15$; ☆ · ☆ production of ϵ for $\tau_p/\tau_f = 0.52$; +···+ destruction of ϵ for $\tau_p/T_f = 0.52$.

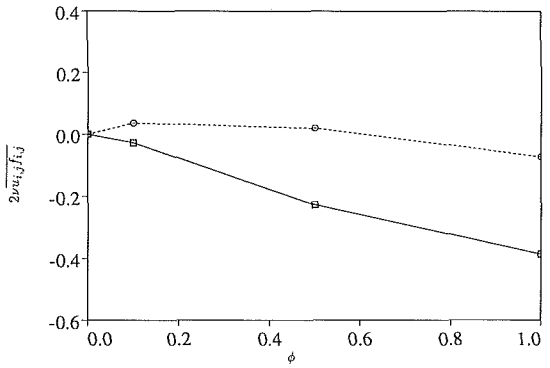

Fig. 4 Effect of mass loading on destruction of ϵ by particles. ⊟——⊟ $\tau_p/T_f = 0.15$; ⊖--⊖ $\tau_p/T_f = 0.52$

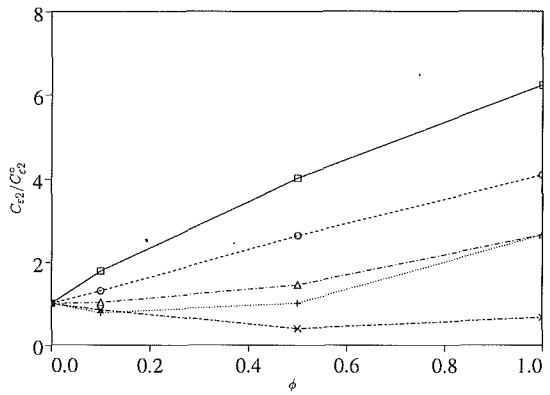

Fig. 5 Effect of mass loading on $C_{\epsilon 2}$. ⊟——⊟ $\tau_p/T_f = 0.14$; ⊖--⊖ $\tau_p/T_f = 0.15$; ☆ · ☆ $\tau_p/T_f = 0.52$; +···+ $\tau_p/T_f = 0.75$; ✳-✳ $\tau_p/T_f = 1.50$.

the destruction term. Therefore, it may be concluded that the effect of particle mass loading is to disrupt the balance between the production and destruction of $\mathfrak{D}$ and that viscous destruction of ϵ is enhanced relative to the production of ϵ. It may also be concluded that selective modification of the turbulence for particles with $\tau_p/T_f = 0.15$, resulting from preferential concentration, causes a more significant disruption of the balance between production and destruction of ϵ. It is important to remember that these changes are not due to the direct action of the particles on the dissipating eddies. Instead, these effects are caused by overall distortion of the turbulence leading to changes in the viscous dissipation.

The exact term in the dissipation equation representing the direct effect of the particle cloud on ϵ (see Eq. (8)) is shown in Fig. 4 for the time constants used in the 64^3 simulations. This figure clearly shows that the lighter particles ($\tau_p/T_f = 0.15$), which exhibit significant effects of preferential concentration, act as a *source* of ϵ for increasing values of the mass loading. It may also be observed from Fig. 4 that particles with a time constant $\tau_p/T_f = 0.52$ dissipate ϵ at smaller mass loadings but also become a source of ϵ at higher mass loadings. Figure 4 can now be used to provide an explanation of the fact that ϵ is larger for simulations in which light particles modify the turbulence (see Fig. 2). Note that the results in Fig. 3 would lead one to conclude that the dissipation rate of the fluid would be less for flows with lighter particles. However, Fig. 4 shows that the effect of preferential concentration of lighter particles is to cause the particle cloud to act as a source of ϵ. Thus, it is the effect of lighter particles acting as a production of ϵ which causes the dissipation rate of the fluid to be larger for cases in which these particles modify the turbulence.

3.3 Effect of Mass Loading on Model Constants. The model for the destruction of dissipation term, $\mathfrak{D}$, in the ϵ equation requires specification of $C_{\epsilon 2}$ in (11). The effect of mass loading on the model constant $C_{\epsilon 2}$ is shown in Fig. 5 for each of the particle time constants used in the simulations. The value of the constant, $C^0_{\epsilon 2}$, for the baseline case ($\phi = 0$) is approximately 0.6 for both the 32^3 and 64^3 results. As is evident from the figure there is little change in $C_{\epsilon 2}$ with increased mass loading for the heavier particles. The figure also shows that $C_{\epsilon 2}$ obtained from simulations in which lighter particles modify the turbulence increases significantly as the mass loading is increased. This increase in $C_{\epsilon 2}$ can be interpreted using Fig. 3 which showed that the effect of mass loading on the production and destruction of $\mathfrak{D}$ was to significantly diminish the production by vortex stretching relative to the viscous destruction term. Since the model for $\mathfrak{D}$ represents a sink of ϵ, increased viscous destruction relative to the production implies that $C_{\epsilon 2}$ must increase. The results in Fig. 5 clearly show that selective modification of the turbulence by lighter particles invalidates the assumption that the single-phase model constants are unaffected by the presence of a dispersed phase which can modify the turbulence.

It is important to emphasize that the results in Fig. 5 demonstrate the profound effect of selective modification, resulting from preferential concentration, on engineering turbulence models such as $K-\epsilon$. As shown by Squires and Eaton (1991a), particle transport in turbulence can be instructively viewed in terms of the various structures, or flow zones, present in turbulent flows (e.g., eddying regions, streaming regions, convergence zones, etc.). Selective modification of the various zones in a turbulent flow will be different, due to the varying concentrations of particles in each zone. As shown by Squires and Eaton (1991a), for the most preferentially concentrated particles, convergence zones occupy about 4–5 percent of the total volume but the average particle number density in these regions is over twice the global mean while eddying regions typically occupy 9–10 percent of the flow volume but the average number density in eddy zones is less than half the global number density. For increasing particle mass loadings, selective modification clearly disrupts the dynamics of the turbulence, resulting in an increase in $C_{\epsilon 2}$.

Finally, it may also be remarked that, as shown by Fig. 5, $C_{\epsilon 2}/C^0_{\epsilon 2}$ increases with larger mass loading and decreasing τ_p/T_f. Remembering that in the limit of $\tau_p/T_f \to 0$ one should expect that $C_{\epsilon 2}/C^0_{\epsilon 2} \to 1$, this then implies the existence of some value of τ_p/T_f for which $C_{\epsilon 2}/C^0_{\epsilon 2}$ is maximum. The existence of maximum is difficult to determine since for small values of τ_p/T_f the volumetric concentration of particles becomes very large in order to obtain increasing mass loadings and the assumption of dilute suspensions, implicit in this work, is no longer valid. Thus, in this study it was not possible to determine

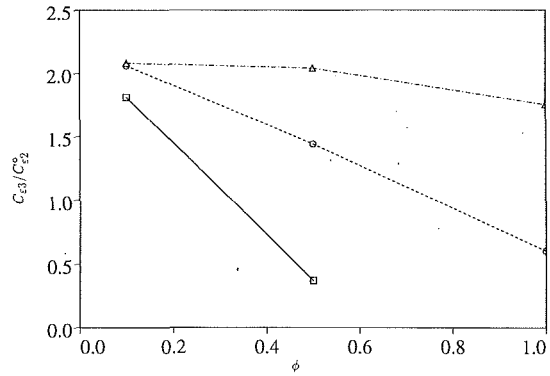

Fig. 6 Effect of mass loading on $C_{\epsilon 3}$. ⊟——⊟ τ_p/T_f = 0.52; ⊖--⊖ τ_p/T_f = 0.75; ☆·☆ τ_p/T_f = 1.50.

whether there exists an "optimal" value of τ_p/T_f yielding a maximum in $C_{\epsilon 2}/C^0_{\epsilon 2}$.

The model for the destruction of dissipation by particles, $\mathfrak{D}_p$, in the ϵ equation requires specification of $C_{\epsilon 3}$. Shown in Fig. 6 are the values of $C_{\epsilon 3}$ for each of the three largest time constants and all mass loadings used in the simulations. Similar to the effect observed in Fig. 5, values of $C_{\epsilon 3}$ for simulations in which heavier particles modify the turbulence are relatively insensitive to increased mass loading. It may also be observed from the figure, however, that $C_{\epsilon 3}$ decreases for increasing mass loading with lighter particles. Since the dissipation of turbulence energy by particles, ϵ_p, is greater than zero for the flows examined in this study, the model for $\mathfrak{D}_p$ given by (12) assumes the effect of particles in the ϵ equation is to provide a sink for the dissipation rate. However, the results in Fig. 4 show that selective modification of the turbulence caused by lighter particles results in a production of ϵ for some mass loadings. This implies that the model constant $C_{\epsilon 3}$ must be less than zero for cases in which particles act as a source of ϵ. The figure only shows cases for which the particles attenuate ϵ. It should be noted that in $K-\epsilon$ computations of particle-laden turbulence the constant $C_{\epsilon 3}$ is usually tuned to yield good agreement with a particular laboratory experiment. The fact that there exists a wide range of values of $C_{\epsilon 3}$ reported in the literature may be due in part to preferential concentration of particles and selective modification of turbulence.

4 Summary and Conclusions

An evaluation of $K-\epsilon$ models for particle-laden turbulence has been made using data from DNS of particle-laden isotropic turbulence. Results from the present study indicate that for values of the mass loading below approximately 0.2 no significant changes to the single-phase model coefficients are needed. However, the effect of selective modification of the turbulence, caused by preferential concentration of light particles, significantly attenuates production of ϵ by turbulent vortex stretching. The disruption in the balance between production and destruction of ϵ by lighter particles results in a significant increase in $C_{\epsilon 2}$ for increasing mass loading. Therefore, assumptions that the "single-phase" terms in the $K-\epsilon$ model are unchanged by turbulence modification are in error. Selective modification of turbulence caused by preferential concentration of light particles was also found to lead to a production of ϵ by the particle cloud. Production of ϵ by lighter particles causes the dissipation rate of the fluid to be larger when lighter particles modify the turbulence as opposed to heavier particles. For flows in which particles act as a production of ϵ the model constant $C_{\epsilon 3}$ representing the effect of particles on ϵ must be negative. Thus, modeling the effect of particles on ϵ analogously to the way in which the destruction of dissipation is modeled is not accurate.

It is also worthwhile to comment as to the effect of the drag law on the results in this study. The particle equation of motion employed in the present work has been based on Stokes law of resistance about a single particle and is valid for small particle Reynolds numbers. In many instances of practical importance the particle Reynolds number will be large enough such that a linear drag law is no longer valid. Relevant in this regard is the recent work by Wang and Maxey (1993) on preferential concentration and settling velocity in isotropic turbulence. Their study showed that effects of preferential concentration were also significant for particle motion governed by a non-linear drag law. Furthermore, for flows in which the density difference between particles and fluid is large, the effects of drag non-linearity will be relatively weak for most problems of practical interest. Thus, the results of this study are generally applicable to those flows in which the drag law is non-linear; turbulence modeling of these flows will then be equally challenging.

Finally, the present formulation of the $K-\epsilon$ model appears to be appropriate for flows in which the particles remain randomly distributed. However, the "constants" show strong variation with flow parameters when the particles are light enough to become preferentially concentrated in regions of high strain rate and low vorticity. Experiments have shown that strong preferential concentration occurs in free shear flows for light particles (see Longmire and Eaton, 1992 or Lazaro and Lasheras, 1992; Fessler et al. (1993). The direct numerical simulations by Squires and Eaton (1991a) have shown that preferential concentration occurs in homogeneous flows for about a ten-fold range of particle time constants centered on τ_p/T_f = 0.15. It may be necessary to resort to large-eddy simulation or other techniques which better represent the instantaneous structure of the turbulence in order to adequately predict flows in this regime.

Acknowledgment

Partial support for this work has been provided by NSF Grant No. CTS-9005998 and NIOSH Grant No. OH03052-02.

References

Azevedo, J. L. T., and Pereira, J. C. F., 1991, "Calculation of Free and Confined Gas-Multiple Size Particle Swirling Jets," ASME FED , Vol. 110, *Turbulence Modification in Multiphase Flows*, Michaelides, E. E., Fukano, T., and Serizawa, A., eds. pp. 111–117.

Berlemont, A., Desjonqueres, P., and Gouesbet, G., 1990, "Particle Lagrangian Simulation in Turbulent Flows," *International Journal of Multiphase Flow*, Vol 16, No. (1), pp. 19–34.

Chen, C. P., and Wood, P. E., 1985, "A Turbulence Closure Model for Dilute Gas-Particle Flows," *Canadian Journal of Chemical Engineering*, Vol. 63, p. 349.

Chen, C. P., 1986, "Calculation of Confined Gas-Particle Two-Phase Turbulent Flows," AIAA paper 86-0219, presented at the 24th Aerospace Sciences Meeting, Reno, Nevada.

Crowe, C. T., 1982, "Review: Numerical Methods for Dilute Gas-Particle Flows," ASME JOURNAL OF FLUIDS ENGINEERING, Vol. 104, pp. 297–303.

Elghobashi, S., and Abou-Arab, T. W., 1983, "A Two-Equation Model for Two-Phase Flows," *Physics of Fluids*, Vol. 26, (4), pp. 931–938.

Elghobashi, S., Abou-Arab, T., Rizk, M., and Mostafa, A., 1984, "Prediction of the Particle-Laden Jet With a Two-Equation Turbulence Model," *International Journal of Multiphase Flow*, Vol. 10, (6), pp. 697–710.

Elghobashi, S. E., and Truesdell, G. C., 1993, "On the Two-Way Interaction Between Homogeneous Turbulence and Dispersed Solid Particles. I: Turbulence Modification," *Physics of Fluids*, Vol. 5, (7), p. 1790.

Fessler, J. R., Kulick, J. D., and Eaton, J. K., 1993, "Preferential Concentration of Heavy Particles in a Turbulent Channel Flow," Submitted to *Physics of Fluids*.

Gore, R. A., and Crowe, C. T., 1989, "Effect of Particle Size on Modulating Turbulence Intensity. *International Journal of Multiphase Flow,* Vol. 15, (2), pp. 279–285.

Launder, B. E., Reece, G. J., and Rodi, W., 1975, "Progress in The Development of a Reynolds-Stress Turbulence Closure," *Journal of Fluid Mechanics*, Vol. 68, p. 537.

Longmeir, E. K., and Eaton, J. K., 1992, "Structure of a Particle-Laden Round Jet," *Journal of Fluid Mechanics*, Vol. 236, pp. 217–257.

Lazaro, B. J., and Lasheras, J. C., 1992, "Particle Dispersion in the Devel-

oping Free Shear Layer. Part 2. Forced Flow," *Journal of Fluid Mechanics*, Vol. 235, pp. 179–221.

Modarress, D., Wuerer, J. and Elghobashi, S., 1982, "An Experimental Study of a Turbulent Round Two-Phase Jet," AIAA paper 82-0964, presented at the AIAA/ASME Third Joint Thermophysics, Fluids, Plasma and Heat Transference Conference, St. Louis, MO.

Modarress, D., Tan, H., and Elghobashi, S., 1984, "Two-Component LDA Measurement in a Two-Phase Turbulent Jet," *AIAA Journal*, Vol. 22, pp. 624–630.

Mostafa, A. A., Mongia, H. C., 1987, "On the Modeling of Turbulent Evaporating Sprays: Eulerian Versus Lagrangian Approach," *International Journal of Heat and Mass Transfer*, Vol. 30, pp. 2583–2593.

Mostafa, A. A., Mongia, H. C., McDonnell, V. G., and Samuleson, G. S., 1989, "Evolution of Particle-Laden Jet Flows: A Theoretical and Experimental Study," *AIAA Journal*, Vol. 27, (2), pp. 167–183.

Reynolds, W. C., 1976, *Annual Review of Fluid Mechanics*, Vol. 8, p. 183.

Rizk, M. A., and Elghobashi, S. E., 1989, "A Two-Equation Turbulence Model for Dispersed Dilute Confined Two-Phase Flows," *International Journal of Multiphase Flows*, Vol. 15, (1), pp. 119–133.

Rodi, W., 1980, "Turbulence Models and Their Applications in Hydraulics, International Associate for Hydraulic Research, Delft, The Netherlands.

Sheun, J-S., Solomon, A. S. P., Zhang, Q-F., and Faeth, G. M., 1985, "Structure of Particle-Laden Jets: Measurements and Predictions," *AIAA Journal*, Vol. 23, (3), pp. 396–404.

Smith, L. M., and Reynolds, W. C., 1991, "The Dissipation-Range Spectrum and the Velocity-Derivative Skewness in Turbulent Flows," *Physics of Fluids*, Vol. 3, (5), p. 992.

Squires, K. D., and Eaton, J. K., 1990, "Particle Response and Turbulence Modification in Istropic Turbulence," *Physics of Fluids*, Vol. 2, pp. 1191–1203.

Squires, K. D., and Eaton, J. K., 1991a, "Preferential Concentration of Particles by Turbulence," *Physics of Fluids*, Vol. 3, (5, part 2), pp. 1169–1178.

Squires, K. D., and Eaton, J. K., 1991b, "Measurements of Particle Dispersion Obtained from Direct Numerical Simulations of Isotropic Turbulence," *Journal of Fluid Mechanics*, Vol. 226, pp. 1–35.

Wang, L. P., and Maxey, M. R., 1993, "Settling Velocity and Concentration Distribution of Heavy Particles in Homogeneous Isotropic Turbulence," *Journal of Fluid Mechanics*, Vol. 256, p. 27.

Particle Mixing and Volumetric Expansion in a Vibrated Granular Bed

M. L. Hunt

S. S. Hsiau

K. T. Hong

Division of Engineering and Applied Science,
California Institute of Technology,
Pasadena, CA 91125

The present experiments are an investigation of the expansion and mixing that occur in a horizontal bed of particles subjected to vibrational accelerations in the direction parallel to gravity. The particles are colored-glass balls of uniform size; three different bed heights are examined of 6, 9, and 12 particle diameters. The vibrational frequency and amplitude are controlled separately to cover a range of acceleration levels from 1 to 5.5 times gravitational acceleration. The expansion results show that above a critical frequency, the bed begins to expand and the bed solid fraction decreases. This result is independent of the vibrational amplitude. Above a second critical frequency, the thickest beds show a further decrease in solid fraction; the minimum value of solid fraction for all bed heights is approximately 0.21 ± 0.03. The mixing results indicate that the mixing times decrease significantly with the expansion of the bed. However, the mixing times are greater as the bed depth increases. Unlike the expansion results, the mixing times depend on the amplitude of the vibration. A simple analysis of the flow is performed using a self-diffusion coefficient developed from dense-gas kinetic theory. The analysis qualitatively agrees with the experiments for the largest vibrational velocities and for the thinnest beds.

Introduction

Many food industries handle, store, and transport food products and staples in a granular or particulate form. Often vibratory systems are used to dry and mix grains, seeds, sugar, and other particulate materials (Suzuki et al., 1980; Pakowski et al., 1984; Yu et al., 1992). The drying process and the associated heat transfer effects are influenced by the degree of mixing of the material caused by the vibrational motion. However, many drying analyses assume a perfect mixing of the material within the bed (Pakowski et al., 1984). In addition to drying applications, vibratory motions are also used in other applications such as pharmaceutical, powder metallurgy, and food industries. In these environments, the vibratory motion is used to sort particulate materials according to particle size.

In the present work, only the mixing aspects of the vibratory particulate systems are addressed. The materials that are considered are dry, noncohesive, and not affected by electrostatic charges. The materials are also uniform in size so that segregation effects are not considered. The purpose of the work is to investigate the one-dimensional mixing process for different vibrational accelerations, frequencies and for different bed heights. The experiments are conducted by placing a horizontal layer of blue spheres over a layer of red spheres and observing the mixing process. This experiment differs from the recent work by Zik and Stavans (1991) in which the spreading of a vertical strip of differently colored particles was monitored. In that study the diffusion coefficient was determined by measuring the lateral spread of the tracer particles for different vibrational speeds.

Although there are few studies in the literature that directly address mixing in vibrated beds, there are several works that examine the mechanics of the vibratory motion on a particulate bed. As the bed acceleration is increased beyond gravitational acceleration, the vibration causes some particles within the bed to go into free flight and a small gap can be observed between the particle layer and the base (Thomas et al., 1989; Douady et al., 1989). If the flight time of the particles is shorter than the period of vibration of the shaker, the particles collide with the surface with little rebound. The material then appears to ride with the surface until the downward acceleration of the plate again exceeds gravitational acceleration.

The recent study by Brennen et al. (1992) examined the expansion of a vibrated bed for various acceleration amplitudes, frequencies, and bed heights. In the experiments, a paper lid was used to impose an external pressure on the particles, and to enable the observation of the extent of the bed expansion. Their experiments show that as the acceleration level is increased, a critical level is passed in which a significant expansion of the bed occurs. The critical acceleration was close to 2 times gravitational acceleration, and increased slightly with the thickness of the bed. The authors suggest that this sudden change in bed height reflects a bifurcation in the dynamic response of the bed.

Contributed by the Fluids Engineering Division for publication in the JOURNAL OF FLUIDS ENGINEERING. Manuscript received by the Fluids Engineering Division July 12, 1993; revised manuscript received February 16, 1994. Associate Technical Editor: M. W. Reeks.

In a study by Savage (1988), a bed of material was subjected to a nonuniform vibration of the lower bed surface. The surface was flexible so that the maximum displacement occurred in the center of the bed and decreased to zero at the edges. By using tracer particles, the flow exhibited a circulation pattern with an upward velocity at the center and a downward motion along the side walls. A similar circulation was also found by Ratkai (1976) in which the vibration of the bottom plate was also nonuniformly distributed. However, the recent work by Knight et al. (1993) showed a convection cell present for a bed in which the vibrating surface remained horizontal. In these experiments, the vibration was not continuous but consisted of a series of discrete accelerations. The results indicated that the convection cells were driven by frictional interactions between the particles and the walls of the container. If the container surfaces were smooth and slippery, convection was suppressed; if the walls were roughened, the particles adjacent to the container walls moved downward, while the material in the center moved upward. The downward motion was faster than the motion of the upward plug.

In addition to these studies, there are many papers that include the air flow within the bed, and examine the effects of the air motion on the bed dynamics (Gutman, 1976; Akiyama and Kurimoto, 1988). As described in the review of Pakowski et al. (1984), the effects of the air motion are generally important in relatively thick beds with particles of diameter less than 1 mm.

Granular Flows

Over the past decade, there has been increasing interest in the general area of flows of granular materials such as flows of sand, seeds, tablets, or food products (see reviews such as Campbell, 1990; Jaeger and Nagel, 1992). The experimental research in this area has progressed rather slowly because of the difficulty in experimental measurements. However, the analytical work has received more attention. One of the approaches in modeling flows of granular material is to employ concepts from dense-gas kinetic theories (Lun et al., 1984; Jenkins and Richman, 1985). The motivating concept behind the work is that the particle movements in dense solid flows are not affected by the fluid, and instead depend on the collisions between the particles and with the bounding surfaces. In this respect, the motions resemble molecular motions in gases. Although the mathematical formulations from gas kinetic theories are useful for developing constitutive relations for granular flows, there are many differences in the mechanisms that govern the collisional behavior for the two different systems. Granular flows are often dense and may involve multiparticle collisions. The particles are also frictional and inelastic, so that energy is dissipated within the flow. In addition, granular flows must also be driven by a shearing forces, by gravity or by external vibrations.

One of the concepts used throughout the granular flow literature is the term granular temperature (Lun et al., 1984; Campbell, 1990). The granular temperature is not a thermodynamic temperature, but is a measure of the specific kinetic energy of the flow, similar to the thermodynamic temperature in gases. The granular temperature, Υ, is defined as one-third of the ensemble average of the sum of the squares of the three fluctuating velocity components. An increase in the granular temperature reflects an increase in the random motion of the individual particles within the flow.

Most of the work in granular flows has concentrated on momentum transport relations. In the past few years, however, several studies have investigated mixing and diffusion processes (Hsiau and Hunt, 1993a,b; Savage, 1993). Using two different kinetic theory approaches, Hsiau and Hunt (1993a) and Savage (1993) developed an analytical expression for the self-diffusion coefficient, D,

$$D=\frac{d(\pi\Upsilon)^{1/2}}{8(1+e_p)\nu g_0(\nu)}. \tag{1}$$

In the above equation, d is the particle diameter, e_p is the coefficient of restitution defined as the particle rebound velocity to impact velocity, ν is the solid fraction, and $g_0(\nu)$ is the radial distribution function evaluated when the particles are in contact. The distribution function is introduced in dense gas studies to account for the increase in particle collisions, and to account for the finite size of the particles. The function $g_0(\nu)$ is evaluated from the Carnahan and Starling approximation for molecular gases,

$$g_0(\nu)=\frac{2-\nu}{2(1-\nu)^3}. \tag{2}$$

This form of $g_0(\nu)$ has been used for uniform granular flows with solid fractions less than 0.5 (Lun et al., 1984).

Apparatus and Procedure

The experiments are performed in a glass-walled rectangular box that is driven in a vertical direction by an eccentric drive mechanism. Figure 1 is a schematic representation of the facility. The shaker is driven by a radial bearing that is off-center from the shaft extension of the variable-speed motor. The drive mechanism can be replaced to change the vibrational amplitude, z_o. In the current experiments two different values of z_o are used: 0.3 cm and 0.5 cm measured from the central shaft position. The shaker is supported by two steel shafts that are guided by four linear bearings. The vibrational frequency is varied by changing the rotational speed of the motor; the range for the current experiments covers from 600 rpm to 1200 rpm ($\pm$10 rpm). The rotational speed of the motor is measured with tachometer in revolutions per minute, and this value is converted to the angular frequency ω. The amplitude of the vibrational acceleration is computed from the product of the displacement and the square of the angular frequency, $z_o\omega^2$. The vibrational speed is found from $z_o\omega$. For the current conditions the magnitude of the acceleration ranges from 2 to 5.5 g where g is gravitational acceleration.

The front and back walls are tempered glass for visual observation of the bed. The distance between the plates is 3.8 cm; the width of the bed is 19.1 cm, and the height is 50.8 cm. The side walls and base are made from aluminum. For most of the current experiments the depth of the channel was decreased to 1.9 cm by placing a plexiglass plate between the glass walls. This decrease in depth reduced the amount of material that was used in each experiment. As mentioned in the experimental section, the results from the 1.9 cm deep bed were compared to results in 3.8 cm bed; there are no discernable

Nomenclature

C = color concentration
d = particle diameter
D = diffusion coefficient
e_p = coefficient of restitution
g = gravitational acceleration
g_0 = radial distribution function
h = height of bed
m = mass of bed
t = time
v = velocity
z = coordinate in direction parallel to vibration
z_o = vibrational amplitude
ν = solid fraction
Υ = granular temperature
ω = angular frequency

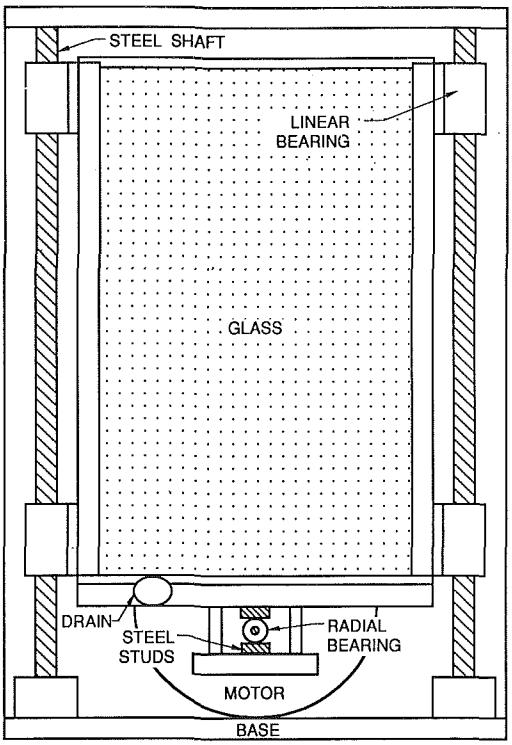

Fig. 1 Schematic representation of the vertical shaker

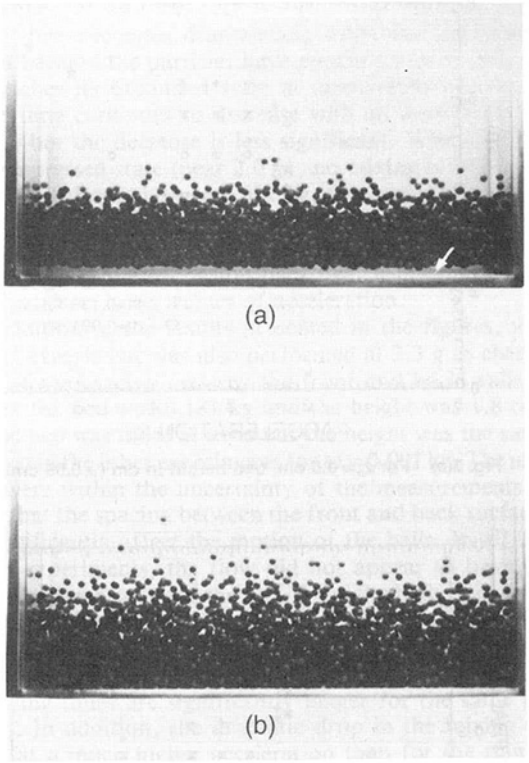

Fig. 2 Photographs of the bed for $m = 0.091$ kg and $z_o = 0.5$ cm: (*a*) arrow indicating the gap that appears when the plate has separated from the bed, (*b*) the bed recontacting the plate

difference between the experimental results. No further attempts were made to ascertain the variations as a function of depth within the bed.

The experiments used red and blue colored-glass balls. The balls are spherical and are 3.01 mm (standard deviation of 0.054 mm) in diameter. The density of the balls is 2490 kg/m^3. The preliminary experiments indicated that the response of the particulate bed to vibratory motions was highly dependent on the surface conditions of the particles and the walls. If the particles were dyed spheres instead of colored-glass balls or if the particles were roughened with a layer of debris, the top surface of the bed formed a wave pattern similar to that shown in the work by Douady et al. (1989). The wave pattern depended on the vibrational acceleration level. However, if the spheres were cleaned and smooth, there were no waves on the upper surface of the bed. As a consequence, the colored-glass balls and the internal surfaces of the shaker were cleaned after every 2 to 3 experimental runs. In addition, electrostatic charge effects appeared to become important after the shaker was run for an extended period of time. To minimize the effects, the surfaces of the shaker were also sprayed with an antistatic fluid. For all of the experimental results presented, the electrostatic forces did not appear to be affecting the motions of the balls.

The mixing process was observed through the front polished-glass plate. The experiments were prepared by placing a layer of red balls on the bottom of the shaker, and overlaying a layer of blue balls of equal amount. The rotational speed of the motor was preset before the experiment commenced. The motor was then started, and the images recorded at a rate of 60 images per second with a video recorder. A frame-grabber board connected to a personal computer was used to evaluate the change in the color distribution over time. The digital images were enhanced to sharpen the color contrast between the red and blue balls. After the enhancement, the red colors appeared white (a digital value of 1.0) and the blue appeared black (value of 0.0). As the mixing progressed, the digital images were evaluated by selecting different horizontal and vertical windows within the bed. All of the images were taken at the same point in the vibration cycle when the bed was in its most compact state. For each window, the average color was calculated to obtain the average color concentration at that bed location. If all of the selected windows within the bed had an average color concentration between 0.495 and 0.505, the bed was determined to be well mixed, and the time was referred to as the mixing time. This definition of the mixing time was chosen to correspond with the definition used in the analysis of the particle diffusion process. The measurement of the mixing times were repeatable within ± 0.2 s.

Expansion Results

Experiments were performed using three different bed masses: 0.091, 0.136, and 0.181 ± 0.004 kg. These correspond with a height at rest of 1.8 cm (roughly 6 particle layers), 2.7 cm (9 layers), and 3.6 cm (12 layers), respectively. Figure 2 shows photographs for a bed with mass of 0.091 kg. The first photo shows the bed just after the vibrating plate has separated from the beads, and indicates a small gap between the particles and the bottom plate. At this point, the plate is moving downward at an acceleration greater than gravitational acceleration. As the plate continues to drop, the bed expands as the particles fall to the surface. The second photo, 2b, shows the bed after some of the particles have impacted the lower surface. Many of the upper particles appear to be in free flight while the particles closer to the surface appear to be resting on the plate. As the plate rises, the bed is compressed, and then the cycle is repeated. For bed of greater mass and hence greater height, the vibration cycle is similar to that for the thinner bed; however, the region of the bed close to the vibratory surface appears to be denser even in the most expanded state.

As shown by the photographs the maximum height that the bed attains is difficult to assess from the motion of individual particles. As a result, a thin sheet of paper was placed on top of the bed, and the change in height of the bed for different

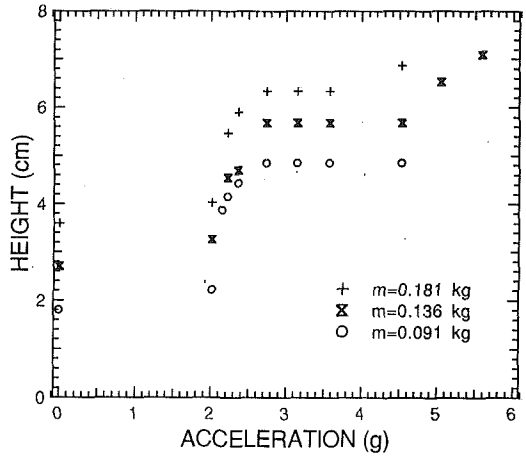

Fig. 3(*a*) For $z_o = 0.5$ cm, bed height in cm (± 0.05 cm)

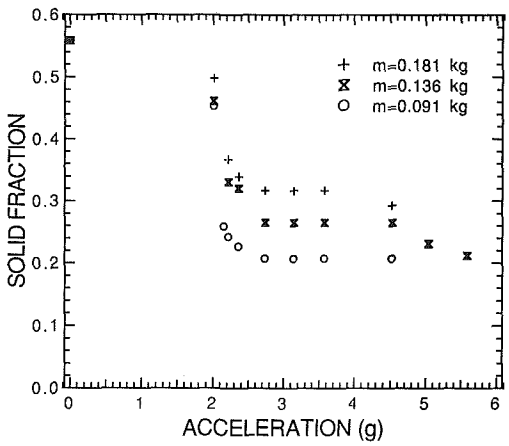

Fig. 3(*b*) Bed solid fraction (± 0.03)

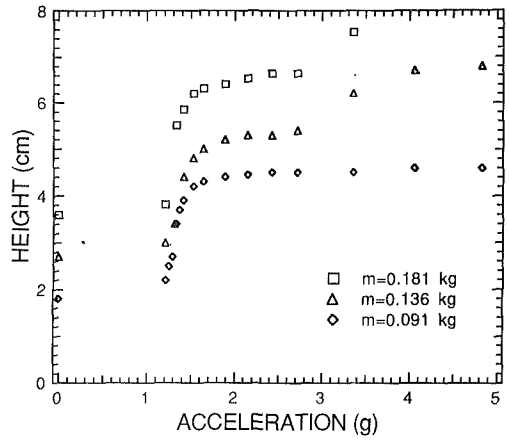

Fig. 4(*a*) For $z_o = 0.3$ cm, bed height in cm (± 0.05 cm)

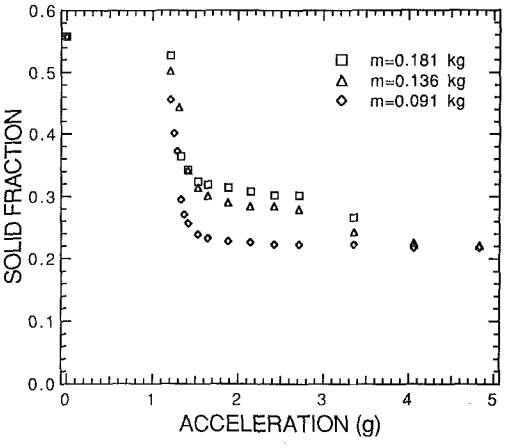

Fig. 4(*b*) Bed solid fraction (± 0.03)

accelerations was determined from the height of paper lid as recorded on the video images. The lid was light enough that it did not appear to affect the expansion. The results for the expansion test for $z_o = 0.5$ cm are shown in Fig. 3(*a*) as a function of acceleration in *g*'s. The figure also shows the initial height of the beds are rest. The height of the bed remains constant for these experiments until the acceleration increases to a value greater than 2 *g*. As the acceleration level is increased, the bed height increases significantly, by a factor of 2.7 for the thinnest bed ($m = 0.091$ kg) and a factor of 1.8 for the thickest bed ($m = 0.181$ kg). For each bed mass, the bed height reaches a plateau at approximately 2.8 *g*. For accelerations greater than 4.5 *g*, the two thicker beds indicate a further expansion.

In Fig. 3(*b*) the data are replotted in terms of average solid fraction, ν, as a function of acceleration. The solid fraction is defined as the ratio of the solid volume to the bed volume, and is calculated from the mass of the beads within the bed divided by the product of the bead density, height of the bed and the cross-sectional bed area. For the different heights, the bulk solid fraction at rest is 0.56. As the acceleration is increased, the solid fraction decreases to a value of approximately 0.21 ± 0.03 for the thinnest bed. For the thicker beds, the solid fraction decreases with an increase in acceleration and reaches a plateau, and then continues to decrease for accelerations greater than 4 *g*.

In Fig. 4(*a*), similar results are presented, but the vibrational amplitude has been reduced to $z_o = 0.3$ cm. As in the previous figure, the height of the bed increases significantly with acceleration; however, the increase occurs at a much lower acceleration level—approximately 1.3 *g* compared with 2.0 *g*. The height of the bed appears to reach a local maximum at roughly 1.8 *g*. In addition, for the two beds of mass 0.136 and 0.181 kg, the beds expand further for accelerations greater than 3.0 *g*. In terms of solid fraction as shown in Fig. 4(*b*), the three different bed heights reach the same minimum solid fraction of approximately 0.22 ± 0.03 for accelerations greater than 4 *g*.

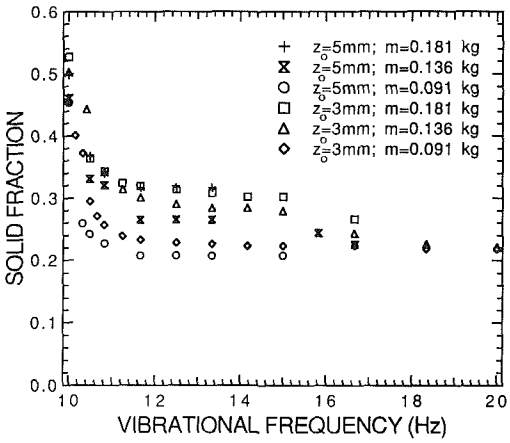

Fig. 5 Bed solid fraction as a function of vibrational frequency

The average solid fraction values are also plotted as a function of vibrational frequency ($\omega/2\pi$) in hertz as shown in Fig. 5. As a function of frequency the data for the two different

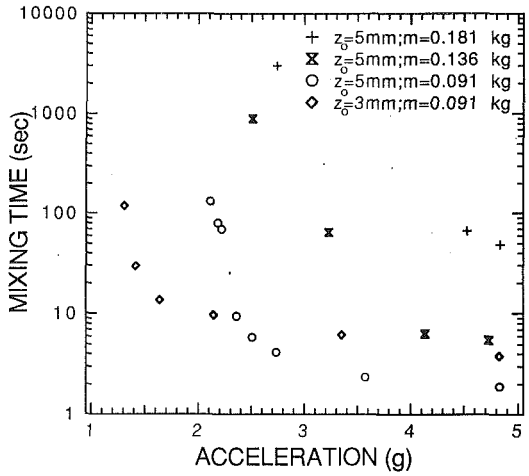

Fig. 6 Mixing time of the bed in seconds (±0.2 s) as a function of acceleration

values of vibrational amplitude coincide for the same bed heights. All of the data indicate a critical frequency of 10 Hz at which the expansion process begins. As the frequency is increased above this value—or as the period of vibration is decreased from 0.1 s—the bed continues to decrease in solid fraction. The rate of decrease in solid fraction with increasing frequency does depend on bed height, but does not appear to be dependent on vibrational amplitude. For frequencies greater than about 18 Hz, the beds have approximately the same minimum solid fraction of 0.21 ± 0.03.

The solid fraction of a randomly-packed stationary bed is generally close to 0.64; since the solid fractions for the present measurements are based on an average bed height, the solid fraction is less due to the packing variations near the solid walls and to the use of the paper lid that may not be in contact with all of the upper layer of particles. It should be emphasized that the solid fractions are also based on the maximum expansion of the bed, and thus represent the minimum value during the vibration cycle. Observations of the bed indicate that the local solid fraction decreases with distance from the base plate. However, it was impossible to determine the distribution from the imaging results. The void regions within the bed could not be accurately determined because as the bed expanded the particles behind the first layer of particles would appear in the images.

Mixing Results

The results from the mixing experiments are shown in Fig. 6. As described in the introduction, the bed is prepared using several layers of blue particles overlaying an equal thickness of red particles. The mixing time is determined from the digital images. For $z_o = 0.5$ cm, the three different values of bed height are used. For $z_o = 0.3$ cm, only the thinnest bed height is studied.

For the $m = 0.091$ kg and $z_o = 0.5$ cm experiment at the lowest acceleration shown (2.1 g), the mixing time is over two minutes. As the acceleration is increased the mixing time decreases significantly. At 2.4 g, the mixing time has decreased by a factor of 12 to 9.3 s. For higher accelerations, the mixing time continues to decrease, but the decrease is not as significant. An additional experiment was also performed for this mass of material at an acceleration of 2.0 g. The mixing time, however, was well over 90 minutes; by this time, several of the beads appeared to adhere to the plexiglass back surface, indicating that electrostatic forces were affecting the mixing process. The experiments at this low acceleration were not continued. In comparing the expansion results (Fig. 3) with the mixing time results (Fig. 6), the data for the thin bed indicates that the mixing time decreases dramatically when the bed begins to expand because the particles have greater mobility. When the bed reaches its expanded state at approximately 2.8 g, the mixing time continues to decrease with an increase in acceleration, but the decrease is less significant. When the bed is in a compressed state (near 2.0 g), no mixing is apparent.

For $z_o = 0.3$ cm and $m = 0.091$ kg, the results are similar to that for $z_o = 0.5$ cm; however, the dramatic drop in the mixing time occurs at lower values of acceleration. This finding is consistent with the expansion data, which indicates that the bed expands at lower values of acceleration.

In addition to the results presented in the figures, an additional experiment was also performed at 2.3 g to check the effect of the spacing between the front and back walls. The mass of the bed was 0.181 kg and the height was 1.8 cm, so that the bed was twice as deep but the height was the same as that used in the other experiments for $m = 0.091$ kg. The mixing times were within the uncertainty of the measurements indicating that the spacing between the front and back surface did not significantly affect the motion of the balls. In all of the current experiments, the flow did not appear to have a circulation pattern, nor did the motion of the balls appear to be different in the region close to the aluminum side walls.

The results for $z_o = 0.5$ cm, $m = 0.136$ kg, and for $m = 0.181$ kg show similar trends as that for the thinner bed; however, the mixing times are significantly longer for the same acceleration. In addition, the dramatic drop in the mixing times occurs at a much higher acceleration than for the thin bed. The difference between the mixing times for the different beds depends on the bed thickness, but also depends strongly on the bulk solid fraction of the bed. The mixing times again continue to decrease even though the bed did not show further expansion with increased acceleration.

A simple analysis of the mixing problem can be performed by utilizing some of the granular flow concepts. As mentioned earlier, the kinetic theory ideas have been used as an approach to examine the transport processes in granular flows. For the current problem, if the mixing is assumed to be diffusive, the following equation can be written,

$$\frac{\partial C}{\partial t} = \frac{\partial}{\partial z}\left(D\frac{\partial C}{\partial z}\right). \tag{3}$$

In the one-dimensional transient diffusion equation given above C is the color concentration, z is measured from the base of the vibrating plate, and D is the diffusion coefficient. For the current experiment, the appropriate boundary conditions for the problem are that the concentration gradient is zero both at the vibrating surface ($z = 0$) and at the top of bed ($z = h$),

$$\frac{\partial C}{\partial z} = 0 \quad \text{at} \quad z = 0 \quad \text{and} \quad z = h. \tag{4}$$

Using red beads to be $C = 1.0$ and blue to be $C = 0.0$, the initial condition at $t = 0$ is

$$C = 1.0 \quad \text{for} \quad z < h/2 \tag{5a}$$

and

$$C = 0.0 \quad \text{for} \quad z > h/2. \tag{5b}$$

If the diffusion coefficient is assumed to be constant throughout the layer, this equation can be integrated using separation of variables. In the long time limit, the concentration distribution is given by the first two terms of the series,

$$C(z, t) = \frac{1}{2} + \frac{2}{\pi}\cos\left(\pi\frac{z}{h}\right)\exp\left(-\frac{\pi^2 Dt}{h^2}\right). \tag{6}$$

The mixing time is then calculated by evaluating the expression for the concentration at $z = 0$. When $C(z = 0, t)$ is equal to 0.505, the difference in the color concentration variation from the bottom to the top is less than 0.01, which is consistent with

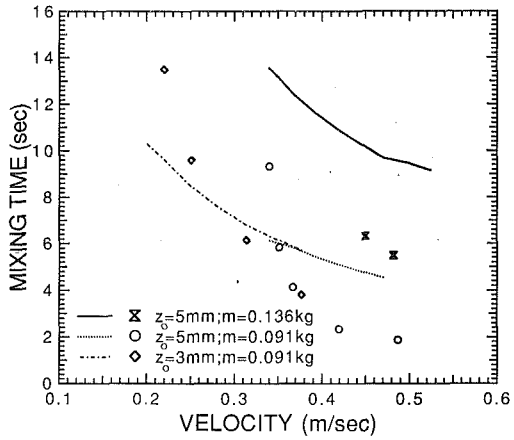

Fig. 7 Mixing time as a function of vibration velocity. The lines are based on the kinetic theory calculations for each of the bed heights.

the definition for the mixing time used in the experiments. This occurs when the time is equal to t_{mix} as given below,

$$t_{\text{mix}} = \frac{h^2}{\pi^2 D} \ln\left(\frac{2}{0.005\pi}\right). \tag{7}$$

The mixing time can then be evaluated if an expression for the diffusivity is known in terms of the vibrational parameters.

As described in an earlier section of the paper, Hsiau and Hunt (1993a) and Savage (1993) developed analytical expressions based on dense gas kinetic theory for self-diffusion coefficient for a granular flow. The diffusion coefficient depends on the square-root of the granular temperature and the particle diameter and is inversely proportional to the solid fraction and to the radial distribution function. In the current experiments, the bulk solid fraction can be estimated for a given vibrational frequency and bed height. However, the local particle velocities, and hence the granular temperature were not measured. From experimental observations, the particles near the vibrating surface appear to move with the surface. Using this velocity as an estimate for the vertical velocity component (Savage, 1988), the granular temperature can be estimated by assuming that the other velocity components are zero,

$$\Upsilon = \frac{1}{3}(v_x^2 + v_y^2 + v_z^2) \approx \frac{1}{3}(\omega z_o)^2. \tag{8}$$

With this expression for the granular temperature, the diffusion coefficient is

$$D = \frac{d(\pi/3)^{1/2}\omega z_o}{8(1+e_p)\nu g_0(\nu)}. \tag{9}$$

An estimate of the diffusion time can be made using this value of the diffusion coefficient. Then the mixing time becomes

$$t_{\text{mix}} = \frac{h^2}{\pi^2} \frac{8(1+e_p)\nu g_0(\nu)}{d(\pi/3)^{1/2}\omega z_o} \ln\left(\frac{2}{0.005\pi}\right). \tag{10}$$

Figure 7 shows the mixing times as a function of vibrational speed, $z_o\omega$. The curves represent the calculated times based on Eq. (10). The data that are shown are for experiments in which the bed has reached an expanded state. Hence for $z_o = 0.5$ cm and $m = 0.091$ kg, the data are for accelerations greater than 2.3 g; for the same mass and with $z_o = 0.3$ cm, the data include accelerations greater than 1.6 g; for $m = 0.136$ kg, the data are for values greater than 4 g. The data for $m = 0.181$ kg are not included. For a given acceleration, the height of the bed and the bulk solid fraction are determined from the experimental values as shown in Figs. 3, 4, and 6, and these terms are then used in Eq. (10). The coefficient of restitution is taken as $e_p = 0.95$ (Hsiau and Hunt, 1993a).

Both the data and the kinetic theory analysis indicates that the mixing times should decrease with increasing vibrational velocity. However, except for the data at the lowest velocities, the calculated times over predict the experimental results. This comparison suggests that if the diffusion equation is applicable to the mixing process, the diffusion coefficient is under estimated. One possible reason may be due to the assumed value of the granular temperature. The particle velocities may in fact be larger than that of the base plate which would tend to increase the granular temperature. In addition, the values of the bed height and the solid fraction are determined when the bed is in its most expanded state.

As previously noted, the mixing of the balls are assumed to follow a diffusive process that can be modeled with a one-dimensional diffusion equation. In addition, the diffusion coefficient is assumed to be independent of time and depth within the bed. However, the diffusion coefficient depends on the solid fraction and granular temperature, and visual observations of the bed indicate a decrease in solid fraction and an increase in the particle velocities relative to the base motion as a function of the distance from the base plate. These variations with depth and time within the vibration cycle may also impact the calculation of the mixing time.

Summary and Conclusions

The experimental results show that the expansion of the bed increases significantly beyond a critical frequency (10 Hz), and that the expansion does not depend on the amplitude of the vibration. However, it is important to note that in these experiments the ratio of vibrational amplitude to particle diameter is one or slightly larger ($z_o/d = 1.0$ or 1.67). The effect of the vibrational amplitude may be significant if the ratio of these two lengths is significantly larger or smaller than unity. For the thicker beds, there appeared to be a second critical frequency beyond which the beds exhibited a further expansion, suggesting that all of the beds may reach a minimum solid fraction if the vibrational frequency is large enough.

The mixing results indicate that the mixing times decrease significantly as the bed reaches an expanded state. For the thickest bed (approximately 12 ball diameters) the mixing time is 25 times longer than for the thinnest bed (approximately 6 ball diameters) at the highest acceleration studied (4.8 g for $z_o = 0.5$ cm). The theoretical predictions for the mixing times show qualitative agreement and indicate a decrease with increasing vibration velocity. The analysis, however, is based on many assumptions that are probably not valid in the current experiments. A more detailed study should include measurements of the local particle velocities and the solid fraction—quantities that are difficult to measure—but which are vitally important to the understanding of particulate flows.

In closing, these studies were conducted with the intent of minimizing any convective motion within the bed so that the results could be compared to a simple diffusion model. The convective motions were minimized by using smooth side walls, and using highly-spherical balls of uniform size. Without these measures, a recirculation pattern was noted. In addition, if the bed contained particles that varied in diameter, there also appeared to be some segregation according to size. The inclusion of these effects modify the mixing process enough so that a simple diffusion analysis would not be sufficient to model the flow. However, in actual engineering applications these effects are important, and will be the subject of future studies.

References

Akiyama, T., and Kurimoto, H., 1988, "Compressible Gas Model of Vibrated Particle Beds," *Chemical Engineering Science*, Vol. 43, pp. 2645–2653.

Brennen, C. E., Ghosh, S., and Wassgren, C., 1993, *Vertical Oscillation of a Bed of Granular Material*, Powders & Grains 93, C. Thornton, ed., Balkema Publishing, Rotterdam, pp. 247–252.

Campbell, C. S., 1990, "Rapid Granular Flows," *Annual Review of Fluid Mechanics*, Vol. 22, pp. 57–92.

Douady, S., Fauve, S., and Larouche, C., 1989, "Subharmonic Instabilities and Defects in a Granular Layer under Vertical Vibrations," *Europhysics Letters*, Vol. 8, pp. 621–627.

Gutman, R. G., 1976, "Vibrated Beds of Powders. Part I: A Theoretical Model for the Vibrated Bed," *Transactions for the Institution of Chemical Engineers*, Vol. 54, pp. 174–183.

Hsiau, S. S., and Hunt, M. L., 1992, "Kinetic Theory Analysis of Flow-Induced Particle Diffusion and Thermal Conduction in Granular Material Flows," ASME *Journal of Heat Transfer*, Vol. 115, pp. 541–548.

Hsiau, S. S., and Hunt, M. L., 1993, "Shear-Induced Particle Diffusion and Longitudinal Velocity Fluctuations in a Granular-Flow Mixing Layer," *Journal of Fluid Mechanics*, Vol. 251, pp. 299–313.

Jaeger, H. M., and Nagel, S. R., 1992, "Physics of the Granular State," *Science*, Vol. 255, pp. 1523–1531.

Jenkins, J. T., and Richman, M. W., 1985, "Kinetic Theory for Plane Flows of a Dense Gas of Identical, Rough, Inelastic, Circular Disks," *Physics of Fluids*, Vol. 28, pp. 3485–3494.

Lun, C. K. K., Savage, S. B., Jeffrey, D. J., and Chepurniy, N., 1984, "Kinetic Theories for Granular Flow: Inelastic Particles in Couette Flow and Slightly Inelastic Particles in a General Flow Field," *Journal of Fluid Mechanics*, Vol. 140, pp. 223–256.

Knight, J. B., Jaeger, H. M., and Nagel, S. R., 1993, "Vibration-Induced Size Separation in Granular Media: The Convection Connection," *Physical Review Letters*, Vol. 70, pp. 3728–3731.

Pakowski, Z., Mujumdar, A. S., and Strumillo, C., 1984, "Theory and Application of Vibrated Beds and Vibrated Fluid Beds for Drying Processes," *Advances in Drying*, Vol. 3, A. S. Mujumdar, ed., Hemisphere Publishing, pp. 245–306.

Ratkai, G., 1976, "Particle Flow and Mixing in Vertically Vibrated Beds," *Powder Technology*, Vol. 15, pp. 187–192.

Savage, S. B., 1988, "Streaming Motions in a Bed of Vibrationally Fluidized Dry Granular Material," *Journal of Fluid Mechanics*, Vol. 194, pp. 457–478.

Savage, S. B., 1993, "Disorder, Diffusion, and Structure Formation in Granular Flows," *Disorder and Granular Media*, D. Bideau, ed., Elsevier Science Publishers, Amsterdam, pp. 255–285.

Suzuki, K., Hosaka, H., Yamazaki, R., and Jimbo, G., 1980, "Drying Characteristics of Particles in a Constant Drying Rate Period in Vibro-Fluidized Bed," *Journal of Chemical Engineering*, Japan, Vol. 13, pp. 117–122.

Thomas, B., Mason, M. O., Liu, Y. A., and Squires, A. M., 1989, "Identifying States in Shallow Vibrated Beds," *Powder Technology*, Vol. 57, pp. 267–280.

Yu, S. H., Ma, B. J., and Weng, Y. Q., 1992, "Drying Performance and Heat Transfer in a Vibrated Fluidized Bed," *Drying '92*, A. S. Mujumdar, ed., Elsevier Science Publishers, Amsterdam, pp. 731–740.

Zik, O., and Stavans, J., 1991, "Self-Diffusion in Granular Flows," *Europhysics Letters*, Vol. 16, pp. 255–258.

B. J. Azzopardi
Department of Chemical Engineering,
University of Nottingham,
Nottingham NG7 2RD UK

J. C. F. Teixeira
Escola de Engenheria,
Universidade do Minho,
Braga, Portugal

Detailed Measurements of Vertical Annular Two-Phase Flow—Part I: Drop Velocities and Sizes

Phase anemometry and laser diffraction techniques have been employed to measure drop sizes in annular two-phase flow. The former technique also provides drop velocities. When converted to the same basis, the drop size distributions from the two techniques are in agreement. Drop velocities were 20 percent below the corresponding local velocities for the gas. Standard deviations of the drop velocities were 10 to 65 percent higher than those for the gas.

Introduction

The simultaneous flow of gas and liquid in a duct or pipe can produce a large number of spatial configurations of the phases due to the deformable interface between them. However, for many years it has been realized that for certain combinations of flow rates these configurations can be characterized by a common description. For example, in vertical upflow at high gas rates, part of the liquid flows as a film on the channel walls while the rest is carried as drops by the gas flowing in the center of the channel. This type of behavior is usually termed annular or annular-mist flow. This flow pattern is important as it occurs of many pieces of industrial equipment such as boilers and gas/condensate wells. Design of such equipment requires knowledge of first-order parameters such as pressure drop. However, there is also a need for more detailed information such as film thickness or the split of liquid between drops and film. These are necessary for models of pressure drop with a sound physical basis as well calculation of heat transfer and processes such as erosion and erosion/corrosion.

Though there are a number of publication which report drop sizes, hitherto, only the papers by Lopes and Dukler (1987) and Tayali et al. (1990) provide information on drop velocities. The first work shows drops to be traveling at velocities significantly below that of the gas. The approach used did not consider drops below 100 μm, a size range that could contain a fraction of the liquid traveling as entrained drops; ignoring these drops could result in the deduced mean drop sizes significantly larger than the correct values. The results of Tayali et al. (1990), whose equipment could handle drops in the size range 75–1500 μm, indicate smaller drop sizes than those measured by Lopes and Dukler (1987) for the equivalent flow conditions. The values of axial drop velocity reported by Tayali et al. were closer to the gas velocities than those observed by Lopes and Dulker. Lopes and Dukler indicate that drop velocities increase with drop size and with distance from the center line. In contrast, Tayali et al. find smaller drops travel faster than large ones and that the fastest drops are at the pipe center.

This paper reports measurements on drop sizes and velocities made in vertical annular flow. Related measurements on gas velocities and turbulence are given in Part II, Azzopardi and Teixeira (1994). Details of measurements using the laser diffraction technique are given by Azzopardi (1985) and Teixeira et al. (1988).

Experimental Arrangement

Flow Rig. Measurements were made in a vertical test section of 0.032 m internal diameter. The rig, shown schematically in Fig. 1, is supplied from the laboratory compressed air main. The air-flow rate is measured by an orifice plate before being mixed with the metered water flow in the test section. Beyond the test section, the two-phase mixture is separated; air is released to the atmosphere while the water is returned to the stock tank. The gas is introduced at the bottom of the vertical test section. The liquid is injected through a porous wall section mounted a few diameters from the bottom. Measurements were made at the top of the test section, 120 diameters from the liquid entry point. For the range of flow rates studied, this length was sufficient for the split of liquid between film and drops to be reasonably close to equilibrium values.

Special test sections are required to allow for the entry of the light beams and for the exit of the scattered light without their being distorted by the curved tube wall and the highly disturbed film interface. Small tubes were inserted through the pipe wall and the liquid film (when present) with flat windows (25 mm diameter, 3 mm thick and flat to $\lambda/2$) placed about 75 mm from the inside pipe wall. A small purge flow was directed at the inside of the windows to keep them drop free. The purge flow rate was kept as low as possible so as not to affect the measurements. Preliminary tests and the single-phase turbulence measurements reported in Part II, which used the same purge rates, indicate that it has no noticeable effect on the measurements. The diameters of the inlet and outlet tubes

Contributed by the Fluids Engineering Division for publication in the JOURNAL OF FLUIDS ENGINEERING. Manuscript received by the Fluids Engineering Division October 7, 1993; revised manuscript received February 15, 1994. Associate Technical Editor. O. C. Jones.

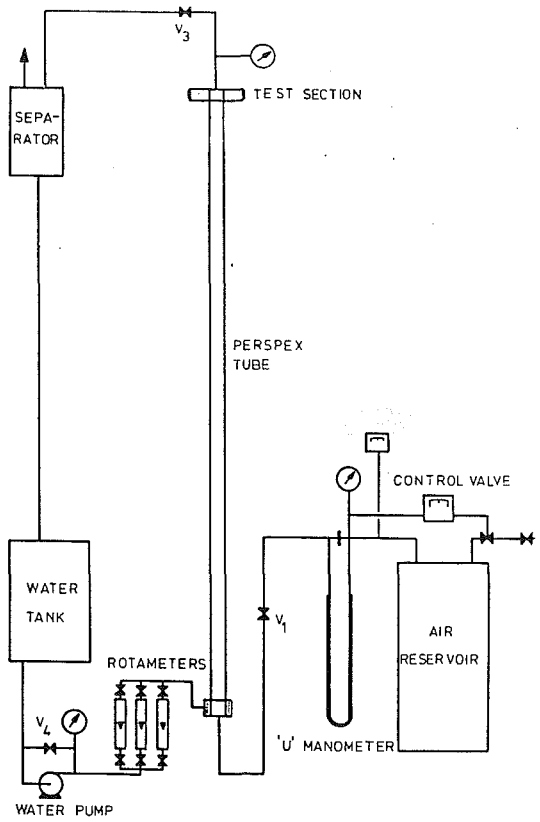

Fig. 1 Experimental facility

were 5 mm and 11 mm, respectively, while they both protruded 5 mm from the pipe wall. Though it might be expected that these tubes could disturb the flows and cause recirculation region to be formed, these are expected downstream of the tubes and not to affect the measurements. For the flow rates used, mean and maximum film thicknesses were estimated to lie in the ranges 0.1 to 0.4 and 0.5 to 2 mm, respectively.

Phase Doppler Anemometry. Simultaneous measurements of drop size and velocity were made using a Phase Doppler Anemometry technique. The beam of a 15 mW HeNe laser was split into two equal intensity beams 15 mm apart. They are focused by a 310 mm focal length lens (crossing angle 2.77 deg) and the scattered light collected at three positions (at an offset of approximately 30 deg from the forward direction). This arrangement produces an instrument with a wide dynamic range and from whose signals sphericity can be determined, Livesley (1988). Filtering of the signals is carried using an opto-electronic approach (Bossel et al., 1972) and the signals are processed to yield the frequency of the doppler burst (and hence velocity) and phase lag between signals from two detectors (and hence size) can be determined. A microcomputer

Table 1 Drop velocity and size data

G_G	G_L	r/R	u_d	u'_d	$-S$	K	$-r_c$	d_{32}
(kg/m²s)		(−)	(m/s)			(−)		μm
24.5	15.9	0.00	13.8	2.1	0.87	4.13	0.55	209
		0.25	12.9	2.2	0.91	3.73	0.52	190
		0.50	7.1	1.4	0.65	3.23	0.38	182
31.8	15.9	0.00	19.6	2.5	1.40	5.81	0.47	144
		0.25	16.1	2.2	0.84	3.86	0.39	140
		0.50	17.2	2.9	0.78	3.52	0.22	131
31.8	31.7	0.00	17.5	2.3	0.63	3.30	0.50	143
		0.25	16.2	2.4	0.60	3.16	0.40	135
		0.50	17.4	3.2	0.66	3.21	0.25	127
31.8	47.6	0.00	17.5	2.6	0.58	3.13	0.49	155
		0.25	16.3	2.5	0.44	3.21	0.43	144
		0.50	17.1	3.3	0.53	3.17	0.23	136
43.7	15.9	0.00	23.1	2.5	1.26	5.26	0.50	127
		0.25	21.1	2.6	1.12	4.46	0.32	117
		0.50	19.5	2.9	0.87	3.93	0.19	115
55.6	15.9	0.00	29.0	2.5	1.49	6.21	0.45	110
		0.25	27.1	3.1	1.28	5.26	0.32	108
		0.50	24.4	3.5	0.78	4.50	0.06	106
55.6	31.7	0.00	30.3	2.7	1.22	5.96	0.49	115
		0.25	28.1	2.9	1.07	4.58	0.34	99
		0.50	24.1	3.6	0.62	3.81	0.06	96
55.6	47.6	0.00	30.7	2.6	1.06	5.29	0.37	114
		0.25	28.5	2.9	0.89	4.47	0.28	99
		0.50	24.3	3.6	0.42	3.30	0.14	89

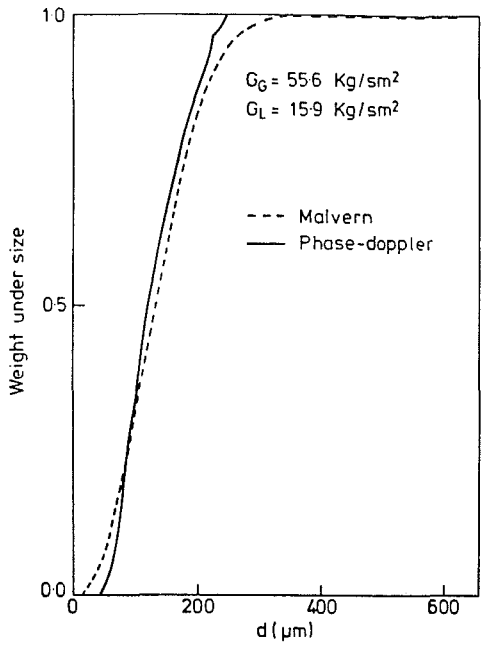

Fig. 2 Comparison between the phase Doppler technique and the laser diffraction: cumulative fraction of drops

Nomenclature

c_D = drag coefficient (−)
d = drop diameter (μm)
d_{10} = linear average drop diameter (μm) ($\Sigma n_i d_i / \Sigma n_i$)
d_{32} = sauter mean diameter (μm) ($n_i d_i^3 / n_i d_i^2$)
G_G = gas mass flux (flow rate per unit flow area) (kg/m²s)
G_L = liquid mass flux (flow rate per unit flow area) (kg/m²s)
g = gravitational acceleration (m/s²)
K = kurtosis
N = total number of drops
n_i = numbers of drops of size d_i
R = pipe radius (m)
r = radial position (m)
r_c = correlation coefficient (−)
S = skewness
t = time (s)
u = vector of velocity (m/s)
$\bar{u}$ = mean velocity (m/s)
u'_d = standard deviation of drop velocity (m/s)
γ = density ratio
λ = wavelength of light (nm)

Subscripts

d = drop
G = gas
i = individual drop
r = radial
z = axial

Table 2 Example of gas and drop velocity profiles (gas mass flux = 43.7 kg/m^{2}s; liquid mass flux = 15.9 kg/m^{2}s)

Dimensionless radius (r/R)	Gas velocity (m/s)	Drop velocity (m/s)
0	29.8	23.1
0.25	28.9	21.1
0.50	26.4	19.5

Table 3 Variation of standard deviations of drop and gas velocity

Gas superficial velocity (m/s)	Standard deviation of drop velocity/mean drop velocity	Gas turbulence intensity/mean gas velocity
13.6	0.15	0.1
17.7	0.13	0.08
24.3	0.11	0.07
30.9	0.09	0.06

calculates the velocity and size and sorts and stores the data. For the optical geometry in these experiments, the size range is 30–650 μm. Because of the gaussian distribution of intensity of the laser beams, the effective probe volume will be larger for bigger drops at a given trigger level. A correlation has been made for this as described by Brazier et al. (1988) and Teixeira (1988).

Accuracy. Water flow rates were measured by rotameters, which were calibrated by weighing a timed efflux. They could be read within 3 percent. Air-flow rates were measured by a standard orifice plate. The pressure drop across the orifice plate was measured by a water manometer which could be read to within 1 percent. Similarly, gas pressure and hence density could also be determined with an accuracy of better than 1 percent.

The accuracy of the phase doppler anemometry equipment has been tested by making measurements of drops created by a Bergland-Liu mono-sized drop generator, Negus et al. (1989). Their experiments indicate that the results should be accurate to within ± 2 percent.

Results

Information on drop sizes and velocities was acquired for gas mass fluxes in the range 24.5 to 55.6 kg/m^{2}s and liquid mass fluxes between 15.9 and 47.6 kg/m^{2}s. Values of means and higher moments are given in Table 1. For each run, data are based on between 1250 and 1400 individual validated measurements.

Discussion

Drop size distribution information has been gathered under identical flow conditions using the phase doppler and laser diffraction techniques. Full details for the latter technique are given in the papers by Azzopardi (1985) and Teixeira et al. (1988). Differences are to be expected in the data "as measured" as the two techniques make different measurements; the diffraction technique measures a time/space average across a pipe diameter while the phase doppler measures point values. However, if an allowance is made for spatial variations and for size/velocity relationships, the data can be reduced to the same basis. Teixeira (1988) gives details of the convertions. Such correction results in maximum differences between the Sauter mean diameters from the two methods of 10 percent with most data showing much smaller differences. Figure 2 shows that there is good correspondence between the data from the two instruments. Similar agreement between the two measurement methods has been observed by Brazier et al. (1988), who studied the drops formed by a spray nozzle.

Mean drop velocities show a similar radial distribution as those for the gas but with values about 20 percent lower, Table 2. The mean drop velocities are approximately equal to the gas superficial velocity. Similar trends are shown at other flow rates. Table 3 shows that the standard deviation of the drop velocity (nondimensionalized by the mean; $1/u_d \sqrt{1/n\{(u_{di}-\overline{u}_d)^2\}}$ increases from the centerline toward the interface.

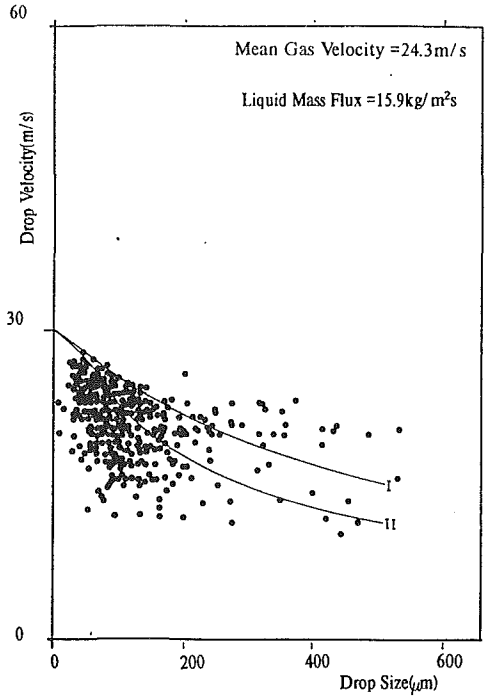

Fig. 3 Effect of drop size on drop velocity

Examination of the data indicates that the equivalent values for the gas (turbulence intensity/mean velocity) are 10 to 65 percent lower than these values for the drops. Table 3 also shows a noticeable dependence on gas velocity. The distribution of drop velocities differs slightly from a gaussian as the peak is skewed toward the gas velocity. This follows from the fact that drops are created with very low velocities while there is an upper limit at the gas velocity. It is interesting to note that the calculations of Schadel et al. (1990) predict slip velocities which are about 20 percent of the gas velocity.

There is a trend for smaller drops to be traveling at higher velocities, Fig. 3. In addition, it can be seen that there is a wider range of velocities at smaller drop sizes. This can be explained by the fact that smaller drops will be most strongly affected by gas turbulence which can cause acceleration and deceleration in the lateral direction and so increase and decrease the time taken for drops to arrive at the probe volume and widen the range of axial velocities that they could achieve. Larger drops, being less susceptible to turbulence, will show a narrower range of lifetimes and hence velocities. It is of interest that one of the only other sources of drop velocity data, Lopes and Dukler (1987), shows a completely different trend of drop velocity with drop size; larger velocities were obtained for the bigger drops. An explanation based on the effect of turbulence on the drag coefficient was suggested by those authors. In addition, it is noted that those authors were working at conditions which resulted in the churn-annular flow ($u_G^* = 0.77$–1.37). For the present experiments $u_G^* = 1.03$–2.34.

Table 1 shows that mean drop sizes and velocities decrease as the interface is approached. This is in contrast with the measurements of Lopes and Dukler (1987). However, drop size measurements by Andreussi et al. (1978) and Tayali et al. (1990) also show a maximum in drop sizes at the center of the channel.

Sizes and velocity are not strongly correlated. The correlation coefficient, defined as

$$r_c = \frac{\Sigma(u_{di} - \overline{u_d})\Sigma(d_i - d_{10})}{(\Sigma(u_{di} - \overline{u_d})^2 \Sigma(d_i - d_{10})^{0.5}} \quad (1)$$

is small and decreases as the interface is approached. Values are listed in Table 1. These show that it also decreases with gas velocity and, in the center of the channel, with liquid flow rate.

Calculations have been carried out to establish phenomena which are important in determining the velocities which drops achieve. The motion was considered as two dimensional and the drag equations written as

$$\frac{du_{dz}}{dt} = \frac{(1-\gamma)}{\gamma} g - \frac{3}{4} c_D \frac{|u_d - u_G|}{\gamma d} (u_{dz} - u_{Gz}) \quad (2)$$

$$\frac{du_{dr}}{dt} = -\frac{3}{4} c_D \frac{|u_d - u_G|}{\gamma d} (u_{dr} - u_{Gr}) \quad (3)$$

where c_d is calculated using the relative velocity $|u_d - u_G|$ and the equation of Teixeira (1988) which takes account of the effect of gas turbulence on the drag coefficient. γ is the density ratio. The initial value of u_{dr} was calculated from the equation of Andreussi and Azzopardi (1983). The results of Lopes and Dukler (1987) confirm that this equation gives values of the correct magnitude for larger drops. A value of 3 m/s was used for u_{dz} (this was taken from measurements of disturbance wave velocity, Azzopardi (1986), these disturbance waves are the source of drops). The equations were integrated up to the time that the drop reaches the centerline. The predictions give values which pass through the middle of the data except for the smallest drop sizes as shown in Fig. 3. The large quantity of small drops with lower velocities is probably caused by their susceptibility to the effect of turbulent eddies which can increase the rate of lateral dispersion of the drops, i.e., either toward or away from the wall, so that some arrive at the centerline earlier than might be expected from Newtonian calculations. Consequently, they will have lower axial velocities. With larger drops, which are less susceptible to the effect of eddies, this effect is negligible. Predictions obtained assuming that the drops have a constant transverse velocity and ignoring the effect of turbulence on the drag law show significant under prediction at the larger sizes indicating that these effects are important. This appears to contradict the experimental finding of Andreussi and Azzopardi (1983) that drops travel with a constant traverse velocity. However, the drops observed in that case were >300 μm and calculations have shown that, though these larger drops do maintain an approximately constant transverse velocity, smaller drops experience a significant transverse retardation, as might be expected. Estimates indicate that, for the range of flow rates listed in Table 1, mean film thickness were in the range 0.1 to 0.4 mm.

Conclusions

From the above it can be concluded that:

(1) The phase doppler technique produces drop size distributions similar to those from a laser diffraction instrument. However, comparison is only possible if conversions have been made so that both are measuring under the same conditions of space time averaging.

(2) Mean drop velocities were seen to be about 20 percent below the corresponding local values for the gas. The averaged drop velocity was approximately the same as the superficial gas velocity. A weak correlation has been found between the velocity and size of drops. Factors which affect this relationship have been identified.

Acknowledgments

The experimental work described in this paper was undertaken as part of the Underlying Research Programme of the UKAEA at their Harwell Laboratory.

References

Andreussi, P., Romano, G., and Zanelli, S., 1978,"Drop Size Distribution in Annular Mist Flow," 1st Int. Conf. on Liquid Automisation and Spray Systems, Tokyo.

Andreussi, P., and Azzopardi, B. J., 1983, "Droplet Deposition and Interchange in Annular Two-Phase Flow," *International Journal of Multiphase Flow*, Vol. 9, pp. 681–695.

Azzopardi, B. J., 1985, "Drop Sizes in Annular Two-Phase Flow," *Experiments in Fluids*, Vol. 3, pp. 53–59.

Azzopardi, B. J., 1986, 'Disturbance Wave Frequencies, Velocities and Spacing in Vertical Annular Two-Phase Flow," *Nuclear Engineering and Design*, Vol. 92, pp. 121–133.

Azzopardi, B. J., and Teixeira, J. C. F., 1994, "Detailed Measurements of Vertical Annular Two-Phase Flow—Part II: Gas Core Turbulence," ASME JOURNAL OF FLUIDS ENGINEERING, published in this issue, pp. 796–800.

Bossel, H. H., Miller, W. J., and Meier, G. E. A., 1972, "Noise-Cancelling Signal-Difference Method for Optical Velocity Measurements," *Journal of Physics E*, Vol. 5, pp. 893–896.

Brazier, K., Gillespie, R. F., Dalzell, W., and Livesley, D. M., 1988, "Bias Corrections to Size Distribution and Concentrations in Phase-Doppler Particle Measurement," AERE R13270, UKAEA.

Livesley, D. M., 1988, "Strengths and Limitations of the Phase Doppler Technique for Simultaneous Measurements of Particle Velocity and Size," AERE R13113, UKAEA.

Lopes, J. C. B., and Dukler, A. E., 1987, "Droplet Dynamics Vertical Annular Flow," *American Institute of Chemical Engineers Journal*, Vol. 33, pp. 1013–1024.

Negus, C. R., Bosley, R. B., Martin, S. R., and Wallace-Sims, G. R., 1989, "Use of the Phase-Difference Technique for Droplet Sizing in the Aerosol Range," 3rd Annual Conf. Aerosol Soc., Birmingham, March 20–22, Paper 1.7, pp. 37–42. Also AEA Technology Report AEA-InTec-0043, Oct. 1990.

Schadel, S. A., Leman, G. W., Binder, J. L., and Hanratty, T. J., 1990, "Rates of Atomisation and Deposition in Vertical Annular Flow," *International Journal of Multiphase Flow*, Vol. 16, pp. 363–374.

Tayali, N. E., Bates, C. J., and Yeoman, M. L., 1990, "Drop Size and Velocity Measurements in Vertical Developing Annular Two-Phase Flow," 3rd Int. Conf. on Laser Anemometry Advances and Application, Swansea, U.K., 26–29 Sept.

Teixeira, J. C. F., 1988, "Turbulence in Annular Two Phase Flow," PhD thesis, University of Birmingham, U.K.

Teixeira, J. C. F., Azzopardi, B. J., and Bott, T. R., 1988, "The Effects of Inserts in Annular Two-Phase Flow," 2nd U.K. National Heat Transfer Conference, Glasgow.

B. J. Azzopardi
Department of Chemical Engineering,
University of Nottingham,
Nottingham, NG7 2RD U.K.

J. C. F. Teixeira
Escola de Engenheria,
Universidade do Minho,
Braga, Portugal

Detailed Measurements of Vertical Annular Two-Phase Flow—Part II: Gas Core Turbulence

Laser anemometry techniques have been employed to measure gas velocities in annular two-phase flow. Mean velocities and Reynold's stresses in the gas appear to be similar to those in corresponding rough pipes. However, turbulence intensities are higher than the values corresponding to flow over a wall with a roughness equivalent to the film interface.

Introduction

Current, physically based, models for annular-mist flow take into account not only the split of liquid between film and drops but also the constant interchange that occurs between them. One of the latest versions of such models, Hewitt and Govan (1990), gives good predictions of experimental data over wide ranges of parameters. Nevertheless, the models are still strongly dependent on empirical correlations for closure. Recently, Abolfadl and Wallis (1985) and Owen and Hewitt (1987) have suggested that knowledge of the turbulence might permit some of the empiricism to be removed. They propose that an effect of the presence of the drops is to suppress the level of turbulence in the gas core which would result in a modified log law for the velocity profile.

An examination of the published literature reveals nothing has been published on turbulence in the gas core of annular flow. A small number of papers were found which report mean velocity profiles, Gill et al. (1964), Adorni et al. (1961), Subbotin et al. (1975), and Kirillov et al. (1978).

There is some information from other types of two-phase pipe flow. A recent review by Hetsroni (1989) reveals that measurements have been made of the continuous phase turbulence in both gas-solid and liquid-solid flows. Maeda et al. (1980), Lee and Durst (1982), and Tsuji et al. (1982, 1984) have reported data for gas-solid flow while Zisselmar and Molerus (1979) investigated liquid-solid flows. From these it can be seen that turbulence intensities increase or decrease from the single-phase values. For smaller particles there is a suppression of turbulence, though the degree of suppression diminishes with particle concentration. For larger particles the turbulence intensity is enhanced the increase being directly dependent on concentration. Gore and Crowe (1989) show that these effects can be quantified by consideration of the ratio between particle size and a characteristic length scale of the turbulence. Ratios below 0.1 result in suppression, higher values correspond to an increase in turbulence. However, it must be remembered that these two-phase flows differ from annular flow in two fundamental aspects. First, there is no liquid film present. In annular flow this can act as a rough wall. The second difference relates to steady state. Though this is achieved in the fluid-solid flows, in annular flow with its constant creation of drops from the film there can only be a dynamic steady state, i.e., there will always be freshly created drops present.

This paper reports measurements on gas phase turbulence made in vertical annular flow. Measurements were first carried out with single-phase gas flow to check the measurement technique/test section combination was working correctly. Related measurements on drop sizes and velocities are given in Part I, Azzopardi and Teixeira (1993).

Experimental Arrangement

Flow Rig. Measurements were made in a vertical test section of 0.032 m internal diameter. The rig is described in detail in Part I, Azzopardi and Teixeira (1994).

Special test sections are required to allow for the entry of the light beams and for the exit of the scattered light without their being distorted by the curved tube wall and the highly disturbed film interface. Small tubes were inserted through the pipe wall and the liquid film (when present) with flat windows (25 mm diameter, 3 mm thick and flat to $\lambda/2$) placed about 75 mm from the inside pipe wall, Fig. 1(*a*). The diameters of the inlet and outlet tubes were 5 mm and 11 mm, respectively, while they both protruded 5 mm from the pipe wall. Though it might be expected that these tubes could disturb the flows and cause recirculation region to be formed, these are expected downstream of the tubes and not to affect the measurements. For the flow rates used, mean and maximum film thicknesses were estimated to lie in the ranges 0.1 to 0.4 and 0.5 to 2 mm, respectively.

Figure 1(*b*) indicates the locations within the pipe cross section at which measurements were made.

Visibility Technique. Velocity measurements in the gas core were obtained with a laser doppler technique using light scattered from 1 μm polystyrene spheres inserted into the gas flow. This size had been chosen as calculations had shown that they

Contributed by the Fluids Engineering Division for publication in the JOURNAL OF FLUIDS ENGINEERING. Manuscript received by the Fluids Engineering Division October 7, 1993; revised manuscript received February 15, 1994. Associate Technical Editor: O. C. Jones.

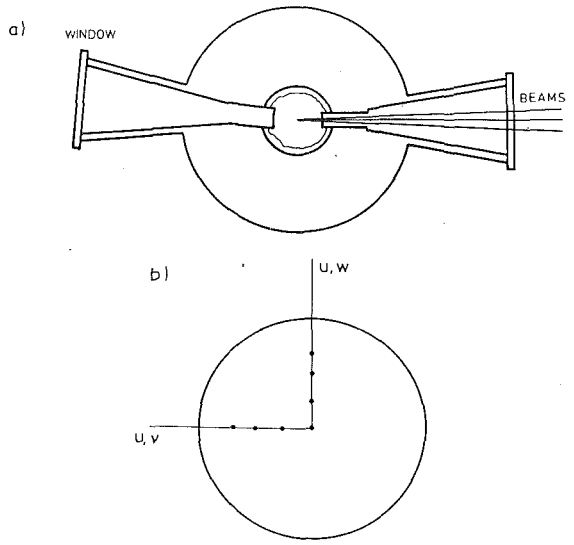

Fig. 1 *(a)* **Schematic location of positions at which measurement were made with LDA; (*b*) arrangement for optical access into the gas core**

would be good flow followers. Signals from these tracer particles were discriminated from those arising from drops by use of the amplitude as well as the visibility (ratio of ac to dc components—which is size dependent) of the doppler bursts.

The light from the blue (λ = 488 nm) and green (λ = 514.5 nm) lines of a 50 mW cw Argon ion laser are selected by means of a color selective beam splitter and narrow band filters. The light is steered through different paths by mirrors before being brought to the same line by a beam splitter. In each one of these paths, the light is focussed (by a 160 mm focal length lens) on to a rotating grating. This has two functions:

(*i*) to split each beam into several *n* order (0, 1, . .) beams from which only the two first order beams are used;

(*ii*) when rotated, to shift the frequency of each first order beam.

The gratings diffract the light at two perpendicular directions to obtain two components of velocity. The motor driving each grating has a separate controller to keep its speed constant throughout the experiments.

The two first order beams from each line (separated from the others using a mask) are collimated by a 300 mm focal length lens which gives a beam expansion of about 2:1. This was carried out to reduce the size of the probe volume and so improve the size resolution of the system. Another 300 mm lens focusses the beams into the probe volume, the crossing angles were 5.1 deg for the green and 4.83 deg for the blue. Scattered light is collected at 6 deg off axis with a 9.5 deg collection angle by a 300 mm lens and focussed by a 250 mm lens onto a 250 μm pinhole. This size ensures that only scattered light from the center of the probe volume is collected, thus improving the signal quality: light scattered from the outermost regions of the probe volume is rejected, and the chances of multiple occupancy of the probe volume is reduced.

The blue and green scattered lights are separated by color selective beams splitters and narrow band filters and then collected by two photodetectors. The analogue signals are amplified and, then, digitized by a Data Lab. DL1080, 2 channel, 20 MHz transient recorder, before being transferred to a Digital PDP11 microcomputer, where the signals are processed.

An important aspect of signal processing in two-phase flow is the discrimination of the tracer particles from the larger water drops. Using a suitable optical design and by correct selection of trigger levels, the amplitude and visibility of the doppler signal (Bates et al., 1981, Klaifas et al., 1987) were used to perform such discrimination. This combination is understood to be the most reliable and can distinguish between the tracer particles and larger drops passing through the edge of the probe volume.

Accuracy. The accuracy of the metering methods for the inlet gas and liquid flow rates are discussed in Part I. The LDA technique for gas velocity measurements was checked in tests using a glass sphere mounted on a rotating glass disk. In addition, the data abstraction part of the instrumentation was checked using electronically generated signals. Both indicated that accuracies were better than 3 percent. The probe volume was positioned at different places in the test section by moving the illumination and light collection systems which were both mounted on the same support. This could be positioned within 2.5 10^{-4} m, giving dimensional radial positions accurate to better than 1 percent. Where wall shear stress and hence friction factor are determined from the extrapolation of Reynold's stress data to the wall, the accuracy is $\pm$29 percent due to the uncertainty in fitting a line through data points.

Results

For single-phase flow, simultaneous measurements of axial and either radial or circumferential velocities were made for Reynolds numbers in the range 57,000 to 142,100. In the case of annular flow, the same measurements were made for gas mass fluxes in the range 24.5 to 55.6 kg/m^{2}s and liquid mass fluxes between 15.9 and 47.6 kg/m^{2}s. An example of the dis-

Nomenclature

d_t = tube diameter (−)
f = friction factor (−)
G = mass flux (mass flow rate per unit cross-sectional area) (kg/m^{2}s)
K = kurtosis (−)
l = turbulence length scale (m)
n = power law exponent (−)
R = pipe radius (m)
r = distance from centerline (m)
S = skewness (−)
U = cross section averaged velocity (m/s)
u = time averaged local velocity (m/s)
u' = axial turbulence intensity (m/s)
u_* = friction velocity ($\sqrt{\tau_w/\rho}$ or $\sqrt{\tau_i/\rho}$) (m/s)
v' = radial turbulence intensity (m/s)
w' = circumferential turbulence intensity (m/s)
$u'v'$, $u'w'$ = Reynolds stress (m^2/s^2)
y = distance from the wall (m)
z = axial distance (m)
Re = Reynolds number $G_G d_t/\mu_G$) (−)
dp/dz = pressure gradient (N/m^3)
ϵ_g = void fraction (−)
λ = wavelength of light (nm)
μ = dynamic viscosity (kg/ms)
ρ = density (kg/m^3)
τ = shear stress (N/m^2)

Subscripts

c = gas/droplet core
G = gas
i = interface
L = liquid
LE = entrained liquid
MAX = maximum value (i.e., at centerline)
w = wall

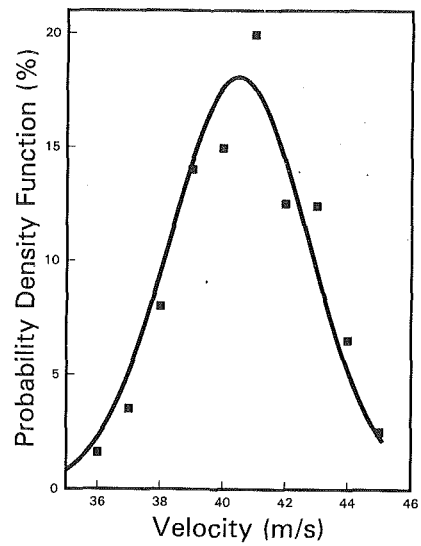

Fig. 2 Probability distribution function of the gas velocity: comparison with a Gaussian function

tribution of axial velocities is shown in Fig. 2. This shows that the data is reasonably well described by a gaussian function. Tables 1 and 2 list the mean axial velocity as well as the three components of turbulence intensity and the axial/radial Reynolds stress ($u'v'$). The other component of Reynolds stress which could be determined ($u'w'$) and the mean values of radial and circumferential velocities were found, within the experimental accuracy, to be zero. In all runs, the results reported were based on 400 realizations.

Discussion

Single Phase Gas Velocity and Turbulence. Data were obtained with gas flowing alone in order to prove the combination of the laser doppler technique, the test section and the purge flow used to keep the windows free of drops during two-phase flow runs. These experiments were carried out at the same purge flow as in the two-phase runs, the minimum value to keep the windows clean.

The results obtained in the present experiments for single phase flow were very similar to published data, e.g., Laufer (1954), for both mean axial velocity and all three components of turbulence intensity. The data show the same radial trends as Laufer's data and when turbulence intensities were nondimensionalized with respect to the friction velocity, there was good agreement of absolute values. Wall shear stresses were deduced from linear extrapolation of Reynolds stresses to the wall. The resulting values were in reasonable agreement with those determined from pressure drop measurements and those calculated from the standard Blasius equation ($f = 0.079/\mathrm{Re}^{1/4}$). Values from all three approaches, in the form of friction factors, are shown in Fig. 3.

The mean axial velocity profiles were found to fit an equation of the form

$$\frac{u}{u_{\mathrm{MAX}}} = \left(\frac{y}{R}\right)^{1/n} \tag{1}$$

where u_{MAX} is the maximum velocity in the channel, y is the distance from the wall, and R is the pipe radius. Flow rates, obtained from integration of Eq. (1) with the correct u_{MAX} and n, agreed with those determined from the orifice plate in the inlet line to within $+2.8/-0.8$ percent. Figure 4 shows that values of $1/n$ (Eq. (1)) and friction factors from the present data lie on the same line as the data of Nikuradse (1932) and Nunner (1956).

The higher moments, skewness (S) and flatness or kurtosis (K), of the distribution of measured values were determined

Table 1 Gas velocity and turbulence data—single phase flow

Re_G	U_G	u_*^+	r/R	u	u'	v'	w'	$-u'v'$
—	m/s	m/s	—		m/s			m^2/s^2
57000	17.7	0.84	0.00	20.74	0.98	0.85	0.85	0.00
			0.25	20.21	1.07	0.97	0.97	0.13
			0.50	18.80	1.48	0.95	0.86	0.37
			0.69	17.50	1.56	1.07	1.13	0.49
78000	24.3	1.09	0.00	28.28	1.05	0.94	0.94	0.00
			0.25	27.57	1.21	1.05	0.94	0.37
			0.50	25.98	1.60	1.25	1.26	0.52
			0.69	24.03	1.83	1.30	1.36	0.81
99600	30.9	1.39	0.00	36.09	1.40	1.12	1.12	0.00
			0.25	35.21	1.51	1.15	1.29	0.65
			0.50	33.10	1.99	1.45	1.55	0.92
			0.69	31.20	2.39	1.53	1.67	1.36
120900	37.5	1.65	0.00	43.67	1.58	1.29	1.29	0.00
			0.25	42.85	1.91	1.43	1.44	0.65
			0.50	40.50	2.21	1.54	1.71	1.44
			0.69	38.50	2.50	1.70	1.96	1.84
142100	44.1	1.84	0.00	51.53	1.61	1.51	1.51	0.00
			0.25	50.60	2.15	1.46	1.48	0.89
			0.50	48.40	2.64	1.79	1.86	1.63
			0.69	45.80	2.95	1.89	2.13	2.37

$^+$Value from extrapolation of $u'v'$ to interface

Table 2 Gas velocity and turbulence data—two phase flow

G_G	G_L	G_{LE}	r/R	u	u'	v'	w'	$-u'v'$
kg/m^2s			—		m/s			m^2/s^2
24.5	15.9	0.86	0.00	17.7	1.69	1.30	1.30	0.00
			0.25	17.2	1.96	1.40	1.52	0.39
			0.50	15.3	2.59	1.80	-	0.70
31.8	15.9	0.96	0.00	22.1	1.78	1.49	1.49	0.00
			0.25	21.7	2.09	1.63	1.80	0.53
			0.50	19.5	2.91	1.90	-	1.03
31.8	31.7	2.92	0.00	22.4	2.30	1.87	1.87	0.00
			0.25	21.9	2.59	1.90	2.12	0.68
			0.50	19.6	3.18	2.14	-	1.49
31.8	47.6	5.20	0.00	22.7	2.82	2.25	2.25	0.00
			0.25	22.0	3.00	2.15	2.48	0.90
			0.50	19.7	3.40	2.51	-	1.64
43.7	15.9	1.43	0.00	29.8	1.99	1.63	1.63	0.00
			0.25	28.9	2.44	1.74	1.91	1.03
			0.50	26.4	3.30	1.90	-	1.61
55.6	15.9	2.19	0.00	37.4	2.17	1.77	1.77	0.00
			0.25	36.0	2.51	1.85	-	1.21
			0.50	33.1	3.41	2.28	-	2.04

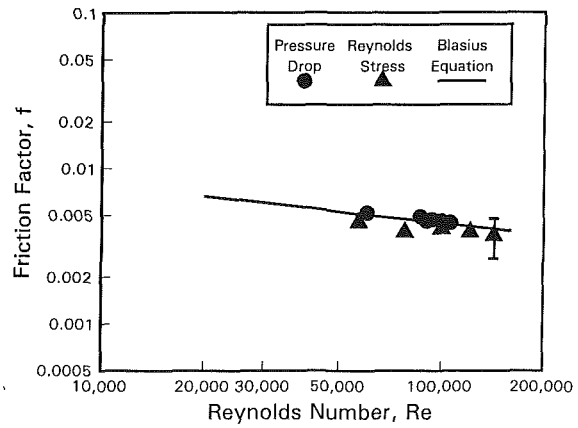

Fig. 3 Comparison of friction factors obtained from pressure drop and extrapolation of Reynolds stress to the wall

for u', v', w', and $u'v'$. The calculated values of the fluctuating components of the velocity were found to vary between -0.5 and 0.1 (S) and 2.8 and 3.3 (K). These values, close to those expected for a gaussian distribution (S = 0 and K = 3), confirm the random nature of the turbulent flow. Similar val-

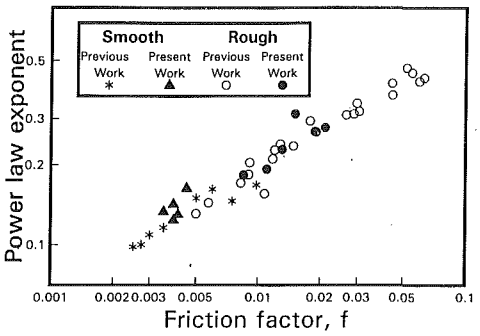

Fig. 4 Power law exponent/friction factor relationship for smooth and rough walled pipes

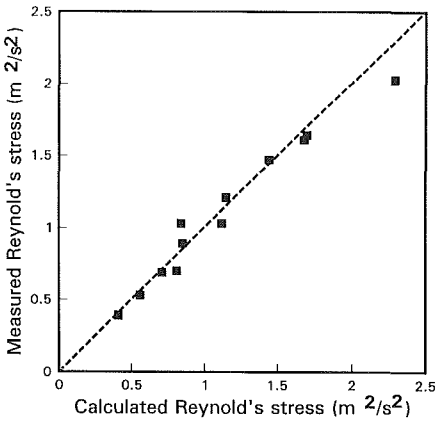

Fig. 5 Comparison between the measured Reynold's stress and that calculated from a force balance in the gas core

ues are found in Batchelor (1951) and Wood and Antonia (1975). The joint probability distribution function for $u'v'$ was shown by Antonia et al. (1973) to be a function of the correlation coefficient $u'v'/(uv)$, when both u' and v' are normally distributed. In such a case, the skewness and kurtosis values would vary between 0 and -2.82 and 9 and 15, respectively. The present values of K range from 9 to 16.3.

From the agreement between present data and that published, it was concluded that the combination of measurement technique, test section and gas purge employed in the present work gave accurate measurements for known conditions and that it could be used with confidence in the more novel application of annular two-phase flow.

Annular Flow Gas Velocity and Turbulence. In the case of annular flow, mean velocity profiles could also be described by Eq. (1). Values of $1/n$ were larger than the equivalent single-phase data values. However, when plotted against friction factor (determined from extrapolation of Reynolds stress data to provide wall shear stresses) the values lie on the same line as data measured by Nikuradse (1932) and Nunner (1956) in rough walled pipes, Fig. 4. Flow rates, obtained from integration of Eq. (1) with the correct constants, agreed with those determined from the orifice plate in the inlet line to within $-2/-6.7$ percent.

The shear stress in the gas core is related to the Reynolds stress through

$$\tau = -\rho\,\overline{u'v'} \tag{2}$$

A force balance on an element of fluid (assuming that the drops are uniformly distributed about the cross section) yields

$$\tau = \frac{r}{2}\left(-\frac{dp}{dz} - \rho_c g - g(\rho_L - \rho_c)(1-\epsilon_g)\right) \tag{3}$$

Combining Eqs. (2) and (3) and using pressure drop values from similar experiments allows values of Reynolds stress to

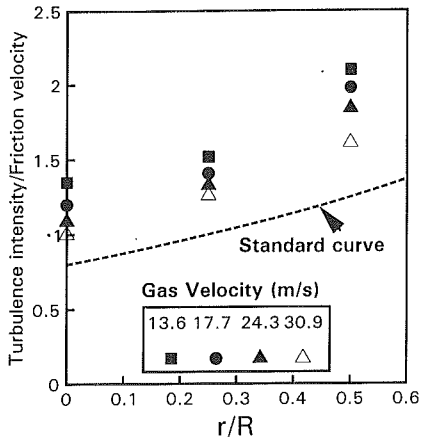

Fig. 6 Effect of the gas velocity on turbulence intensities in annular flow (liquid mass flux = 15.9 kg/m^{2}s)

Table 3 Ratio of turbulence intensity to friction velocity (gas mass flux = 43.7 kg/m^{2}s)

Drop mass flux / gas mass flux	Dimensionless radius (r/R)		
	0	0.25	0.5
0	0.8	1.0	1.25
3	1.2	1.41	1.98
9.2	1.39	1.56	1.9
16.3	1.57	1.65	1.82

be calculated. Figure 5 shows that these are in reasonable agreement with the measured values.

Data from published literature indicate that, in both smooth and rough walled pipes, the radial profiles of turbulent intensities follow a standard curve when nondimensionalized with the correct friction velocity. The present data have been analyzed in this way using values deduced from the two-phase pressure drop. Figure 6 shows that the results to lie 25–96 percent above the values determined from the interfacial shear stress (standard value). The effect of drop concentration can be seen in the data listed in Table 3.

Use of the two-phase friction velocity should have allowed for the effects of turbulence arising from the rough liquid film interface. Kada and Hanratty (1960) suggested that particles much smaller than the most energetic eddies will follow the eddy for part of its lifetime and take up energy. Thus turbulent energy of the eddy will be transformed to kinetic energy of the particle. The larger particles, because of higher values of Reynolds number, will tend to create turbulence (in their wake) near the scale of the most energetic eddies and so increase the turbulence intensity of the gas. Drop velocities reported in Part I of this paper (Azzopardi and Teixeira, 1994) have been found to be significantly less than the corresponding gas velocities (and hence than the velocities of the eddies). This implies that contact times are small and little energy can be transferred from eddy to drop in spite of the drops being much smaller than the most energetic eddies. However, the large differential velocity will result in drop Reynolds numbers at which vortex shedding from the drops (and hence additional turbulence) will occur.

The change in the turbulence intensity of the gas ([value for two-phase flow minus the standard value]/standard value) is plotted against the ratio of drop size to characteristic turbulence length scale in Fig. 7 as suggested by Gore and Crowe (1989). The Sauter mean diameter was used as the characteristic drop size and the length scale was determined from the simple equation suggested by Hutchinson et al. (1971) - 0.2R. Length scales determined from the Reynolds stress and the gradient of the mean velocity profile gave similar results. In contrast to those data from gas-solid and liquid-solid flows, the present

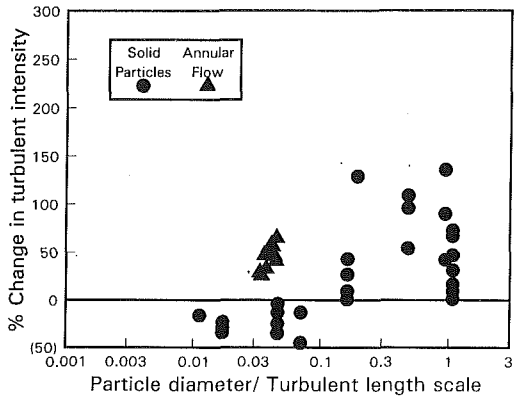

Fig. 7 Change in turbulence intensity as a function of the length scale ratio

Table 4 Effect of rate of entrainment on the increase in turbulence intensity over standard values

% Change in turbulence intensity	Rate of entrainment per unit area of surface (kg/m^2s)
50	8.4
36	8.6
25	15.7
74	49.3
96	74.5

data show that there was an increase in turbulence intensity above the standard value, even though the drop size/length scale ratio was below 0.1, probably for the reasons discussed above.

An attempt to quantify the above concepts has been produced by Theofanous and Sullivan (1982). They consider that in a dispersed flow, the shear on the wall and that on the dispersed phase (drops) should both be taken into account. They defined a new friction velocity which depended on the sum of the shear stresses on the wall and on drops. Turbulence intensities were then determined from the assumption that it is equal to the friction velocity. Turbulence intensities calculated in this manner were reasonably close to the measured values. However, the assumptions on which the theory is based require further strengthening.

Further support for the idea that the increase in turbulence intensity is due to newly created drops is seen in Table 4. The increase in turbulence intensity tends to increase with the rate of entrainment. Increasing in the amount of new drops increases the augmentation of turbulence.

The higher order moments of the velocity distributions show features similar to those observed in single phase flow: the computed values of the skewness and kurtosis are in the same range as those discussed above single phase flow.

Conclusions

From the above it can be concluded that:

(1) Measurements of turbulence in single-phase gas flow indicate that the LDA system employed in these tests gave reliable results.

(2) Though mean velocity and Reynolds stress data for annular flow show good correspondence to that for equivalent rough pipes, Turbulence intensities (even when nondimensionalized by the correct friction velocity) were higher than the values that would normally be found in a pipe with a wall roughness equivalent to that of the film interface. Vortex shedding from slow moving drops was suggested as the source of this extra turbulence.

Acknowledgments

The experimental work described in this paper was undertaken as part of the Underlying Research Programme of the UKAEA at their Harwell Laboratory.

References

Abolfadl, M., and Wallis, G. B., 1985, "A Mixing Length Model for Annular Two Phase Flow," *Physico-Chemical Hydrodynamics*, Vol. 6, pp. 49–68.

Adorni, N., Casagrande, I., Cravarolo, L., Hassid, A., and Silvestri, M., 1961, "Experimental Data on Two-Phase Flow: Liquid Film Thickness, Phase and Velocity Distribution, Pressure Drops in Vertical Gas-Liquid Flow," C.I.S.E. report no. R 35.

Antonia, R. A., Atkinson, J. D., and Luxton, R. E., 1973, "Comments on Statistical Characteristics of Reynolds Stress in a Turbulent Boundary Layer," *Physics of Fluids*, Vol. 16, p. 956.

Azzopardi, B. J., and Teixeira, J. C. F., 1994, "Detailed Measurements of Vertical Annular Two-Phase Flow—Part I: Drop Velocities and Sizes," ASME JOURNAL OF FLUIDS ENGINEERING, published in this issue, pp. 792–795.

Bates, C. J., Yeoman, M. L., Roberts, P. J., and Dalzell, W. D., 1981, "Developments of a Laser System for the Simultaneous Measurement of Particle Size and Particle Velocity," UKAEA Report AERE R-10210.

Batchelor, G. K., 1951, "Pressure Fluctuations in Isotropic Turbulence," *Proceedings of the Cambridge Philosophical Society*, Vol. 47, pp. 359–374.

Gill, L. E., Hewitt, G. F., and Lacey, P. M. C., 1964, "Sampling Probe Studies of the Gas Core in Annular Two Phase Flow II," *Chemical Engineering Science*, Vol. 19, pp. 665–682.

Gore, R., and Crowe, C. T., 1989, "Effects of Particle Size on Modulating Turbulence Intensity," *International Journal of Multiphase Flow*, Vol. 15, pp. 279–285.

Hetsroni, G., 1989, "Particles-Turbulence Interaction," *International Journal of Multiphase Flow*, Vol. 15, pp. 735–746.

Hewitt, G. F., and Govan, A. H., 1990, "Phenomena and Predictions in Annular Two-Phase Flow," *Advances in Gas-Liquid Flows*, ASME FED Vol. 99, HTD Vol. 155, pp. 41–55.

Hutchinson, P., Hewitt, G. F., and Dukler, A. E., 1971, "Deposition of Liquid or Solid Dispersion from Turbulent Gas Streams: A Stochastic Model," *Chemical Engineering Science*, Vol. 26, pp. 419–439.

Kada, H., and Hanratty, T. J., 1960, "Effect of Solids on Turbulence in a Fluid," *American Institute of Chemical Engineers Journal*, Vol. 6, pp. 624–630.

Kirillov, P. L., Smogolev, I. P., Suvurov, M. Ya., Shumsky, R. V., and Stein, Yu. Yu., 1978, "Investigation of Steam-Water Flow Characteristics at High Pressures," *Proc. 6th Int. Heat Transfer Conf.*, Toronto, Canada, 7–11 Aug., Vol. 1, pp. 315–320.

Kliafas, Y., Taylor, A. M. K. P., and Whitelaw, J. H., 1987, "Errors in Particle Sizing by LDA Due to Turbidity in the Laser Beams," *Experiments in Fluids*, Vol. 5, pp. 159–176.

Laufer, J., 1954, "The Structure of Turbulence in Fully Developed Pipe Flow," NACA Report 1174.

Lee, S. L., and Durst, F., 1982, "On the Motion of Particles in Turbulent Duct Flows," *International Journal of Multiphase Flow*, Vol. 8, pp. 125–146.

Maeda, M., Hishida, and Furutani, T., 1980, "Optical Measurements of Local Gas and Particle Velocity in an Upward Flowing Gas-Solid Suspension," *Polyphase Flow and Transport Technology*, p. 211, Century 2_ETC, San Francisco, CA.

Nikuradse, J., 1932, "Gesetzmassigkeiten der turbulenten stromung in glatten rohren," VDI-Forschungsheft 356.

Nunner, W., 1956, "Waermeubergang und druckfall in rauhen rohren," VDI-Forschungsheft 455.

Owen, D. G., and Hewitt, G. F., 1987, "An Improved Annular Two-Phase Flow Model," *Proc. 3rd Int. Conf. on Multiphase Flow*, The Hague, The Netherlands, Paper C1.

Subbotin, V. I., Kirillov, P. L., Smogalev, I. P., Suvorov, M. Ya., Stein, Yu. Yu., and Shumsky, R. V., 1975, "Measurement of Some Characteristics of a Steam-Water Flow in a Round Tube at Pressures of 70 and 100 atm," ASME Paper No. 75-WA/HT-21.

Theofanous, T. G., and Sullivan, J., 1982, "Turbulence in Two-Phase Dispersed Flows," *Journal of Fluid Mechanics*, Vol. 116, pp. 343–362.

Tsuji, Y., and Morikawa, Y., 1982, "LDV Measurements of an Air-Solid Two Phase Flow in a Horizontal Pipe," *Journal of Fluid Mechanics*, Vol. 120, pp. 385–409.

Tsuji, Y., Morikawa, Y., and Shiomi, H., 1984, "LDV Measurements of an Air-Solid Two Phase Flow in a Vertical Pipe," *Journal of Fluid Mechanics*, Vol. 139, pp. 417–434.

Wood, D. H., and Antonia, R. A., 1975, "Measurements in a Turbulent Boundary Layer Over d-type Roughness," ASME *Journal of Applied Mechanics*, Vol. 42, pp. 591–597.

Zisselmar, R., and Molerus, O., 1979, "Investigation of Solid-Liquid Pipe Flow with Regard to Turbulence Modification," *Chemical Engineering Journal*, Vol. 18, pp. 233–239.

Kenji Katoh
Associate Professor,
Department of Mechanical Engineering,
Osaka City University,
Sugimoto 3, Sumiyoshiku, Osaka 558,
Japan

Hideomi Fujita
Professor,
Department of Mechanical Engineering,
Nagoya University,
Furocho, Chikusaku, Nagoya 464, Japan

Masato Takaya
Honda R&D Co., Ltd.,
Tochigi R&D Center,
Shimotakanezawa 4630,
Hagacho, Hagagun,
Tochigi Pref. 321-33, Japan

Flow Patterns of Falling Liquid Film Observed Near an Obstacle

The purpose of this study is to investigate the flow patterns of a falling liquid film as observed near an obstacle on a flow channel. In this report, a bend on the channel was chosen as the obstacle and the behavior of a ring-shaped swelling of the liquid film, which appears near the obstacle at a low flow rate, is considered. The Weber number at which the swelling shifts from upstream to downstream of the bend is theoretically estimated. The experimental results for the swelling behavior agree well with those of the above theory. Moreover, in order to investigate the characteristics of the stationary wave observed in the upstream side of the swelling, the wavelength and the damping rate of the amplitude were measured by the needle contact method and agree with theory.

1 Introduction

It is well known that the characteristics of falling liquid film flow are changed by an obstacle on the wall, which produces a remarkable effect on the performance of apparatus dealing with heat or mass transfer. In earlier reports, the authors investigated the effect of the obstacle on the flow characteristics (Fujita et al., 1984; Fujita et al., 1986). The flow patterns near the obstacle changed variously with the flow rate and could be classified into several typical patterns.

When the flow rate is small, the film flow stagnates and a liquid swelling is observed above the obstacle. Just above the swelling, a stationary wave driven by liquid surface tension occurs (Katoh and Fujita, 1990). When the flow rate becomes sufficiently large, the liquid film separates from the wall at the obstacle and forms a free film flow. The authors discussed the condition for which the film flow separates from the wall, which is related to the problem of "dryout" (Katoh et al., 1988). In this report, we study the film flow at low flow rate, for which the flow does not separate from the wall. First, the mechanism for the formation of the liquid swelling is investigated both theoretically and experimentally. Next, the behavior of the stationary wave observed above the swelling is studied.

2 Experimental Method

2.1 Outline of Experimental Apparatus. The experimental apparatus is almost the same as that used by the authors in the preceding reports (Fujita et al., 1984; Fujita et al., 1986). The outline is shown in Fig. 1. The liquid flowing out from

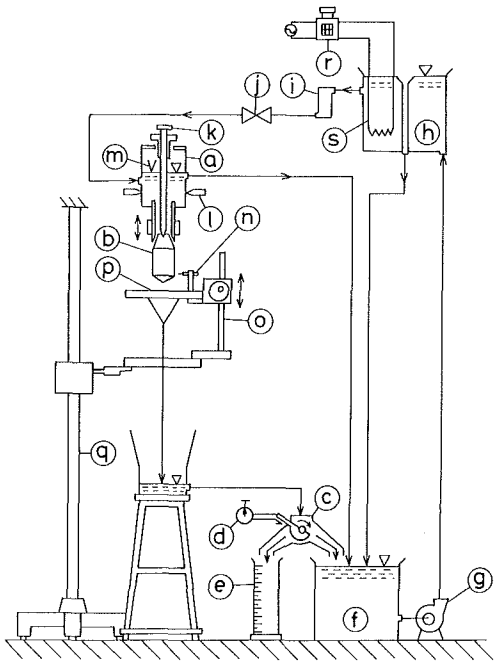

(a) Distributor (b) Test cylinder
(c) Flow direction switching device
(d) Stopwatch (e) Vessel for flow rate measurement
(f) Lower tank (g) Pump (h) Upper tank (i) Filter
(j) Regulating valve (k) Center
(l) Device for adjusting distributor axis
(m) Thermocouple (n) Needle probe (o) Height gauge
(p) Probe fixing table (q) Support (r) Transformer
(s) Heater

Fig. 1 Experimental apparatus

Contributed by the Fluids Engineering Division for publication in the JOURNAL OF FLUIDS ENGINEERING. Manuscript received by the Fluids Engineering Division October 16, 1992; revised manuscript received February 15, 1994. Associate Technical Editor: D. M. Bushnell

Table 1 Properties of the test liquids

Liquid	t °C	ρ kg/m^3	ν X10^{-6}m^2/s	σ N/m
Water	25.0±0.5	993±1	0.893±0.002	0.0730±0.0005
Ethanol(15%)	20.0±0.5	975±1	1.872±0.002	0.0445±0.0005
Ethanol(30%)	20.0±0.5	954±1	2.796±0.002	0.0340±0.0005

the slit-type distributor (a) flows down on the outer wall of the vertical cylinder (b) and a falling liquid film is formed. After the flow rate is measured, the liquid is collected in lower tank (f) and is then pumped up to upper tank (h), from where it flows into the distributor again.

2.2 Test Channel and Liquid. In this experiment, a brass cylinder with a bend was used as a test channel as shown in Fig. 2. Although there may be many kinds of obstacles with various configurations in practical engineering apparatus, the bend with simple geometry was chosen as the obstacle to obtain a basic understanding of the flow physics and behavior near the obstacle.

The liquid film flows out from (a) shown in Fig. 2 and down along the vertical wall. At (b), the film flow is influenced by the bend and various flow patterns appear as the flow rate changes. The bend angles ϕ as shown in Fig. 2 were changed from 45 deg to 90 deg with 15 deg intervals.

To investigate the effect of the liquid properties, 3 kinds of test liquid were used; water and 15 and 30 percent water-ethanol solutions. The properties are shown in Table 1, in which ρ, ν, and σ indicate density, kinematic viscosity, and surface tension, respectively.

2.3 Needle Contact Method. The configuration of the film surface was measured by the needle contact method (Fujita et al., 1984). As shown in Fig. 1, the needle probe (n) was attached to height gage (o) through table (p) in order to measure the film thickness at various positions on the test cylinder (b). In this report, the film thickness at any position was defined as the average of 4 circumferential points of the test cylinder (90 deg interval). The uncertainty of the measured film thicknesses is about 2/100 mm (95 percent coverage). The error is mainly caused by the fact that the film flow is not completely axisymmetric near the bend and the thickness changes circumferentially. Even though the distributor axis is carefully adjusted, it is observed that the flow "leans" slightly at some circumferential locations. This is considered to be an inevitable characteristic of the film flow near the obstacle.

3 Typical Flow Patterns Observed Near the Obstacle.

Using the test channel described in Section 2.2, the flow patterns of the film flow near the obstacle were observed for various flow rates and test liquids. Three typical patterns were observed as shown in Fig. 3. From the experimental results obtained by the authors in earlier studies, almost the same flow patterns as Fig. 3 appeared for other obstacles with different geometry, such as a protuberance and a step (Fujita et al., 1984; Fujita et al., 1986). Therefore, the classification into

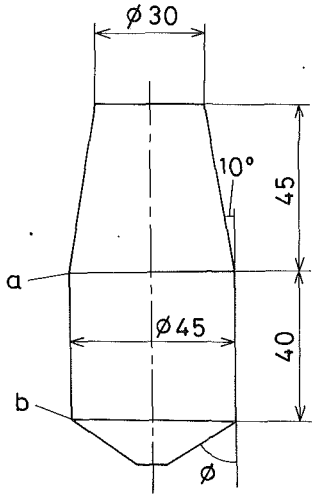

Fig. 2 Test channel

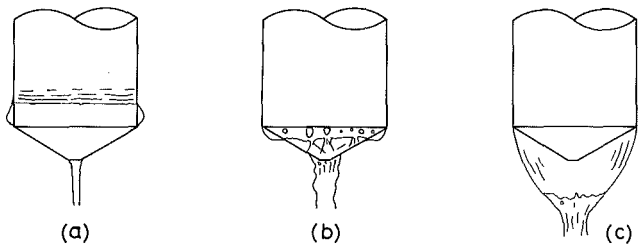

Fig. 3 Typical flow patterns. (*a*) Liquid swelling and stationary wave; (*b*) state in which the swelling in (*a*) shifts from upstream to downstream of bend at larger flow rate than (*a*); (*c*) state in which liquid film separates from bend at larger flow rate than (*b*)

3 patterns, as shown in Fig. 3, may be generally applicable for a wide range of obstacles.

Figure 3(a) shows the flow pattern which appears at a low flow rate. Upstream of the bend, a ring-shaped swelling and a stationary wave driven by surface tension were observed. Increasing the flow rate from the case of Fig. 3(a), the stationary wave disappears and the swelling shifts below the bend as shown in Fig. 3(b). Bubbles were observed to mix into the swelling. As the flow rate increases, the bubbles inside the swelling become larger and eventually merge with one another circumferentially. The flow then separates from the wall at the bend and forms the free film flow shown in Fig. 3(c).

In the above flow patterns, the condition for which the flow pattern changes from Fig. 3(b) to Fig. 3(c) was previously discussed by the authors (Katoh et al., 1988). In the present study, we consider the behavior of the liquid swelling and the stationary wave as shown in Fig. 3(a).

4 Behavior of Liquid Swelling Observed Near Obstacle

It can be considered that the swelling shown in Figs. 3(a)

Nomenclature

$\overline{U}$ = average film velocity
We = Weber number ($=\rho\overline{U}^2\delta/\sigma$)
α = wave number
δ = film thickness
δ_{max} = thickness of liquid swelling
η = damping rate of wave amplitude
g = gravitational acceleration
$h(x)$ = configuration of stationary wave
M = momentum of film flow
Re = Reynolds number ($=\overline{U}\delta/\nu$)
$U(y)$ = velocity distribution of film flow
λ = wave length
ν = kinematic viscosity
ρ = density
σ = surface tension
ϕ = angle of bend
Ψ = stream function
$\overline{\ }$ = *nondimensional quantity*

and 3(b) is formed by flow stagnation due to the resistance of the obstacle. It is important from an engineering viewpoint to understand the behavior of this swelling because the heat or mass transfer coefficient becomes small at the position where the swelling exists. Here, we consider the condition in which the swelling observed above the bend disappears and shifts below as shown in Figs. 3(a) and 3(b).

4.1 Swelling Shape. Figure 4 shows the film surface profile near the bend measured by the needle contact method as stated in Section 2.1. Each plot in the figures indicates the film thickness δ along on the wall. In the figures, We indicates the Weber number and is defined by the following expression;

$$\mathrm{We}=\frac{\rho\overline{U}^2\delta}{\sigma} \tag{1}$$

where $\overline{U}$ indicates the average film velocity. Figure 4 clearly shows that the swelling moves from the upstream side of the bend to the downstream side as the Weber number We increases from We$\approx$0.5 to 1.0. When the swelling is formed upstream of the bend, the film surface is nearly parallel to the wall on the downstream side of the bend.

4.2 Theoretical Consideration of Swelling Formation. Figure 5 indicates the force balance acting on the control surface ABCD near the bend above which swelling exists. As shown in Figs. 4(a) and 4(c), the liquid film flows parallel to the wall at the cross sections AB and CD. M_1 and M_2 in the figure indicate the momentum of the film flow passing through AB and CD, respectively. The resultant surface tension σ acting on B and D has a component in the upward direction because the stream line of the film flow changes its direction at the bend. Because of the resistance of this upward force, the flow stagnates and the swelling appears. When the momentum of

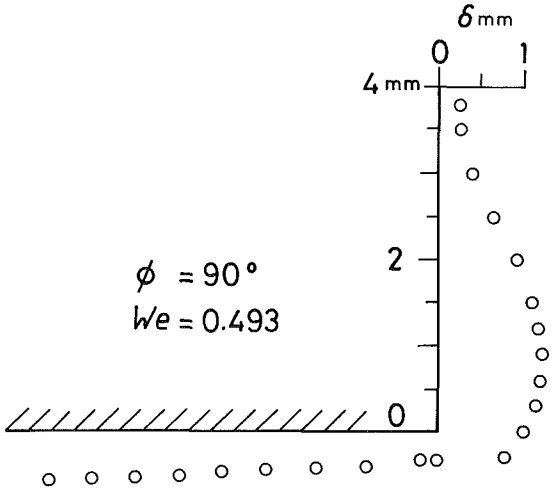

Fig. 4(a) ϕ = 90 deg, We = 0.493

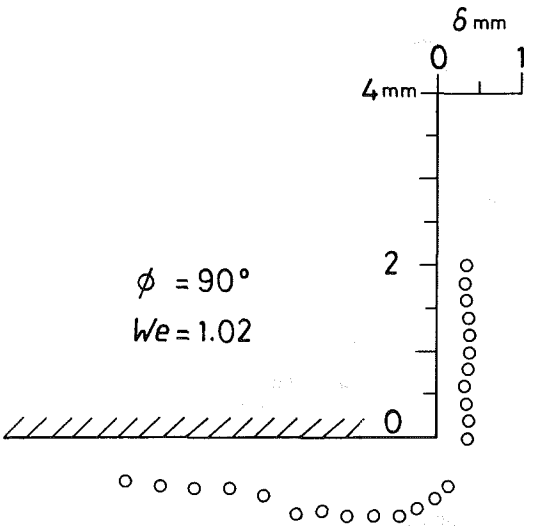

Fig. 4(b) ϕ = 90 deg, We = 1.02

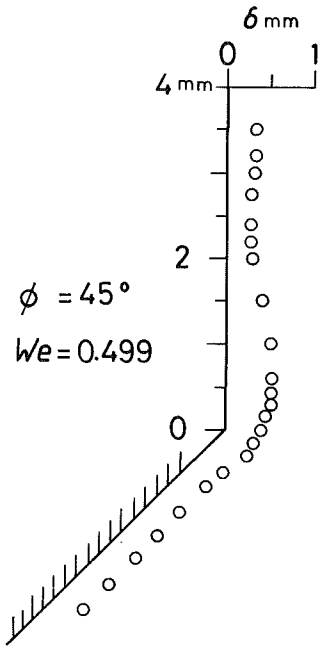

Fig. 4(c) ϕ = 45 deg, We = 0.499

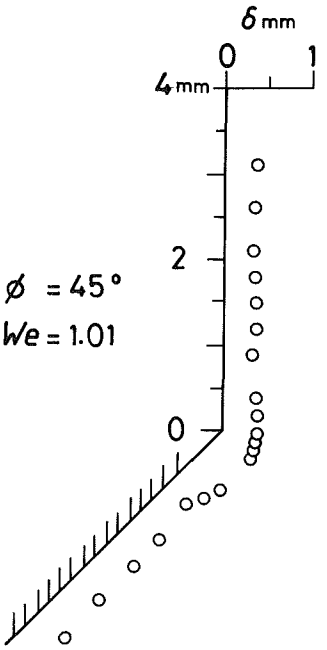

Fig. 4(d) ϕ = 45 deg, We = 1.01

Fig. 4 Swelling shape

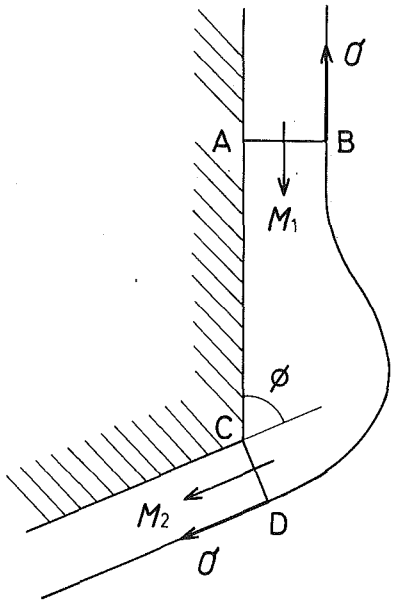

Fig. 5 Force balance on the swelling

the film flow is smaller than the upward resistance at a low flow rate, the swelling is formed and its downward gravitational force is added to satisfy the force balance.

In the light of the above consideration, the swelling appears above the bend if the decrease of downward momentum at the bend ($M_1 - M_2 \cos\phi$) is smaller than the upward resistance of surface tension. Hence the condition that the swelling disappears and shifts below the bend can be written as follows;

$$M_2 \cos\phi - M_1 = \sigma(\cos\phi - 1) \tag{2}$$

The derivation of Eq. (2) did not consider the effects of gravitational and viscous forces acting on the film. This is because the gravitational force is balanced with the viscous force for laminar film flow on a smooth wall as indicated in Nusselt's theory (Nusselt, 1923). The swelling must be caused by other than the gravitational and viscous forces, which balance each other in the equilibrium state. In the above discussion, we considered that the change in the direction of the surface tension and the momentum at the bend is the cause of the swelling.

The horizontal component momentum M_2 downstream of the bend can be obtained by the following expression.

$$M_2 \sin\phi = \sigma \sin\phi \tag{3}$$

By inserting Eq. (3) into Eq. (2), we may write the condition in which the swelling shown in Fig. 5 disappears and shifts below the bend as follows;

$$M_1 = \sigma \tag{4}$$

The momentum of the film flow on the upstream side of the bend M_1 can be calculated using the velocity distribution $U(y)$ as:

$$M_1 = \int_0^\delta \rho U^2 dy \tag{5}$$

where y indicates the distance from the wall. Since the swelling appears for laminar flow at a small flow rate, we can use the velocity distribution of Nusselt's theory as

$$U(y) = \frac{g}{2\nu}(2\delta y - y^2) \tag{6}$$

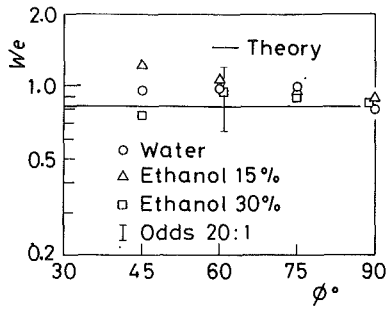

Fig. 6 Weber number at which a shift of the swelling occurs

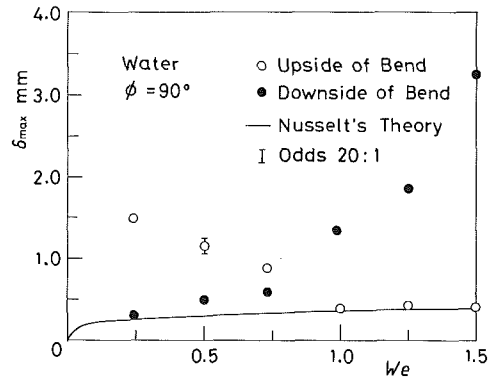

Fig. 7 The swelling film thickness above and below bend

where g is the gravitational acceleration. Substituting Eq. (6) into Eq. (5), M_1 can be obtained as:

$$M_1 = 1.2\rho\overline{U}^2\delta \tag{7}$$

Substituting Eq. (7) into Eq. (4) and arranging the expression by use of the Weber number We, the condition of Eq. (2) can be rewritten as follows:

$$\mathrm{We} = 0.83 \tag{8}$$

It is noted that the swelling shifts below the bend can be determined only by We and they are independent of the bend angle and the liquid properties.

4.3 Experimental Results. To confirm the validity of the above consideration, we measured the Weber number by visual inspection for conditions where the swelling shifts below the bend. The results are shown in Fig. 6. The measured values agree with theory for various bend angles and test liquids. However, the uncertainty of the data measured by gross observations is about ±20 percent and is somewhat large as shown in Fig. 6. We therefore measured the maximum film thickness of swelling δ_{max} above and below the bend by the needle contact method. Figure 7 shows an example of the measurement results, in which the inequality of δ_{max} measured above and below the bend is reversed between We = 0.75 and We = 1.0. After the reversal occurs, the thickness δ_{max} above the bend agrees with that calculated by Nusselt's theory. Hence the liquid surface on the upstream side of the bend is considered to be smooth.

5 Behavior of Stationary Wave Appearing Above Obstacle

When the swelling appears above the obstacle, a stationary

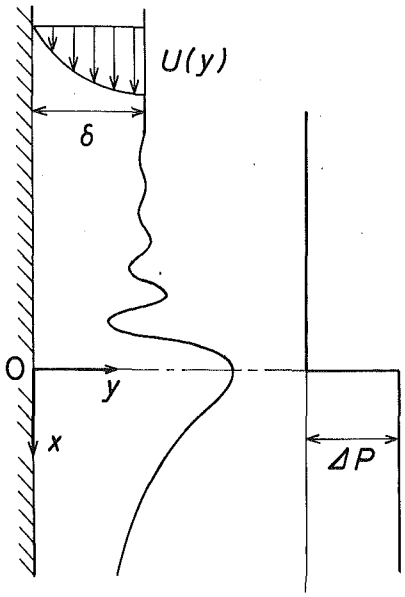

Fig. 8 Flow system of the stationary wave

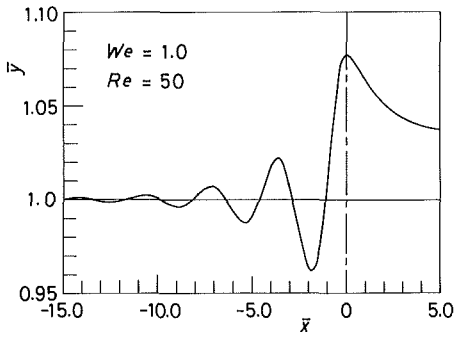

Fig. 9 Calculated configuration for the stationary wave

wave can be observed on the film surface above the swelling as shown in Fig. 8. The origin indicated in Fig. 8 corresponds to the position of the obstacle. This stationary wave is due to the pressure increase inside the film produced by the obstacle and is driven by the liquid surface tension. The wave profile is stationary because the velocity of wave propagation in the upward direction is equal to that of the falling film flow. The authors previously analyzed this phenomena to study the mechanism of wave attenuation by viscosity (Katoh and Fujita, 1990).

5.1 Theoretical Analysis of Stationary Wave Profile. As stated above, the disturbance given by the obstacle, namely, the sudden pressure increase, is the cause of the stationary wave. It can be shown that the magnitude and the distribution of the pressure increase influences only the amplitude and the phase of the wave motion and not the wave characteristics such as wave length or damping rate of wave amplitude (Katoh and Fujita, 1990). Therefore, for simplicity, the effect of the obstacle is replaced by a simple pressure increase, a step function with magnitude ΔP at the obstacle as shown in Fig. 8. The effect of the distribution of the pressure increase on the wave characteristics will be investigated experimentally.

We consider the flow system in which the small disturbance caused by the stationary wave is superimposed on the laminar film flow according to Nusselt's theory. The disturbance is assumed sufficiently small to be treated by the linear approximation. The stream function of the motion caused by the disturbance is expanded in Fourier series and the component for a wave number $\overline{\Psi}_\alpha$ is indicated by the following expression:

$$\overline{\Psi}_\alpha = \overline{\psi}_\alpha(\overline{y}) e^{i\overline{\alpha}\overline{x}}$$

where $\overline{\alpha}$ is the nondimensionalized wave number. Substituting the above equation into the Navier-Stokes equation, the following differential equation can be obtained for $\overline{\psi}_\alpha(\overline{y})$:

$$\overline{\psi}_\alpha'''' - \{2\overline{\alpha}^2 + 1.5i\overline{\alpha}\mathrm{Re}(2\overline{y} - \overline{y}^2)\}\overline{\psi}_\alpha'' + \{-3i\overline{\alpha}\mathrm{Re} + \overline{\alpha}^4 + 1.5i\overline{\alpha}^3\mathrm{Re}(2\overline{y} - \overline{y}^2)\}\overline{\psi}_\alpha = 0 \quad (9)$$

where $'$ indicates differentiation by $\overline{y}$. Moreover, i is the imaginary unit and Re indicates Reynolds number ($\mathrm{Re} = \overline{U}\delta/\nu$). Equation (9) is nondimensionalized by the film thickness δ and the average film velocity $\overline{U}$.

The boundary conditions of Eq. (9) are given as follows:

$$\overline{y} = 0: \quad \overline{\psi}_\alpha = 0 \quad (10)$$

$$\overline{y} = 0: \quad \overline{\psi}_\alpha' = 0 \quad (11)$$

$$\overline{y} = 1: \quad \overline{\psi}_\alpha'' + \overline{\alpha}^2\overline{\psi}_\alpha = 0 \quad (12)$$

$$\overline{y} = 1: \quad \overline{\psi}_\alpha''' - (3\overline{\alpha}^2 + 1.5i\overline{\alpha}\mathrm{Re})\overline{\psi}_a' + \left(\frac{i\overline{\alpha}^3 Re}{1.5\,\mathrm{We}}\right)\overline{\psi}_\alpha = \Delta\overline{P}\cdot\mathrm{Re} \quad (13)$$

The solution $\overline{\psi}_\alpha(\overline{y})$ of Eqs. (9)–(13) was obtained numerically by Adam's method with the aid of the superposition method for boundary problems of linear differential equations (Shinozaki, 1976). The profile of the stationary wave $\overline{h}(\overline{x})$ can be calculated from the kinetic condition at the liquid surface by use of ψ_α as:

$$\overline{h}(\overline{x}) = \int_{-\infty}^{\infty} -\overline{\psi}_\alpha(1) e^{i\overline{\alpha}\overline{x}} d\overline{\alpha} \quad (14)$$

Figure 9 shows an example of the calculated wave profiles. $\overline{y} = 1.0$ of vertical axis in Fig. 9 corresponds to the mean film thickness obtained by Nusselt's theory. The stationary wave with constant wave length appears on the liquid surface in the region upstream of the obstacle of $\overline{x} = 0$. It is shown that the wave amplitude damps gradually by a constant rate due to viscous effects.

5.2 Experimental Results. The wave length λ and damping rate η of the stationary wave were measured for water and for a 30 percent ethanol solution by use of the needle contact method as stated in Section 2. η indicates the damping rate of wave amplitude per wave length and can be defined by

$$\eta = 1 - A_2/A_1$$

where A_1 and A_2 are the amplitudes of the adjacent two waves, respectively. Figures 10 and 11 provide a comparison of measured λ and η with the theory described in Section 5.1. The uncertainty of the measured η values is large. This is due to the small amplitude of the stationary wave (about 0.1 mm).

To investigate the effect of the magnitude and distribution of the pressure increase, the results measured for two kinds of obstacles (i.e., a bend of $\phi = 90$ deg and a 1.5 mm height rib with square cross section) are shown in Figs. 10(a) and 11(a) for water. For a 30 percent ethanol solution, λ and η could not be measured for the bend because of the too small amplitude of the stationary wave, and hence only the results for the rib are shown in Figs. 10(b) and 11(b).

5.2.1 Wave Length. Figure 10 shows both experimental and theoretical results for the wave length λ. As shown in the figure, λ decreases as the Weber number We increases. As stated above, the propagation velocity of the stationary wave is equal to the film velocity. Since the propagation velocity becomes larger with increasing We, the energy of the wave motion also becomes larger. Generally, the smaller the wave length, the larger the wave energy. The above variation of λ

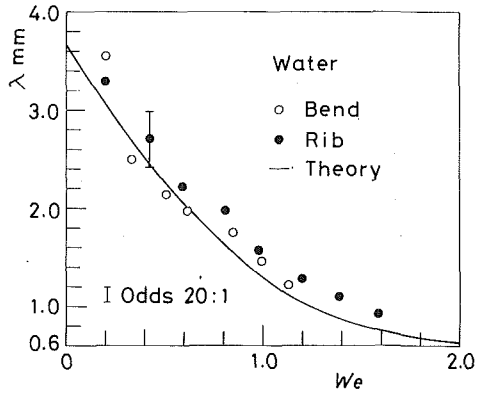

Fig. 10(*a*) Water

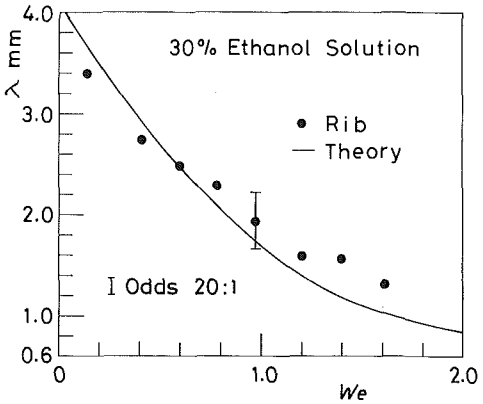

Fig. 10(*b*) 30 percent ethanol solution

Fig. 10 Wave length of the stationary wave

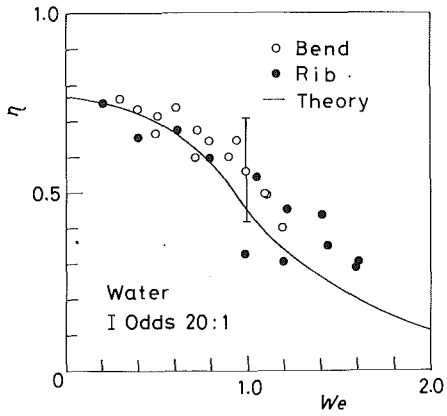

Fig. 11(*a*) Water

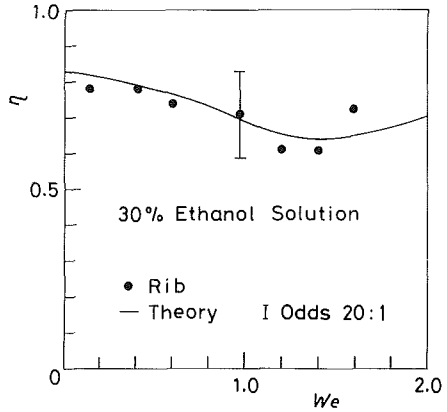

Fig. 11(*b*) 30 percent ethanol solution

Fig. 11 Damping rate of the stationary wave amplitude

with We results from the fact that small waves with large energy appear at high flow rates corresponding to large film velocity.

The theoretical results agree with the experimental ones and describe well the tendency of measured values as shown in Figs. 10(*a*) and (*b*).

5.2.2 Damping Rate of Wave Amplitude. Figure 11 shows both experimental and theoretical results of the damping rate of wave amplitude η for water and 30 percent ethanol solution. For water, η decreases monotonously with We within the range of this experiment. Since the Reynolds number Re increases with We for the system treated in this report, the viscous effect becomes relatively weak compared to the inertia force. As a result, η decreases with increasing We as stated above.

For a 30 percent ethanol solution, however, although η decreases in the region of small We in the same manner as for water, η has a tendency to increase in the region of We larger than a certain value. This result is closely related to the difference in liquid properties between the water and the 30 percent ethanol solution; that is, the viscosity of ethanol solution is much larger than that of water and, conversely, the surface tension of ethanol solution is smaller than that of water (see Table 1). The behavior of η in the region of large We for ethanol solution may be expressed as follows. The viscous force decreases as We and Re increase. At the same time, however, the surface tension, which is the driving force of the wave motion, also clearly decreases as We increases, as seen from the definition of We. Since the relation $We \propto Re^{5/3}$ holds for the laminar film flow under study, the driving force of the wave motion decreases more rapidly than the viscous force. In the case of an ethanol solution with small surface tension and large viscosity, the driving force becomes extremely small at large We, and the viscous effect becomes relatively large. Hence the damping rate η increases in the range of large Weber numbers.

For the water results shown in Figs. 10(*a*) and 11(*a*), λ and η were measured for two kinds of obstacles as stated above. As seen in the figures, the results are very similar. This means that the shape of the obstacle, that is, the magnitude and the distribution of the pressure increase imposed on the film flow, does not affect the characteristics of the stationary wave as would be expected from our preceding report (Katoh and Fujita, 1990).

Moreover, Fig. 11 shows that the measured and theoretical damping rate η agree, as did the wave lengths. These results verify the theory earlier proposed by Katoh and Fujita (1990).

6 Conclusions

To clarify the effect of an obstacle on falling liquid film flow, a bend was chosen as a representative obstacle due to its simple geometry. The behavior of the liquid swelling and the stationary wave appearing above the obstacle at a low flow rate was investigated both experimentally and theoretically. The principal results are summarized as follows.

(1) The force balance on the swelling was utilized to derive the condition wherein the swelling shifts from the upside to the downside of the bend. This condition is dependent only on Weber number We and is independent of the liquid properties and the bend angle. The Weber number at which the shift of the swelling occurs can be obtained as $We = 0.83$ by use of Nusselt's velocity distribution.

(2) The behavior of the swelling was investigated by observation and measurements of the swelling thickness. The results showed the validity of the theory as stated in (1).

(3) The profile of the stationary wave appearing above the swelling was measured by the needle contact method. The

measured wave length and damping rate agreed with the theory presented earlier by Katoh and Fujita (1990).

(4) The wave length of the stationary wave λ tended to decrease monotonically as We increases for both water and a 30 percent ethanol solution. On the other hand, the damping rate η decreases monotonically with We for water, whereas for an ethanol solution η increases in the region of We larger than a certain value. This result indicated that the behavior of the damping rate is closely related to the ratio of the viscosity to the surface tension, which is the driving force of the wave motion.

Acknowledgment

The authors thank Mr. Shiraki of Nagoya University for his assistance in manufacture of the experimental apparatus.

References

Fujita, H., Takahama, H., and Katoh, K., 1984, "Falling Water Films over a Ring Attached to a Vertical Cylinder (Flow Configuration and Film Thickness)," *Bulletin of Japanese Society of Mechanical Engineers*, Vol. 27, pp. 2126–2133.

Fujita, H., Katoh, K., and Takahama, H., 1986, "Falling Water Films on a Vertical Cylinder with a Downward Step," *International Journal of Engineering Science*, Vol. 24, pp. 1405–1418.

Katoh, K., Fujita, H., and Osakabe, T., 1988, "Behavior of Falling Liquid Films on a Vertical Cylinder with a Salient Edge," *Proceedings of 25th National Heat Transfer Symposium of Japan* (in Japanese), Vol. 2, pp. 178–180.

Katoh, K., and Fujita, H., 1990, "Viscous Damping of Stationary Wave Formed near an Obstacle in a Channel," ASME JOURNAL OF FLUIDS ENGINEERING, Vol. 112, pp. 185–191.

Nusselt, W., 1923, "Wärmeaustäusch am Berieselungskühler," *VDI-Zeitschrift*, Vol. 67, pp. 206–210.

Shinozaki, T., (edited by Shinozaki, T., and Matsushita, Y.), 1976, *Introduction of Numerical Calculation to Engineers* (in Japanese), Corona-Corp., Vol. 2, pp. 117–127.

Spin-Up From Rest of a Two-Layer Liquid in a Cylinder

Kwan Yeop Kim

Jae Min Hyun

Department of Mechanical Engineering,
Korea Advanced Institute of
Science and Technology,
373-1 Kusong-dong Yusungku,
Taejon, 305-701, Korea

A numerical and analytical study is made of spin-up from rest of a two-layer liquid in a rapidly rotating cylinder. The overall system Ekman number is small. The density of the top layer is smaller than that of the bottom layer ($\rho_1/\rho_2<1.0$), but the ratio of the individual layer kinematic viscosities is arbitrary ($\nu_1/\nu_2<1.0$ or $\nu_1/\nu_2>1.0$). The highlights of the analytical model, which is based on amended formulations of the Wedemeyer-Gerber-Homicz flow configurations, are briefly recapitulated. Comprehensive numerical solutions are secured to the time-dependent Navier–Stokes equations. The numerical solutions are validated by comparing the maximum interface displacements with the available experimental data as well as the analytical model predictions. Descriptions are made of the prominent characteristics of the interface shape for the two regimes of $\nu_1/\nu_2<1.0$ and $\nu_1/\nu_2>1.0$. Details of the azimuthal and meridional flow structures are illustrated by exploiting the numerical solutions. The computed meridional flows are compatible with the basic assumptions embedded in the development of the analytical model. Sequential plots of the radial profiles of azimuthal velocities are presented. These show that the global spin-up process is substantially accomplished over ($E_n^{-1/2}\Omega^{-1}$), where E_n denotes the value of the smaller Ekman number of the two layers. The numerical study gives credence to the reliability and accuracy of the simplified analytical model.

1 Introduction

The transient motion of a viscous fluid, in response to an abrupt change in the rotation rate of the container, is given a general term "spin-up." The basic flow configuration of a homogeneous fluid, completely filled in a vertically-mounted axisymmetric cylinder, was treated in a classical treatise by Greenspan and Howard (1963). They dealt with the situations when the container rotation rate was altered by a small amount from $\Omega_i=\Omega-\Delta\Omega$ to $\Omega_f=\Omega$, $\Delta\Omega/\Omega_f\ll 1$, therefore, linearized methods were applicable. For most practical systems, the overall Ekman number is small, $E\{=\nu/\Omega H^2\}\ll 1$, in which ν is the fluid kinematic viscosity and H the characteristic dimension of the container. It was clearly demonstrated that the essential dynamic ingredients were the Ekman suction mechanism and the concomitant radially-inward meridional circulations in the interior core. Consequently, the major phase of transient motions is substantially accomplished over the spin-up time scale $O(E^{-1/2}\Omega^{-1})$. This physical picture has since been validated by several numerical and experimental investigations (see, e.g., Warn-Varnas et al., 1978). The essential elements of spin-up dynamics were succinctly outlined in a review paper by Benton and Clark (1974).

The spin-up from an initial state of rest, i.e., $\Omega_i=0$, $\Omega_f=\Omega$, constitutes a nonlinear problem. Wedemeyer (1964), building upon the ideas of Howard and Greenspan, put forward an elegant flow model, which captured the principal characteristics of the transient process. The role of the Ekman pumping remains to be qualitatively the same as for the linearized spin-up. With several physically plausible assumptions, Wedemeyer's model produces a simplified formulation for the axisymmetric interior core region. The qualitative correctness of this model has been verified by numerical as well as experimental results (see, e.g., Weidman, 1976; Kitchens, 1980; Hyun et al., 1983).

The above-referenced studies on spin-up, relating to the Wedemeyer model, were concerned with the situations in which a homogeneous fluid completely filled the enclosed cylinder. A natural extension of the model is the transient flow configuration of a two-layer liquid system in a closed cylinder. Specifically, it is proposed here to explore the spin-up from rest of two layers of immiscible liquids. For gravitational stability, the density of the upper layer is lower than that of the lower layer. It is important to note that the kinematic viscosities of the two liquids may assume arbitrary values. It is emphasized here again that, for the flow configuration of present concern, the upper lid of the cylindrical container is a fully closed rigid wall.

The transient dynamics of this problem are of relevance to technological applications, such as centrifugal separation of biological and chemical substances (Berman et al., 1978). As to the spin-up of a two-layer liquid, a generalized linear mathematical formulation was developed by Pedlosky (1967), but it was limited to very small Froude numbers. For larger variations in Froude numbers, the deformation of interface was examined, both analytically and experimentally, by Berman et al. (1978). However, their interest was restricted to small de-

Contributed by the Fluids Engineering Division for publication in the JOURNAL OF FLUIDS ENGINEERING. Manuscript received by the Fluids Engineering Division June 24, 1993; revised manuscript received April 25, 1994. Associate Technical Editor O. C. Jones.

viations from the state of a pre-existing rigid-body rotation. A theoretical analysis was made by Baker and Israeli (1981) for the spin-up from rest of a two-layer liquid. However, this model was directed strictly to the cases when the interface deformation from the horizontal plane was negligibly small.

Recently, Lim et al. (1993) produced experimental measurements of the transient interface shape during spin-up from rest of a two-layer liquid. Parallel efforts were expended in Lim et al. to amend the original Wedemeyer model to describe the spin-up from rest of a two-layer liquid system. These were closely in line with the earlier endeavors of Goller and Ranov (1968) and Homicz and Gerber (1987), who constructed a modified Wedemeyer model to tackle the spin-up of a liquid with a free surface. Of particular interest is the case when the kinematic viscosity of the upper layer (ν_1) is larger than that of the lower layer (ν_2). The upper layer reaches the final rigid-body rotation faster than the lower layer. Therefore, at intermediate times, the pressure in the upper layer, due to the centrifugal forces, is lower in the central axis and higher in the peripheral region. Consequently, the originally-horizontal interface rises in the central region at early stages of spin-up. As the lower layer also attains the rigid-body rotation of the final state, the interface sinks down in the center in the later stages of spin-up. In the final state, the interface assumes the parabola shape, the lowest point being at the center, which is characteristic of a perfectly rigid-body rotation. These time-dependent features were also revealed in the linearized analyses by Berman et al. (1978).

With a view to toward complementing the preceding analytical and experimental efforts, this paper presents the full-dress numerical solutions to the governing equations. The numerical approaches will produce a wealth of data to disclose the details of both azimuthal and meridional flows. The numerical results will be illuminated for two cases, which are prototypical of the two qualitatively different flow regimes, i.e., $\nu_1/\nu_2 > 1.0$ and $\nu_1/\nu_2 < 1.0$. The time evolutions of the interface, azimuthal and meridional flow structures are displayed. These results provide descriptions of the major dynamical elements that are involved in the transient process. Another aim here is to validate the predictions of the modified Wedemeyer-type analytical model by cross-checking its predictions against the present numerical computational results. These exercises will place into proper perspective the capabilities of the analytical undertakings, which are essentially based on the classical Wedemeyer model.

2 Mathematical Formulation

Consider a vertically mounted right closed circular cylinder of radius R and height H. At the initial state, two homogeneous, immiscible liquids of depth $(H-h_0)$ and h_0 fill completely the cylinder at rest, and the interface shape is horizontal

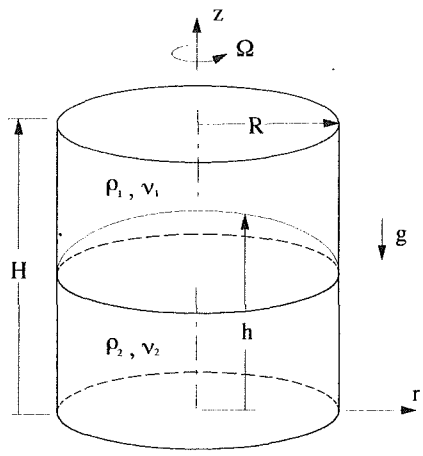

Fig. 1 Schema of flow configuration

at $z = h_0$. For a gravitationally stable setup, the density of the lower (upper) layer is $\rho_2(\rho_1)$, and $\rho_2 > \rho_1$. The subscripts 1 and 2 denote, respectively, the conditions in the upper and lower layers. However, the kinematic viscosities of the two layers (ν_1 and ν_2) may assume arbitrary values. These physical properties are taken to be constant. At the initial instant $t = 0$, the cylinder is abruptly set to rotate, about its vertical longitudinal z-axis, at rotation rate Ω. The task is to describe the ensuing time-dependent axisymmetric liquid motions inside the spinning cylinder. A schema of the flow configuration is shown in Fig. 1.

The fluid motions are governed by the full, time-dependent axisymmetric Navier–Stokes equations. These equations, written in cylindrical coordinates (r,θ,z) with corresponding velocity components (u,v,w), are

$$\frac{\partial(\rho u)}{\partial t}+\frac{1}{r}\frac{\partial}{\partial r}(\rho r u^2)+\frac{\partial}{\partial z}(\rho w u)-\rho\frac{v^2}{r} = -\frac{\partial p}{\partial r}+\frac{1}{r}\frac{\partial}{\partial r}\left(2\mu r\frac{\partial u}{\partial z}\right)+\frac{\partial}{\partial z}\left[\mu\left(\frac{\partial u}{\partial z}+\frac{\partial w}{\partial r}\right)\right]-\frac{2\mu u}{r} \quad (1a)$$

$$\frac{\partial(\rho w)}{\partial t}+\frac{1}{r}\frac{\partial}{\partial r}(\rho r u w)+\frac{\partial}{\partial z}(\rho w^2) = -\frac{\partial p}{\partial z}+\frac{1}{r}\frac{\partial}{\partial r}\left(\mu r\frac{\partial w}{\partial r}\right)+\frac{1}{r}\frac{\partial}{\partial r}\left(\mu r\frac{\partial u}{\partial z}\right)+\frac{\partial}{\partial z}\left(2\mu\frac{\partial w}{\partial z}\right)-\rho g \quad (1b)$$

$$\frac{\partial(\rho v)}{\partial t}+\frac{1}{r}\frac{\partial}{\partial r}(\rho r u v)+\frac{\partial}{\partial z}(\rho w v)+\rho\frac{uv}{r} = \frac{1}{r}\frac{\partial}{\partial r}\left(\mu r\frac{\partial v}{\partial r}\right)+\frac{\partial}{\partial z}\left(\mu r\frac{\partial v}{\partial z}\right)-\frac{v}{r^2}\frac{\partial}{\partial r}(r\mu) \quad (1c)$$

Nomenclature

Ar = aspect ratio of the container
E = the Ekman number $(\nu/\Omega R^2)$
E_n = smaller Ekman number of the two layers
F_j = the Froude number $(\Omega^2 R^2/g_j H)$
H = dimensional height of the container
h = dimensional height of the interface
h_c = dimensional height of the interface at the center
h_0 = initial interface level
g_j = reduced gravity
R = dimensional radius of the container
r_d = radial position where the interface has a local minimum level
p = pressure
t = time
t_1 = instant when the interface at the center reaches the lowest level
(u,v,w) = velocity components corresponding to (r,θ,z) coordinates
(r,θ,z) = (radial, azimuthal, vertical) coordinates in the cylindrical system
ν = kinematic viscosity of fluid
μ = viscosity of fluid
ρ = density of fluid
Ω = rotation rate of the container, rad/s
ψ = meridional stream function

Subscript

1 = index for the upper fluid
2 = index for the lower fluid

$$\frac{1}{r}\frac{\partial}{\partial r}(ru)+\frac{\partial w}{\partial z}=0 \tag{2}$$

In the above, p denotes the pressure, μ the coefficient of viscosity.

The governing equations are supplemented by the associated initial and boundary conditions. At the initial state of rest, the conditions are:

$$\text{at } t<0, \quad u=v=w=0 \tag{3a}$$

$$\rho=\rho_1,\ \mu=\mu_1 \quad h_0<z\le H \tag{3b}$$

$$\rho=\rho_2,\ \mu=\mu_2 \quad 0\le z<h_0 \tag{3c}$$

The boundary conditions can be stated as

$$u=w=0,\ v=R\Omega \qquad \text{at } r=R; \tag{4a}$$

$$u=0,\ \frac{\partial(v/r)}{\partial r}=\frac{\partial w}{\partial r}=0 \quad \text{at } r=r_i; \tag{4b}$$

$$u=w=0,\ v=r\Omega \qquad \text{at } z=0 \text{ and } z=H. \tag{4c}$$

In Eq. (4*b*), the boundary condition at the axis is applied at r_i, a small but non-zero value. This is necessary to avoid the singularity at the axis, and these steps have been customarily invoked (see e.g., Warn-Vanas et al., 1978). In passing, in the present formulation, the azimuthal flow are shown as observed by an external observer on an inertial coordinate system. This choice has been selected such that the initial field is motionless and the final state is a rigid-body rotation in the entire interior of the cylinder (e.g., Wedemeyer, 1964, Warn-Varnas et al., 1978).

The above system of equations is subject to numerical integration. After having undergone extensive tests, a version of finite-difference numerical method was selected. An explicit scheme of first-order accuracy was chosen for the time derivatives, and second-order differencings were applied to the spatial derivative terms. For the convective terms, the power-law scheme of Patankar (1980) was adopted. In order to capture the deforming profile of the interface between the two liquids, the VOF method, as documented by Hirt et al. (1981), was utilized. The Poisson equation for pressure was solved by making use of the projection method, which was proposed by Chorin (1968). This has the advantage in dealing with the boundary conditions for the two-layer system. For most calculations, the mesh points were (50×100) in the $(r\text{-}z)$ plane. Grid stretchings were implemented to cluster more grid points near the solid boundaries as well as near the interface region. Grid- and time increment-convergence tests were conducted for several exemplary computations, and the present mesh network and time interval were shown to produce adequate results. All the computations were executed on a CRAY-2S supercomputer. For typical runs, approximately one hour of CPU time was needed for one case of computation.

3 Results and Discussion

A total of twelve computational runs were performed. In line with the fundamental notions of the present study, the Froude numbers are $O(1)$ and the Ekman numbers are very small. Accordingly, the effects of surface tension and fluid property variations were not included. The cylinder dimensions were $R=4.5$cm, $H=20.42$cm, thus $H/R=4.54$. These were designed to facilitate direct comparisons with the experiments of Lim et al. (1993). In the ensuing discussions, the results of the following two exemplary runs, representing the two regimes of $\nu_1/\nu_2<1.0$ and $\nu_1/\nu_2>1.0$, will be scrutinized.

Set 1: $\rho_1/\rho_2=0.7465$, $\nu_1/\nu_2=0.1$, $E_1=1.33\times10^{-3}$, $E_2=1.33\times10^{-2}$, $h_0/H=0.5$;

Set 2: $\rho_1/\rho_2=0.7465$, $\nu_1/\nu_2=10.0$, $E_1=1.33\times10^{-2}$, $E_2=1.33\times10^{-3}$, $h_0/H=0.5$,

in which $E_1=\nu_1/\Omega R^2$, $E_2=\nu_2/\Omega R^2$.

In order to check the sensitivity of the results to grid and time interval, comparison exercises were made by using two grids (30×60) and (80×150) in addition to the present (50×100) grid. The time increment was $(\Delta t=0.002)$. The convergence criterion was that the relative changes of variables were smaller than 1.0×10^{-4}. These tests showed that the variations in computed results were less than 1.0 percent.

Before proceeding further, it is advantageous to recapitulate the highlights of the analytical developments. As remarked earlier, the fundamental Wedemeyer model for a completely-filled homogeneous fluid in a cylinder has occupied the centerstage for the study of spin-up from rest. Lim et al. (1993) extended this basic model to the spin-up flows of a two-layer liquid system. For flows of small Ekman numbers, the transient flow field is divided into an essentially inviscid interior core and the boundary layers on the solid boundary walls. In each layer of liquid, a simplified form of momentum equation is adopted:

$$\frac{\partial v_j}{\partial t}+u_j\left(\frac{\partial v_j}{\partial r}+\frac{v_j}{r}\right)=E_j\Omega R^2\left[\frac{\partial^2 v_j}{\partial r^2}+\frac{\partial}{\partial r}\left(\frac{v_j}{r}\right)\right] \tag{5}$$

where $j=1, 2$ to indicate the upper and lower layer, respectively.

A key element in the model developments is the postulation of a functional relationship linking the radial (u) and azimuthal (v) velocity components. Lim et al. took note of the methodologies of Homicz and Gerber (1987), which dealt with the spin-up from rest of a liquid with a free surface. The crux of these heuristic arguments, enriched with physical insights, is that the radial velocities in the interior core are made up of the contributions from the Ekman layers and from the deformation of the free surface. This is an admittedly crude approximation; however, as stressed by Goller and Ranov (1968) as well as by Homicz and Gerber (1987), this is a necessary task in order to construct a workable model. It has been amply demonstrated that the predictions based on these analytical models capture the gross features of spin-up flows of a liquid with a free surface (see, e.g., Choi et al., 1989, 1991). In an analogous manner, Lim et al. (1993) postulated that, for spin-up flows of a two-layer liquid, the radial velocities in the interior core are driven by the Ekman layer pumpings at the endwall disks and by the deformation of the interface. Combining these considerations, a functional relationship linking u and v is derived. With this step in place, Eq. (5) can now be numerically integrated to yield $v_j(r,t)$ in each layer. The transient shape of the interface $h(r,t)$ may be determined by considering a force balance (Goller and Ranov, 1968).

$$\frac{\partial h}{\partial r}=\frac{1}{R\Omega^2}\left[F_2\frac{v_2^2}{r}-F\frac{v_1^2}{r}\right], \tag{6}$$

in which the Froude number $F_j=(\Omega R)^2/g_jH$, $g_j\equiv g(\rho_2-\rho_1)/\rho_j$, $j=1,2$ for the upper and lower layer, respectively. Upon integration, Eq.(6) reduces to

$$h(r,t)=h_c+\frac{1}{R\Omega^2}\left[F_1\int_r^R\frac{v_1^2}{\zeta}\,d\zeta-F_2\int_r^R\frac{v_2^2}{\zeta}\,d\zeta\right], \tag{7}$$

$$h_c=H-\frac{1}{R^3\Omega^2}\left[F_1\int_0^R v_1^2\,rdr+F_2\int_0^R v_2^2 rdr\right],$$

The calculation procedures are straightforward. Once $v_j(r,t)$ are determined, the meridional flow field in each layer can be computed, and the transient interface shape $h(r,t)$ may be described by Eq. (7).

In the first, verifications of the present numerical solutions are conducted by checking the numerical data against the meas-

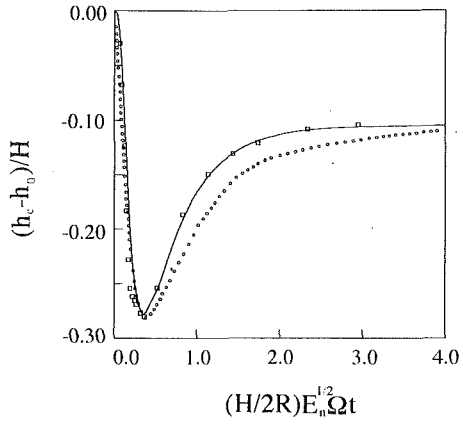

Fig. 2(*a*)

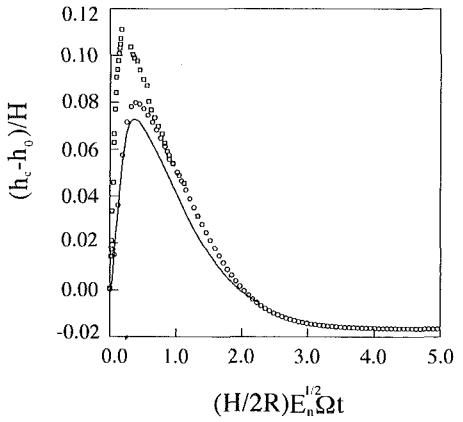

Fig. 2(*b*)

Fig. 2 Time history of the interface displacement at the axis, h_c. The present numerical results are shown, by ——, the analytical model predictions by ○, and the laboratory measurements by □. E_n denotes the smaller Ekman number of the two layers. Maximum experimental uncertainty in the interface height is ±0.025. Conditions are (*a*) R = 4.5cm, H = 20.42cm, ν_1/ν_2 = 0.1, ρ_1/ρ_2 = 0.7465, $E_1 = 1.33 \times 10^{-3}$, $E_2 = 1.33 \times 10^{-2}$, h_0/H = 0.5; (*b*) R = 6.0cm, H = 22.40cm, ν_1/ν_2 = 30.0, ρ_1/ρ_2 = 0.872, $E_1 = 1.31 \times 10^{-3}$, $E_2 = 4.35 \times 10^{-5}$, h_0/H = 0.5.

urements as well as the analytical model predictions. For this purpose, the data for the interface displacement at the central axis h_c are selected for specific comparisons. In the experiment, the interface change is the largest at the axis, and, therefore, it is relatively easy to monitor h_c. In addition, the displacement of interface at the central axis is least distorted by the lens effect caused by the cylindrical shape of the container.

Figure 2 illustrates the outcome of such comparisons. Figure 2(*a*) typifies the behavior of transient interface deformation at the axis, h_c, when the viscosity of the top layer is smaller than that of the bottom layer, $\nu_1/\nu_2 < 1$. At small times, the bottom layer gains angular velocity faster than the top layer. Therefore, the pressure in the bottom layer in the central region is smaller than in the periphery. Consequently, the interface at the center dips to a low level. In the intermediate stage, the interface contour reaches the lowest level. However, as spin-up of both layers progresses, the top layer also reaches the solid-body rotation at large times. The interface deformation at the center gradually approaches the steady-state value. In the final stage, both layers are in rigid-body rotation at rotation rate Ω; at this state, the profile of the interface takes the well-known equilibrium parabolic shape:

$$\frac{h_{\text{rigid}}}{H} = \frac{h_0}{H} + \frac{\Omega^2 R^2}{4gH}\left[2\left(\frac{r}{R}\right)^2 - 1\right] \tag{8}$$

Figure 2(*a*) clearly depicts this characteristic behavior of the evolution of h_c. The three sets of data are shown to be mutually consistent. In particular, the experimental data and the present numerical solutions are in good agreement.

In the opposite case of $\nu_1/\nu_2 > 1$, Fig. 2(*b*) also demonstrates fair agreement among the three sets of data. In this case, at small times, the top layer gains angular momentum faster than the bottom layer. This implies that the pressure at the center in the top layer is smaller than near the periphery. The interface bulges upward in the central region in the early phase. In the intermediate stage, the bottom layer also gains angular velocity, and the upward displacement of the central portion of the interface is retarded. Therefore, the upward bulging of the interface at the center h_c reaches the highest point. After this instant, h_c begins to recede. In the latter part of the process, both layers tend to rigid-body rotation, and the interface shape approaches the pertinent paraboloid, Eq. (8). The evolution of h_c, as displayed in Fig. 2(*b*), is captured equally well by the experiment, analytical prediction and the numerical solutions. The comparisons in Fig. 2 are representative of several other verification exercises for the present numerical solutions. These cross-checks clearly establish the accuracy and reliability of the present numerical simulation model. The results of numerical computations will now be used to disclose the significant details of flow, which have hitherto not been available by other means of investigation.

The transient shape of the interface profile is depicted in Figs. 3 and 4. Fig. 3 is typical of the time-dependent interface contour for $\nu_1/\nu_2 < 1.0$. As emphasized previously, the bottom layer spins up faster than the top layer. As a consequence, at small times, the interface sags downward in the central area and rises upward in the periphery. The interface deformation in the early phase is exhibited in Fig. 3(*a*). For the parameter set of Fig. 3, the downward displacement of interface at the center reaches the lowest level at approximately $\Omega t_1 \cong 22.0$. In the time period $0 < t < t_1$, the difference in angular velocities between the bottom and top layer is large. This situation can easily be seen in Eq. (6) as well. The faster spin-up of the bottom layer than the top layer makes $(v_2 - v_1)$ large, and the slope of the interface becomes steep. The interface profiles of Fig. 3(*a*) are illustrative of these situations. After this time instant, as the top layer gains more angular velocities as a result of spin-up, the difference in angular velocities between the two layers diminishes. Referring to Eq. (6), as the difference $(v_2 - v_1)$ is reduced, the slope of interface also decreases. Consequently, as shown in Fig. 3(*b*), the interface shape evolves slowly to the steady-state parabola of Eq. (8). The global adjustment of the interface takes place over the time span, which is scaled with $E_n^{-1/2}\Omega^{-1}$, where E_n denotes the smaller value of the two Ekman numbers for the two layers.

The evolution of interface profiles for $\nu_1/\nu_2 > 1.0$ needs careful examination. As remarked earlier, at small times, the top layer is spun up faster than the bottom layer. Therefore, the interface rises (sinks) at the center (periphery). This early-time behavior is consistent with the numerical results shown in Fig. 4(*a*). For the parameter set of Fig. 4, the interface deformation of this type continues to approximately $\Omega t_1 \cong 18.0$. Again, this time period corresponds to the situations when $(v_1 - v_2)$ is large. After t_1, as the bottom layer is also spun-up, the interface slope becomes less steep as $(v_1 - v_2)$ decreases in magnitude. The interface profile approaches slowly the final-state parabola of Eq. (8). The overall time of adjustment is characterized by $E_n^{-1/2}\Omega^{-1}$, and the numerical results of Fig. 4 are in accord with this observation.

A closer inspection of the slopes of the interface, $\partial h/\partial r$, shown in Figs. 3 and 4, is revealing. For the profiles in Fig. 3, $\partial h/\partial r > 0$ in the whole flow field throughout the entire spin-up process. This is characteristic of the situation when $\nu_1/\nu_2 < 1.0$. However, for the profiles in Fig. 4, the interface profiles for $\nu_1/\nu_2 > 1.0$ in the intermediate stages contain a mini-

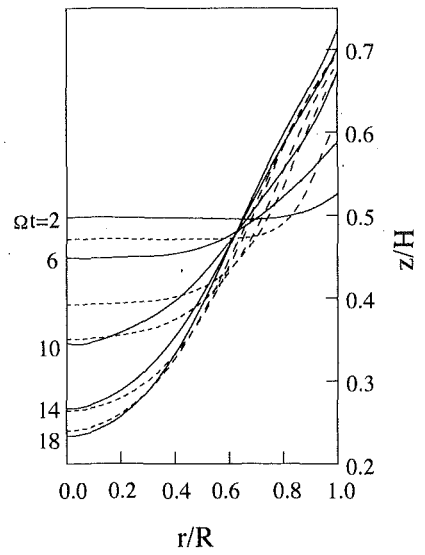

Fig. 3(*a*)

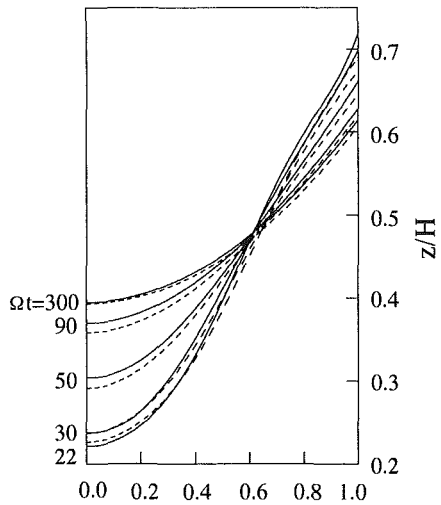

Fig. 3(*b*)

Fig. 3 Sequential plots of the interface profile for Set 1. Solid lines indicate the present numerical results, and dotted lines the analytical model predictions.

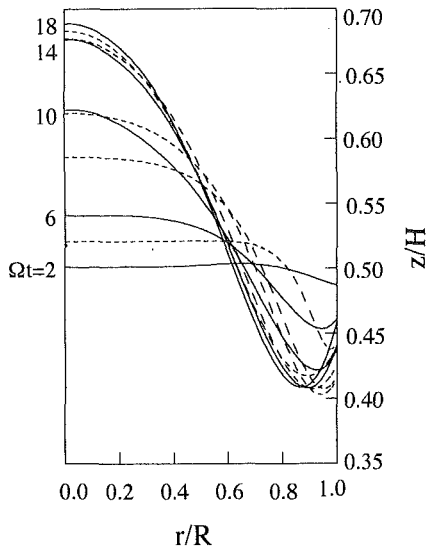

Fig. 4(*a*)

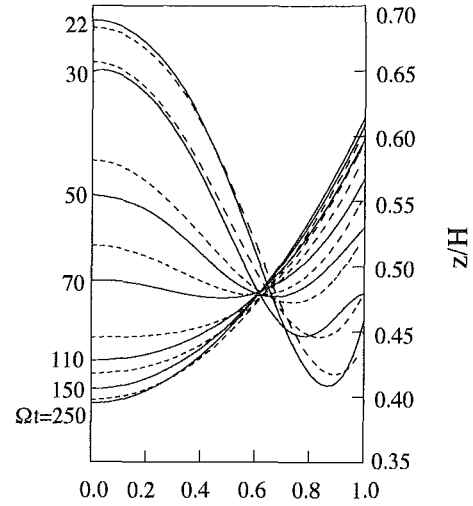

Fig. 4(*b*)

Fig. 4 Same as a in Fig. 3, except for Set 2.

mum point at a radial location close to the sidewall, say $r_d/R \cong 0.85$. In the vicinity of this point r_d, the interface contour reaches a local minimum. At radii larger than r_d, the interface rises sharply until it hits the sidewall. This radial profile near the sidewall is characteristic of the flow patterns for $\nu_1/\nu_2 > 1.0$. As described previously, in the intermediate stages, say $10.0 < \Omega t < 25.0$ for the parameter set of Fig. 4, the fluids close to the sidewall have already been sufficiently spun-up in both layers. Therefore, at large radii very close to the sidewall, $v_1 \cong v_2 \cong r\Omega$, and, consequently, $\partial h/\partial r > 0$ in this region [Eq. (6)]. However, at small and moderate radii, the difference in angular velocity between the two layers, $v_1 - v_2$, is still appreciable. The slope of the interface in these areas is, accordingly, $\partial h/\partial r < 0$ [see Eq. (6)]. The radially-descending interface profile at moderate radii and the rapidly-ascending interface profile very close to the sidewall are joined at this point r_d. As time elapses, the degree of spin-up in the two layers becomes equalized and, consequently, $v_1 - v_2$, becomes small. Therefore, the location of the point r_d in the interface profile moves radially inward. Also, the magnitudes of the slopes in the vicinity of the point r_d are reduced. At large times, as both layers are substantially spun up, the profile tends to the steady-state parabola of Eq. (8), and the point r_d is located on the central axis. These characterizations of the transient interface profile are consistent with the basic physical reasoning advanced earlier by Berman et al. (1978). It is also noteworthy that the qualitative aspects of the interface evolutions are portrayed well by both the present numerical solutions and the predictions of the analytical model of Lim et al.

Figures 5 and 6 exemplify the sequential plots of the ψ-field, where the streamfunction for meridional flow, ψ, is defined such that $u = r^{-1}\,\partial\psi/\partial z$ and $w = -r^{-1}\partial\psi/\partial r$. It is noted that the details of transient meridional flows have not been presented by laboratory observations. The magnitudes of meridional flows are very small, and thus the experimental measurements of u and w are difficult. Figure 5 is representative of the cases $\nu_1/\nu_2 < 1.0$. Notice that, at very small times, the meridional flows are concentrated near the top and bottom endwall disks and around the interface [see Fig. 5(*a*)]. At very small times, the no-slip and impermeability conditions imposed on the top and bottom endwall disks lead to formation of the Ekman layers. The Ekman flux produced near each endwall disk is closed by Stewartson layer at the sidewalls. This picture is qualitatively consistent with the well-documented spin-up

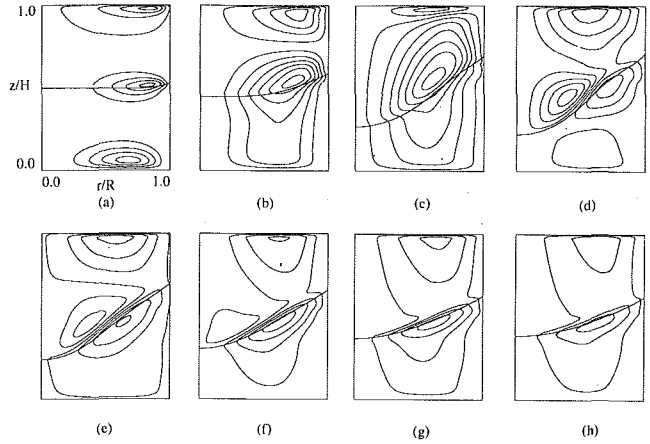

Fig. 5 Plots describing the meridional flow field for Set 1. Values of ψ are normalized by $E_1^{1/2}\,\Omega R^3$. (*a*) $\Omega t = 2.0, \psi_{min} = -0.415, \psi_{max} = 0.499, \Delta\psi = 0.115$; (*b*) $\Omega t = 6.0, \psi_{min} = -0.567, \psi_{max} = 0.950, \Delta\psi = 0.151$; (*c*) $\Omega t = 14.0, \psi_{min} = -0.221, \psi_{max} = 0.659, \Delta\psi = 0.070$; (*d*) $\Omega t = 22.0, \psi_{min} = -0.162, \Delta\psi = 0.041$; (*e*) $\Omega t = 30.0, \psi_{min} = -0.111, \psi_{max} = 0.078, \Delta\psi = 0.031$; (*f*) $\Omega t = 50.0, \psi_{min} = -0.079, \psi_{max} = 0.010, \Delta\psi = 0.018$; (*g*) $\Omega t = 90.0, \psi_{min} = -0.021, \psi_{max} = 0.000, \Delta\psi = 0.005$; (*h*) $\Omega t = 120.0, \psi_{min} = -0.008, \psi_{max} = 0.000, \Delta\psi = 0.003$.

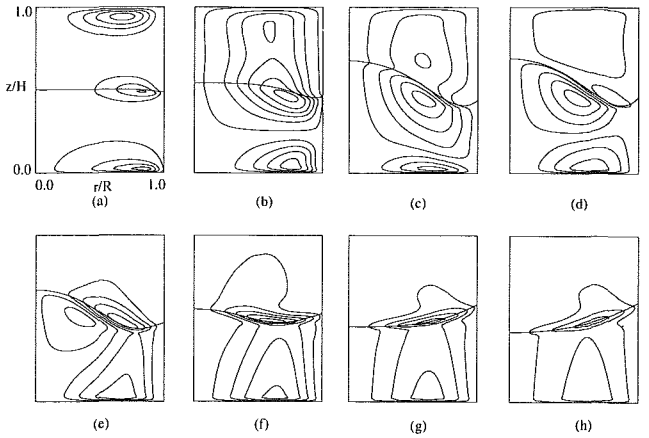

Fig. 6 Plots describing the meridional flow field for Set 2. Values of ψ are normalized by $E_2^{1/2}\Omega R^3$. (*a*) $\Omega t = 2.0, \psi_{min} = -0.499, \psi_{max} = 0.415, \Delta\psi = 0.114$; (*b*) $\Omega t = 6.0, \psi_{min} = -0.726, \psi_{max} = 0.568, \Delta\psi = 0.130$; (*c*) $\Omega t = 14.0, \psi_{min} = -0.443, \psi_{max} = 0.297, \Delta\psi = 0.092$; (*d*) $\Omega t = 18.0, \psi_{min} = -0.269, \psi_{max} = 0.242, \Delta\psi = 0.073$; (*e*) $\Omega t = 26.0, \psi_{min} = -0.083, \psi_{max} = 0.238, \Delta\psi = 0.053$; (*f*) $\Omega t = 50.0, \psi_{min} = -0.002, \psi_{max} = 0.125, \Delta\psi = 0.025$; (*g*) $\Omega t = 90.0, \psi_{min} = 0.000, \psi_{max} = 0.042, \Delta\psi = 0.010$; (*h*) $\Omega t = 120.0\ \psi_{min} = 0.000, \psi_{max} = 0.020, \Delta\psi = 0.007$.

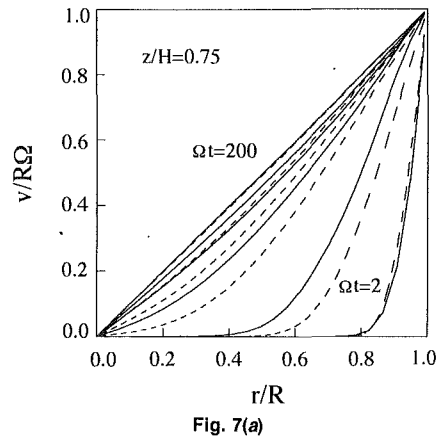

Fig. 7(*a*)

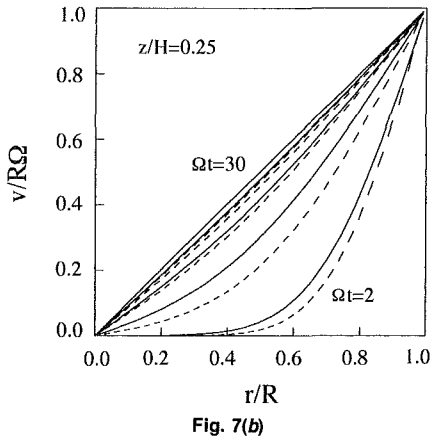

Fig. 7(*b*)

Fig. 7 Radial profiles of the angular velocity for Set 1. Frame (*a*) portrays $v/R\Omega$ in the upper layer ($z/H = 0.75$) and Frame (*b*) in the lower layer ($z/H = 0.25$). The numerical results are shown by ——, and the analytical predictions by ·····. Times for the curves are (*a*) $\Omega t = 2.0, 10.0, 30.0, 50.0, 70.0, 200.0$; and (*b*) $\Omega t = 2.0, 6.0, 14.0, 22.0, 30.0$.

from rest of a single fluid. Some analytical endeavors were made to delineate the flow structure in these boundary layers as well as in the corner regions (e.g., Wedemeyer, 1974; Benton and Clark, 1974), which show rather complex features. Certainly, the validity of model requires that the system Ekman number should be small. However, if Ω is extremely large, flow instabilities and non-axisymmetry are expected to take place, which would render the present model inapplicable. In the present paper, the objective is to portray the gross characteristics of global axisymmetric flow features. Examination of detailed flow structures of time-dependent evolution of boundary layers is beyond the scope of the present paper; those efforts will be dealt with in a subsequent paper. At small times, the meridional flows in the bottom layer weaken since the fluid in this region has already been appreciably spun-up. However, due to large differences in azimuthal velocities across the interface, the meridional flows in the top layer, driven by the interface, intensify [see Fig. 5(*c*)]. Furthermore, the deformation of interface is notable, and these two effects give rise to vigorous meridional flows. In the intermediate stages, as the top layer also gains considerable angular velocities, the meridional flows in the top layer also subside. At large times, the meridional flows are vanishingly small, as both layers reach solid-body rotation. Notice the difference in the scales of ψ used in the plots of Fig. 5. The overall pictures of both the azimuthal and meridional flows are in line with the global flow structure described earlier.

Figure 6 illuminates the transient flow structures for the case of $\nu_1/\nu_2 > 1.0$. The initiation of the meridional flows at very early times near the two endwall disks and around the interface is discernible. The meridional flows grow to large values in the bottom layer at small times [see Fig. 6(*b*)]. The deformation of the interface and the associated meridional flow field are clearly demonstrated in Fig. 6.

The present numerical results are corroborative of the basic assumptions incorporated in the amended Wedemeyer-Gerber-Homicz analytical model. In particular, the results are in support of the postulation that the u-velocity fields in the interior are contributed mostly by the radial flows driven in the Ekman layers and by the deformation of interface.

In an effort to appraise the capability of the modified analytical model, quantitative assessments of the time-dependent azimuthal flows are made. Figure 7 shows the radial distributions of v-field for the case of Set 1 [$\nu_1/\nu_2 < 1.0$]. Clearly, in the top (bottom) layer, spin-up is substantially accomplished over the time span $\Omega t \cong 200.0$ ($\Omega t \cong 30.0$). These are consistent with the basic notion that the major phases of the flow adjustment are attained over the spin-up time scales in the respective layer, i.e., $(2R/H)E_j^{1/2}\,\Omega t \sim O(1)$. The above time spans

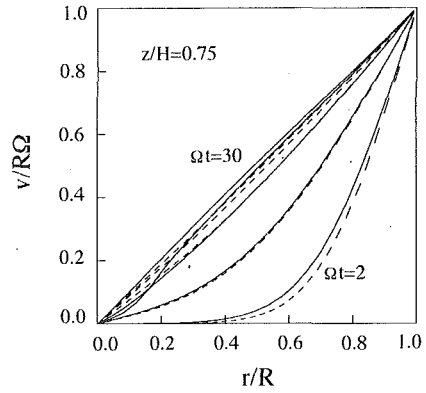

Fig. 8(*a*)

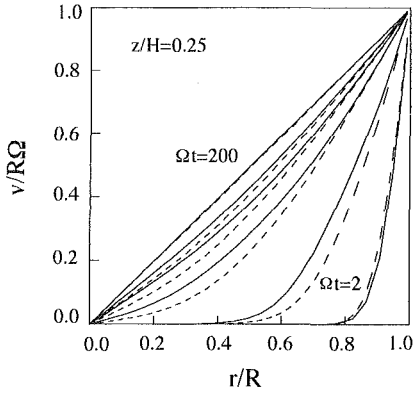

Fig. 8(*b*)

Fig. 8 Same as in Fig. 7, expect for Set 2. Times for the curves are (*a*) Ωt = 2.0, 6.0, 14.0, 22.0, 30.0; (*b*) Ωt = 2.0, 10.0, 30.0, 50.0, 70.0, 200.0.

may indeed be re-expressed as $(2R/H)E_1^{1/2}\ \Omega t \cong 3.215$ $[(2R/H)E_2^{1/2}\ \Omega t \cong 1.525]$, which are in conformity with the above observations. In a similar manner, the results for Set 2 $[\nu_1/\nu_2 > 1.0]$ are displayed in Fig. 8. These direct comparisons of Figs. 7 and 8 establish that the predictions of the analytical model are compatible with the present numerical results.

4 Conclusion

The present numerical model is shown to generate accurate and stable solutions for the transient flow fields. The numerical computational results are in accord with the available experimental data for the interface deflection at the center. Reliable numerical results are obtained for both cases of $\nu_1/\nu_2 < 1.0$ and $\nu_1/\nu_2 > 1.0$.

Details of the time-dependent structures of azimuthal and meridional flows are secured. The radially-inward propagating velocity shear fronts are discernible in both layers. The transient meridional flow fields are supportive of the basic contentions of the modified analytical model. The meridional flows are concentrated to the Ekman layers on the endwall disks as well as to the vicinity of the interface. The global features of the two-layer spin-up flows are substantially accomplished over the spin-up time scale $O(E_n^{-1/2}\Omega^{-1})$, where E_n denotes the smaller value of the Ekman numbers for the two layers.

The time-evolving radial profiles of the azimuthal velocity fields are exhibited. For both situations of $\nu_1/\nu_2 < 1.0$ and $\nu_1/\nu_2 > 1.0$, the modified Wedemeyer analytical model is seen to yield the results which are largely compatible with the numerical results. These verification exercises establish that the Gerber-Homicz-Wedemeyer model can indeed be amended successfully to tackle the salient flow characteristics of the spin-up from rest of a two-layer liquid system.

Acknowledgments

Appreciation is extended to the referees who provided constructive and informative comments. The suggestions of the referees led to improvements in the revised manuscript. This was supported in part by research grants from the Korea Science and Engineering Foundation and the Advanced Fluids Engineering Research center at Pohang, Korea.

References

Baker, G. R., and Israeli, M., 1981, "Spin-up from Rest of limmiscible Fluids," *Studies in Applied Mathematics*, Vol. 65, pp. 249–268.

Benton, E. R., and Clark, A. Jr., 1974, "Spin-Up," *Annual Review in Fluid Mechanics*, Vol. 6, pp. 259–280.

Berman, A. S., Bradford, J., and Lundgren, T. S., 1978, "Two-Fluid Spin-Up in a Centrifuge," *Journal of Fluid Mechanics*, Vol. 84, Part 3, pp. 411–431.

Choi, S, Kim, J. W., Hyun, J. M., 1989, "Experimental Investigation of the Flow with a Free Surface in an Impulsively Rotating Cylinder," ASME JOURNAL OF FLUIDS ENGINEERING, Vol. 111, pp. 439–442.

Choi, S., Kim, J. W., Hyun, J. M., "Transient Free Surface Shape in an Abruptly Rotating, Partially Filled Cylinder," ASME JOURNAL OF FLUIDS ENGINEERING, Vol. 113, 1991, pp. 245–249.

Chorin, A., 1968, "Numerical Solution of the Navier-Stokes Equations," *Mathematics of Computation*, Vol. 22, pp. 745–762.

Goller, H., and Ranov, T., 1968, "Unsteady Rotating Flow in a Cylinder with a Free Surface," ASME *Journal of Basic Engineering*, Vol. 90, No. 4, pp. 445–454.

Greenspan, H. P., and Howard, L. N., 1963, "On a Time Dependent Motion of a Rotating Fluid," *Journal of Fluid Mechanics*, Vol. 17, Part 3, pp. 385–404.

Hirt, C. W., and Nichols, B. D., 1981, "Volume of Fluid (VOF) Method for the Dynamics of Free Boundaries," *Journal of Computational Physics*, Vol. 39, pp. 201–225.

Homicz, H., and Gerber, N., 1987, "Numerical Model for Fluid Spin-Up from Rest in a Partially Filled Cylinder," ASME JOURNAL OF FLUIDS ENGINEERING, Vol. 109, pp. 195–197.

Hyun, J. M., Leslie, F., Fowlis, W. W., and Warn-Varnas, A., 1983, "Numerical Solutions for Spin-Up from Rest in a Cylinder," *Journal of Fluid Mechanics*, Vol. 127, pp. 263–281.

Kitchens, C. W. Jr., 1980, "Navier-Stokes Solutions for Spin-Up in a Filled Cylinder," *AIAA Journal*, Vol. 18, No. 8, pp. 929–934.

Lim, T. G., Choi, S. M., and Hyun, J. M., 1993, "Transient Interface Shape of a Two-Layer Liquid in an Abruptly Rotating Cylinder," ASME JOURNAL OF FLUIDS ENGINEERING, Vol. 115, pp. 324–329.

Patankar, S. V., *Numerical Heat Transfer and Fluid Flow*, 1980, McGraw-Hill, New York.

Pedlosky, J., 1967, "The Spin Up of a Stratified Fluid," *Journal of Fluid Mechanics*, Vol. 28, pp. 463–479.

Warn-Varnas, A., Fowlis, W. W., Piacsek, S., and Lee, S. M., 1978, "Numerical Solutions and Laser-Doppler Measurements of Spin-Up," *Journal of Fluid Mechanics*, Vol. 85, pp. 609–639.

Wedemeyer, E. H., 1964, "The Unsteady Flow within a Spinning Cylinder," *Journal of Fluid Mechanics*, Vol. 20, Part 3, pp. 383–399.

Weidman, P. D., 1976, "On the Spin-Up and Spin-Down of a Rotating Fluid. Part 1: Extending the Wedemeyer Model. Part II: Measurements and Stability," *Journal of Fluid Mechanics*, Vol. 77, Part 4, pp. 685–735.

Computational Study of Disk Driven Rotating Flow in a Cylindrical Enclosure

E. Lang

K. Sridhar

N. W. Wilson

Department of Mechanical Engineering,
University of Windsor,
Windsor, Ontario, Canada N9B 3P4

The problem of steady laminar flow in a stationary cylinder driven by a rotating disk at the top was studied numerically. Three governing equations in cylindrical coordinates were solved by the spatially second-order and temporally first-order accurate ADI method. The flow was characterized by three bulk quantities, namely the torque coefficient and the primary and secondary volumetric flow rates. Calculation of the torque coefficient presented a difficulty because the velocity gradient is singular where the rotating disk and the stationary cylinder meet. This problem was overcome by specifying a gap between the disk and cylinder in the boundary conditions. The results obtained compared favourably with previous experimental results. The relevant parameters for the problem were the rotational Reynolds number, the aspect ratio and the gap. The ranges investigated were as follows: Reynolds number from 1 to 10^5; aspect ratio from 0.02 to 3; and gap size from 0.1 to 10 percent of the cylinder radius. The results showed that the bulk quantities were dependent on the Reynolds number and the aspect ratio. The torque coefficient was also dependent on the gap, while the volumetric flow rates were only weakly dependent on the gap. For high aspect ratios, the bulk quantities approached constant values.

Introduction

Rotating fluid flow is important in many areas of engineering. The main features of confined rotating flow are a primary flow in the direction of rotation and a secondary flow perpendicular to the first (see Fig. 1). In this case, the torque required to rotate the disk and the volumetric flow rates are particularly important.

Analytical calculations of the torque were done by von Kármán (see Schlichting, 1968), Schultz-Grunow (1935), and Schmieden (1928). Theodorsen and Regier (1944) give a review of this type of work. Daily and Nece (1960) used analytical and experimental methods to find the torque for low aspect ratios.

Computational solutions of the torque present a unique problem: the velocity gradient is singular where the rotating disk meets the stationary sidewall, and this prevents calculation of the torque. Lugt and Abboud (1987) gave an asymptotic form for this singularity and pointed out that the torque results obtained by computational methods by Pao (1972) and Bertelà and Gori (1982) are questionable.

This work addressed the torque problem by specifying a gap between the rotating disk and the sidewall in the boundary conditions. The full laminar Navier–Stokes equations were solved using ADI (alternating-direction implicit) solvers. The three parameters which govern the flow and their ranges are as follows: Re, the Reynolds number (1 to 10^5), δ, the aspect ratio (0.02 to 3.00), and b, the gap (0.001 to 0.10). From the results, the torque coefficient, C_m, and the primary and secondary volumetric flow rates, Q_p and Q_s, were obtained, and the effects of varying the parameters were determined. Only laminar calculations were attempted because of time and resource constraints.

Governing Equations

The geometry of the flow and coordinate system used are shown in Fig. 1. The governing equations of Lugt and Abboud (1987) were used. The flow is assumed axisymmetric ($\partial/\partial\theta = 0$) and, therefore, can be described by three equations in cylindrical coordinates (r,θ,z): the equations for the stream function, ψ, and the vorticity, ζ, define the secondary flow and a Navier–Stokes equation defines the primary flow, v (see Fig. 1). For this type of flow, Lugt and Haussing (1973) showed that a fluid particle will spiral around the cylinder.

In nondimensional form, the governing equations are

$$\frac{\partial\psi}{\partial t}=\delta^2\frac{\partial^2\psi}{\partial r^2}-\frac{\delta^2}{r}\frac{\partial\psi}{\partial r}+\frac{\partial^2\psi}{\partial z^2}-r\zeta, \tag{1}$$

$$\frac{\partial\zeta}{\partial t}+\frac{\partial(u\zeta)}{\partial r}+\frac{\partial(w\zeta)}{\partial z}-2\frac{v}{r}\frac{\partial v}{\partial z}=\frac{1}{\mathrm{Re}}\left[\frac{\partial^2\zeta}{\partial r^2}+\frac{1}{r}\frac{\partial\zeta}{\partial r}-\frac{1}{r^2}\zeta+\frac{1}{\delta^2}\frac{\partial^2\zeta}{\partial z^2}\right], \tag{2}$$

Contributed by the Fluids Engineering Division for publication in the JOURNAL OF FLUIDS ENGINEERING. Manuscript received by the Fluids Engineering Division November 12, 1992; revised manuscript received February 24, 1994. Associate Technical Editor: O. Baysal.

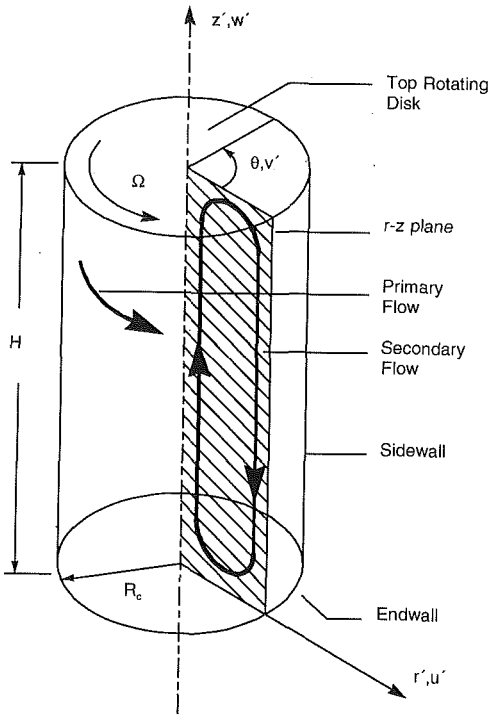

Fig. 1 Geometry and coordinate system

$$\frac{\partial v}{\partial t}+\frac{\partial(uv)}{\partial r}+\frac{\partial(wv)}{\partial z}+2\frac{uv}{\partial r}$$
$$=\frac{1}{\mathrm{Re}}\left[\frac{\partial^2 v}{\partial r^2}+\frac{1}{r}\frac{\partial v}{\partial r}-\frac{1}{r^2}v+\frac{1}{\delta^2}\frac{\partial^2 v}{\partial z^2}\right]. \quad (3)$$

These have been nondimensionalized using

$$t'=\Omega t', \quad r=\frac{r'}{R_c} \quad z=\frac{z'}{H},$$
$$u=\frac{u'}{\Omega R_c}, \quad v=\frac{v'}{\Omega R_c}, \quad w=\frac{w'}{\Omega R_c},$$
$$\psi=\frac{\psi'}{\Omega R_c^2 H}, \quad \zeta=\frac{H}{\Omega R_c}\zeta',$$

where the superscript prime denotes dimensional variables. Note that v is discontinuous at $r = 1$ and $z = 1$.

The boundary conditions are as follows:

$$\text{for } 0\le r\le 1 \text{ and } z=0, \quad u=v=w=\psi=0; \quad (4a)$$
$$\text{for } r=1 \text{ and } 0\le z\le 1, \quad u=v=w=\psi=0; \quad (4b)$$
$$\text{for } 0\le r<1 \text{ and } z=1, \quad u=w=\psi=0,\ v=r; \quad (4c)$$
$$\text{for } r=0 \text{ and } 0<z<1, \quad u=v=\psi=\zeta=0,\ \partial w/\partial r=0. \quad (4d)$$

For some cases, grid points were clustered near the boundaries by transforming the (r,z) physical domain into the (ξ,η) computational domain by using a stretching function given by Anderson et al. (1984). For ξ, the transformation is

$$\xi=\alpha_r+(1-\alpha_r)\frac{\ln\left[\dfrac{\gamma_r+(2\alpha_r+1)r-2\alpha_r}{\gamma_r-(2\alpha_r+1)r+2\alpha_r)}\right]}{\ln\left[\dfrac{\gamma_r+1}{\gamma_r-1}\right]}. \quad (5)$$

The parameters α_r and γ_r control the location and degree of grid refinement, respectively. If $\alpha_r = 0$, the grid is refined near $r = 1$ only; if $\alpha_r = 0.5$, it is refined near $r = 0$ and $r = 1$. The grid becomes uniform as $\gamma_r \to \infty$, while $\gamma_r = 1$ is a singular point which packs all the grid points onto the boundaries. For η, an equivalent transformation was used.

Numerical Procedure

The governing equations were solved using an ADI method (see Roache, 1982). The second-order spatial differencing is central, and the first-order temporal differencing is time linearized. Programs were in FORTRAN using double precision on an IBM 4381 computer. The finite-difference equations and programs can be found in Lang (1992).

The vorticity at a no-slip boundary was evaluated using a first-order form. For example, on the endwall

$$\zeta_{i,1}^n=\frac{2(\psi_{i,2}^n-\psi_{i,1}^n)}{r_i\Delta z^2}+O(\Delta z). \quad (6)$$

The subscripts denote the grid points in the r- and z-directions and the superscript, the iteration step. Roache (1982) indicates that for stability this is the safest form to use. Lugt and Haussling (1973) compared results from a first-order with a second-order form and reported no difference.

The convergence criterion used was that for all i, j and $\psi_{ij}^n \neq 0$

$$\max\left|\frac{\psi_{ij}^n-\psi_{ij}^{n-1}}{\psi_{ij}^n}\right|\le 10^{-5}.$$

To determine program accuracy, a grid refinement test was done using the uniform grids 121×121, 101×101, 81×81, 41×41,and 21×21 with Re = 500 and 1000. Comparisons were made of ψ, ζ and v at $r = z = 0.50$ and $r = z = 0.10$, and of ζ at $r = 0.50$ and $z = 1.00$. These data were normalized using the values at the 121×121 grid. For the 101×101 to 21×21 grids, the maximum deviations at Re = 500 were 1.01, 1.01, 1.08, and 0.74, while at Re = 1000, they were 1.02, 1.06, 1.36, and 2.77. The worst case, 2.77, was for ζ at $r = z = 0.10$. To ensure that there were grid points both on the edge of the disk and within the gap, a much smaller grid spacing was used in most cases. Grids as high as 201×101 were used. It was, therefore, concluded that the results from the grid refinement test proved the accuracy of the solution method.

In addition, comparisons were made with the flow visual-

Nomenclature

b = gap = $(R_c-R_d)/R_c$
C_m = torque coefficient
H = height of cylinder
Q_p = primary volumetric flow rate
Q_s = secondary volumetric flow rate
(r,θ,z) = cylindrical coordinates
$(r_{v.c.},z_{v.c.})$ = position of the vortex center
R_c = radius of cylinder
R_d = radius of disk
Re = rotational Reynolds number = $\Omega R_c^2/\nu$
t = time
u = velocity in r-direction = $1/r\partial\psi/\partial z$
v = velocity in θ-direction
w = velocity in z-direction = $-1/r\partial\psi/\partial r$
α,γ = stretching parameters
δ = aspect ratio = H/R_c
Δ = difference in variable
ζ = vorticity = $\partial u/\partial z - \delta^2\partial w/\partial r$
ν = kinematic viscosity
(ξ,η) = transformed (r,z) coordinates
ρ = density
ψ = stream function
Ω = angular velocity of rotating disk

ization study of Escudier (1984) and the computational studies of Lugt and Abboud (1987) and Lopez (1990). The present work compared favorably with these. Details, including contour plots of ψ, can be found in Lang (1992). Finally, during program development, it was found that the solution converged to the same results from different initial conditions.

Bulk Characteristics

The flow was characterized by three bulk quantities: the primary volumetric flow rate, Q_p, is the amount of fluid flow around the axis of symmetry; the secondary volumetric flow rate, Q_s, is the amount of fluid flow in the rz-plane; the torque coefficient, C_m, is the torque required to rotate the disk. These are given by

$$Q_p = \delta \int_0^1 \int_0^1 v dr dz, \tag{7}$$

$$Q_s = 2\pi\delta r_{\text{v.c.}} \int_0^{z_{\text{v.c.}}} u dz, \tag{8}$$

$$C_m = \frac{8\pi}{\delta \text{Re}} \int_0^{R_d} \left.\frac{\partial v}{\partial z}\right|_{z=1} r^2 dr. \tag{9}$$

These were nondimensionalized using

$$Q_p = \frac{Q_p'}{\Omega R_c^3}, \quad Q_s = \frac{Q_s'}{\Omega R_c^3}, \quad C_m = \frac{2\int_0^{R_d} dM'}{\frac{1}{2}\rho\Omega^2 R_c^5},$$

where Q_p' and Q_s' are the dimensional equivalents of Eqs. (7) and (8), and dM' is an element of moment. The factor 2 in the numerator is used because C_m is usually defined for a disk submerged in a fluid; therefore, both sides provide drag.

Discussion of Results

Validation of the Torque Method. When C_m is calculated using Eq. (9), a problem arises because the discontinuity of v at $r = 1$ and $z = 1$ makes $\partial v/\partial z$ singular there. Since the singularity is at a corner point and there are no mixed derivatives in the equations of motion, the finite-difference equations are not affected; therefore, previous computational studies which did not calculate the torque could ignore the problem. Clearly, a method is required to deal with the singularity. Pao (1972) assumed a constant boundary layer on the disk near the tip. Specifically, he assumed that on the disk, the term $(1/r)\partial v/\partial z$ was constant across the last grid spacing. He then calculated C_m for Re 1 to 400 using a 41×41 uniform grid with $\delta = 1$.

In this study, Pao's method was used to calculate the torque coefficient with $\delta = 1$ and Re = 1, 10, 100, 500 and 1000 using the uniform grids 21×21, 41×41 and 81×81. For the 41×41 grid, the results were the same as Pao's. Across the grids, however, there was a maximum deviation of about 50 percent, which showed no sign of converging as the grid was refined; therefore, Pao's method is grid dependent. The reason is that as the grid is refined, the second last grid point gets closer to the wall causing the velocity gradient to increase.

The singularity results from assuming that there is no gap between the rotating disk and the sidewall, but physically there must be a gap. For this work, the gap was included as part of the boundary conditions by dividing the top of the computational domain into two parts: the section occupied by the rotating disk had the boundary conditions of Eq. (4*c*), while for the gap, two possibilities were considered. The first was to assume that the flow in the gap approximates cylindrical Couette flow (Schlichting, 1979); therefore,

$$v_c = v(r) = \frac{(1-b)^2}{1-(1-b^2)^2}\left[\frac{1}{r} - r\right]. \tag{10}$$

The second was to assume symmetry which would be true if the rotating disk was suspended midway in the cylinder. The boundary conditions, are, respectively,

$$\text{for } 1-b<r<1 \text{ and } z=1, \quad u=w=\psi=0,\ v=v_c, \tag{11a}$$

$$\text{for } 1-b<r<1 \text{ and } z=1, \quad w=\psi=\zeta=\partial u/\partial z=\partial v/\partial z=0 \tag{11b}$$

For simplicity, it was assumed that the thickness of the disk was zero.

Using the same set of parameter as were used with Pao's method, boundary conditions (11) were used to calculate C_m. For Eqs. (11*a*) and (11*b*), the maximum deviations across the grids were about 5 and 10 percent, respectively. The one exception at Re = 1000 with a 21×21 grid was about 15 percent; this was because the results were less accurate there. In contrast to Pao's method, the results converged as the grid was refined. Therefore, it was concluded that both sets of boundary conditions gave consistent results and were not grid dependent. In addition, when the two methods were compared, the difference was about 10 percent at low Re and 1.5 percent at high Re. Therefore, it was concluded that the essential requirement necessary to calculate C_m is to include the gap in the boundary conditions in some consisted manner. Because of constraints of time and computer resources, only Eq. (11*a*) was used; however, when results were compared to the work of other researchers, symmetry conditions were used when appropriate.

Daily and Nece's (1960) experimental determination of the torque provided an opportunity to test the above method. They used $\delta = 0.0127$ to 0.217, Re = 10^3 to 10^7, and $b = 0.00633$. Up to Re = 10^5, they reported that the flow was laminar; this was confirmed by the present results. The flow remains laminar at such high Re because Re is based on Ω, and since the primary flow is parallel to the rotation, the tendency is for a thin boundary layer to form on the disk where most of the rotational effect is confined.

For laminar flow, they identified two regimes. In Regime I, the boundary layers on rotating disk and the endwall are merged, the velocity profile is linear and there is no secondary flow. Their correlation for Regime I is

$$C_m = \frac{2\pi(1-b)^4}{\delta \text{Re}} \tag{12}$$

In Regime II, the boundary layers are separated by a core of fluid rotating at a constant angular velocity. Their correlation for Regime II is

$$C_m = \frac{3.70\delta^{1/10}(1-b)^{39/40}}{\text{Re}^{1/2}}. \tag{13}$$

The factor $(1-b)$ occurs because Re is based on R_c, but the integral limit of Eq. (9) is R_d.

Figure 2 compares these correlations with the present results. The calculations were done using condition boundary (11*b*) on a 601×13 grid for $\delta = 0.02$ and on a 601×61 grid for $\delta = 0.10$; $b = 0.0063$ and Re = 1 to 10^6. The stretching transformation given by Eq. (5) was used; otherwise, it would have been very difficult to place a grid point on the disk edge with $b = 0.0063$.

For $\delta = 0.02$, excellent agreement was obtained between experimental and computational results with some deviation around Re = 20,000 and 100,000. At Re = 20,000, there is a transition from Regime I to II. Daily and Nece reported a smooth transition between regimes, and this accounts for the variation shown in the computational results. It is believed that the deviation around Re = 100,000 is due to a transition to a turbulent regime.

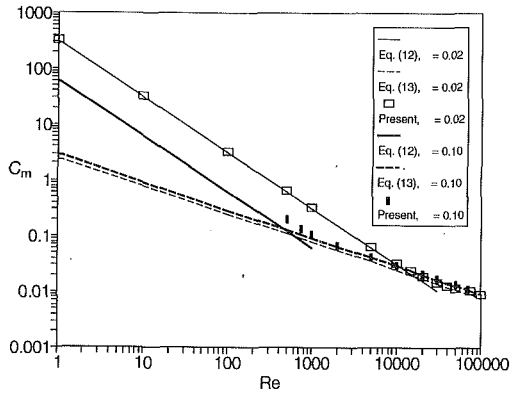

Fig. 2 Comparison of computational results with the experimental results of Daily and Nece (1960), Eqs. (12) and (13), for δ = 0.02 and 0.10

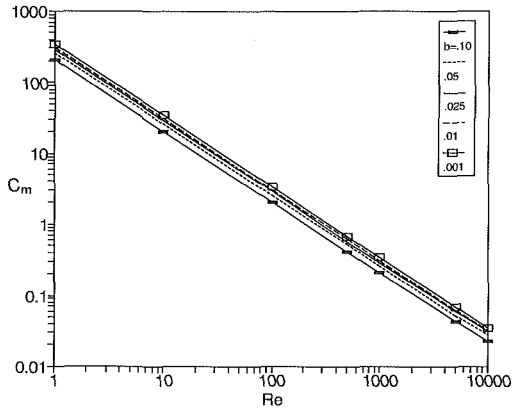

Fig. 3 Torque coefficient for δ = 0.02

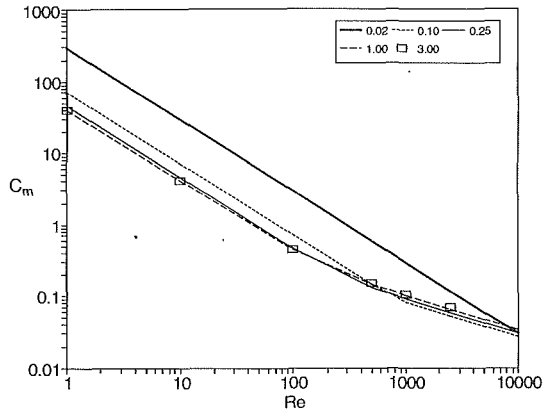

Fig. 4 Torque coefficient with δ given in the legend and b = 0.025

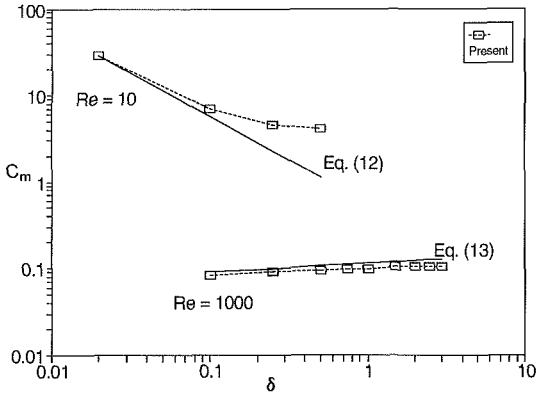

Fig. 5 Comparison of Eqs. (12) and (13) with computational method for Re = 10 and 1000 with b = 0.025

For δ = 0.10, there was very good agreement with the experimental results for Re > 1000, while for Re $\leq$ 1000, there was a significant variation. The two lowest points in the figure are for Re = 500 and 750; however, the lowest Re for which Daily and Nece gave results was about 700, i.e., they gave no results in Regime I; therefore, it cannot be concluded that Eq. (12) is valid here. For Re = 100,000, which Daily and Nece reported as near a turbulent region, the solution did not converge.

Torque Results. Computational solutions were obtained for different parameter combinations: δ = 0.02 to 3.00, Re = 1 to 10,000, and b = 0.001 to 0.10. The maximum grid used was 201×101, and uniform grids were used in most cases. The following criteria were used to choose the grid size: keep the grid square as δ changed, force a node point onto the edge of the disk, and place at least one grid point inside the gap. It was found by numerical experiments that the last criterion was necessary to obtain consistent results. Boundary conditions (11*a*) were used. Only the more important results will be presented here, but a complete set of data is given by Lang (1992).

Figure 3 gives C_m for δ = 0.02 and various b. For each b, C_m was determined for Re = 1, 10, 100, 500, 1000, and 10,000, and the grids used varied from 501×11 to 801×17. Nonuniform grids were used for b = 0.001; otherwise, it would have been necessary to use an even finer grid for such a low value of b. The C_m curves are straight and decrease as Re increases. As b decreases, C_m increases as a result of the edge effect: at the edge of the disk $v = R_d$, but at the sidewall v = 0; therefore, the velocity gradient, and with it C_m, increases as b decreases; therefore, C_m is nonlinear with respect to b. For example, at Re = 1, C_m = 206.8, 257.4, 287.0, 309.5, 334.5, 339.6 at b = 0.10, 0.05, 0.025, 0.01, 0.002, 0.001, respectively. C_m is almost linear from b = 0.01 to 0.025, but then increases more rapidly as b decreases.

Figure 4 gives C_m for b = 0.025 and various δ. For δ > 0.02, the curves can be divided into three regions: two straight lines joined by a crossover region. The crossover region starts around Re = 750 for δ = 0.10 and 100 for the rest. For δ = 0.10, this corresponds well with the experimental results of Daily and Nece (1960) shown in Fig. 2. For δ = 0.02, there was no crossover region, but from Fig. 2, it can be seen that there should be one starting around R = 20,000. For δ = 3.00, C_m was calculated only for Re $\leq$ 2500, since experimental work by Escudier (1984) showed that above about δ = 1.75 the flow becomes unstable for Re > 2500; specifically, an oscillating separation bubble forms on the axis of symmetry.

Calculations were also done with b = 0.10 to 0.01 for each δ as in Fig. 3. It was found that C_m varied with b in a manner similar to Fig. 3. For the first region, the curves are parallel and well spaced; for example, at δ = 0.25 and Re = 1, the difference between C_m at b = 0.10 and 0.01 is about 150 percent. For region three, however, the difference has decreased, so that at Re = 10^4 it is about 35 percent.

Figure 5 shows the ranges of validity of Eqs. (12) and (13). For Eq. (12), the value of Re should place C_m in Regime I; however, the two curves quickly diverge and at δ = 0.10 the difference is already about 20 percent. It is concluded that the linear velocity profile assumption is only valid for very small δ. It should be noted, though, that Daily and Nece did not report experimental results for Re this low. For Eq. (13), δ starts at 0.10, the first value for which Regime II should hold. Agreement is extremely good for all values with a maximum

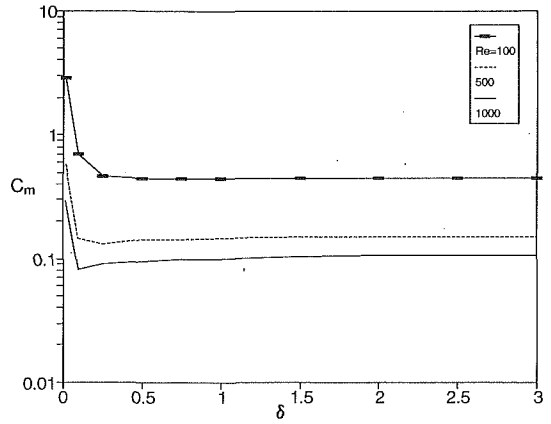

Fig. 6 Torque coefficient as a function of δ with $b = 0.025$

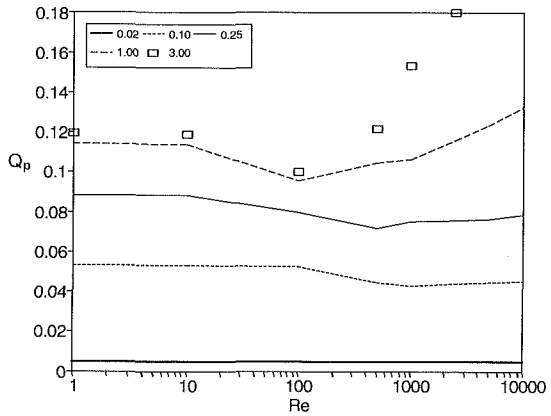

Fig. 7 Primary volumetric flow rates with δ given in the legend and $b = 0.025$

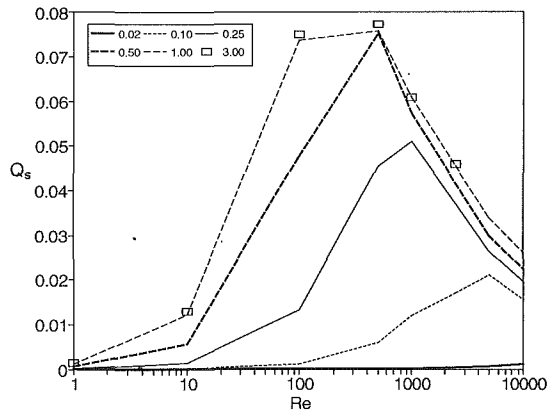

Fig. 8 Secondary volumetric flow rates with δ given in the legend and $b = 0.025$

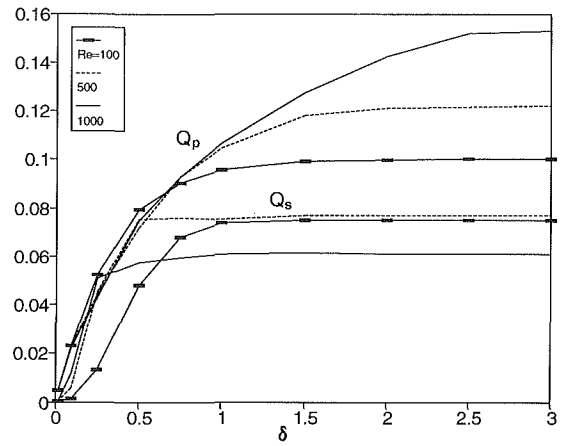

Fig. 9 Volumetric flow rates as a function of δ with $b = 0.025$

deviation of about 20 percent at $\delta = 3.0$. Since Daily and Nece reported results only for $\delta = 0.0127$ to 0.0217, this agreement is remarkable. One point of caution should be made: they used $b = 0.006\,33$, and as seen above, the effect of decreasing b is significant; therefore, it might be questionable if Eq. (13) would still hold for lower values of b.

Figure 6 shows the effect of δ on C_m. After an initial rapid drop, C_m becomes constant.

Finally, a comparison was made with the often used Schultz-Grunow correlation. Schultz-Grunow (1935) derived an analytical formula for C_m by assuming that there are boundary layers on the disk and endwall and that the remaining fluid core rotates at a constant angular velocity. He ignored the effect of the sidewall (the edge effect) and obtained the correlation

$$C_m = \frac{2.67}{\sqrt{\mathrm{Re}}}(1-b)^4. \tag{14}$$

For $\delta = 0.50$ and $b = 0.025$ at Re = 1, 10, 100, 500, 1000, 5000, and 10,000, the ratios of C_m from the computational results to C_m from the Schultz-Grunow correlation are 17.0, 5.37, 1.83, 1.30, 1.24, 1.27, and 1.31. For $\delta = 0.10$ and 3.00, the ratios at Re = 1000 were 1.07 and 1.38. Therefore, for Re $\geq$ 1000, Eq. (14) gives very good results for small δ, and an acceptable first approximation for $\delta > 0.10$. At lower Re, the correlation is invalid. Equation (14) would not be applicable for very small δ, because the boundary layers would not be separated.

Primary and Secondary Volumetric Flow Rates. The volumetric flow rates, Q_p and Q_s, are important for the design of mixing vessels and in understanding fluid flows in the environment. There are few published values for these rates; Bertelà and Gori (1982) published some, but only for coarse grids with a limited range of parameters.

First the effect of b on Q_p and Q_s is considered. Q_p and Q_s were calculated for $\delta = 0.25$ with $b = 0.10$, 0.05, 0.025 and 0.01. At Re = 1.0, the variation was about 5 percent for both Q_p and Q_s (C_m had a variation of 60 percent). Therefore, Q_p and Q_s are weakly dependent on b, and this was true for all δ. The one exception was at $\delta = 0.02$ where the variation of Q_s was about 15 percent at high Re and went to 90 percent at lower values. However, at lower Re, Q_s is of order 10^{-8}; therefore, this variation is probably not significant.

Figures 7 and 8 give the effect of varying δ on Q_p and Q_s. For Q_p, the variation with respect to Re is small for lower δ and moderate at higher ones. For example, at $\delta = 0.25$, the difference between minimum and maximum values of Q_p is about 20 percent, while at $\delta = 3.0$, it is about 45 percent. For Q_s, the variation is much larger. For example, at $\delta = 0.25$, the minimum is 1.3×10^{-4} and the maximum is 5.1×10^{-2}. In addition, for $\delta = 0.10$, 0.025 and 0.50, Q_s has a sharp maximum which is associated with the minimum of Q_s and the crossover region of C_m described previously. Also, Q_p is greater than Q_s except for $\delta = 0.25$ and 0.50 where Q_s exceeds Q_p at the maximum of Q_s. The figures also show that as Q_p decreases, Q_s increases and vice versa.

Figure 9 shows the effect of δ on Q_p and Q_s. For lower δ, Q_p increases and then reaches a constant value. All the curves cross over around $\delta = 0.75$, and above this point the higher Re, the higher Q_p. For Q_s, the rate of increase at small aspect ratios is much greater, and a constant value is achieved more quickly. For high δ, the lowest value of Q_s is at Re = 1000,

followed by 100 and then 500, since Q_s is maximum at Re = 500.

Conclusions

It has been shown that previous computational determinations of C_m were inaccurate because the singularity of the velocity gradient where the rotating disk meets the sidewall was not dealt with adequately. This problem was overcome by including a gap in the boundary conditions between the rotating disk and the sidewall. This method was shown to be accurate based on the experimental results of Daily and Nece (1960). This method was simple and easy to apply. It was found that the most important feature in dealing with C_m was to treat the boundary conditions in a consistent fashion. C_m was a function of Re, δ, and b. For high δ, however, it tended to a constant value. Extrapolating the empirical formula of Daily and Nece for Regime II, Eq. (13), beyond the δ of their work gave very good results for high δ. This was not the case for Regime I, Eq. (12), which was only valid for $\delta \ll 1$. The Schultz-Grunow correlation, Eq. (14), was valid only for Re $\geq$ 1000. The error in this range of Re varied from about 5 to 40 percent.

Q_p and Q_s are functions of Re and δ. For higher aspect ratios, they tended to a constant. They are weak functions with respect to b. Q_p is greater than Q_s, except for a few points at low δ. As Re was varied, Q_p and Q_s varied in phase with each other: as one decreased, the other increased and vice versa.

Acknowledgments

The authors wish to express their gratitude to Drs. R. M. Barron and K. R. Kumar for useful discussions. In addition, the assistance rendered by the computer consultants at the University of Windsor, especially Mrs. J. Sreedharan, and the assistance of Mrs. Barbara Carr in helping to prepare the manuscript are gratefully acknowledged. This study was financially supported through a University of Windsor Post-graduate Scholarship and grants from the Natural Science and Engineering Research Council of Canada (Grant Numbers A-2190 and A-1403).

References

Anderson, D. A., Tannehill, J. C., and Pletcher, R. H., 1984, *Computational Fluid Mechanics and Heat Transfer*, Hemipshere Publishing Corporation, Washington, pp. 249–250.

Bertelà, M., and Gori, F., 1982, "Laminar Flow in a Cylindrical Container with a Rotating Cover," ASME JOURNAL OF FLUIDS ENGINEERING, Vol. 104, pp. 31–39.

Daily, J. W., and Nece, R. E., 1960, "Chamber Dimension Effects on Induced Flow and Frictional Resistance of Enclosed Rotating Disks," ASME *Journal of Basic Engineering*, Vol. 82, pp. 217–232.

Escudier, M. P., 1984, "Observations of the Flow Produced in a Cylindrical Container by a Rotating Endwall," *Experiments in Fluids*, Vol. 2, pp. 189–196.

Lang, E., 1992, "A Computational Study of Torque and Volumetric Flow Rates in a Confined Rotating Fluid and Optimum Iteration Parameters in Cavity Flow," Ph.D. dissertation University of Windsor, Windsor, Ontario, Canada.

Lopez, J. M., 1990, "Axisymmetric Vortex Breakdown. Part 1. Confined Swirling Flows," *Journal of Fluid Mechanics*, Vol. 221, pp. 533–552.

Lugt, H. J., and Abboud, M., 1987, "Axisymmetric Vortex Breakdown With and Without Temperature Effects in a Container with a Rotating Lid," *Journal of Fluid Mechanics*, Vol. 179, pp. 179–200.

Lugt, H. J., and Haussling, H. J., 1973, "Development of Flow Circulation in a Rotating Tank," *Acta Mechanica*, Vol. 18, pp. 255–272.

Pao, H.-P., 1972, "Numerical Solution of the Navier-Stokes Equations for Flows in the Disk-Cylinder System," *Physics of Fluids*, Vol. 15, pp. 4–11.

Roache, P. J., 1982, *Computational Fluid Dynamics*, Hermosa Publishers, Albuquerque, pp. 91–95, 141.

Schlichting, H., 1968, *Boundary-Layer Theory*, 6th Ed., McGraw-Hill, New York, pp. 93–99.

Schlichting, H., 1979, *Boundary-Layer Theory*, 7th Ed., McGraw-Hill, New York, p. 87.

Schmieden, C., 1928, "Über den Widerstand einer in einer Flüssigkeit rotierenden Scheibe," *Zeitschrift für angewandte Mathematik und Mechanik*, Vol. 8, pp. 460–479.

Schultz-Grunow, F., 1935, "Der Reibungswiderstand Rotierender Scheiben in Gehäusen," *Zeitschrift für angewandte Mathematik und Mechanik*, Vol. 15, pp. 191–204.

Theodorsen, T., and Regier, A., 1944, "Experiments on Drag of Revolving Disks, Cylinders, and Streamline Rods at High Speeds," NACA Report No. 793.

Flow of Newtonian and Non-Newtonian Fluids in a Concentric Annulus With Rotation of the Inner Cylinder

J. M. Nouri

J. H. Whitelaw

Imperial College of Science,
Technology and Medicine,
Mechanical Engineering Department,
Thermofluids Section,
Exhibition Road,
London England SW7 2BX

Mean velocity and the corresponding Reynolds shear stresses of Newtonian and non-Newtonian fluids have been measured in a fully developed concentric flow with a diameter ratio of 0.5 and at a inner cylinder rotational speed of 300 rpm. With the Newtonian fluid in laminar flow the effects of the inner shaft rotation were a uniform increase in the drag coefficient by about 28 percent, a flatter and less skewed axial mean velocity and a swirl profile with a narrow boundary close to the inner wall with a thickness of about 22 percent of the gap between the pipes. These effects reduced gradually with bulk flow Reynolds number so that, in the turbulent flow region with a Rossby number of 10, the drag coefficient and profiles of axial mean velocity with and without rotation were similar. The intensity of the turbulence quantities was enhanced by rotation particularly close to the inner wall at a Reynolds number of 9,000 and was similar to that of the nonrotating flow at the higher Reynolds number.

The effects of the rotation with the 0.2 percent CMC solution were similar to those of the Newtonian fluids but smaller in magnitude since the Rossby number with the CMC solution is considerably higher for a similar Reynolds number. Comparison between the results of the Newtonian and non-Newtonian fluids with rotation at a Reynolds number of 9000 showed similar features to those of nonrotating flows with an extension of non-turbulent flow, a drag reduction of up to 67 percent, and suppression of all fluctuation velocities compared with Newtonian values particularly the cross-flow components. The results also showed that the swirl velocity profiles of both fluids were the same at a similar Rossby number.

1 Introduction

Rotating flows in annular passages with rotation of the inner cylinder are important and have application in bearings, rotating-tube heat exchangers, and drilling of oil wells where mud flows between the drill shaft and the well casing to remove cuttings and friction-generated heat. The drilling fluids usually have non-Newtonian properties and the rheological requirements are that they should have low effective viscosity, consistent with transporting drilled cuttings back to surface, and high effective yield stress to keep solids in suspension during stationary periods. Thus the variation of viscometric viscosity and the velocity characteristics can be important. The present investigation is an extension of that of Nouri et al. (1993) and reports measurements of pressure and velocity of two Newtonian fluids and a non-Newtonian fluid in a concentric annulus, at Reynolds numbers up to those of fully turbulent flow and with rotation of the inner shaft.

Contributed by the Fluids Engineering Division for publication in the JOURNAL OF FLUIDS ENGINEERING. Manuscript received by the Fluids Engineering Division June 25, 1993; revised manuscript received February 10, 1994. Associate Technical Editor: J. A. C. Humphrey.

Previous investigations of nonrotating Newtonian flows in concentric annuli, and a few in eccentric annuli, include those of Brighton and Jones (1964), Quarmby (1967), Jonsson and Sparrow (1966), Smith et al. (1968), Lawn and Elliot (1971), Kacker (1973), and Rehme (1974) and a detailed survey has been given by Nouri et al. (1993). Previous experiments in rotating flow in circular ducts and annular passages are scarce. The early work of White (1964) in axially rotating pipe flow showed that the flow resistance was reduced by up to 40 percent at high Reynolds numbers and that rotation stabilized a laminar flow with delay in transition to turbulence to a higher Reynolds number (Cannon and Kays, 1969). In concentric annulii with diameter ratios larger than 0.85, the investigation of Yamada (1962) showed that the flow resistance in laminar flow increased sharply when the inner shaft was rotating and decreased with increase in axial bulk flow.

Here the inner shaft was rotated at 300 rpm with rotational Reynolds numbers, defined as $\mathrm{Re}_\omega = \omega R_{in} S/\nu$ where ω, R_{in}, S and ν are the inner shaft angular velocity, inner shaft radius, the gap between two cylinders and fluid viscosity respectively, of 398 and 1930 for the Newtonian fluids and, 317 and 507

Table 1 Newtonian flow properties

(*a*) Aqueous solution of Glycerol

	$N=0.0$ rpm	$N=300$ rpm
Outer diameter (D_0, mm)	40.3	40.3
Inner diameter (D_{in}, mm)	20.0	20.0
Hydraulic diameter (D_0-D_{in}, mm)	20.3	20.3
Volume flow rate ($\times 10^{-3}$, m^3/s)	0.351	0.351
Inner shaft tip velocity (V_t, m/s)	0.0	0.314
Bulk velocity (U_b, m/s)	0.366	0.366
Bulk Reynolds number (Re, $\times 10^3$)	0.95	0.95
Reynolds number of rotation (Re_w, $\times 10^3$)	0.0	0.4
Rossby number (R_{os})	0.0	2.38
Swirl number (S_N)	0.0	0.33
Glycerol temperature (°C)		25.0 ± 0.02
Density of the glycerol (ρ, kg/m^3)		1134.0
Kinematic viscosity of the glycerol (ν, $\times 10^{-6}$ m^2/s)		7.89
Refractive index of the glycerol at λ = 589.6 nm		1.41

(*b*) Mixture of 31.8 percent tetraline in turpentine

	$N=0.0$ rpm		$N=300$ rpm	
Volume flow rate ($\times 10^{-3}$, m^3/s)	0.69	2.06	0.69	2.06
Inner shaft tip velocity (V_t, m/s)	0.0	0.0	0.314	0.314
Bulk velocity (U_b, m/s)	0.72	2.14	0.72	2.14
Bulk Reynolds number (Re, $\times 10^3$)	9.0	26.6	9.0	26.6
Reynolds number of rotation (Re_w, $\times 10^3$)	0.0	0.0	1.93	1.93
Rossby number (R_{os})	0.0	0.0	4.5	13.9
Swirl number (S_n)	0.0	0.0	0.16	0.03
Mixture temperature (°C)				25.0 ± 0.02
Density of the mixture (ρ, kg/m^3)				896.0
Kinematic viscosity of the mixture (ν, $\times 10^{-6}$ m^2/s)				1.63
Refractive index of the mixture at λ = 589.6 nm				1.489

for the non-Newtonian fluid. The bulk-flow Reynolds numbers, based on bulk-flow velocity, U_b, hydraulic diameter, d_h, and fluid viscosity, for the Newtonian fluids were 950, 9000, and 26,600 and for the 0.2 percent aqueous solution of CMC 1,220, and 9,000.

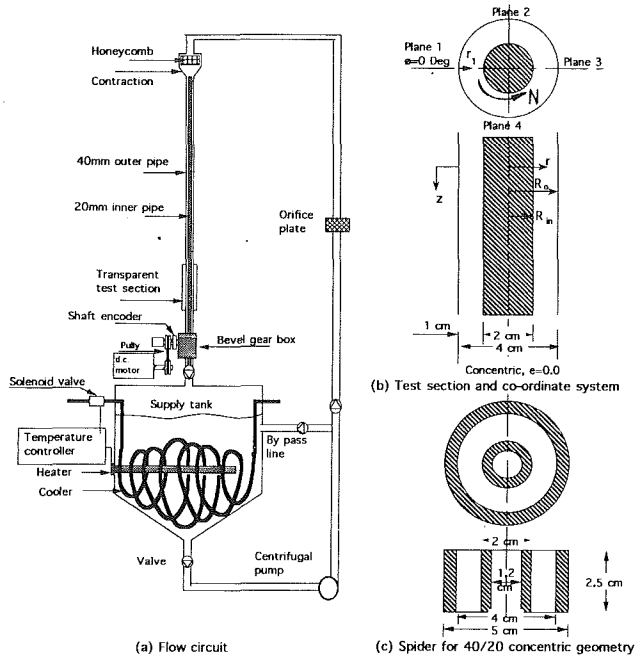

Fig. 1 Flow configuration and the coordinate system

A useful nondimensional parameter to characterize the rotating flows is the ratio of the rotational Reynolds number to that of bulk-flow Reynolds number as

$$R_{os}=\frac{2U_b}{\omega R_{in}} \tag{1}$$

which represents the ratio of Coriolis to inertial forces and is referred to as the Rossby number with values listed in Table 1 for Newtonian and non-Newtonian fluids at different bulk Reynolds numbers.

The flow configuration and instrumentation are described briefly in the following section and the results presented and discussed in the third section. The paper ends with a summary of the more important findings.

2 Flow Configuration and Instrumentation

The flow arrangement is identical to that of Nouri et al. (1993) and is shown on Fig. 1 with the details of the test section and coordinate system in Fig. 1(*b*). A centrifugal pump delivered the working fluid from a supply tank to a chamber where,

Nomenclature

C_f = skin- friction coefficient
d_h = hydraulic diameter
d_r = drag reduction
D_{in} = inner cylinder diameter
D_0 = outer pipe diameter
r = radial coordinate
r_1 = radial distance from the outer wall
r_2 = radial distance from the inner wall
N = inner cylinder rotational speed, rpm
R_{in} = inner cylinder radius
R_0 = outer pipe radius
R_{os} = Rossby number, $2U_b/\omega R_{in}$
Re = bulk flow Reynolds number, $U_b d_h/\nu$
Re_ω = rotational Reynolds number, $\omega R_{in} S/\nu$
S = the gap between the inner and outer wall
S_N = swirl number
$\tilde{u}$, $\tilde{v}$ and $\tilde{w}$ = r.m.s. velocity fluctuations in z, r and θ directions
$u_{\tau_{in}}$ = inner wall shear velocity, $\sqrt{(\tau_{in}/\rho)}$
u_{τ_0} = outer wall shear velocity, $\sqrt{(\tau_0/\rho)}$
$\overline{U},\overline{V},\overline{W}$ = mean velocity components in z, r and θ directions
U_b = bulk velocity
U^+ = $u_{\tau_{in}}/U$ or u_{τ_0}/U
V_t = inner cylinder tip velocity
Y^+ = $r_1 u_{\tau_0}/\nu$ or $r_2 u_{\tau_{in}}/\nu$
z = axial coordinate
$\frac{\partial P}{\partial z}$ = axial wall pressure drop
γ = shear rate
λ = laser light wave length
μ_w = viscosity at the wall for polymer solution
ν = fluid kinematic viscosity
θ = angular coordinate
ρ = fluid density
τ = shear stress
τ_{in} = inner wall shear stress
τ_0 = outer wall shear stress
ω = inner cylinder angular velocity

Table 2 Non-Newtonian flow properties and properties of 0.2 percent aqueous solution of CMC

	$N=0.0$ rpm		$N=300$ rpm	
Volume flow rate ($\times 10^{-3}$, m^3/s)	0.59	2.67	0.59	2.65
Inner shaft tip velocity (V_t, m/s)	0.0	0.0	0.314	0.314
Bulk velocity (U_b, m/s)	0.616	2.78	0.616	2.76
Viscosity at wall (μ_w, $\times 10^{-3}$ kg/m.s)	10.3	6.3	9.8	6.19
Effective Reynolds number (Re, $\times 10^3$)	1.22	9.0	1.25	9.0
Reynolds number of rotation (Re_w, $\times 10^3$)	0.0	0.0	0.32	0.51
Rossby number (R_{os})	0.0	0.0	4.0	17.5
Swirl number (S_N)	0.0	0.0	0.14	0.024
CMC temperature (°C)				25.0 ± 0.02
Density of the CMC (ρ, kg/m^3)				1000.0
Refractive index of CMC at $\lambda = 589.6$ nm				1.33

after passing through a section of honeycomb and contraction, it flowed into the annular passage with an outer brass pipe of nominal inside diameter, D_0, of 40.3 mm and 2.0 m long and an inner stainless steel rod of 20 mm diameter, D_{in}. The bulk flow was measured by a calibrated orifice plate with precision better than 3 percent for Newtonian flow, and with 0.2 percent CMC the orifice plate underestimated the values of bulk velocities by 16 percent when compared with those obtained from integration of mean velocity profiles and this was corrected accordingly. The bulk mass flow rate was constant with rotation up to 350 rpm within measuring uncertainties.

Two Newtonian fluids were selected so as to allow the use of laser-Doppler velocimetry, without limitations imposed by refraction, and to be able to measure in the laminar flow region. For the former purpose, a mixture of 31.8 percent tetraline in turpentine was selected and maintained at a constant temperature of 25 ± 0.02°C. Further details on the use of refractive-index-matching techniques have been provided by Nouri et al. (1988). The second fluid, an aqueous solution of Glycerol, was selected to obtain pressure and velocity measurements in laminar flow.

The non-Newtonian fluid was a 0.2 percent aqueous solution of sodium carbomethyl cellulose (CMC, a weakly elastic shear-thinning polymer), the same as that used by Nouri et al. (1993), and its viscometric properties are known from Pinho and Whitelaw (1990, 1991) to be stable. The viscometric power law relating shear stress τ to shear rate γ

$$\tau = 0.04\ \gamma^{0.75} \qquad (2)$$

is appropriate in the range of shear rates from 140 to 12,000 s^{-1}.

The test section was machined from a rectangular block of plexiglass with an arrangement identical to that of Nouri et al. (1993). In the case of rotation a four-leg support was fixed half way between the inlet pipe and the test section, $30D_0$ upstream of the test section, with legs of 1.5mm diameter. With this arrangement, measurements could be performed up to 350 rpm with inner shaft oscillation amplitude measured to be less than ± 0.1mm; this measurement used the waist of a single laser beam in grazing incidence on the shaft surface to monitor its movement. To insure fully developed flow in the measuring section, the length of the straight pipe upstream of the test section was 2.32m, corresponding to 116 hydraulic diameters or 58 outer-pipe diameters, with a uniform step at the inlet in order to produce an artificially thickened boundary layer. The inner shaft was driven by a d.c. motor via a bevel gear box located down stream of the test section as shown in Fig. 1(*a*), and the rotational speed was measured using an optical shaft encoder which provided a train of 2000 pulses per revolution. The maximum variation in the shaft rotational speed did not exceed ± 0.5 percent of the shaft periphery velocity. The temperature of the liquids was controlled to 25.0 ± 0.02°C so that, in the case of mixture flow, its refractive index was 1.489 and identical to that of the plexiglass material used to form the test section. The bulk flow conditions and properties of the Newtonian and non-Newtonian fluids are given in Tables 1 and 2.

Table 3 Characteristics of optical arrangement

Focal length of the focusing lens (mm)	300.0
Half angle of the beam interaction (degrees)	5.98
Fringe spacing (μm)	3.04
Number of fringes without frequency shift	20
Diameter of the control volume at $1/e^2$ intensity in air (μm)	61.0
Length of the control volume at $1/e^2$ intensity in air (μm)	580.0
Maximum frequency shift (MHz)	± 3.0
Frequency to velocity conversion (ms^{-1}/MHz)	3.04

The effective viscosities listed in Table 2 and used in the calculation of effective Reynolds number were obtained by determining the average wall shear stress from pressure measurements and then dividing by the shear rate determined from the power law relationship for 0.2 percent CMC (Eq. (2)). Similar rheological measurements to those of Pinho and Whitelaw (1990) were carried out with 0.2 percent CMC solutions and the viscosity results were all within 5 percent. These results also confirmed that the 0.2 percent CMC degraded by less than 10 percent after six hours of operation.

Static pressures were measured with holes of 0.5mm diameter distributed longitudinally and circumferentially in the outer diameter. The static pressures were read from a calibrated manometer bank with ± 1 mm resolution. The specific gravity of the manometer fluid was 1.88 giving a height range of 20-400mm. The maximum uncertainties at the lower range for the Newtonian turbulent flow and polymer solution were of the order of ± 5 and ± 2.5 percent, respectively.

The swirl numbers of Tables 1 and 2 were calculated as a ratio of the axial flux of the angular momentum to that of axial momentum (Beer and Chigier, 1972); the axial and angular momentum were obtained by integrating the mean axial and tangential velocity profiles.

The laser-Doppler velocimeter was identical to that described by Nouri and Whitelaw (1991) and comprised a 5 mW helium-neon laser, diffraction-grating unit to divide the light beam and provide frequency shift, a focusing lens to form the control volume in the test section, a lens located on the axis to collect forward-scattered light, a pin hole and a photomultiplier. The principal characteristics of the optics system are given in Table 3. The signal from the photomultiplier was processed by a frequency counter interfaced to a microprocessor and led to ensemble-averaged values of mean and rms velocities. The Reynolds shear stresses were obtained from rms velocity measurements in planes at ± 45 degrees of the main flow as suggested by Melling and Whitelaw (1976). A detailed discussion on the uncertainties associated with the velocity measurements and their correction is given by Nouri et al. (1993) and is not repeated here. In brief, the maximum uncertainties in mean and rms values with nonmatched fluids (i.e., glycerol and 0.2 percent CMC) were 2.5 and 5 percent, respectively, after applying the corrections for velocity gradient broadening. With the refractive index matched fluid, no correction was necessarily for velocity gradient broadening, since the smaller diameter of the control volume was aligned along the plane of the velocity gradient, and the corresponding maximum uncertainties were lower than those with the non-matched fluids.

3 Results and Discussion

The results are presented in two subsections dealing with

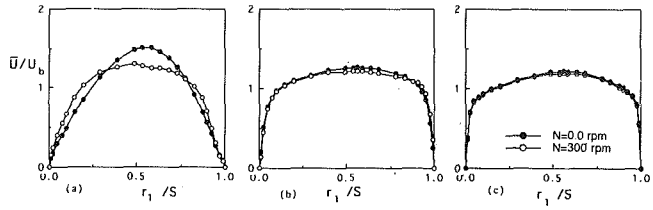

Fig. 2 Rotating and nonrotating axial mean velocity profiles of the Newtonian fluid flow: (*a*) Re = 950; (*b*) = 9,000

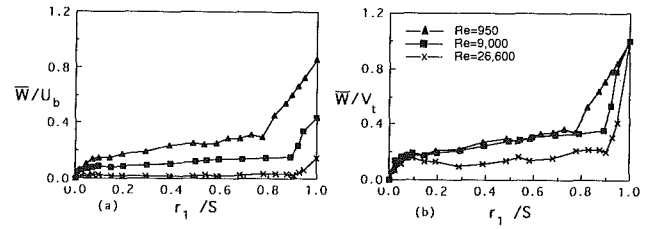

Fig. 3 Tangential mean velocity profiles of the Newtonian fluid flow with an inner shaft rotational speed of 300 rpm: (*a*) normalized with bulk velocity; (*b*) normalized with tip velocity

Newtonian and non-Newtonian rotating flows respectively. All velocity results have been normalised with bulk velocities, U_b, with the tangential component normalized with the inner shaft tip velocity, V_t, or U_b and the distances are normalized with the gap between the outer and inner walls. S, which was 10.15mm.

3.1 Rotating Flow With Newtonian Fluid. Preliminary measurements of mean velocity profiles of the nonrotating flows on four quadrants and at locations separated by a distance of 5 hydraulic diameters confirmed symmetry within 0.01 U_b and led to integrated bulk velocities within 1 percent of each other. Similar confirmation was obtained with the rotating flows but with slightly higher uncertainties of 0.015 U_b and 2 percent.

Figure 2 presents the results of rotating and nonrotating flows at bulk Reynolds numbers of 950, 9000, and 26,600 with corresponding Rossby numbers of 2.38, 4.5, and 13.9 and at the lowest Reynolds number, Fig. 2(*a*), the rotation makes the profile of the axial velocity flatter and less skewed with a maximum velocity of 1.3 U_b, which is 13.5 percent less than that without rotation and with a steeper velocity gradient close to the inner and outer walls. This difference in maximum velocity reduces with Reynolds number so that it is 5 percent at a Reynolds number of 9000 and is zero at 26,600 suggesting a value above which rotation ceases to affect the mean flow. The results also show that the mass flow rates, obtained by integrating the velocity profiles of the rotating and non-rotating flows at all three Reynolds numbers, were within 1.5 percent of each other and similar to those obtained from the orifice plate.

The swirl velocity profiles of Fig. 3 decrease rapidly from the inner wall and form a thin boundary layer and with more gradual decrease toward the outer wall. The penetration of the swirling flow into the bulk flow is reduced with increase in axial flow so that the thicknesses of the inner-wall boundary layer at bulk Reynolds numbers of 950, 9000 and 26,600 are 0.22S, 0.113S, and 0.094S, respectively. The rotation had little effect on the radial mean velocity which was less than 2 percent of the bulk velocity, as for non-rotating flow.

Figure 4 compares the results of rotating and nonrotating flows at the Reynolds number of 9000 and shows that the axial mean velocity profile with rotation is flatter than without rotation with an increase in the rms velocity, Fig. 4(*b*), of up to 16 percent close to the center of the gap. The radial and tangential rms velocities of the rotating flow, Figs. 4(*c*) and (*d*), are larger than without rotation particularly the tangential component which extends throughout cross-section with maximum differences of 25 and 49 percent close to the inner wall for the radial and tangential components respectively. The distribution of $\overline{uv}/U_b^2$, Fig. 4(*e*), is almost linear across the annular gap with and without rotation and its magnitude is again higher with rotation close to the inner wall with a maximum value of 3.9×10^{-3} which is some 25 percent larger than without rotation. The locations of zero $\overline{uv}/U_b^2$ coincide with those of the maximum axial velocities for both flows. The variations of $\overline{uw}/U_b^2$ coincide with those of the maximum axial velocities for both flows. The variations of $\overline{uw}/U_b^2$ with the rotating flow, unlike the zero value without rotation, are near linear with a zero value close to the centre of the gap and with magnitudes comparable to those of $\overline{uv}/U_b^2$ which indicates angular transport of longitudinal momentum.

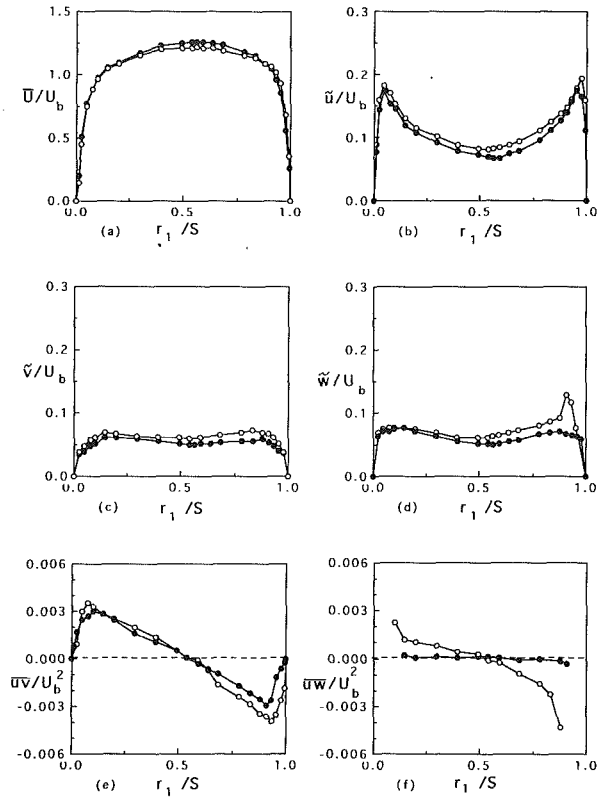

Fig. 4 Rotating and nonrotating flow velocities of the Newtonian fluid with Reynolds number of 9000: (*a*) axial mean velocity, (*b*) axial rms velocity; (*c*) radial rms velocity; (*d*) tangential rms velocity; (*e*) $\overline{uv}$ cross correlation; (*f*) $\overline{uw}$ cross correlation. For symbols see Fig. 2.

The bulk Reynolds number of 26,600 represents a fully developed turbulent flow and the results of Fig. 5 show that the rotating and nonrotating flows are similar except for the turbulence quantities close to the inner wall which are higher with rotation. In particular, the $\overline{uw}/U_b^2$ cross-correlation has a trend similar to that of the lower bulk Reynolds number, Fig. 5(*f*) but with smaller magnitude. The results emphasis that the turbulence quantities are affected by rotation although there was no effect on mean axial values.

The wall shear stresses of the Newtonian fluid at the inner and outer walls were calculated with the procedure described by Nouri et al. (1993), that is from pressure measurements and the location of maximum axial mean velocity with the equations obtained from momentum equation for fully developed, axisymmetric, steady and incompressible flow

$$\tau_0 = -\left(\frac{\partial P}{\partial z}\right)\left[\frac{R_o^2 - R_m^2}{2R_0}\right] \qquad (2)$$

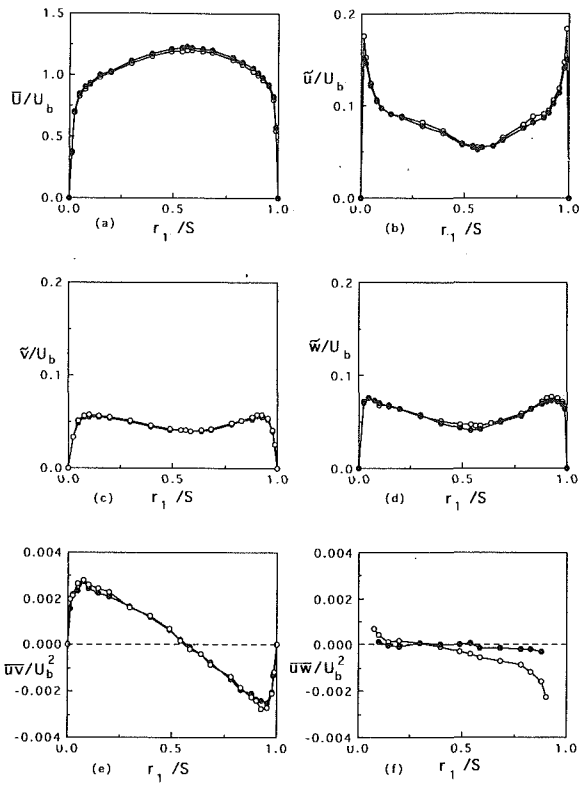

Fig. 5 Rotating and non-rotating flow velocities of the Newtonian fluid with Reynolds number of 26,600; (*a*) axial mean velocity; (*b*) axial rms velocity; (*c*) radial rms velocity; (*d*) tangential rms velocity; (*e*) $\overline{uv}$ cross correlation; (*f*) $\overline{uw}$ cross correlation, For symbols see Fig. 2.

$$\tau_{\text{in}} = -\left(\frac{\partial P}{\partial z}\right)\left[\frac{R_m^2 - R_{\text{in}}^2}{2R_{\text{in}}}\right] \tag{3}$$

where τ_0 and τ_{in} are the outer and inner wall shear stresses and R_m is the location of maximum axial mean velocity. Figure 6 presents the near-wall profiles for rotating and non-rotating flows at bulk Reynolds numbers of 9000 and 26,600 in law of the wall coordinates and confirms logarithmic regions similar to that of the accepted law of the wall at both Reynolds numbers and without rotation. With the lower Reynolds number and rotation, the logarithmic region of the inner and outer walls is shifted down by about 10 percent, in accordance with the increase in the axial pressure drop, and this difference is negligible at the higher Reynolds number.

The average skin-friction coefficient was obtained from pressure measurements as

$$C_f = \left(\frac{\partial P}{\partial z}\right)\left[\frac{d_h}{2\rho U_b^2}\right] \tag{4}$$

for Reynolds numbers from 400 to 6500 with the aqueous solution of glycerol and 7000 to 30,000 with the turpentine/tetraline mixture and its variation with Reynolds number is shown in Fig. 7(*c*). In the laminar flow region, the results show that the values of C_f without rotation agree with the correlation curve of Shah and London ($C_f = 23.8\,\text{Re}^{-1}$) and that transition is at a Reynolds number just above 2000. The flow resistance with rotation is 28 percent higher than without, up to the location of transition, and can be expressed by $C_f = 33\,\text{Re}^{-1}$. This difference decreases gradually with Reynolds number after transition and becomes less than 1.5 percent at Reynolds numbers of 4,100 and 18,000 with the Glycerol solution and mixture fluid, respectively, corresponding to Rossby numbers of 10 and 9.1; this means that the effect of rotation would be negligible at or below these values. This uniform increase of flow resistance with rotation of the inner cylinder and its subsequent

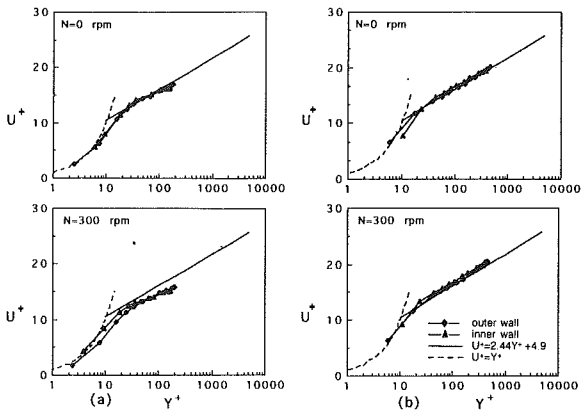

Fig. 6 Rotating and non-rotating axial mean velocity profiles of the Newtonian fluid in law of the wall coordinates: (*a*) RE = 9,000, (*b*) Re = 26,600.

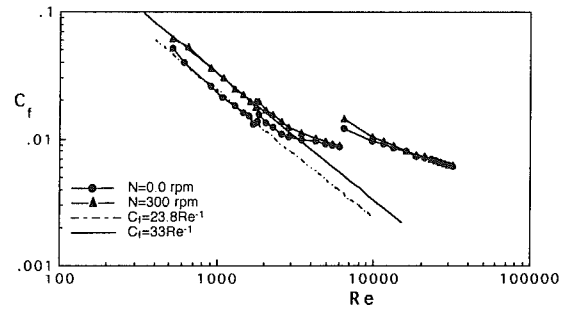

Fig. 7 Skin friction coefficient of the Newtonian fluid as a function of Reynolds number

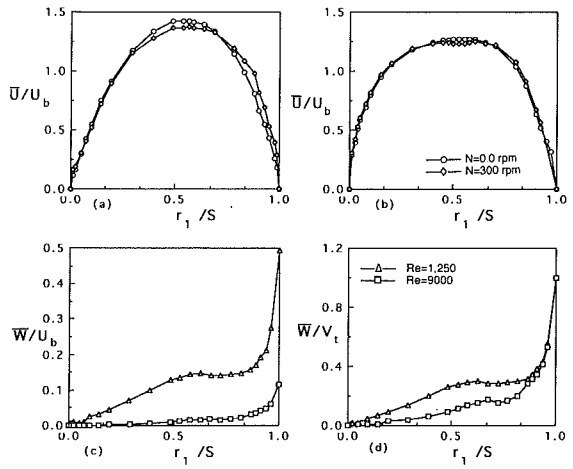

Fig. 8 Rotating and nonrotating mean velocity profiles of the 0.2 percent CMC solution: (*a*) and (*b*) axial component at RE = 1250 and 9000, respectively, (*c*) and (*d*) tangential component normalized with bulk and tip velocities, respectively

decrease to become the same as the non-rotating value is consistent with the findings of Yamada (1962) in concentric annulii with diameter ratios larger than 0.85.

3.2 Rotating Flow With Non-Newtonian Fluid. The axial mean velocities of the 0.2 percent CMC solution at effective Reynolds numbers of 1220 and 9000 are presented in Figs. 8(*a*) and (*b*) for rotating and nonrotating flows. At the lower Reynolds number, the axial mean velocity profile with rotation is flatter and less skewed with a maximum velocity of $1.36U_b$, which is 5 percent less than without rotation, and this difference is much smaller than that obtained with the Newtonian fluid

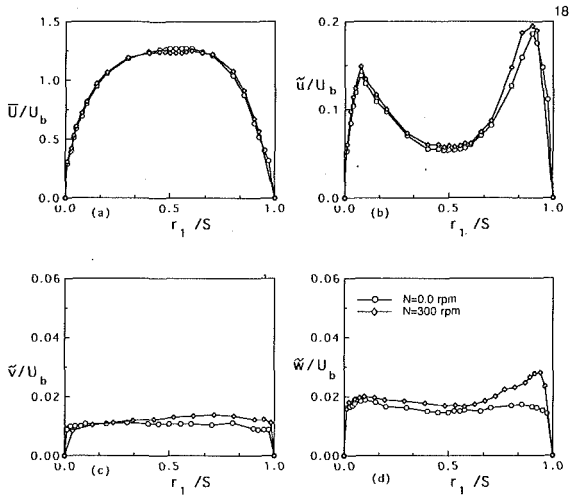

Fig. 9 Rotating and nonrotating flow velocities of the 0.2 percent CMC solution with Reynolds number of 9000: (*a*) axial mean velocity; (*b*) axial rms velocity; (*c*) radial rms velocity; (*d*) tangential rms velocity

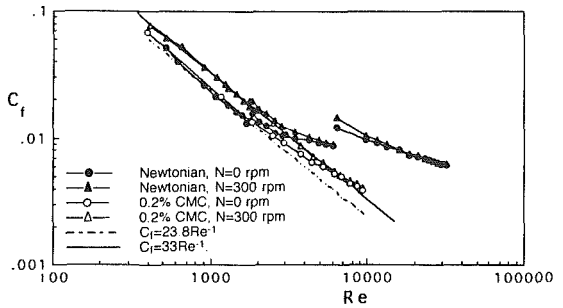

Fig. 10 Skin friction coefficient of the Newtonian and non-Newtonian fluids as a function of Reynolds number

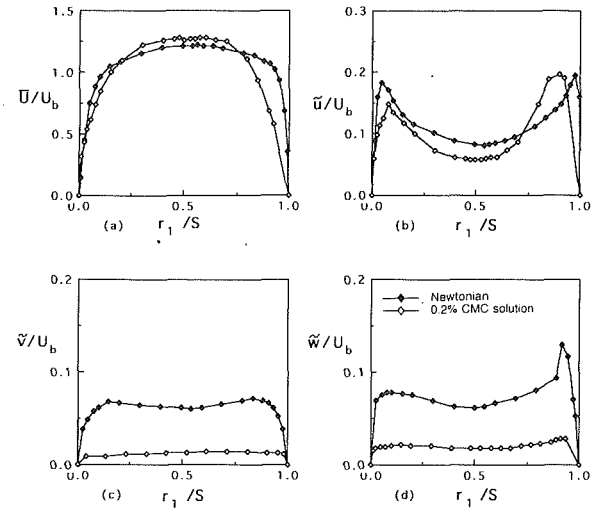

Fig. 11 Comparison of the Newtonian and non-Newtonian fluid flows with Reynolds number of 9000 and an inner shaft rotational speed of 300 rpm: (*a*) axial mean velocity; (*b*) axial rms velocity; (*c*) radial rms velocity; (*d*) tangential rms velocity

for a similar Reynolds number; this is expected since the Rossby number with the Newtonian fluid is half that with the 0.2 percent CMC solution. As with the Newtonian fluid, this difference reduces with Reynolds number to become negligible at a Reynolds number of 9000. The swirl velocity profiles at the two bulk Reynolds numbers, Figs. 8(*c*) and (*d*) show similar variations to that of the Newtonian fluid with penetration into the bulk flow reduced with increase in the axial flow and with an inner boundary-layer thickness around 0.1S at both effective Reynolds numbers.

Figure 9 shows that the axial mean velocities are similar with and without rotation for the Reynolds number of 9000 and the axial rms velocities, Fig. 9(*b*), are higher by up to 12 percent. The radial and tangential rms velocities, Figs. 9(*c*) and (*d*), are higher with rotation particularly the tangential component which extends through the whole cross-section with maximum differences of 21 and 43 percent close to the inner wall for the radial and tangential components respectively. Thus, turbulence quantities were affected by rotation although mean values were not.

The non-Newtonian variation of C_f for a nonrotating flow, Fig. 10, is the same as that obtained by Nouri et al. (1993) with an extended range of non-turbulent flow and drag reduction of 63 percent (defined as $d_r = 100 \times [(C_{f_n} - C_{f_p})/C_{f_n}]$ where suffixes n and p represent the skin-friction coefficient for Newtonian and non-Newtonian fluids) at the highest Reynolds number of 9000. The values of C_f with rotation are again uniformly higher by about 27 percent than without rotation up to a Reynolds number of 2500 and reduce with Reynolds number to become the same at a value of 5200, which corresponds to a Rossby number of 12.5. The drag reduction with rotation is about 67 percent at a Reynolds number of 9000 which is higher than without rotation. The CMC near-wall velocity profiles of the rotating and nonrotating flows at a Reynolds number of 9000, not presented here, were found to be similar since neither the mean velocity profile nor the drag coefficient was affected by the rotation and the profiles had logarithmic regions which lay between the usual law of the wall and that of the maximum drag reduction asymptote and conformed to an expression which was different for the inner and outer walls, similar to those presented by Nouri et al.

Figure 11 allows comparison of mean and rms velocities of Newtonian and 0.2 percent CMC solutions at a Reynolds number of 9000 with rotation and shows that the axial mean velocity profile of the Newtonian fluid is flatter than that of 0.2 percent CMC with steeper velocity gradients close to the walls. These features are also present with the nonrotating flows, as shown by Nouri et al., but with a lesser magnitude which is expected because the Rossby number with the Newtonian fluid is smaller than that with non-Newtonian fluid, so that the effects of rotation on Newtonian fluid are much greater. As with nonrotating flow, the turbulence intensities of Figs. 11(*b*) to (*d*) for the non-Newtonian fluid with rotation decrease more than the Newtonian values particulary the radial and tangential components so that they are smaller by 4.5 and 4 times, and these differences are larger than those obtained with the nonrotating flow (about 3.5 times with both components.) The suppression of turbulence intensities is due to the preferential orientation of the polymer solution and the increased resistance of the stretched molecules to deformation.

Swirl mean velocities for the Newtonian and non-Newtonian fluids at Reynolds numbers of around 1000 and 9000 are presented in Figs. 12 and indicate that those of the non-Newtonian fluid are much smaller which implies that the penetration of swirl into the bulk flow is greater with the Newtonian fluid. This is because the Rossby numbers with the Newtonian fluid are smaller although the bulk Reynolds numbers are the same. It is also evident that the swirl velocities with both fluids decrease monotonically with increase in Rossby number and that the swirl velocity profiles of Newtonian and non-Newtonian fluids are similar. It is also clear that a combination of the bulk Reynolds number and the Rossby number is needed to characterize rotating flows.

Drag reduction with polymer solutions is a direct result of the thickening of the sublayer due to the expansion of molecules with a mechanism that had been explained for example by

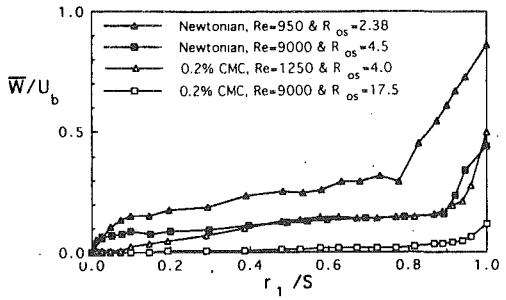

Fig. 12 Comparison of the swirl velocity of the Newtonian and non-Newtonian fluids at an inner shaft rotational speed of 300 rpm

Lumley (1977) and Durst et al. (1982) and which causes suppression of turbulence intensities and therefore a reduction in drag coefficient and higher values of U^+. The presence of these effects is evident with the present results for the 0.2 percent CMC solution. The effect of the rotation in turbulent flow is the enhancement of the turbulence intensities particularly the cross-flow components, an increase in drag coefficient, and lower values of U^+ which is opposite to that of drag reduction. In addition, the rotation of the inner shaft introduces angular transport across planes normal to the angular axis which, in the case of eccentric-annulus flow, would have the effect of creating a more uniform flow between the smallest and largest gaps.

4 Conclusions

The following statements summarize the more important conclusions.

1 The results with the nonrotating Newtonian fluid are consistent with those of Nouri, Umur and Whitelaw (1993) and provide confidence in the measurement accuracy. With rotation of the inner shaft at Rossby numbers of 2.38 to 17.5, the axial laminar-flow velocity profiles became flatter than those without rotation and this difference reduced with increase in bulk flow Reynolds number or increase in Rossby number so that turbulent-flow profiles were the same. The near inner- and outer-wall velocity profile with rotation did not conform to the law of the wall with values below that of nonrotating flow. The swirl velocity profiles indicated a thin boundary layer close to the inner wall and this decreased with bulk-flow Reynolds numbers of 950, 9000 and 26,600 to 0.22S, 0.11S and 0.094S.

2 The intensity of the fluctuations was enhanced by rotation at Reynolds and Rossby numbers of 9000 and 4.5 with increases in u, v, w and $\overline{uv}$ of 16, 25, 49, and 25 percent, respectively, close to the inner wall and reduced to less than 5 percent at Reynolds numbers of 26,600 and 13.9. The values of $\overline{uw}$ showed the existence of angular diffusion comparable to that of radial diffusion at a Rossby number of 4.5 which decreased to one third at 13.9.

3 The effects of rotation on the 0.2 percent CMC solution were similar to those of the Newtonian fluid, but to a lesser extent because the Rossby numbers with the CMC solution were much larger than for Newtonian fluids at similar effective Reynolds numbers.

4 Average skin-friction coefficients with Newtonian and non-Newtonian fluids increased by about 28 percent with rotation in laminar flow and, after transition, decreased with increase in bulk Reynolds number until they became the same as those without rotation at Rossby numbers of 9.5 and 12.5 for the Newtonian fluid and 0.2 percent CMC solutions, respectively. At these Rossby numbers, the effect of the rotation on the axial mean velocity was also negligible. With the polymer solution and rotation, the extension of the non-turbulent flow was evident with a drag reduction of order of 67 percent at a Reynolds number of 9000 which was higher than that without rotation.

5 The penetration of the swirling flow into the bulk flow was greater with the Newtonian fluid, at the same effective Reynolds number, causing a flatter axial mean velocity profile and the swirl velocity profiles were similar with both fluids at similar Rossby numbers. All velocity fluctuations of the polymer solution were suppressed particularly in the cross-stream direction, as for the flow without rotation, due to the molecular stretching of the polymer solution.

Acknowledgments

Financial support from the British Petroleum PLC is gratefully acknowledged. Frequent meetings with Professor M. P. Escudier of the University of Liverpool and Dr. C. Lockyear and colleagues at British Petroleum were of considerable benefit to the research.

References

Beer, J. M., and Chigier, N. A., 1972, *Combustion Aerodynamics*, Applied Science Publisher LTD, London.

Brighton, J. A., and Jones, J. B., 1964, "Fully Developed Turbulent Flow in Annuli," ASME *Journal of Basic Engineering*, Vol. 86, pp. 835–844.

Cannon, J. N., and Kays, W. M., 1969, "Heat Transfer to a Fluid Flowing Inside a Pipe Rotating About its Longitudinal Axis," ASME *Journal of Heat Transfer*, Vol. 91, pp. 135–139.

Durst, F., Haas, R., and Interthal, W., 1982, "Laminar and Turbulent Flows to Dilute Polymer Solution: A Physical Model," *Rheo. Acta.*, Vol. 21, pp. 572–577.

Jonsson, V. K., and Sparrow, E. M., 1966, "Experimental on Turbulent Flow Phenomena in Eccentric Annular Ducts," *J. Fluid Mech.*, Vol. 25, pp. 65–68.

Kacker, S. C., 1973, "Some Aspects of Fully Developed Turbulent Flow in Noncircular Ducts," *J. Fluid Mech.*, Vol. 57, pp. 583–602.

Lawn, C. J., and Elliott, C. J., 1971, "Fully Developed Turbulent Flow Through Concentric Annuli," C.E.G.B. Rep RD/B/N, 1878.

Lumley, J. L., 1977, "Drag Reduction in Two Phase and Polymer Flows," *The Physics of Fluids*, Vol. 20, pp. 64–71.

Melling, A., and Whitelaw, J. H., 1976, "Turbulent Flow in a Rectangular Duct," *J. Fluid Mech.*, Vol. 78, pp. 289–315.

Nouri, J. M., Whilelaw, J. H., and Yianneskis, M., 1988, "A Refractive Index Matching Technique for Solid/Liquid Flows," *Laser Anemometry in Fluid Mechanics*, Vol. 3, pp. 335–346.

Nouri, J. M., Whitelaw, J. H., 1991, "Particle Velocity Characteristics of Dilute to Moderately Dense Suspension Flows in Stirred Reactors," *Int. J. Multiphase Flow*, Vol. 18, No. 1, pp. 21–23.

Nouri, J. M., Umur, H., and Whitelaw, J. H., 1993, "Flow of Newtonian and Non-Newtonian Fluids in Concentric and Eccentric Annuli," *Journal of Fluid Mechanics*, Vol. 253, pp 617–641.

Pinho, F. T., and Whitelaw, J. H., 1990, "Flow of Non-Newtonian Fluids in a Pipe," *J. Non-Newtonian Fluid Mechanics*, Vol. 34, pp. 129–144.

Pinho, F. T., and Whitelaw, J. H., 1991, "The Flow of Non-Newtonian Fluids Over A Confined Baffle," *J. Fluid Mech.*, Vol. 226, pp. 475–496.

Quarmby, A., 1967, "An Experimental Study of Turbulent Flow in Concentric Annuli," *Int. J. Mech. Sci.*, Vol. 9, pp. 205–221.

Rehme, K., 1974, "Turbulent Flow in Smooth Concentric Annuli with Small Radius Ratios," *J. Fluid Mech.*, Vol. 64, pp. 263–287.

Shah, R. K., and London, A. L., 1978, *Laminar Flow Forced Convection in Ducts*, Academic Press New York.

Smith, S. L., Lawn, C. J., and Hamlin, M. J., 1968, "The Direct Measurement of Wall Shear Stress in an Annulus," C.E.G.B. Rep RD/B/N 1232.

White, A., 1964, "Flow of a Fluid in an Axially Rotating Pipe," *J. Mech. Eng. Science*, Vol. 6, pp. 47–52.

Yamada, Y., 1962, "Resistance of a Flow Through an Annulus With an Inner Rotating Cylinder," *Bulletin of JSME*, Vol. 5, No. 18, pp. 302–310.

Ventilated Flow Between Corotating Disks With Large Obstructions in a Fixed Cylindrical Enclosure

(Data Bank Contribution*)

D. Gor

J. A. C. Humphrey
Fellow ASME

R. Greif
Fellow ASME

Thermofluids Laboratory,
Department of Mechanical Engineering,
University of California at Berkeley,
Berkeley, CA 94720

Time-resolved laser-Doppler velocimeter measurements of the circumferential velocity component were obtained for the flow between the center pair of four disks of common radius R_2 corotating at angular velocity Ω in a fixed, cylindrical enclosure. Mean and rms profiles of this velocity component were obtained for two disk rotation speeds (300 and 3600 rpm), two relatively thick tapered obstructions (long and short) placed radially inward midway between each pair of disks, and three ventilation conditions (unventilated, blowing, and sucking) resulting from an imposed inter-disk radial throughflow. The profiles were determined at four circumferential locations downstream of the respective obstructions; radially along the midplane, and axially at selected radial locations. The profiles for the unventilated flow case show that the circumferential component of motion signficantly accelerates near the hub, in the region between the tip of the obstruction and the rotating hub. Elsewhere, this component of motion is significantly decelerated. The presence of ventilation, whether directed radially outward or inward, significantly affects the flow field only in the region immediately around the hub, and far downstream of the obstruction where it increases both the mean and rms velocities. Analysis of the time records suggests that the observed increases in the rms values are due to the circumferentially periodic nature of the radial ventilation condition. These observations are, for the most part, independent of the disk speed of rotation and the length of the obstructions. A comparison of present unventilated flow results with the corresponding results of Usry et al. (1993), who used much thinner obstructions, reveals the extent to which increasing the obstruction blockage ratio induces larger levels of flow unsteadiness.

Introduction

Rotating flows are of considerable fundamental and practical interest, especially in computer, turbomachinery and chemical reactor equipment. In particular, the trend in the computer industry to produce smaller disk drives rotating at higher speeds requires an improved understanding of fluid motion in the inter-disk spaces. Specifically, the effects of obstructions and radial throughflow (ventilation) on the inter-disk flow are not well documented or satisfactorily resolved. The present research extends earlier experimental work performed by Gor et al. (1993) and Usry et al. (1993) by exploring for the first time the *simultaneous* effects of ventilation and obstruction on the inter-disk flow.

The configuration of interest, shown in Fig. 1, involves four, centrally clamped disks corotating in a fixed cylindrical enclosure. The literature relevant to this configuration has been reviewed by Schuler et al. (1990), Humphrey et al. (1991) and, more recently in relation to the effects of ventilation and obstructions, by Gor et al. (1993) and Usry et al. (1993), respectively. In particular, Usry et al. (1993) observed that a long thin obstruction ($t/H = 0.21$, $L/(R_2+a-R_1) = 0.62$) inserted radially inward appears to disrupt the periodicity of circumferentially distributed large-scale flow structures with intensified axial component of vorticity while reducing the mean circumferential velocity component and substantially increasing the corresponding rms values in the wake of the obstruction. Numerical calculations by Humphrey et al. (1992) and Usry (1992) show that the presence of the obstruction reinforces the sense of the cross-stream motion induced by the rotating disks. For the short obstruction of Usry et al. (1993) ($t/H = 0.21$, $L/(R_2+a-R_1) = 0.31$), this works to restore the flow pattern characteristic of an unobstructed geometry

*Data have been deposited in the JFE Data Bank. To access the file for this paper, see instructions on p. 892 of this issue.

Contributed by the Fluids Engineering Division for publication in the JOURNAL OF FLUIDS ENGINEERING. Manuscript received by the Fluids Engineering Division July 13, 1993; revised manuscript received April 1, 1994. Associate Technical Editor: F. White.

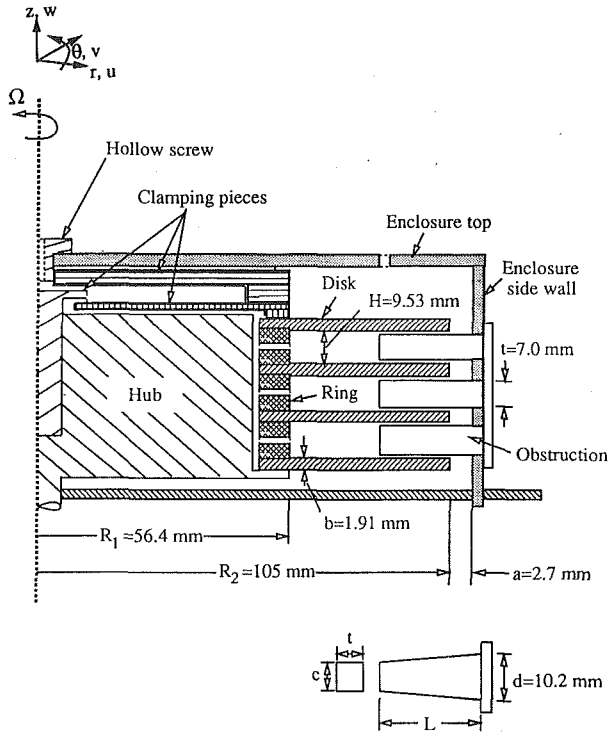

Fig. 1 Schematic of the experimental test section. In the absence of ventilation, the disk spacer rings and the cylindrical enclosure are replaced with identical solid pieces and the hollow screw is absent. The insert shows a plan view of one of the obstructions. For the long obstruction, c = 6.9 mm and L = 31.8 mm; for the short obstruction, c = 8.5 mm an L = 15.9 mm.

within one disk rotation cycle, thus minimizing the influence of the far wake of the obstruction on the interdisk flow. Schuler et al. (1990) list and discuss the major experimental studies involving unventilated geometries.

To date, with the exception mentioned below, all major investigations performed in ventilated enclosures with corotating disks have involved unobstructed flows. The most relevant here are the studies of Szeri et al. (1983a, b), Chang et al. (1989, 1990), Abrahamson et al. (1991), Humphrey et al. (1992), and Gor et al. (1993). (We note also the important, but less relevant, contributions of Hide and Titman (1967), Owen et al. (1985), and Chew and Rogers (1988) where the enclosure corotates with the disks, thus eliminating the element of circumferential shearing along the curved enclosure wall which is of paramount importance to the present flow.) In particular, Abrahamson et al. (1991) visualized the effects of radial outflow and Gor et al. (1993) quantified the effects of radial outflow and radial inflow. Radial throughflow, introduced via openings in the disk spacers, displaces the central core of fluid originally in solid-body rotation, thickens the disk Ekman layers, and changes the number and size of the circumferentially distributed structures with axial vorticity present in the flow. In an obstructed, ventilated flow configuration, Abrahamson et al (1991) observed that a relatively thin obstruction (t/H = 0.38, $0.25 \le L/(R_2-R_1) \le 0.50$) redirects part of the outward-directed throughflow radially inward. Gor et al. (1993) list and discuss the most relevant studies involving unobstructed ventilated geometries.

Perhaps the most informative study performed to date on the *separate* effects of obstructions and ventilation on inter-disk flows is that of Humphrey et al. (1992). In that work, the authors first showed that the power loss, P, due to viscous dissipation in an unventilated disk stack of n-1 disks with n radial obstructions, correlates according to

$$P=\frac{n\mu^2\Omega R_2}{\rho}\left(2C_1+C_2\frac{H}{R_2}\right)\left(\frac{\mathrm{Re}}{1-tL/(HR_2)}\right)^{m+3/2} \quad (1)$$

where C_1, C_2, and m are experimentally determined constants. It is clear that as $tL/(HR_2)\rightarrow 1$, P becomes very large. Via numerical calculation, Humphrey et al. (1992) then showed that in an unobstructed ventilated geometry radial outflow has the potential for stabilizing inter-disk fluid motion but increases dissipation, while radial inflow has the potential for destabilizing inter-disk fluid motion but decreases dissipation. These important findings point to the need to extend the experimental data base and improve the understanding of the *combined* effects of ventilation and obstructions in enclosed corotating disk flows.

The Experiment

Except for the differences noted below, the present experimental apparatus and measurement methodology are as reported in Gor et al. (1993). The test section is shown in Fig. 1. Its corotating parts for the obstructed ventilated configuration consisted of four aluminum disks, each pair separated by an aluminum ring which had 24 equally-spaced circular holes of diameter 3/16 in. The ring openings allowed for a positive radial outflow (blowing) or negative radial inflow

Nomenclature

Alphanumeric

- a = disk-to-enclosure side wall spacing
- b = disk thickness
- c = obstruction width at tip
- d = obstruction width at base
- f = frequency of mean flow oscillation in Hz
- H = inter-disk spacing
- L = obstruction length
- n_N = number of occurrences of N
- N = $(=60f/\Omega)$ normalized value of f
- N_h = number of holes in disk spacer ring
- Q = total radial throughflow rate
- r = radial coordinate
- R = $(=r/R_2)$ normalized radial coordinate
- R_h = radius of hole in disk spacer ring
- R_1 = disk inner radius
- R_2 = disk outer radius
- Re = $(=\Omega R_2^2/\nu)$ Reynolds number
- Ro = $(=V_o/V_t)$ Rossby number
- t = obstruction thickness
- v = mean circumferential velocity component
- v_{rms} = root mean square (rms) circumferential velocity component
- V = $(=v/\Omega r)$ normalized mean circumferential velocity component
- V_{rms} = $(=v_{\mathrm{rms}}/\Omega r)$ normalized rms circumferential velocity component
- V_0 = $(=Q/3\pi N_h R_h^2)$ average throughflow velocity at R_1 between center pair disks
- V_t = $(=\Omega R_2^2)$ circumferential velocity of disk at $r = R_2$
- z = axial coordinate, relative to midplane between center pair of disks
- Z = $(=z/H)$ normalized axial coordinate
- θ = circumferential coordinate; also angular location downstream of obstruction
- μ = fluid dynamic viscosity
- ν = $(=\mu/\rho)$ fluid kinematic viscosity
- ρ = fluid density
- Ω = disk rotation rate in radians/second (also in rpm)

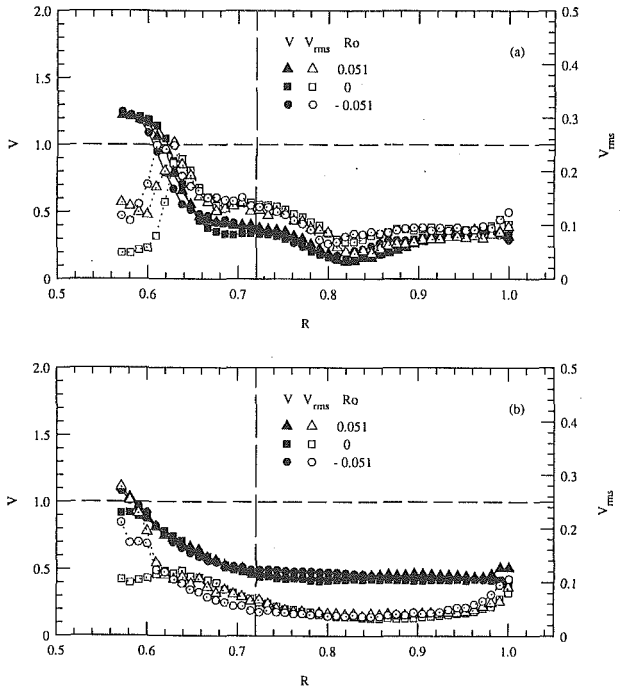

Fig. 2 Mean and rms circumferential velocities versus radial position along the midplane between the center pair of the four disks corotating at 300 rpm with and without ventilation: (*a*) 25 deg and (*b*) 90 deg downstream of the long thick obstruction.

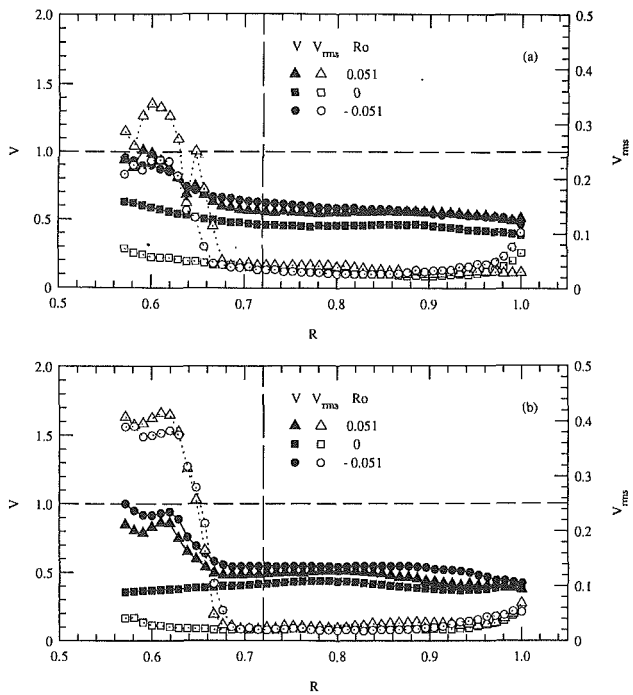

Fig. 3 Mean and rms circumferential velocities versus radial position along the midplane between the center pair of the four disks corotating at 300 rpm with and without ventilation: (*a*) 180 deg and (*b*) 270 deg downstream of the long thick obstruction.

(sucking) of air. Three clamping pieces secured the disks and rings onto a rotating hub, and a fixed cylindrical Plexiglas enclosure surrounded these moving components. Five holes symmetrically drilled through the top of the enclosure allowed the ventilation condition. An opening in the side wall enabled the insertion of a thick tapered radial obstruction midway between each pair of disks. Two obstructions were used: a long obstruction ($t/H = 0.73$, $L/(R_2+a-R_1) = 0.62$) and a short one ($t/H = 0.73$, $L/(R_2+a-R_1) = 0.31$), with the dimensions given in Fig. 1. The corresponding test section for the obstructed unventilated configuration was similar to that just described, except that the enclosure top and the disk spacer rings were replaced by identical solid pieces and the hollow screw shown in Fig. 1 was removed.

In all cases the circumferential velocity component was measured between the center pair of disks using the laser-Doppler velocimetry (LDV) technique. The test section was seeded with micron size mineral oil particles in sufficient concentration to yield instrument-validated data rates ranging between 100 Hz (for low velocities) to 1000 Hz (for high velocities). Measurements were made along the radial direction in the midplane, and along the axial direction at various radial locations. Mean velocities, rms velocities, and energy spectra were obtained from the velocity time records. The data from which the mean and rms values were determined by ensemble averaging consisted of 2500 samples of velocity, with less than 1 percent falling beyond five standard deviations from the mean. The total cumulative uncertainties for the mean and rms velocities were ± 3 and ± 4 percent, respectively, in most of the flow.

The total radial throughflow for either the blowing or sucking condition was determined by means of one of four rotameters, depending on the flow range, to guarantee an average random uncertainty of less than ± 2 percent. Further details concerning the test section, the implementation of the ventilation condition, the measurement techniques, and the experimental uncertainties are available in Gor et al. (1993).

Results and Discussion

Detailed measurements of the mean and rms circumferential velocity component were made for: two disk rotation rates (300 and 3600 rpm, corresponding to $Re = 2.2 \times 10^4$ and 2.66×10^5, respectively); two thick tapered obstruction types (one long and one short) introduced radially inward midway between each pair of disks; three ventilation conditions (unventilated, blowing, and sucking); and, four angular locations downstream of the obstruction. Radial profiles were obtained along the midplane between the center pair of disks, while axial profiles were taken at selected radial locations. For the blowing and sucking conditions, the total radial throughflow rate imposed was such that $Ro = \pm 0.051$ for 300 rpm and $Ro = \pm 0.038$ for 3600 rpm. In these experiments it was not possible to keep the Rossby number constant for both disk rotation rates due to pressure-related mechanical limitations of the apparatus.

The complete data set has been deposited with the *Journal of Fluids Engineering* from which it is available upon request. Selected experimental results are presented here in two parts: the first examines the ensemble-averages mean and rms velocity profiles while the second discusses the flow unsteadiness.

Discussion of Mean and RMS Velocity Results. Selected radial profiles of the mean and rms circumferential velocity component plotted in Figs. 2–7 show data obtained for the two obstruction types at the two rotation speeds. (In these plots, the dashed vertical line denotes the tip of the obstruction in the inter-disk space, while the dashed horizontal line at $V = 1$ is the value of the circumferential velocity corresponding to solid-body rotation.) The results in Fig. 8 compare present measurements with corresponding data obtained by Schuler et al. (1990) and Usry et al. (1993).

Consider first the data obtained at 300 rpm for the long thick obstruction (Figs. 2 and 3). The mean velocity profiles show that immediately downstream of the obstruction (25 deg) the flow behind the obstruction is substantially decelerated while that in the region between the obstruction tip and the rotating hub is accelerated. This is true for all ventilation

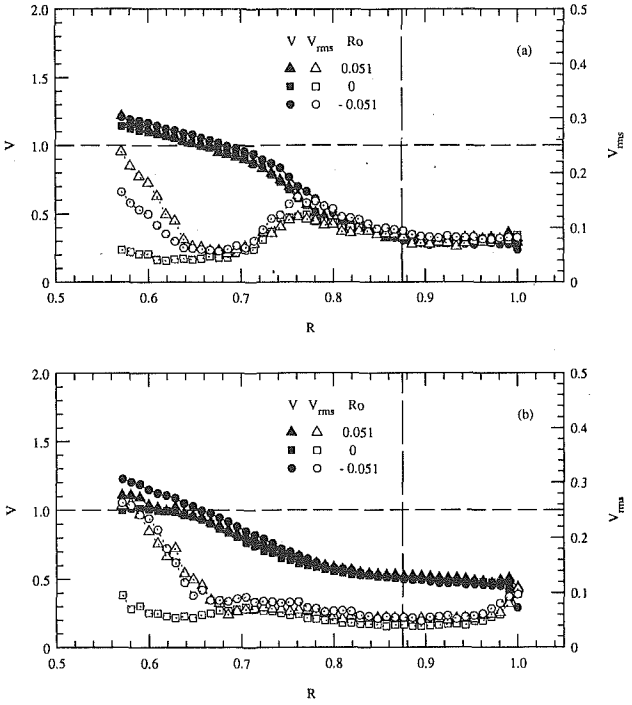

Fig. 4 Mean and rms circumferential velocities versus radial position along the midplane between the center pair of the four disks corotating at 300 rpm with and without ventilation: (*a*) 25 deg and (*b*) 90 deg downstream of the short thick obstruction.

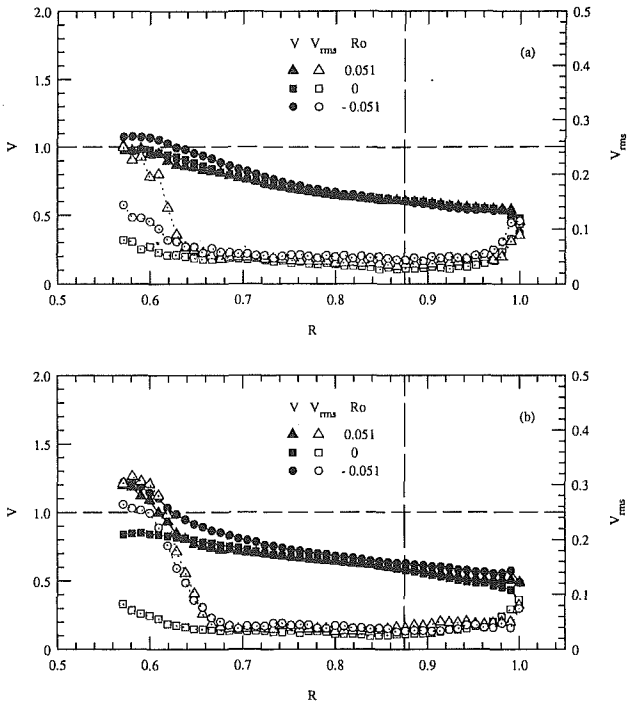

Fig. 5 Mean and rms circumferential velocities versus radial position along the midplane between the center pair of the four disks corotating at 300 rpm with and without ventilation: (*a*) 180 deg and (*b*) 270 deg downstream of the short thick obstruction.

conditions. At the other downstream locations (90, 180, and 270 deg), the mean velocity remains low in the wake of the obstruction. However, at the 180 and 270 deg locations, ventilation (either blowing or sucking) results in higher values of the mean velocity in the region between the obstruction tip and the rotating hub.

The corresponding variations in the rms velocity profiles in Figs. 2 and 3 are even more pronounced. Immediately downstream of the long obstruction (25 deg), the rms velocities behind the obstruction range between 5 and 16 percent, irrespective of the ventilation condition. In the region between the obstruction tip and the rotating hub, the rms values rise to 26 percent but drastically decrease as the hub is approached. The reduction in the rms velocities is much stronger for the unventilated flow case than for either of the ventilated conditions. Further downstream, especially at the 180 and 270 deg locations, the rms values for both the ventilated and unventilated flows is everywhere smaller than the values at the 25 deg location, *except in the region between the obstruction tip and the rotating hub*, where values as large as 44 percent are attained in the ventilated flow cases only. Abrahamson et al. (1991) have shown that the presence of an inter-disk obstruction induces a circumferential pressure variation capable of altering the circumferential symmetry of the radial ventilation condition, here reflected in the increase of the rms velocity near the hub, downstream of the obstruction.

Collectively, these rms velocity data suggest that in the immediate vicinity of the obstruction its effect is to mitigate the influence of the radial component of motion (induced by blowing or sucking) on the circumferential rms velocity by accelerating the flow circumferentially in the region between the obstruction tip and the rotating hub. Futher downstream, as the flow relaxes from the effect of the contraction, the radial component of motion induces very large values of the circumferential rms velocity near the hub. It is important to note that, at the relatively low Reynolds number corresponding to 300 rpm, the large values of the rms velocity near the hub are not due to turbulent mixing. They are due, instead, to large

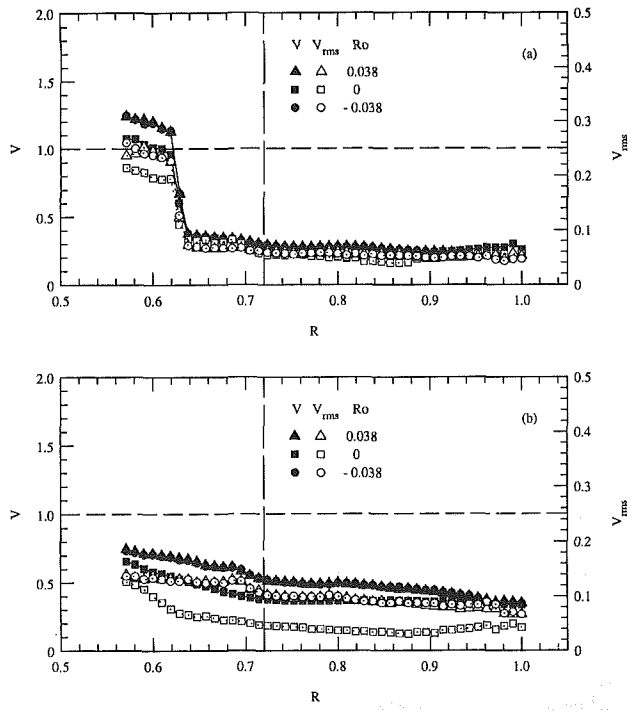

Fig. 6 Mean and rms circumferetial velocities versus radial position along the midplane between the center pair of the four disks corotating at 3600 rpm with and without ventilation: (*a*) 25 and (*b*) 90 deg downstream of the long thick obstruction.

and regular pulsations of the circumferential velocity component induced by the periodic radial component of motion, as detected by the stationary optical probe volume.

Inspection of the corresponding mean and rms velocity profiles obtained at 300 rpm for the short thick obstruction, in Figs. 4 and 5, shows a behavior for the circumferential com-

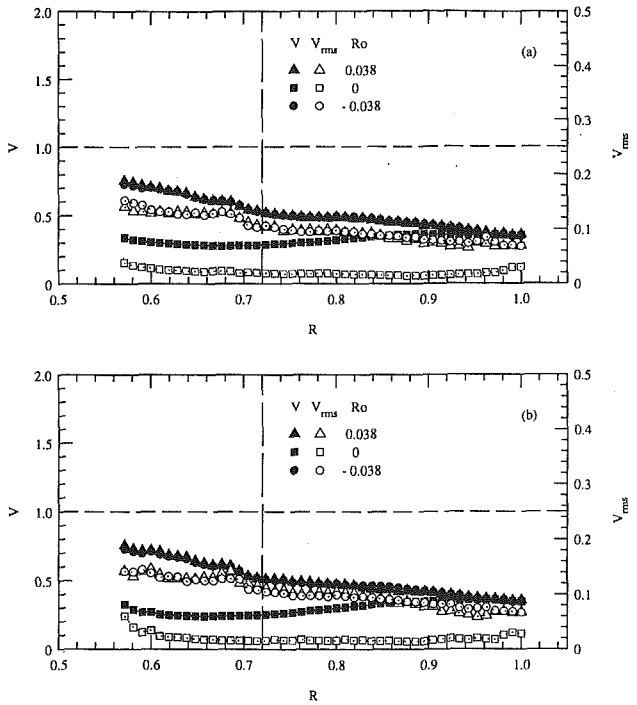

Fig. 7 Mean and rms circumferential velocities versus radial position along the midplane between the center pair of the four disks corotating at 3600 rpm with and without ventilation: (*a*) 270 deg and (*b*) 330 deg downstream of the long thick obstruction.

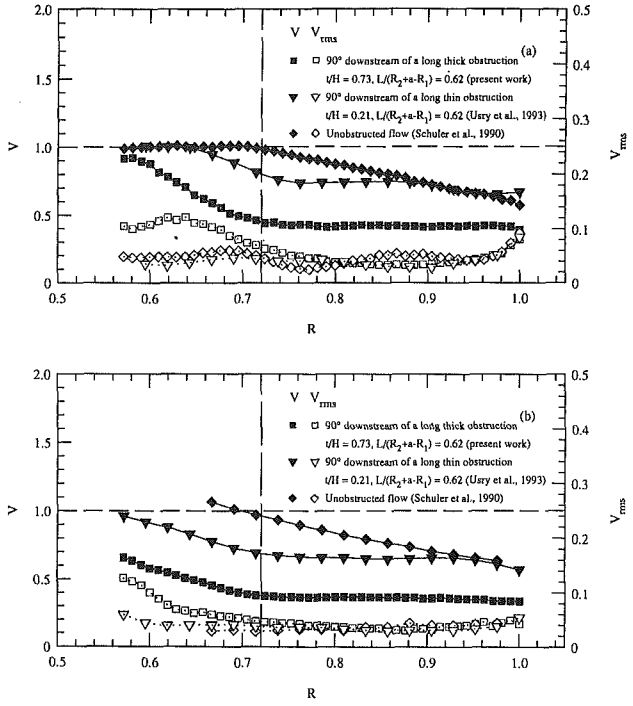

Fig. 8 Comparison among mean and rms circumferential velocities versus radial position along the midplane between the center pair of four disks corotating at (*a*) 300 and (*b*) 3600 rpm for the unventilated flow condition

ponent of motion in broad agreement with that just discussed for the long obstruction, but scaled to reflect the shorter obstruction penetration depth. However, the rms velocity data shown in Fig. 4(*a*) differ in an important way from the corresponding data shown in Fig. 2(*a*). For the short obstruction, the acceleration of the flow in the region between the obstruction tip and the rotating hub is less than in the case of the long obstruction. As a result, the radial component of motion is affected less in the vicinity of the short obstruction and is capable of a stronger influence on the circumferential component of motion, yielding much larger values of the circumferential rms velocity near the hub at the 25 deg location, just downstream of the contraction.

Mean and rms velocity profiles obtained at 3600 rpm for the long thick obstruction are shown in Figs. 6 and 7 for four downstream locations (25, 90, 270, 330 deg). The results differ markedly from the corresponding data for the same obstruction at 300 rpm, shown in Figs. 2 and 3. Except for the 25 deg location, at 3600 rpm both the mean and the rms velocities show relatively little variation with radial position on the midplane. As in the case at 300 rpm, the differences between blowing and sucking are also small but, nevertheless, significant relative to the unventilated flow case. Especially noteworthy are the much smaller values of the rms velocity near the hub at the 270 and 330 deg locations for the flow at 3600 rpm. These results suggest that at high speeds of rotation the influence of ventilation on the velocity rms penetrates less deeply into the inter-disk space, presumably because of the more rapid entrainment of the ventilating flow by the disk Ekman layers.

The mean and rms velocity profiles shown in Fig. 8 allow an examination of the effect of varying the obstruction blockage ratio. These radial profiles were obtained for unventilated flow conditions at 300 and 3600 rpm and include measurements for the long obstructions of the present work as well as measurements obtained by Usry et al. (1993) using thinner obstructions with $t/H = 0.21$, $L/(R_2+a-R_1) = 0.62$. The unobstructed flow measurements made by Schuler et al. (1990) at the same rotation rate are also included for comparison. (Note that all these data were measured at different times in the same test section so that, aside from the obstruction dimensions, all other dimensions remain unchanged.) Even though restricted to a 90 deg plane downstream of the obstructions, the profiles quantify both the amount and the radial extent by which an increase in blockage translates into a reduction of the circumferential velocity component and an increase in the rms values. A noteworthy difference between the rms velocity profiles for the cases with long obstructions is the persistence of relatively large values of the rms velocity near the hub for the thicker obstruction of the present work. Since these are all unventilated flows, the higher rms velocity is attributed to a stronger interaction between the tip of the thicker obstruction and the flow shearing past it.

Discussion of Unsteady Velocity Results. The mean and rms values of the circumferential velocity component, discussed above, were obtained by averaging the time records for velocity obtained at each point in the flow. The slotted autocorrelation technique of Bell (1986) was used to obtain autocorrelations of the velocity records at selected positions in the flow. Fast Fourier transforms of the autocorrelations yielded the corresponding energy spectra, samples of which are provided in Gor (1993). The values of frequency for which the energy in each spectrum exceeded a threshold of about half the value of the highest energy peak were determined. This procedure ensured the detection of all major flow oscillations at low frequencies. The values of frequency, f, so obtained were then normalized by $\Omega/60$ to obtain the dimensionless quantity N.

The validated velocity data rate ranged between 100 and 1000 Hz allowing the resolution of velocity waveforms with frequencies ranging from 17 to 170 Hz, approximately. However, because of the random arrival of velocity data in LDV, the binning procedure in the slotted technique reduces the high frequency end of the autocorrelation, and hence of the energy spectrum, to about 135 Hz. These are only approximate num-

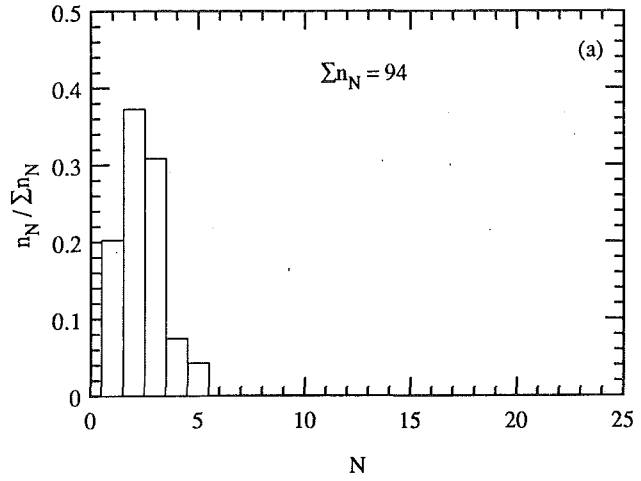

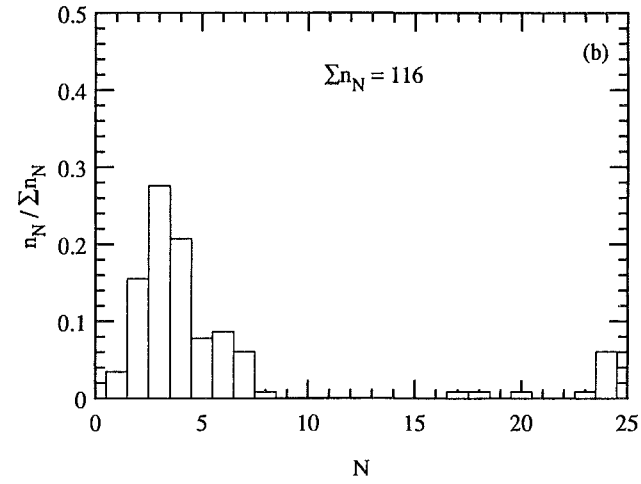

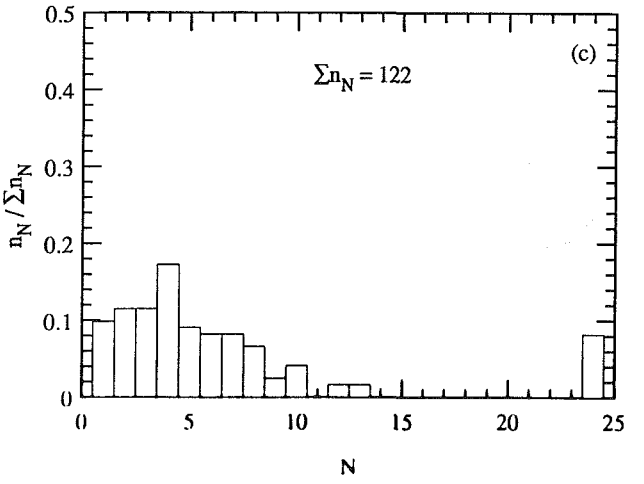

Fig. 9 Total relative frequency, $n_N / \Sigma n_N$, of the dimensionless oscillating flow frequency, N, for data measured along the midplane between the center pair of the four disks corotating at 300 rpm with and without ventilation, 180 deg downstream of the long thick obstruction: (*a*) Ro = 0, (*b*) Ro = 0.051, (*c*) Ro = −0.051. The total population size, Σn_N, is indicated in each figure.

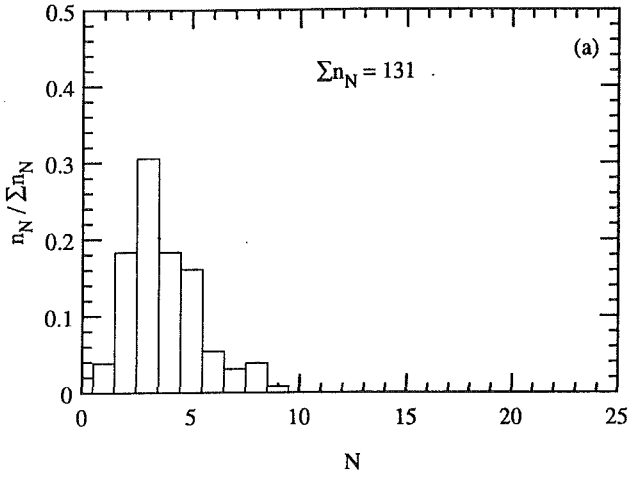

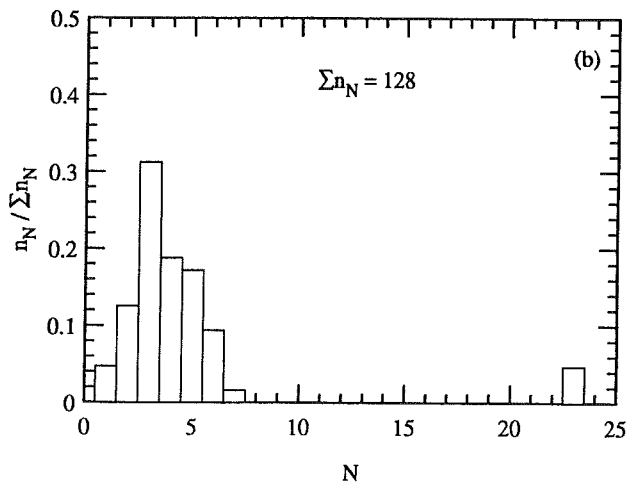

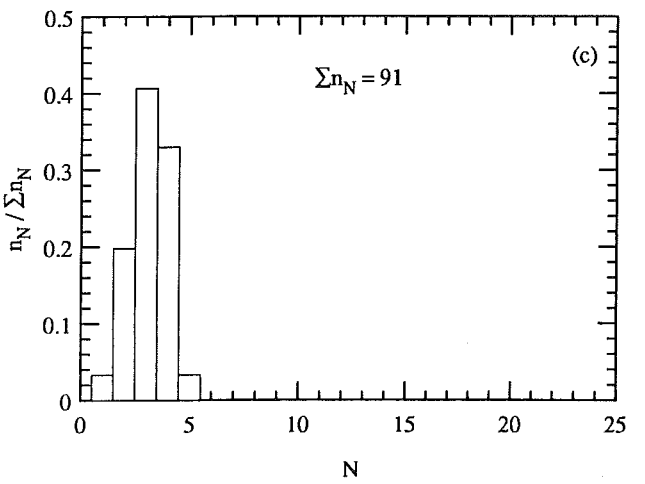

Fig. 10 Total relative frequency, $n_N / \Sigma n_N$, of the dimensionless oscillating flow frequency, N, for data measured along the midplane between the center pair of the four disks corotating at 300 rpm with and without ventilation, 180 deg downstream of the short thick obstruction: (*a*) Ro = 0, (*b*) Ro = 0.051, (*c*) Ro = −0.051. The total population size, Σn_N, is indicated in each figure.

bers intended to illustrate that, for the purposes of this work, the values of N were accurately resolved for the data obtained at 300 rpm but not for the data at 3600 rpm.

Values of N as a function of R, obtained on the midplane between the center pair of disks at $\theta = 180°$C for 300 rpm, are available in Gor (1993). The measurements were made for both the long and short obstruction, with and without ventilation. From these data it was possible to obtain the frequency distributions of N integrated over R, shown in Figs. 9 and 10. In the case of an unobstructed unventilated geometry identical to the present one, Usry et al. (1993) find $N = 2$ for the same flow conditions. It this work, however, N is not necessarily

an integer. Its value ranges between 1 and 6 for the unventilated flow, and between 1 and 24 when either blowing or sucking are imposed. Thus, for example, the histogram for the case of the long thick obstruction in an unventilated flow, Fig. 9(*a*), yields $N \approx 2$ as the most probable value of N, but it also indicates that $N \approx 1$ and 3 have high probabilities of occurrence. In contrast, the likelihood of values of $N > 3$ is small, and values of $N > 5$ were not observed for this case. The ventilated flow cases in Figs. 9(*b*)–(*c*) show similar distributions of N, the details of which depend on the direction of the imposed radial throughflow. Thus, the distribution for the case with sucking (Ro $= -0.051$) is broader than for the case with blowing (Ro $= 0.051$). The larger range in the values of N for the sucking conditions is consistent with the more unstable nature of this flow relative to one with blowing. For both ventilation cases, $N \approx 24$ emerges as a significant value, corresponding to the number of ventilation holes in the rotating ring.

Similar results for the short thick obstruction at 300 rpm are plotted in Fig. 10. Relative to the long obstruction case, these results show a much broader distribution for N (ranging from $N \approx 1$ to 9) for the case of unventilated flow, and a much narrower distribution with the sucking condition imposed. A value of $N \approx 23$ is detected for the case of blowing but not for sucking. In these histograms, $N \approx 3$ is the most probable value independent of the ventilation condition. (Recall that $N = 2$ is the expected value for an unobstructed, unventilated flow.)

While the above results are limited to the 180 deg plane downstream of the obstructions, corresponding data measured at other streamwise locations reveal the circumferential dependence of the low frequency histograms. Thus, for example, we find that for a short obstruction at the 25 deg location a sucking condition results in a larger range of N. In contrast, for a long obstruction at the same location, the sucking condition yields a narrower distribution of N. A clear explanation for this behavior is not presently available and is the subject of continuing work.

Conclusions

Measurement of the mean and rms circumferential component of velocity between pairs of disks corotating in a cylindrical enclosure show that radial obstructions with large blockage ratios significantly alter the flow in the region between the obstruction tip and the rotating hub. If, in addition, ventilation (blowing or sucking) is imposed, additional disturbances to the flow, evident as unusually large increases in the rms velocity, arise downstream of the obstructions, especially in the region of flow corresponding to the space between the obstruction tip and the rotating hub. For the two speeds of rotation of this work, the relatively large increases in the rms velocity of the ventilated flow relative to the unventilated flow are primarily due to the circumferentially periodic nature of the ventilation condition and the effect on ventilation of the circumferential pressure variation induced by the obstruction. The above observations are independent of the obstruction type used. Analysis of the instantaneous velocity time records for the data at 300 rpm reveals that *simultaneously obstructing and ventilating* an inter-disk flow has the effect of increasing the range of low frequency oscillations arising in the flow.

Given the trend in the computer industry toward smaller but faster rotating and highly obstructed disk storage devices, power consumption per unit volume due to viscous dissipation will not necessarily decrease. In principle, as shown by Humphrey et al. (1992), a sucking ventilation condition could be imposed to reduce dissipation but, as noted in that study and here, this may be accompanied by undesirable flow instability. Additional experimental and computational investigations for conditions more closely approximating those of the practical devices, and in which the possible advantages of streamlined obstructions are explored, are required to advance fundamental understanding and definitively establish the impact of ventilation on the highly obstructed flows characteristic of future disk storage devices.

Acknowledgments

The authors are grateful to the Computer Mechanics Laboratory of the Department of Mechanical Engineering at the University of California at Berkeley, and the IBM Almaden Research Center in San Jose, California, for the financial support of this work. The first author acknowledges additional funding in the form of a National Science Foundation Graduate Fellowship. Our thanks go to John Morton and Ron Phillips at Berkeley for their assistance with manufacturing parts of the test section.

References

Abrahamson, S. D., Chiang, C., and Eaton, J. K., 1991, "Flow Structure in Head Disk Assemblies and Implications for Design," *Advances in Information Storage Systems*, Vol. 1, pp. 111–132.

Bell, W. A., 1986, "Spectral Analysis of Laser Velocimeter Data with the Slotted Correlation Method," *Proceedings of the AIAA/ASME Fourth Fluid Mechanics, Plasma Dynamics and Lasers Conference.*

Chang, C. J., Humphrey, J. A. C., and Greif, R., 1990, "Calculation of Turbulent Convection Between Corotating Disks in Axisymmetric Enclosures," *International Journal of Heat and Mass Transfer*, Vol. 33, No. 12, pp. 2701–2720.

Chang, C. J., Schuler, C. A., Humphrey, J. A. C., and Greif, R., 1989, "Flow and Heat Transfer in the Space Between Two Corotating Disks in a Axisymmetric Enclosure," ASME *Journal of Heat Transfer*, Vol. 111, pp. 625–632.

Chew, J. W., and Rogers, R. H., 1988, "An Integral Method for the Calculation of Turbulent Forced Convection in a Rotating Cavity with Radial Outflow," *International Journal of Heat and Mass Transfer*, Vol. 9, No. 1, pp. 37–48.

Gor, D., 1993, "Experimental Investigation of the Effects of Ventilation in Corotating Disk Flows," Ph.D. thesis, University of California at Berkeley.

Gor, D., Humphrey, J. A. C., and Greif, R., 1993, "Ventilated Flow in the Unobstructed Space Between Corotating Disks in a Cylindrical Enclosure," ASME JOURNAL OF FLUIDS ENGINEERING, Vol. 115, pp. 398–407.

Hide, R., and Titman, C. W., 1967, "Detached Shear Layers in a Rotating Fluid," *Journal of Fluid Mechanics*, Vol. 29, pp. 39–60.

Humphrey, J. A. C., Chang, C.-J., Li, H., and Schuler, C. A., 1991, "Unobstructed and Obstructed Rotating Disk Flows: A Summary Review Relevant to Information Storage Systems," *Advances in Information Storage Systems*, Vol. 1, pp. 79–110.

Humphrey, J. A. C., Schuler, C. A., and Iglesias, I., 1992, "Analysis of Viscous Dissipation in Disk Storage Systems and Similar Flow Configurations," *Physics of Fluids A*, Vol. 4, pp. 1415–1427.

Owen, J. M., Pincombe, J. R., and Rogers, R. H., 1985, "Source-Sink Flow Inside a Rotating Cylindrical Cavity," *Journal of Fluid Mechanics*, Vol. 155, pp. 233–265.

Schuler, C. A., Usry, W., Weber, B., Humphrey, J. A. C., and Greif, R., 1990, "On the Flow in the Unobstructed Space Between Shrouded Corotating Disks," *Physics of Fluids A*, Vol. 2, No. 10, pp. 1760–1770.

Szeri, A. Z., Schneider, S. J., Labbe, F., and Kaufman, H. N., 1983a, "Flow Between Rotating Disks (Part 1, Basic Flow)," *Journal of Fluid Mechanics*, Vol. 134, pp. 103–131.

Szeri, A. Z., Schneider, S. J., Labbe, F., and Kaufman, H. N., 1983b, "Flow Between Rotating Disks (Part 2, Stability)," *Journal of Fluid Mechanics*, Vol. 134, pp. 133–154.

Usry, W. R., 1992, "Investigation of the Flow Between Obstructed Corotating Disks in Enclosures," Ph.D. thesis, University of California at Berkeley.

Usry, W. R., Humphrey, J. A. C., and Greif, R., 1993, "Unsteady Flow in the Obstructed Space Between Disks Corotating in a Cylindrical Enclosure," ASME JOURNAL OF FLUIDS ENGINEERING, Vol. 115, pp. 620–626.

Performance Analysis of Viscous Flow Computations on Various Parallel Architectures

D. Drikakis

E. Schreck

F. Durst

Lehrstuhl für Strömungsmechanik,
Universität Erlangen-Nürnberg,
Cauerstr. 4, D-91058 Erlangen,
Germany

A study on the performance of parallel viscous flow computations on various parallel architectures is presented. An implicit computational fluid dynamics code was utilized to solve the axisymmetric compressible Navier-Stokes equations, and parallelization of the code was obtained by the grid partitioning technique. Several hardware and software issues, such as, different communication possibilities and their effect on the parallel performance, the numerical and parallel efficiency for single grid and mesh-sequencing solutions, double and single precision calculations, and the effect of the number of processors on the computing time and the parallel performance, were investigated. Calculations for laminar and turbulent benchmark cases were performed on four parallel platforms and the results were compared with corresponding computations done on the Cray Y-MP utilizing only one processor. A theoretical model for the prediction of the parallel efficiency was also derived and it was verified for single grid and mesh-sequencing solutions by comparing the measured efficiencies with those of the predicted ones.

1 Introduction

The desire to solve increasingly more complex problems has always surpassed the computing capabilities of the day, and has thus provided a driving force in recent years for the extensive development of parallel computing machines. Scientific breakthroughs are expected to be achieved with Teraflop provisions, quoting examples in the area of: aerospace and automotive industry, chemical industry, and material design. There are several parameters that can be used to describe or classify a parallel system, such as, the type and number of processors, the presence or absence of a global control mechanism, the synchronous versus asynchronous operation, and the processor interconnections.

A Multiple Instruction Multiple Data (MIMD) parallel computing architecture can be classified as shared or distributed memory machine. Codes, using shared memory, are simpler to write, but conflicts exist in memory access, and the memory bandwidth prevents this architecture from being truly scalable. For distributed memory architectures, there is the possibility of parallel memory access without conflict, since each processor has its local memory. However, difficulties exist in writing programs for such systems since without communication libraries, writing of software to perform the communication between is left up to user.

Research on parallel CFD is continuously growing with the development of new solvers and the investigation of parallelization strategies (Reinsch et al., 1992; Pelz et al., 1993; Agarwal, 1989; Simon, 1991; Drikakis et al., 1993). However, aside from the development and application of numerical methods in parallel systems, systematic investigations of the factors influencing the parallel performance are also needed. The performance of solvers on different platforms depends on several hardware characteristics, such as, the set-up time required to enable message passing, the time needed to perform one floating point operation, the rate at which data are transferred between the processors, and the communication procedure. In addition, factors that are related to the iterative schemes, and acceleration techniques can also influence the performance of parallel computations.

In the present study some of the above issues which influence the performance of Navier-Stokes computations, as well as the scalability of the these computations on different parallel architectures, were investigated. For this purpose, a parallel Navier-Stokes code based on an implicit Riemann solver and the mesh-sequencing technique has been employed. Results for the computing time and total efficiencies on various number of processors are presented for the single grid and mesh-sequencing solutions. Furthermore, the computations are compared with one processor calculations on the parallel platforms, as well as, with one processor calculations on the Cray Y-MP machine. The efficiency of the parallel computations is studied in terms of the parallel, numerical, and total efficiency. The performance of the parallel computations was also analyzed by developing a theoretical model for the prediction of the parallel efficiency. This model can be used for single grid and mesh-sequencing solutions and for various parallel systems.

Contributed by the Fluids Engineering Division for publication in the JOURNAL OF FLUIDS ENGINEERING. Manuscript received by the Fluids Engineering Division March 9, 1993; revised manuscript received March 22, 1994. Associate Technical Editor: O. Baysal.

2 The Parallel Navier-Stokes Solver

2.1 Governing Equations and Numerical Discretization. The governing equations used in the present study are the axisymmetric Navier-Stokes equations. The Navier-Stokes equations can be written in dimensionless form and for a general curvilinear coordinate system as:

$$(JQ)_t + E_\xi + G_\zeta + J\frac{\tilde{G}+\bar{G}}{z} = \frac{1}{\mathrm{Re}}\left(R_\xi + S_\zeta + J\frac{\tilde{S}+\bar{S}}{z}\right) \quad (1)$$

The inviscid fluxes were discretized by a finite volume Riemann solver (Eberle, 1987), which uses an upwind interpolation scheme up to third-order accuracy for the calculation of the conservative variables on the cell faces. The viscous terms are discretized by central differences, except for the cross derivatives where an "upwind-type" scheme (Chakravarthy, 1988) was used.

The Navier-Stokes equations were solved by a first-order unfactored implicit method. The unfactored implicit solution was succeeded by a Newton-type method constructing a sequence of approximations q^ν such that $\lim_{\nu>1} q^\nu \mapsto Q^{n+1}$, where ν denotes the subiteration state. Consequently, the equations are written as:

$$J\frac{\Delta q^{\nu+1}}{\Delta t} + (A^\nu \Delta q^{\nu+1})_\xi + (C^\nu \Delta q^{\nu+1})_\zeta + (C_{\mathrm{vis}}^{th,\nu}\Delta q^{\nu+1})_\zeta = J\frac{Q^n - q^\nu}{\Delta t} - \mathrm{RHS} \quad (2)$$

where n, $n+1$ are the previous and present time steps, respectively, while the right-hand side (RHS) term is:

$$\mathrm{RHS} = E_\xi^n + G_\zeta^n - \frac{1}{\mathrm{Re}}(R_\xi^n + S_\zeta^n) + \frac{J}{z}\left(\tilde{G}+\bar{G} - \frac{1}{\mathrm{Re}}\tilde{S} - \frac{1}{\mathrm{Re}}\bar{S}\right) \quad (3)$$

On the left-hand side of Eq. (2), the thin layer viscous Jacobian $C_{\mathrm{vis}}^{th,\nu}$ was used for steady-state calculations instead of the full viscous Jacobians, thus saving computational time. The solution at the subiteration level $\nu+1$ was updated as:

$$q^{\nu+1} = q^\nu + \Delta q^{\nu+1} \quad (4)$$

Equation (2) is solved by a Gauss-Seidel relaxation scheme while holding constant the RHS:

$$\mathrm{DIAG}\bullet(\Delta q^{\nu+1})_{i,k}^{(m)} + \mathrm{ODIAG} \bullet(\Delta q_{i-1,k}^{\nu+1,m}, \Delta q_{i,k+1}^{\nu+1,m-1}, \Delta q_{i,k-1}^{\nu+1,m}, \Delta q_{i+1,k}^{\nu+1,m-1}) = \omega\bullet\mathrm{RHS} \quad (5)$$

where the under-relaxation factor, ω, compensated for the errors of different spatial orders of accuracy on the right and left-hand side of Eq. (4). DIAG is a diagonal block matrix at the point (i,k) and ODIAG( ) represents the off-diagonal elements. In the present computations m, and ν were retained constant with values $m=4$, and $\nu=2$.

For high Reynolds' number flows the well known Baldwin-Lomax (Baldwin and Lomax, 1987) algebraic turbulence model was used.

2.2 Grid Partitioning. The parallelization strategy was based on the grid-partitioning method. The computational domain was subdivided into nonoverlapping subdomains and each subdomain is assigned to one processor. The values at the subdomains boundaries were exchanged at each time step between the neighboring processors. The same code can be run on one processor, as well as on a multi-processor environment. For simple geometries under consideration, and for turbulent flows, grid partitioning in one direction is preferred, thus avoiding the modification of the algebraic turbulence model. In the parallel version of the algorithm the relaxation procedure was not the same as that of the corresponding one implemented in the serial version because all the values Δq at the subdomain boundaries were considered from the previous relaxation step.

Nomenclature

Q = conservative solution vector
E, G = inviscid fluxes
R, S = viscous fluxes
$\bar{G}, \tilde{G}, \bar{S}, \tilde{S}$ = axisymmetric terms
J = Jacobian of the coordinate transformation
ξ, ζ = curvilinear coordinates
x, z = Cartesian coordinates
Re = Reynolds number
q = intermediate solution in the Newton-type method
A, C = Jacobians of the inviscid flux vectors
S_n = speedup of parallel computations
$C_{\mathrm{vis}}^{th,\nu}$ = viscous thin layer Jacobian
E_n^{tot} = total efficiency of parallel computations
E_n^{par} = parallel efficiency
E_n^{num} = numerical efficiency
E_n^{lb} = load balancing efficiency
$i_{n,l}$ = number of outer iterations at the grid level l and for calculations on n processors
N_{var} = number of variables
N_{BC} = number of boundary cells
N_{WC} = number of cells in the wake region
N_{nb} = number of the neighbors' subdomains
N_{db} = number of bytes per boundary cell
N^C = number of cells of the whole computational domain
$N_n^{C,l}$ = number of cells per processor at the grid level l
l_{ms} = number of grid levels used in the mesh-sequencing technique
l = mesh-sequencing level
T_n^{calc} = calculation time on n processors
T_n^{com} = communication time on n processors
T_1 = execution time on one processor
T_n = execution time on n processors
t_n^{glob} = global communication time for calculations on n processors
t_n^{loc} = local communication time for calculations on n processors
τ = calculation time per iteration and per control volume
R_{tr} (Mbytes/s) = rate at which data are transferred between processors
t^{set} (μs) = set-up time for communication

Superscripts

ν = Newton subiteration
m = Gauss-Seidel subiteration
n = time step
calc = calculation
com = communication

Subscripts

n = number of processors

These values were updated on the boundaries of each subdomain after each relaxation step by exchanging information with the neighboring processors.

2.3 Mesh-sequencing (Multi-Level) Technique. The mesh-sequencing technique was employed in order to create an initial condition on the fine mesh, which is better than the uniform flow field condition. Hence, the initial guess on the fine mesh was obtained by solving the equations on coarser meshes using the mesh-sequencing technique. The coarse meshes on each subdomain were defined by eliminating every second line of the finer mesh. With the grid subdivided into stripes (i.e., one-dimensional grid partitioning) the number of cells on each processor at the grid level l is:

$$N_n^{C,l} = \frac{N^C}{n \cdot 2^{l_{ms}-l}} \tag{6}$$

where for $l=1$ is defined the coarsest grid of the mesh-sequencing.

3 Efficiency Analysis

The most widely used performance metrics for the investigation of parallel computations are the traditional or relative speedup S_n and the total efficiency E_n^{tot}, defined as:

$$S_n = \frac{T_1}{T_n}, \quad E_n^{\text{tot}} = \frac{T_1}{nT_n} \tag{7}$$

One drawback of the *relative speedup* metric is that it tends to reward slower processors, and inefficient compilation with higher speedup (Sun and Gustafson, 1991), while it suppresses the speedup of efficient algorithms (e.g., multigrid). On the other hand, the *relative speedup* and the total efficiency can be used for the performance analysis of parallel algorithms and systems, if additional data about the hardware characteristics, e.g., communication time, and time needed for one floating point operation, are given. In this paper the total efficiency factor is used while measured data for the hardware characteristics are provided. The ideal efficiency of parallel computations would be 100 percent, which corresponds to a speedup n, but this efficiency can never be achieved due to the following factors:

1. The time needed for local and global communication (parallel efficiency, E_n^{par}),
2. An increase in the number of iterations necessary to fulfill the convergence criterion. This is due to the changes of the algorithm required for its parallelization (numerical efficiency E_n^{num}),
3. The idle time of some processors due to a different problem size per processor (load balancing efficiency E_n^{lb})

Consequently, the total efficiency can be written as the product of the above factors:

$$E_n^{\text{tot}} = E_n^{\text{par}} E_n^{\text{num}} E_n^{\text{lb}} \tag{8}$$

In this paper all subdomains are considered of the same size, and thus, the load balancing effects are ignored. The *numerical efficiency* is defined as the ratio of the total number of floating point operations per cell in the serial algorithm to the total number of operations in the parallel algorithm on n processors, required to reach the same convergence criterion. For the present, unfactored algorithm inner iterations, which are the Newton subiterations (ν) and the Gauss-Seidel relaxations (m), are executed at each time step. These inner iterations can be retained constant at each time step with values $m=4$, and $\nu=2$, as it is indicated by numerical experiments. Thus, the numerical efficiency is only affected by the increase in the number of outer iterations, due to the modification of the Gauss-Seidel relaxation at the subdomain boundaries, as it was already mentioned in the previous section.

The parallel efficiency represents the time loss in a parallel computation due to the local and global communication, and it is defined as:

$$E_n^{\text{par}} = \frac{T_n^{\text{calc}}}{T_n^{\text{calc}} + T_n^{\text{com}}} = \frac{1}{1 + T_n^{\text{com}}/T_n^{\text{calc}}} \tag{9}$$

One of the goal of the present paper is to develop a model for the prediction of the *parallel efficiency*. The latter can be achieved if the calculation and communication times are expressed in terms of hardware parameters, grid sizes and iteration counts. For the mesh sequencing technique the calculation time can be defined as:

$$T_n^{\text{calc}} = \sum_{l=1}^{l=l_{ms}} (N_n^{C,l} \cdot \tau \cdot i_{n,l}) \tag{10}$$

The communication is composed by the *local* and *global* communication times:

$$T_n^{\text{com}} = t_n^{\text{loc}} + t_n^{\text{glob}} \tag{11}$$

The former describes the exchange of interface information between the neighboring subdomains, and the latter, the gathering of information (e.g., level of residuals) from all the processors to the "master" and the broadcasting of other information (e.g., decision on convergence) from the master to all the other processors. For the present algorithm *local* communication is needed for the exchange of the conservative variables between neighboring subdomains, after each Newton subiteration ν, as well as, for the values Δq at the subdomain boundaries, at each Gauss-Seidel relaxation m. The communication time needed for the exchange of each variable Q or Δq can be expressed as:

$$t^{\text{set}} + \frac{N_{db} \cdot N_{BC}}{R^{tr}} \tag{12}$$

where N_{BC} is the number of cells on each column of the subdomain boundary if, for sake of simplicity, one-dimensional grid partitioning is considered. Consequently, for the exchange of the variables Q and Δq the communication time per outer iteration of each grid level can be written as:

$$t_a = 2 \cdot N_{nb} \cdot \left[2 \cdot \nu \cdot N_{\text{var}} \left(t^{\text{set}} + \frac{N_{db} \cdot N_n^{C,l}}{R^{tr}} \right) + m \cdot \nu \cdot N_{\text{var}} \cdot \left(t^{\text{set}} + \frac{N_{db} \cdot N_n^{C,l}}{R^{tr}} \right) \right] \tag{13}$$

The factor of two in front of the first term into the brackets is inserted because two columns of each subdomain boundary are exchanged. This is due to the third-order interpolation scheme used in combination with the Riemann solver. Furthermore, local communication needs in the wake region if a C-type grid topology is used. In this case, the communication is obtained cell by cell for each variable. Consequently, for the exchange of the variables Q and Δq in the wake region the communication time per outer iteration of each grid level can be written as:

$$t_b = 2 \cdot \left[\nu \cdot N_{\text{var}} \cdot N_{\text{WC}} \cdot \left(t^{\text{set}} + \frac{N_{db}}{R^{tr}} \right) + m \cdot \nu \cdot N_{\text{var}} \cdot N_{\text{WC}} \cdot \left(t^{\text{set}} + \frac{N_{db}}{R^{tr}} \right) \right] \tag{14}$$

The factor of 2 at the beginning of the right-hand side in Eqs. (13) and (14) is because each processor sends and receives data. Finally, combining Eqs. (13) and (14), the total local communication time is:

$$t_n^{\text{loc}} = 2 \cdot N_{\text{var}} \cdot \nu \cdot \sum_{l=1}^{l=l_{ms}} i_{n,l} \cdot [N_{nb} \cdot (t^{\text{set}} + N_{db} \cdot N_n^{C,l}/R^{tr})(m+2) + N_{\text{WC}} \cdot (t^{\text{set}} + N_{db}/R^{tr})(m+1)] \tag{15}$$

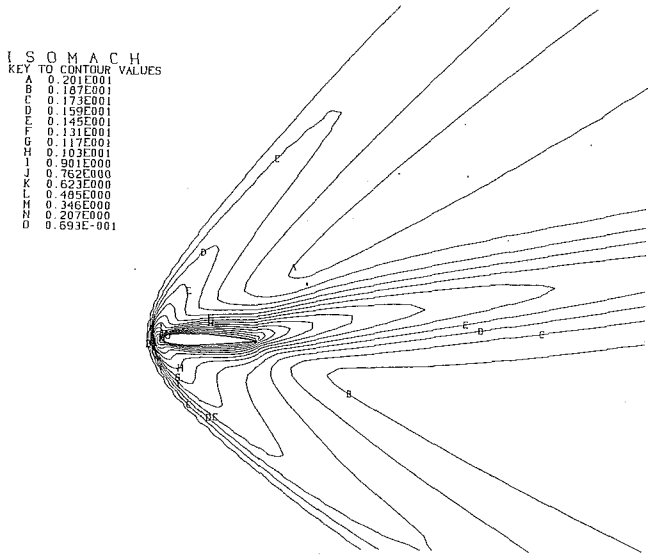

Fig. 1 Iso-Mach contours for the laminar supersonic flow $M_\infty = 2$, Re = 106, $a = 10$ deg over a NACA 0012 airfoil

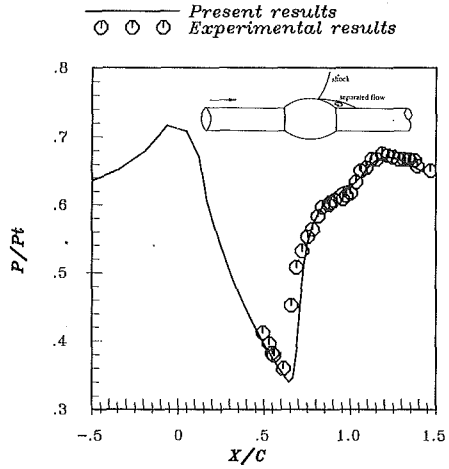

Fig. 2 Comparison of numerical solution with the experimental results (Johnson et al., 1982) for the wall pressure distribution (benchmark II)

Global communication is needed for checking the convergence after each outer iteration. The convergence is checked by the variation $\Delta Q = Q^{n+1} - Q^n$ of the conservation variables between two time steps. Consequently, the communication corresponding to this checking per outer iteration is:

$$t_c = 2 \cdot n \cdot N_{\text{var}} \cdot \left(t^{\text{set}} + \frac{N_{db}}{R^{tr}} \right) \tag{16}$$

Furthermore, if checking of the convergence after each Newton subiteration and Gauss-Seidel relaxation is desired, then the RHS (Eq. (3)) and the quantity $\max_{i,k} \left(\sum_{j=1}^{j=4} \Delta Q_j \right)$, where $j = 1,4$ for the four conservative variables, have to be checked, respectively. The communication corresponding to this checking per outer iteration is:

$$t_d = 2 \cdot n \cdot \nu \cdot (1 + m) \cdot \left(t^{\text{set}} + \frac{N_{db}}{R^{tr}} \right) \tag{17}$$

Consequently, the combination of Eqs. (16) and (17) gives the global communication time for the whole computation:

$$t_n^{\text{glob}} = 2 \cdot n \cdot [N_{\text{var}} + \nu \cdot (1 + m)] \cdot \left(t^{\text{set}} + \frac{N_{db}}{R^{tr}} \right) \cdot \sum_{l=1}^{l=l_{ms}} i_{n,l} \tag{18}$$

In the above formulas, the parameter N_{db} takes the value four and eight, for single and double precision calculations, respectively.

By using the measured values of t^{set}, τ and R^{tr}, Eqs. (8), (9), (10), (11), (15), and (18) can be used to predict the parallel efficiency of the given algorithm on a parallel system, as function of the number of processors. In order to verify the model in the next section, the efficiencies are calculated and compared with the measured ones.

At a fixed grid size, the efficiency decreases as the number of processors is increased. Furthermore, for a fixed number of processors the efficiency increases as the grid is refined. This behavior is due to the following factor. When the number of cells in each direction is increased by a factor of two, the calculation time of each processor increases by a factor of four, but the number of boundary cells, and, therefore the communication time, increases by a factor of two (ignoring setup time). Thus the calculation time varies linearly with the number of cells while the communication time varies as the square root of the number of cells. Hence, the ratio of the communication to the calculation time is reduced as the grid is refined, and the efficiency increases.

4 Results and Discussion

Two viscous compressible flows were selected, as benchmarks for the parallel calculations. The first (benchmark I) was the laminar supersonic flow $M_\infty = 2$, Re = 106, $a = 10$ deg over a NACA 0012 airfoil. In Fig. 1, the iso-Mach contours over the airfoil are shown. The second (benchmark II) was the high Reynolds number transonic flow $M_\infty = 0.875$, $\text{Re} = 13.6 \times 10^6/\text{m}$ over an axisymmetric bump. In Fig. (2) the pressure distribution over the bump surface and the comparison with the experimental results (Johnson et al., 1982) is shown.

4.1 Effects of Different Communication Possibilities on Parallel Performance. The efficiency of parallel computations strongly depends on interprocessor communication, which is a hardware characteristic, different from system to system. A parallel system can sometimes offer more than one communication possibility, which has a different setup time. In this paper, the effect of different communication possibilities on parallel performance is investigated on two parallel systems.

The first is the Meiko Computing Surface with 64 T800 transputers, each with a clock rate of 25 MHz and 4MB memory. In this system, the four transputer links are connected to routing chips which can be programmed to establish the desired configuration. Each transputer can be connected to at most four physical neighbors and one transputer is connected to the host. The configurations used were the ring and the surface of the cylinder (thorus). A development toolset, CSTools, makes possible the implementation of parallel applications and supports process communication on transputers without taking care of the physical architecture constraints. Two communication possibilities between the processors are available: (i) four hardwired links (channels) with very short setup time but communication only with the four nearest neighbors; (ii) transports; a soft link that can be established at run time to any processor but with longer setup time. Results for the parallel efficiency (benchmark I) using the channel's, and transports communication are shown in Table 1 for calculations performed on 10 and 30 processors, respectively. Significant differences exist especially for smaller grid sizes and larger number of processors. Thus, due to the faster communication, channel's communication is proposed for computations where grid partitioning can result in subdomains with only four neighbors.

Table 1 Parallel efficiency on the Meiko Computing Surface for different grid sizes and number of processors, using the transports and channels communications

		E_n^{par} (%)		
		61 × 11	122 × 22	244 × 44
10 procs.	Meiko (*channels*)	92.7	96.0	99.3
	Meiko (*transports*)	81.4	92.1	97.1
30 procs.	Meiko (*channels*)	80.2	92.7	96.8
	Meiko (*transports*)	55.5	80.8	92.8

Table 2 Performance characteristics of parallel platforms used with one or more communication possibilities

Computer	t^{set} (μs)	R_{tr} (MB/s)	$1/\tau$ (MFlops)	t^{set}/τ
Meiko (*channels*)	22	1.4	0.45	10
Meiko (*transports*)	180	1.4	0.45	81
Parsytec (*helios*)	1340	1.4	0.35	469
Parsytec (*parix*)	70	1.2	0.35	24.5
Parsytec (*message ports*)	180	1.3	0.35	63
Parsytec (*dumb links*)	56	1.3	0.35	20
KSR-1	110	7.3	5	550
Convex Meta	370	8	20	7400

The latter is possible when simple geometries are considered, while for complex geometries with more than one interface per subdomain boundary the transport communication must be used.

Different communication possibilities were also tested for a Parsytec system which uses the T805 transputer, with a clock rate of 30 MHz. For this system four communication possibilities exist: (i) dumb links, similar but somewhat slower than the above Meiko channels, (ii) message ports with more software support and flexibility but still slower; (iii) input/output of the Helios operating system, the most comfortable but the slowest option; and (v) the Parix operating system, the fastest communication possibility. A comparison of the speedup factor on the Parsytec using the Parix, and the Helios operating system is shown in Fig. 3 for the benchmark (I). The calculations were performed on a 244×44 grid. It is seen that computations performed using 120 processors, have a speedup factor of about 17 percent higher when the Parix operating system is used instead of Helios. The difference in the speedup corresponds to a total efficiency difference of 14 percent. Consequently, the Parix operating system is used due to the faster communication it offers.

Two other parallel machines used in this work were the KSR-1 from Kendall Square Research and the Convex Meta. The KSR-1 consists of proprietary processors each with 40 MFlops peak performance and 32 MBytes memory. It is a so-called virtual shared memory machine. This system was programmed with the TCGMSG message-passing library from Argonne National Laboratories. The Convex Meta consists of 10 HP 9000/735 workstations which are connected with a FDDI-ring. The major parameters influencing the performance of parallel computations are: (i) the setup time, t^{set}, required to enable message passing; (ii) the time needed to perform one floating-point operation, τ, and (iii) the rate at which data is transferred between processors, R_{tr}. In Table 2 the performance characteristics for the parallel systems used, including characteristics of different communication possibilities, are shown. In the following paragraphs it will be shown that the ratio t^{set}/τ is the most crucial parameter for describing parallel computing efficiency.

4.2 Efficiency of the Mesh-Sequencing Technique and the Single Grid Method. An investigation of the *numerical* and *parallel* efficiency, for the single grid method and the mesh sequencing technique, was obtained for the benchmark (I) on the Parsytec system. In Table 3, results for the number of iterations, as well as, for the parallel and total efficiency are shown for the single grid method and the mesh-sequencing technique. In addition, the number of iterations on each grid level is also presented for the mesh-sequencing technique. The total efficiency was calculated by measuring the computing times, on one and n processors, respectively. The parallel efficiency was measured by using a fixed number of outer iterations. Consequently, $E_n^{num} = 100$ percent, and thus, the total efficiency is equal to the parallel efficiency. The results in Table 3 show that when the number of processors increases, the number of outer iterations also increases, especially on the fine grid. For computations performed on 60 processors using the single grid method, the increase in the number of iterations corresponds to a numerical efficiency of 99 percent. As was mentioned in the previous sections, this increase is due to the parallelization of the implicit part of the method. In the coarse grid levels of the mesh-sequencing technique, the number of iterations remains almost unchanged when the number of processors is increased. This is due to the fact that parallelization of the implicit solution results in a larger number of iterations when the residual level is lower. In the coarse grid levels the calculations are terminated when the residuals are two orders of magnitude larger than the steady-state convergence criterion. Hence, on this residual level grid partitioning does not significantly influence the numerical efficiency, at least, for the present computations. According to the above results, for the performance of the present solver the *parallel* efficiency seems to be more significant than the numerical efficiency.

Table 3 Investigation of the number of iterations (numerical efficiency), parallel efficiency, and total efficiency on the Parsytec system, for the single-grid method and the mesh sequencing technique applied to the benchmark I

	Single grid solver			Mesh-sequencing solver				
	iterations	efficiencies		iterations on the grid levels			efficiencies	
n	244×44	E_n^{par}	E_n^{tot}	61×11	122×22	244×44	E_n^{par}	E_n^{tot}
1	1547	100	100	109	82	627	100	100
10	1547	96.4	96.4	110	84	628	96.4	96.2
30	1552	92.4	92.1	110	84	630	91.8	91.3
60	1562	86.9	86.1	110	84	640	85.0	83.8

Table 4 Computing time and total efficiencies for the single-grid and the mesh-sequencing on the Meiko, Parsytec, and Cray Y-MP machines. Results for 64-bits and 32-bits arithmetic (benchmark I, grid 243 × 43, SG: single-grid method; MS: mesh-sequencing technique).

		Computing time (h) & (E_n^{tot} %), grid 244 × 44				
		1 proc.	10	30	60	120
Meiko	64-bit, SG	93.32 (100)	9.46 (98.6)	3.23 (96.3)	1.66 (93.7)	- - - - -
	32-bit, SG	67.40 (100)	6.79 (99.3)	2.32 (96.8)	1.19 (94.4)	- - - - -
	MS	28.08 (100)	2.84 (98.9)	0.97 (96.5)	0.50 (93.6)	- - - - -
Parsytec	SG	59.37 (100)	6.16 (96.4)	2.15 (92.1)	1.15 (86.1)	0.61 (81.1)
	MS	24.64 (100)	2.56 (96.2)	0.9 (91.3)	0.49 (83.8)	0.26 (79.0)
Cray Y-MP, (1 processor) SG: 0.7355 h, MS: 0.30642 h						

Furthermore, the mesh-sequencing technique and the single grid method have been compared for benchmarks (I), and (II), in Tables 4, and 5, respectively. The calculations were performed on the Meiko and Parsytec systems. The acceleration factor, using the mesh-sequencing technique, is 2.4 and 1.4 for the laminar (benchmark I) and turbulent (benchmark II) flow, respectively. The total efficiency is higher when the single grid method is used instead of the mesh sequencing technique, because in the latter case a part of the computations is performed on coarser meshes where the *parallel* efficiency reduces according to the analysis of Section 3.

4.3 Double and Single Precision Computations. The effect of 32-bit and 64-bit arithmetic on the parallel performance was studied using the Meiko system and the benchmark (I)

Table 5 Computing time, and total efficiency for the benchmark II, for various grid sizes and number of processors on the Meiko Computing Surface (SG: single-grid method; MS: mesh-sequencing technique)

grid	solution method	Computing time (h) & (E_n^{tot}%) (Meiko) 1 proc.	4	8	10	20	40
42×22	SG	2.244	0.5817	0.2988	0.2417	0.124	0.074
		(100)	(96.44)	(93.88)	(92.84)	(90.48)	(75.81)
82×42	SG	36.79	9.373	4.74	3.8	1.965	1.047
		(100)	(98.13)	(97)	(96.82)	(93.61)	(87.85)
	MS	25.68	6.55	3.32	2.66	1.38	0.744
		(100)	(98)	(96.7)	(96.54)	(93)	(86.3)
162×82	SG	275.92[a]	69.68	35.07	28.41	14.27	7.37
		(100)	(99.0)	(98.35)	(97.12)	(96.7)	(93.6)
	MS	193[a]	48.9	24.66	19.92	10.05	5.24
		(100)	(98.67)	(97.83)	(96.9)	(96)	(92.1)

[a]estimated

Table 6 Computing time, and total efficiency for the benchmark II, for various grid sizes and number of processors on the Parsytec machine (single-grid algorithm)

grid	Computing time (h) & (E_n^{tot} %) (Parsytec) 1 proc.	4	8	10	20	40
42×22	1.975	0.5188	0.272	0.2252	0.1228	0.0756
	(100)	(95.17)	(90.76)	(87.7)	(80.41)	(65.31)
82×42	32.4	8.3	4.247	3.413	1.794	0.997
	(100)	(97.59)	(95.36)	(94.93)	(90.3)	(81.24)
162×82	242.19[a]	61.638	31.117	25.07	12.756	6.656
	(100)	(98.23)	(97.3)	(96.6)	(94.93)	(90.97)

[a]estimated

Table 7 Computing time, and total efficiency for the benchmark II, for various grid sizes and number of processors on the KSR-1 machine; comparison with the Cray Y-MP (single-grid algorithm)

grid	Computing time (h) & (E_n^{tot} %) (KSR-1) 1 proc	2	4	8
42 × 22	0.22	0.1288	0.077	0.05814
	(100)	(85.4)	(71.4)	(47.3)
82 × 42	3.5156	1.9337	1.038	0.6118
	(100)	(91)	(84.7)	(71.8)
162 × 82	26.4755	13.93	7.21	3.912
	(100)	(95)	(91.8)	(84.6)
Cray Y-MP (1 processor), grid 162x82; computing time: 3.0 h				

Table 8 Computing time, and total efficiency for the benchmark II, for various grid sizes and number of processors on the Convex Meta (single-grid algorithm)

grid	Computing time (h) & (Total Efficiency %) (Convex Meta) 1 proc.	2	4	8	10
82 × 42	0.579	0.332	0.228	0.176	0.169
	(100)	(87.2)	(63.50)	(41.12)	(34.26)
162 × 82	4.412	2.273	1.271	0.782	0.697
	(100)	(97.0)	(86.78)	(70.52)	(63.30)

(Table 4). For a 64-bit arithmetic the computing time is higher and the total efficiencies lower, in comparison with the corresponding computations performed with a 32-bit arithmetic. For the present solver numerical experiments showed that a 32-bit arithmetic provides satisfactory results, and thus the following computations were performed with single precision.

4.4 Single Processor and Mulit-Processor Solutions on Various Parallel Systems. A comparison between the Meiko, Parsytec, and Cray Y-MP systems is shown in Table 4 for the benchmark (I) case. Results for the benchmark (II) are shown in Tables 5, 6, 7, and 8 for computations performed on the Meiko, Parsytec, KSR-1 and Cray Y-MP, and Convex Meta, respectively. In these tables, the computing time and total efficiencies for various number of processors are shown. For the computations performed on one T800 or T805 using the finest grid, an extreme computing time was needed. In these

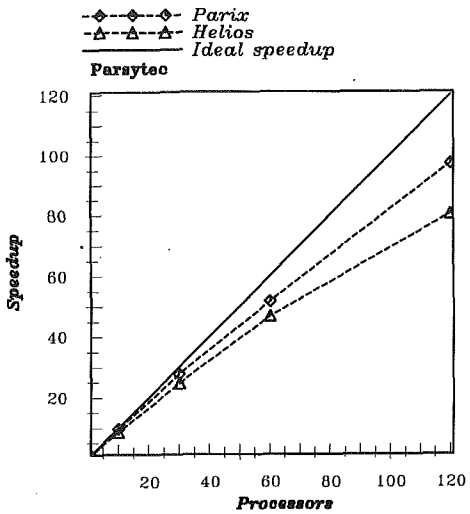

Fig. 3 Comparison between the Parix and Helios operating systems for the speedup on the Parsytec machine using the benchmark I (grid 243 x 43)

cases the computing time, on one T800 or T805 transputer, has not been measured, but has been estimated by first performing the computations on a Sun-ELC workstation. From these computations the number of iterations was determined, and thus, the execution time on one T800 and T805 transputers was easily estimated.

In Tables 4–8 it is seen that the highest efficiencies are obtained for parallel systems with the smallest t^{set}/τ ratio (see Table 2). For systems with high t^{set}/τ ratio (e.g., KSR-1, Convex Meta) the effect of communication is extremely significant when using small grid sizes. The transputer systems present very satisfactory efficiencies even on the coarse grids. For finer grids the differences between the transputer systems and the KSR-1 or Convex Meta machines are significantly less. Furthermore, longer computing times are observed for the transputer systems than for the KSR-1 or the Convex Meta machines, and this is due to the slow T800 and T805 transputers. The fastest solution is achieved on the Convex Meta system, which provides a very satisfied run time in comparison with the transputer systems or the Cray Y-MP. This is actually a workstation cluster system and one of the differences it has to that of a traditional parallel system is the imbalance between communication and arithmetic performance. Therefore, the efficiency is always worse than a transputer system, but the wall clock time is much shorter. The calculations on one processor of the Cray Y-MP were performed using vectorization of the programme loops. This "poor" vectorization results in six times faster computations than the scalar ones. The computing times on the parallel platforms are satisfactory in comparison with the corresponding times on one processor of the Cray Y-MP.

4.5 Prediction of the Parallel Efficiency. The theoretical model for the parallel efficiency was verified by comparing predicted with measured efficiencies on the Meiko system. These comparisons were obtained for the benchmark (I), and they are shown for both the single grid method and the mesh-sequencing technique in Fig. 4(*a*, *b*) respectively. The agreement between measured and predicted efficiencies is satisfactory. The theoretical model can be effectively used as a measure index before computations are performed on a large number of processors.

5 Conclusions

Hardware and software issues influencing the performance of parallel computations were investigated by employing a

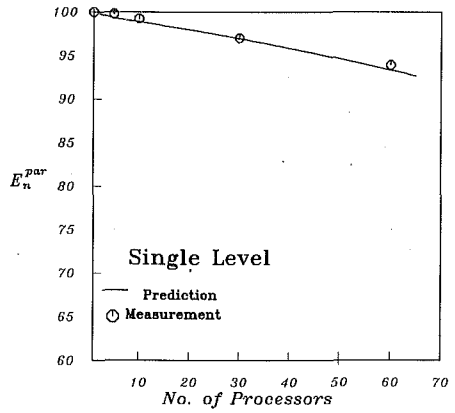

(a)

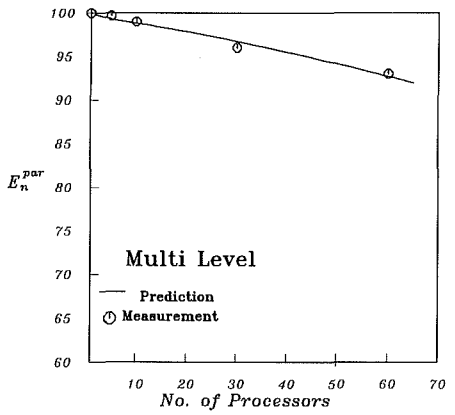

(b)

Fig. 4 Comparison of the predicted and measured values of the parallel efficiency for the benchmark (I); (*a*) single level (one grid), (*b*) multi-level (mesh-sequencing)

parallel Navier-Stokes code. The computations on four parallel architectures revealed the ratio of communication setup time to the time needed for one floating point operation, (t^{set}/τ), as the critical hardware parameter for the communication, and thus, for the parallel efficiency of computations. The highest efficiency was always achieved for the smallest t^{set}/τ ratio. Furthermore, the computing time must seriously be considered for the characterization of a parallel platform. The communication procedure can also strongly affect the performance of parallel computations, and this factor has to be taken into account when the parallel platform used has more than one communication possibility.

It seems the parallel efficiency is more decisive than the numerical one for the present algorithm. The mesh-sequencing technique presents slightly lower total efficiency than the single grid method but it results in less computing time. The effects of the grid partitioning on the numerical efficiency of the coarse grid levels in the mesh-sequencing technique seem to be weak. A theoretical model for the parallel efficiency was also developed and the computations showed good agreement between measured and predicted efficiencies. The performance analysis, as well as, the computations with different grids and on various number of processors showed a reduction in the total efficiency when the number of processors increases and the gird size is considered constant. Furthermore, for a constant number of processors the performance is higher when the grid size (i.e., the load per processor) is increased. Finally, a 64-bit arithmetic results in a computing time increase and a total efficiency reduction.

Acknowledgments

The financial support from the Bavarian Ministry of Education and the Bavarian Science Foundation, is greatly appreciated. The authors would also like to thank Dr. G. Papadopoulos for his comments on the manuscript.

References

Agarwall, R. K., 1989, "Development of a Navier-Stokes Code on a Connection Machine," *Proceedings of the 9th AIAA Computational Fluid Dynamics Conference*, Buffalo, NY, June 13–15, 1989, AIAA Paper 89-1939, pp. 103–108.

Baldwin, B. S., and Lomax, H., 1978, "Thin Layer Approximation and Algebraic Model for Separated Turbulent Flows," AIAA 16th Aerospace Sciences Meeting, 78-257, Huntsville, AL.

Chakravarthy, S. R., "High Resolution Upwind Formulation for the Navier-Stokes Equations," VKI Lecture Series, Computational Fluid Dynamics, 1988-05.

Drikakis, D., and Schreck, E., 1993, "Parallel Multi-Level Calculations for Viscous Compressible Flows," *Proceedings of ASME Fluids Engineering Conference*, June 20–24, Washington, DC, FED-Vol. 156, CFD Algorithms and Applications for Parallel Processors, O. Baysal, and W. Saxena, eds., Book No. H00796-1993.

Eberle, A., 1987, "Characteristic Flux Averaging Approach to the Solution of Euler's Equations," VKI Lecture Series, Computational Fluid Dynamics, 1987-04.

Johnson, D. A., Horstman, C. C., and Bachalo, W. D., 1982, "Comparison Between Experiment and Prediction for a Transonic Turbulent Separated Flow," *AIAA Journal*, Vol. 20, pp. 737–744.

Pelz, R. B., Ecer, A., and Häuser, J., 1993, *Proceedings of the Conference on Parallel Computational Fluid Dynamics '92*, Elsevier Science Publishers.

Reinsch, K. G., Schmidt, W., Ecer, Häuser, A., and Periaux, J., 1992, *Proceedings of Parallel Computational Fluid Dynamics '91*, Elsevier Science Publishers.

Simon, H. D., 1991, "Partitioning of Unstructured Problems for Parallel Processing," *Computing Systems in Engineering*, Vol. 2, No. 2/3, pp. 1356–1480.

Sun, X-H., and Gustafson, J. L., 1991, "Toward a Better Parallel Performance Metric," *Parallel Computing*, Vol. 17, pp. 1093–1109.

A. H. M. Kwong

A. P. Dowling

Cambridge University
Engineering Department,
Trumpington Street,
Cambridge CB2 1PZ, United Kingdom

Unsteady Flow in Diffusers

The flow in a diffuser is unsteady in the range of optimum pressure recovery; diffusers can therefore be a major source of noise in pipework systems. A theory is developed to predict the frequency of this noise and good agreement with experimental results, for both conical and rectangular diffusers, is demonstrated. The acoustics of the duct to which a diffuser is connected are found to have a crucial effect on the unsteady flow within the diffuser, a point which has been overlooked previously in the literature. Once this is recognized, it is possible to reconcile experimental results for air and water diffusers.

1 Introduction

Diffusers are used extensively in pipework systems to slow down a mean flow, converting its kinetic energy into a pressure rise. Much attention has been given to the mean flow in diffusers. That flow is characterized by a nondimensional pressure recovery coefficient $\overline{C}_p$, which is defined to be the mean pressure difference across the diffuser, $\overline{\Delta p}$, non-dimensionalized on the mean dynamic head at inlet to the diffuser, $\rho \overline{u_1^2}/2$. $\overline{C}_p$ is found to depend strongly on the diffuser geometry and the aerodynamic blockage at inlet to the diffuser, and only weakly on other flow parameters like Reynolds number, Mach number, velocity profile and turbulence level at inlet (Japikse, 1984).

Fox and Kline (1962) and Runstadler et al. (1975) give performance maps for rectangular diffusers of length L_D, width W_1 and divergence angle 2θ, as illustrated in Fig. 1. The various flow regimes are described by Kline (1959). For very small divergence angles there is no appreciable reversed flow in the diffuser. But, as 2θ is increased for fixed W_1/L_D, the adverse pressure gradient along the diffuser causes flow separation, with an appreciable back-flow within the diffuser. The flow in the diffuser is then highly unsteady, a phenomenon which is commonly referred to as "transitory stall." As 2θ is increased still further, the stall becomes fully developed. In this regime the main flow follows one wall and is relatively steady. Finally, at still larger divergence angles, the flow separates from both walls forming a jet. McDonald and Fox (1966) identify a similar set of flow regimes and performance maps for conical diffusers.

In a rectangular diffuser with fixed W_1/L_D, the nondimensional pressure recovery is maximal for 2θ approximately equal to 10 deg, the precise value depending on the other flow parameters. This is in the transitory stall regime. Our aim is to predict the frequency of the transitory stall. Diffusers could then be designed to operate in this regime, with their frequency of flow oscillation well away from any structural resonances of the pipework. Diffusers are commonly used to slow down a flow for subsequent burning. The frequencies of any combustion oscillations could also be avoided in a similar way.

Transitory stall has been mentioned by many researchers but few quantitative studies are reported. The earliest was on rectangular water diffusers. Smith and Kline (1974) used flow visualization to determine the period T_s of fluctuations in the exit velocity. They found that their observed periods of transitory stall could be scaled according to $\overline{u}_1 T_s/(L_W \sin 2\theta) = 180 \pm 60$, where L_W is the diffuser wall length. This scaling was derived from limited data, involving just two mean flow speeds and three diffuser wall lengths. In the same paper, Smith and Kline reported four results for air diffusers which were found to have a similar scaling. However, when Smith and Layne (1979) set out to repeat the air diffuser experiments, they found a different behavior. They proposed $\overline{u}_1 T_s/(L_W \sin 2\theta) \simeq 4000$ with 40 percent scatter in the data points, again based on two inlet velocities and three diffuser lengths. A second shorter time-scale ($\overline{u}_1 T_s/(L_W \sin 2\theta) \simeq 1000$) was also observed, contrary to the previous water experiments where only one time-scale was found. Smith (1978) attempted to collapse these stall periods onto a revised parameter. In order to account for the difference between air and water diffusers, he proposed a further scaling on inlet Reynolds number Re_1. By simply multiplying the previous nondimensional parameter by the factor Re_1^{α}, he found that for the longer time-scale, he

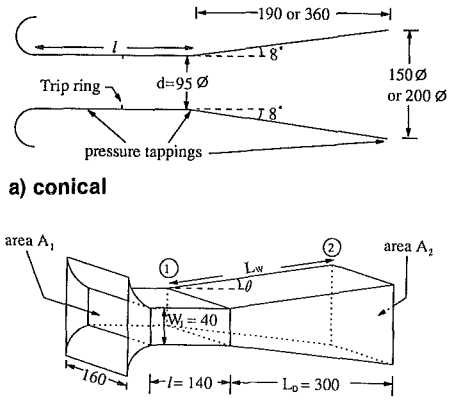

Fig. 1 The dimensions of the diffusers

Contributed by the Fluids Engineering Division for publication in the JOURNAL OF FLUIDS ENGINEERING. Manuscript received by the Fluids Engineering Division March 9, 1993; revised manuscript received March 22, 1994. Associate Technical Editor: R. L. Panton.

could bracket 95 percent of the available data to $S = \bar{u}_1 T_s \mathrm{Re}_1^{\alpha} / (L_W \sin 2\theta) = 0.10 \pm 0.04$, with $\alpha = -0.825$. For the shorter time scale, the same parameter gave $S = 0.026 \pm 0.006$. Smith recommended that this new correlation should be treated with some caution, since it was established using data from only four different Reynolds numbers.

An experimental investigation of transitory stall, in both rectangular and conical air diffusers, is described in Section 2. In these experiments, we find that the stall frequency does not scale on Smith's parameter as the flow conditions change. Moreover, the geometry of the duct to which a diffuser is connected is found to have significant effects on the stall frequency. This leads to the conclusion that transitory stall is not solely a function of the diffuser but also of its unsteady coupling to the connecting devices. Consequently, there is a need for a more careful analysis than a single nondimensional timescale.

A theory is developed in Section 3 to calculate the frequency of transitory stall. It takes full account of the acoustics of the connecting devices and gives good agreement with our experimental frequencies for air diffusers. Moreover, on applying the same theory to Smith and Kline's (1974) experiments, we successfully obtain the stall frequencies in their water experiments.

2 Experiment

Experiments were conducted on both conical and rectangular diffusers. The inlet pipe has a smooth entrance, followed by a section of straight ducting of variable length l and the same cross-section as the diffuser inlet. Trip-rings can be inserted into the inlet pipe to alter the inlet blockage to the diffuser. The diffuser exhausts into a $1.82 \times 1.21 \times 1.21$ m^3 plenum chamber which in turn is connected to an axial blower by 12.5 m of ducting of 0.18 m diameter.

Two conical diffusers were investigated. Each diffuser has divergence angle $2\theta = 16$ deg, inlet diameter $d = 95$ mm. Their length/diameter ratios are 2 and 4, leading to area ratios of 2.4 and 4.5, respectively. The geometries of the two diffusers are summarized in Fig. 1(*a*). These geometries are taken from the performance map produced by McDonald and Fox (1966), where they are reported to be in the "transitory" and "fixed intermittent transitory" stall regimes, respectively. Three different inlet pipe lengths were used, $l = 0$, 200 and 400 mm. The inlet blockage to the diffuser could be varied between 0 and 16 percent by changes in the length of the inlet pipe and/or by the insertion of various trip-rings. The flow in the diffusers was investigated for mean inlet velocities $\bar{u}_1$ in the range 22 to 62 m/s ($\mathrm{Re}_d \simeq 1.4 \times 10^5 - 4.0 \times 10^5$).

Experiments on the rectangular diffuser have concentrated on the effects of diffuser divergence angle. Figure 1(*b*) shows the dimensions of the rectangular diffuser. The diffuser length/inlet height ratio is 7.5 and the inlet aspect ratio is 4. During the experiment, the wall angle 2θ was varied from 8 to 30 deg and the mean inlet velocity from 21 to 47 m/s ($\mathrm{Re}_1 \simeq 5.5 \times 10^4 - 1.3 \times 10^5$), while the inlet blockage was maintained at 13 ± 1 percent.

Pressure measurements are made by two Druck PDCR 800 pressure transducers (range ± 70 mbar with a corresponding output of ± 17 mV). The first stage of amplification uses a low noise OP-27G operational amplifier by Analog Devices. The transducers are connected to the diffuser and the inlet pipe through plastic hoses and tappings of diameter 2.5 mm mounted flush in the walls. At frequencies of interest (less than 25 Hz), attenuation and phase errors induced by these connections are negligible in theory (Tijdeman, 1975). The diffuser inlet gauge pressure, p_1, is measured on the straight inlet pipe immediately upstream of the sloping wall. The exit pressure, p_2, is measured on the sloping wall just before flow is discharged into the plenum chamber. The recovery pressure, Δp, is measured directly by a pressure transducer connected across these two positions. The transducer accuracy, as calibrated by the manufacturer (<0.06 percent full-scale), leads to errors of less than ± 1 percent within our data range.

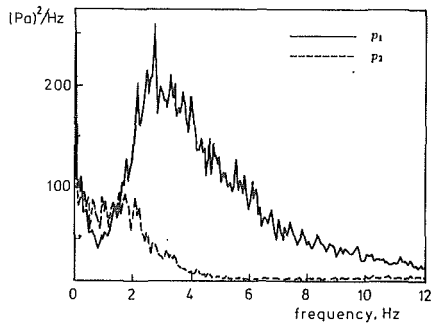

Fig. 2 The power spectral density of pressure fluctuations in a conical diffuser of length/diameter ratio 4, $\bar{u}_1 = 30$ m/s and $l = 400$ mm.

Volume flow rate and inlet velocity may be deduced from the static pressure p_i measured at one inlet diameter (conical) or one inlet width W_1 (rectangular) downstream of the intake end of the straight inlet section (for the $l = 0$ mm case in conical diffuser, p_i is taken to be equal to p_1). Here the area blockage is found by hot-wire measurements to be less than 0.5 percent. By assuming an inviscid uniform flow at this section and neglecting the inertial term in the unsteady Bernoulli's equation, the instantaneous inlet dynamic head can be equated to the instantaneous gauge pressure p_i. Including the uncertainties in pressure measurement, this gives a maximum total error of ± 5 percent in unsteady measurements of the dynamic head and of ± 3 percent in time-averaged inlet velocity and volume flow rate measurements.

Time-history measurements are made by feeding the preamplified transducer signals to a 12-bit Microlink data acquisition system. A 80 Hz cut-off loss-pass anti-aliasing analogue filter is used for each logging channel at the sampling rate of 200 Hz. The maximum error due to quantization is 0.5 percent. Spectral data are collected by a Hewlett-Packard 5420B digital signal analyzer.

Conical Diffuser Results. Typical spectra for p_1 and p_2 are shown in Fig. 2. The power spectral density of p_1 has a peak at around 3 Hz, while fluctuations in p_2 are weaker and contain frequencies from about 4 Hz to the steady state. Comparison of the spectra for different inlet velocities and diffuser configurations shows that the amplitude of the fluctuations increases with increasing inlet velocity and diffuser length, in agreement with Smith and Layne's (1979) observations of rectangular diffusers. The unsteady power is reduced by increasing the inlet blockage.

The dependence on inlet velocity of the frequency of the peak in the p_1-spectrum is summarized in Table 1. In contradiction to Smith's nondimensional scaling, the frequency actually decreases with increasing velocity. The frequency reduces with increasing diffuser length. It is found not to be affected by inlet blockage, but is influenced by the length of the inlet ducting (Table 2). This leads us to believe that the unsteady flow is not solely a function of the diffuser, but that it also depends on the connecting devices.

We introduce an unsteady pressure recovery coefficient, $C_p(t)$, defined to be the instantaneous pressure difference across the diffuser, $\Delta p(t)$, divided by the instantaneous dynamic head at inlet. The pressure difference $\Delta p(t)$ is measured directly. We have already noted that the inlet dynamic head can be deduced from $p_i(t)$ in the inlet pipe with an error of ± 5 percent. Hence $C_p(t) \simeq -\Delta p(t)/p_i(t)$. The time history of the pressure recovery coefficient is shown in Fig. 3. It is unlikely that a total washout of stall occurs, because the in-

Table 1 The variation of the frequency of the peak in the p_1-spectrum, f_s with $\overline{u}_1$ for conical diffuser of length/diameter ratio 4, l = 400 mm.

$\overline{u}_1(m/s)$	Experimental peak frequency (Hz)	Calculated frequency (Hz)
23	3.2	2.98
30	3.0	2.76
36	2.7	2.46
46	2.0	1.84

Table 2 The variation of the frequency of the peak in the p_1-spectrum with l for the conical diffuser of length/diameter ratio 4 and $\overline{u}_1$ = 30 m/s.

$l(mm)$	Experimental peak frequency (Hz)	Calculated frequency (Hz)
0	4.7	4.58
200	3.8	3.34
400	2.7	2.76

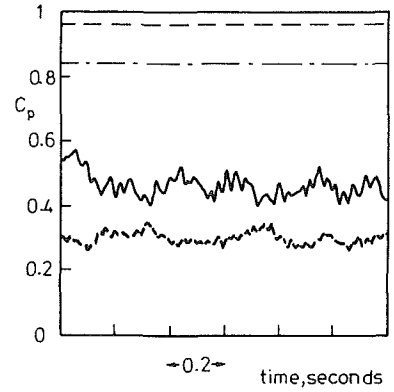

Fig. 3 The pressure recovery coefficient, $C_p = \Delta p/(\rho u_1^2/2)$, for the conical diffusers, $\overline{u}_1$ = 30 m/s, length/diameter ratio 4, — instantaneous C_p, - - ideal C_p; length/diameter ratio 2, · · · instantaneous C_p, - · - · ideal C_p

stantaneous values of C_p are always much less than the ideal values.

Flow visualization, with both tufts and smoke, was used to investigate the stall movement. The tufts were observed to reverse direction over a time interval of several seconds. While the tufts are pointing upstream, indicating reversed flow at those locations, they flicker rapidly both perpendicular to and sideways along the wall at a frequency of several Hertz. The flickering indicates local stall movements, while the reverses in tuft direction must be caused by a major shift in the position of the stall. To clarify the interpretation, smoke was injected at the bottom of the diffuser and a video made of the flow. The smoke is observed either to fill up a whole stall cell or to be carried straight down the diffuser in periods of seconds. Furthermore, at times when the smoke is trapped inside the stall cell, the whole stall can be observed to oscillate in the streamwise direction at a frequency of several Hertz. The most vigorous oscillations, however, are at the upstream edge, where the separation point is seen to move between the throat up to half way along the diffuser. As the smoke in a stall cell at the bottom of the diffuser is washed away, without exception, a stall forms at the top. This is visualized by tufts at the top suddenly reversing direction to point upstream. Therefore, the stall is not washed out, but rather switches intermittently from side to side. This explains why all the measured instantaneous values of C_p are so much less than the ideal values (Fig. 3).

We therefore have two modes of unsteadiness. The first is associated with oscillations of the upstream edge of the stall cell. It has a strong amplitude and a distinctive frequency. The

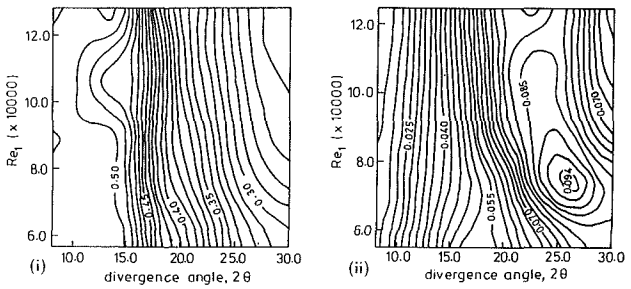

Fig. 4 Contours of (i) C_p and (ii) $C'_{p_{rms}}$ as functions of divergence angle 2θ and inlet Reynolds number for the rectangular diffuser

second mode is a consequence of shifts of the whole stall from one side of the diffuser to the other. It occurs relatively infrequently and intermittently, and only has a weak effect on the value of C_p. Most of our attention is given to the first mode of oscillation which is both stronger and more periodic.

Rectangular Diffuser Results. Flow visualization, with smoke in the rectangular diffuser, shows vigorous oscillation of the upstream edge of the stall cells, just as in the conical diffuser. The stall cells are to be found mostly in the corners and switch from one corner to another over an interval of seconds in an apparently random way.

Measured values of $\overline{C}_p$ and $C'_{p_{rms}}$ are shown in Fig. 4, where $C'_{p_{rms}}$ is the rms value of the pressure rise across the diffuser nondimensionalized on the mean inlet dynamic head (Smith and Layne, 1979). Over the range of 2θ investigated, all instantaneous values of C_p are too low for total stall wash-out and, as for the conical diffuser, the unsteadiness is due to alterations in the stall position. This is in contradiction with Smith and Layne's (1979) suggestion that there are complete stall washouts. However, since their $C'_{p_{rms}}$ is actually slightly smaller than ours (Smith and Layne, 1979, Figs. 2-4), it is likely that their observed low frequency oscillations were a result of stall switches like ours. At small diffuser angles, $2\theta \leq 12.5$ deg, $\overline{C}_p$ rises with increasing 2θ and is independent of Re_1. Maximum recovery occurs at 2θ around 10 to 14 deg. The closely spaced contours from $\overline{C}_p = 0.48$ to 0.35 suggest a rapid growth of stall as 2θ increases from 16 to 22 deg. We see from Fig. 4 (ii) that this is accompanied by a continuous rise in unsteadiness. A similar observation was made by Smith and Layne (1979). The maximum unsteadiness is found to occur at around 2θ = 21 to 26 deg at high Re_1. This agrees with Smith and Layne's observation of maximum unsteadiness for 2θ in the range 20 to 24 deg at high Re_1. The amplitudes of the fluctuations are also comparable.

Figure 5 shows typical power spectral densities of p_1. Just as for the conical diffuser, there is a local peak in the pressure spectrum. For low values of 2θ ($2\theta \leq 16$ deg), this peak occurs around 3 to 5 Hz, and is labeled f_s. A comparison of Fig. 5*a* (i)–(ii) and Fig. 5*b* (i)–(ii) shows that for this range of 2θ the frequency of peak unsteadiness decreases with increasing inlet velocity. A similar observation was made for the 16 deg conical diffuser (Table 1). Higher inlet velocity also tends to make the spectrum broader. Increasing 2θ from 16 to 20 deg leads to an abrupt change in the spectral composition. We have already noted that there is a dramatic drop in $\overline{C}_p$ and a rise in flow unsteadiness in this range. A comparison of Fig. 5*a* (ii) and (iii) or Fig. 5*b* (ii) and (iii) shows that this is accompanied by the spectral peak moving to a higher frequency and becoming broader. For $2\theta \geq 20$ deg, the frequency of peak unsteadiness in p_1 tends to increase for higher inlet velocity as suggested by Smith and Kline's (1974) scaling.

We clearly have two different types of unsteady flow with an abrupt transition between them. For $2\theta \leq 16$ deg, the frequency of peak unsteadiness tends to decrease with inlet

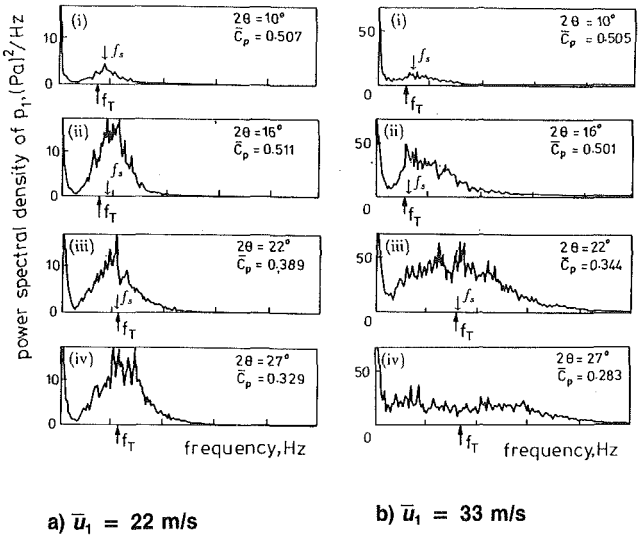

a) $\bar{u}_1$ = 22 m/s b) $\bar{u}_1$ = 33 m/s

Fig. 5 The variation in the spectral density of inlet pressure p_1 with divergence angle 2θ for the rectangular diffuser. f_T is the theoretical frequency, calculated using the steady-stall model in (i), (ii) and the lag-law in (iii), (iv). f_s marks the peak in the pressure (f_s is used in Fig. 6).

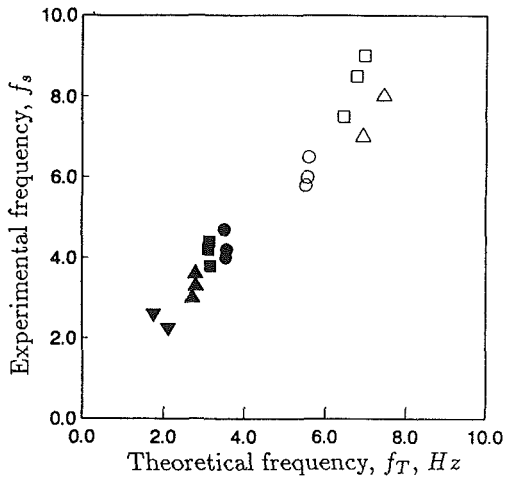

Fig. 6 Comparison of experimental and theoretical frequencies for: • $\bar{u}_1$ = 22 m/s, ■ $\bar{u}_1$ = 29 m/s, ▲ $\bar{u}_1$ = 33 m/s, ▼ $\bar{u}_1$ = 39 m/s. Closed symbols are for $2\theta \leq 16$ deg and are calculated using the steady stall model Eq. (8). Open symbols are for $2\theta \geq 20$ deg and are calculated using the lag-law Eq. (13).

velocity. This is the range of most practical significance because it encompasses the divergence angles giving maximum mean pressure recovery. For $2\theta \geq 20$ deg, the frequencies of oscillation tend to be higher, more broad-band and increase with increasing inlet velocity. Flow visualization shows the stall to be highly unsteady for this range of divergence angles. Some of these trends are summarized in Fig. 6.

3 Theory

Since the fluctuations are of low frequency, the inlet pipe and the diffuser are so compact that the flow in them can be treated as incompressible. Application of the unsteady form of Bernoulli's equation along a streamline from ambient conditions to the inlet of the diffuser gives

$$p_1 + \frac{1}{2}\rho u_1^2 + \rho \frac{\partial}{\partial t}\int_0^1 \mathbf{u}\cdot\mathbf{dl} = p_a. \tag{1}$$

Since the inlet pipe is straight and of length l with uniform cross-sectional area, this may be rewritten for linear perturbations of frequency ω as

$$\hat{p}_1 + \rho\bar{u}_1\hat{u}_1 + \rho i\omega L_{in}\hat{u}_1 = 0, \tag{2}$$

where the overbar denotes a mean value and the circumflex a complex amplitude. L_{in} is the effective length of the inlet pipe. Levine and Schwinger (1948) showed that $L_{in} = l + 0.3D$ for an inlet pipe of circular cross-section. We therefore take $L_{in} = l + 0.3(4A_1/\pi)^{1/2}$ for a rectangular diffuser of inlet area A_1 and modest aspect ratio. Although this end correction is found to have little effect on the numerical results.

Even within the diffuser the flow outside the stall cell can be considered to be inviscid. Let u_{c_2} denote the velocity at exit from the diffuser in this inviscid core flow. Then Bernoulli's equation applied along the diffuser to the core flow gives

$$p_1 + \frac{1}{2}\rho u_1^2 = p_2 + \frac{1}{2}\rho u_{c_2}^2 + \rho\frac{\partial}{\partial t}\int_1^2 u_c dx. \tag{3}$$

If we assume that the velocity varies approximately linearly along the diffuser core flow, this equation simplifies to

$$\hat{p}_1 + \rho\bar{u}_1\hat{u}_1 = \hat{p}_2 + \rho\bar{u}_{c_2}\hat{u}_{c_2} + \frac{1}{2}i\omega\rho L(\hat{u}_1 + \hat{u}_{c_2}), \tag{4}$$

where L is the effective length of the diffuser. The end correction for low frequency oscillations in a circular pipe of diameter D, with a mean exit flow, is $0.13D$ (Rienstra, 1981). We therefore take $L = L_D + 0.13(4\bar{A}_{c_2}/\pi)^{1/2}$, where $\bar{A}_{c_2}$ is the cross-sectional area of core flow at the diffuser exit. Although once again the end correction does not alter the results significantly.

The plenum volume V_p is sufficiently large for compressibility effects to be significant. Essentially, it behaves like the bulb of a Helmholtz resonator. Applying continuity from the diffuser entrance to the plenum exit yields $\rho A_1 u_1 = V_p(\partial\rho_p/\partial t)$ when the flow at the plenum exit is steady. For fluctuations of frequency ω, this can be rewritten in the form

$$\rho A_1\hat{u}_1 - \frac{i\omega V_p}{c^2}\hat{p}_2 = 0, \tag{5}$$

where c is the speed of sound.

The transfer function between p_2 and u_1 can be measured to confirm this relationship. We find that Eq. (5) predicts this transfer function well for all but very low frequencies (<2 Hz, see Kwong, 1992, Fig. 2.39). For these very low frequencies the flow at the plenum exit is unsteady and the propagation of acoustic waves along the exhaust ducting from the plenum exit to the blower must be taken into account. Once these are included the theoretical transfer function has a more complicated form and agrees well with the low frequency measurements (Kwong, 1992, Fig. 2.38).

One further equation, describing the unsteady flow in the diffuser, is required to determine the frequency of stall oscillations. In our experiments on the conical diffuser and the rectangular diffuser ($2\theta \leq 16$ deg), we found that the unsteadiness was primarily due to the stall altering position within the diffuser. Our first stall model assumes volume of the stall cell within the diffuser, the rate of entrainment into the stall cell and the core flow exit area to be constant. Then continuity gives

$$u_1 A_1 = u_{c_2} A_{c_2}, \tag{6}$$

where the core exit area A_{c_2} is equal to $A_1/(1 - \bar{C}_p)^{1/2}$. We refer to this as the "steady stall" model.

Elimination of $\hat{p}_1$, $\hat{p}_2$, $\hat{u}_1$, and $\hat{u}_{c_2}$ from Eqs. (2), (4), (5), and (6) leads to an eigenvalue equation for ω, the frequency of oscillation. The roots are

$$\omega = \pm\left[\omega_0^2 - \frac{\bar{u}_1^2}{4L_{eq}^2}\left(\frac{A_1}{A_{c_2}}\right)^4\right]^{1/2} + \frac{i}{2}\frac{\bar{u}_1}{L_{eq}}\left[\frac{A_1}{A_{c_2}}\right]^2. \tag{7}$$

L_{eq} is the equivalent length of the diffuser and inlet pipe:

$$L_{eq} = L_{in} + \frac{1}{2} L\left(1 + \frac{A_1}{A_{c_2}}\right), \tag{8}$$

and $\omega_0 = c(A_1/L_{eq}V_p)^{1/2}$ is the Helmholtz resonance frequency.

Note that when there is no mean flow the eigenfrequency is just the Helmholtz resonance frequency. In general, Real(ω) gives the frequency of oscillation, while Im(ω) describes the damping. The frequency, f_T, given by Eq. (7) agrees well with the measurements on the conical diffuser. It accurately predicts the variation of frequency with inlet velocity and inlet length (Tables 1 and 2). It also gives reasonable agreement with the observed frequency of oscillation in rectangular diffusers with small divergence angles ($2\theta \leq 16$ deg) as shown by the results in Figs. 5 and 6. In particular, the predicted frequency decreases as $\bar{u}_1$ increases in agreement with the experimental results. Moreover, it is clear from Eq. (7) that the nondimensional damping factor increases with inlet velocity. This is compatible with the broadening of the frequency spectrum at higher $\bar{u}_1$, as noted from Fig. 5.

At large divergence angles ($2\theta \geq 20$ deg), flow visualization showed the flow in the rectangular diffuser to be highly unsteady. In this regime we do not believe that fluctuations in u_1 are immediately mimicked by changes in u_{c_2} as in the "steady stall" model. Instead, we expect a sudden increase in u_1 to either cause the stall cell to retreat downstream or to increase the rate of entrainment of stalled fluid into the core. In either case, u_{c_2} is prevented from building up suddenly. We describe this time delay in the response of u_{c_2} through a lag equation:

$$\tau_d \frac{du_{c_2}}{dt} = u_{c_{2ss}} - u_{c_2}. \tag{9}$$

$u_{c_{2ss}}$ is the steady-state value of u_{c_2} corresponding to the instantaneous value of u_1 (i.e., $u_{c_{2ss}} = u_1 A_1/A_{c_2}$). Note that for $\tau_d = 0$, Eq. (9) reduces to the steady stall model. In general, τ_d is the time constant of the diffuser's response. Typically we might expect it to be of the order of the travel time through the diffuser, i.e., of order $L_d/\bar{u}_c$. A similar lag equation has been used by Greitzer (1976) to describe the time delay between changes in pressure ratio and mass flow rate in a compressor.

As a check on the lag equation, we applied it to the nonlinear build up of stall in a wide-angled rectangular diffuser. Stall can be virtually eliminated from this diffuser by using wall jets to inject high momentum fluid into the wall region of the diffuser. When the jets are switched off, the stall builds up. Using the measured $u_1(t)$, Eq. (9) can be integrated with respect to time to give $u_{c_2}(t)$. A prediction for $\Delta p(t)$ then follows from the unsteady Bernoulli Eqs. (1) and (3). For $\tau_d = L_d/\bar{u}_{c_2}$, this prediction closely matches the measured $\Delta p(t)$ (Fig. 7).

For linear perturbations of frequency ω the lag law in Eq. (9) simplifies to

$$\hat{u}_{c_2} = \frac{A_1}{A_{c_2}} \frac{\hat{u}_1}{1 + i\omega\tau_d}. \tag{10}$$

When this is combined with Eqs. (2), (4), and (5) it leads to a cubic equation with real coefficients for $i\omega$. One root of ω is purely imaginary and describes a decaying mode. The other two roots are, in general, complex. Then Real(ω) gives the frequency of oscillation and Im(ω) the damping. This frequency is plotted in Figs. 5 and 6 for a range of experimental conditions. There is reasonably good agreement between the measured frequency of peak unsteadiness and that predicted.

We do not have enough information about the geometry to compare Smith and Layne's (1979) air diffuser results with theory. They report very low frequency oscillations with periods of seconds. Their plenum of volume 3.5 m^3 would not be able to isolate these low frequency disturbances in the diffuser from the unsteady behavior of the compressor and its ducting. Details of the compressor characteristic and the ducting from the plenum to the compressor are needed to calculate such low frequency oscillations.

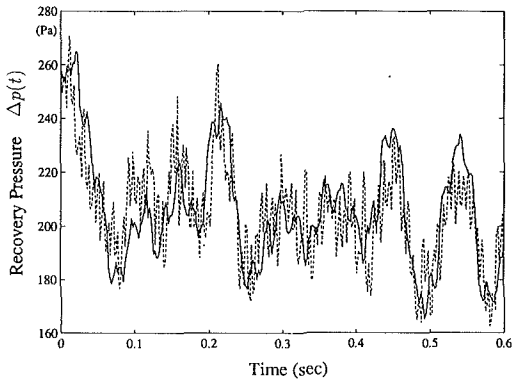

Fig. 7 The time history of $\Delta p(t)$ during stall build up — measured; · · · · calculated from measured $u_1(t)$ using the lag-law

Smith and Kline's (1974) water diffuser exhausts into a tank of surface area A_T, the level of the water in the tank being controlled by a weir of width b. Continuity applied from the diffuser inlet to the weir gives

$$u_1 A_1 = A_T \frac{dh}{dt} + Q_o, \tag{11}$$

where h is the height of the free surface above the weir and Q_o the volume flow rate over the weir. For very low frequency oscillations we can use the quasi-steady result, $Q_o = 2C_D bh(2gh)^{1/2}/3$ (Massey, 1983), where C_D is the discharge coefficient. Linearizing Eq. (11) leads to

$$\hat{u}_1 A_1 = [A_T i\omega + C_D b(2g\bar{h})^{1/2}]\hat{h}, \tag{12}$$

for linear perturbations of frequency ω. Now for low frequency fluctuations the pressure at the diffuser exit, $\hat{p}_2$, is equal to $\rho g\hat{h}$, and hence Eq. (12) can be written as

$$\rho\hat{u}_1 A_1 = \left[\frac{A_T i\omega}{g} + C_D b\left(\frac{2\bar{h}}{g}\right)^{1/2}\right]\hat{p}_2. \tag{13}$$

The first term on the right-hand side of Eq. (13) accounts for the rate of storage of water in the tank, while the last term describes the unsteady mass flowing over the weir.

The frequency of oscillation follows from combining Eq. (13) with Eqs. (2), (4), and (6):

$$\omega = \left[\omega_1^2 - \frac{1}{4}\left(\frac{\bar{u}_1 A_1^2}{L_{eq}A_{c_2}^2} - \frac{C_D b(2g\bar{h})^{1/2}}{A_T}\right)^2\right]^{1/2} + \frac{i}{2}\left(\frac{\bar{u}_1 A_1^2}{L_{eq}A_{c_2}^2} + \frac{C_D b(2g\bar{h})^{1/2}}{A_T}\right) \tag{14}$$

where L_{eq} is defined in Eq. (8) and $\omega_1 = (gA_1/L_{eq}A_T)^{1/2}$. With the mean depth $\bar{H}_T$ and volume of water V_T in the tank, ω_1 can be rewritten as $(gA_1\bar{H}_T/L_{eq}V_T)^{1/2}$. If we replace $g\bar{H}_T$ by c^2, this is directly comparable to the Helmholtz resonance frequency $\omega_o = c(A_1/L_{eq}V_p)^{1/2}$ defined earlier. It is now apparent why the transitory stall frequency in air and water diffusers depends in such a different way on the flow parameters. It is not a Reynolds number effect as postulated by Smith (1978). Rather it occurs because of the different ways in which the mass fluctuates in the downstream plenum, compressibility effects being important in air, and oscillations of the free surface in water. The difference between the two wave speeds describing these effects is considerable, e.g., for water depth of $\simeq 0.5$ m, $c/(gH_T)^{1/2} \approx 150$.

We can check the frequency of oscillation predicted by Eq.

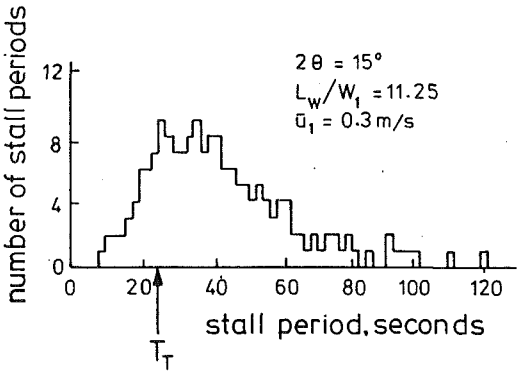

Fig. 8 Histogram of stall periods for a water diffuser (from Smith and Kline, 1974). T_T is the theoretical period calculated from Eq. (14).

(14) by comparing it with Smith and Kline's (1974) experimental results. In their Fig. 4 (reproduced here in Fig. 8) they give a histogram for the stall periods of a water diffuser with $\bar{u}_1 = 0.3$ m/s, $W_1 = 25.4$ mm, $L_{in} = 0.3$ m, $2\theta = 15$ deg, $L_W/W_1 = 11.25$ and an inlet aspect ratio of 10. The pressure recovery coefficient is not reported and we take $\bar{C}_p = 0.5$. The sketch of the discharge tank (Smith and Kline, 1974, Fig. 2) suggests $b = 0.6$ m and $A_T = 1.5$ m^2. For a typical discharge coefficient $C_D = 0.6$ (Massey, 1983), $\bar{h} = 15$ mm follows from the mean of Eq. (11). Substitution of these values of the parameters into Eq. (14) leads to a period of oscillation of 23.5 seconds. We see from a comparison with the data in Fig. 8 that this agrees well with Smith and Kline's observations.

4 Conclusions

The frequency of transitory stall oscillations is affected by the unsteady coupling between the diffuser and other pipework components. Having recognized this, a theory has been developed that satisfactorily predicts the frequency for both air and water diffusers.

We have observed an abrupt change in the nature of the unsteady flow in a diffuser as the divergence angle is increased. The change happens as 2θ increases from about 16 to 20 deg and accompanies a rapid drop in mean pressure recovery. For $2\theta \leq 16$ deg, we have developed a model to describe the system theoretically. This is the range of most practical significance because it includes the divergence angles which give maximum mean pressure recovery. The theory simply assumes the effective core passage area within the diffuser to be independent of time. Predicted frequencies of oscillation follow from coupling the unsteady flow in the diffuser to the appropriate boundary condition. Good agreement is found between the measured frequencies of peak unsteadiness and these predictions. For large divergence angles, $2\theta \geq 20$ deg, the frequencies of oscillation tend to be higher and the spectrum is more broadband. Flow visualization shows the stall to be highly unsteady and stall motion needs to be included into the theoretical model. We describe this by a simple lag law and once again obtain satisfactory agreement with the experimental results.

Acknowledgment

This work was carried out while A. H. M. K. was in receipt of studentships from Magdalene College Cambridge and the CVCP. This financial support is gratefully acknowledged.

References

Fox, R. W., and Kline, S. J., 1962, "Flow Regime Data and Design Methods for Curved Subsonic Diffusers," ASME *Journal of Basic Engineering*, Vol. 84, pp. 303–312.

Greitzer, E. M., 1976, "Surge and Rotating Stall in Axial Flow Compressors. Part I: Theoretical Compression System Model," ASME *Journal of Engineering for Power*, Vol. 98, pp. 190–217.

Japikse, D., 1984, "Turbomachinery Diffuser Design Technology," The Design Technology Series, Concepts ETI, Vermont.

Kline, S. J., 1959, "On the Nature of Stall," ASME *Journal of Basic Engineering*, Vol. 81, pp. 305–320.

Kwong, A. H. M., 1992, "Active Boundary Layer Control in Air Diffusers," Ph.D. thesis, Cambridge University.

Levine, H., and Schwinger, J., 1948, "On the Radiation of Sound From an Unflanged Circular Pipe," *Physical Review*, Vol. 73, pp. 383–406.

Massey, B. S., 1983, *Mechanics of Fluids*, Van Nostrand Reinhold.

McDonald, A. T., and Fox, R. W., 1966, "An Experimental Investigation of Incompressible Flow in Conical Diffusers," *International Journal of Mechanical Science*, Vol. 8, pp. 125–139.

Smith, C. R., 1978, "Transitory Stall Time-Scales for Plane-Wall Air Diffusers," ASME JOURNAL OF FLUIDS ENGINEERING, Vol. 100, pp. 133–135.

Smith, C. R., and Kline, S. J., 1974, "An Experimental Investigation of the Transitory Stall Regime in Two-dimensional Diffusers," ASME JOURNAL OF FLUIDS ENGINEERING, Vol. 96, pp. 11–15.

Smith, C. R., and Layne, J. L., 1979, "An Experimental Investigation of Flow Unsteadiness Generated by Transitory Stall in Plane-Wall Diffusers," ASME JOURNAL OF FLUIDS ENGINEERING, Vol. 101, pp. 181–185.

Rienstra, S. W., 1987, "On the Acoustic Implications of Vortex Shedding from an Exhaust Pipe," ASME *Journal of Engineering for Industry*, Vol. 103, pp. 378–384.

Runstadler, P. W., Dolan, F. X., and Dean, R. C., Diffuser Data Book, TN-186 Creare Inc. Science and Technology, 1975.

Tijdeman, H., 1975, "On the Propagation of Sound Waves in Cylindrical Tubes," *Journal of Sound and Vibration*, Vol. 39, pp. 1–33.

Measurements of the Turbulence Structure Downstream of a Tube Bundle at High Reynolds Numbers

U. Karnik
Novacor Research & Technology Corporation,
2928-16 St., N.E.
Calgary, Alberta
Canada T2E 7K7

Mean and turbulent velocity profiles are measured in natural gas at a static pressure of approximately 5200 kPa and a Reynolds number of around 7×10^6. These measurements are obtained by conventional hot film anemometry suitably modified for use in a natural gas environment. Measurements are taken in a 102.26 mm nominal diameter pipe following a development length of around 76D. The mean velocity profile and the turbulence intensities at this location are typical for a fully developed pipe flow. Further, measurements downstream of a 19 tube bundle flow conditioner are also presented. The tube bundle is traversed downstream of a 90 degree, long radius ($r = 1.5D$) elbow and the measurements are taken at 19D downstream of the elbow exit. Measurements include those of the axial mean and turbulent velocities and the integral length scales. It is found that the decay of turbulence is slower and the magnitude of the length scale is smaller in comparison to measurements at lower Reynolds numbers. Orifice meter comparisons, performed in a 19D test section (meter run), confirm earlier findings that turbulence is one of the factors that affects orifice meter accuracy.

Introduction

Past research, mostly initiated by the natural gas industry, has established a correlation between mean velocity profiles and orifice metering accuracy. Recently, Karnik et al. (1994) have postulated that orifice metering error can also be attributed to turbulence. Following their measurements in an air loop ($\text{Re} \approx 1 \times 10^5$) they conclude that for the same mean velocity profile higher turbulence intensity could result in a higher pressure difference across the orifice plate and hence a lower discharge coefficient (C_d) and vice versa.

Turbulence profiles have also been measured downstream of installations and tube bundles by Morrow and Park (1992) and Mattingly and Yeh (1991). The former use a single hot film in a nitrogen loop ($\text{Re} \approx 9 \times 10^5$) where as the latter use LDV in a water loop ($\text{Re} \approx 1 \times 10^5$). Some measurements of Morrow and Park (1992) and Park et al. (1992) support the above theory. For example, Park et al. (1992) state that in one of their experiments, a nearly ideal mean velocity profile with a turbulence intensity significantly lower than Laufer's reference value resulted in a +0.45 percent shift in C_d. Also, Morrow and Park (1992) show measurements for two configurations where although the mean velocity profiles are similar the turbulence intensities are quite different. If the hypothesis proposed by Karnik et al. (1994) is applied then their measured shift in C_d can be predicted.

Thus, it appears that turbulence is indeed one of the factors responsible for metering error. Measurements at lower Reynolds numbers are usually extrapolated to higher Reynolds numbers. However, this extrapolation involves some uncertainty, particularly if high accuracy is desired. Hence, it was thought worthwhile to explore the measurement of turbulence intensity in natural gas at conditions typical for the natural gas industry.

Experimental Facility

Experiments were conducted in a 102.26 mm nominal diameter pipe loop at NOVA's gas dynamic test facility. The static pressure was around 5200 kPa. At an average velocity of around 16.6 m/s, the pipe Reynolds number was evaluated to be 7×10^6. The experimental set up is shown in Fig. 1. The reference profile was measured at the exit of a 76D, specially fabricated, single honed spool piece with a measured roughness of around 2.54 μm. (100 μin.). In the case of the two elbows in plane, the separation between the elbows was around 10D and the profiles downstream of the second elbow were similar to those of a single 90 degree elbow (Karnik et al., 1991). A single elbow ($r = 1.5D$) is a typical installation prevalent in the natural gas industry. A 19-tube bundle, meeting AGA standards, is commonly used to eliminate flow non-uniformities resulting from such installations. The present tube bundle consisted of 19 tubes arranged in a concentric pattern. Each tube had an internal diameter of 18.16mm and an outside diameter of 20.70 mm.

The traversing assembly (positioning uncertainty of ± 0.7 mm.) shown in Fig. 2 allowed the use of two platinum hot films and their accompanying Pitot-static tubes. This arrangement provided the capability of near wall measurements. The hot films were powered by means of a constant temperature anemometer via an intrinsically safe barrier. The barrier en-

Contributed by the Fluids Engineering Division for publication in the JOURNAL OF FLUIDS ENGINEERING. Manuscript received by the Fluids Engineering Division June 9, 1993; revised manuscript received March 21, 1994. Associate Technical Editor: R. Arndt.

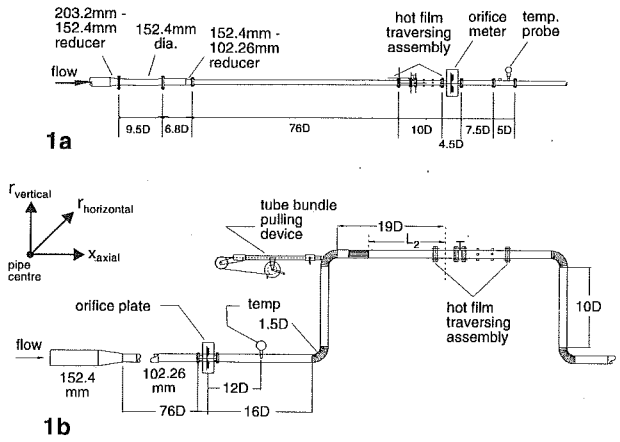

Fig. 1 Experimental facility

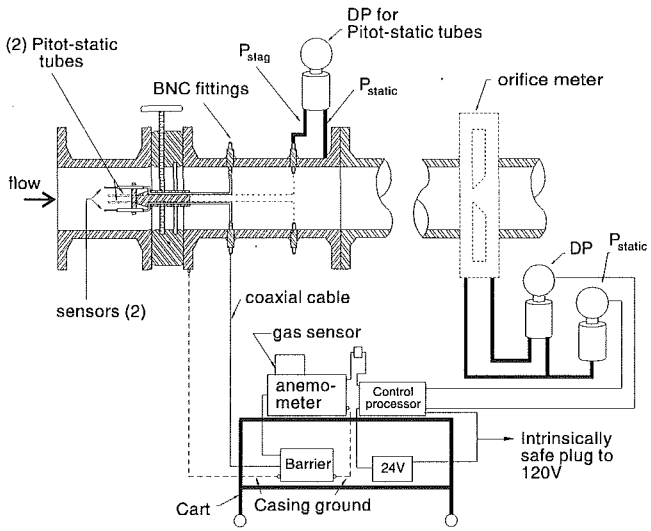

Fig. 2 Instrumentation at the NOVA gas dynamic test facility

sured that the total energy supplied to the hot film was within safe limits. In order to ensure that, in the worst case, the hot film temperature did not run away to values beyond auto-ignition, the power to the anemometer was controlled by means of a control processor. The control processor was triggered by means of the pressure difference across a reference orifice plate and the static pressure in the pipe. The former ensured that there was always sufficient flow over the hot film to cool it and the latter ensured that the static pressure was in the range used for the heat transfer calculations.

The hot film signals were corrected for departures of density and temperature from calibration conditions. The gas temperature was monitored by means of a thermowell accurate to within 0.1 °C. The changes in the gas composition were insignificant and the hot film signal was not corrected for the same. The output from the anemometer was filtered at around 5 kHz and the amplified signal was sampled at frequencies above the Nyquist requirement to prevent aliasing. In order to obtain reliable statistics, 50 records each consisting of 1024 samples were stored for post processing.

The dynamic pressure from the Pitot-static tubes was measured by means of a differential pressure transmitter (range ≈ 25 kPa). Note that the static holes were located on the tube. At the orifice plate, the differential pressure was measured by means of a differential transmitter (range ≈ 50kPa) whereas the static pressure at the wall was measured by means of a static pressure transmitter (range ≈ 6900 kPa). The transmitters had an accuracy of 0.1 percent of range.

Calibration

Ideally, the calibration of a hot film probe should be performed in uniform flow with low turbulence intensity. However, given the difficulties involved with frequent piping changes, it was decided that the hot films be calibrated in situ.

The mean velocity profile at 76D, measured by means of the Pitot-static tubes, indicated that the profile was symmetric. Hence, each hot film was calibrated with respect to its closest Pitot-static tube. The probes were positioned such that the hot film and the Pitot-static tube were equally spaced about the pipe center. This ensured that they were subjected to the same velocity. The maximum possible error in velocity, due to positioning inaccuracy, by adopting such a procedure was estimated to be around 0.6 percent.

In the case of the sliding tube bundle, calibration was performed with the tube bundle at $L_2 = 0.4D$, since the velocity in the core region was nearly uniform. The possible error in velocity resulting from positioning inaccuracy and departure from uniformity was estimated to be, at worst, around 1.5 percent.

To account for the fact that the flow is turbulent, with an intensity of around 4 percent of the centerline velocity, the data for calibration was sampled such that 10,240 data points were averaged for a period of 10.24 s. A typical calibration of the two sensors is shown in Fig. 3. The response of voltage to velocity appears to be nearly linear which is unlike a typical hot film signal. However, this is not surprising, since the cooling rates in the present facility are very high when compared to conventional measurements at ambient conditions. A typical rms error on the calibration curve is around 0.1 m/s.

Nomenclature

C = correction for ϵ; a function of ϵ^+
C_d = orifice discharge coefficient
D = pipe diameter
E = anemometer bridge output
L_2 = distance from tube bundle exit to orifice/hot film
L_e = entrance length
L_{xx} = Eulerian axial integral length scale
R = pipe radius
Re = Reynolds number based on pipe diameter
R_{xx} = axial auto correlation function
U = local mean axial velocity
U_{cl} = centerline mean axial velocity
$c(\xi,f)$ = Bouge and Metzner correction coefficient
f = Darcy friction factor
n = exponent in the velocity profile power law
r = radial distance from the pipe center = $1 - y$
u = instantaneous fluctuating axial velocity
u_* = friction velocity
u^+ = U/u_*
u' = rms axial turbulent velocity
x = axial distance
y = distance from the pipe wall
y^+ = yu_*/ν
ϵ = pipe roughness height
ϵ^+ = $\epsilon u_*/\nu$
τ = temporal separation
ν = fluid kinematic viscosity
ξ = y/R

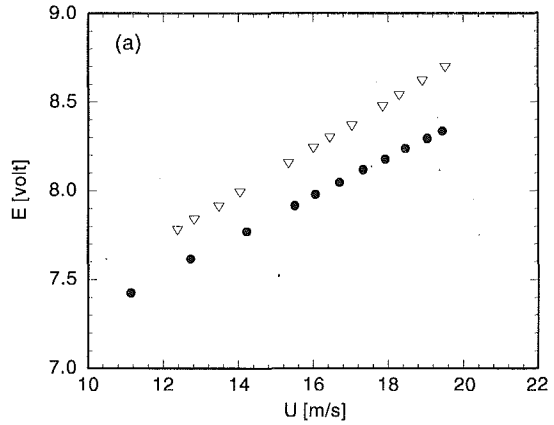

Fig. 3 Calibration of hot films in natural gas. • hot film 1; ▽ hot film 2

Fully Developed Flow

Velocity Profiles. A commonly accepted expression governing the velocity profile for a fully developed flow is

$$\frac{U}{U_{cl}} = \left[\frac{y}{R}\right]^{1/n}. \tag{1}$$

The value of n, which is usually dependent on the Reynolds number and friction factor, is empirically determined by fitting curves to experimental data obtained at different Reynolds numbers. Nikuradse's (1932) measurements were used to obtain some typical values of n (see Schlichting, 1979). The maximum Reynolds number covered was 3.2×10^6. Another empirical method would be to estimate n via the friction factor (Nunner, 1956, reported by Hinze, 1975) as

$$n = \frac{1}{\sqrt{f}}. \tag{2}$$

The above equation was obtained by curve fitting the smooth and rough pipe experimental data of Nunner (1956) and Nikuradse (1932, 1933) as reported by Hinze (1975). The expression is valid and fairly accurate for $f < 0.1$. However, it is important to accurately determine the value of the friction factor for the given situation.

The friction factor can be evaluated accurately by measuring the pressure drop along the test section. In the absence of such measurements, the Colebrook (1939) equation, which is identical to the Moody (1944) diagram, can be used if the relative roughness of the pipe and the Reynolds number are known. The Colebrook equation is given as

$$\frac{1}{\sqrt{f}} = -2.0 \log\left[\frac{\epsilon/D}{3.7} + \frac{2.51}{(\mathrm{Re})f^{1/2}}\right]. \tag{3}$$

In the present case, by honing the pipe, a measured roughness of around 2.54 μm (100 μ in.) was achieved. In the range $0.635\ \mu\mathrm{m} < \epsilon < 5.08\ \mu\mathrm{m}$, the value of n, as predicted by equation (2), is bounded by $10.5 < n < 9.5$.

The power law has a deficiency in the fact that its application cannot be extended to the center of the pipe. Also, the value of n is a function of the Reynolds number. In order to present a universal velocity profile applicable to all Reynolds number, the logarithmic law was proposed. The general form of the logarithmic law for smooth pipes is

$$u^+ = A \log(y^+) + B \tag{4}$$

The values of the constants A and B are determined by fitting Eq. (4) to available experimental data (see Clauser, 1956; Patel, 1965; Hinze, 1975; and Schlichting, 1979 among others). There appears to be no consensus on the exact value of these constants. This is to be expected since the prevailing experimental conditions for the available data may vary slightly in each case.

A drawback of Eq. (4) is that, firstly, it does not have a zero derivative at the center of the pipe and more importantly the data in the outer layer deviate from the equation significantly (Clauser, 1956; Patel, 1965; Hinze, 1975; White, 1984). To account for this fact, a number of corrections exist (see Hinze, 1975) which can be applied to the above equation. The one most commonly used by the natural gas industry (for example, Morrow and Park, 1992) is the one presented by Bouge and Metzner (1963). This correction modifies, Eq. (4) as

$$u^+ = 5.57 \log(y^+) + 5.57 + c(\xi, f). \tag{5}$$

where the correction coefficient is given by

$$c(\xi, f) = 0.05\sqrt{\frac{8}{f}} \exp\left(-\frac{(\xi - 0.8)^2}{0.15}\right). \tag{6}$$

The constants in Eq. (6) and the correction coefficient were determined such that they fitted the smooth pipe data of Laufer (1954) and Nikuradse (1932).

To account for pipe roughness, Eq. (6) has to be further corrected. The effect of pipe roughness (Clauser, 1956; Schlichting, 1979; White, 1984) is a constant offset in the logarithmic law. Thus, the correction is usually applied in the form of a subtraction to the constant B in the logarithmic law. The magnitude of the correction is dependent on the nondimensional roughness of the pipe (ϵ^+) and it takes the form (Schlichting, 1979).

$$\Delta B = A \log(\epsilon^+) - C \tag{7}$$

Thus, the velocity profile given by Eq. (5) can be re-written as

$$u^+ = 5.57 \log\left(\frac{y}{\epsilon}\right) + 5.57 + c(\xi, f) + C \tag{8}$$

In the present case, for a roughness 2.54 μm, the value of ϵ^+ is around 6.34. This value implies that the present measurements are near the lower limit of the transition region ($5 < \epsilon^+ \leq 70$). Using the data of Nikuradse (1932, 1933) as presented by Schlichting (1979), the value of C is around 4.0.

Measurements

Reference Profiles. In order to establish that hot film anemometry could be successfully used in natural gas at elevated pressures, it was decided that the technique should be tested in a fully developed flow. For a Reynolds number of 7×10^6, empirical expressions (White, 1986) estimate the entrance length to be around 61D. It was possible to fabricate a single unflanged spool piece which was 76D long. This length was believed to be sufficient to achieve a fully developed flow.

The mean velocity profiles taken simultaneously by the hot films and the Pitot-static tubes are shown in Fig. 4. The measurements with the Pitot-static tubes serve as a confirmation of the mean velocity profile measured by the hot film. The uncertainty in the measurement of velocity with the Pitot-tube is estimated to be ± 0.5 percent.

In order to account for discrepancies due to possible drifts in flow rate during the traverse, the velocity at each point was normalized with the average velocity measured by means of a reference orifice plate. Further, due to practical difficulties involved in the calibration of the hot films, an accurate estimation of the absolute velocity was not to be expected. In some cases, the velocity measured by the hot film and the Pitot-static tube disagreed by almost four percent. Thus, to minimize the magnitude of the error due differences in the measuring techniques or drifts in the hot film calibration, the velocity ratios at each location were normalized with the measured centerline velocity ratio.

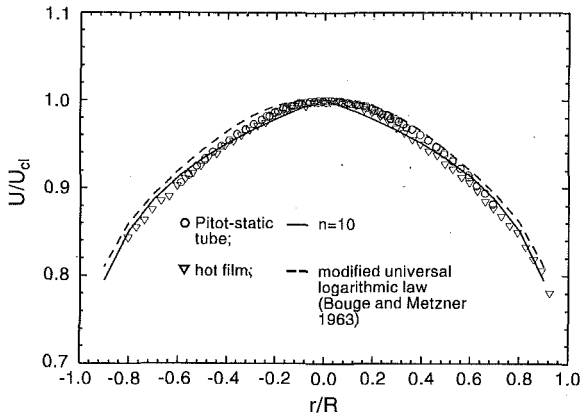

Fig. 4 Mean velocity profile at reference location (vertical traverse)

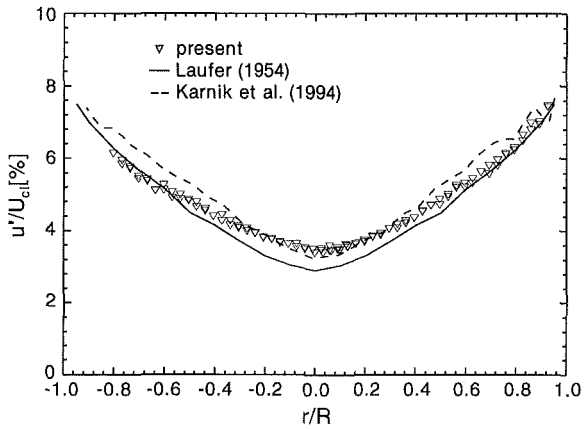

Fig. 5 Axial turbulence intensity at reference location (vertical traverse)

It can be seen that the profile measured with the hot films is comparable to that measured with the Pitot-static tubes. The profiles are symmetric and a regression fit to the data indicates that the value of n is around 9.5. For the regression, the data near the core were omitted since the power law is not valid in this region. If one uses Eq. (2), with a value of 2.54 μm as the roughness in the Colebrook equation, then, for Re = 7×10^6, the predicted value of n for a fully developed flow is 10.0. This is in reasonable agreement with the present data. The present data are also compatible with Eq. (8). Thus, for all practical cases, this profile can be considered to be fully developed.

Measurements of the rms velocities normalized by the centerline mean velocity are shown in Fig. 5. The measurement uncertainty in the turbulence intensity is around ± 5 percent. Also, shown alongside are the measurements taken in the air loop by Karnik et al. (1994) and those of Laufer (1954). It can be seen that the present measurements are comparable to the generally accepted values in a fully developed flow. If the turbulence intensity is used as an indication, then the present flow can be accepted to be fully developed.

The integral length scale is a measure of the typical size of the energy containing eddies of the flow. It is also sometimes used to estimate the *mixing length scale.* The measure of the length scale is of particular interest to researchers attempting to simulate such a flow with computational codes. In the present investigation, the Eulerian integral length scale of the axial velocity component in the axial direction is evaluated from the temporal auto correlation coefficient by using Taylor's *frozen flow* approximation as

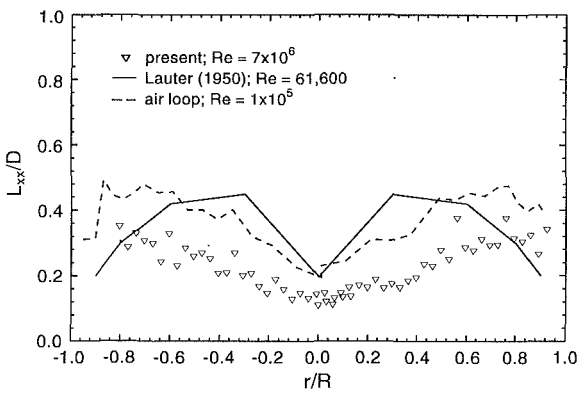

Fig. 6 Integral length scale in a fully developed pipe flow

$$L_{xx} = U \int_0^\infty R_{xx}(\tau) d\tau \tag{9}$$

where τ is the time delay. The temporal auto correlation coefficient, R_{xx}, defined as

$$R_{xx}(\tau) = \frac{\overline{u(t)u(t+\tau)}}{u'^2} \tag{10}$$

is evaluated from discrete data and integrated to the first zero. The accuracy of this procedure has been documented by Comte-Bellot and Corrsin (1971) and it has been successfully used, for example, by Tavoularis and Corrsin (1981) and Tavoularis and Karnik (1989) in uniformly sheared flows and Sreenivasan et al. (1980) in a grid generated, nearly isotropic turbulent flow. It has been shown by Tavoularis and Corrsin, (1981) that in the fully turbulent region, the structure of the pipe flow is quite similar to a uniformly sheared turbulent flow.

Measurements of the length scale (uncertainty $\approx \pm 10$ percent) in the present flow and in the air loop are presented in Fig. 6 along with Laufer's (1950) data for a fully developed channel flow. Although the data obtained from the air loop is comparable to Laufer's data, the magnitude of the length scale appears to be lower at high Reynolds numbers.

For pipe flows, the length scale is approximated to scale with distance from the wall (Tennekes and Lumley, 1972). For low Reynolds numbers, measurements indicate that this is indeed true. In the turbulent regime, the maximum magnitude of the length scale at off center locations is around 0.4D as also noted by Hinze (1975). At this center of the pipe the value of the length scale decreases. One reason for this behavior could be that the magnitude of the axial length scale possibly depends on the magnitude of imposed velocity shear available to stretch the turbulent eddy in the axial direction.

Hence, considering the data for the measurements in air, it seems appropriate that at the center of the pipe the magnitude of the length scale is at a minimum and it increases as one moves away from the center where the velocity gradients, in comparison to the center, are larger. Thus, in natural gas the mean velocity profile being flatter ($n \approx 10$) in comparison to the profile in air ($n \approx 7$), it seems reasonable that the magnitude of the scales are smaller at larger Reynolds numbers. Also, since the value of y^+ is large, the near wall region is not captured and the measurements reveal features of the core spread over the cross-section of the pipe.

Profiles Downstream of 19-Tube Bundle With a Single 90 deg Elbow and a 19D Meter Run. Measurements of the mean velocity profiles, in the plane of the elbow, are presented in Fig. 7. It has been shown (Mattingly and Yeh, 1991) that the tube bundle eliminates secondary flow emanating from a single elbow. Hence, a single hot film probe should be suitable for

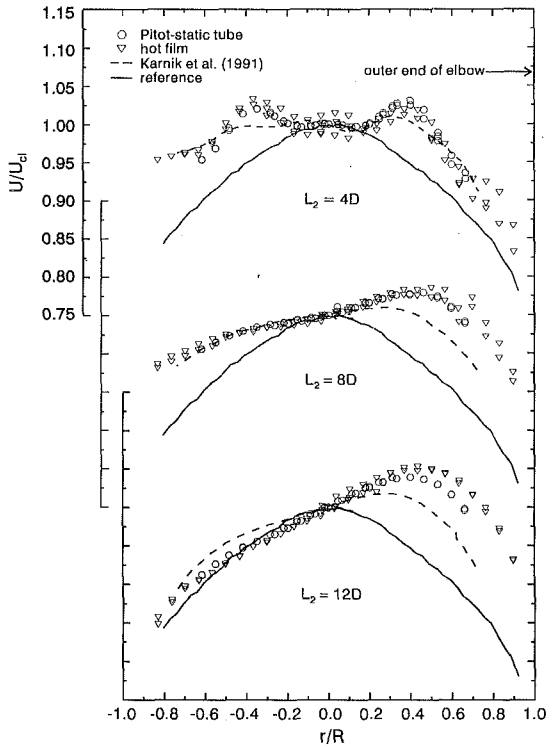

Fig. 7 Axial mean velocity profiles downstream of the tube bundle in the plane of the elbow (vertical profiles)

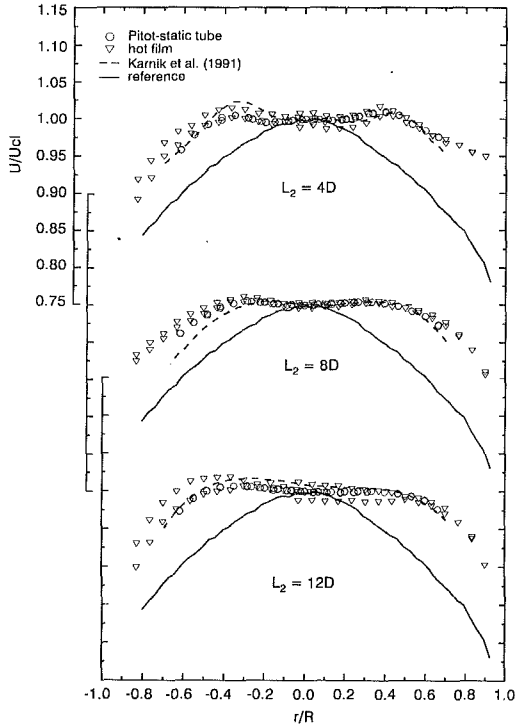

Fig. 9 Horizontal profiles of the axial mean velocity downstream of the tube bundle

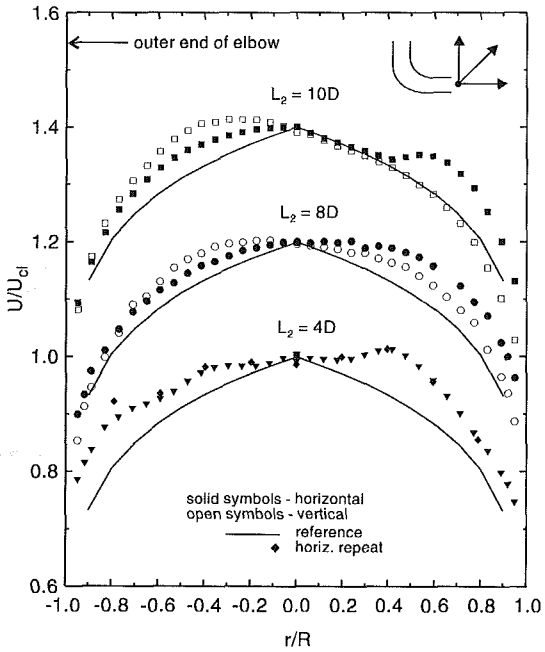

Fig. 8 Mean axial velocity profiles downstream of a tube bundle at low Reynolds numbers; taken from Karnik et al. (1994). Note: each profile following L_2 = 4D is successively offset by 0.2 units.

the present measurements. For comparison, the measurements in air (Karnik et al., 1994) at Re = 1×10^5 are shown alongside in Fig. 8. Note that for the latter measurements, the outer end of the elbow is at $r/R = -1.0$. Once again the velocities are normalized by the centerline value. In cases where the centerline value was not available, the velocities closest to the center were averaged. Two traverses were performed and in some cases a scatter, within the previously mentioned accuracy, was seen in the data. Note that the hot film location was fixed at 19D from the elbow exit and the tube bundle was moved axially to vary the position L_2.

The hot film measurements are once again comparable to those obtained by means of the Pitot-static tubes. Also, the present measurements are comparable to those obtained under similar conditions by Karnik et al. (1991). Any differences could be attributed to the fact that, in the present case, the traverse was at ≈18D instead of 19D. Also, the effect of rotation of the tube bundle during the pulling of the tube bundle could be a contributing factor.

For L_2 = 4D, the wakes of the tube bundle are still evident. At L_2 = 8D, measurements in natural gas, at Re = 7×10^6, exhibit a velocity profile which is much flatter than the reference profile. At this location, the effect of the elbow is visible and as the tube bundle is pulled further away from the measuring station i.e. closer to the elbow, the profile generated by the elbow seems to have passed unconditioned through the tube bundle as seen at L_2 = 12D. This phenomenon has been observed in other similar experiments. The measurements at lower Reynolds numbers also exhibit a similar behavior. However, for L_2 = 4D and 8D, the velocity profiles are not much flatter than the reference profile.

The horizontal axial mean velocity profiles are shown in Fig. 9. Once again the present data (Pitot-static tube and hot film) are comparable to those of Karnik et al. (1991). In comparison to the low Reynolds number data, the profiles at higher Reynolds number appear to be much flatter than the reference profiles.

The axial rms velocities, normalized by the centerline mean velocity, downstream of the tube bundle are shown in Fig. 10. Also shown are the measurements of Karnik et al. (1994) in air. Discrepancies in the values of the horizontal and vertical traverse in the present measurements are possibly due to the inaccurate axial positioning of the tube bundle. Such uncertainties were estimated to be around ±0.125D. The discrepancy, as expected, is larger for the locations closest to the tube bundle.

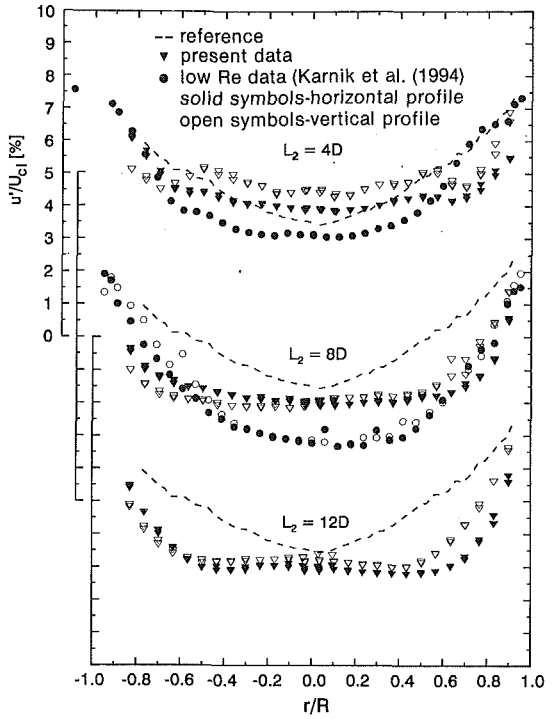

Fig. 10 *Profiles of the turbulence intensity downstream of the tube bundle*

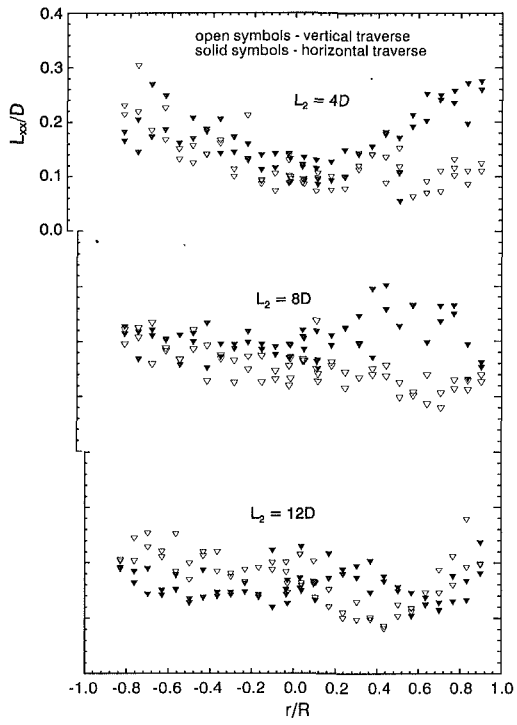

Fig. 12 *Axial integral length scale downstream of a tube bundle with an elbow*

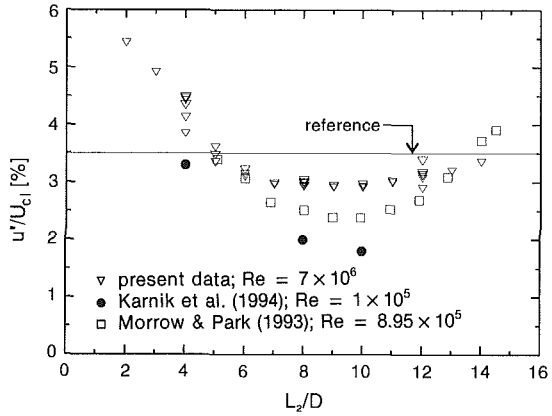

Fig. 11 *Axial rms turbulence intensities along centerline*

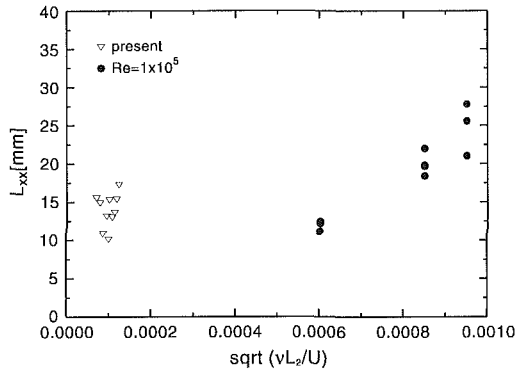

Fig. 13 *Development of axial Eulerian integral length scale along centerline downstream of the tube bundle*

In the present measurements, as expected, the turbulence intensity is high at L_2 = 4D. It is also higher than the reference value in contrast to the measurements in air. As the tube bundle is moved away the intensity decreases but the decay rate is not as high as observed in air. A plot of the centerline turbulence intensity (Fig. 11) indicates that the decay at lower Reynolds numbers is greater than that at higher Reynolds numbers. This is to be expected since the viscous forces decrease relative to the inertial forces as the Reynolds number is increased. As expected the data of Morrow and Park (1993) lie in between the low Reynolds number and high Reynolds number case.

The profiles at L_2 = 8D and L_2 = 12D indicate that the intensity is fairly constant at around 3.0 percent in the core region and increases near the wall. Considering the nearly linear velocity gradient in the major portion of the pipe cross-section (Fig. 7), the feature is not unlike a nearly transversely homogeneous flow (Tavoularis and Karnik, 1989). A constancy of turbulence intensity is exhibited by the data at low Reynolds numbers except that the intensity of around 1.8 percent is much lower than the reference value.

The distributions of the integral length scales, L_{xx}, are presented in Fig. 12. The magnitude of random error in the estimation of the scale (Tavoularis and Karnik, 1989) could be around 7 percent. Since the frozen flow hypothesis is being used, in the present case, considering the inaccuracy in measuring the magnitude of the mean velocity, this error could be higher. This is quite evident as one considers the scatter in the data.

The scale imposed on the flow is of the size of the tubes (tube I.D. = 18mm) as seen for L_2 = 4D. The measurements indicate a near transverse homogeneity, particularly in regions of a nearly linear velocity gradient. The magnitude of the scale increases rather slowly with increasing L_2. This is to be expected since (as for isotropic turbulence) the scales should to grow proportional to $(\nu t)^{0.5}$ (Hinze, 1975) where $t = x/U$ is the mean convective time for a turbulent eddy.

The growth of the scales along the centerline are shown in Fig. 13. The length scales appear to exhibit a nearly linear growth (from 12mm to 25mm) with downstream distance for low Reynolds numbers. However, for larger Reynolds numbers, the scale imposed by the tube bundle survives and the

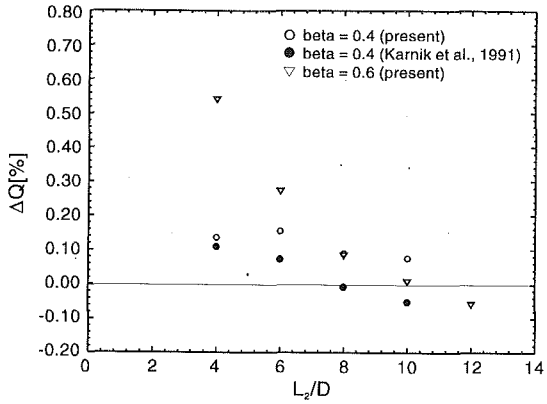

Fig. 14 Orifice meter comparison tests

growth is not as distinct as in the case of the lower Reynolds number. The data appears to be scattered in the range of 10mm to 15mm). Another reason for this nondistinct growth could be that, as seen from Fig. 6, the magnitude of the length scale is not far from that in a fully developed flow.

Orifice Meter Comparison

In order to extend the conclusions of Karnik et al. (1994), on turbulence and orifice meter accuracy, to high Reynolds numbers, orifice meter comparisons were performed in a 19D meter run. The test orifice meter was placed at 19D from the exit of the elbow (replacing the hot film assembly in Fig. 1(*b*)) and the reference orifice meter was placed at the exit of the 76D spool piece. The tube bundle was traversed axially and meter comparisons were conducted for various positions of the tube bundle exit with respect to the test orifice plate. The Reynolds numbers for these were in the range $1\times10^6<\mathrm{Re}<4\times10^6$.

In order to eliminate any errors that may be associated with the use of two differential pressure transmitters (at the test and reference locations), the output of each transmitter was balanced by subjecting the transmitters to the same differential pressure simultaneously. This procedure was followed before comparing the performance of the orifice meters for a given location of the tube bundle. Such a procedure also eliminated any bias that may arise due to possible drifts in the calibration of the pressure transmitters. The pressure taps are located in the horizontal plane for both orifice meters at $r/R = 1.0$.

The results of the meter comparisons are shown in Fig. 14. Each data point is an average of 10 measurements with the maximum standard deviation being 0.035 percent. Also shown, are the measurements of Karnik et al. (1991) for a similar configuration. Note that the reference meter for the latter test was preceded by a 41D straight section which consisted of a 34.7D approach section and a 6.3D upstream spool piece. Within the uncertainty of the experimental data (around ±0.2 percent), as expected, the orifice plated with a beta ratio (orifice diameter to pipe diameter) of 0.4 appears to be least affected by the position of the tube bundle. For the orifice plate with a beta ratio of 0.6, the zero error occurs at around 8D. Discrepancies between the present results and those of Karnik et al. (1991) could be attributed to differences in the reference conditions and experimental inaccuracies.

The mean velocity profiles at the location of the zero error are flatter than the profile at the reference location as seen in Fig. 7 and 9. This implies, as according to Karnik et al. (1994), that the turbulence intensity should be lower than that at the reference location. An examination of the turbulence intensity (Figs. 10 and 11) indicates that this is indeed the case. Thus, it could be concluded that turbulence is indeed one of the factors affecting orifice meter accuracy.

However, in comparison to the low Reynolds number results, it can be seen that at the zero error location, the mean velocity profiles in the high Reynolds number flow are much flatter than the reference. In the low Reynolds number case, the turbulence intensity was around 1.8 percent. Thus, for the present case, the turbulence intensity should be lower than 1.8 percent since reference values in the two cases are similar. Measurements do not indicate such an occurrence. Thus, although turbulence intensity is one of the factors affecting orifice meter accuracy, there appear to be other factors involved. To gain more insight into the mechanism of fluid flow interaction with orifice meter accuracy, further studies are warranted.

Concluding Remarks

The present measurements have demonstrated the successful use of hot film anemometry to measure mean and turbulent flow characteristics in natural gas at elevated pressures. It has also been established that for the given experimental conditions, the velocity profile after 76D is, for all practical purposes, fully developed. Hot film anemometry has subsequently been used to measure the velocity flow field downstream of a tube bundle providing details of the structure of the flow at high Reynolds numbers.

It was found that, as expected, the turbulence intensity at higher Reynolds numbers exhibited a slower decay than that seen at lower Reynolds numbers. Although the uncertainty in the measure of the length scale is high, the magnitude of the integral length scales appear to be lower than that measured at lower Reynolds numbers. The dominance of the inertial forces at high Reynolds numbers is also evident from the fact that the mean velocity profiles develop rather slowly when compared to their counterparts at low Reynolds numbers.

Orifice meter comparisons have confirmed the findings of Karnik et al. (1994) that turbulence is one of the parameters affecting orifice meter accuracy. The present measurements have provided a comparison between low Reynolds number and high Reynolds number flows and will serve as a useful data base for computational procedures.

Acknowledgment

The author would like to acknowledge the assistance of Ian Williamson and Shane Fry in performing the experiments. The discussions with Dr. Kamal Botros, Skip Kiland of TSI, Malcolm Franklin of MTL and Richard Parlby of CSA were very useful. Acknowledgment is also due to Kelvin Corbiell and Glenn Funfer for their assistance with the control processor. The work presented here is part of a flow metering research program sponsored by Nova Corporation of Alberta and the permission to publish it is hereby acknowledged.

References

Bouge, D. C., and Metzner, A. B., 1963, "Velocity Profiles in Turbulent Pipe Flow," *Industrial and Engineering Chemistry Fundamentals*, Vol. 2, pp. 143–149.

Colebrook, C. F., 1938-39, "Turbulent Flow in Pipes, With Particular Reference to the Transition Between the Smooth and Rough Pipe Laws," *Journal of the Institute of Civil Engineers*, London, Vol. 11, pp. 133–136.

Clauser, F. H., 1956, "The Turbulence Boundary Layer," *Advances in Applied Mechanics*, Vol. 4, pp. 1–51.

Comte-Bellot, G., and Corrsin, S., 1971, "Simple Eulerian Time Correlation of Full and Narrow Band Velocity Signals in Grid Generated Isotropic Turbulence," *Journal of Fluid Mechanics*, Vol. 48, pp. 273–335.

Hinze, J. O., 1975, *Turbulence*, 2nd Edition, McGraw-Hill, New York.

Karnik, U., Jungowski, W. M., and Botros, K. K., 1991, "Effects of Flow Characteristics Downstream of Elbow/Flow Conditioner on Orifice Meter," 9th North Sea Flow Measurements Workshop, Bergen, Norway, Part 2, pp. 1–37.

Karnik, U., Jungowski, W. M., and Botros, K. K., 1994, "Effects of Tur-

bulence on Orifice Meter Performance," *Journal of Offshore Mechanics and Arctic Engineering*, Vol. 116, pp. 77–85.

Laufer, J., 1950, "Investigation of Turbulent Flow in a Two-Dimensional Channel," NACA Technical Note 2123.

Laufer, J., 1954, "The Structure of Turbulence in Fully Developed Pipe Flow," NACA Report 1174.

Mattingly, G. E., and Yeh, T. T., 1991, "Effects of Pipe Elbows and Tube Bundles on Selected Types of Flow Meters," *Flow Measurement and Instrumentation*, Vol. 2, pp. 4–13.

Moody, L. F., 1944, "Friction Factors for Pipe Flow," *Trans. ASME*, Vol. 66, pp. 671–684.

Morrow, T. B., and Park, J. T., 1993, "Installation Effects on Orifice Meter Performance," Gas Research Institute Topical Report 93/0054, Metering Research Program.

Morrow, T. B., and Park, T. J., 1992, "Effects of Tube Bundle Location on Orifice Meter Error and Velocity Profiles," *Proceedings of the 11th International Conference on Offshore Mechanics and Arctic Engineering*, Calgary, Canada, Vol. V, Part 2, pp. 13–18.

Nikuradse, J., 1932, "Gesetzmässigkeit der Turbulenten Strömung in Glatten Rohren," *Forschg. Arb. Ing.-Wes.*, No. 356.

Nikuradse, J., 1933, "Strömungsgesetze in rauhen Rohren," *Forschg. Arb. Ing.-Wes.*, No. 361.

Nunner, W., 1956, "Wärmeübergang und Druckabfall in rauhen Rohren," *VDI-Forschungsheft*, No. 455.

Park, J. T., Morrow, T. B., Yeh, T. T., and Mattingly, G. E., 1992, "Effect of Velocity Profile From Tee and Tube Bundle Flow Conditioner on Orifice Meters," *International Gas Research Conference*, Vol. III, Orlando, FL, pp. 223–233.

Patel, V. C., 1965, "Calibration of the Preston Tube and Limitations on Its Use in Pressure Gradients," *Journal of Fluid Mechanics*, Vol. 23, Part I, pp. 185–208.

Schlichting, H., 1979, *Boundary-Layer Theory*, McGraw-Hill, New York.

Sreenivasan, K. R., Tavoularis, S., Henry, R., and Corrsin, S., 1980, "Temperature Fluctuations and Scales In Grid Generated Turbulence," *Journal of Fluid Mechanics*, pp. 100.

Tavoularis, S., and Corrsin, S., 1981, "Experiments in a Nearly Homogeneous Shear Flow With a Uniform Mean Temperature Gradient," *Journal of Fluid Mechanics*, Vol. 104, pp. 311–347.

Tavoularis, S., and Karnik, U., 1989, "Further Experiments on the Evolution of Turbulent Stresses and Scales in Uniformly Sheared Turbulence," *Journal of Fluid Mechanics*, Vol. 204, pp. 457–478.

Tennekes, H., and Lumley, J. L., 1972, *A First Course in Turbulence*, MIT Press, Massachusetts.

White, F. M., 1986, *Fluid Mechanics*, McGraw-Hill, New York.

A New Correlation for Pressure Drop in Arrays of Rectangular Blocks in Air-Cooled Electronic Units

M. Molki
Department of Mechanical Engineering,
Esfahan University of Technology,
Esfahan, Iran

M. Faghri

O. Ozbay

Department of Mechanical Engineering
and Applied Mechanics,
University of Rhode Island,
Kingston, RI 02881

An experimental work is carried out to investigate the pressure drop and to visualize the flow field in the entrance region of an array of rectangular modules attached to the lower wall of a duct. The modules are positioned in an in-line arrangement to simulate the geometry often encountered in the cooling passages of electronic units. The investigation is performed in both laminar and turbulent regions with Reynolds number ranging from 400 to 15,000. The geometric parameters range from $H/L = 0.125$ to 1.5 and $S/L = 0.125$ to 0.5, while the value of B/L is fixed to 0.5. The flow visualization revealed a highly separated region on the first module of the array. The pressure drops are correlated for the range of Re, H/L, and S/L employed in this work.

Introduction

This paper describes an experimental study of pressure drop in the entrance region of an array of rectangular blocks in a duct. The main focus of the work is to present a correlation for pressure drop and also to provide some qualitative information on the nature of the flow field in this region. The geometry investigated is similar to those encountered in electronic equipment, and in particular, to those employed in computer industry.

A search of literature revealed a number of studies related to this investigation. Sparrow et al. (1982, 1983) have reported heat transfer and pressure drop in arrays of rectangular modules with barrier and missing modules. The focus of their work was to study the effect of missing modules and barriers on thermal-hydraulic behavior of rectangular arrays. Their pressure results for no-barrier arrays without missing modules were obtained for one particular geometry around Reynolds number of 6900.

In an experimental effort, Lehmann and Wirtz (1985) have studied the effect of streamwise spacing and length on convection from an array of two-dimensional modules. They also performed visualization tests in the periodically fully developed region of the duct and obtained some information on the nature of flow field in this region. The pressure drops reported in this reference is limited to Re = 1000, 2000, and 3000. Some pressure results are also reported by Moffat et al. (1985) for rather tall and widely spaced cubical elements.

For sparse arrays of elements, the pressure drop is mainly determined by form drag and thus the pressure coefficient is independent of Reynolds number. In this connection, the pressure drop coefficients reported in some publications are independent of Re (e.g., Moffat et al., 1985), while the others (e.g., Tai and Lucas, 1985; Souza Mendes and Santos, 1987; and Hollworth and Fuller, 1987) have shown their pressure results in terms of Re.

Another issue of importance in flow through array of rectangular blocks is to determine the flow regime. In a paper by Garimella and Eibeck (1992), the onset of transition from laminar to turbulent is investigated. They concluded that, in a three dimensional situation, transition is not only a function of flow rate and geometry, but also is a function of location in the array. They have further stated that the transition Re (based on channel height) varies from 700 to 1900, and by increasing the streamwise spacing between the elements, the transition occurs at lower Reynolds numbers.

In the present study, an array of rectangular blocks (modules) is positioned along the lower wall of a rectangular duct. These blocks, which represent a model for the modular electronic components, are arranged in an in-line fashion. The geometric variables, namely the module dimension (L), the module height (B), the inter-module spacing (S), and the height of the flow passage between the module and the opposite wall of the duct (H), are varied in such a manner that $B/L = 0.5$, $S/L = 0.125, 0.33, 0.5$, and $H/L = 0.125, 0.25, 0.5, 0.75, 1$, and 1.5. These dimensions are close to those often encountered in the computer industry. The working fluid is air, and the Reynolds number based on H and the air velocity in the bypass channel (i.e., the channel formed between the top surface of modules and the opposite wall of the duct) range from 400 to 15,000.

Contributed by the Fluids Engineering Division for publication in the JOURNAL OF FLUIDS ENGINEERING. Manuscript received by the Fluids Engineering Division April 3, 1993; revised manuscript received May 2, 1994. Associate Technical Editor: W. S. Saric.

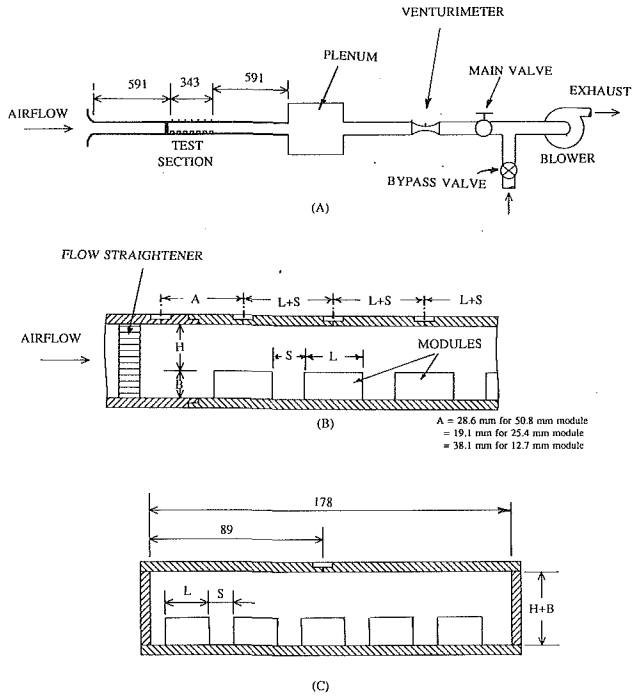

Fig. 1 Schematic view of the experimental setup (not to scale). (A) the overall view, (B) side view of the test section, (C) cross-sectional view of the test section. All dimensions are in millimeter.

In this study, the experiments are carried out in two directions. The first is to measure and to correlate pressure drop in the entrance region of the array of rectangular modules. The second is to complement the problem by flow visualization and to gain more insight into the nature of the flow field.

A search of literature did not indicate any correlation for pressure drop in the entrance region. As will be noted shortly, all flow and geometric parameters such as Re, X (distance along the array), H/L, and S/L, are brought together in a single correlation.

The Experimental Apparatus and Procedure

The schematic view of the experimental setup is shown in Fig. 1. Laboratory air is drawn into the apparatus through a bell-mouth inlet geometry. It then passes through a flow development section (559 mm), flow straightener, test section, flow redevelopment section (591 mm), venturimeter, and main valve, and then leaves the flow circuit through the blower operating in suction mode.

The air flow is adjusted by the main valve. There is also available a bypass valve which allows for a more precise control of the air flow. The flow rate is measured by a precalibrated venturimeter.

Table 1 Geometrical dimensions of the test section

TEST SECTION NO.	B/L	S/L	H/L	B [mm]	L [mm]	H [mm]	S [mm]
1	0.5	0.125	0.125	25.4	50.8	6.4	6.4
2	0.5	0.125	0.25	25.4	50.8	12.7	6.4
3	0.5	0.125	0.5	25.4	50.8	25.4	6.4
4	0.5	0.33	0.25	12.7	25.4	6.4	8.4
5	0.5	0.33	0.5	12.7	25.4	12.7	8.4
6	0.5	0.33	0.75	12.7	25.4	19.1	8.4
7	0.5	0.5	0.5	6.4	12.7	6.4	6.4
8	0.5	0.5	1	6.4	12.7	12.7	6.4
9	0.5	0.5	1.5	6.4	12.7	19.1	6.4

The test section and the corresponding upstream and downstream ducts have a rectangular cross section. The width of the cross section is equal to $W = 178$ mm, but its height ($H + B$ in Figs. 1(B) and (C)), depending on the dimensions of the array, varies from 12.8 and 76.2 mm.

An in-line array of rectangular modules are deployed along the lower wall of the test section. The dimensions, as noted in Figs. 1(B) and (C), are $S = 6.4$ and 8.4 mm, $H = 6.4$, 12.7, 19.1, and 25.4 mm, $L = 12.7$, 25.4, 50.8 mm, and $B = 6.4$, 12.7, and 25.4. From the combination of these dimensions nine test sections are fabricated with dimensions shown in Table 1. In all cases, B/L is equal to 0.5. The number of rectangular blocks depends on the test section number. For test sections (1 to 3), (4 to 6), and (7 to 9) the number of modules along and across the test section are, respectively, 5×3, 8×5, and 15×9.

The pressure taps are located at the upper wall. As shown in Fig. 1(B), the first tap is located a distance A upstream of the second tap, and the other taps are equally spaced. The distance A for the first tap depends on the test section and is equal to 28.6 (for $L = 50.8$), 19.1 (for $L = 25.4$), and 38.1 (for $L = 12.7$) mm. In the spanwise direction, the pressure taps are located in the middle of the cross section and just above the central module (Fig. 1(C)). The location of all pressure taps in terms of their distance from the first tap is shown in Table 2. It should be noted that the number of pressure taps for test sections 1 to 3 are more than what is shown in Fig. 1(B) (see Table 2 for exact location of pressure taps).

Prior to the onset of a data run, the proper test section is selected and assembled. Then, to prevent air from leaking into the test section, all suspected joints are sealed by silicon rubber, and they are thoroughly tested for leaks with the aid of soap solution.

Once the test section is properly assembled, the air flow is activated and adjusted for a given flow rate. After a warm-up period, the setup is ready for pressure readings. The pressure signals are transmitted via plastic tubing to a (1 or 10 torr) pressure transducer and an electronic manometer, which are interfaced with an IBM PC. The computer scans the pressure signals for 22 seconds. It is noteworthy that this arrangement could resolve pressure to within 10^{-5} mm Hg. Each experiment is repeated twice and the results are averaged to obtain a data

Nomenclature

A_1 = inlet cross sectional area of venturimeter, $(\pi/4)D_1^2$
B = module height, Fig. 1(B)
C_D = flow coefficient of venturimeter, $C_D = Q[(D_1/D_2)^2 - 1]^{0.5}/[A_1(2\Delta P/\rho_1)^{0.5}]$
D_1 = inlet diameter of venturimeter
D_2 = throat diameter of venturimeter
f_{2H} = friction factor, Eq. (4)
H = distance between top surface of modules and the opposite wall, Fig. 1(B)
K = pressure drop coefficient, Eq. (3)
K^+ = modified pressure drop coefficient, Eq. (8)
L = plane dimension of square module, Figs. 1(B) and (C)
P_i = air pressure at the ith pressure tap, Eq. (3)
P_0 = air pressure at the first pressure tap, Eq. (3)
Q = volume flow rate, Eq. (2)
Re = Reynolds number, Eq. (1)
S = inter-module spacing, Figs. 1(B) and (C)
V = air mean velocity in bypass channel, Eq. (2)
W = duct width, Fig. 1(C), $W = 178$ mm
X = streamwise axial coordinate
ν = kinematic viscosity, Eq. (1)
ρ = density, Eq. (4)

Table 2 Location of pressure taps

	TEST SECTIONS 1,2,3	TEST SECTIONS 4,5,6	TEST SECTIONS 7,8,9
TAP NO.	X [MM]	X [MM]	X [MM]
1	0	0	0
2	14.3	19.1	38.1
3	28.6	52.9	57.2
4	42.9	86.7	76.3
5	57.2	120.5	95.4
6	71.4	154.3	114.5
7	85.7	188.1	133.6
8	100.0	221.9	152.7
9	114.3	255.7	171.8
10	128.6	289.5	190.9
11	142.9		210
12	157.2		229.1
13	171.5		248.2
14	185.7		267.3
15	200.0		286.4
16	214.3		305.5
17	228.6		324.6
18	242.9		
19	257.2		
20	271.5		

Table 3 The precision limits for the measured parameters

parameter	precision limit
barometric pressure	±0.1 mm Hg
venturimeter inlet gage pressure	$\pm 10^{-5}$ mm Hg
pressure drop across the venturimeter	$\pm 10^{-5}$ mm Hg
pressure drop across the laminar-flow element	$\pm 10^{-5}$ mm Hg
inlet air temperature	±0.6 °C
laminar-flow element	±1% of volume flow rate
duct width, W	±0.1 mm
distance between top of modules and the opposite wall, H	±0.1 mm
module height, B	±0.1 mm
inlet and throat diameters of venturimeter	±0.1 mm
pressure gradient, dP/dX	twice the standard deviation of the slope of P-X plot
test section gage pressure	$\pm 10^{-5}$ mm Hg

Table 4 Estimated typical uncertainties

parameter	uncertainty, %
venturimeter coefficient, C_D	2.8
Reynolds number, Re	2.9
pressure drop coefficient, K	6.1
friction factor, f_{2H}	15.3

point. A total of 1420 data points are reported in this paper and are used to obtain the pressure drop correlation.

All nine test sections are entirely made of plexiglass so that they can also be used in flow visualization experiments. The flow visualization method used in this work is the so-called oil-lampblack technique.

The results of this investigation are presented in terms of Reynolds number Re with the conventional definition,

$$\mathrm{Re} = \frac{VH}{\nu} \tag{1}$$

In this equation, V is the mean velocity of air in the bypass channel above modules and is related to the volume flow rate as,

$$V = \frac{Q}{WH} \tag{2}$$

The pressure drops are nondimensionalized and expressed as,

$$K = \frac{P_0 - P_i}{0.5\rho V^2} \tag{3}$$

where K is the pressure drop coefficient.

In the periodically fully developed region, the pressure drops are converted to friction factor defined as,

$$f_{2H} = \frac{-\left(\frac{dP}{dX}\right)2H}{0.5\rho V^2} \tag{4}$$

Experimental Uncertainty

Prior to the onset of experimental runs, the venturimeter was calibrated with the aid of a laminar-flow element. The parameters recorded during the calibration process and the respective measurement uncertainties are listed in Table 3. The precision limits seen in the table are the smallest interval between the scale markings (least count) of the perspective instruments. The bias limit for instruments was negligible. The sensitivity coefficients were evaluated using the data reduction FORTRAN program. The results were then combined through the root-sum-square expression to obtain uncertainties (Kline, 1985; and Abernethy et al., 1985).

Using these guidelines, the uncertainty of venturimeter coefficient is found to be ± 0.027 with $C_D = 0.971 \pm 2.8$ percent. Other uncertainty values are summarized in Table 4.

Flow Visualization

The flow pattern in the entrance region of the array of modules was revealed by the application of oil-lampblack technique. The technique is relatively simple, but it may not be suitable for any type of flow field. The detailed description of oil-lampblack visualization technique is described by Sparrow et al. (1981).

The first step is to make a suitable mixture of oil and lampblack. In this study, it was found that the automatic transmission oil gives the best result. The mixture is subsequently applied to the top surface of the module, and thus creating a uniform glossy black surface.

When the airflow is initiated, the mixture moves under the action of shear exerted by the air, and the streaks that form on the surface reveal the pattern of flow field adjacent to the wall. The development of the surface patterns is visually observed during the visualization run. The experience gained from these visual observations together with the information reflected by the streaks are used to describe the flow field.

The photographic evidence of the flow field is shown in Fig. 2. The photograph shows the top view of the flow patterns near the top surface of the first three modules of the array. These patterns are obtained for the modules with $S/L = 0.125$, and $H/L = 0.125$, at $\mathrm{Re} = 15{,}000$. The main flow is from let to right, and the scale below the photograph shows the distance from the leading edge of the first module in centimeters.

Special features of the flow are flow separation at the leading edge of the first module, reattachment of air flow at about 1.8 cm from the leading edge (nearly $L/3$), and the formation

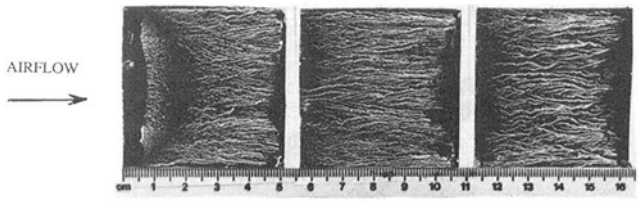

Fig. 2 Flow visualization patterns (Re = 15,000, L = 50.8 mm, S/L = 0.125, H/L = 0.125)

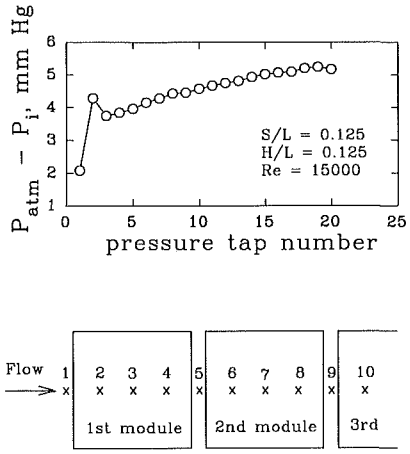

Fig. 3 Pressure distribution versus tap number at Re = 15,000, S/L = 0.125, and H/L = 0.125

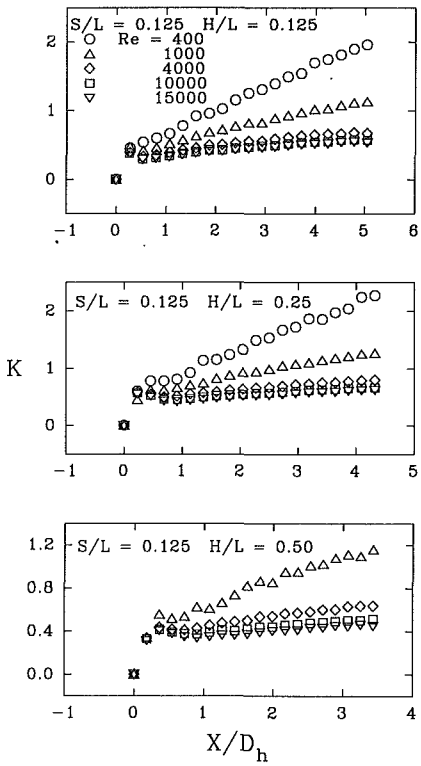

Fig. 4 Distribution of pressure drop coefficient in terms of axial distance for S/L = 0.125

of a recirculating bubble in between. The curved dark line which starts at the lower left corner of the first module and extends to 1.8 cm downstream and subsequently returns to the upper left corner, is the line of flow reattachment.

The recirculating bubble is located between the line of reattachment and the leading edge of the first module. In this region, air moves upstream near the wall to meet the incoming separated flow. The dark area extending from the zero of scale to about 0.5 cm downstream (see the scale below the photograph in Fig. 2) is simply an area of rather weak shear stress. Beyond the line of reattachment, the air flows downstream toward the other modules of the array.

The patterns clearly show that the flow field near the first module of the array is three dimensional. This is also confirmed by the observations of Chou and Lee (1988) who employed a two-module array in their experiments. Further downstream, the air appears to flow along the direction of main stream and there is no clear evidence of flow separation.

Another message from these photographs is that, at S/L = 0.125 (i.e., the value at which the visualization experiments were performed), there is no clear indication that the flow penetrates into the inter-modular gaps, as is often observed for larger values of S/L (e.g., see Chou and Lee, 1988). However, the sharp edges of the modules are expected to be conducive to flow separation, and possibly the flow separates behind the modules. This is even more possible at higher Reynolds numbers. If this is true, then the pressure results may reflect a lack of dependence on Re especially at higher Re.

Pressure Results

Pressure distribution along the flow at Re = 15,000, S/L = 0.125, and H/L = 0.125 is shown in Fig. 3. The lower diagram in this figure is prepared to show the location of pressure taps (marked with X) relative to the modules. As seen, the first tap is located just upstream of the leading edge of the first module. The ordinate in Fig. 3 indicates the air pressure with respect to the atmosphere $P_{atm} - P_i$, so that an increase in the ordinate reflects a drop in pressure.

Examination of the graph indicates that pressure decreases rapidly from the first tap to the second one, while there is a slight pressure recovery for the next pair of taps. From this point on, the air pressure continuously decreases. The rapid pressure drop between the first and second taps occurs at a point where flow is separated from the wall and the recirculating zone has reduced the effective cross section of the airflow. Beyond this point, the flow expands and the pressure is somewhat recovered.

Pressure distributions along the flow direction are shown in Figs. 4 to 6. The abscissa X/D_h is the axial distance from the first pressure tap divided by the hydraulic diameter of the duct ($D_h = 2W(H+B)/(W+H+B)$). The ordinate K is the pressure drop coefficient as defined in Eq. (3).

Examination of these figures indicate a fairly rapid drop in air pressure as flow enters the array of modules. Further downstream however, the pressures at similar locations approach a fully developed state and decrease linearly. When the numerical values of pressure data at respective locations were closely examined, it was found that a fully developed state has been reached after the 2nd, 3rd, and 4th modules in test sections numbered (1, 2, 3), (4, 5, 6), and (7, 8, 9), respectively.

Another noteworthy feature in these figures is the independence of K from Re when Re is greater than 4000. At higher Re, the possible flow separation behind the modules is intense. In this case, the drag force exerted by the modules on air flow are determined by form drag and the effect of wall friction is negligible. It is known that form drag, and thus K, is nearly independent of Re.

Fully developed pressure drops are expressed in terms of friction factor, f_{2H}, in Fig. 7. As stated in the preceding paragraph, there are two mechanisms that govern the pressure drop in the array, namely the form drag and wall friction. At larger inter-modular spacing, the flow is governed by form drag, while at smaller spacing the wall friction is dominant. The data points in Fig. 7 indicate that as S/L is increased, the f_{2H} values become less dependent on Re.

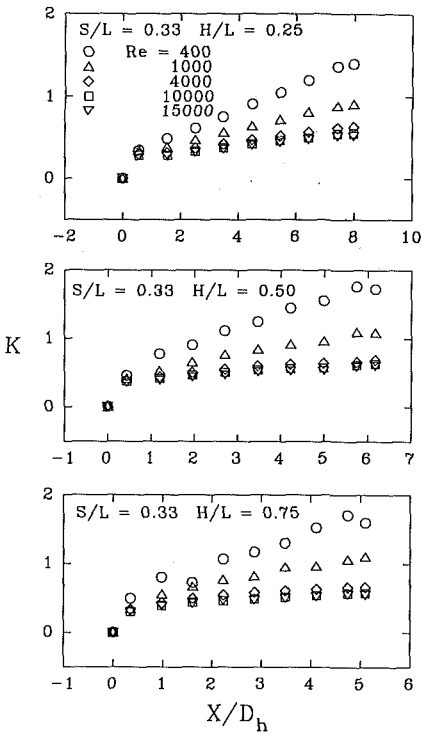

Fig. 5 Distribution of pressure drop coefficient in terms of axial distance for $S/L = 0.33$

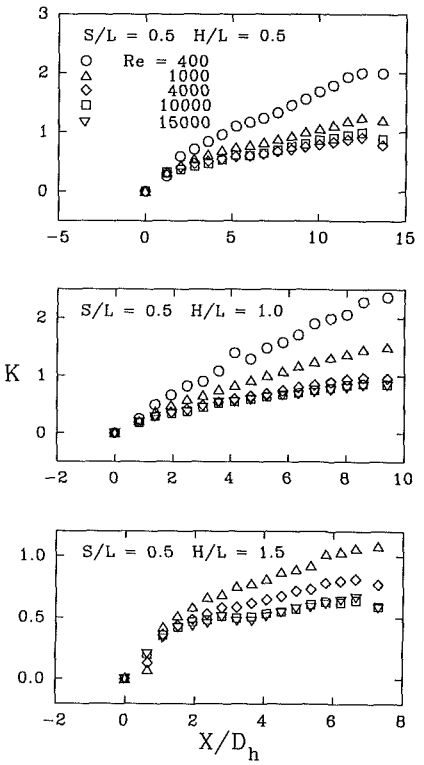

Fig. 6 Distribution of pressure drop coefficient in terms of axial distance for $S/L = 0.5$

Also shown in Fig. 7, are the laminar flow results of Asako and Faghri (1988) (at $B/L = 0.375$ as compared to 0.5 in this investigation), their turbulent results (Asako and Faghri, 1991, at $B/L = 0.5$), and the laminar Hagen-Poiseuille flow in parallel plate channel indicated by 48/Re. There is generally a close agreement between the data, and the minor differences seen in the laminar region is perhaps due to difference in B/L values.

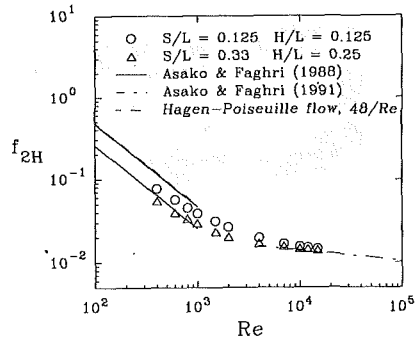

Fig. 7 Friction factor and comparison with literature

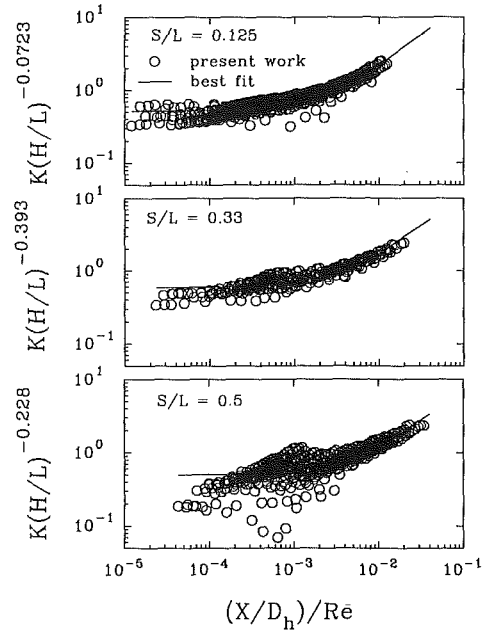

Fig. 8 The first step in correlating pressure data ($S/L = 0.125$, 0.33, and 0.5)

As a first step in obtaining a correlation for the pressure data, we combine the different H/L values with the pressure drop coefficient K in Fig. 8. In addition to the experimental data, the figure also shows the best fit through the points. The equation for the solid lines, obtained through a least-squares curve fitting procedure, are

$$K\left(\frac{H}{L}\right)^{-0.0723} = 165.33\frac{\left(\frac{X}{D_h}\right)}{\mathrm{Re}} + 0.518 \tag{5}$$

$$K\left(\frac{H}{L}\right)^{-0.393} = 114.21\frac{\left(\frac{X}{D_h}\right)}{\mathrm{Re}} + 0.588 \tag{6}$$

$$K\left(\frac{H}{L}\right)^{-0.228} = 71.68\frac{\left(\frac{X}{D_h}\right)}{\mathrm{Re}} + 0.498 \tag{7}$$

The standard deviations of data from the correlations 5 to 7 are, respectively, 0.0677, 0.0760, and 0.1187. With these numbers, the respective correlations are good to within ± 17.0, ± 16.9, and ± 30.1 percent.

Further attempt to correlate all data points and to present them by a single equation requires the definition of modified pressure drop coefficient as

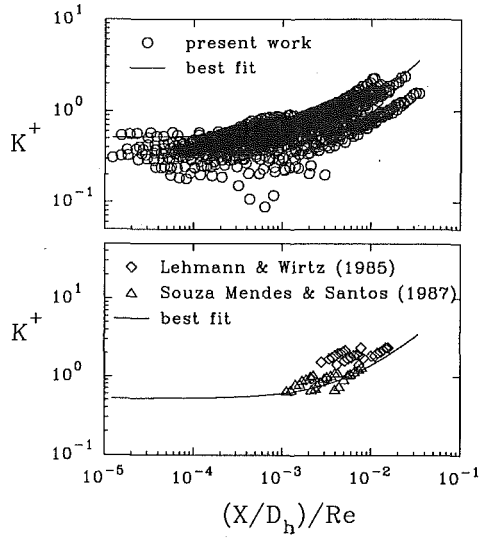

Fig. 9 Modified pressure drop coefficient for all data points

$$K^+ = K\left(\frac{H}{L}\right)^{2.559(S/L)^{2.81}} \tag{8}$$

The upper graph in Fig. 9 presents a total of 1420 data points. The figure indicates that the data points have been brought together relatively well, and they are represented by the equation

$$K^+ = 87.223\frac{\left(\frac{X}{D_h}\right)}{\mathrm{Re}} + 0.515 \tag{9}$$

The standard deviation of data from correlation is 0.1899 and the correlation is good to within ± 54.4 percent. Further, the standard deviation of coefficients 87.223 and 0.515 are, respectively, $\sigma_1 = 1.493$ and $\sigma_2 = 0.6579 \times 10^{-2}$, corresponding to $\pm 2\sigma_1/87.223 = \pm 3.4$ percent and $\pm 2\sigma_2/0.6579 \times 10^{-2} = \pm 2.6$ percent uncertainty.

This equation provides a means for estimating the pressure drop in the entrance region of an array of rectangular blocks when $400 \le \mathrm{Re} \le 15000$, $B/L = 0.5$, $0.125 \le S/L \le 0.5$, and $0.125 \le H/L \le 1.5$.

To compare this correlation with literature, the pressure results of Lehmann and Wirtz (1985) and those of Souza Mendes and Santos (1987) are shown in the lower graph. There are a number of differences between these investigations. Lehmann and Wirtz studied the problem for $B/L = 0.25$, $0 \le S/L \le 1$, and $0.25 \le H/L \le 0.75$, which are somewhat different from the geometric parameters of the present study. In addition, their test section geometry was two dimensional. The pressure results reported by Souza Mendes and Santos (1987) are for $B/L = 3/8$, $S/L = 0.25$, and $H/L = 5/8$. Despite all the differences, the level of agreement seen in Fig. 9 is relatively good.

Concluding Remarks

This experimental investigation revealed the patterns of fluid flow and the results of pressure drop in the entrance region of an array of rectangular modules in a duct. The array of modules are considered to be a model for circuit boards used in electronic equipment.

Flow visualization indicated the presence of a highly separated flow on top of the first module, followed by flow reattachment and recirculation. It was further found that flow reattachment is curved, and thus the flow field is thoroughly three dimensional. Further downstream, the flow visualization could not present a clear evidence of flow separation. However, the pressure results indicate that at higher values of Re, the flow is possibly separated behind the downstream modules.

Pressure drop results are presented and correlated through the definition of a modified pressure drop coefficient. This correlation is good to within ± 54.4 and is a convenient tool for estimating the pressure drop in arrays of rectangular blocks.

Acknowledgment

This work was supported by a grant from IBM corporation. Esfahan University of Technology supported Dr. M. Molki during his sabbatical leave.

References

Abernethy, R. B., Benedict, R. P., and Dowdell, R. B., 1985, "ASME Measurement Uncertainty," ASME JOURNAL OF FLUIDS ENGINEERING, Vol. 107, pp. 161-164.

Asako, Y., and Faghri, M., 1988, "Three-Dimensional Heat Transfer and Fluid Flow Analysis of Arrays of Square Blocks Encountered in Electronic Equipment," *Numerical Heat Transfer*, Vol. 13, pp. 481-498.

Asako, Y., and Faghri, M., 1991, "Parametric Study of Turbulent Three-Dimensional Heat Transfer of Arrays of Heated Blocks Encountered in Electronic Equipment," *Heat Transfer in Electronic Equipment*, HTD-Vol. 171, pp. 135-141.

Chou, J. H., and Lee, J., 1988, "Reducing Flow Nonuniformities in LSI Packages by Vortex Generators," *Cooling Technology for Electronic Equipment* (by W. Aung), Hemisphere, pp. 113-124.

Garimella, S. V., and Eibeck, P. A., 1992, "Onset of Transition in the Flow Over a Three-Dimensional Array of Rectangular Obstacles," ASME *Journal of Electronic Packaging*, Vol. 114, pp. 251-255.

Hollworth, B. R., and Fuller, H. A., 1987, "Heat Transfer and Pressure Drop in a Staggered Array of Aircooled Components," *Proceedings of the International Symposium on Cooling Technology for Electronic Equipment*, Honolulu, pp. 732-748.

Kline, S. J., 1985, "The Purposes of Uncertainty Analysis," ASME JOURNAL OF FLUIDS ENGINEERING, Vol. 107, pp. 153-160.

Lehmann, G. L., and Wirtz, R. A., 1985, "The Effect of Variations in Stream-Wise Spacing and Length on Convection from Surface Mounted Rectangular Components," ASME HTD, Vol. 48, pp. 39-47.

Moffat, R. J., Arvizu, D. E., and Ortega, A., 1985, "Cooling Electronic Components: Forced Convection Experiments with an Air-Cooled Array," *Heat Transfer in Electronic Equipment*, ASME HTD, Vol. 48, pp. 17-27.

Souza Mendes, P. R., and Santos, W. F. N., 1987, "Heat-Transfer and Pressure Drop Experiments in Air-Cooled Electronic-Component Arrays," *J. Thermophysics*, Vol. 1, pp. 373-378.

Sparrow, E. M., Molki, M., and Chastain, S. R., 1981, "Turbulent Heat Transfer Coefficients and Fluid Flow Patterns on the Faces of a Centrally Positioned Blockage in a Duct," *Int. J. Heat Mass Transfer*, Vol. 24, pp. 507-519.

Sparrow, E. M., Niethammer, J. E., and Chaboki, A., 1982, "Heat Transfer and Pressure Drop Characteristics of Arrays of Rectangular Modules Encountered in Electronic Equipment," *Int. J. Heat Mass Transfer*, Vol. 25, pp. 961-973.

Sparrow, E. M., Vemuri, S. B., and Kadle, D. S., 1983, "Enhanced and Local Heat Transfer, Pressure Drop, and Flow Visualization for Arrays of Block-Like Electronic Components," *Int. J. Heat Mass Transfer*, Vol. 26, pp. 689-699.

Tai, C. C., and Lucas, V. T., 1985, "Thermal Characterization of a Card-on-Board Electronic Package," *Heat Transfer in Electronic Equipment*, ASME HTD, Vol. 48, pp. 49-57.

Discrete Vortex Simulation of Pulsating Flow Behind a Normal Plate

Hyung Jin Sung
Professor.
Mem. ASME

Young Nam Kim
Graduate Student.

Jae Min Hyun
Professor.
Mem. ASME

Department of Mechanical Engineering,
Korea Advanced Institute of Science
and Technology,
373-1 Kusong-dong, Yusong-ku,
Taejon, Korea
305-701

A numerical study is made of the separated flow behind a flat plate. The plate is placed normal to the direction of the approach flow. The oncoming freestream velocity contains a pulsating part, $U_\infty = U_0(1+A_0\cos f_p t)$. The temporal behavior of vortex shedding patterns is scrutinized over broad ranges of the two externally specified parameters, i.e., the pulsation amplitude ($A_0 \leq 0.6$), and the dimensionless pulsation frequency, ($f_p \leq 0.32$). A version of the discrete vortex method is utilized. The variable-position nascent vortex technique is applied, and it proves to be adequate for pulsating approach flows. The numerical results clearly capture the existence of lock-on when f_p exceeds a threshold value. The modulation of vorticity shedding is also detected when f_p is reasonably low. The influence of A_0 on the flow characteristics is examined in detail. As A_0 increases to a moderate value (e.g., $A_0 \leq 0.6$), an appreciable broadening is seen of the range of f_p for which lock-on occurs. Based on the numerical results, three characteristic flow modes in the wakes are identified. These findings are qualitatively consistent with the existing flow-visualization studies for a cylinder.

1 Introduction

Flow about a bluff body constitutes an important element of modern fluid dynamics research. In particular, vortex shedding and wake patterns emanating from the separation points are of vital interest to the designers of engineering structures. The solid structures may develop flow-induced oscillations, and these phenomena are of concern to the construction and operation of high-performance technological systems.

The studies of flow characteristics about bluff bodies have been concentrated to geomerically simple configurations. The most widely dealt with are cylinders and flat plates placed in a uniform, steady approach stream. A good deal of experimental observations have been accumulated on the vortex shedding patterns behind bodies of simple geometries (e.g, Chen and Ballengee, 1971; Hatfield and Morokovin, 1973). The principle results are illustrated in the form of the behavior of the Strouhal number (St) with the Reynolds number, which describes the periodic nature of vortex shedding in the wake. Also of usefulness are the integrated surface pressures, which turn up in the drag (C_D) and lift coefficient (C_L) experienced by the body. Extensive experimental endeavors, using wind- and water-turnnels, have substantially deepened our understanding of the salient dynamic features that arise in the interaction of a steady uniform flow with a bluff body.

In the present paper, we shall address the topic of flow about a flat plate, placed normal to the approach flow direction, when the oncoming freestream contains significant amounts of pulsating components. In many realistic situations, oscillating velocity components are embedded in the oncoming stream. An example can be found in wind-tunnel testings; the freestream normally contains pulsating components due to the fan/compressor motions. It is also important to recognize that the major characteristics in the wake of a pulsating flow demonstrate features which are qualitatively different from the case of a nonpulsating counterpart. One prominent technical issue is the lock-on phenomenon of the shedding frequency on the imposing frequency of the pulsation. The lock-on has been discussed widely in unsteady dynamics, and the physical implications of the lock-on on coupled flow-body systems have been rigorously investigated (Hussain and Ramjee, 1976, Barbi et al., 1986).

The purpose of this work is to portray the unsteady dynamics of a pulsating oncoming free stream about a flat plate by utilizing numerical simulations. It is remarked here that much of the essential unsteady behavior may be depicted by the computational methods with vortices. Variations of these methods have been widely utilized for a class of flow problems, and the principal features of the techniques have been documented (e.g., Sarpkaya, 1975, Kiya and Arie, 1980, Chein and Chung, 1988, Smith and Stansby, 1989). In particular, the discrete vortex method has been shown to be a powerful tool to describe the separated flow of a non-pulsating approach stream at high Reynolds numbers. The crux of the method is that the separated flow is modeled by a combination of two ingredients. One is the inviscid potential flow, which is generated by the oncoming flow. The other is the time-dependent behavior of the discrete vortices, which are shed in the neighborhoods of the separation points. The effect of viscosity and

Contributed by the Fluids Engineering Division for publication in the JOURNAL OF FLUIDS ENGINEERING. Manuscript received by the Fluids Engineering Division December 14, 1992; revised manuscript received February 23, 1994. Associate Technical Editor: A. F. Ghoniem.

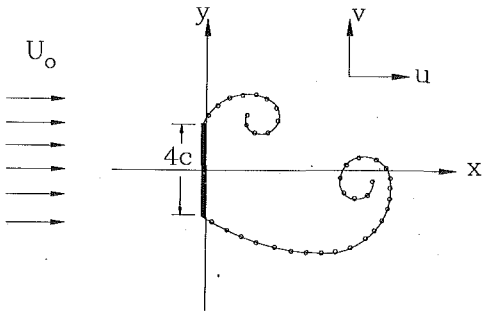

Fig. 1 Definition sketch and coordinate system

the reduction of the strength of circulation of vortices after shedding are accounted for accordingly by invoking physically meaningful conceptual models. The highlights of this technique, together with the modifications in the computational schemes implemented in the present endeavors, will be briefly recapitulated. It should be mentioned here that much of the numerical procedures are well-established. No claims are made as to the development of original and/or innovative numerical schemes.

The emphasis of this paper is placed on analyzing the time-dependent separated flows emanating from the two edges of the plate when the oncoming stream contains considerable pulsations. The primary advantage of the numerical simulations is that wide ranges of the relevant flow parameters can be encompassed. It would be highly desirable to conduct experiments which could lead to direct time-history comparisons with the numerical results. However, presently, no laboratory experimental data on this particular flow condition are available to establish the accuracy and limitations of the numerical techniques. The major mission of the present paper is directed to clarifying the qualitative character of flow. The wealth of numerical results will be examined in light of the existing information based on similar, related experimental setups. First, the viability of the present numerical simulation procedure is ascertained by repeating calculations of the nonpulsating flow solutions. Several key features of the flow are thoroughly delineated, and the predictions of the present simulations are found to be consistent with the preceding analyses. However, for the case of a pulsating oncoming stream, there is a conspicuous lack of published information on numerical methodologies. The present numerical method is shown to produce reliable and physically acceptable solutions over broad ranges of the two parameters, i.e., the amplitude (A_0) and frequency of pulsation (f_p) in the approach flow. Based on these computational results, assessments are made of the interrelationship between the dominant vortex shedding frequency f_s and f_p. The present numerical results confirm the existence of lock-on, which indicates that $f_s = 0.5f_p$ when f_p exceeds a certain threshold value. These are in support of the prior experimental measurement data (Hussain and Ramjee, 1976 and Barbi et al., 1986). Examinations are made as to the effect of pulsation amplitude on the boundaries of f_p in which lock-on takes place. Systematic evaluations of the time histories of vortex shedding lead to the observation that, as A_0 increases, lock-on is expected to occur over an increasingly broader range of f_p. Another principal outcome of these numerical simulations is the characterization of the global wake pattern as f_p encompasses a wide range. The present findings about a normal flat plate demonstrate qualitatively similar characteristic flow modes to those illustrations obtained by the previous experimental visualizations using a cylinder (Barbi et al., 1986).

2 The Model

A definition sketch of the flow configuration is shown in Fig. 1, together with the Cartesian coordinates (x,y) and the corresponding velocity components (u,v). The flat plate is, of height $4c$, placed perpendicular to the approach flow. As stated earlier, the approach freestream is assumed to be

$$U_\infty = U_0(1 + A_0 \cos f_p t) \tag{1}$$

For the present problem, the discrete vortex model is adopted. This has been successfully employed by several authors (e.g., Kiya and Arie, 1977; 1980, Chein and Chung, (1988) to tackle a variety of separated flows. As reviewed in the literature (Sarpkaya, 1988), the crux of this method is to represent the shear layer emanating from the separation points by an array of discrete vortices, which are termed the nascent vortices. The motion of the shear layers is depicted by the evolving arrays of vortices which are introduced into the wake.

For the geometry at hand, in line with Kiya and Arie (1980), the flat plate in the physical z-plane is mapped, by using the Joukowsky transformation, into a circle in the transformed ζ-plane (see Fig. 2). As remarked by Kiya and Arie, such a transformation is useful to render a convenient problem formulation.

Following Kiya and Arie (1980), a system of image vortices is constructed in the transformed plane such that the condition of zero normal velocity at the surface of the circle is satisfied. In the ensuing developments, nondimensional quantities are adopted by adopting $2c$ and $2c/U_0$ for reference scales for length and time, respectively.

The complex velocity-potential $F(\zeta)$ for the total flow in the transformed plane is made up of the potential due to the approach flow and the potential induced by the vortices:

$$F(\zeta) = -U_\infty\left(\zeta e^{-i\alpha} + \frac{c^2}{\zeta} e^{i\alpha}\right) + \sum_{k=1}^{m} \frac{i\Gamma_{kp}}{2\pi} \log(\zeta - \zeta_{kp}) - \sum_{k=1}^{m} \frac{i\Gamma_{kp}}{2\pi} \log\left(\zeta - \frac{c^2}{\zeta_{kp}}\right) - \sum_{k=1}^{m} \frac{i\Gamma_{kg}}{2\pi} \log(\zeta - \zeta_{kq}) + \sum_{k=1}^{m} \frac{i\Gamma_{kg}}{2\pi} \log\left(\zeta - \frac{c^2}{\zeta_{kq}}\right) \tag{2}$$

where Γ_{kp} and ζ_{kp} denote, respectively, the circulation and the location of the kth p-vortex, Γ_{kq} and ζ_{kq} the circulation and the location of the kth q-vortex, as displayed in Fig. 2. As in

Nomenclature

A_0 = pulsation amplitude
c = raidus of circle in the transformed ζ-plane
C_D = drag coefficient
C_L = lift coefficient
C_p = pressure coefficient
f_p = pulsation coefficient
f_s = shedding frequency
f_{so} = natural shedding frequency
f_m = modulated frequency, $|f_p - f_s|$
St = Strouhal number
t = time
Δt = time interval
U_0 = free stream velocity
u, v = mean velocity in x- and y-direction, respectively
z = complex coordinate in the physical z-plane
ϵ = shear layer thickness
ζ = complex coordinate in the transformed ζ-plane
Γ = circulation
Γ_{kp}, Γ_{kq} = strength of circulation of kth p-vortex and kth q-vortex, respectively
F = complex velocity potential
σ = cutt-off radius

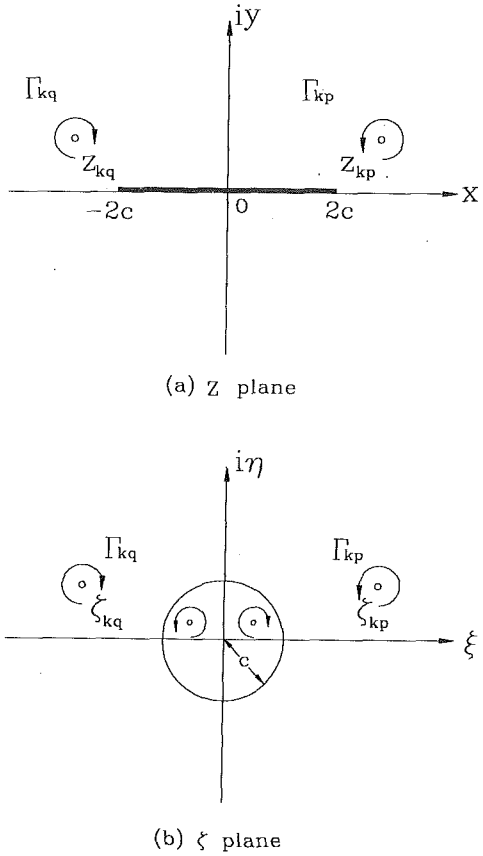

Fig. 2 Schematic configurations of (*a*) physical *z*- and (*b*) transformed ζ-planes

the notation of Sarpkaya (1975) and Kiya and Arie (1977; 1980), the *p*- and *q*- vortex indicate counter-clockwise and clockwise vortices, respectively. An overbar indicates the complex conjugate and *c* denotes the radius of circle in the transformed ζ-plane (Kiya and Arie, 1980).

The velocity in the physical *z*-plane is therefore expressed as

$$u_k - iv_k = \frac{d}{d\zeta}\left[F(\zeta) - \frac{i\Gamma_k}{2\pi}\log(\zeta-\zeta_k)\right]\frac{1}{f'(\zeta)}\Big|_{\zeta=\zeta_k} - \frac{i\Gamma_k}{4\pi}\frac{f''(\zeta_k)}{[f'(\zeta_k)]^2} \quad (3)$$

where $z = f(\zeta)$ is the transform function, Γ_k the circulation about z_k, $F(\zeta)$ the complex potential, ζ_k is the mapping point of z_k. The last term in (3) represents Routh's correction (Sarpkaya, 1988), which takes care of the geometrical effects stemming from the transformation of the planes.

A key element of the present numerical model lies in the determination of the strengths and positions of the nascent vortices. In the previous development of Kiya and Arie (1980) for nonpulsating flows, the positions of the nascent vortices were fixed, at some points very close to the edges of the flat plate. However, several earlier attempts in accordance with the above-stated method of fixed-position nascent vortices, failed to yield converged solutions for the present problem of pulsating approach flows. Careful assessments of the numerical results, together with a systematic reformulation of the numerical procedures, lead to the following conclusion. In order to obtain numerically stable solutions for pulsating flows, the positions of the nascent vortices should be allowed to vary, within some localized areas, near the edges of the plate. This technique turns out to be complementary to the method of Kiya and Arie (1980), which is effective for the case of pulsating approach flows.

The plausibility argument for the present method of variable-position nascent vortices is that, for a pulsating approach flow, the precise positions of the separation points would also oscillate in small localized regions near the edges. It should be pointed out that Sarpkaya (1975) and Chein and Chung (1988) developed the basic ideas of variable-position nascent vortices. In line with this physical picture, the positions of the nascent vortices should be permitted to vary, while satisfying certain physically imposed constraints. In the present development, it is noted that the Kutta condition should be enforced at both edges of the plate, i.e., in the transfomed ζ-plane,

$$(dF/d\zeta)_{\zeta=\pm 0.5} = 0. \quad (4)$$

Furthermore, the rate of vorticity shedding at the separation point is governed by the well-known relationship (e.g., Evans and Bloor, 1977):

$$\frac{d\Gamma}{dt} = \frac{1}{2}U_s^2 \quad (5)$$

in which, Γ is the total circulation and U_s is the velocity at the outer edge of the separated shear layer with a very small width ϵ. In passing, it is mentioned that Eq. (5) represents an approximation. A more precise form would include a term which corresponds to the flow at the inner edge of the shear layer. In the present case, Eq. (5) is adopted, under the assumption that the outer flow velocity is much larger in magnitude than the inner flow velocity (Sarpkaya, 1975; Kiya and Arie, 1977, 1980; Kiya et al., 1982; Nagano et al. (1982; Chein and Chung, 1988). In the original discrete vortex method, the no-slip condition is not applied for the boundary condition for tangential velocity at the wall.

In the actual solution procedure, Eqs. (4) and (5) are solved at each calculation step to determine the values of Γ and ϵ. It is important to note that the edges of the plate in the *z*-plane are mapped onto the real axis in the ζ-plane, thereby indicating the absence of the imaginary parts. This fact greatly simplifies the calculations; Eq. (4), i.e., the Kutta condition, was found to be easily amenable to a Newton-type iterative method at each time step. The iterations, starting from some educated initial guesses for Γ and ϵ near the edges of the plate, were continued until a suitable convergence criterion was met. In the wake region, the convection of vortices was simulated by employing the Adams-Bashforth-type scheme:

$$z_k^{n+1} = z_k^n + 0.5(3u_k^n - u_k^{n-1})\Delta t. \quad (6)$$

The time interval was set to be sufficiently small to enable detailed descriptions of the prominent characteristics of the evolving flows. As the flow field develops, decays of vortices take place due mainly to the viscous effects, the interaction of vortices with the solid boundaries and the interaction of vortices with the solid boundaries and the interactions of vortices of opposite signs. As pointed out by Sarpkaya (1988), the discrete vortex method does not directly deal with the viscosity effects. Several models have been proposed to address this aspect (Evans and Bloor, 1977; Nagano et al., 1982; Smith and Stansby, 1989; Blevins, 1991), although a precise treatment of viscosity remains to be an unresolved problem. The current status of model capabilities in this regard should be borne in mind. In the present paper, the experimental findings of Nagano et al. (1982) are cited to obtain an estimate of vorticity decays. In view of these experimental measurements, the vorticity decay is modeled as

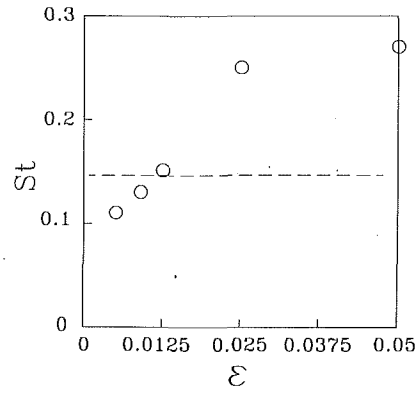

Fig. 3 Variation of the Strouhal number (St) with the position of the nascent vortex (ϵ)

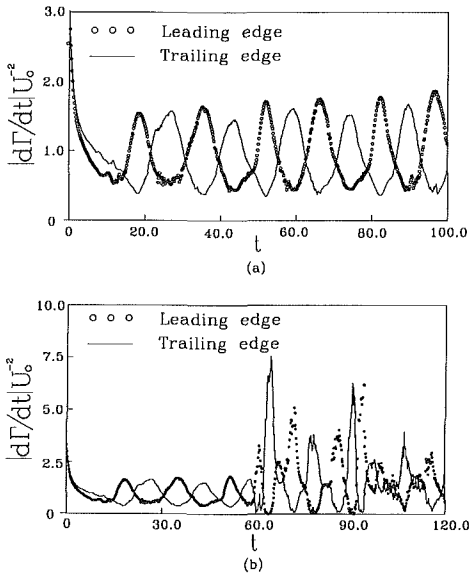

Fig. 4 Temporal variation of the rate of vorticity shedding, as computed by the fixed-position nascent vortex method. (*a*) nonpulsating flow ($A_0 = 0$) (*b*) pulsating flow ($f_p = 0.14$, $A_0 = 0.1$)

$$\frac{\Gamma(t)}{\Gamma_n} = 0.99 \qquad 0 < t < 2.0$$

$$\frac{\Gamma(t)}{\Gamma_n} = 1 - \exp\left(-\frac{60.0}{t}\right) \qquad 2.0 < t < 8.0 \qquad (7)$$

$$\frac{\Gamma(t)}{\Gamma_n} = 0.60 \qquad t > 0.8$$

in which Γ_n is the initial strength, $\Gamma(t)$ the circulation at time t. In this connection, the cut-off vortex model, proposed by Chorin (1973), was adopted in the present work. This was needed to take care of the singularity of an inviscid point vortex. The value of the cut-off radius was determined in a manner similar to that of the preceding investigations (Kiya et al., 1982).

In the course of actual computations, the number of vortices increases in the flow field as time elapses. In order to keep the computational economy within a manageable limit, the vortices that have negligible influence on the gross flow characteristics are removed from the computational domain. To this end, the vortices that have crossed over the line $y = 15.0$ are eliminated from the computations. Systematic studies have been made by repeating the computations for $y = 15.0$, 20.0 and 30.0. The resulting variations in the global flow features of interest were found to be very small (less than 1.0 percent), and $y = 15.0$ was chosen in the ensuing calculations.

In the actual calculations, no computations were made in the region very close to the solid plate, say, within a distance of 0.05. In this region, owing to the proximity of the image vortices, unreasonably high velocities are expected to occur. In order to bypass these difficulties, the afore-stated method of Chorin (1973) was employed. This is admittedly not a completely satisfactory remedy. However, as was amply discussed in the preceding accounts (Sarpkaya, 1988), in light of the lack of a better model, this approach is pursued in the present work.

In all the flows computed in the present numerical experiments, a quasi-periodic flow pattern was achieved typically at times t larger than 40.0

3 Results and Discussion

First, it is important to ascertain the reliability and accuracy of the present numerical procedures. This forms an integral part of the overall validation efforts. The assessments of the present methods will be made by comparing the numerical results against the data of the well-confirmed case studies.

Kiya and Arie (1980), in executing the conventional discrete vortex method using the fixed-position nascent vortices, stressed the significance of an accurate determination of the precise location of the nascent vortex. For the case of a uniform nonpulsating approach flow to a flat plate, Fig. 3 shows the behavior of the Strouhal number (St) as a function of the location of the fixed-position nascent vortex. Here, the position of the nascent vortex is fixed at distance ϵ from the edge of the plate. As displayed in Fig. 3, at around $\epsilon = 0.0125$, the value of St yields excellent agreement with the prior results of Kiya and Arie (1980).

The inadequacy of the fixed-position nascent vortex method for the case of pulsating approach flows is exemplified in Fig. 4. Using the value $\epsilon = 0.0125$, as selected in Fig. 3, the history of the rate of vortex shedding, for the case of a non-pulsating uniform freestream, is demonstrated in Fig. 4(*a*). The observed Strouhal number is St = 0.146, which is consistent with the existing data in the literature (Kiya and Arie, 1980). In summary, when the approach stream is a uniform non-pulsating flow, the fixed-position nascent vortex method, as proposed by Kiya and Arie (1980), is found to be capable of producing satisfactory simulations.

As briefly mentioned in the Introduction, however, the fixed-position nascent vortex method, when applied to the case of pulsating approach flows, fails to yield converged solutions. Numerous attempts, with varying values of ϵ, time step, and cut-off radius, have been shown to be unsuccessful to generate stable simulations. The result of Fig. 4(*b*) is prototypical of the diverging solutions that are obtained after some intermediate times. This clearly calls for an improved version of the fixed-position nascent vortex technique. The rationale is that, since the approach flow contains pulsating parts, the initial release positions of the nascent vortices should also be flexible, while satisfying the underlying physical constraints described earlier.

The capabilities of the present variable-position nascent vortex method are examined by comparing its predictions against the existing data. For this purpose, calculations were repeated, employing the present technique, for the uniform nonpulsating flow about a normal flat plate. Table 1 lists the comparisons of the present output against the available data in the literature. Notice that in Table 1, the calculation scheme of Kiya and Arie (1980) is based on the aforestated fixed-position nascent vortex method. Clearly, as expected, the present predictions are in broad agreement with the prior works.

Now, the performance of the present computation scheme, incorporating the variable-position nascent vortices, for the

Table 1 Comparisons of St, C_D, C_L with other computational and experimental data

	St	C_D	C_L
Present	0.146	1.97	0.00
Kiya and Arie (Cal.)	0.150	2.00	—
Fage and Johansen (Exp.)	0.146	1.85	0.00
Roshko (Exp.)	0.143	—	—

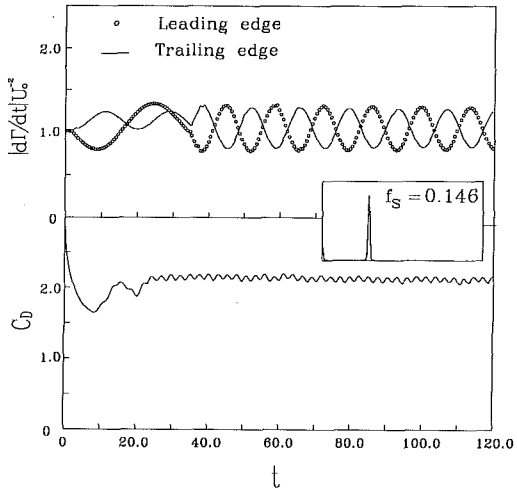

Fig. 5 Temporal variations of the rate of vorticity shedding and C_D, as computed by the variable-position nascent vortex method

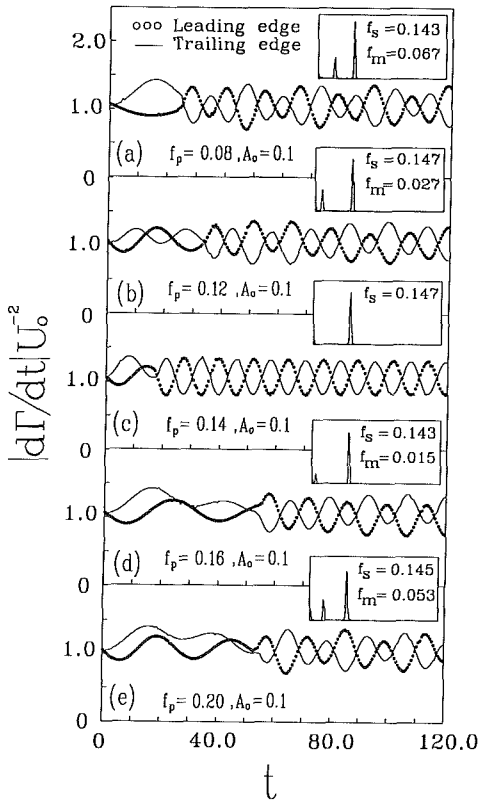

Fig. 6 Temporal variations of the rate of shedding of vorticity for $0.03 \le f_p \le 0.20$. $A_0 = 0.1$

case of a pulsating approach flow is inspected. For all the cases calculated in the present study, the computed results consistently exhibited high degrees of stability and excellent convergence characteristics. The usefulness of the method of variable-

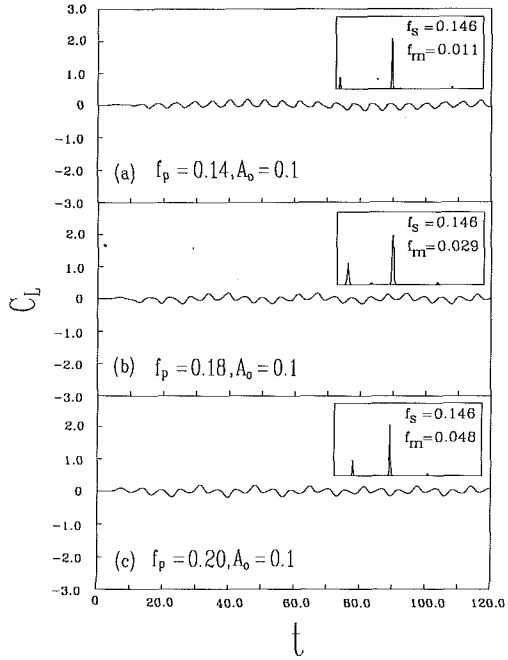

Fig. 7 Temporal variations of the instantaneous lift coefficient (C_L)

position nascent vortices was stressed earlier by Sarpkaya (1975) and Chein and Chung (1988), and the present results are supportive of these assertions. Figure 5 depicts a representative set of the present numerical results, plotted in the form of time-dependent behavior of vortex shedding and the integrated quantity such as C_D. Obviously, the computed data reveal that quasi-periodic flow patterns are attained after nearly $t \cong 40.0$. It should be mentioned here that, for the case of pulsating approach flows, there are no experimental measurement data to validate the present numerical predictions. However, it is encouraging that the present computational scheme does produce highly stable and reasonably accurate results for the cases of both the usual nonpulsating approach flows and the pulsating freestreams. The central objective of the present numerical efforts, as remarked previously, is to scrutinize the eminent time-dependent characteristics, notably the lock-on phenomenon, of the global flow field when a pulsating freestream approaches the normal flat plate. The reliability and stability of the present numerical scheme are adequate in serving the above-defined purpose of the present numerical experiments. Based on this reasoning, we shall now proceed to explore the salient temporal characteristics of the wake flow behind the plate, which are influenced by the pulsating oncoming stream. In the ensuing discussions, the externally controllable nondimensional parameters are: the nondimensional pulsation frequency of the approach flow f_p, and the amplitude of pulsation A_0. In the actual computations, the parameter ranges were: $f_p = 0.0 \sim 0.4$, $A_0 = 0.0 \sim 0.6$. For most of the preceding experimental work involving pulsating flows, the maximum amplitude of pulsation has been usually rather small, typically in the neighborhood of $A_{0max} \cong 0.1$.

As in Kiya and Arie (1980), the computed result of the rate of vorticity shedding was chosen to be the major physical quantity for detailed examination. Figure 6 exemplifies the histories of this quantity, together with the output of its Fast Fourier Transformation (FFT). For the illustrated results of Fig. 6, the amplitude is set at a reasonably small value $A_0 = 0.1$, while f_p encompasses a wide range $0.08 \le f_p \le 0.20$. Figure 6 discloses that the primary natural shedding frequency remains to be substantially unchanged $f_s \cong 0.145$, as the externally specified pulsation frequency f_p is altered. This indicates that,

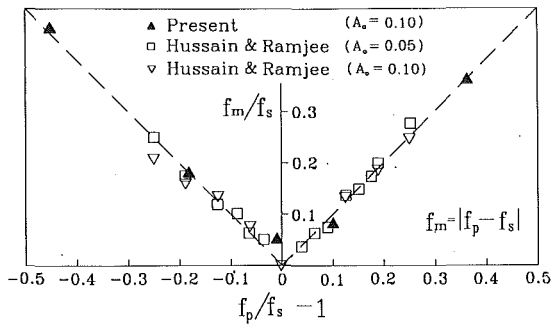

Fig. 8 Modulation frequency f_m as a function of pulsation frequency f_p

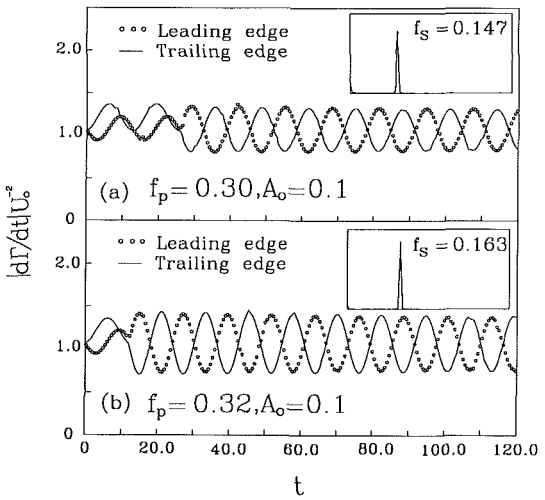

Fig. 9 Effects of A_0 on the rate of vorticity shedding. (*a*) f_p = 0.30, A_0 = 0.1, (*b*) f_p = 0.32, A_0 = 0.1

when the amplitude of pulsation is small, the dominant frequency of the Karman vortex street in the wake is not affected much by the presence of pulsation in the approach freestream. This observation is intuitively plausible, and it is in qualitative agreement with the experimental data of Hatfield and Morkovin (1973) for a bluff body when the pulsation amplitude is rather small ($A_0 \cong 0.08$).

A closer inspection of the time histories in Fig. 6 reveals that the vorticity shedding rate is modulated at a lower frequency, f_m. This modulation frequency f_m is visible in the FFT analysis. As demonstrated in the experiment of Hussain and Ramjee (1976) for a bluff body, this modulation frequency f_m is seen to be related to the difference between the externally-enforced pulsation frequency and the natural shedding frequency, i.e., $f_m \sim |f_p - f_s|$. The present results indicate the existence of the modulation frequency f_m, which has long been recognized in experimental unsteady dynamics. The significance of the modulation frequency, $f_m \sim |f_p - f_s|$, is also discernible in the temporal behavior of such an integrated physical quantity as the instantaneous lift coefficient, C_L, as exhibited in Fig. 7.

The entire computational results, obtained for reasonably small pulsation amplitudes ($A_0 \leq 0.1$), are assembled in Fig. 8, which provides a confirmation of the relationship between the three principal frequencies. These data, which include the present calculations and the associated experimental measurements (Hussain and Ramjee, 1976), are mutually consistent and are in accord with the relationship $f_m \sim |f_p - f_s|$.

Now, as the pulsation frequency is increased further, e.g., f_p = 0.30 ~ 0.32 in Fig. 9, A_0 being unchanged (A_0 = 0.1), the numerically constructed temporal behavior shows a dramatic qualitative change from that of lower values of f_p. The vortex shedding patterns are substantially periodic, with the dominant frequency f_s being close to one-half of the pulsation frequency, $f_s \sim 0.5 f_p$. The time-histories of Fig. 9, for f_p = 0.30 and f_p = 0.32, together with their FFT analyses, attest to the above findings. This is a manifestation of the celebrated physical phenomenon "lock-on." As described by experiments of Barbi et al. (1986) for a cylinder, when the lock-on is established, the flow field in the wake is characterized by well-defined large-scale structures which evolve at a specific dominant frequency. It is worth mentioning that lock-on is expected when the pulsation frequency f_p exceeds a certain threshold value. In the experiments of Hussain and Ramjee (1976) for a circular cylinder, the lock-on phenomenon was not conspicuous. The nonappearance of lock-on can be attributed to the fact that, in their experiment, the maximum value of f_p used was restricted due to inherent physical limitations of their experimental apparatus.

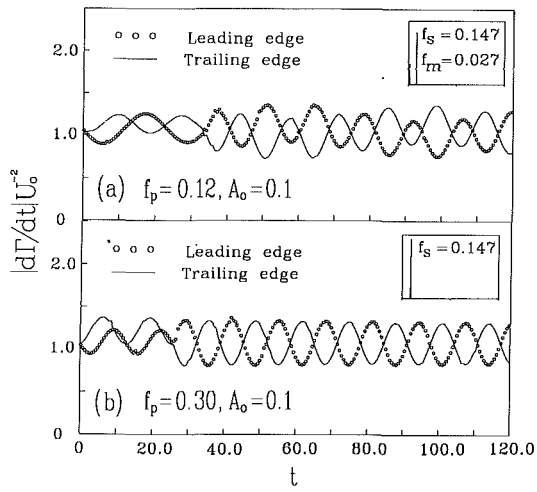

Fig. 10 Effects of f_p on the rate of vorticity shedding. (*a*) f_p = 0.12, A_0 = 0.1 (*b*) f_p = 0.30, A_0 = 0.1

Summarizing the numerical results for the entire gamut of f_p, a conclusion emerges that the patterns of vortex shedding can be classified into two qualitatively distinctive regimes in Fig. 10. When f_p is reasonably low, the temporal behavior is characterized by beating at f_m, where $f_m \sim |f_p - f_s|$. The Strouhal number is thus governed primarily by the natural shedding frequency. On the other hand, when f_p is above a threshold value, lock-on is the principal physical phenomenon. The shedding frequency is nearly one-half of the pulsation frequency, $f_s \sim 0.5 f_p$. When this takes place, the temporal behavior is highly organized and the vortex shedding pattern evolves at a specific well-defined frequency.

The foregoing discussions were conducted when the pulsation amplitude is fixed at a reasonably small value, A_0 = 0.1. As addressed by Barbi et al. (1986) for a cylinder, the effect of pulsation amplitude A_0 on the resulting flow characteristics poses a crucial issue. For this purpose, the frequency diagrams are constructed for two different pulsation amplitudes. In Fig. 11, lock-on implies the frequency relationship $f_s = 0.5 f_p$, which is represented by the straight dotted line. When A_0 is low (see o marks in the figure for A_0 = 0.1), the threshold pulsation frequency f_p for lock-on is approximaltey $f_p/f_{so} \approx 1.9$, where f_{so} is the natural shedding frequency. Clearly, when $f_p/f_{so} \leq 1.9$, the shedding frequency f_s is nearly constant ($f_s/f \cong 1.0$), and it is independent of f_p. When A_0 is large, (see Δ marks in the figure for A_0 = 0.6), lock-on is initiated at a smaller value of f_p, i.e., $f_p/f_{so} \geq 0.9$ for lock-on for A_0 = 0.6. It is also interesting to note that, when f_p is slightly less than the threshold value, f_s also takes a slightly smaller value. This aspect, which is disclosed by the present numerical results, is in qual-

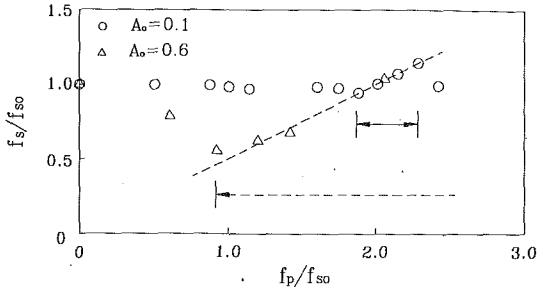

Fig. 11 The relationship among the vortex shedding frequency f_s, pulsation frequency f_p, and natural shedding frequency f_{so}

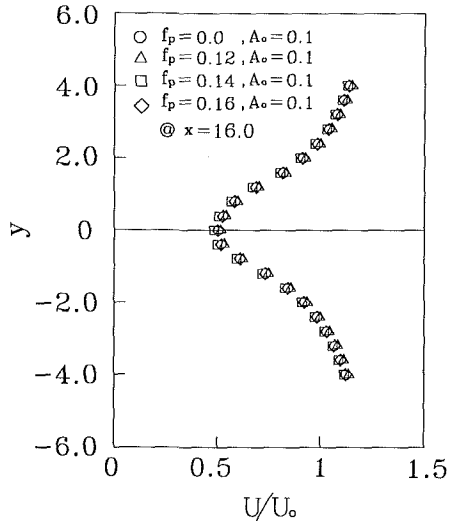

Fig. 12 Averaged velocity field behind the normal plate. x = 16.0

itative agreement with the prior experimental observations of Barbi et al. (1986). Further systematic evaluations of the threshhold frequencies for lock-on, as influenced by the pulsation amplitude A_0, are carried out. As displayed in Fig. 11, the important observation is that, as A_0 increases, the ranges of f_p in which lock-on takes place are widened in both directions of f_p. The broadening of the range of f_p for lock-on is appreciable as A_0 increases to moderate and large values.

Based on the wealth of numerical results, it is useful to characterize the velocity field in the wake. An exemplary profile is plotted in Fig. 12. Clearly, the averaged velocity profile in the wake is quite insensitive to the pulsation frequency. These findings are in qualitative consistency with the experimental observations of Hussain and Ramjee (1976).

It is recalled that, for the case of a cylinder, Barbi et al. (1986) performed extensive flow visualization studies. Their experimental results illustrated the three characteristic flow modes as f_p varies over a range, as demonstrated in Fig. 13. In the present study, similar characterizations are attempted by constructing the flow field by using the numerical results. In Fig. 14, plots are presented for three selective values of f_p = 0.08, 0.14 and 0.32. These, respectively, are prototypical of the qualitatively distinct conditions: when f_p is very small, when f_p is increased to a value slightly smaller than the threshold value for lock-on, and when f_p is slightly larger than the threshold value for lock-on. Figure 14 exhibits the time evolutions of wake patterns of the above three modes.

Plots in Fig. 14(*a*) are for f_p = 0.08, a small value. The vortex pattern is qualitatively similar to the conventional Karman vortex street. The vortex shedding occurs alternatively over the natural cycle. At this low value of f_p, the flow pattern arising from the frequency modulation is not discernible. Fig-

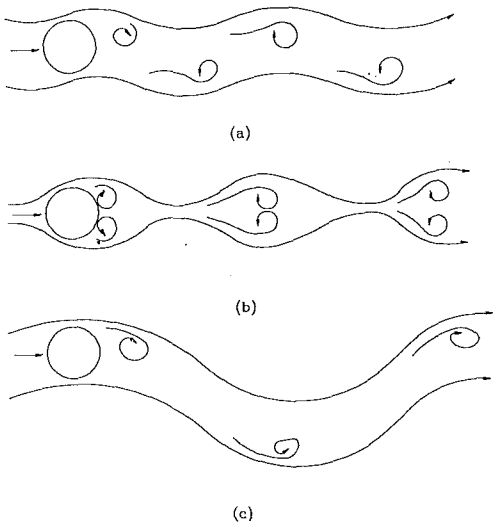

Fig. 13 Flow mode characterizations for a cylinder. Cases (*a*), (*b*), and (*c*) correspond to the experimental conditions of Barbi et al. (1986).

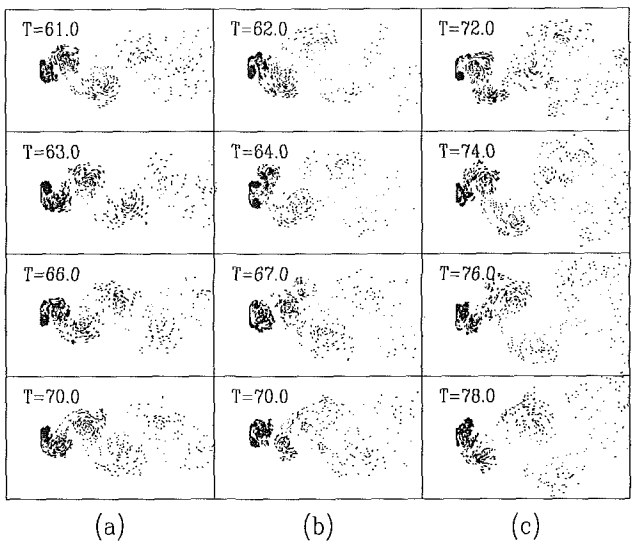

Fig. 14 Characterizations of flow modes. (*a*) f_p = 0.03, A_0 = 0.1, (*b*) = f_p = 0.14, A_0 = 0.1, (*c*) f_p = 0.32, A_0 = 0.1, A_0 = 0.1.

ure 14(*b*) is representative of the conditions of moderate values of f_p, but f_p being slightly less than the lock-on threshold frequency. The patterns showing the progressive frequency attraction are seen. Two symmetric vortices are shed simultaneously during one cycle. These features are in fair consistency with the patterns sketched in Fig. 13(*b*).

When f_p is in the lock-on range, as shown in Fig. 14(*c*), the vorticity shedding is vigorous. The vortex tends to stay closer to the plate during its formation and growth stages. A vortex then absorbs the counter-rotating vortex and this process creates a sudden rolling of the wake toward the opposite side. It is also apparent that the width of the entire wake region increases. The numerically constructed visualization of Fig. 14 are demonstrative of the qualitative similarities between the present results and the experimental observations of Barbi et al. (1986) for a cylinder.

Concluding Remarks

A version of the discrete vortex simulation was applied to calculate the separated flow behind a plate placed normal to the approach flow with a pulsating component. Modifications based on physical constraints are introduced into the com-

putational schemes, which lead to variable-position nascent vortex techniques. This proved to be effective in dealing with the cases of pulsating approaching flows. When f_p is reasonably small, the vortex shedding frequency f_s is nearly constant and is independent of f_p. The time histories of vortex shedding, however, are modulated at a lower frequency $f_m \sim |f_p - f_s|$. The present numerical simulations manifest the existence of lock-on phenomenon, i.e., $f_s \sim 0.5 f_p$, when f_p is higher than a certain threshold value. These results are consistent with the prior experimental observations. The range of f_p, in which lock-on takes place, is substantially broadened as A_0 increases. It is found that the averaged velocity profile in the wake is insensitive to the pulsation frequency. The numerically constructed flow visualizations identify the characteristic flow modes over a range of f_p. These flow regimes show qualitative similarities to the prior experimental observations for a cylinder.

Acknowledgment

Appreciation is extended to the referees who provided detailed and helpful comments. The suggestions of the referees led to improvements in the revised paper.

References

Barbi, C., Favier, D. P., Maresca, C. A., and Telionis, D. P., 1986, "Vortex Shedding and Lock-on of a Circular Cylinder in Oscillatory Flow," *Journal of Fluid Mechanics*, Vol. 170, pp. 527–544.

Blevin, R. D., 1991, "Application of the Discrete Vortex Method to Fluid-Structure Interaction," ASME *Journal of Pressure Vessel Technology*, Vol. 113, pp. 437–445.

Chen, C. F., and Ballengee, D. B., 1971, "Vortex Shedding from Circular Cylinders in an Oscillating Freestream," *AIAA Journal*, Vol. 9, pp. 340–349.

Chein, R., and Chung, J. N., 1988, "Discrete-vortex Simulation of Flow over Inclined and Normal Plates," *Computers & Fluids*, Vol. 16, No. 4, pp. 405–427.

Chorin, A. J., 1973, "Numerical Study of Slightly Viscous Flow," *Journal of Fluid Mechanics*, Vol. 57, pp. 785–796.

Evans, R. A.,and Bloor, M. I. G., 1977, "The Starting Mechanism of Wave-induced Flow Through a Sharp-edged Orifice," *Journal of Fluid Mechanics*, Vol. 82, pp. 115–128.

Hatfield, H. M., and Morkovin, H. V., 1973, "Effect of an Oscillating Free Stream on the Unsteady Pressure on a Circular Cylinder," ASME JOURNAL OF FLUIDS ENGINEERING, Vol. 95, pp. 249–254.

Hussain, A. K. M. F., and Ramjee, V., 1976, "Periodic Wake behind a Circular Cylinder at Low Reynolds Numbers," *Aeronautical Quarterly*, Vol. 123, pp. 123–142.

Kiya, M., and Arie, M., 1977, "A Contribution to an Inviscid Vortex-shedding Model for an Inclined Flat Plate in Uniform Flow," *Journal of Fluid Mechanics*, Vol. 82, pp. 223–240.

Kiya, M., and Arie, M., 1980, "Discrete-vortex Simulation of Unsteady Separated Flow behind a Nearly Normal Plate," *Bulletin of JSME*, Vol. 23, No. 183, pp. 1451–1458.

Kiya, M., Sasaki, K., and Arie, M., 1982, "Discrete-vortex Simulation of a Turbulent Separation Bubble," *Journal of Fluid Mechanics*, Vol. 120, pp. 219–244.

Kuwahara, K., 1978, "Study of Flow past a Circular Cylinder by an Inviscid Model," *Journal of Physical Society, Japan*, Vol. 45, pp. 292–297.

Nagano, S., Naito, M., and Takata, H., 1982, "A Numerical Analysis of Two-dimensional Flow past a Rectangular Prism by a Discete Vortex Model," *Computers and Fluids*, Vol. 10, No. 4, pp. 243–259.

Sarpkaya, T., 1975, "An Inviscid Model of Two-dimensional Vortex Shedding for Transient and Asympotically Steady Separated Flow over an Inclined Plate," *Journal of Fluid Mechanics*, Vol. 68, pp. 109–128.

Sarpkaya, T., 1988, "Computational Methods With Vortices-The 1988 Freeman Scholar Lecture," ASME JOURNAL OF FLUIDS ENGINEERING, Vol. 111, pp. 5–52.

Smith, P. A., and Stansby, P. K., 1989, "An Efficient Surface Algorithm for Random-particle Simulation of Vorticity and Heat Transport," *Journal of Computational Physics*, Vol. 81, pp. 349–371.

Navier-Stokes Simulation of the Flow Around an Airfoil in Darrieus Motion

Ko-Foa Tchon

Ion Paraschivoiu

Department of Mechanical Engineering,
Ecole Polytechnique de Montreal,
C. P. 6079, Succursale Centre-Ville,
Montreal (Quebec) H3C 3A7, Canada

In order to study the dynamic stall phenomenon on a Darrieus wind turbine, the incompressible flow field around a moving airfoil is simulated using a noninertial stream function-vorticity formulation of the two-dimensional unsteady Navier-Stokes equations. Spatial discretization is achieved by the streamline upwind Petrov-Galerkin finite element method on a hybrid mesh composed of a structured region of quadrilateral elements in the vicinity of solid boundaries, an unstructured region of triangular elements elsewhere, and a layer of infinite elements surrounding the domain and projecting the external boundary to infinity. Temporal discretization is achieved by an implicit second order finite difference scheme. At each time step, a nonlinear algebraic system is solved by a Newton method. To accelerate computations, the generalized minimum residual method with an incomplete triangular factorization preconditioning is used to solve the linearized Newton systems. The solver is applied to simulate the flow around a NACA 0015 airfoil in Darrieus motion and the results are compared to experimental observations. To the authors' knowledge, it is the first time that the simulation of such a motion has been performed using the Navier-Stokes equations.

Introduction

Darrieus vertical axis wind turbines offer an advantageous alternative to horizontal axis wind turbines because of their mechanical simplicity and their independence from wind direction. However, the Darrieus rotor aerodynamics are particularly complex to analyze and involve dynamic stall. The dynamic stall phenomenon results from the unsteady separation of the boundary layer from the surface of the rotating blades. It is characterized by dynamic delay of stall to angles significantly beyond the static stall angle, and by massive recirculating regions moving downstream over the surface of the airfoil (McCroskey, 1977; Carr, 1988). The unsteady forces due to the passage of this vorticity produce a lift and a nose down moment much greater than the corresponding static stall loads. The aeroelastic response to this phenomenon may cause structural fatigue and even stall flutter leading to catastrophic failure. Dynamic stall can thus become, in many cases, the primary limiting factor in the performance of the turbine. Therefore, in order to predict the aerodynamic performances of such structures and supply aerodynamic loading information to structural dynamic codes, a numerical model must be able to capture the complex aerodynamics encountered by a vertical axis rotor blade, and more particularly the dynamic stall phenomenon.

Several methods have been investigated in order to simulate this kind of aerodynamics. These methods can be classified in two categories: the semi-empirical methods and the theoretical methods. Semi-empirical methods, such as the Gormont, MIT, and indicial models, predict dynamic stall load variations within engineering accuracy. Their application range is, however, limited to the type of airfoil and motion used in the experiments from which they were derived. Moreover, these models cannot predict the local aerodynamics such as the evolution of the boundary layer or pressure distribution, both of which are essential to study the dynamic stall phenomenon or to optimize the airfoil shape of the turbine blades. For such tasks, theoretical methods must be used. Coupled viscous-inviscid methods have first been considered. However, dynamic stall involves large regions of recirculating flow so that Navier-Stokes equations must be considered to account for the important viscous effects present even in regions far from the wall. Although Navier-Stokes solvers have been used to simulate dynamic stall (Shida et al., 1987; Daube et al., 1989; Tuncer et al., 1990; Visbal, 1990), most of the studies were concerned with helicopter retreating-blade stall or agile fighter aircraft. All these studies have thus considered pitching motions and none have considered the rotation motion encountered by the blades of a Darrieus turbine. The present project was thus initiated in order to develop a Navier-Stokes solver able to simulate the flow around an airfoil in Darrieus motion, i.e., the motion experienced by an airfoil on a curved-blade Darrieus vertical axis wind turbine.

The first step of this project resulted in a finite element computer code able to simulate the dynamic stall on a NACA

Contributed by the Fluids Engineering Division for publication in the JOURNAL OF FLUIDS ENGINEERING. Manuscript received by the Fluids Engineering Division November 20, 1992; revised manuscript received March 21, 1994. Associate Technical Editor: O. Baysal.

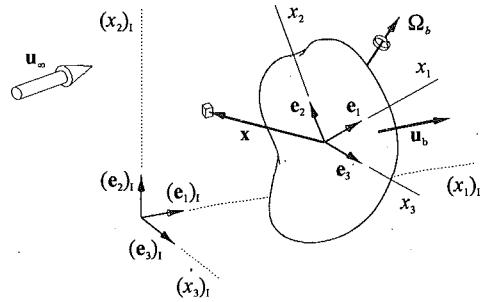

Fig. 1 Noninertial frame of reference

0018 oscillating in pitch at a Reynolds number of 10^4 (Tchon and Paraschivoiu, 1990). The computed flow matched experimental visualizations previously conducted in a water tunnel (Tchon, 1989). However, this code fell short of the prime objective of simulating a Darrieus motion. The main problems were the difficulty of determining adequate conditions on the external boundary for the Darrieus motion and poor control of the density of the structured mesh in critical flow regions. The second step of this project addressed these problems by using a hybrid structured-unstructured computational mesh and infinite elements (Tchon, 1993). The unstructured mesh regions were used to have a better control of the mesh density and the infinite elements simplified the external boundary conditions for the Darrieus motion. The present paper describes the resulting solver and its application to the simulation of the flow around an airfoil in Darrieus motion.

Governing Equations

For wind turbine applications, the fluid can be considered incompressible and is governed by the time averaged Navier-Stokes equations, i.e., the continuity equation

$$\nabla \cdot \bar{\mathbf{u}} = 0 \tag{1}$$

and the momentum equation

$$\frac{D\bar{\mathbf{u}}}{Dt} + 2\boldsymbol{\Omega}_b \times \bar{\mathbf{u}} + \boldsymbol{\Omega}_b \times \boldsymbol{\Omega}_b \times \mathbf{x} + \dot{\boldsymbol{\Omega}}_b \times \mathbf{x} + \dot{\mathbf{u}}_b = -\nabla\left(\frac{\bar{p}}{\rho} + \frac{2}{3}k\right) + \frac{\partial}{\partial x_i}\nu_e\left(\frac{\partial u_i}{\partial x_j} + \frac{\partial u_j}{\partial x_i}\right) \tag{2}$$

in which the Boussinesq hypothesis has been introduced and where $\nu_e = \nu + \nu_t$ is an effective viscosity while k is the turbulent kinetic energy. These two equations are expressed in a noninertial frame of reference $\mathbf{e}_1\mathbf{e}_2\mathbf{e}_3$ moving at a velocity $\mathbf{u}_b$ and rotating with the solid body at a velocity $\boldsymbol{\Omega}_b$ in order to simulate its motion without using a deforming mesh (Fig. 1). Note that, in Fig. 1, the subscript I indicates the inertial frame and the vector $\mathbf{u}_\infty$ corresponds to the wind velocity. This vector $\mathbf{u}_\infty$ represents the the constant part of the translation velocity of the body while the vector $\mathbf{u}_b$ represents the variable part. The term $\mathbf{u}_b$ is not necessary to simulate a Darrieus motion but is nonetheless introduced in order to keep the formulation as general as possible. Turbulence effects can be introduced by using a turbulence model to determine the eddy viscosity ν_t. However, only laminar flow are presently considered and ν_t is thus set to zero.

Since three-dimensional simulations are presently too expensive, the study was limited to two dimensional cases for which it is advantageous to introduce the stream function-vorticity formulation. To avoid undefined conditions at infinity, this formulation is expressed in terms of the perturbation stream function ψ and the perturbation vorticity ω defined by

$$-\mathbf{e}_3 \times \nabla\psi \equiv \bar{\mathbf{u}} + \boldsymbol{\Omega}_b \times \mathbf{x} + \mathbf{u}_b - \mathbf{u}_\infty \tag{3}$$

$$\omega \equiv (\nabla \times \bar{\mathbf{u}} + 2\boldsymbol{\Omega}_b) \cdot \mathbf{e}_3 \tag{4}$$

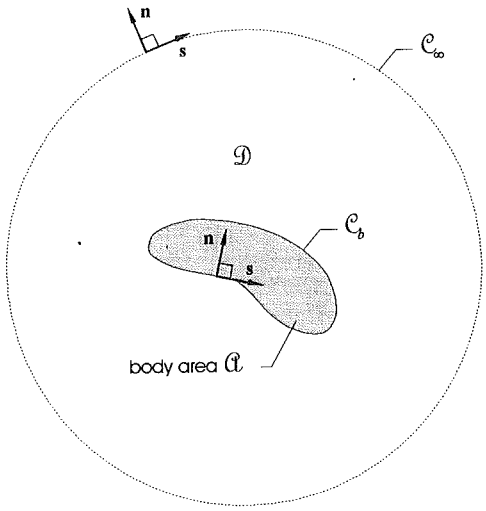

Fig. 2 Spatial domain

Taking the curl of Eqs. (2) and (3) yields the stream function-vorticity formulation, i.e., the vorticity transport equation

$$\frac{\partial\omega}{\partial t} + \nabla \cdot (\omega\bar{\mathbf{u}} - (\nabla\nu_e\omega + 2\mathbf{S}_\omega)) = 0 \tag{5}$$

where

$$\mathbf{S}_\omega = \begin{Bmatrix} \dfrac{\partial\nu_e}{\partial x_1}\dfrac{\partial^2\psi}{\partial x_2^2} - \dfrac{\partial\nu_e}{\partial x_2}\dfrac{\partial^2\psi}{\partial x_1\partial x_2} \\ \dfrac{\partial\nu_e}{\partial x_2}\dfrac{\partial^2\psi}{\partial x_1^2} - \dfrac{\partial\nu_e}{\partial x_1}\dfrac{\partial^2\psi}{\partial x_1\partial x_2} \end{Bmatrix} \tag{6}$$

and the stream function compatibility equation

$$\nabla^2\psi + \omega = 0 \tag{7}$$

defined on a computational domain $\mathcal{D}$ enclosed by an external boundary $\mathcal{C}_\infty$ and an internal solid boundary $\mathcal{C}_b$ (Fig. 2). Note that the term $\mathbf{S}_\omega$ in Eq. (5) can be dropped because it is identically equal to zero for laminar flows and negligible for turbulent flows (Sugavanam and Wu, 1982).

The main advantages of using stream function-vorticity variables compared to primitive variables, i.e., the velocity and pressure, are threefold. First, the compressibility constraint, i.e., the continuity condition, is satisfied automatically by the definition of the stream function. Second, the kinematics and kinetics of the flow, expressed, respectively, by the stream function compatibility equation and the vorticity transport equation, are effectively decoupled from the thermodynamics, expressed by the pressure equation. The pressure assumes thus the role of an engineering parameter to be derived a posteriori from the vorticity and stream function fields, reducing thereby the number of simultaneous unknowns from three to two. Third, all noninertial effects due to the motion of the frame of reference enter the stream function-vorticity formulation only through initial and boundary conditions (Speziale, 1987).

On the other hand, the stream function-vorticity formulation has traditionally been known for several problems. The first problem is that, at the solid wall $\mathcal{C}_b$, normal and essential conditions corresponding to the no-slip condition are available for the stream function but none for the vorticity

$$\psi = \psi_b - \frac{1}{2}\boldsymbol{\Omega}_b\mathbf{x}^2 + \mathbf{e}_3 \times (\mathbf{u}_b - \mathbf{u}_\infty) \cdot \mathbf{x} \tag{8}$$

$$\nabla\psi \cdot \mathbf{n} = (\boldsymbol{\Omega}_b \times \mathbf{x} + \mathbf{u}_b - \mathbf{u}_\infty) \cdot \mathbf{s} \tag{9}$$

where ψ_b is a constant while $\mathbf{s}$ and $\mathbf{n}$ are respectively the unit vector tangent and normal to $\mathcal{C}_b$ (Fig. 2). This problem is bypassed by extending to the unsteady formulation an ap-

proach that solves the compatibility equation and the vorticity transport equation simultaneously and uses the redundant information on the stream function to determine the vorticity on solid boundaries (Peeters et al., 1987; Gunzburger and Peterson, 1988). This approach has also been found to improve numerical stability at high Reynolds numbers (Van Dam and Hafez, 1989).

A second problem is that the stream function on solid walls is known only up to a constant, ψ_b in present case. For simply connected domains, this constant can be arbitrarily set to a reference value but, for multiply connected domains, there is a different constant for each internal boundary. These constants are unknown a priori and need to be determined as part of the solution. The additional conditions needed to fix these constants can, however, be easily deduced by integrating the momentum equation along each internal boundary and by requiring that the pressure be a single-valued function (Gunzburger and Peterson, 1988), yielding the following expression

$$\oint_{\mathcal{C}_b} (\omega\bar{\mathbf{u}} - \nabla \nu_e \omega)\cdot \mathbf{n} d\mathcal{C} = 2\dot{\Omega}_b \mathcal{A} \tag{10}$$

where $\mathcal{A}$ is the cross section area of the body surrounded by $\mathcal{C}_b$.

The third problem traditionally attributed to the stream function-vorticity formulation is that the usual weak formulation of the pressure equation involves second order derivatives of the stream function and has no obvious boundary conditions. This problem is avoided by using a modified pressure, which can be related to the total pressure head,

$$P = \frac{\bar{p}}{\rho} + \frac{2}{3}k + \frac{1}{2}(\mathbf{e}_3 \times \nabla\psi + \mathbf{u}_b - \mathbf{u}_\infty)^2 + \Omega_b \mathbf{x}\cdot\nabla\psi \tag{11}$$

where k is the kinetic turbulent energy, and the following form of the pressure equation, obtained by taking the divergence of Eq. (2),

$$\nabla\cdot\left(\nabla P - \mathbf{e}_3 \times \left(\frac{\partial}{\partial t}\nabla\psi - \omega\bar{\mathbf{u}} + \nabla\nu_e\omega\right)\right) = 0 \tag{12}$$

The following natural condition can then be imposed on solid boundaries

$$\left(\nabla P - \mathbf{e}_3 \times \left(\frac{\partial}{\partial t}\nabla\psi - \omega\bar{\mathbf{u}} + \nabla\nu_e\omega\right)\right)\cdot\mathbf{n} = \Omega_b \mathbf{u}_b \cdot \mathbf{s} \tag{13}$$

while the pressure P is set to a finite reference value, usually zero, at free stream.

For the present study, an additional problem arises at the external boundary from the Darrieus motion. Usually the external boundary is divided into an inlet region where the stream function and vorticity are considered to take known values corresponding to free stream, and an outlet region where a relaxed condition is imposed to allow wake convection. In a non-inertial domain, this outlet region is relatively limited for a pitching motion, but, for a Darrieus motion, a limited outlet region cannot be defined because the wake position will vary with respect to the azimuth angle from 0 to 360 deg. To avoid a moving outlet region, infinite elements are used to effectively project the external boundary to infinity (Zienkiewicz et al., 1983). Along this infinite external boundary $\mathcal{C}_\infty$, no outlet region needs to be defined and simple free stream conditions can be imposed everywhere, i.e., $\psi = \omega = P = 0$.

Discretization

Spatial discretization of the governing equations is achieved by the streamline upwind Petrov-Galerkin (SUPG) finite element method to avoid spurious oscillation of the solution (Tezduyar et al., 1988). The finite element formulation associated with Eqs. (5) and (7) are, respectively,

$$0 = \int_{\mathcal{D}} \left(W^\psi \frac{\partial\omega}{\partial t} - \nabla W^\psi \cdot (\omega\bar{\mathbf{u}} - \nabla\nu_e\omega)\right) d\mathcal{D} + \sum_e \int_{\mathcal{D}} \delta W^\psi \left(\frac{\partial\omega}{\partial t} + \nabla\cdot(\omega\bar{\mathbf{u}} - \nabla\nu_e\omega)\right) d\mathcal{D} + \oint_{\mathcal{C}_b} W^\psi(\omega\bar{\mathbf{u}} - \nabla\nu_e\omega)\cdot\mathbf{n} d\mathcal{C} \tag{14}$$

and

$$0 = \int_{\mathcal{D}} (\nabla W^\omega \cdot \nabla\psi - W^\omega\omega) d\mathcal{D} - \oint_{\mathcal{C}_b} W^\omega (\Omega_b \times \mathbf{x} + \mathbf{u}_b - \mathbf{u}_\infty)\cdot\mathbf{s} d\mathcal{C} \tag{15}$$

where W^ψ and W^ω are weighting functions and δW^ψ is a Petrov-Galerkin perturbation of W^ψ. The formulation for δW^ψ can be found in Tezduyar et al. (1988). The finite element formulation of the pressure Eq. (12) is

$$0 = \int_{\mathcal{D}} \nabla W^P \cdot \nabla P d\mathcal{D} - \int_{\mathcal{D}} \nabla W^P \cdot \mathbf{e}_3 \times \left(\frac{\partial}{\partial t}\nabla\psi - \omega\bar{\mathbf{u}}\nu\nabla_e\omega\right) d\mathcal{D} - \oint_{\mathcal{C}_b} W^P \Omega_b \mathbf{u}_b \cdot \mathbf{s} d\mathcal{C} \tag{16}$$

where W^P is a weighting function. Within each element the variables are approximated by using shape functions $N_j^\omega(\mathbf{x})$, $N_j^\omega(\mathbf{x})$, and $N_j^P(\mathbf{x})$ and nodal values $\psi_j(t)$, $\omega_j(t)$, and $P_j(t)$

$$\psi(\mathbf{x},t) \approx \psi^h(\mathbf{x},t) = \sum_j N_j^\psi(\mathbf{x})\psi_j(t) \tag{17}$$

$$\omega(\mathbf{x},t) \approx \omega^h(\mathbf{x},t) = \sum_j N_j^\omega(\mathbf{x})\omega_j(t) \tag{18}$$

$$P(\mathbf{x},t) \approx P^h(\mathbf{x},t) = \sum_j N_j^P(\mathbf{x})P_j(t) \tag{19}$$

and weighting functions W^ψ, W^ω, and W^P correspond to N^ω, N^ψ, and N^P, respectively. Note that W^ψ does not correspond to N^ψ but rather to N^ω while W^ω corresponds to N^ω in order to avoid a singular matrix system when $N^\psi \neq N^\omega$ (Gunzburger and Peterson, 1984).

An unstructured computational mesh of triangular element was first considered in order to have a better mesh density control in critical regions of the flow. However, to accommodate high Reynolds flows and ease the future introduction of an algebraic turbulence model, a hybrid mesh was eventually preferred and included a structured region of highly stretched quadrilateral elements in the vicinity of solid boundaries, an unstructured region of triangular elements elsewhere, and layer of inifinite elements (Zienkiewicz et al., 1983) surrounding the domain and projecting the external boundary to infinity. Within each element, a linear interpolation is used for all the variables.

Temporal discretization at a time step k is achieved by second order accurate finite differences as follows

$$\left.\frac{\partial\omega}{\partial t}\right|_{x,t^k} \approx \sum_j N_j^\omega(\mathbf{x}) \frac{3\omega_j^k - 4\omega_j^{k-1} + \omega_j^{k-2}}{\Delta t^k + \Delta t^{k-1}} \tag{20}$$

$$\left.\frac{\partial}{\partial t}\nabla\psi\right|_{x,t^k} \approx \sum_j \nabla N_j^\psi(\mathbf{x}) \frac{3\psi_j^k - 4\psi_j^{k-1} + \psi_j^{k-2}}{\Delta t^k + \Delta t^{k-1}} \tag{21}$$

where $\Delta t^{k-1} = t^{k-1} - t^{k-2}$ and $\Delta t^k = t^k - t^{k-1}$. To avoid stability problems, an implicit iterative scheme was chosen and the time step size is thus controlled by accuracy considerations only.

The element equations resulting from the spatial and temporal discretizations are assembled to form two global algebraic matrix systems: a linear one for the pressure and a

nonlinear one for the stream function and the vorticity. The pressure system has to be solved only when the aerodynamic coefficients are needed and is thus relegated to a post processing operation. The coupled stream function-vorticity system must, however, be solved iteratively for each time step using a Newton method. Direct solution of the linearized Newton systems is expensive, both in computational time and storage, and may not be justified for an unsteady simulation. That is why a generalized minimum residual (GRMES) method with an incomplete triangular factorization (ILU) preconditioning is used instead (Saad and Shultz, 1983).

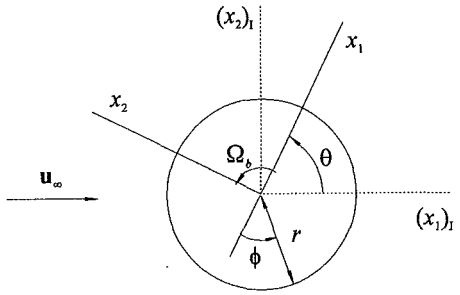

Fig. 3 Circular cylinder—combined translation and rotation motion

Numerical Results

To validate this solver, the flow around a circular cylinder was computed (Tchon, 1993). A combined translation and rotation motion (Fig. 3) was chosen for its computational closeness to the Darrieus motion and because ample experimental and numerical data is available. For such a motion, it is usual to consider a frame of reference translating with the cylinder and to impose a tangential velocity on the surface of the cylinder to simulate its rotation. However, this approach is valid only for a circular cylinder rotating about its center. To prove that a combined rotation and translation motion can be simulated for a non-axisymmetric body and any axis of rotation, a frame translating and rotating with the cylinder was considered instead. The motion was thus simulated by placing the cylinder at the center of the mesh, acting as the origin of the noninertial frame of reference and the axis of rotation, and imposing a constant rotational velocity Ω_b and a constant freestream velocity $\mathbf{u}_\infty$.

The two cases presented here consider a rotation to translation velocity ratio $\lambda = \Omega_b r/u_\infty$ of 0.5 and Reynolds numbers $\mathrm{Re}_\infty = 2u_\infty r/\nu$ of 200 and 500, respectively. The computational mesh was composed of a structured region of 900 quadrilateral elements around the cylinder, an unstructured region of 4606 triangular elements, and a layer of 20 infinite elements located at 20 radii from the cylinder center. The cylinder itself was covered by 180 quadrilateral elements with a constant thickness

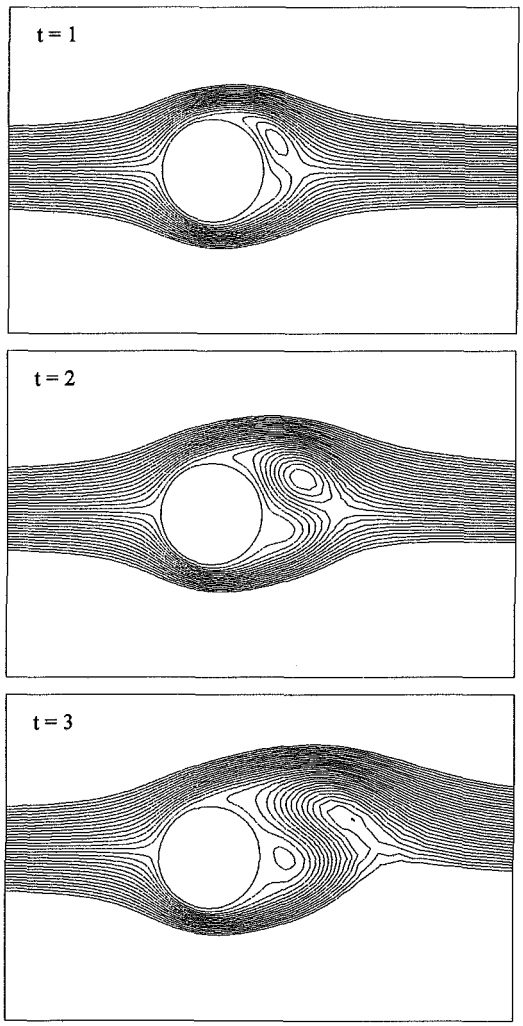

Fig. 4(*a*)

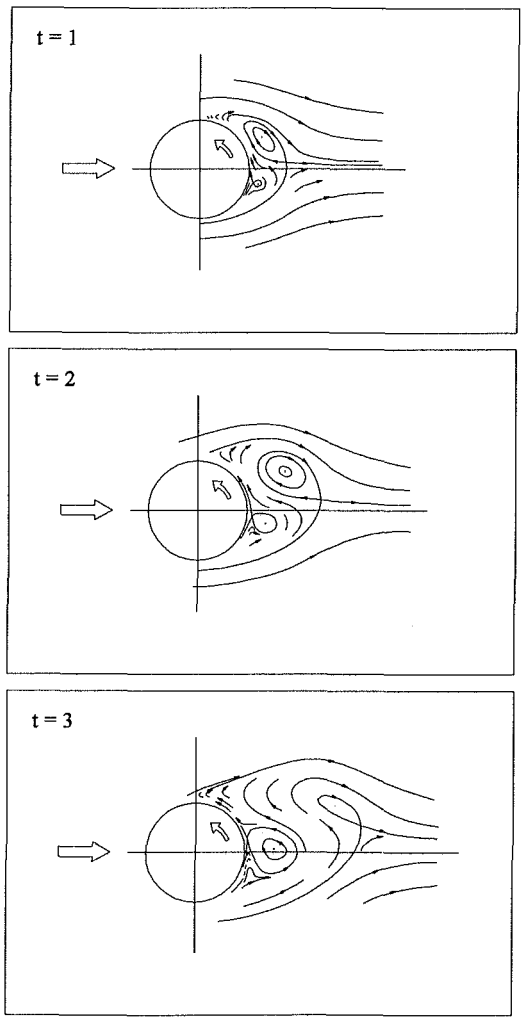

Fig. 4(*b*)

Fig. 4 Circular cylinder—streamlines for $\lambda = 0.5$ and $\mathrm{Re}_\infty = 200$: (*a*) computed; (*b*) experimental (Coutanceau and Ménard, 1985)

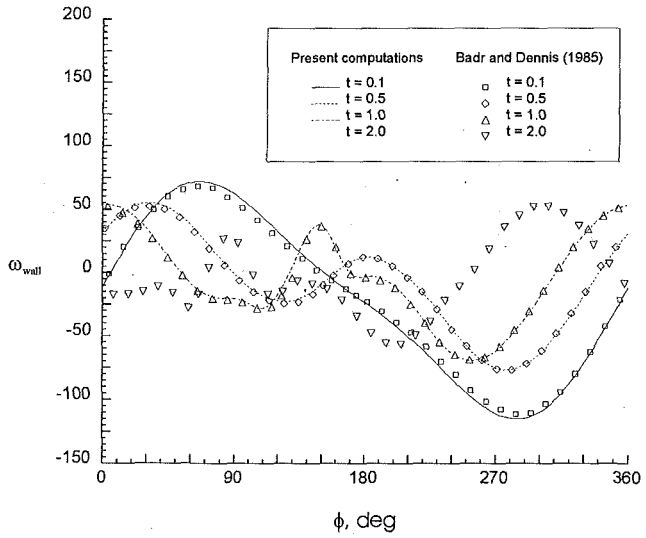

Fig. 5 Circular cylinder—surface vorticity distribution for $\lambda = 0.5$ and $Re_\infty = 500$

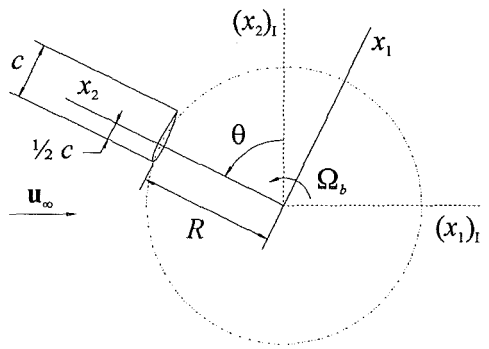

Fig. 6 NACA 0015 airfoil—Darrieus motion

of $0.0038r$. Starting from rest, the flow was computed up to a nondimensional time $u_\infty t/2r$ of 3.0, corresponding to a total rotation of 172 deg, with a time step varying from 0.0001 to 0.01. For $\lambda = 0.5$ and $Re_\infty = 200$, Fig. 4 shows that the experimental visualizations of Coutanceau and Ménard (1985) match the computed streamlines, defined as

$$\psi + \frac{1}{2}\Omega_b^2 \mathbf{x}^2 - \mathbf{e}_3 \times (\mathbf{u}_b - \mathbf{u}_\infty) \cdot \mathbf{x} = \psi_b \pm n0.025 \qquad (22)$$

where $n = 1$ to 15. For $\lambda = 0.5$ and $Re_\infty = 500$, Fig. 5 compares the computed surface vorticity distribution with numerical results from Badr and Dennis (1985). Note that these results were recalibrated to match the definition of ω and ϕ used in the present paper. The good agreement between the two sets of curves confirms the validity of the present method.

After this validation, the solver was used to simulate the flow around a NACA 0015 airfoil in Darrieus motion. This motion is a combined translation and rotation motion corresponding to the path of a Darrieus rotor blade cross section (Fig. 6), and it is characterized by the tip speed ratio $\Omega_b R/u_\infty$ and the chord to radius ratio c/R. Its simulation was achieved by simply decentering the airfoil by a distance R from the origin of the noninertial frame of reference, i.e., the center of the mesh, and imposing a constant rotational velocity Ω_b and a constant free stream velocity $\mathbf{u}_\infty$.

The simulation was performed for a blade Reynolds number $Re_b = \Omega_b Rc/\nu$ of 6700, a tip speed ratio of 2.5 and a chord to radius ratio of 0.25. The computational mesh was composed of a structured region of 3120 quadrilateral elements around

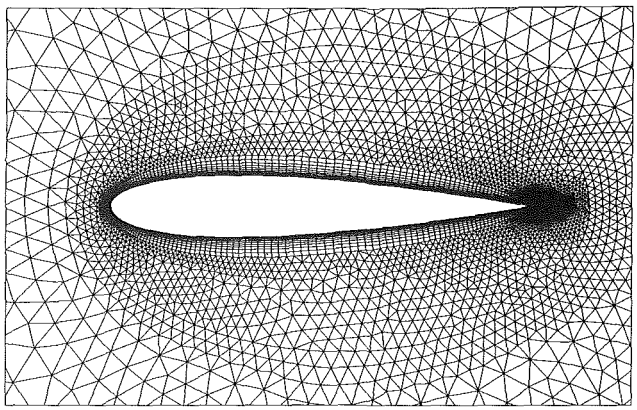

Fig. 7(a)

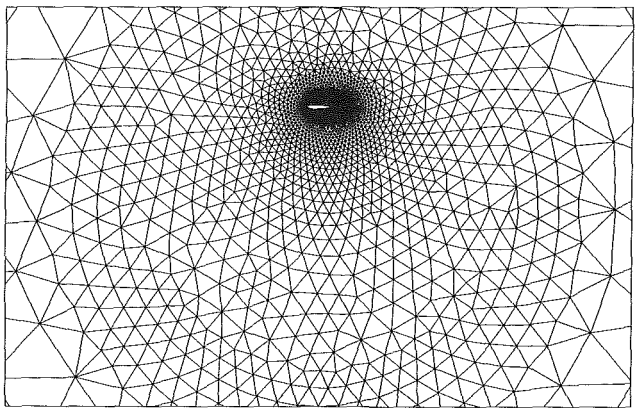

Fig. 7(b)

Fig. 7 NACA 0015 airfoil—computational mesh: (a) near field; (b) far field

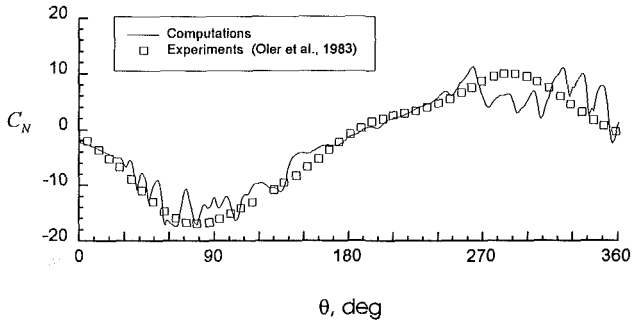

Fig. 8 NACA 0015 airfoil—normal force evolution

the airfoil, an unstructured region of 10308 triangular elements elsewhere and a layer of 20 infinite elements located at 80 chords from the mesh center (Fig. 7). The airfoil surface was covered by 260 elements of minimum thickness and length of $0.0002c$ and $0.0003c$ respectively. Starting from rest, the flow was computed up to a nondimensional time $u_\infty t/c$ of 10.08, corresponding to one complete rotation. The time step was fixed at 0.0014 to be able to follow the flow evolution correctly and a total of 7200 time steps was required. In Figs. 8 and 9, the computed normal force coefficient $C_N = 2\mathbf{F}_b \cdot \mathbf{e}_2/\rho_\infty u_\infty^2 c$ and tangential force coefficient $C_T = 2\mathbf{F}_b \cdot \mathbf{e}_1/\rho_\infty u_\infty^2 c$ are compared with experimental data from Oler et al. (1983). Note that $\mathbf{F}_b$ is the resultant force acting on the airfoil. It should be pointed out that the experiments were conducted at a blade Reynolds number of 67,000 while the computations were limited to 6700 in order to stay in laminar flow. The tangential force does not match the experimental data, but has at least

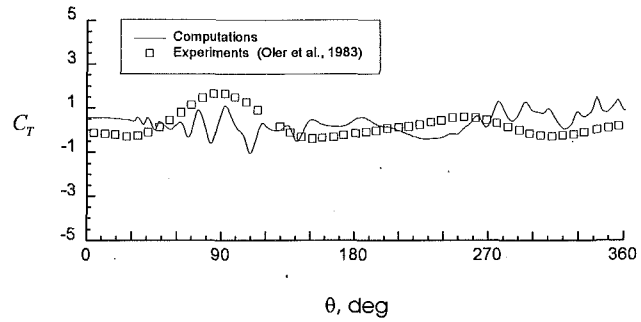

Fig. 9 NACA 0015 airfoil—tangential force evolution

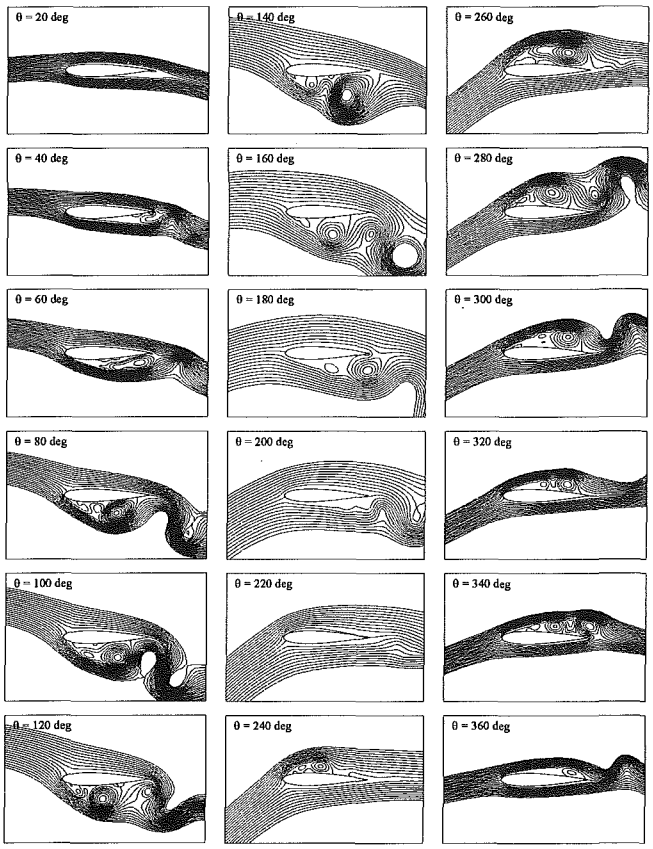

Fig. 10 NACA 0015 airfoil—computed streamlines

the same magnitude. On the other hand, the computed normal force seems to follow more or less the experimental measures. However, its evolution presents multiple peaks that do not appear in the experiments. Although the present simulation was limited to only one rotation, the main reason for this discrepancy is not the starting effects but rather the difference in Reynolds numbers and its consequences on the flow structure. To illustrate the computed flow structure, Fig. 10 presents the evolution of streamlines defined by

$$\psi + \frac{1}{3}\,\Omega_b^2\,\mathbf{x}^2 - \mathbf{e}_3 \times (\mathbf{u}_b - \mathbf{u}_\infty)\cdot\mathbf{x} = \psi_b \pm n0.05 \qquad (23)$$

where $n = 1$ to 10. During the first half of the rotation, dynamic stall occurs in the interval 25 deg $\leq \theta \leq$ 195 deg on the inner surface of the airfoil and, during the second half, it occurs in the interval 230 deg $\leq \theta \leq$ 360 deg on the outer surface. This dynamic stall generates multiple alternating leading edge and trailing edge vortices. These vortices are the cause of the peaks in the computed C_N and C_T curves. However, in the experiments of Oler et al. (1983), dynamic stall occurs in the interval 100 deg $\leq \theta \leq$ 140 deg on the inner surface and in the interval 265 deg $\leq \theta \leq$ 290 deg on the outer surface. Furthermore, only one vortex is shed during each half rotation. These differences between the computed and experimental flow structures result from the differences in Reynolds numbers. The experiments have been performed for a blade Reynolds number 10 times higher than the computational one and for which the turbulence effects are no longer negligible. Since turbulence tends to stabilize the boundary layer, dynamic stall occurs at higher effective angles of attack and corresponds to a smaller azimuthal region. Turbulence also tends to coalesce vorticity in one big blob explaining the observation of only one vortex for each half rotation during the experiments. Although a direct simulation at a blade Reynolds number of 67,000 instead of 6700 could be possible, it would require either an extremely fine mesh or an excessive use of artificial diffusion that would corrupt the results. For high Reynolds numbers, an adequate turbulence model has thus to be introduced in the solver.

However, before taking on this problem, the computational efficiency of the solver has to be improved. For the Darrieus motion, computations took indeed 3 minutes per time step, resulting in a total of 360 hours per rotation, on an IBM 3090 mainframe and were limited to only one rotation due to CPU time restrictions. This poor performance results from an inadequate vectorization of the present computational code which achieves only around 10 Mflops although the IBM 3090 vector processor is rated at a maximum of 80 Mflops. Vectorization is thus the key to this efficiency problem. However, good vectorization is generally more difficult to achieve on unstructured or hybrid meshes than on structured ones because of heavy use of indirect addressing. That is why structured meshes tend to exhibit faster CPU times per node but usually require much more mesh nodes. Thus any comparison with other solvers should by done not only on the same machine and for similar problems, i.e., moving airfoils, but also using the same type of mesh structure. In this perspective, the performance of the present solver, expressed in terms of CPU time per node per swept pitching or rotation angle, is effectively comparable to the performance of similar solvers on scalar workstations. This been said, the present code should nevertheless be optimized to take advantage of vector mainframes and reduce the total computing time per rotation to a more acceptable level on these machines.

Concluding Remarks

In the present study, the unsteady flow around an airfoil in Darrieus motion was simulated. To the authors' knowledge, such a simulation has not been previously attempted using the Navier–Stokes equations and it shows a promising approach to the study and prediction of dynamic stall on airfoils in Darrieus motion. However, the efficiency of the present solver should be improved to reduce the computational time per rotation to an acceptable level before taking on more complex problems, such as turbulent flows.

Acknowledgments

The present work was supported by Energy, Mines and Resources Canada under contract No. 23440-0-9457/01-SS.

References

Badr, H. M., and Dennis, S. R. C., 1985, "Time-dependent Viscous Flow Past an Impulsively Started Rotating and Translating Circular Cylinder," *Journal of Fluid Mechanics*, Vol. 158, pp. 447-488.

Carr, L. W., 1988, "Progress in Analysis and Prediction of Dynamic Stall," *Journal of Aircraft*, Vol. 25, No. 1, pp. 6-17.

Coutanceau, M., and Ménard, C., 1985, "Influence of Rotation on the Near-Wake Development Behind an Impulsively Started Circular Cylinder," *Journal of Fluid Mechanics*, Vol. 158, pp. 399-446.

Daube, O., Ta Phuoc, L., Dulieu, A., Coutanceau, M., Ohmi, K., and Textier, A., 1989, "Numerical Simulation and Hydrodynamic Visualization of Transient

Viscous Flow Around an Oscillating Aerofoil," *International Journal for Numerical Methods in Fluids*, Vol. 9, pp. 891–920.

Gunzburger, M. D., and Peterson, J. S., 1984, "On the Finite Element Approximation of the Streamfunction-Vorticity Equations," *Computer Methods for DPEs V*, IMACS Conference, pp. 47–56.

Gunzburger, M. D., and Peterson, J. S., 1988, "On Finite Element Approximations of the Streamfunction-Vorticity and Velocity-Vorticity Equations," *International Journal for Numerical Methods in Fluids*, Vol. 8, pp. 1229–1240.

McCroskey, W. J., 1977, "Some Current Research in Unsteady Fluid Dynamics—The 1976 Freeman Scholar Lecture," ASME JOURNAL OF FLUIDS ENGINEERING, Vol. 99, pp. 8–39.

Peeters, M. F., Habashi, W. G., and Dueck, E. G., 1987, "Finite Element Stream Function-Vorticity Solutions of the Incompressible Navier-Stokes Equations," *International Journal for Numerical Methods in Fluids*, Vol. 7, pp. 17–27.

Oler, J. W., Strickland, J. H., Im, B. J., and Graham, G. H., 1983, "Dynamic Stall Regulation of the Darrieus Turbine," SANDIA Report SAND83-7029.

Saad, Y., and Schultz, M., 1983, "GMRES: A Generalized Minimum Residual Algorithm for Solving Nonsymmetric Linear Systems," Research Report YALEU/DCS/RR-254.

Shida, Y., Kuwahara, K., Ono, K., and Takami, H., 1987, "Computation of Dynamic Stall of a NACA-0012 Airfoil," *AIAA Journal*, Vol. 25, No. 3, pp. 408–413.

Speziale, C. G., 1987, "On the Advantages of Vorticity-Velocity Formulation of the Equations of Fluid Dynamics," *Journal of Computational Physics*, Vol. 73, pp. 476–480.

Sugavanam, A. and Wu, J. C., 1982, "Numerical Study of Separated Turbulent Flow over Airfoils," *AIAA Journal*, Vol. 20, No. 4, pp. 464–470.

Tchon, K. F., 1989, "Flow Visualization Investigation of Dynamic Stall on a Pitching Airfoil," AIAA Paper 89-0842.

Tchon, K. F., 1993, "Simulation Numérique du Décrochage Dynamique Sur un Profil D'aile en Mouvement de Rotation," Ph.D. thesis, École Polytechnique de Montréal.

Tchon, K. F., and Paraschivoiu, I., 1990, "Finite Element Simulation of Unsteady Two-Dimensional Incompressible Viscous Flows," *Canadian Aeronautics and Space Journal*, Vol. 36, No. 4, pp. 236–246.

Tezduyar, T. E., Glowinsky, R., and Liou, J., 1988, "Petrov-Galerkin Methods on Multiple Connected Domains for the Vorticity-Stream Function Formulation of the Incompressible Navier–Stokes Equations," *International Journal for Numerical Methods in Fluids*, Vol. 8, pp. 1269–1290.

Tuncer, I. H., Wu, J. C., and Wang, C. M., 1990, "Theoretical and Numerical Studies of Oscillating Airfoils," *AIAA Journal*, Vol. 28, No. 9, pp. 1615–1624.

Van Dam, C. P., and Hafez, M., 1989, "Comparison of Iterative and Direct Solution Methods for Viscous Flow Problems," *AIAA Journal*, Vol. 27, No. 10, pp. 1459–1461.

Visbal, M. R., 1990, "Dynamic Stall of a Constant-Rate Pitching Airfoil," *Journal of Aircraft*, Vol. 27, No. 5, pp. 400–407.

Zienkiewicz, O. C., Emson, C., and Bettess, P., 1983, "A Novel Boundary Infinite Element," *International Journal for Numerical Methods in Engineering*, Vol. 19, pp. 393–404.

D. K. Ota
Member Technical Staff.

S. R. Chakravarthy
Manager, CFD Department.

Computational Fluid Dynamics Department,
Rockwell International Science Center,
1049 Camino Dos Rios,
Thousand Oaks, CA 91360

T. Becker

T. Sturzenegger

Rockwell Golde,
Frankfurt, Germany

Computational Study of Resonance Suppression of Open Sunroofs

A 2-D computational study of flow over a fully open sunroof of a car with a passenger compartment has been done on a scalar workstation. The critical velocity for resonance in the passenger compartment has been determined. A wind deflector angle study has been done to determine an adequate angle to suppress the resonance. A validation case of computing the resonance condition of the flow over a 3:1 depth to length rectangular cavity has also been done. These resonance studies show the potential of using scalar workstations for a CFD design study.

Introduction

Computational Fluid Dynamics (CFD) has been widely used in the aerospace community. As the cost of computing decreased with more efficient CFD codes and faster computers, the commercial community has been able to use CFD more and more. In the automotive sunroof design community, the scalar workstation environment is fairly common due to its lower cost compared with mainframes. For aeroacoustical analysis of the sunroofs, road tests are typically done, since the automotive car companies may not allow the sunroof companies into their proprietary wind tunnel tests. Since the workstation environment already exists at the sunroof companies, it would be of great interest to be able to do CFD on the workstations and get useful aeroacoustical information to assist in the design of the sunroofs.

The main goals of the current project are to see if CFD technology can be successfully transferred to the automotive sunroof community and help in the design of sunroofs. In a road test or a wind tunnel test, the main effect that the engineers are looking for is the "boom" phenomenon. The boom phenomenon is a low frequency resonance (10–50 Hz) of the passenger compartment with the sunroof fully open. It is assumed that the passenger compartment is behaving like a Helmholtz Resonator. This boom phenomenon usually occurs between 40–90 km/hr (11–25 m/s). Once this resonance condition is found, the engineers employ various techniques to suppress the resonance. The main technique is to place a wind deflector at the front of the sunroof opening. The road test or wind tunnel test is used to optimize the angle and the shape of the wind deflector. Once this is done, the aeroacoustical design of the sunroof is complete.

Contributed by the Fluids Engineering Division for publication in the JOURNAL OF FLUIDS ENGINEERING. Manuscript received by the Fluids Engineering Division April 3, 1993; revised manuscript received February 24, 1994. Associate Technical Editor: O. Baysal.

This project deals with the development of a CFD code optimized for scalar workstations. Because the computation of flow over an open sunroof will result in an acoustical oscillating signal, the computation is time-dependent. Time-dependent CFD computations can take a great deal of CPU-time to reach statistically steady answers. Because of the time constraint and the use of scalar workstations, the open sunroof computation will be limited to 2-D analysis.

In a 2-D analysis, any 3-D effects such as vortex spillage effects on the sides of the sunroof will be neglected. Also wind deflector parameters can only be wind defector length and angle. The edge shape or holes in the wind deflector cannot be modeled.

In this 2-D analysis, the ability of the CFD code to find the resonance condition (boom phenomenon) of a 2-D car passenger compartment with a fully open sunroof will be studied. Also the effect of varying wind deflector angles will be studied.

If this 2-D analysis technique is useful, this type of analysis may help automotive sunroof designers in understanding the noise mechanisms, correlating the noise directly to certain flow structures. Other higher velocity modes such as the higher frequency "whistling" mode of the tilted sunroof can also be studied. Other mechanisms such as ventilation can be studied for their suppression/augmentation effect on the acoustical environment within the passenger compartment.

Golde Code

The Golde Code (Ota, 1992) is an optimized scalar workstation code which has been developed from the USA-series code (Chakravarthy et al., 1988). This flow solver is a implicit multi-zonal structured grid solver for the 3-D Reynolds-averaged compressible Navier-Stokes equations. Steady-state and unsteady time dependent flows can be computed. This code can be up to third order accurate based on the total

variation diminishing (TVD) formulation for the convective terms within a finite-volume framework. The TVD option can be turned off for low Mach number flows. Several Riemann solvers are available for defining the fluxes at cell faces, Roe's approximate solver being the one most commonly used. One turbulence model is included which is an algebraic modified Baldwin-Lomax model incorporating Goldberg's treatment for separated flow regions. A law of the wall boundary condition option is available. The interval between cells to the turbulence model can be set by the user. The capability to solve inviscid or viscous perfect gas flows exists. The code permits flexible specification of point-wise boundary conditions, using either templates or user-coded subroutines. This is a full 3-D solver which can also be used for 2-D computations. For efficient 2-D computations, special 2-D subroutines have been added to speed up 2-D computations.

Scalar optimizations have been incorporated which help the speed of the code on scalar workstations. On a scalar workstation, faster code is created when the number of operations is reduced, therefore all metrics and derivatives are computed once and stored. Viscous terms are computed only if an estimate for the viscous term is larger than a user defined tolerance. The following additional options are used when running on a scalar workstation. A law of the wall boundary condition is utilized which allows for use of coarser grid near wall which allows the total number of grid points needed for a problem to be approximately half as much as a grid required for "solve to the wall" no-slip boundary conditions. The turbulence model is called every fifth time step instead of every time step.

A more detailed description of the code is not included since the main purpose is not to document the code itself but to describe a use of CFD in extreme conditions (relatively coarse grid/large time steps) where the results are still potentially useful in a design environment.

Frequency Estimates

Cavities or resonators are excited by the oscillations of the shear layer over its opening caused by vortex shedding. Resonance occurs when the vortex shedding frequency of the shear layer matches the acoustical frequency of the cavity or the resonator shape.

Vortex Shedding Frequency Estimates. There are many references for formulas for estimates of vortex shedding frequencies for shear layers. The following formula due to Franke and Carr (Blevins, 1990) is valid for turbulent boundary layers.

$$f_v=\frac{1}{3}\left(n-\frac{1}{4}\right)\frac{U_\infty}{L_N},\ n=1,\ 2,\ 3,\ \ldots \tag{3.1}$$

where U_∞ is the freestream velocity, L_N is the length of the opening of the cavity (sunroof opening), n is the shear wave mode number or the number of vortices present across the opening. The modes $n = 1$, 2, or 3 are commonly present in shear layers; higher modes $n > 3$ are not typically observed experimentally (Blevins, 1990).

Equation (3.1) is used to determine an estimate for vortex shedding frequency given a velocity or vice versa.

Deep Cavity Resonance Frequency Estimates. East (1966) did an experiment where he developed the following formula for the resonant frequency for a 3:1 depth to length ratio cavity.

$$f_a=0.18\,\frac{c}{H} \tag{3.2}$$

where c is the speed of sound, and H is the depth of the cavity.

Equation (3.2) is used to get an estimate for the resonance frequency which is then used in Eq. (3.1) ($f_v = f_a$) to get an estimate for the velocity range required to get resonance in a deep cavity.

Helmholtz Resonator Frequency Estimates. The passenger car interior with an open sunroof can be modeled as a Helmholtz resonator. Blevins (1984) has the following formula for the resonance frequency for a Helmholtz resonator.

$$f_a=\frac{c}{2\pi}\left[\frac{A}{1.21(V+AH_N)H_1}\right]^{1/2} \tag{3.3}$$

where

$$H_1=\left\{H_V+L_O+(H_N+L_O)\left[1+\frac{H_N+L_O}{2H}+\frac{A(H_N+L_O)}{2V}+\frac{A(H_N+L_O)}{3V}\,\frac{H_N+L_O}{H}\right]\right\}\times\frac{V}{V+A(H_N+L_O)}\,\frac{H}{H+H_N+L_O} \tag{3.4}$$

where c is the speed of sound of the fluid, A is the cross-sectional area of the neck, H_N is the height of the neck, V is the volume of the cavity without the neck, H is the height of the resonator cavity from the bottom to the neck, $L_O = 0.24r$ where r is the radius of the neck (if the neck is not circular, r is a characteristic radius), and H_V is the form factor where

$$H_V=\frac{A}{VH}\int_0^H\frac{x\left[\int_0^x A_V(\eta)\,d\eta\right]dx}{A_V(x)} \tag{3.5}$$

where x is the coordinate from the bottom of the resonator and $A_V(x)$ is the cross-sectional area of the cavity at each station x.

For the 2-D passenger compartment interior, only approximate "averaged" constant values for L, H, A, and A_V are used. This simplifies (3.5) to the following

$$H_V=\frac{AH^2}{3V} \tag{3.6}$$

with $V = LHW$ and $A = WL_N$ where L_N is the length of the cavity opening and L is the length of the cavity.

For the 2-D cavity and passenger car, the width of the geometry is assumed to be "large" (width set to $W = 10.0$ m). The characteristic radius used is

$$r=\frac{1}{2}\left[\frac{L_N}{2}+\frac{W}{2}\right] \tag{3.9}$$

Equation (3.3) is used to get an estimate for the resonance frequency which is then used in Eq. (3.1) ($f_v = f_a$) to get an estimate for the velocity range required to get resonance in a Helmholtz resonator.

3.1 Depth to Length Ratio Cavity

This case is chosen because East (1966) has done an experimental resonance study on deep cavities where he developed an empirical formula (Eq. (3.2)). The Golde code is used to computationally find resonance and to see how well the computational results, experimental measurements and empirical formula compare. Aeroacoustics of cavities for subsonic and supersonic flows have been extensively studied computationally (Venkatapathy et al., 1987; Dougherty, et al., 1990; Baysal and Stallings, 1988; Srinivasan and Baysal, 1991).

Problem Setup. The length of the cavity L_N is set to 0.4 meters. This is a typical opening of a fully open sunroof. The depth of the cavity H is set to 1.2 meters (3:1 ratio). Using Eq. (3.2), with $c = 343.8$ m/s, the resonance frequency for this cavity is $f_a = 51.6$ Hz. Using Eq. (3.1), the estimated velocity for this resonance is $U_\infty = 83.4$ m/s for the $n = 1$ mode; $U_\infty = 35.7$ m/s for the $n = 2$ mode. These two modes are chosen, since East (1966) observed that mainly the $n = 1$

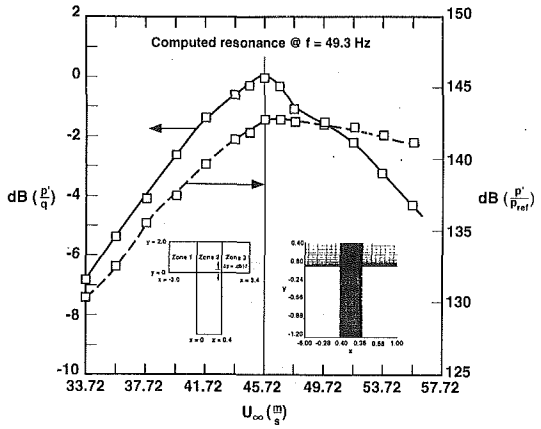

Fig. 1 Sound level based on p'/q versus U_∞ (left scale) Sound level based on p'/p_{ref} versus U_∞ (right scale). Layout of 3 zone grid also shown.

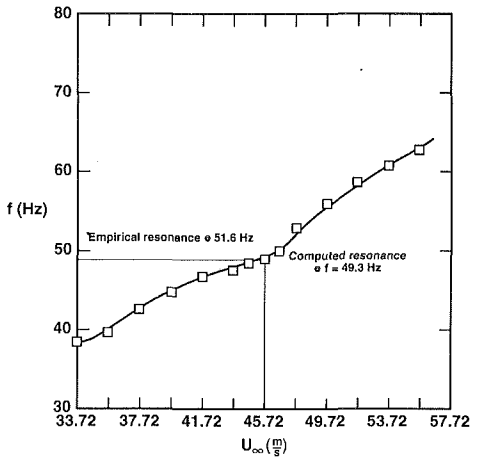

Fig. 2 Dominant frequency versus U_∞

and $n = 2$ modes are present. This indicates that the velocity associated with the resonance should be in the range U_∞ = 35–85 m/s.

Computational Setup. The computational grid for this problem has been set up as a 3 zone problem (zone1:40x30, zone2:40x69; zone3:40x30), as shown in Fig. 1. Viscous clustering for law of the wall boundary conditions is set by putting the first point off walls at Δy = 0.0017 m. No clustering in the streamwise direction is used. An arbitrary initial boundary layer thickness δ = 0.09 m was imposed at the inflow computation boundary. Pressure and temperature are set to Standard Atmospheric conditions.

Finding Resonance. To find resonance, a series of time-accurate computations must be done, changing freestream velocity U_∞. Each computation must be postprocessed for a decibel (dB) sound level based on p'/q, where

$$p' = \sqrt{\frac{1}{T}\int_t^{t+T} (p-\overline{p})^2 dt}$$

which is the root mean square pressure, $\overline{p}$ is the mean pressure and $q = 1/2\,\rho_\infty U_\infty^2$ which is the freestream dynamic pressure. A plot of dB based on p'/q versus velocity U_∞ will show a maximum value at resonance where $dB(p'/q) = 20\log_{10}(p'/q_{k,l})$. This measure of resonance is used by East (1966).

The freestream velocity range for resonance is estimated to be U_∞ = 35–85 m/s. The initial velocity chosen is U_∞ = 35.72 m/s. The next two runs were at U_∞ = 33.72 m/s and U_∞ = 37.72 m/s. The decibel levels were checked to verify that the slope of the curve is positive, meaning that the resonance peak would be at still higher velocities. If it were negative, then velocities less than 33.72 m/s would need to be computed. A total of twelve computations were done, with the velocities ranging from 33.72 m/s to 55.72 m/s at intervals of 2.0 m/s. A CFL number of 25.0 was used; each computation was run 25,000 steps. For frequencies of about 50 Hz, a CFL number of 25.0 will set a time step which will have about 500 time steps per period. For each run, decibel levels based on p' and p'/q were computed, along with the dominant frequencies computed from an FFT.

Figure 1 shows the plot of $dB(p'/q)$ versus U_∞. This plot shows that resonance occurs at U = 45.72 m/s which is in the initial range estimated by Eqs. (3.1) and (3.2). The data are calculated at the midpoint of the front face of the cavity. Figure 1 also shows the decibal level based on p' versus U_∞ where $dB(p'/p_{ref}) = 20\log_{10}(p'/p_{ref})$; $p_{ref} = 1.9738 \times 10^{-10}$ atm. This shows the decibel level in the range of 135–140, which is in the range of decibel level of subsonic cavities (Blevins, 1990). Figure 2 shows the plot of dominant frequency versus U_∞. This shows the resonance frequency is 49.3 Hz which is very close to the estimated value of 51.6 from Eq. (3.2).

Grid and CFL Number Study. For U_∞ = 33.72 m/s, a grid study and a CFL number study were done to check the numerical dependence of the pressure signals on these two parameters.

Two computations have been done to see the effect of the grid. The first grid is the grid used for this study which has 40 points normal to the cavity opening with the first point off the wall at .0017 m. The outer boundary for this grid is placed at 2 m from the cavity wall. The second grid used for the grid sensitivity check has 30 points normal to the cavity opening with the first point off the wall at .0022 m. The outer boundary for this grid is placed at 1.5 m from the cavity wall.

For the freestream velocity of U = 33.72 m/s and CFL = 25, computations on these two grids resulted in frequencies which differed by 2 Hz. This results in an error estimate of the frequencies of about 4 percent for a fixed CFL number.

The CFL number was varied from 2.5 to 25.0. All computed frequencies were within 10 percent of the estimated frequency (Eq. (3.1)) for the n = 2 mode. At the lower CFL numbers, the frequencies become very similar.

The dominant frequency can be seen to be much more convergent for CFL numbers less than 20. The dominant frequency may be slightly different at higher CFL numbers, however, it still stays in the range given by the frequency estimates.

Running the problem at the higher CFL numbers can introduce larger time errors (due to the first order accurate time algorithm and cross-factorization error) which can result in much different frequencies. For this case, it has been shown that the computed frequencies are not unreasonable for the chosen CFL.

To get the best turn-around-time for each case, the time-accurate runs must be run at a CFL number (Δt) which gives enough time steps per period of the dominant frequencies and a fine enough grid to resolve the shear layer flow over the open sunroof.

The computed pressure oscillations are hydrodynamic, directly being generated by the vortices being shed off the leading edge of the cavity. Once these pressure oscillations are generated, they are convected into the cavity. These pressure waves are of the order 0.0001 compared to a freestream pressure level of order 1.0. It is felt that the grid and time step studies give confidence that the pressure oscillations are acoustically correct.

It is felt that with the original grid density, and the chosen

CFL number that the computed frequencies are good enough for a design environment where getting the result in the shortest amount of time on a scalar workstation is very important.

Boundary Layer Thickness Study. Equation (3.1) is a fairly crude estimate of vortex shedding frequency since it does not include any parameters of the shear layer or incoming boundary layer. These are considered important in determining the vortex shedding frequency (Blevins, 1990). Blevins shows that as a boundary layer thickness is decreased, higher modes will be present (Blevins, 1990). Higher modes mean that higher vortex shedding frequencies will exist (refer to Eq. (3.1)).

At the resonance velocity, $U_\infty = 45.72$ m/s, two other boundary layer thickness were run, $\delta = 0.009$ m which is 10 times smaller, and $\delta = 0.0$ m (no incoming boundary layer). At the lowest velocity, $U_\infty = 33.72$ m/s, $\delta = 0.009$ m was run. Computationally the effect of higher frequencies with smaller boundary layer thickness is seen; $f = 49$ Hz for $\delta = 0.09$, $f = 70$ Hz for $\delta = 0.0$.

This explains why Eq. (3.1) gives only velocity estimates for the vortex shedding frequency. The constant in Eq. (3.1) is not really a constant but a function of boundary layer thickness, shear layer thickness, etc. For other formulas (with different constants) for vortex shedding frequency, the range of velocities for resonance is 35.7–49.6 m/s (Blevins, 1990). This range can partially be explained by the effect of boundary layer thickness. Computationally it is found that for the resonance frequency of 51.5 Hz, the resonance velocity is 34.0 m/s for $\delta = 0.009$ m/s, but 45.72 m/s for $\delta = 0.09$ m. This observation must be remembered when reviewing the differences between the estimated frequencies from Eq. (3.1) and the computations. However, it is highly desirable to provide the proper boundary layer thickness if possible.

The main conclusion is that computationally the same trend is seen as in experiments as boundary layer thickness is changed. This effect of boundary layer thickness along with the relative error introduced by using relatively coarse grid and large time steps means that "exact" frequencies may not be computed, but physically consistent frequencies are computed to see realistic trends for design.

Conclusion: Effectiveness for Resonance Analysis. The flow over the 3:1 depth to length ratio cavity has been computed for a range of velocities. Resonance was found to be very close to the empirical formula for resonance frequency. Twelve computations were necessary to plot out the resonance curve. Each computation was computed out to 25,000 steps, taking about two days real time on a dedicated scalar workstation. This computational setup includes compromises in grid resolution and CFL number selection. These compromises were shown to be acceptable since finer grid or smaller CFL will increase the time for each run. Frequency resolution so that about 500 time steps per period is obtained seems to give good results. This validation case shows that by using the Golde code, resonance frequency and velocity can be found computationally on a dedicated scalar workstation.

Passenger Car Interior

This case is chosen to see if the Golde code can computationally find resonance in a passenger car interior and demonstrate resonance suppression using a wind deflector.

Problem Setup. A 2-D centerline description of a passenger car is used for this problem. This includes hood angle, windshield, roofline, rear window, passenger compartment interior, and front seat. The car from which this geometry is derived has a corresponding road test for the "boom" phenomenon. The road test data will be used for comparison (Golde, 1991).

Using Eq. (3.3), with approximate values for the sunroof opening, $L_N = 0.4$ m; the depth of the passenger compartment, $H = 0.89$ m; the length of the passenger compartment, $L = 2.24$ m; and $c = 343.8$ m/s; the resonance frequency for this passenger compartment interior is $f_a = 24.6$ Hz. Using Eq. (3.1), the estimated velocity for this resonance is $U_\infty = 39.8$ m/s for the $n = 1$ mode; $U_\infty = 17.0$ m/s for the $n = 2$ mode. This indicates that the velocity associated with the resonance should be in the range $U_\infty = 17$–40 m/s.

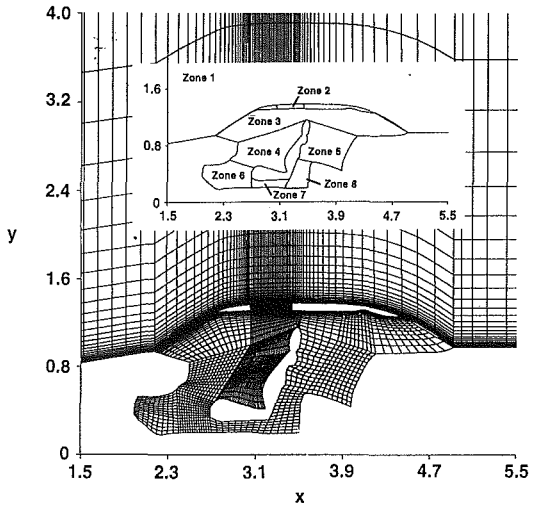

Fig. 3 8 zone grid for the passenger car interior

Computational Setup. The computational grid for this problem has been set up as a 8 zone problem (7715 total grid points) as shown in Fig. 3. Viscous clustering for law of the wall boundary conditions setting the first point off walls at $\Delta y = 0.001$ m. No clustering in the streamwise direction is used. An arbitrary initial boundary layer thickness $\delta = 0.0254$ m was imposed at the inflow computation boundary. Within the passenger compartment, inviscid flow type coarse grids are used. With this coarse grid resolution of the interior, it is hoped that the pressure waves will still generate a fairly realistic acoustic environment. Pressure and temperature are set to Standard Atmospheric conditions.

Finding Resonance. To find resonance, the same method for the cavity problem is used. The freestream velocity range for resonance is estimated to be $U_\infty = 17$–40 m/s. The initial velocity chosen is $U_\infty = 17.0$ m/s. The next two runs were at $U_\infty = 15.5$ m/s and $U_\infty = 18.5$ m/s. The decibel levels were checked to verify that the slope of the curve is positive, meaning that the resonance peak would be at still higher velocities. For this case, the slope was negative meaning that the resonance peak is less than $U_\infty = 17.0$ m/s. A total of six computations were done, with the velocities ranging from 11.0 m/s to 18.5 m/s at intervals of 1.5 m/s. A CFL number of 50.0 was used; each computation was run 25,000 steps. For frequencies of about 25 Hz, a CFL number of 50.0 will set a time step which will have about 500 time steps per period. This CFL criteria seemed to give good results for the cavity. For each run, decibel levels based on p'/p_{ref} and p'/q were computed, along with the dominant frequencies computed from a FFT.

Figure 4 shows the plot of p'/q versus U_∞. This plot shows that resonance occurs at $U = 14.0$ m/s, which is not much less than the low end velocity estimated by Eq. (3.1) and (3.2). The two lines show the resonance behavior of data measured at locations corresponding to a passenger's ear location if seated at the front and back seats. Figure 4 also shows the decibel level based on p'/p_{ref} versus U_∞. The road test had sound levels at resonance of about 115 dB (Golde, 1991) which is right in the range of the computed sound level. The two different measures of sound of Fig. 4 should be similar except for a shift proportional to the dynamic pressure. The discrep-

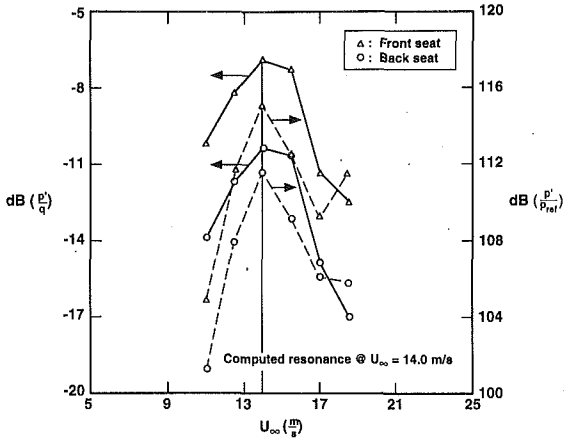

Fig. 4 Sound level based on p'/q versus U_∞ (left scale)
Sound level based on p'/p_{ref} versus U_∞ (right scale)

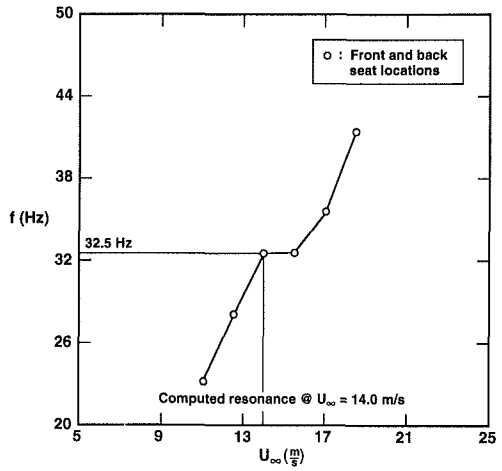

Fig. 5 Dominant frequency versus U_∞.

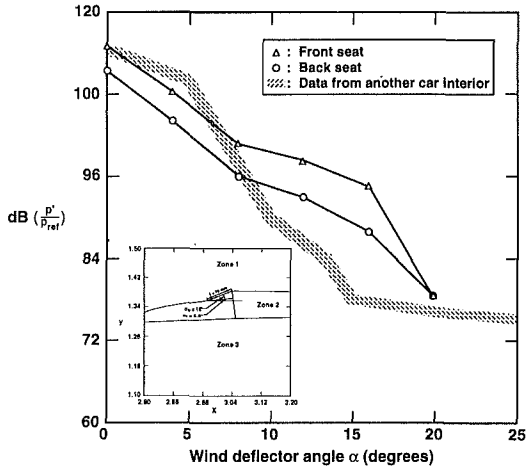

Fig. 6 Sound level based on p'/q versus wind deflector angle α_w.
Insert shows wind deflector geometry.

ancy seen at the higher velocities is showing that the computation is being pushed close to the limits of acceptable numerical accuracy. This discrepancy may be fixed by running the higher velocities (higher dominant frequencies) at lower CFL numbers to keep the time resolution of each frequency constant. Figure 5 shows the plot of dominant frequency versus U_∞. This shows that the resonance frequency is 32.5 Hz which is a little higher than the estimated value of 24.6 Hz from Eq. (3.2). The road test shows resonance at about 20–22 Hz (Golde, 1991).

Grid and CFL Number Study. Two computations have been done to see the effect of the grid using the law of the wall boundary condition. The first grid is the grid used for this study with 115 × 40 points with the first point off the wall at .0007 m. This grid (zone 1) encloses the passenger compartment. The outer boundary for this grid is placed at about 15 m for the passenger compartment. The second grid used for grid sensitivity check has 115 × 30 points with the first point off the wall at .0010 m. The outer boundary for this grid is placed at about 10 m from the passenger compartment. For the freestream velocity of U = 17.0 m/s and CFL = 50, results of both grids are very similar with the frequencies differing by 3 Hz. This results in an error estimate of the frequencies of about 9 percent for a fixed CFL number.

The different outer boundary locations did not significantly change the computed frequencies which means that the frequencies seen are not dominated by any numerical reflection off the outer boundaries.

For U_∞ = 17.0 m/s, a CFL number study was done to check the numerical dependence of the pressure signals on this parameter.

The CFL number was varied from 5.0 to 80.0. All computed frequencies were between the estimated frequencies (Eq. (3.1)) for the n = 2 and the n = 3 modes. At the lower and higher CFL numbers, the frequencies become very similar (close to the n = 2 mode).

This shows again that to guarantee accurate frequencies, low CFL numbers should be used, however, again it can be seen that at the higher CFL numbers, the computed frequencies are not unreasonable.

As with the computation of flow over the cavity, it is felt that the current compromises with grid resolution and CFL number to get reasonable turn-around-time per case on a scalar workstation for a design environment do not degrade the computational results severely.

Wind Deflector Angle Study: Resonance Suppression. There are many methods for suppressing the resonance ("boom") of a passenger compartment. The automotive sunroof industry and the aerospace bomb bay acoustic environment groups have devised techniques such as deflectors at the front of the opening, ramps at the back of the opening, and venting air into the passenger compartment (Rockwell, 1978). For this study, the effect of wind deflector ramp angle will be studied.

The wind deflector length is arbitrarily set to 70 mm. The insert of Fig. 6 shows the wind deflector at an angle of 16 deg to the roof angle (total angle = 21.8 deg). The roof angle is 5.8 deg.

Six wind deflector angle cases were run from 0–20 deg in intervals of 4 deg. Each case was run for 25,000 steps and run at a CFL number equal to 50. These results are plotted in Fig. 6. The suppression of the resonance is seen very clearly as the sound level in the front and back seat both are reduced by −25 dB with the wind deflector angle equal to 16 deg. To show that the overall trend is correct, a shaded hashed region shows the data from a wind tunnel test of a different car (Porsche, 1992).

Conclusion: Effectiveness for Resonance Analysis. The flow over a 2-D passenger car interior has been computed for a range of velocities. Resonance was found to be reasonably close to the empirical formula for resonance frequency. Six computations were necessary to plot out the resonance curve. Each computation was computed out to 25,000 steps, taking about 3 days real time on a dedicated scalar workstation. This computational setup includes compromises in grid resolution

and CFL number selection. These compromises were shown to be acceptable since finer grid or smaller CFL will increase the time for each run. A wind deflector study was also done. This demonstrated that the resonance can be suppressed with a large enough wind deflector angle. This validation case shows that by using the Golde code, resonance frequency and velocity can be found computationally on a dedicated scalar workstation. Also optimum wind deflector angle to suppress resonance and decrease the sound level in the passenger compartment can also be found computationally.

Conclusion

The Golde code has been used for computing flow over a 3:1 depth to length ratio cavity and a 2-D passenger compartment interior. Both cases compared well against available empirical formulas and experimental data. These projects have all been done on a dedicated scalar workstation. These time-accurate computations need about 2–3 days per case. For the 2-D passenger compartment, the resonance and wind deflector angle studies took about 1 month. Faster scalar workstations are always being developed which means the same resonance and wind deflector studies would be done that much faster. The Golde code shows much promise in helping the automotive sunroof engineer using dedicated scalar workstations to understand more about the resonance and the suppression of the resonance in passenger car interiors with fully open sunroofs.

The 2-D passenger car interior which was computationally tested did not have a complete experimental data set available. Much experimental data is automobile manufacturer proprietary and not readily available for the sunroof design engineers. It is hoped that a complete wind tunnel test for a passenger car with a fully opened sunroof with a resonance and wind deflector study can be made available for the next test of this computationally capability. It would be a much more complete validation of this promising capability.

References

Baysal, O., and Stallings, Jr., R. L., 1988, "Computational and Experimental Investigation of Cavity Flowfields," *AIAA Journal*, Vol. 26, No. 1, pp. 6–7.

Blevins, R. D., 1984, *Formulas for Natural Frequency and Mode Shape*, Van Nostrand Reinhold, New York. Reprinted by Krieger, Malabar, FL.

Blevins, R. D., 1990, *Flow-Induced Vibration*, Van Nostrand Reinhold, New York.

Chakravarthy, S. R., and Szema, K.-Y., 1988, "Unified 'Nose-to-Tail' Computational Method for Hypersonic Vehicle Applications," AIAA Paper 88-2564.

Dougherty, N. S., Holt, J. B., Nesman, T. E., and Farr, R. A., 1990, "Time-Accurate Navier-Stokes Computations of Self-Excited Two-Dimensional Unsteady Cavity Flows," AIAA Paper No. 90-0691.

East, L. F., 1990, "Aerodynamically Induced Resonance in Rectangular Cavities," *Journal of Sound and Vibration*, Vol. 3, No. 3, pp. 277–287.

Golde, 1991, Rockwell Golde Internal Report V77 3024.0, "Twinflex Windabweiser, Wummern bei verschiedenen WAW—Blattlangen im Opel Corsa," Oct. 30.

Ota, D. K., 1992, "Rockwell Golde Code On-line User Manual," *Version 92.8*, Aug.

Porsche, 1992, Porsche Internal Report 975/75-564, "Schiebedachuntersuchungen an einem Porsche-Prototypen," May 27.

Rockwell, D., 1978, "Review-Self-Sustaining Oscillations of Flow Past Cavities," ASME JOURNAL OF FLUIDS ENGINEERING, Vol. 100, June, pp. 152–164.

Srinivasan, S., and Baysal, O., 1991, "Navier-Stokes Calculations of Transonic Flows Past Cavities," ASME JOURNAL OF FLUIDS ENGINEERING, Vol. 113, No. 3, pp. 368–376.

Venkatapathy, E., Lombard, C. K., and Nagaraj, N., 1987, "Numerical Simulation of Compressible Flow Around Complex Two-Dimensional Cavities," AIAA Paper No. 87-0116.

Journal of Fluids Engineering

Technical Briefs

Assessment of the Martin-Hou Equation for Modeling a Nonclassical Fluid

G. Emanuel[1]

Nomenclature

A, B = Clausius-II functions
b, k, A_i, B_i, C_i = Martin-Hou constants
f_i = Martin-Hou temperature functions
p = pressure
T = temperature
v = specific volume
Z_c = critical compressibility

Subscripts and Superscript

c = critical point
f = liquid side of the coexistence curve
g = vapor side of the coexistence curve
r = reduced variable
$*$ = experimental equilibrium vapor pressure

Introduction

A nonclassical fluid exhibits retrograde behavior, see Thompson et al. (1986), or negative nonlinearity, see Cramer (1991). Both aspects, which are not mutually exclusive, occur in the vicinity of the vapor side of the coexistence curve for a gas consisting of large molecules, such as the Freons. A van der Waals equation of state is often used to model nonclassical behavior when simple, qualitative trends are desired. For accurate results, the Martin-Hou equation is used, see Martin and Hou (1955), Martin et al. (1959), Martin (1967), and Burnside (1973). This equation requires a relatively large number of constants and the use of a computer. Accurate nonclassical results, however, require a self-consistent thermodynamic model, especially in the vicinity of the vapor side of the coexistence curve. This note shows that the Martin-Hou equation does not necessarily fulfill this expectation. For purposes of clarity, several other state equations are also discussed.

Discussion

In reduced variable form, the van der Waals equation is

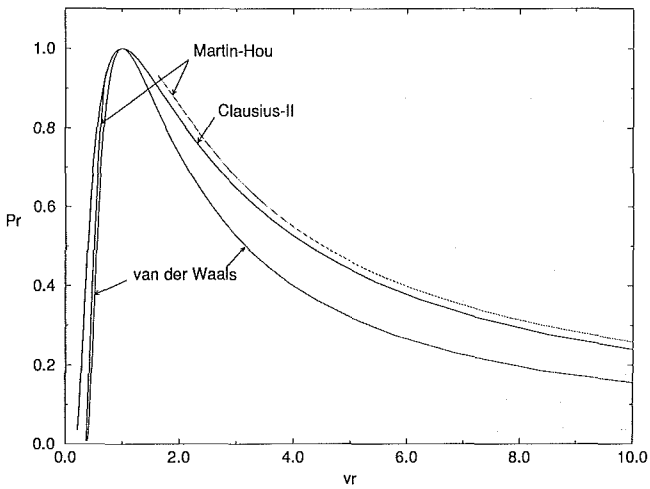

Fig. 1 The coexistence curve according to van der Waals, Clausius-II, and the Martin-Hou-I equations of state

$$p_r = \frac{8T_r}{3v_r - 1} - \frac{3}{v_r^2}$$

and this relation requires no empirical constants. The Martin-Hou equation can be written as

$$p = \sum_{i=1}^{5} \frac{f_i(T)}{(v-b)^i} \tag{1a}$$

$$f_i = A_i + B_i T + C_i e^{-kT_r} \tag{1b}$$

where $A_1 = C_1 = 0$ and B_1 is the gas constant. The constants in these equations can be evaluated by the procedure in Martin and Hou (1955), or by a least square fit to data, as is done by Mears et al. (1969) for sulphur hexafluoride (SF_6).

Figure 1 is a conventional p_r, v_r plot, where the Martin-Hou curve is for SF_6 (Mears et al., 1969). Also shown is a Clausius-II curve (Emanuel, 1987), given by

$$p_r = \frac{4T_r}{A} - \frac{3}{T_r B^2}$$

where

$$A = 1 + 4Z_c(v_r - 1),\ B = 1 + \frac{8}{3} Z_c(v_r - 1)$$

and the one free parameter, Z_c, equals 0.286 for SF_6. (The Clausius-II equation is a special case of the Martin-Hou equation.) The figure illustrates the generally accepted view that van der Waals equation is not accurate on the vapor side. Agreement between the Clausius-II and Martin-Hou equations is better. As evident in the following discussion, however, this agreement may be fortuitous.

The Mears et al. paper provides extensive SF_6 experimental vapor pressure data. Their curve fit to this data is denoted as

[1]Professor, School of Aerospace and Mechanical Engineering, University of Oklahoma, Norman, OK 73019.

Contributed by the Fluids Engineering, Division of The American Society of Mechanical Engineers. Manuscript received by the Fluids Engineering Division December 11, 1993; revised manuscript received May 10, 1994. Associate Technical Editor: D. P. Telionis.

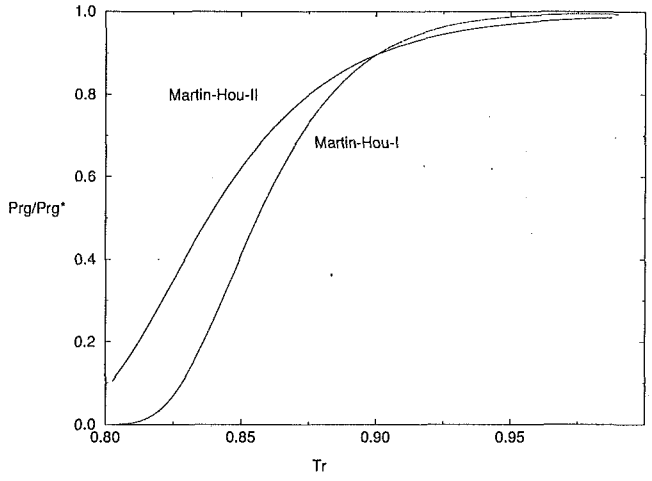

Fig. 2 Vapor pressure comparison for two Martin-Hou equations, where p^*_{rg} is based on experimental data for SF_6

$p^*_{rg}(T_r)$. They separately use p-v-T data for their least-square Martin-Hou equation, hereafter denoted with a I. These data include the critical point along with one other vapor pressure point, which is located near the critical point. Thus, the overwhelming bulk of the vapor pressure data is not used for evaluating the constants in Eqs. (1).

We next assess the consistency of the vapor pressure curve with the Martin-Hou-I equation. The vapor pressure can, most easily, be determined from a thermal state equation using the Maxwell construction

$$\int_{v_f}^{v_g} v\left(\frac{\partial p}{\partial v}\right) dv = 0$$

along a $T_r \leq 1$ isotherm. For Eqs. (1), this yields

$$\left\{B_1 T\left[\ln(v-b) - \frac{b}{v-b}\right] - \sum_{i=2}^{5} \frac{f_i(T)}{i-1}\frac{iv-b}{(v-b)^i}\right\}_g = \left\{B_1 T\left[\ln(v-b) - \frac{b}{v-b}\right] - \sum_{i=2}^{5} \frac{f_i(T)}{i-1}\frac{iv-b}{(v-b)^i}\right\}_f \quad (2)$$

which is equivalent to the usual chemical potential condition.

Equations (1) and (2) provide the Martin-Hou vapor pressure, denoted as p_{rg} (where $p_{rf} = p_{rg}$). A Martin-Hou-I comparison with p^*_{rg} is shown in Fig. 2. Also shown is a similarly determined curve, labeled Martin-Hou-II, which is based on the Martin and Hou (1955) procedure, and where the coefficients for SF_6 were graciously supplied by Prof. Cramer. This later comparison deviates significantly from unity when T_r is below about 0.95. The first comparison starts to deviate from unity at a slightly lower temperature. In both cases, the accuracy of the Martin-Hou equations is poor below $T_r = 0.9$.

The Martin-Hou equation is not expected to be very accurate at specific volumes below about $0.7v_c$, e.g., see Burnside (1973). Liquid side accuracy, however, is not the issue. The use of a separate equation for the vapor pressure that is not consistent with the thermal equation of state, as is found in Mears (1969) and Burnside (1973), can result in significant discontinuities in various thermodynamic properties at the coexistence curve. This approach is particularly inappropriate for the modeling of nonclassical fluid behavior. Although the discussion focusses on SF_6, it is not limited to just this vapor.

Acknowledgments

I would like to thank Prof. M. S. Cramer for his helpful comments. The calculations were ably performed by K. K. Leung and A. J. Haridas.

References

Burnside, B. M., 1973, "Thermodynamic Properties of Five Halogenated Hydrocarbon Vapour Power Cycle Working Fluids," *Journal of Mechanical Engineering and Science*, Vol. 15, pp. 132–143.

Cramer, M. S., 1991, "Nonclassical Dynamics of Classical Gases," *Nonlinear Waves in Real Fluids*, A. Kluwick, ed., Springer-Verlag.

Emanuel, G., 1987, *Advanced Classical Thermodynamics*, AIAA Education Series, p. 154.

Martin, J. J., and Hou, Y.-C., 1955, "Development of an Equation of State for Gases," *AIChE Journal*, Vol. 1, pp. 142–151.

Martin, J. J., Kapoor, R. M., and De Nevers, N., 1959, "An Improved Equation of State for Gases," *AIChE Journal*, Vol. 5, pp. 159–160.

Martin, J. J., 1967, "Equations of State," *Industrial and Engineering Chemistry*, Vol. 59, pp. 34–52.

Mears, W. H., Rosenthal, E., and Sinka, J. V., 1969, "Physical Properties and Virial Coefficients of Sulfur Hexafluoride," *Journal Physical Chemistry*, Vol. 73, pp. 2254–2261.

Thompson, P. A., Carofano, G. C., and Kim, Y.-G., 1986, "Shock Waves and Phase Changes in a Large-Heat-Capacity Fluid Emerging from a Tube," *Journal of Fluid Mechanics*, Vol. 166, pp. 57–92.

Journal of Fluids Engineering

Discussion

Characteristics of Swirling Flows in a Circular Pipe[1]

M. Padmanabhan[2]. The experiments conducted by the authors are for relatively high initial swirl intensities. So, ranging from 0.58 to 1.12, and the authors show the swirl decay rate to be independent of the swirl intensity and Reynolds number, Re, for the test Re range of 60,000 to 125,000. However, previous experiments, Padmanabhan and Janik (1980), conducted in a 254 mm pipe with water, for lower So values of 0.07 to 0.35 and Re range of 100,000 to 250,000, indicated the swirl decay rate to be a function of initial swirl intensity So and Re. Do the authors have any explanation of likely reasons for this difference? Are there any compressibility effects in the author's tests using air?

A more common expression for swirl decay, as given by Baker and Sayer (1974) and Padmanabhan and Janik (1980), is given by

$$\frac{K}{Ko} = e\left(\frac{-\beta x}{D}\right)$$

where K and Ko denote the angular momentum fluxes at $X=x$ and at $X=0$, respectively, X being the distance along the pipe of diameter D, and β is a swirl parameter. It will be interesting to see a plot of β against So and Re using the authors data for comparison with the corresponding information at lower So values given by Padmanabhan and Janik (1980) and Baker and Sayer (1974).

Additional References

Baker, D. W., and Sayer, C. L., 1974, "Decay of Swirling Turbulent Flow of Incompressible Fluids in Long Pipes," *Flow-Its Measurement and Control in Science and Industry*, Instrument Society of America, Vol. 1, pp. 301–312.

Padmanabhan, M., and Janik, C. R., 1980, "Swirling Flow and Its Effect on Wall Pressure Drop within Pipes," *Symposium on Vortex Flows*, ASME Winter Annual Meeting, Chicago, IL, pp. 65–75.

Authors' Closure

I have read with interest the recent discussion written by Dr. Padmanabhan. In our paper, the following swirl number is defined to express swirl intensity of swirling flow.

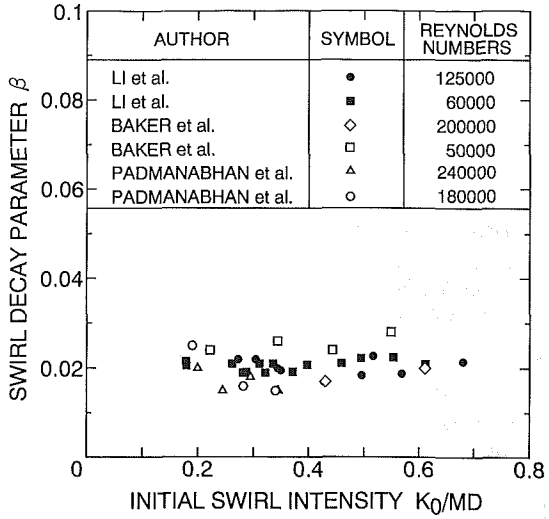

Fig. 1 Dependence of the swirl decay parameter on initial swirl intensity and Reynolds number

$$S = \frac{2\pi\rho \int_0^R uwr^2\,dr}{R2\pi\rho \int_0^R u^2 r\,dr} \tag{1}$$

Baker et al. and Padmanabhan et al. have used the following expression to definite swirl decay, given by

$$\frac{K}{K_0} = \exp\left(-\frac{\beta x}{D}\right) \tag{2}$$

Where $K = 2\pi\rho \int_0^R uwr^2\,dr$ and K_0 is the angular momentum fluxes at $X=x$ and at $X=0$, respectively, β is the swirl decay parameter, axial momentum is expressed as $M = (\pi\rho U_m D^2)/4$. The swirl intensity accounts for the product K/MD.

In Fig. 1 the variation of β against K_0/MD and R_e, which are evaluated using our experimental data by expression (2), is presented. It is found that the swirl decay rate is independent of initial swirl intensity and Reynolds number for K_0/MD greater than 0.18 ($S_0 = 0.36$) with R_e range of 60,000 to 125,000. The data from Baker et al. and Padmanabhan et al. with various K_0/MD and R_e are also compared with our results in Fig. 1, and the agreement is satisfactory.

Until now the relations of β, K_0/MD and R_e are not very clear. In our experimental range, it can be concluded that for fully developed turbulence swirl flow with middle and high initial swirl intensity, the swirl decay rate is only a function of x/D. According to the experimental results from Baker et al. and Padmanabhan et al., the swirl decay rate can be expressed as a function of initial swirl intensity and Reynolds number for low Reynolds number and weak initial swirl flow. These conclusions are valid whether for water or air.

[1]By Hui Li and Yuji Tomita, Technical Brief published in the June 1994 issue of the JOURNAL OF FLUIDS ENGINEERING, Vol. 116, pp. 370–373.

[2]Vice President, Alden Research Laboratory, Inc., 30 Shrewsbury Street, Holden, MA 01520.